Bio-MEMS

Technologies and Applications

EDITED BY

Wanjun Wang • Steven A. Soper

CRC Press
Taylor & Francis Group
Boca Raton London New York

CRC Press is an imprint of the
Taylor & Francis Group, an informa business

CRC Press
Taylor & Francis Group
6000 Broken Sound Parkway NW, Suite 300
Boca Raton, FL 33487-2742

Printed in the United States of America on acid-free paper
10 9 8 7 6 5 4 3 2 1

International Standard Book Number-10: 0-8493-3532-9 (Hardcover)
International Standard Book Number-13: 978-0-8493-3532-7 (Hardcover)

Library of Congress Cataloging-in-Publication Data

BioMEMS : technologies and applications / edited by Wanjun Wang and Steven A. Soper.
p. cm.
Includes bibliographical references and index.
ISBN 0-8493-3532-9 (alk. paper)
1. BioMEMS. I. Wang, Wanjun, 1958- II. Soper, Steven A.

TP248.25.B54B56 2006
660.6--dc22 2006045665

Visit the Taylor & Francis Web site at
http://www.taylorandfrancis.com

and the CRC Press Web site at
http://www.crcpress.com

Table of Contents

Preface

Applications of microelectromechanical systems (MEMS) and microfabrication have spread to different fields of engineering and science in recent years. Perhaps the most exciting development in the application of MEMS technology has occurred in the biological and biomedical areas. In addition to key fluidic components, such as microvalves, pumps, and all kinds of novel sensors that can be used for biological and biomedical analysis and measurements, many other types of so-called micro total analysis systems (TAS) have been developed. The advantages of such systems are that microvolumes of biological or biomedical samples can be delivered and processed for testing and analysis in an integrated fashion, thereby dramatically reducing the required human involvement in many steps of sample handling and processing. This helps to reduce the overall cost of measurement and time, while improving the sensitivity in most cases.

Many books have been published on these subjects in recent years, but most of them have focused primarily on various fabrication technologies with a few application areas highlighted. Unfortunately, in this burgeoning area, only a couple of books have been directed specifically toward biomedical MEMS. As MEMS applications spread to all corners of science and engineering, more and more universities and colleges are offering courses in the bio-MEMS area. In comparison with other MEMS areas, which typically involve different engineering disciplines, such as the mechanical, electrical, and optical fields, the development of bio-MEMS devices and systems involves a truly interdisciplinary integration of basic sciences, medical sciences, and engineering. This is the primary reason bio-MEMS is still in the earliest stages of development in comparison with electrical and mechanical sensing devices and systems. Due to the complexity and interdisciplinary nature of bio-MEMS, it is critical to include a diverse range of expertise in the composition of a book that attempts to cover the bio-MEMS area from both a fabrication and application point of view. This is the reason we have assembled a large group of leading researchers actively working in basic science, engineering, and biomedical areas to contribute to this book. *Bio-MEMS: Technologies and Applications* is divided into three sections:

1. Basic Bio-MEMS Fabrication Technologies
2. Microfluidic Devices and Components for Bio-MEMS
3. Sensing Technologies and Bio-MEMS Applications

The book targets audiences in the basic sciences and engineering, both industrial engineers and academic researchers. Efforts have been made to ensure

that while enough topics on the cutting edge of bio-MEMS research are covered, the book is still easy to read. In addition to structurally organizing the book from basic materials to advanced topics, we have made sure that each chapter and subject area are covered beginning with basic principles and fundamentals. Because of the shortage of suitable textbooks in this area, this collection is designed to be reasonable for graduate education as well as working application engineers who are interested in getting into this exciting new field.

About the Editors

Wanjun Wang received his B.S. in mechanical engineering from Xian Jiaotong University of China in 1982. He received his M.S. and Ph.D. degrees in mechanical engineering from the University of Texas at Austin in 1986 and 1989, respectively. He joined the faculty of the mechanical engineering department of Louisiana State University, Baton Rouge, in 1994 and has been teaching and doing research in microfabrication and MEMS for more than 13 years. His main research specialty has been in UV-LIGA microfabrication technology, especially in the UV lithography of ultra-thick SU-8 resist and applications in microfluidics, micro-optics, and micro-sensors/actuators. In the last 10 years, he has received research funding in MEMS and microfabrication from many state and federal agencies, such as the National Science Foundation, the National Institutes of Health, and the Board of Regents of Louisiana. Dr. Wang has authored or co-authored more than seventy papers in technical journals and proceedings of conferences. Dr. Wang has also received five patents for sensors and actuators, as well as for microfluidic and micro-optic components. He has also taught courses in the areas of sensors and actuators, instrumentations, MEMS and microfabrication technologies for many years. He is currently a senior member of IEEE, and a member of ASME and SPIE.

Prof. Steven A. Soper received his Ph.D. in bioanalytical chemistry from the University of Kansas (KU) in 1989. While at KU, he received several awards, such as the Huguchi Distinguished Doctoral Candidate Award and the American Chemical Society Award for research in analytical chemistry (sponsored by the Pittsburgh Conference). Following graduation, Dr. Soper accepted a postdoctoral fellowship at Los Alamos National Laboratory, where he worked on single molecule detection methods for the high-speed sequencing of the human genome. As a result of this work, he received an R&D 100 award in 1991.

Dr. Soper joined the faculty at Louisiana State University (LSU) in the fall of 1991 as an assistant professor. He was promoted to associate professor in 1997 and to full professor in 2000. In 2002, Steven received a chaired professorship in chemistry at LSU (William L. & Patricia Senn, Jr. Chair). His research interests include micro- and nanofabrication of integrated systems for biomedicine, chemical modification of thermoplastic materials, ultra-sensitive fluorescence spectroscopy (time-resolved and steady-state), high-resolution electrophoresis, sample preparation methods for clinical analyses, and microfluidics. As a result of his efforts, he has secured extramural funding from such agencies as the National Institutes of Health,

Whitaker Foundation, American Chemical Society, Department of Energy, and the National Science Foundation. Steven has published over 160 manuscripts in various research publications and is the author of three patents. In addition, Steven has given approximately 165 technical presentations at national/international meetings and universities since 1995. Steven is now the director of a major multi-disciplinary research center at LSU, which is funded through the NSF.

Prof. Soper has received several awards for his research accomplishments while at LSU, including the Outstanding Untenured Researcher (Physical Sciences, Louisiana State University, 1995) presented by Phi Kappa Phi; Outstanding Researcher in the College of Basic Sciences (Louisiana State University, 1996); and Outstanding Science/Engineering Research in the state of Louisiana (2001). In 2006, Dr. Soper was awarded the Benedetti-Pichler Award in Microchemistry.

Prof. Soper is also involved in various national activities, such as serving on review panels for the National Institutes of Health, the Department of Energy, and the National Science Foundation. In addition, he serves on the advisory board for several technical journals including *Analytical Chemistry* (A-page editorial board), *Journal of Fluorescence*, and *The Analyst*.

Contributors

Gang Chen Department of Chemistry, Fudan University, Shanghai, China

Wendy D. Dominick Rieveschl Laboratories for Mass Spectrometry, Department of Chemistry, University of Cincinnati, Cincinnati, Ohio, U.S.A.

Celeste Frankenfeld Department of Pharmaceutical Chemistry, The University of Kansas, Lawrence, Kansas, U.S.A.

Carlos D. García Department of Chemistry, The University of Texas at San Antonio, San Antonio, Texas, U.S.A.

Jost Goettert The J. Bennett Johnston, Sr. Center for Advanced Microstructures and Devices, Louisiana State University, Baton Rouge, Louisiana, U.S.A.

Charles S. Henry Department of Chemistry, Colorado State University, Fort Collins, Colorado, U.S.A.

Mateusz L. Hupert Department of Chemistry, Louisiana State University, Baton Rouge, Louisiana, U.S.A.

Lianji Jin Rieveschl Laboratories for Mass Spectrometry, Department of Chemistry, University of Cincinnati, Cincinnati, Ohio, U.S.A.

Ryan T. Kelly Environmental Molecular Sciences Laboratory, Pacific Northwest National Laboratory, Richland, Washington, U.S.A.

Kabseog Kim HT MicroAnalytical, Inc., Albuquerque, New Mexico, U.S.A.

Jeong-Bong (J-B.) Lee Department of Electrical Engineering, University of Texas at Dallas, Richardson, Texas, U.S.A.

Patrick A. Limbach Rieveschl Laboratories for Mass Spectrometry, Department of Chemistry, University of Cincinnati, Cincinnati, Ohio, U.S.A.

Yuehe Lin Pacific Northwest National Laboratory, Richland, Washington, U.S.A.

Susan Lunte Department of Pharmaceutical Chemistry, The University of Kansas, Lawrence, Kansas, U.S.A.

A. Maha Mechanical Engineering Department, Louisiana State University, Baton Rouge, Louisiana

Justin S. Mecomber Rieveschl Laboratories for Mass Spectrometry, Department of Chemistry, University of Cincinnati, Cincinnati, Ohio, U.S.A.

Dimitris E. Nikitopoulos Professor, Mechanical Engineering Department, Louisiana State University, Baton Rouge, Louisiana, U.S.A.

Daniel Oerther Department of Civil and Environmental Engineering, University of Cincinnati, Cincinnati, Ohio, U.S.A.

Ian Papautsky Department of Electrical and Computer Engineering, University of Cincinnati, Cincinnati, Ohio, U.S.A.

Sunggook Park Mechanical Engineering Department, Louisiana State University, Baton Rouge, Louisiana, U.S.A.

Helmut Schift Laboratory for Micro- and Nanotechnology, Paul Scherrer Institut, Villigen, Switzerland

Li Shi Mechanical Engineering Department, The University of Texas at Austin, Austin, Texas, U.S.A.

Steven A. Soper Department of Chemistry, Louisiana State University, Baton Rouge, Louisiana, U.S.A.

Wanjun Wang Department of Mechanical Engineering, Louisiana State University, Baton Rouge, Louisiana, U.S.A.

Malgorzata. A. Witek Department of Chemistry, Louisiana State University, Baton Rouge, Louisiana, U.S.A.

Adam T. Woolley Department of Chemistry and Biochemistry, Brigham Young University, Provo, Utah, U.S.A.

Ren Yang Department of Mechanical Engineering, Louisiana State University, Baton Rouge, Louisiana, U.S.A.

Choongho Yu Materials Sciences Division, Lawrence Berkeley National Laboratory, Berkeley, California, U.S.A.

Jeffrey D. Zahn Department of Bioengineering, Pennsylvania State University, University Park, Pennsylvania, U.S.A.

1

Introduction

Wanjun Wang and Steven A. Soper

CONTENTS

The last decade has been an exciting period for people working in the fields of microelectromechanical systems (MEMS) and microfabrication technologies. Starting from the earliest devices in electromechanical transducers, such as accelerometers and pressure sensors, which are among the most commercially successful MEMS devices and systems, the technologies have observed a rapid expansion into many different fields of engineering, physical sciences, and biomedicine. MEMS technologies are assisting in bridging the gap between computers, which work in the digital domain, with the analog world in which we live. For example, various sensors and actuators may be produced using MEMS technologies, and these sensors and actuators can then be used as interfaces between computers and the physical environment for the purposes of information processing and intelligent control.

In recent years, one of the most exciting progresses in MEMS applications is the rapid evolution of biological-microelectromechanical systems (bio-MEMS). In addition to basic components, such as microchannels, microvalves, micropumps, micromixers and microreactors for flow management at microscopic volumes, various novel sensor and detection platforms have been reported in the microfluidic and bio-MEMS fields. Many of the so-called micro total analysis systems (μTAS), or lab-on-a-chip systems have also been reported, and will offer new paradigms in biomedicine and biology, in particular the ability to perform point-of-care measurements. The advantages

of such systems are the microvolumes of biological or biomedical samples that can be delivered and processed for testing and analysis in an integrated fashion, therefore dramatically reducing the required human involvement in many steps of sample handling and processing, and improving data quality and quantitative capabilities. This format also helps to reduce the overall cost and time of the measurement and at the same time improves the sensitivity and specificity of the analysis.

Though it is believed that the long-term impact of MEMS technologies on our life will be similar to that made by the microelectronics industry, the market for MEMS products has grown at a much slower pace than many people had expected. In comparison with the market development history associated with the microelectronics and computer industries, the market for MEMS is much more diversified with highly specialized, individual categories of products with specifically targeted applications. The research and development efforts are therefore very diversified, often requiring multidisciplinary teams to work collaboratively to build effectively operating systems. In addition, it is often desired that the researchers and product development engineers also possess multidisciplinary backgrounds—a requirement that is often extremely hard to meet. This may be particularly true for the field of bio-MEMS. In comparison with other MEMS subareas, which typically involve only different engineering disciplines such as mechanical, electrical, and optical engineers, the development of bio-MEMS involves a truly interdisciplinary integration of basic sciences, medical sciences, material sciences, and engineering. Functioning in an interdisciplinary endeavor requires researchers to possess the ability to cross-communicate, work in a team-directed fashion, and compartmentalize research tasks. This is a primary reason why bio-MEMS science and engineering, as well as the systems they produce, are evolving at a relatively slow rate of development in comparison with electrical and mechanical sensing devices and systems, whose developments primarily depended upon a specific discipline.

There have been many high-quality books published in the general areas of design and fabrication technologies of MEMS devices and systems. Most of these books have focused on silicon-based technologies, such as surface micromachining, and wet and dry etching technologies (RIE and DRIE processes). As bio-MEMS technologies develop and many educational institutions begin to offer courses on this subject matter, textbooks covering both the fundamental fabrication technologies in a variety of different substrates (Si, thermoplastics, ceramics, etc.), metrology, and device characterization as well as the latest technology applications are needed. While there are a number of seminal books covering conventional MEMS-based technologies, there are very few that focus on the design and fabrication of bio-MEMS devices and systems. There are several reasons for this phenomenon. The first is that bio-MEMS technology is still in a much earlier stage of development in comparison to other MEMS technologies. The second, and perhaps the most important one, is that the topics to be covered in a bio-MEMS

textbook are so widely diversified that it is virtually impossible for a single author to fully understand or become expert in all of the relevant areas of expertise required to build effective bio-MEMS devices and systems. This is also the main reason why an edited book that includes contributions on different subjects from specialized researchers who work on the frontiers of bio-MEMS from both the basic science and engineering realms is highly desirable. As editors, we were fortunate enough to have a group of well-recognized researchers and educators as contributors in their specific areas of expertise, and to cover both fundamental knowledge and the latest research progresses in various areas of importance to bio-MEMS.

This book was prepared with the intent of targeting two main areas. First, we wanted to cover enough fundamental materials so that it could be used as a textbook for classes at either the graduate or senior undergraduate levels. This book may also be suitable for those people who are not currently in the bio-MEMS field and may need to learn the fundamentals in order to enter the field. Second, with enough application examples covered and the latest research progress presented, the book may also be used as a reference for scientists or engineers who work in the bio-MEMS field to provide a guide as to what has been accomplished in many related areas to date.

Because the materials to be covered in a bio-MEMS book are so widely diversified, to be able to cover all the key contents in a limited space is definitely a challenge. Some compromises and balances were obviously needed in compiling the contents of this book in order to cover relevant areas in bio-MEMS, but also to make it manageable for the reader. In this book, topics on microfabrication technologies focus primarily on nonsilicon-based methods. There are two reasons for this decision. First, there are already numerous books available on silicon-based microfabrication technologies and interested readers can always refer to these books. Secondly, the current trends in bio-MEMS seem to be in the direction of using nonsilicon-based fabrication technologies and materials. Because biologists and chemists have long used nonsilicon materials, such as glasses and polymers (PMMA, polycarbonate, etc.), various surface treatment technologies have been developed and processes are well understood. Micro- and nanoreplication using molding, imprinting or hot-embossing technologies also help to reduce the batch fabrication cost, making these substrates very appealing for bio-MEMS-related application areas.

Because the potential readers of this book may have various educational backgrounds, it was also necessary to balance the fundamental fabrication principles with the advanced contents, as well as the scientific and engineering materials. To be able to serve readers who are interested in learning the fundamentals of bio-MEMS technologies as well as researchers who work in the field and need a good reference book, efforts were made by the contributors of this book to balance fundamental knowledge with the latest advancements in related subject areas. In addition, the readers with engineering backgrounds may have difficulty in fully understanding the

biological or biomedical aspects of the materials covered in these chapters. The same may hold true for readers with basic science or life science backgrounds when reading the engineering sections of this book. The authors of each chapter have tried to include some basic introduction references to allow readers to obtain relevant background materials to augment those that are presented herein.

1.1 Main Contents and Organization of the Book

The contents in this book can be generally divided into three basic sections:

1. Basic Bio-MEMS Fabrication Technologies (Chapters 2, 3, 4, and 5);
2. Microfluidic Devices and Components for Bio-MEMS (Chapters 6, 7, 8, and 9);
3. Sensing Technologies and Bio-MEMS Applications (Chapters 10, 11, 12, 13, 14, 15, and 16).

1.1.1 Microfabrication Technologies

In this section, we focused on nonsilicon-based micro- and nanofabrication technologies, such as LIGA—a combination of deep-etch x-ray lithography with synchrotron radiation (LI), electroforming (G = Galvanoformung [German]), and molding (A = Abformung [German]), or UV-LIGA (using ultra violet lithography instead of x-ray lithography), hot-embossing, nanoimprinting, and so forth. Because UV lithography of SU-8 has become a popular choice for a lot of researchers in recent years, this topic is covered in Chapter 2. In addition to the basic lithography processing steps and optimal processing conditions, example applications in microfluidic devices and micro-optic devices are also presented. Chapter 3 provides a very detailed presentation on the LIGA process. Applications of LIGA technologies in fabricating polymer bio-MEMS are also introduced. Nanoimprint lithography (NIL) is a low cost and flexible patterning technique particularly suitable for fabrication of nanoscale components for biological applications. Its unique advantages are that both topological and chemical surface patterns can be generated at the micro- and nanometer scales. Chapter 4 presents an overview of NIL technology with the focus on the compatibility of materials and processes used for biological applications. Examples are also presented to demonstrate how NIL technology can be employed to fabricate devices used to understand and manipulate biological events. Hot embossing is another reasonably fast and moderately inexpensive technique used to replicate microfluidic elements in thermoplastics. In the hot-embossing process, polymer and the prefabricated master containing the prerequisite

structural elements are heated above the glass transition temperature (or softening point) of the thermoplastic, then a controlled force is applied under vacuum. The assembly is cooled below the glass transition temperatures and de-embossed. The technology offers the advantage of a relatively simpler replication process with few variable parameters and high structural accuracy, and is well suited for a wide range of microfluidic applications from rapid prototyping to high-volume mass fabrication. Chapter 5 presents an introduction to hot embossing for microfluidic lab-on-a-chip applications. Following an introduction to polymer characteristics, fabrication of masters for hot embossing and the process itself will be examined in detail.

1.1.2 Microfluidic Devices and Components for Bio-MEMS

In most bio-MEMS, it is commonly required to prepare, deliver, or manipulate microscopic amounts of biosamples or reagents in either microchannels and/or microchambers. Fluid behavior at the microscale is often different from those at macroscales. For example, factors such as surface tension may become dominant in microfluidic devices and systems. When the size of biological samples, such as cells, are close to those of the flow channels through which the samples are delivered, the dynamics of the flow may not be readily predicted based on conventional fluid dynamics. Significant research efforts have been made in the last decade in the area of microfludics, basic components, and fabrication technologies. Many novel devices and systems have been reported in the field. In this book, conventional fluid dynamics was not presented because the topic has been covered in numerous textbooks. Instead, we have focused on the fundamental principles, the design and fabrication of basic microfluidic components such as micropumps, micromixers, flow cytometers, and so forth, for sample extraction, preparation, and manipulations. Information on microfluidics and sample preparation is presented in Chapters 6 through 9.

Micropumps are used for sample delivery and manipulation. They are among the most important components in most microfluidic devices and systems. In Chapter 6, operation principles of commonly used micropumps are presented, analyzed, and compared. Representative fabrication procedures are also presented and discussed. Mixing is of significant importance to realizing lab-on-a-chip microscale reactors and bioanalysis systems because the reactions carried out on the micro- or even nanoscale in such devices require the on-chip mixing of samples and reagents. Unfortunately, to mix microvolumes of fluids in microfluidic systems is always a very difficult task due to diffusional constraints. The topic of mixing on the microscale has been at the forefront of research and developmental efforts over roughly the last fifteen years because the technological thrust toward miniaturization of fluidic systems began. Chapter 7 covers the basic principles of mixing techniques on the microscale. This chapter also presents a detailed review of various micromixers reported in the field. In order to produce lab-on-a-chip devices,

it is necessary to integrate all of the components for sample preparation (including sample extraction, sample preconcentration, and sample derivatization), sample introduction, separation, and detection onto a single microchip made from either glass, silica, or polymers. In most bio-MEMS, the sample usually undergoes some kind of sample preparation or pretreatment steps prior to being submitted to the actual analysis. This step may involve extracting the sample from its matrix, removing large matrix components from the sample that may mask the analysis or removing interfering species, derivatizing the sample to make it detectable, or performing a sample preconcentration step. Chapter 8 provides a thorough overview of the developments in this field. Another commonly used technology for manipulations (sorting and counting) of biological particles is flow cytometry. A complete microcytometer would require an integrated microfluidic unit for either hydrodynamic or dielectrophoretic focusing of biological entities undergoing sorting, and the optical measurement unit to count the number of sorted species. There are many research reports in the literature detailing advancements in this area. Chapter 9 covers an introduction to the basic principles of flow cytometry and a review of the state-of-the-art in this field.

1.1.3 Sensing Technologies and Bio-MEMS Applications (Chapters 10, 11, 12, 13, 14, 15, and 16)

Because of the enormous variations in biological and biomedical samples, the processing and detection principles required for the analysis of targets are often completely different. There have been numerous bio-MEMS either in commercial applications or reported in the literature that have described the integrated processing of biosamples in a microfluidic platform. It is virtually impossible to cover all of them in the limited space of this book. In addition, bio-MEMS technologies are still in their early stages of development and as such new and novel technologies are constantly evolving with the potential for integration into bio-MEMS. The seven chapters in this section cover some of the representative technologies in this rapidly developing area.

Chapter 11 focuses on the topic of culture-based microchips for the rapid detection of environmental mycobacteria. Because much of the research work in μTAS devices has focused on the use of capillary electrophoresis (CE), materials related to the applications of capillary electrophoresis have been presented in two chapters. Chapter 10 covers an introduction to microchip CE with electrochemical detection (CE-ECD), while Chapter 13 introduces microchip capillary electrophoresis systems for DNA analysis. Bio-MEMS technologies have lead to some breakthroughs in both on-spot and controlled drug delivery as well as new technologies for drug development. Two chapters cover the progress in this area. Chapter 12 provides a complete review of bio-MEMS technologies for drug delivery. Chapter 16 presents studies on pharmaceutical analyses using bio-MEMS. Chapter 14 discusses

the recent advances of bio-MEMS applications in assay development, improved separation performance, and enhanced detection strategies. As the dimensions of processing bio-MEMS elements is reduced, the analysis and detection of the basic building blocks of biology, such as single cells and single molecules, becomes necessary to consider. Chapter 15 offers an overview of novel technologies for single-cell and single-molecule analyses using microfluidic devices.

1.2 Suggestions for Using This Book as a Textbook

Because this book is well organized and covers three major aspects of bio-MEMS technology—fabrication and microfluidics, detection and analysis technologies, and applications—it is suitable as a textbook for either senior-level technical elective courses or graduate courses. However, with fifteen chapters (excluding this chapter) the book is most likely too much to be covered in a typical semester of fourteen to fifteen weeks (45 plus hours for a three-credit-hour course). It is therefore necessary to omit some chapters. Based on the interests and foci of the particular class, it is suggested that one third of the instruction be spent on the microfabrication technologies presented in Chapters 2 through 5, another third devoted to microfluidics offered in Chapters 6 through 9, and the remaining third used for coverage of selected topics on specific devices and systems for different applications, which is encompassed in Chapters 10 through 16.

Part I

Basic Bio-MEMS Fabrication Technologies

2

UV Lithography of Ultrathick SU-8 for Microfabrication of High-Aspect-Ratio Microstructures and Applications in Microfluidic and Optical Components

Ren Yang and Wanjun Wang

CONTENTS

2.1 Introduction

Ultraviolet (UV) lithography of ultrathick photoresist with high-aspect-ratio, high sidewall quality, and good dimensional control is very important for microelectromechanical systems (MEMS) and micro-optoelectromechanical systems (MOEMS). Although x-ray lithography of methyl methacrylate (PMMA) can meet these requirements, the expensive beamlines are not readily available to many researchers. The high cost of x-ray lithography also made it impractical for many applications. As a cheaper alternative, UV lithography of SU-8 has received wide attention in the last few years. As the obtainable results with UV lithography of SU-8 get better and better, ever more applications have been found for the technology in MEMS and MOEMS.

SU-8 resist is a negative tone, epoxy-type photoresist based on EPON™ SU-8 (also called EPIKOTE™ 157) epoxy resin from Shell Chemical, and originally developed by IBM [1–5]. It is commercially available from MicroChem Corp., Newton, Massachusetts. Mixed with a photoinitiator, SU-8 epoxy is dissolved in a standard gamma-butyrolactone (GBL) solvent, which can be replaced by cyclopentanone, and has improved properties. Due to its low optical absorption in the near-UV range, SU-8 can be lithographed in thicknesses of hundreds or thousands of micrometers with very high aspect ratios by standard contact equipment. SU-8 can also be patterned using x-ray or e-beam. Cross-linked SU-8 also has good chemical and physical properties and can serve as excellent structural material for many applications [6–13]. For SU-8s near-UV contact printing, normally broadband near UV light between 320 nm and approximately 450 nm is used for the exposure. With well-controlled lithography conditions, with pressure contact exposure or vacuum contact exposure, cross-linked polymer microstructures with high aspect ratios could be obtained at heights of more than 1000 micrometers [14–20]. Chang and Kim obtained a 1 μm feature size with 25 μm thickness [14]. Ling et al. obtained 360 μm–thick structures with a 14 μm feature size [15]. With the help of a well-collimated proximity ultraviolet source, Dentinger et al. obtained aspect ratios exceeding 20:1 for film thicknesses of 200 to approximately 700 μm [19]. Williams and Wang obtained a 65:1 high-aspect-ratio structure up to 1 μm high with a Quntel aligner [20]. Yang and Wang reported a work covering both numerical simulations and an experimental study of the air gap effect and compensation, with optimal wavelengths of the light source for UV lithography of ultrathick SU-8 resist for high-aspect-ratio microstructures with an aspect ratio of more than 100 and thickness of the resist to more than 2 μm [21].

In this chapter, recent developments in SU-8 lithography of ultrathick SU-8 resist will be presented first, followed by a summary of UV lithography conditions and some processing tips. Finally, some applications of UV lithography of ultrathick SU-8 resist in microfluidics and micro-optics will be demonstrated.

2.2 Numerical Study of Diffraction Compensation and Wavelength Selection

For ultrathick SU-8 lithography, several important parameters need to be carefully controlled: temperature in prebake and postbake, Fresnel diffraction and wavelength-dependent absorption in exposure, and agitated development. Among these parameters, the effects of the absorption spectrum and diffraction on lithography quality are two key factors limiting the sidewall quality of UV lithography of ultrathick SU-8 resist; these will be the topics of this chapter.

2.2.1 Diffraction Caused by Air Gap and Wavelength Dependence of the UV Absorption Rate of SU-8

SU-8 in general has excellent surface planarizing properties. However, as the thickness of SU-8 resist increases, the nonuniformity of the resist can become a serious issue. To fabricate ultrathick, high-aspect-ratio microstructures commonly requires spin-coat resist layers ranging from several hundreds to thousands of micrometers. In such cases, high viscosity SU-8, such as SU-8 50 or SU-8 100, is always preferred. The surface flatness can be a very severe problem, with typical flatness errors of 10 μm to 100 μm. Other factors, such as unintentional tilt in the baking process, dirt particles, curvatures of the substrate or mask, and so forth, may also contribute to reduced surface flatness. The flatness error then forms air gaps between the mask and resist surface, and results in serious diffraction, aerial image distortion, and printing errors.

For the ultrathick photoresist, the absorption of the resist with respect to the light source also greatly affects the lithography quality. As the light beam penetrates the SU-8 resist layer from the top to the bottom, the light intensity drops gradually as the light is absorbed. The top part of the SU-8 resist therefore absorbs more than the bottom part does. There is, therefore, overdosage at the top and underdosage at the bottom. This is one of the major reasons that inexperienced operators often produce mushroom types of microstructures in UV lithography of SU-8. It is also one of the reasons x-ray lithography is normally preferred for high-quality vertical sidewall and high-aspect-ratio structures. The extremely high transmission of the x-ray beam line helps to provide about the same absorption across the entire thickness of the photoresist.

The absorption spectrum of unexposed SU-8 resist shows much higher absorbance at shorter wavelengths than at long wavelengths. Figure 2.1a shows the transmission spectrum of 1 mm–thick unexposed SU-8 100, a thickness close to that used in our experimental study as will be presented in the later sections. The absorption coefficient of unexposed SU-8 at 365 nm (where the photoresist is the most sensitive) is about 4 times that of the absorption coefficient at 405 nm. The shorter wavelength components of light are primarily absorbed by the surface layer, while the longer wavelength components penetrate farther down and expose the bottom part. It is therefore desirable to filter out the wavelengths shorter than (or near) 365 nm to avoid overexposure at the top layer. Longer wavelengths (either *h* line or *g* line) with much lower absorbance are used to permit more energy to reach the bottom part of the thick SU-8 resist layer and to achieve better sidewall profiles. Figure 2.1b shows the measured refractive index of SU-8 as a function of the wavelength.

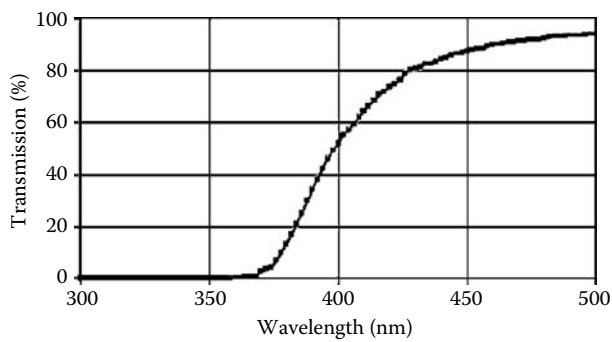

(a)

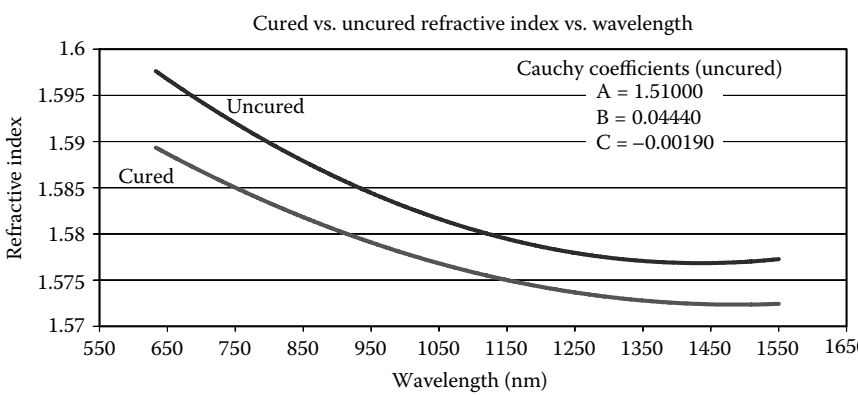

(b)

FIGURE 2.1
Properties of SU-8 resist: (a) transmission of 1 mm–thick unexposed SU-8 film; (b) SU-8 refractive index vs. wavelength. (Courtesy of Mark Shaw, MicroChem Corp., Newton, MA.)

The absorption coefficient of unexposed SU-8 at 436 nm is about 1/3 of that at 405 nm and 1/12 of that at 365 nm. A light source with primarily *g*-line components may therefore be suitable to expose ultrathick SU-8 resist; sidewall quality may also be much better than using 365 nm or 405 nm as a lithography source. Of course, the diffraction effect may become more serious with longer wavelengths.

For ultrathick SU-8 lithography, there are several important parameters to be carefully controlled: temperature in prebake and postbake, Fresnel diffraction and wavelength-dependent absorption in exposure, development processing, and so forth. Normally, optimization of the temperature control in prebake and postbake can minimize the stress of the SU-8 and reduce the possibility of debonding; the Fresnel diffraction and photoresist's absorption cause the aerial image shape to be degraded and the light intensity distribution changed in the cross-section of the light beam in the propagation direction; optimization of the exposure dosage helps to obtain enough dosage for the bottom part of the SU-8 to improve the adhesion and avoid overexposure for the top part.

Fresnel diffraction of the micropatterns on the mask degrades the geometry of the aerial images and reduces the sidewall qualities of the printed microstructures. With increased thickness of the photoresist layers and the mask–photoresist gaps, effects of Fresnel diffraction become more severe and the pattern aerial image distortion more significantly. Full understanding of the Fresnel diffraction is therefore very important to obtaining a high-quality, ultra-high-aspect ratio in UV lithography of thick SU-8 resist.

2.2.2 Numerical Analysis of Diffraction and the Absorption Spectrum on UV Lithography of Ultrathick SU-8 Resist

As collimated light passes through an aperture on the mask in UV exposure, diffraction happens because of the mask patterns' limitation for light wavefront. In lithography, the collimated light source can be considered as infinitely far away, but the mask patterns (i.e., diffracting apertures) are so close to the photoresist (observing screen) that the curvature of the wavefront becomes significant.

Based on Huygens' principle, the diffraction produced by an aperture with an arbitrary shape in an otherwise opaque partition can be stated by the Fresnel-Kirchhoff integral formula:

$$U_p = -\frac{ikU_0 e^{-i\omega t}}{4\pi} \iint \frac{e^{ik(r+r_0)}}{rr_0} [\cos(n,r) - \cos(n,r_0)]ds, \tag{2.1}$$

where $k = 2\pi$, i is the incident light wavelength, U_0 represents spherical monochromatic source waves, r and r_0 stand for positions of a point on the aperture relative to the screen and the source, respectively, (n, r) and (n, r_0)

denote the angles between the vectors and the normal to the surface of integration, and *ds* represents the integration on the surface of the aperture.

For a rectangular pattern on the mask, the diffraction distribution at an arbitrary plane *z* will be:

$$U_p(x,y,z) = \frac{e^{ikz}}{i\lambda z}\int_{u_1}^{u_2} e^{\frac{i\pi u^2}{2}}du \int_{v_2}^{v_1} e^{\frac{i\pi v^2}{2}}dv, \tag{2.2}$$

$$\text{where } u = \sqrt{\frac{2}{\lambda z}}(x - x_0)$$

$$\text{and } v = \sqrt{\frac{2}{\lambda z}}(y - y_0)$$

are Fresnel numbers, *z* is the vertical distance to the photomask pattern, and *x* and *y* are the horizontal distance-to-pattern edges. The integrals in Equation (2.2) are evaluated in terms of the integral known as the Fresnel integral:

$$\int_0^a e^{\frac{i\pi\xi^2}{2}}d\xi = \int_0^a \cos(\frac{\pi\xi^2}{2})d\xi + i\int_0^a \sin(\frac{\pi\xi^2}{2})d\xi\ . \tag{2.3}$$

Patterns such as slit, straightedges, and so forth, can be treated mathematically as modified cases of a rectangular aperture. For other arbitrary pattern shapes in UV lithography, the same method can be used to obtain the aerial light distribution caused by diffraction based on Equation (2.1).

A commercial software called ZEMAX EE (ZEMAX Development Corporation, San Diego, CA), based on the principles as stated in Equations (2.1) through (2.3) were used to simulate Fresnel diffraction in UV lithography of SU-8. Light intensity distribution data were exported from ZEMAX and imported to Excel or Sigma Plot. The effect of the substrate reflectivity (such as silicon substrate, about 0.575 for vertical incident light with a wavelength of 365 nm, and 0.473 for a wavelength of 405 nm) was considered in the numerical simulations.

Using ZEMAX EE software, numerical simulations were conducted for two different cases: (1) with an air gap between the mask and wafer and no compensation; (2) using glycerin liquid compensation. In all the simulations, the slot on the mask was assumed to be 20 μm wide and infinitely long, as shown in Figure 2.2. The ideal distribution of the light intensity without any diffraction effect (entering the slot) is plotted as uniformly distributed.

Numerical simulations were conducted to study the effects of diffraction caused by the air gap, and the diffraction compensation effects using an optical liquid, such as glycerin. In the simulations, the gaps between the mask and resist surface were assumed to be 50 μm, and the slot was assumed

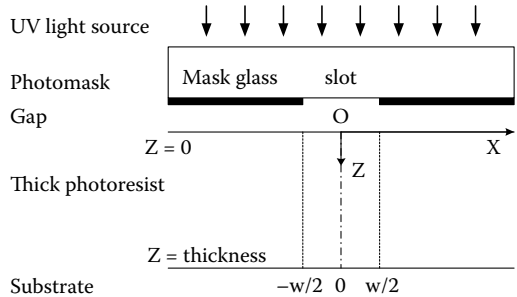

FIGURE 2.2
A slot pattern on a photomask exposed to a collimated UV light source.

to be at 20 μm. The simulation results show that with gap compensation, using glycerin produced improved intensity distribution as compared with the air gap.

Because SU-8 is a negative tone resist, the pattern profile is defined by light intensity higher than the threshold energy to cure SU-8 within the targeted region. With the attenuation of intensity in SU-8 in the vertical direction (Z direction) and diffraction caused by the micropatterns, the aerial dimension of the projection image is varied. The edges of the aerial image are defined as the edges of the Fresnel diffraction pattern with energy higher than the cross-link dosage.

The light intensity in the vertical direction is

$$I = I_0 \cdot e^{-aZ}, \tag{2.4}$$

where a is the absorption coefficient, and Z is the distance in vertical direction from the film's surface. The transmission is then

$$T = I / I_0 = e^{-aZ}. \tag{2.5}$$

Figure 2.3 shows a measured transmission for unexposed SU-8 with a different thickness. As can be seen from the results in Figure 2.3, the intensity of *i*-line light decayed much faster than *h*-line as light penetrated deeper into the resist. The absorption coefficient a is found to be about 0.0031 for the *i*-line and about 0.0005 for the *h*-line. The measured data presented in Figure 2.3 was used in numerical simulations for the combined effects of wavelength dependence of the absorption of unexposed SU-8 and the diffraction. Similarly, a 20 mm opening slot on the mask is assumed. Two different wavelengths, *i*-line and *h*-line, were considered separately. Numerical simulations were conducted to obtain the Fresnel diffraction pattern at the bottom of the resist layer.

After using ZEMAX EE to obtain the light energy distribution at the different depth of the SU-8 resist based on the transmission of SU-8 thick film

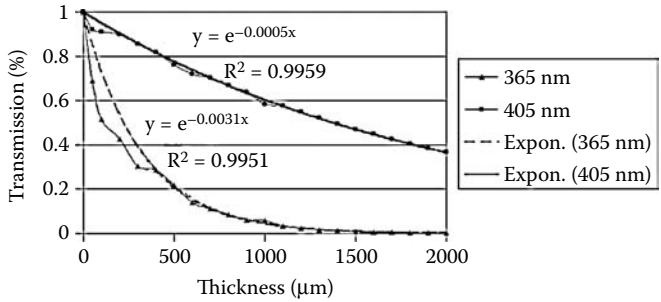

FIGURE 2.3
Measured transmissions for both the *i*-line and *h*-line for different thicknesses of SU-8.

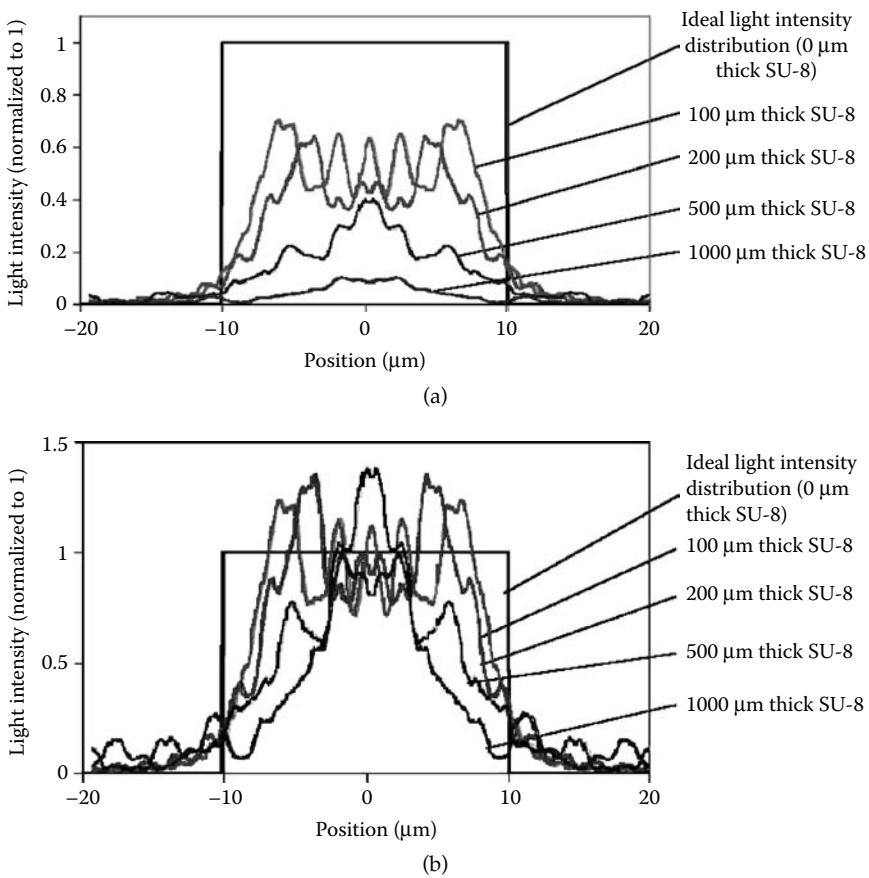

FIGURE 2.4
(a) Fresnel diffraction pattern in the bottom of the resist layer as projected by the *i*-line light source. (b) Fresnel diffraction pattern in the bottom of the resist layer as projected by the *h*-line light source.

as shown in Figure 2.3, a Fresnel diffraction pattern was numerically obtained and is shown in Figure 2.4. Figure 2.4a shows the simulated results for the *i*-line light source and four different resist thicknesses. Figure 2.4b shows the simulation results for the *h*-line light source at different resist thicknesses. Two observations can be made from the results shown in Figure 2.4. First, as the resist thickness increases, the nonuniformity of light intensity caused by diffraction becomes more serious. Second, shorter wavelength light (*i*-line) has less of a problem in diffraction, but the light intensity drops quickly with depth and may have difficulty cross-linking SU-8 resist at the bottom region.

Figure 2.5 shows the simulated sidewall profiles when a 20 μm–wide slot pattern is exposed using *i*-line and *h*-line light sources, respectively [15]. The sidewall profile is defined by the threshold exposure dosage of lithography. The resist in the left side of the threshold boundary line received enough exposure dosage to fully cross-link the resist. The lithography dosage in the resist on the right side of the boundary line is below the required threshold dosage and is removed in the development process. Because of the symmetry of the exposed pattern, only the right half of the exposed region is shown in simulated results in Figure 2.5. The sidewall profiles in Figures 2.5a and 2.5b are for the exposure with a zero gap and 50 μm gap between mask and SU-8 resist, respectively. Several different situations have been examined: *h*-line or *i*-line exposure, air gap, or with glycerin. The simulation results show that glycerin reduces the Fresnel diffraction. With wavelength selection (for example,

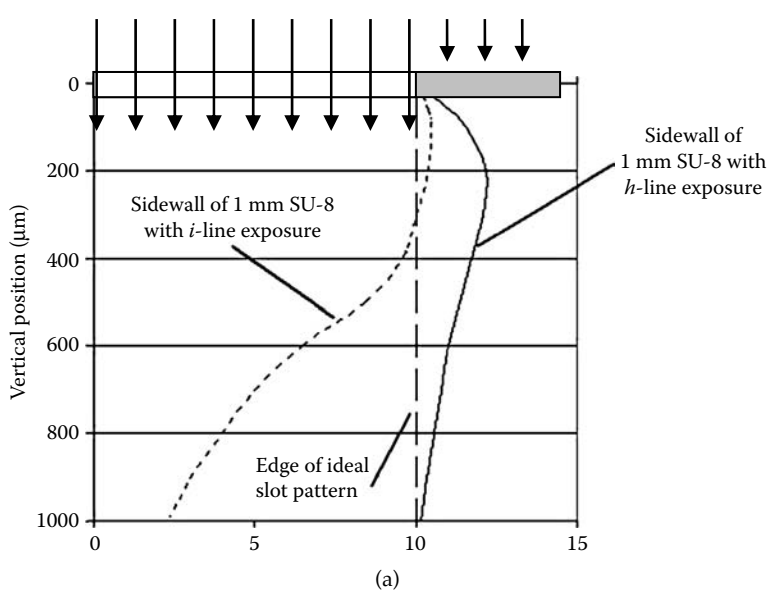

FIGURE 2.5a
The simulated sidewall profiles for a 20 μm–wide slot on the mask. On the left side of these profile lines, the exposure dosage is enough to cross-link the resist. The gap between the mask and SU-8 is assumed to be zero.

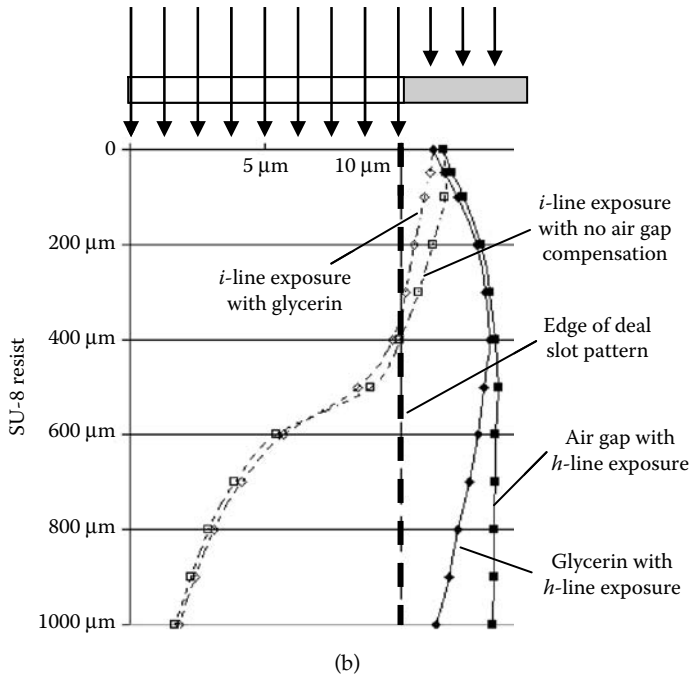

FIGURE 2.5b
The simulated sidewall profiles for a 20 μm–wide slot on the mask with a 50 μm gap between the mask and SU-8. On the left side of these profile lines, the exposure dosage is enough to cross-link the resist.

using an *h*-line-dominated light source), the lithography quality may be further improved. From the foregoing analyses, it can be seen that the wavelength selection played the most important role in optimal lithography of ultrathick SU-8, while the air gap compensation played a secondary role. In comparison with the air gap, glycerin compensation is proved to be marginally better in producing better sidewall profiles.

2.2.3 Development with One-Direction Agitation Force

Development of thick SU-8 film is another challenge in fabrication of high-aspect-ratio microstructures. The SU-8 developer cannot effectively work in ultradeep and narrow structures by simple diffusion and conventional stirring mechanisms. The development may last hours, damage the fine structures, and often is incomplete. Strong agitation is normally used to completely develop the SU-8. However, the strong stirring process or supersonic vibration often produce vibrations in random directions and cause severe vibrations of the microstructures. They may also reduce the sidewall quality, deform or debond some fine patterns, and destroy the high-aspect-ratio microstructures.

In contact lithography, the light source is projected perpendicular to the substrate. With no external agitation, the unexposed SU-8 is developed from the top layer to the bottom layer and is based on diffusion of the SU-8 developer solution. If the direction of the agitation force is perpendicular to the substrate (parallel with the sidewall of the microstructures), the agitation would accelerate the development but not affect the sidewall quality or minimize the possibility of damaging the microstructures. There are two methods of accelerating the development process. One is to immerse the sample in a face-down orientation to take advantage of the gravity force for better convective transport. Another method is to use a megasonics agitation perpendicular to the substrate.

The mechanism of SU-8 development should be understood in the following way: when the SU-8 developer enters the uncross-linked SU-8, a porridgelike region is produced between the SU-8 and the developer. Inside this porridgelike region, as the developer diffuses, the uncross-linked SU-8 dissolves into the SU-8 developer. The concentration of uncross-linked SU-8 is nonuniformly distributed. The concentration decreases closer to the boundary line between the dissolved and the solid sections of the uncross-linked SU-8. With the sample positioned in a face-down orientation, the diffusion and removal of the dissolved SU-8 from the boundary region of the developer and the uncross-linked SU-8 were accelerated by gravity force. This may help to achieve a much higher development rate based on our experience. Our experiments have proved that the development rate for face-down-oriented samples can be at least two times that obtained when the samples were placed in a face-up orientation. SU-8 microstructure edges and trenches were also found to be much cleaner after the development.

With megasonic agitation, when the wave propagates perpendicular to the substrate, much faster development rates can also be achieved. Our experiments found that excellent uniformity of development can also be realized. This technique is commonly used in x-ray Lithographie, Galvahoformung, Abformung (LIGA) processes and has been reported to work well with SU-8. In megasonic agitated development, the range of frequencies is normally several MHz. This reduced wavelength helps to agitate the fluids in the porridgelike region between the uncross-linking SU-8 and the SU-8 developer. This leads to higher dissolved speed and faster development.

2.3 Experimental Results Using Filtered Light Source and Air Gap Compensation for Diffraction

To demonstrate the superiority of the proposed optimal lithography of a filtered light source and gap compensation, we will show three different

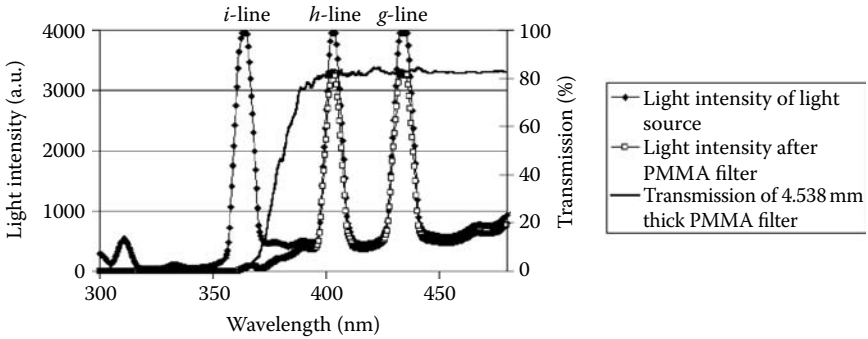

FIGURE 2.6
Light intensity before and after filter for the Oriel UV station at 200 W output.

groups of experiments in this section: (1) a broadband light source without gap compensation, (2) a broadband light source using glycerin for gap compensation; and (3) a filtered light source with PMMA sheet (*i*-line eliminated) and gap compensation using glycerin as suggested here.

A broadband light source was used in a lithography process and a thick plate of PMMA used as an optical filter to eliminate the short wavelength components. The broadband spectra of an Oriel UV station before and after the PMMA filter are shown in Figure 2.6, which were measured using an Ocean Optics S2000 spectrometer. The UV light source has three major spectrum lines: the *i*-line, *h*-line, and *g*-line. A 4.538 mm–thick PMMA plate (not annealed) was used as a filter to eliminate the short wavelength components of the light source of the Oriel UV station. The optical transmission spectrum of a 4.538 mm–thick PMMA sheet without anneal is also shown in Figure 2.6. The transmission of this PMMA sheet is about 0.3% at the *i*-line, 82% at the *h*-line, and 82% at the *g*-line. The PMMA sheet filters out most of the light with a wavelength less than or equal to 365 nm. The spectrum of the Oriel UV station used in this study after filtering with this PMMA sheet was measured and shown in Figure 2.6 where the *i*-line is removed, and the *h*-line and *g*-line are reduced. It was found that light intensity at 365 nm dropped from 15.08 mJ/cm^2 to 0.47 mJ/cm^2, and at 405 nm dropped from 42.08 mJ/cm^2 to 34.15 mJ/cm^2. This result is consistent with that expected from the transmission spectrum of PMMA measured using a spectrometer. Because the absorbance of unexposed SU-8 around the *g*-line ($\lambda = 436$ nm) is only about one-third of that around *h*-line ($\lambda = 404.7$ nm), and total exposure dosage from the light source as shown in Figure 2.6 after PMMA filter is dominated by the *h*-line, the effect of the *g*-line in the lithography of SU-8 will therefore be neglected under such conditions.

The detailed processing conditions for 1150 μm–thick SU-8 100 film are as follows:

1. Clean Si wafer with acetone, IPA (isopropyl alcohol), and DI (deionized) water.
2. Spin coat SU-8 100 at 400 rpm.
3. Level hot plate, bake 10 hours at 110°C, cool down to 60°C inside 1 hour, dwell at 55°C (uncross-linked SU-8's glass temperature is 50°C to approximately 60°C) for 4 hours, cool down to room temperature inside 3 hours.
4. Expose the sample using a broadband light source (with spectrum as shown in Figure 2.6; includes the *i*-line, *h*-line, and *g*-line) with total exposure dosage of 2 J/cm^2, for PMMA filter wavelength selection exposure (with spectrum as shown in Figure 2.6; includes the *h*-line and *g*-line) with total exposure dosage 12 J/cm^2.
5. Postbake at 110°C for 20 minutes, cool down as in step 3.
6. Develop sample using SU-8 developer at 32°C with SONOSYS megasonic actuator driven with a 250 W power supply for 2 hours. The megasonic transducer was placed in a water bath supporting a quartz tank in which the developer and substrate were located. Wafers were facing the megasonic actuator.
7. Rinse sample with IPA several times, dry naturally.

To measure the sidewall quality of the microstructures fabricated using filtered a light source and gap compensation, a 20 μm feature-sized microstructure with a flat edge was removed from the substrate and placed on the measurement stage of the Veeco optical profiler. The R_s (roughness of standard deviation) was then measured along the 1150 μm length. It was found that the roughness of standard deviation (in the light incident direction) was 2.72 μm over the entire length of 1150 μm.

Figure 2.7 shows a group of microcrosses produced with different conditions: (a) broadband light source with no air gap compensation, (b) broadband light source and air gap compensation using a glycerin solution, (c) the filtered light source (*i*-line eliminated) with no air gap compensation, and (d) filtered light source with gap compensation using a glycerin solution.

The minimum designed thicknesses of the crosses achieved are 20 μm for the air gap and 8 μm for the glycerin gap compensation. The dark region in Figure 2.7a was due to the residuals of the development.

The theoretical optical resolution of the line and space of the width b can be estimated by the following equation:

$$b_{\min} = \frac{3}{2}\sqrt{\lambda\left(s + \frac{1}{2}d\right)}$$

where b is the width of line or space, λ is the wavelength of the lithography light, s is the air gap between the mask and the photoresist, and d is the

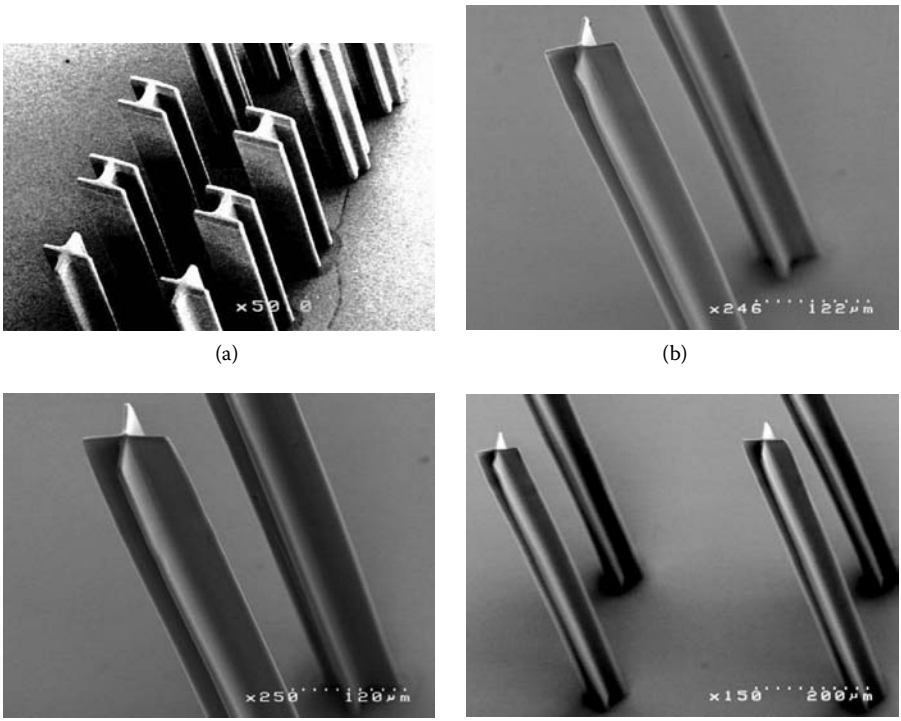

FIGURE 2.7
Cross-patterns made using a filtered light source and three different UV lithography processing conditions. (a) Broadband exposure with no air gap compensation. Crosses with designed thickness of 20 μm and height of 1150 μm. (b) Crosses with designed thickness of 8 μm and height of 1150 μm. Processing conditions: broadband exposure and air gap compensation using glycerin. (c) Crosses with designed thickness of 9 μm and height of 1150 μm. Processing conditions: filtered light source and no air gap compensation. (d) Crosses with designed thickness of 9 μm and height of 1150 μm. Processing conditions: filtered light source and air gap compensation using glycerin.

resist thickness. For 1150 μm–thick SU-8 resist, and assuming no air gap, the optical resolution can be estimated at 21.7 μm for the *i*-line and 22.9 μm for the *h*-line. Because of the low absorption in the *g*-line, the lithography processes in broadband lithography were dominated by the combined effect of the *i*-line and *h*-line, especially the *i*-line. These calculated results are very consistent with what was observed in the experiments for broadband lithography without air gap compensation or using glycerin compensation. The lithography quality of comb structures with a broadband light source becomes quite bad as the feature sizes dropped to about a width of 20 μm and a height of 1150 μm, with some improvement after gap compensation using glycerin. Figure 2.8 shows a comb structure made using a filtered light source and gap compensation with glycerin. It can be seen that the comb structures obtained using the suggested filtered light source and gap

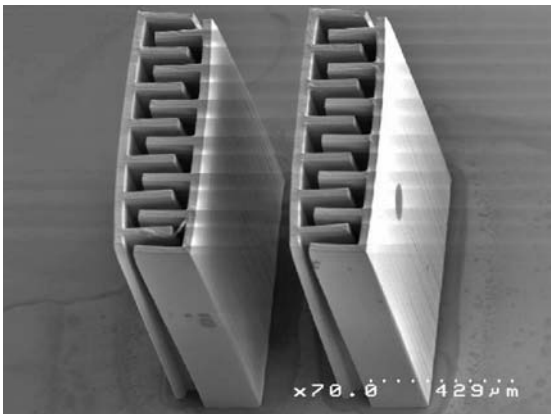

FIGURE 2.8
Comb structures made using filtered light source and gap compensation with glycerin.

compensation with glycerin have excellent sidewall quality and resolutions. Both structures were developed all through and clearly separated. The top fingers are removed together by the liquid surface tension in the drying process.

2.4 Basic Steps for UV Lithography of SU-8 and Some Processing Tips

The standard lithography processing procedures of SU-8 include: (1) pretreat the substrate, spin-coat SU-8; (2) preexposure bake, UV exposure (320 to 450 nm); (3) postexposure bake; and (4) development. The process parameters determine the final quality of the microstructures. The curing process of SU-8 is completed in two steps: formation of acid during optical exposure and thermal epoxy cross-linking during the postexposure bake. A flood exposure or controlled hard bake is recommended to further cross-link the exposed SU-8 microstructures if they are going to be used as parts of the final products. Because most of the publications in the field do not provide detailed lithography conditions, beginners often have to learn from their own experiences and the learning curve can sometimes be exceptionally long. Some basic lithography conditions are provided here as guidelines for those readers who may need something to start from [21–24].

2.4.1 Pretreat for the Substrate

To obtain good adhesion for SU-8 on a substrates, the substrate needs to be cleaned with acetone, IPA, and DI water sequentially, and then dehydrated

at 120°C for 5 to approximately 10 minutes on a hotplate. The substrate may also be primed using plasma asher immediately before spin-coating the resist. In addition, an adhesion promoter may be used as needed. For the applications involving electroplating metals and alloys and stripping of cured SU-8, the vendor of SU-8, MicroChem, recommends using OmniCoat before coating of SU-8.

2.4.2 Spin-Coating SU-8

The thickness of SU-8 film is dependent on several factors: the viscosity of the SU-8 used, the spin speed, and the total number of turns. The vendor of SU-8, MicroChem, provides some spin-coating curves for different SU-8 formulations, such as SU-8 5, SU-8 50, and SU-8 100. Some research labs have also developed their own spin-coat curves based on the particular equipment used. Figure 2.9 shows some typical spin-coating curves of SU-8.

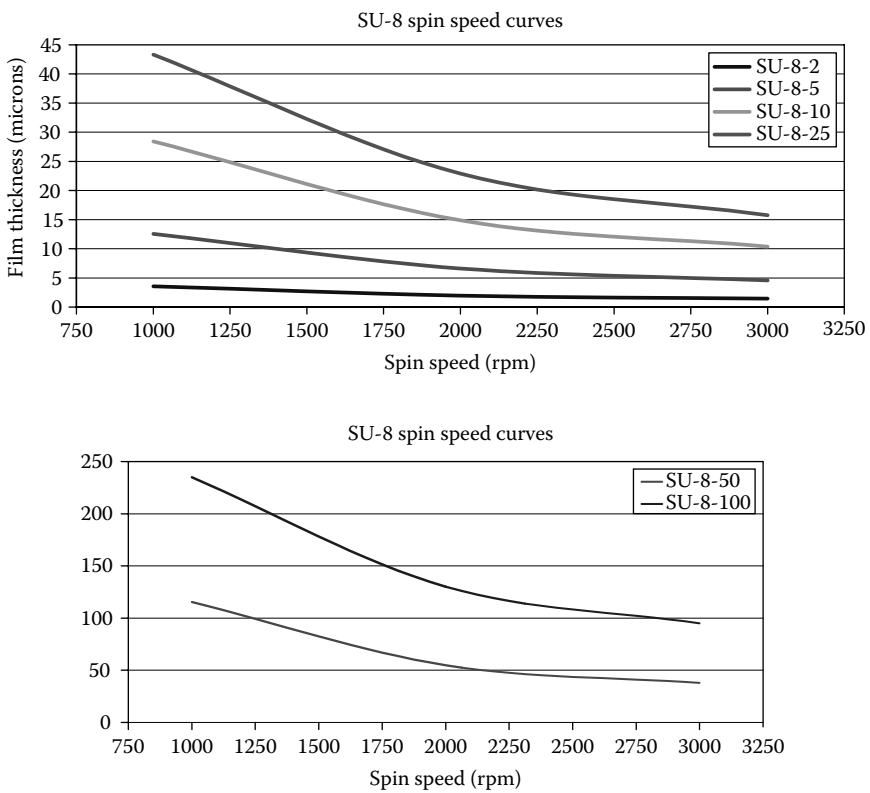

FIGURE 2.9
Selective SU-8 spin-speed vs. film thickness curve. (Courtesy of Mark Shaw, MicroChem Corp., Newton, MA.)

Bubbles formed during the spin-coating step may lead to reduced lithography quality. To eliminate bubbles in resist film, the substrate should be placed on a flat and horizontal plate for 2 to approximately 10 hours before prebake. This is an especially critical step for obtaining good quality of thick SU-8 film.

2.4.3 Soft Bake

The spin-coated sample needs to be soft baked to evaporate the solvent on a leveled hotplate or in convection ovens. The heat transfer condition and ventilation are different for the hotplate and the convection ovens, and the preferred soft baking times are therefore different as shown by the curves for measured soft baking times in Figure 2.10. Ramping and stepping the soft bake temperature is often recommended for better lithography results. The glass temperature of the unexposed SU-8 photoresist is about 50 to approximately 60°C. Figure 2.11 shows a typical soft-baking temperature curve used in our laboratory. This soft-bake process consists of multiple steps of ramping up, dwell, and ramping down. The total cooling time is about 8

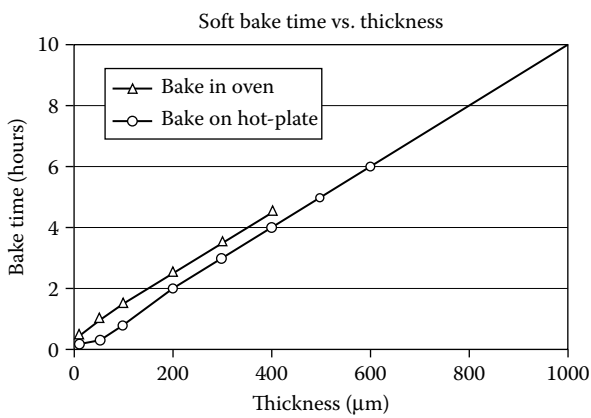

FIGURE 2.10
Soft bake time vs. SU-8 thickness.

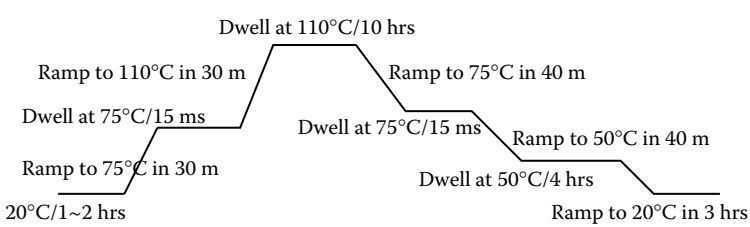

FIGURE 2.11
A selected soft bake profile for 1100 mm–thick SU-8 film.

to approximately 10 hours for a 1000 μm–thick SU-8 resist. For ultrathick SU-8 film (more than 1000 μm thick), a baking temperature of 110°C is used as shown in Figure 2.11. To improve the adhesion of the SU-8 film on substrate coated with Cr/Au film (as commonly used in the UV-LIGA process as the plating seed layer), a 110°C bake temperature is suggested instead of 96°C. At the same time, the bake time should be slightly reduced.

2.4.4 Exposure

A near UV (320 to 450 nm) light source is normally used for lithography of SU-8. As the wavelength of the light source increases, the absorbance of the light reduces and the transmission increases significantly. The transmission increases from 6% at $\lambda = 365$ nm to about 58% as the wavelength increases to 405 nm. SU-8 has high actinic absorption for wavelengths less than 350 nm, but is almost transparent and insensitive for above 400 nm wavelengths. Because of the high absorption of SU-8 for light with shorter wavelengths, a light source dominated by shorter wavelength components often results in overexposure at the surface of the resist and underexposure at the bottom part of the resist layer. This is the main reason that UV lithography of SU using an *i*-line-dominated light source tend to produce microstructures with T-topping geometric distortions. Thickness of the resist is another key parameter that dictates the required dosage of the exposure. Figure 2.12 shows two curves of required exposure dosage and the thickness of SU-8. MicroChem, the vendor of SU-8, advises that the user filter out the light with a wavelength lower than 350 nm to improve lithography quality. After filtering the light components with wavelengths shorter than 350 nm from the light source of the Oriel UV station used in our laboratory, with its spectrum as shown in Figure 2.6, the total exposure dosage ratio between the *i*-line and *h*-line are kept in a range of 1:7 to approximately 1:10 to achieve perfect vertical sidewalls, especially for the SU-8 resist with thickness around 1 mm. For lithography of a very thick resist, multiple exposures are required to avoid

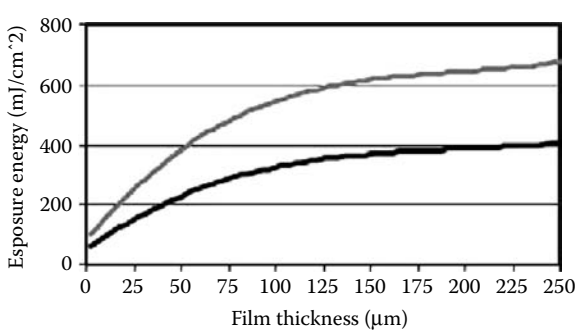

FIGURE 2.12
Exposure dosage vs. film thickness: the preferred exposure dosage should fall between the top and bottom curves. (Courtesy of Mark Shaw, MicroChem Corp., Newton, MA.)

overheating, scattering, and diffusion on the surface of the resist. Typically, exposures need to be separated in 20-second (or less than 400 mJ/cm^2 per time) intervals with 60-second waiting periods in between. For a highly reflective substrate, the effect of the reflection needs to be taken into account in estimating the total exposure time.

2.4.5 Postexposure Bake (PEB)

Postexposure bake (PEB) is performed to cross-link the exposed regions of the SU-8 resist. The cross-link, or the curing step of SU-8, can be achieved at room temperature. Postbaking at a raised temperature helps accelerate the polymerization process [20]. Figure 2.13 shows a typical PEB temperature profile. For resist thickness up to a few hundred micrometers, postbake at 96°C for 15 to approximately 20 minutes is required either on a hotplate or in a convection oven. SU-8's cross-link process may cause significant residual stress, which may cause cracks or debonding. In order to minimize possible residual stresses, wafer bowing, and cracking, rapid cooling from the PEB temperature should be avoided. For resist films with thicknesses more than 1000 micrometers, ramping the PEB temperature down from 96°C should take more than 8 hours. Another possible way to reduce postbake stress is to use lower PEB temperatures, such as 50°C or 55°C, but longer baking times. This method would result in much lower thermal stress in comparison with using a PEB temperature of 96°C.

2.4.6 Development

After exposure and postbake, the sample is then developed by SU-8 developer. Recommended development times can be found in the catalog provided by vendor of SU-8 or your lab's experiment data. The development process can be optimized based on the experiment's agitation rate, development temperature, and SU-8 resist processing conditions. After the sample is developed by SU-8 developer, it is sometimes dipped into a fresh SU-8 developer to rinse, then rinsed with isopropyl alcohol (IPA) for 3 to 5 minutes. If white spots can be observed in the IPA, the SU-8 is underdeveloped.

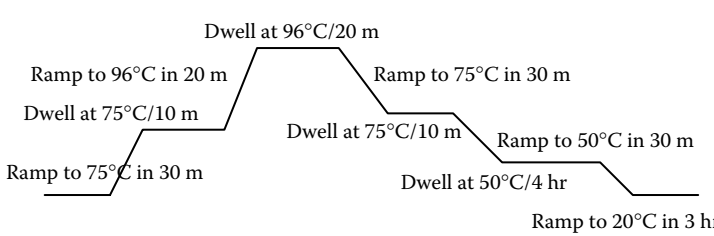

FIGURE 2.13
A possible temperature profile to be followed in PEB for 1100 μm–thick SU-8 film.

The sample needs to be immersed into SU-8 developer or rinsed with fresh SU-8 developer to further development. After the sample is completely developed, it needs to be rinsed using fresh IPA. If possible, avoiding a deionized (DI) water rinse is preferred. Finally, the sample is dried naturally or by nitrogen gas blow.

2.5 Tilted Lithography of SU-8 and Its Application

SU-8 is well suited for the fabrication of three-dimensional microstructures using tilted exposure. A variety of SU-8 resist structures, such as slope, trapezoids, dovetails, as well as various conical shapes, can be fabricated using tilted lithography. In recent years, we have fabricated micromixers [25], out-of-plane microlens [26–28], out-of-plane microlens arrays [30], fiber bundle couplers [31], and three-dimensional hydrofocus components [31].

Because of the refraction of light at the surface of the SU-8 resist, a light beam projected on the resist at an incident angle may propagate at a reduced refraction angle. Based on the refraction index of the SU-8 ($n = 1.668$ at $\lambda = 365$ nm, $n = 1.650$ at $\lambda = 405$ nm), the refraction angle can be approximately calculated to be 25.08° for the *i*-line with a 45° incident angle as shown in Figure 2.14. The critical angle is about 36.8° at 365 nm. If a larger refractive angle is needed, optical liquid and a coupling prism are used to compensate for the light refraction.

The working principle to achieve a bigger refraction angle for SU-8 lithography is shown in Figure 2.15. The positions of the prism, mask, SU-8, and the substrate are as shown in Figure 2.15.

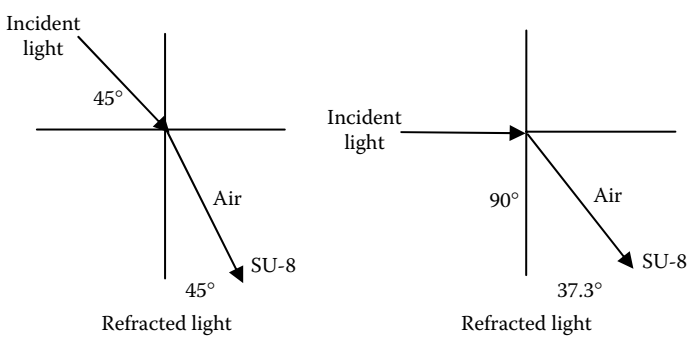

FIGURE 2.14
The refraction of the SU-8 resist may cause the projected light beam to bend over and therefore leading to reduce angle of the light projection. SU-8's refraction and the critical angle (critical angle is about 36.8° at 365 nm).

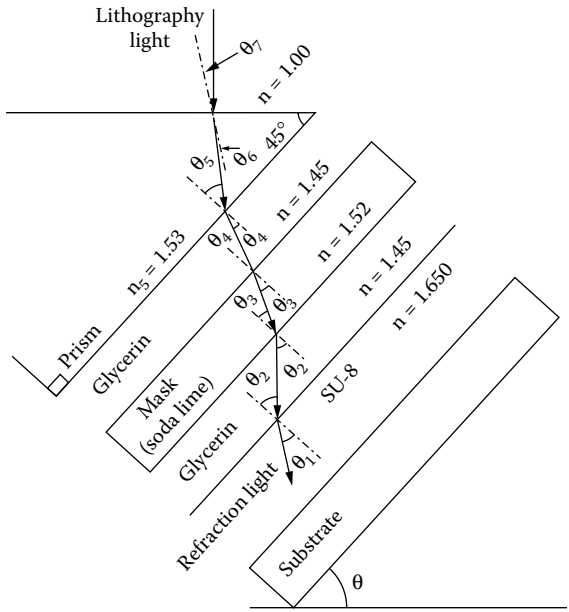

FIGURE 2.15
The working principle to obtain a bigger refraction angle inside SU-8.

If the angle at which the light enters SU-8 resist needs to be θ_1, from Snell's law,

$$n_1 \sin\theta_1 = n_2 \sin\theta_2 = n_3 \sin\theta_3 = n_4 \sin\theta_4 = n_5 \sin\theta_5, \tag{2.6}$$

θ_5 can be obtained as

$$\theta_5 = \sin^{-1}\left(\frac{n_1 \sin\theta_1}{n_5}\right). \tag{2.7}$$

From the geometry relationship, we know

$$\theta_6 = \theta_5 - 45° = \sin^{-1}\left(\frac{n_1 \sin\theta_1}{n_5}\right) - 45°. \tag{2.8}$$

From Snell's law, θ_7 can be obtained:

$$\theta_7 = \sin^{-1}\left(\frac{n_6 \cdot \sin\theta_6}{n_7}\right) = \sin^{-1}\left\{\frac{n_6}{n_7} \cdot \sin\left[\sin^{-1}\left(\frac{n_1 \sin\theta_1}{n_5}\right) - 45°\right]\right\}. \tag{2.9}$$

$$\theta = 45° + \theta_7 \tag{2.10}$$

The substrate therefore needs to be kept at $\theta = 45° + \theta_7$ with the horizontal level (because the light beam in the UV station is always in the vertical direction) to completely compensate for the refraction at the interface to obtain a 45° refractive angle inside the SU-8 photoresist.

2.5.1 Micromixer/Reactor

As an example of tilted lithography of SU-8, we present a novel passive micromixer/reactor based on arrays of spatially impinging microjets, which takes a three-dimensional approach in design and is based on a fabrication process using UV lithography SU-8 photoresist [25].

To mix microvolumes of fluid samples in microfluidic systems is always a challenging task. Because the flow in all microfluidic systems is laminar and has a low Reynolds number, diffusion is the dominant mechanism. Various efforts have been made to improve the mixing process by introducing geometric irregularities in inflow channels to create localized eddies and turbulent flows. Efforts have also been made to use special actuation mechanisms to disturb the flow with such noncontact measures as ultrasound waves. Because it is very difficult to obtain high mixing efficiency with a diffusion mechanism, some reported efforts used active disturbance to create turbulence in the microfluidic systems. An obvious approach to increased diffusion efficiency is to maximize the effective interfacial areas of the two samples to be mixed. According to the scaling law, the most effective way to maximize the effective surface area of liquid is to convert it into plumes of stream. This is the approach we have adopted in our design of the micromixer. The micromixer/reactor has a simple structure and significantly boosts the mixing efficiency by increasing the interfacial contact with the impinging plumes from two opposite arrays of more, but smaller-sized, micronozzles.

The micromixer/reactor is based on large arrays of spatially impinged microjets mixing. The schematic design for the micromixer/reactor is shown in Figure 2.16. Two arrays of micronozzles are in opposite directions. The micronozzles are parallel with the substrate plane. There are two possible ways to arrange the opposite arrays of nozzles: directly opposite orientations or with a designed offset. The two sample fluids are delivered to inlet A and inlet B, respectively. Then they are converted into plumes of streams by the large micronozzle array and driven into the mixing chamber. The mixing processing is three-dimensional with multiplayer spatially impinged jet arrays. This helps to enhance the Reynolds number; increase the effective interfacial areas; convert a higher percentage of the kinetic energy into microscopic molecular

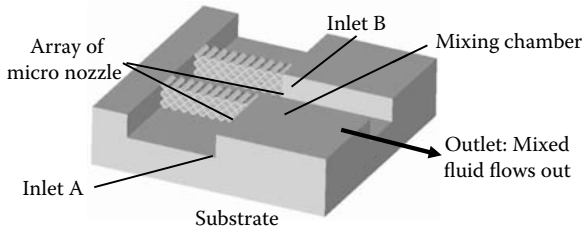

FIGURE 2.16
Schematic design diagram of the micromixer/reactor.

motion, thereby effectively boosting the eddies; increase the Reynolds number in the micromixer chamber; and improve the diffusion effects for mixing.

The Reynolds number at the input channels just before the liquid enters the nozzles is at a very low level (about 0.0002), the micromixer/reactor based on a spatially impinged jet array with an offset can still locally mix the two flows in less than one second. The pressure drop of this micromixer/reactor is about 200 Pa. By increasing flow eddies generated and increased interfacial contacts, the mixers based on arrays of impinging jets with offset have better mixing efficiency. A higher possibility of microjets traveling to the opposite side of the chamber to achieve better interfacial contact with the incoming jets to be mixed gives the mixer with a narrow mixing chamber a higher mixing efficiency. This micromixer/reactor can be easily integrated with other microfluidic components or microfluidic channels for various biochemical, biological, and chemical applications.

The micromixer was fabricated using UV lithography of SU-8. Two optical masks were used: one was used to fabricate the large arrays of micronozzles by tilted exposure; the other was used to form the inlet and outlet channels and sidewalls. As shown in Figure 2.17a, when two arrays of narrow light beams are projected on the photoresist, the intersection forms an array of micronozzle channels. Conventional contact exposure was used to fabricate the inlet and outlet flow channel sidewalls.

In the fabrication process, the substrates were spin-coated with SU-8 100 negative photoresist at 400 rpm for 1100 μm thickness and baked at 110°C for 10 hours, then cooled down to room temperature over an 8-hour time interval. Following exposure, the substrates were postbaked at 96°C for 25 minutes and cooled down to room temperature again over another 8-hour interval. Then samples were developed with megasonic agitation. Figure 2.17b shows a SEM image of the bottom part of a prototype mixer.

A top cover glass was then bonded to it and the inlet and outlet with flow connectors were sealed. The experiment, as shown in Figure 2.18, tested by mixing a fluorescent dye solution and DI water, shows the high mixing efficiency. The micromixer with offset can locally mix the two test solutions in less than one second.

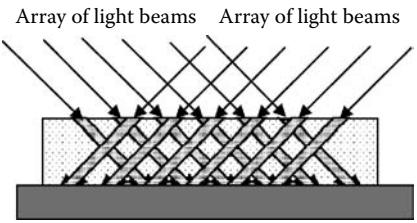

(a)

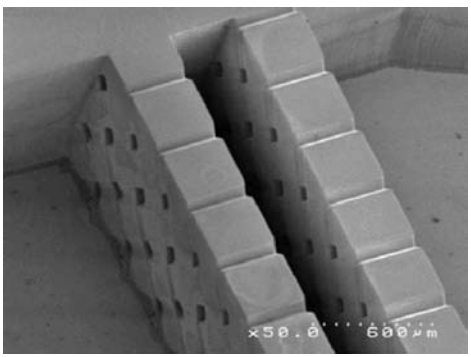

(b)

FIGURE 2.17
Schematic fabrication diagram and SEM image of the fabricated micromixer/reactor. (a) Lithography principle. (b) SEM image of the prototype mixer.

2.5.2 Three-Dimensional Hydrofocus Component for Microcytometer

Flow cytometric devices are very important for biomedical research and clinical diagnostics. The labeled cell is driven to flow through a nozzle so that light scattering or fluorescence measurements can be used for analyses. Many research efforts have been made to develop microcytometers to reduce the device and sample sizes, develop low-cost and single-use disposable devices, and to improve device portability along with low consumption of sample and buffer fluids, and to reduce the biohazard risk level.

The principle of hydrofocusing in a microchannel is based on laminating cells with sheath flow [31]. A small volume of sample flow is injected into a much larger volume of sheath fluid. Both the sheath flow and sample flow require a small Reynolds number. Most of the reported hydrofocusing units for microcytometers based on sheath flow are two-dimensional, which only focuses the samples in the same plane as the substrate. A truly three-dimensional hydrofocusing component can focus the cells along the core stream to flow with an almost uniform velocity.

Based on the three-dimensional hydrofocusing requirements and the microfabrication limitations of SU-8 UV lithography, a three-dimensional hydrofocusing unit for microflow cytometry was designed as shown by the schematic diagram in Figure 2.19. There are three inlets for the hydrofocusing

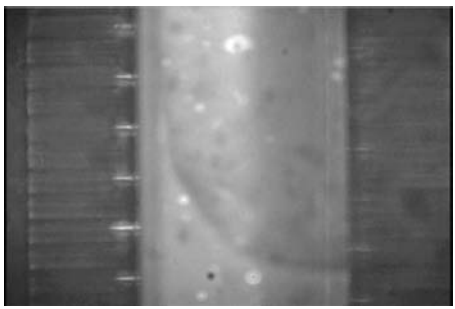

(a)

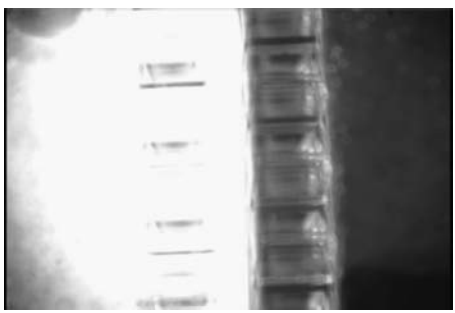

(b)

FIGURE 2.18
Test results for two types of micromixer. (a) Micro-mixer with direct opposition: photography taken 2 mm downstream along the outlet channel. (b) Micro-mixer with offset: 5/6 second locally mixed.

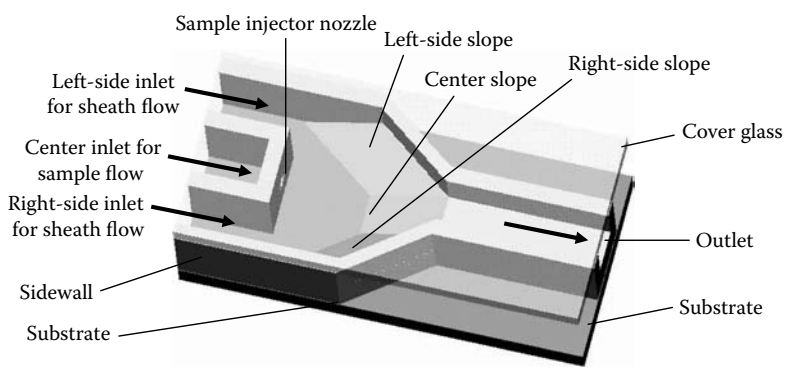

FIGURE 2.19
A schematic diagram of the three-dimensional hydrofocusing unit.

microfluidic unit. Left-side and right-side inlets are for the sheath flow, while the center inlet is for the sample flow. In the center of the end of this sample flow inlet, there is a diamond-shaped nozzle with a width of 100 μm. There are three slopes formed by tilt-exposed, cross-linked SU-8 polymer in which the center slope configured to a 30° angle with the substrate. The flat covering

glass and sloped bottom help focus the flow upward to a central region in the direction perpendicular to the substrate. The left-side slope, right-side slope, and the two sloped sidewalls perpendicular to the substrate assist in achieving flow to the central region in a horizontal direction [31].

In the fabrication process, all the slopes and the sample injection holes were fabricated using tilted exposure. A total of three exposures were required: (1) a 60° angle tilt exposure to achieve slopes having a 30° angle with the substrate, (2) a 45° angle tilt exposure to obtain a suspended sample injection nozzle in the center position of the sample inlet end, and (3) a conventional contact exposure to produce all of the SU-8 sidewalls.

The fabrication procedures were as follows: clean the Si or glass substrate; spin-coat SU-8 100 photoresist to obtain a 500 μm–thick resist layer; soft bake the sample; conduct a 60° tilted exposure of SU-8 with the help of a prism and optical liquid for refraction compensation to obtain slopes tilted at 30° with the substrate; postbake the sample; spin-coat SU-8 100 photoresist to obtain the second 500 μm–thick resist layer; prebake the sample; use a 45° angle tilted exposure of the SU-8 with a correction prism and optical liquid to obtain a suspended sample injector nozzle in the center of the sample inlet end; expose all of the SU-8 sidewalls; postbake the sample; develop with SU-8 developer; bond cover glass, seal inlet and outlet tubes. Figure 2.20 shows three SEM images of a prototype hydrofocusing unit fabricated using the tilted lithography method.

The three-dimensional focusing function of the prototype hydrofocusing unit was tested using a fluorescent dye solution. The images in Figure 2.21 show experimental results that clearly demonstrated the three-dimensional hydrofocusing function. The main advantages of this polymer hydrofocusing

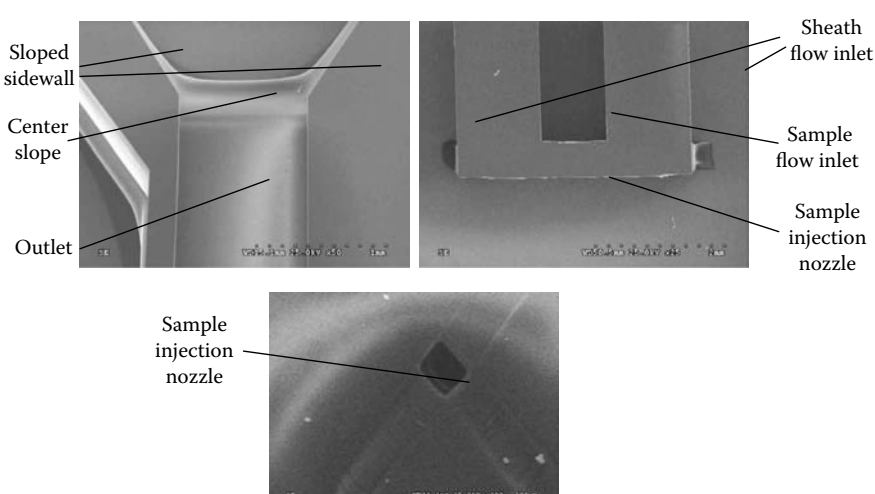

FIGURE 2.20
SEM pictures for the three-dimensional hydrofocusing components.

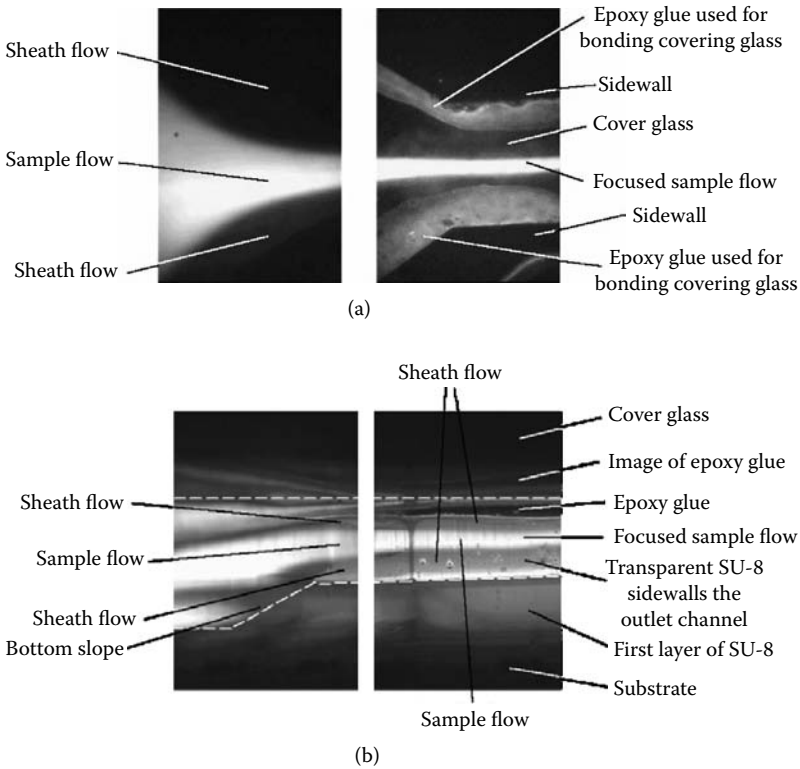

FIGURE 2.21
Three-dimensional hydrofocus function. (a) Top-view image showing the hydrofocusing function in horizontal plane. (b) Side-view image showing the focusing function in vertical direction.

microstructure include its easy fabrication and its ease of integration with other polymer microfluidic and micro-optical components and subsystems.

2.5.3 Out-of-Plane Polymer Refractive Microlens, Microlens Array, Fiber Bundle Aligner

Integrated free-space optical benches are widely used in military, telecommunications, metrology, biochemistry, and so forth. Microlens and microlens arrays are the important components in the integrated micro-optical system. There are two kinds of conventional methods for fabricating the microlens or microlens array. One is based on the surface tension needed to form the microlens, such as reflow photolithographyed photoresist, inject polymer drop, and press polymer through micro holes. Another is based on chemical or physical removal of materials, such as ion-milling, dry-etching, and wet-etching.

The optical axis of microlens arrays fabricated with conventional approaches is normally in the same plane as the substrate because the fabrication process

is based on regular lithography and surface technologies. Integrated optical systems often require the lenses' principal planes to be perpendicular to the substrate on which the system is constructed. One approach is to use a flexible hinge [32,33]. Another is using microstereolithography [34,35].

We reported a method to obtain a quasiparabolic surface for an out-of-plane prealigned polymer microlens [25–29]. This out-of-plane polymer microlens can be easily prealigned with other optical components with no additional adjustment and assembly required, and dramatically reduce the running cost and improve the quality and performance of the optical system. The other optical components also can be fabricated by direct lithography of SU-8. All of the optical components are prealigned with the same optical axis in mask design, and no changes and adjustments between the mask and the photoresist are needed during lithography.

The basic fabrication principle for out-of-plane, prealigned polymer refractive microlenses and microlens arrays can be explained using the schematic diagrams shown in Figure 2.22. The intersection region as shown in Figure 2.22a was double exposed and formed the lens base. The intersected region included four pieces of cylindrical surface with sharp edge lines as shown in Figure 2.22b. The development rate for the unexposed SU-8, single-exposed SU-8, and double-exposed SU-8 are different. By careful control of the exposure dosage and the optimized development time, the double-exposed region formed the microlens or microlens array as shown in Figure 2.22c.

Figure 2.23a shows an SEM image of a sample microlens array fabricated using this method. Figure 2.23b shows the focus function of the out-of-plane microlens and microlens array.

A simple application of the out-of-plane prealigned microlens and microlens array [29] is to design and fabricate an integrated fiber coupler and fiber bundle couplers. The substrate coated with 1100 μm–thick SU-8 100 was soft

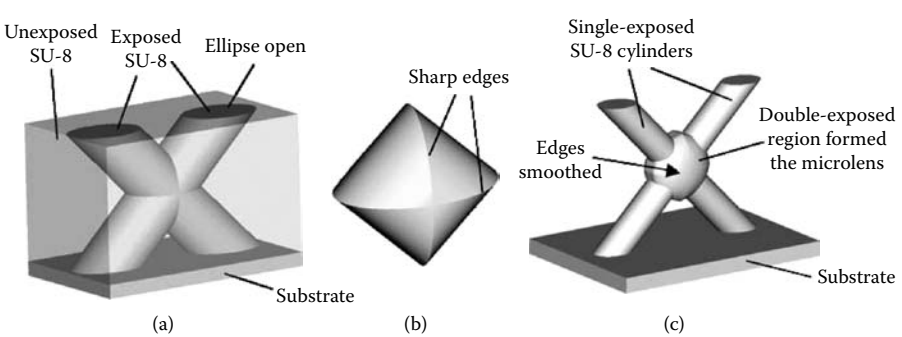

FIGURE 2.22
Combining microstereolithography and thick resist UV lithography for 3D microfabrication. (a) Two cylindrical beams used to expose the negative resist. Exposed regions are kept and the unexposed regions removed in development. (b) The intersection region formed by two cylindrical beams is doubled-exposed and formed the lens base. (c) After development, the sharp edges were rounded and a smoother surface profile is obtained.

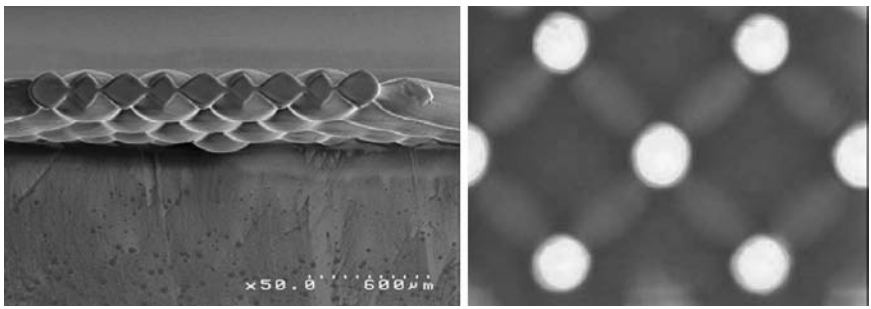

FIGURE 2.23
(a) SEM image of an out-of-plane microlens array. (b) Microlens array and measured focus pads of the out-of-plane microlens and microlens array.

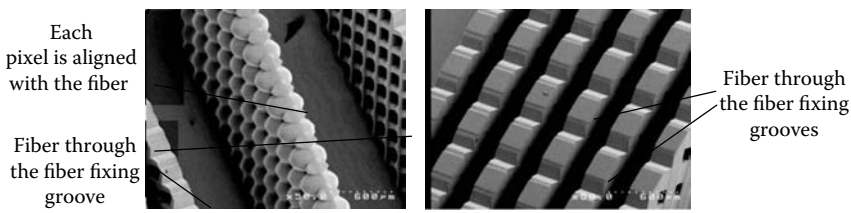

FIGURE 2.24
SEM images of fiber bundle coupler. Each pixel of the microlens array and fiber-fixing grooves are pre-aligned together.

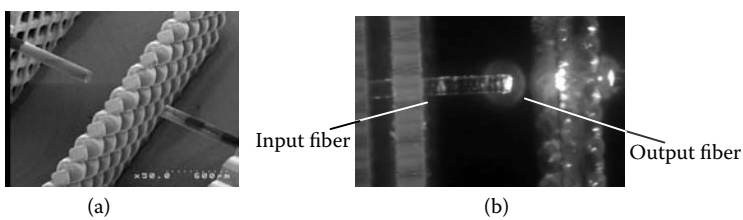

FIGURE 2.25
.(a) SEM image showing one pair of optical fibers inserted in a prototype fiber bundle coupler; (b) optical image of the fiber coupler with light supplied.

baked and tilt exposed for the biconvex microlens or microlens array with optimized exposure dosage. After the exposure for the biconvex microlens or microlens array, a shield mask was placed on the optical mask to cover the regions for the biconvex microlens or microlens array, and exposure for fiber fixing grooves with different exposure dosage was conducted. The sample was then postbaked and developed. The exposed regions of SU-8 formed the microlens array and fiber-fixing grooves as shown in Figure 2.24 [30]. Figure 2.25 shows a photograph of the fiber coupler with just one pair of fibers inserted and light from a laser diode (wavelength of 635 nm) supplied to the fiber pair [30].

2.6 Conclusions

In this chapter, we have presented some detailed discussions on optical lithography of SU-8. Detailed processing tips have been provided. In addition, we have also presented some theoretical and experimental studies on air gap effects on the lithography quality of ultrathick SU-8 resist and the method to compensate for it. The combination effect of diffraction compensation, wavelength selection, and one-direction agitation development is present by ultra-high-aspect-ratio SU-8 microstructures. SU-8 tilted lithography and its application are also presented. Some representative applications of UV lithography of SU-8 in microfluidics and micro-optics have also been presented.

The polymer out-of-plane microlens can be fabricated using direct tilted-lithography of SU-8 resist. The microlens array fabricated this way is perpendicular to the substrate without requiring any assembly or adjustment, and can be designed to any prealigned positions. With optical components prealigned in mask design, it is possible to have all components integrated onto a single platform for an optical bench without any assembly or adjustment required. Unique microfluidic components and systems can also be made using the direct lithography method as demonstrated by the micromixer and the hydrofocusing unit for the microflow cytometer presented in this chapter.

References

[1] N. LaBianca, and J. Delorme, High aspect ratio resist for thick film applications, in *Proceedings of the International Society for Optical Engineering* (*SPIE*), 2438, 846–852, 1998.

[2] H. Lorenz, M. Despont, P. Vettiger, and P. Renaud, Fabrication of photoplastic high-aspect ratio microparts and micromolds using SU-8 UV resist, *Microsyst. Technol*. 4, 143–146, 1998.

[3] K. Lee, N. LaBianca, S. Rishton, and S. Zohlgharnain, Micromachining applications for a high resolution ultrathick photoresist, *J. Vac. Scien. Technol*. B 13, 3012–3016, 1995.

[4] H. Lorenz, M. Despont, N. Fahrni, N. Labianca, P. Vettiger, and P. Renaud, EPON SU-8: A low-cost negative resist for MEMS, in *Proc. of Micro Mechanics Europe '96*, Barcelona, 32–35, 1996.

[5] H. Lorenz, M. Laudon, and P. Renaud, Mechanical characterization of a new high-aspect-ratio near UV-photoresist, *Microelec. Engin*. 41/42, 371–374, 1998.

[6] J. Williams and W. Wang, UV-LIGA fabrication of electromagnetic power microrelays, presented at the International Symposium on Test and Measurement (ISTM/2001), Shanghai, China, June 2001.

[7] C. Oropeza, K. Lian, and W. Wang, "Fracture toughness study on LIGA fabricated microstructures," presented in *Micromachining and Microfabrication*, Photonics West, San Jose, California, January 2003.

[8] D. E. Lee, H.-P. Chen, S. Soper, and W. Wang, An Electrochemical Micropump and Its application in a DNA Mixing and Analysis System, presented in *Micromachining and Microfabrication*, Photonics West, San Jose, California, January 2003.

[9] R. Yang, S. J. Jeong, and W. Wang, UV-LIGA microfabrication of a power relay based on electrostatic actuation, presented in *Micromachining and Microfabrication*, Photonics West, San Jose, California, January 2003.

[10] K.-H. Hang, W. Wang, M. C. Murphy, and K. Lian UV-LIGA microfabrication and test of an AC type micropump based on magnetohydrodynamic (MHD) principle, in *Proceedings of the SPIE Symposium on Microfabrication*, Santa Clara, CA, 20–22 September, 2000.

[11] Y. Konaka and Mark G. Allen, Single and multi-layer electroplated microaccelerometers, in *Proceedings of the IEEE Micro Electro Mechanical Systems (MEMS)*, 168–173, 1996.

[12] H. Lorenz, M. Despont, N. Fahrni, J. Brugger. P. Renaud, and P. Vettiger, High aspect ratio ultrathick, negative-tone near-UV photoresist and its applications for MEMS, *Sensors and Actuators* A, A 64, 33–39, 1998.

[13] L. Dellmann, S. Roth, C. Beuret, L. Paratte, G.-A. Racine, H. Lorenz, M. Despont, P. Renaud, P. Vettiger, and N. de Rooij, Two steps micromoulding and photopolymer high-aspect ratio structuring for applications in piezoelectric motor components, *Microsyst. Technol*. 4, 147–150, 1998.

[14] H. Chang and Y. Kim, UV-LIGA process for high aspect ratio structure using stress barrier and C-shaped etch hole, *Sensors and Actuators A: Physical*, 84, 342–350, 2000.

[15] Z. Ling, K. Lian, and L. Jian, Improved patterning quality of SU-8 microstructures by optimizing the exposure parameters, *Proceedings of the International Society for Optical Engineering* (*SPIE*), 3999, P1019–1027, 2000.

[16] J. O'Brien, P. J. Hughes, M. Brunent, et al., Advanced photoresist technologies for microsystems, *J. Micromech. Microeng*., 11, 353–358, 2001.

[17] J. Zhang, K. L. Tan, G. D. Hong, L. J. Yang, and H. Q. Gong, Polymerization optimization of SU-8 photoresist and its applications in microfluidic systems and MEMS, *J. Micromech. Microeng*., 11, 20–26, 2001.

[18] C. Lin, G. Lee, B. Chang, and G. Chang, A new fabrication process for ultrathick microfluidic microstructures utilizing SU-8 photoresist, *J. Micromech. Microeng*., 12, 590–597, 2002.

[19] P. M. Dentinger, K. L. Krafcik, K. L. Simison, R. P. Janek, and J. Hachman, High aspect ratio patterning with a proximity ultraviolet source, *Microelectronic Engineering*, 61–62, P1001–1007, 2002.

[20] J. Williams and W. Wang, Study on the postbaking process and the effects on UV lithography of high aspect ratio SU-8 microstructure," *J. Microlith., Microfab., Microsyt.*, in press.

[21] R. Yang and W. Wang, Application of optical refractive index liquid and wavelength selection for ultra-high-aspect-ratio UV-lithography of thick SU-8 resist," *Sensor and Actuator B: Chemical*, 110/2, 279–288, 2005.

[22] Y. J. Chuang, T. G. Tseng, and W. K. Lin, Reduction of diffraction effect of UV exposure on SU-8 negative thick photoresist by air gap elimination, *Microsystem Technologies*, 8, 308–313, 2002.

[23] E. Reznikova, V. Namov, and J. Mour, Deep photo-lithography characterization of SU-8 resist layers, *Microsystem Technologies,* 11, 4–5, 282–291, 2005.

[24] S.J. Lee, W. Shi, P. Maciel, and S.W. Cha, Top-edge profile control for SU-8 structural photoresist, in *Proceedings of 15th Biennial University/Government/Industry Microelectronics Symposium*, 389–390, June 30–July 2, 2003, Boise, ID.

[25] R. Yang, J. D. Williams, and W. Wang, A rapid micro-mixer/reactor based on arrays of spatially impinging micro-jets, *Journal of Micromechanics and Microengineering*, 14, 10, 1345–1351, October 2004.

[26] R. Yang and W. Wang, Fabrication of out-of-plane SU-8 refractive microlens using directly lithography method, SPIE Photonics West, San Jose, CA., *Proceedings of the International Society for Optical Engineering* (*SPIE*), 5346, 2004, 151–159, 2004.

[27] R. Yang and W. Wang, Out-of-plane polymer refractive microlens fabricated based on direct lithography of SU-8, *Sensor and Actuators A: Physical*, 113, 1, P71–77, June 15, 2004.

[28] R. Yang and W. Wang, Numerical and experimental study on an out-of-plane pre-aligned refractive microlens fabricated using UV lithography method, *Optical Engineering*, 43, 12, 3096–3103, December 2004.

[29] R. Yang, S. Soper, and W. Wang, Out-of-plane microlens array fabricated using ultraviolet lithography," *Applied Physics Letter*, 86, 16, 161110-1–161110-3, April 2005.

[30] R. Yang, S. A. Soper, and W. Wang, Microfabrication of pre-aligned fiber bundle couplers using ultraviolet lithography of SU-8, *Sensors and Actuators, A*, 127, 1, 123–130, February 28, 2006.

[31] R. Yang, D. L. Feeback, and W. Wang, Microfabrication and test of three-dimensional polymer hydro-focusing unit for flow cytometry applications, *Sensors and Actuators A: Physical*, 118, 2, 259–267, February 2005.

[32] C.R. King, L.Y. Lin, and M.C. Wu, Out-of-plane refractive microlens fabricated by surface micromachining, *IEEE Photonics Technology Letters*, 8, 10, 1349–1351, October 1996.

[33] Yong W. Yi and Chang Liu, Assembly of micro optical components using magnetic actuation, *Sensors and Actuators A*, 78, P205–211, 1999.

[34] K. Ikuta, S. Maruo, and S. Kojima, New micro stereo lithography for freely movable 3D micro structure, *Proceedings of MEMS98*, Heidelberg, Germany. 1998.

[35] A. Bertsch, H. Lorenz, and P. Renaud, 3D microfabrication by combining microstereolithography and thick resist UV lithography, *Sensors and Actuators: A-Physical*, 73, 1–2, 14–23, 1999.

3

The LIGA Process: A Fabrication Process for High-Aspect-Ratio Microstructures in Polymers, Metals, and Ceramics

Jost Goettert

CONTENTS

3.1 The LIGA Process: A Brief History

The LIGA process was initially developed in the late 1970s at the Forschungszentrum Karlsruhe (FZK) as an alternative way to produce very small slotted nozzles for uranium isotope separation [1,2]. These separation nozzles were to be made from metal, with small lateral dimensions of a few micrometers, and several hundred micrometers tall. A large number of them had to be arranged in a cascaded array in order to achieve a high separation yield. While silicon-based MEMS technologies allow batch production of structures with small lateral dimensions, it is the LIGA process—a combination of deep-etch x-ray lithography with synchrotron radiation (LI), electroforming (G = Galvanoformung [German]), and molding (A = Abformung [German])—that was proposed and developed to build these structures.

From its beginning LIGA was in competition with, but also used complementary to, commonly practiced micropatterning techniques such as wet-chemical etching of single-crystalline silicon [3], or dry-etching processes by means of low-pressure plasma [4]. Typical structure geometries are similar, but material choices, including polymers, metals, and ceramics, as well as production methods, are significantly different. Materials for LIGA microstructures can meet a broad range of application requirements, for example, optical transparency, mechanical stiffness and hardness, electrical conductivity, and magnetic properties, and offer additional design freedom to MEMS system engineers [5]. As a consequence, hybrid systems such as millirotational motors, linear motors, micropumps, photonic systems, and various analytical devices assembled with high-precision LIGA components, are currently being developed and introduced into the marketplace [6–12].

The goal of this text is to briefly introduce the reader to the technology basics of the three main LIGA process steps, demonstrate the properties of LIGA microstructures, and provide some examples used in various MEMS applications.

3.2 The LIGA Process: A Brief Introduction

The three main steps of the LIGA process are:

- *Deep x-ray lithography* (DXRL) typically using x-ray photons emitted from a synchrotron source to shadow print microstructures from an x-ray mask in an extremely precise manner into thick resist layers; the actual pattern is produced in a subsequent wet-chemical developing process.
- *Electroplating* is employed to fabricate complementary metal microstructures used either as an end product or mold insert.
- *Molding techniques* such as injection or reaction molding and hot embossing are used to replicate the microstructures in a cost-effective way suitable for mass production in a great variety of materials.

A typical fabrication sequence is illustrated in Figure 3.1 and described in the following text. The absorber pattern of an x-ray mask is transferred into a thick resist layer by shadow printing with synchrotron radiation (step 1). The thick resist layer is applied onto a conductive substrate used as a cathode in the electroplating process. Polymethylmethacrylate (PMMA) or Plexiglas®, a positive resist, and SU-8 [13], an epoxy-based negative resist are commonly used as x-ray resists. Within the irradiated sections, the x-ray photons are absorbed and lead to radiation-induced changes of the resist materials. For example, in PMMA resist, main-chain scissions occur reducing the molecular

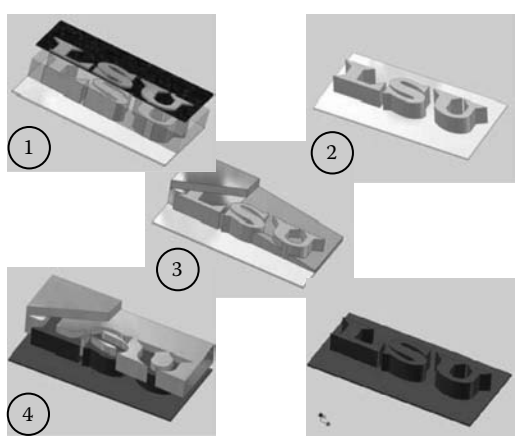

FIGURE 3.1
Typical sequence for the production of microstructures using the LIGA process. The primary pattern is generated by deep x-ray lithography using synchrotron radiation (1) and wet chemical development (2). Next, electroplating typically manufactures metal microstructures as a mold insert (3). Replication techniques (4) such as injection molding or hot embossing enable cost-effective mass production of LIGA parts (5) in a variety of materials.

weight of the irradiated material so that it can be selectively removed in an appropriate developer (step 2). By means of electroplating of metals, including copper, nickel, and nickel alloys, the complementary microstructure pattern is grown from the conductive substrate (step 3). This process can be terminated at the height of the resist template resulting in metal microstructures, or continued up to several millimeters in height forming a massive metal block. After stripping the remaining PMMA resist and further polishing and machining, this block can be used as mold insert for replicating the microstructures into polymers or ceramic materials by employing replication techniques including reaction injection molding, injection molding, or hot embossing (step 4) resulting in a replicated microchip as the final product (step 5).

3.3 Deep X-Ray Lithography Process

Employing x-ray photons for patterning microstructures is, in principle, similar to the use of UV light. However, light source, mask, and resist materials, as well as light–matter interaction are significantly different and will be briefly discussed in the following paragraphs.

3.3.1 Synchrotron Light, Beamlines, and Scanner

In order to cost-effectively use x-rays for patterning of microstructures, a suitable light source like a synchrotron is required. In a synchrotron, charged particles forced onto a circular orbit and traveling nearly at the speed of light are generating a continuous radiation spectrum, so-called synchrotron radiation, ranging from the infrared to the hard x-ray regime [14]. Synchrotron radiation forms a homogeneous narrow fan in the direction of propagation with a Gaussian-shaped profile perpendicular to it.

Synchrotron radiation is a powerful tool for many fields in basic and applied science including physics, chemistry, and biology as well as in microengineering, and a number of dedicated synchrotron light sources have been built and are operated serving the growing demands of the scientific community [15].

Table 3.1 summarizes the basic synchrotron radiation properties and the interested reader will find further information about this powerful scientific tool in [14].

The spectrum and total emitted power are defined by the characteristics of the source, such as maximum electron energy (E) and electron current (I), radius of curvature (r_0) of the bending magnets, and distance of the experiment to the source point. The spectrum of a synchrotron light source can be qualified by the characteristic energy (E_c) or corresponding wavelength (λ_c)

TABLE 3.1

Important Properties of Synchrotron Radiation

Continuous light spectrum ranging from the infrared to the hard x-rays
High intensity
High degree of collimation (nearly parallel light)
Clean environment—light is generated inside an ultrahigh vacuum system
High stability of intensity and source position ensuring predictable experimental parameters
Long beam lifetime (more than 10 hours) allowing experiments with quasi-constant conditions
Well-defined structure enabling time-resolved spectroscopy and imaging experiments

that describes the photon energy at which the power spectrum is divided in half. The basic properties of the light source can be calculated from Equations 3.1 through 3.3 [16]:

Total energy loss per revolution

$$P[kW] = 88.5 \frac{E^4[GeV]}{r_0[m]} I[A] \tag{3.1}$$

Characteristic energy and wavelength, respectively, of the emitted synchrotron spectrum

$$E_c[eV] = 2218 \frac{E^3[GeV]}{r_0[m]}, \quad \lambda_c[\text{Å}] = 5.59 \frac{\mathrm{r_0[m]}}{\mathrm{E^3}[GeV]} \tag{3.2}$$

Vertical opening angle of the emitted light cone

$$\Psi \sim \frac{1}{\gamma} = \frac{m_0 c^2}{E} = 5.1x10^{-4} \frac{1}{E[GeV]} \tag{3.3}$$

For example, using Equation 3.3 the vertical beam width for the CAMD (Center for Advanced Microstructures and Devices at Louisiana State University (LSU) in Baton Rouge, Louisiana) storage ring (electron energy = 1.3 GeV) is calculated to approximately 0.4 mrad resulting in a typical vertical Gaussian intensity distribution of 4 mm full width half maximum (FWHM) at the mask-resist plan at a distance of approximately 10 m from the source point.

In the 1970s, the use of synchrotron radiation as a short wavelength light source was already being intensively discussed for lithographic patterning of small microelectronic circuits [17,18]. X-ray lithography was a serious contender for the next generation lithography (NGL) and dedicated compact synchrotron light sources like HELIOS 1 [19] designed by Oxford Instruments were built and operated successfully [17]. In the early 1980s a second property of x-rays—their large penetration depth into matter—was then

considered for patterning of tall structures using deep x-ray lithography (DXRL) shadow printing [20]. This initial effort grew to the point that today a number of dedicated synchrotron radiation facilities worldwide provide easy access and sufficient beamtime for many users from academia and industry, enabling continuous process improvement and commercial use [21–24].

CAMD at LSU in Baton Rouge, LA, is one of these dedicated synchrotron radiation facilities with a strong program in LIGA technology [25]. The ring delivers light from 8 bending magnets as well as one insertion device—a 7-Tesla superconductive wiggler—to its users, and four microfabrication beamlines offer a large variety of patterning opportunities using soft and hard x-rays. The exposure spectra for the bending magnet and wiggler sources are shown in Figure 3.2, representing typical light spectra used for x-ray lithography.

Figure 3.3 illustrates the schematic setup of an x-ray micromachining beamline at a synchrotron light source. The ultrahigh vacuum x-ray beamline is directly attached to the vacuum system of the electron storage ring. A number of safety components including gate valves, a fast-closing shutter, and photon- and Bremsstrahlungs-shutters ensure both a vacuum- and radiation-safe operation of the beamline. The beamline is terminated by an exposure station or x-ray scanner. The x-ray scanner in its simplest design consists of a vacuum chamber and houses a linear motion stage that moves the mask or substrate assembly vertically across the narrow, collimated synchrotron beam. By using

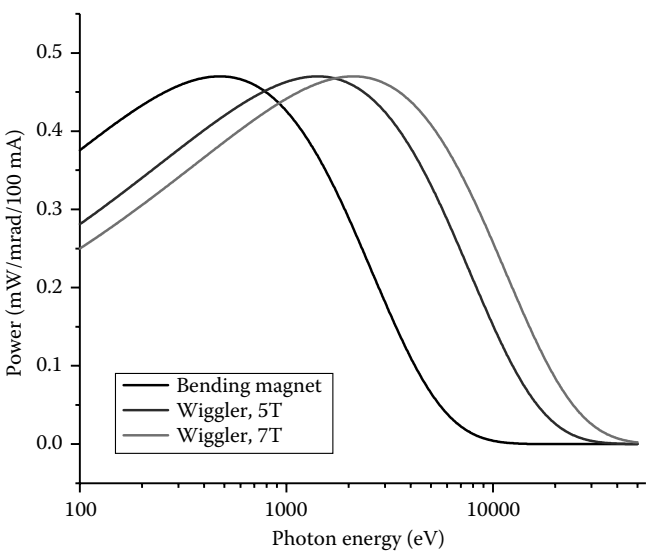

FIGURE 3.2
Power output for an average current of 100 mA as a function of photon energy for different CAMD source points and wiggler operating conditions. The low energy part of the "white spectra" is typically absorbed by a vacuum window made from beryllium resulting in photon energies of the exposure spectrum ranging from 2 keV to 40 keV.

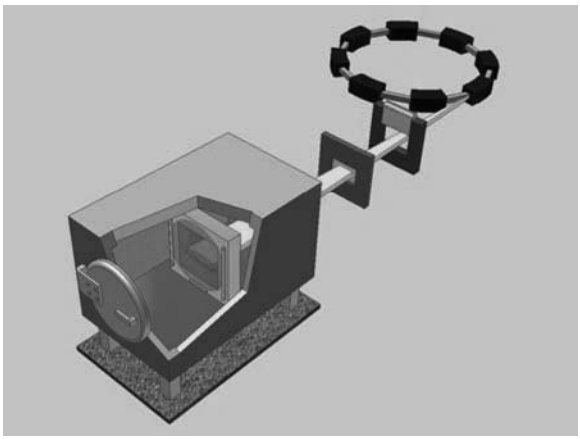

FIGURE 3.3
Schematic of an x-ray beamline attached to an electron storage ring. At the end of the beamline, an exposure station or x-ray scanner houses a linear motion stage carrying the mask and substrate assembly perpendicular or at a desired angle across the synchrotron beam.

this scanning method, a uniform dose deposition across the entire mask field of up to 100 mm is ensured. Typically, the ultrahigh vacuum beamline is terminated by a beryllium foil, so-called window, separating the beamline vacuum system from the vacuum system of the scanner. A filter unit either located in an additional vacuum chamber in front of the exposure station or inside the scanner chamber accommodates different filter materials, which can be inserted into the beam in order to adapt the synchrotron spectrum to the resist thickness.

As an example, commercial scanners operated at CAMD are shown in Figures 3.4a and b. Besides regular normal incident exposures, these scanners also provide more advanced exposure techniques including aligned, tilt, and tilt-and-rotate exposures (DEX 2) as well as large-format exposures (DEX 3), More information about the scanners is available from Jenoptik Mikrotechnik GmbH, Germany.

3.3.2 X-Ray Mask

A critical tool for x-ray lithography is the x-ray mask, which contains the structure design information. Compared with quartz glass masks used in conventional optical and UV lithography, architecture and commercial availability of x-ray masks is significantly different.

While glass is transparent for UV and visible photons, x-ray transparent mask substrates typically consist of low-atomic-number materials. Beryllium, carbon (amorphous or glassy graphite), and polyimide are suitable substrates with acceptable thicknesses ranging from 50 to 1000 μm, while a few micrometer-thin membrane masks from silicon, silicon-nitride, diamond, or titanium offer an alternative option. Mask contrast is achieved

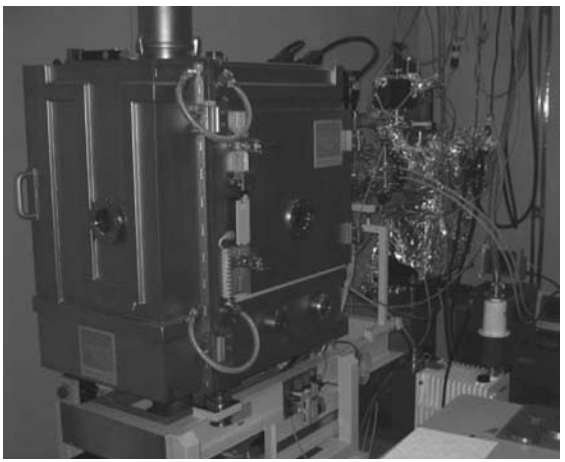

(a)

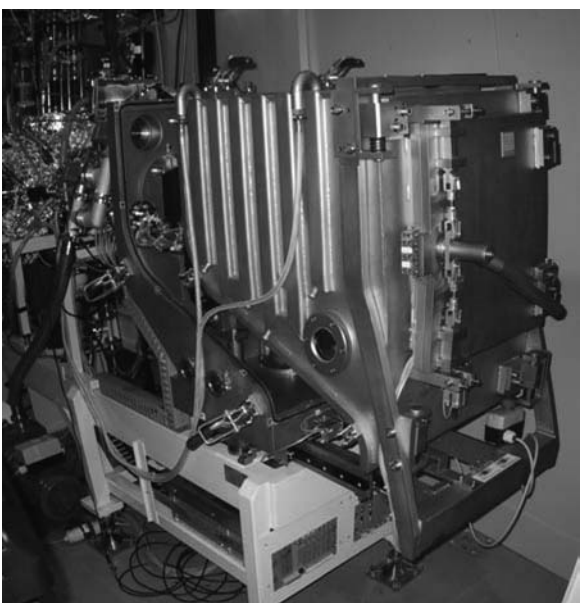

(b)

FIGURE 3.4
(a) DEX 03 scanner inside the radiation hutch at the CAMD XRLM 4 beamline. (b) DEX 02 scanner inside the radiation hutch at the CAMD XRLM 1 beamline.

using high-atomic-number material, typically gold, forming the absorber pattern. The thickness of the gold absorber ranges from a few micrometers when using soft x-ray photons (1 to 4 keV photon energy) up to 50 μm and more when using hard x-ray photons (50 keV) [26]. Due to this wide range of photon energies as well as different specifications regarding resist thickness, resolution, and structure tolerances, no standard mask fabrication process exists, but individual solutions are used [27–32].

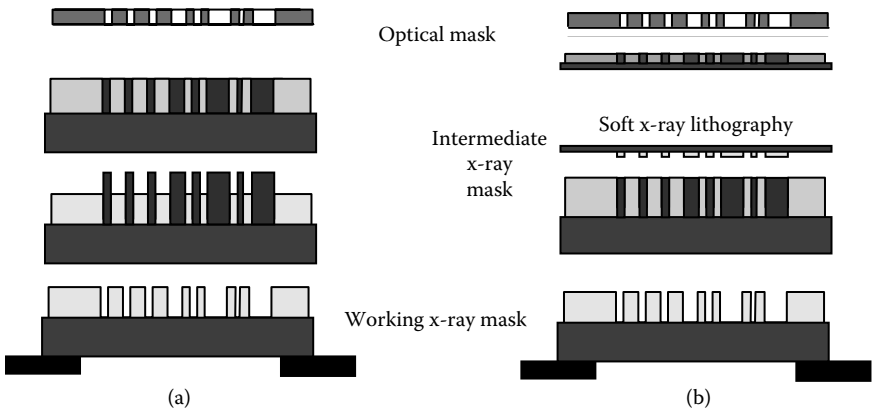

FIGURE 3.5
(a) Optical lithography and gold plating used to fabricate x-ray masks with critical dimensions down to 10 μm. (b) A combination of optical and soft x-ray lithography with subsequent gold plating is used to fabricate x-ray masks with critical dimensions down to 2 μm.

Mask fabrication combines a number of techniques starting with electron or photon or laser beam writing of the initial design onto a chromium or optical mask substrate. The optical mask will then be transferred into a thick optical resist, for example up to 70 μm–thick SU-8, using optical lithography (Figure 3.5a) [32]. After exposure, baking, and development, the resist structure is used as a template and the open areas are filled with gold by electroplating. Resist removal and mask mounting onto a support ring completes the process. Masks fabricated with this rapid prototyping approach have, typically, the smallest feature sizes of 8 μm for a 15 μm–thick resist, which will increase with thicker resist layers. Short mask fabrication times of approximately 3 days is attractive for performing initial exposure tests and is commonly practiced when exploring new designs.

For designs with smaller critical dimensions, the optical lithography is done into a thinner, positive resist (3 to 10 μm thick) and after development approximately 2 to 6 μm–thick gold is electroplated into this template (Figure 3.5b) resulting in the so-called x-ray intermediate mask. Using soft x-rays from a mirror beamline, the pattern is then transferred into a thicker positive resist, for example, 10 to 80 μm PMMA. After development and gold electroplating, a so-called x-ray working mask is completed containing very fine, micrometer-sized structures. Typical fabrication time for working masks is 2 weeks with significantly higher costs compared to the rapid prototyping approach but also superior critical dimensions.

For even smaller, submicrometer critical dimensions, high energy electron beam lithography (100 keV) has to be employed directly into 2 to 3 μm–thick electron beam resist. After development, this pattern serves as a template for gold electroplating resulting in the x-ray intermediate mask, which will then be transferred with soft x-ray into the final working mask, similar to the process scheme illustrated in Figure 3.5b. Figures 3.6a through 3.6c show

different examples of x-ray masks illustrating the wide range of technical solutions available today. Figure 3.6a demonstrates approximately 1 μm small features on an electron-beam-written x-ray intermediate mask [33] (mask fabricated by the Institut für Mikrostrukturtechnik, Forschungszentrum Karlsruhe) and a successful soft x-ray lithography copy into approximately 6 μm–thick PMMA resist performed at the CAMD XRLM 1 mirror beamline (grazing angle of the Cr-coated silicon mirror was 1°).

Typically, the pattern of an x-ray mask can cover an area of up to 85 mm on a 100 mm–wide substrate. However, when using thin membrane masks, a free-standing membrane size with this dimension cannot be fabricated reliably. Instead, smaller open areas are etched into the silicon wafer as illustrated in Figure 3.6b. A third example, an x-ray working mask made on a beryllium substrate, is shown in Figure 3.6c. This mask was copied from an x-ray intermediate mask resulting in a gold height of approximately 30 μm with accurate control of dimensions down to 2 μm.

3.3.3 Resist Application and X-Ray Exposure

PMMA and SU-8 are commonly used x-ray resists, with most of the initial work in LIGA being done in PMMA because of its high resolution and good availability. One challenge is to apply uniform resist layers over a wide range of thickness from micrometers to millimeters. For PMMA, a number of methods including casting and *in-situ* polymerization [34] as well as gluing or solvent bonding of PMMA [35] sheets have been invented and are routinely applied for substrate coating. A main advantage of the latter methods is the use of well-defined, high-molecular-weight PMMA sheets that will be bound to the substrate in a press at room temperature. Uniform resist performance across the entire substrate with minimum stress in the glue layer are unique properties of these methods. The adjustment of the resist height is achieved by fly-cutting the initial PMMA sheet to the desired height within a ± 5 μm tolerance. Figure 3.7a shows an example of a PMMA sheet firmly attached to a silicon substrate and ready for exposure using the solvent bonding method [35]. Substrates suitable for the x-ray lithography process include silicon and ceramic wafers as well as steel and copper blanks. Various methods of surface treatment are employed to ensure good adhesion of the PMMA resist to the substrate surface. The commonly used seed layer on silicon and ceramic wafers is sputter-deposited titanium, which is wet-chemically etched prior to applying the PMMA resist [34]. Best adhesion results on substrates with a titanium surface are achieved through a combined chemical bonding and mechanical locking due to the surface porosity of the wet-etched titanium [34].

In the case of SU-8 resist, single and multiple spin-coating as well as casting are commonly used methods allowing to resist layers to build up to several millimeters in thickness [36,37]. While controlling the solvent contents of

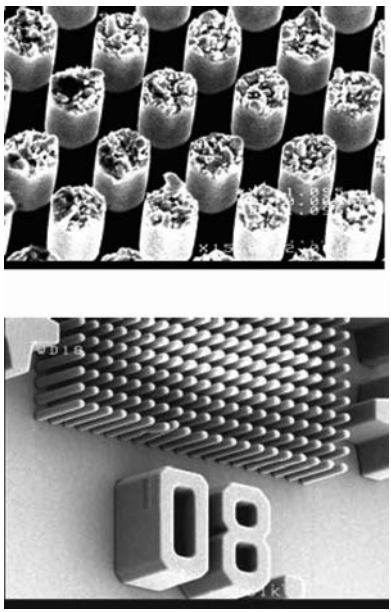

(a)

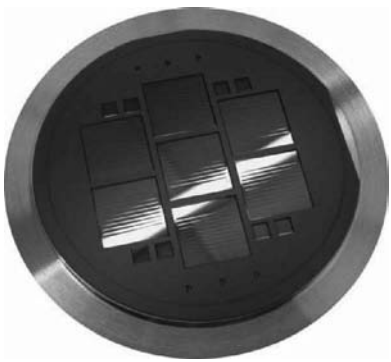

(b)

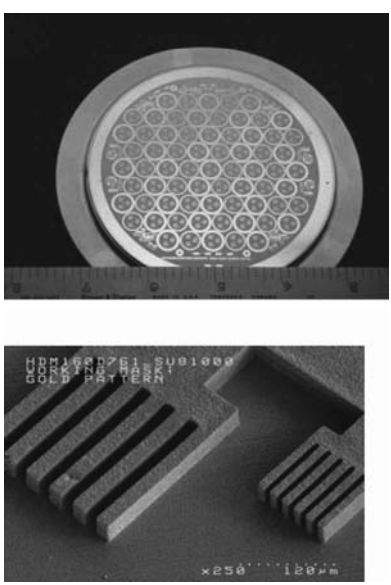

(c)

FIGURE 3.6
(a) Approximately 1 µm–diameter gold post on intermediate mask (top) and copy into approximately 6 µm–thick PMMA resist (bottom). (b) 2 µm–thick silicon nitride mask covering a 4" wafer with seven exposure fields. (c) Be mask with gears and a patterned field of 85 mm ø (top) and detail of Au absorber of test structures (bottom).

(a)

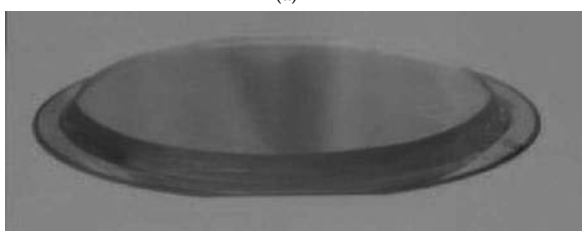

(b)

FIGURE 3.7
(a) Three millimeter–thick PMMA sheet solvent bonded to a silicon substrate. (b) Four millimeter–thick SU-8 layer applied to a silicon substrate using the double-dry chip casting method.

spin-coated SU-8 layers is possible up to a height of approximately 500 μm, thicker layers show a nonuniformity of the solvent contents over the height, and consequently nonuniform lithography performance compromising the structure quality [36].

Although hard x-ray photons easily penetrate through matter, in particular organic materials like resists, photon absorption and energy transfer into the polymer [38] has to be considered when choosing the right exposure conditions. Consequently, the amount of absorbed energy in units of J/cm^3 is a measure for dose instead of the incident power per area commonly used in optical lithography [39]. Furthermore, two dose values are commonly used—the top dose defining the amount of energy absorbed at the resist surface, and the bottom dose indicating the minimum dose required at the resist–substrate interface to fully destroy the resist and make it soluble (see Figure 3.8).

In order to properly expose the resist, the top to bottom dose ratio should not exceed a value of 5 for PMMA resist. This ratio further decreases for thicker resist layers in order to prevent foaming of the surface layer. A third dose is related to the dose that is absorbed underneath the gold absorber. This dose, the so-called critical dose, determines the minimum gold absorber thickness needed to sufficiently absorb the synchrotron radiation.

Dose calculation and optimizing exposure conditions benefit from the properties of synchrotron radiation, namely, that the incident power spectrum can be precisely calculated from the machine and operating parameters.

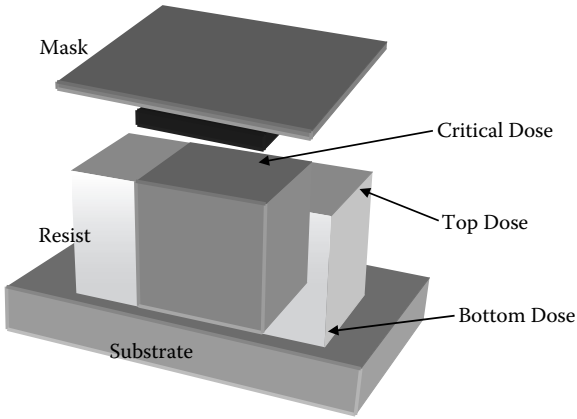

FIGURE 3.8
Exposure doses used in x-ray lithography. *Critical dose:* maximum dose underneath absorber to avoid development. *Top dose:* maximum dose allowed at the top of the resist before foaming or bubble formation occurs. *Bottom dose:* minimum dose required at the resist–substrate interface to completely dissolve the resist.

Beamline properties as well as absorption coefficients from window, mask, filter, and resist materials are included in a program named DOSESIM [40] and offer a convenient way to perform the calculation. The basic equation for dose calculation is presented in Equation 3.4 [41].

$$D(z)[J/cm^3] = 1.421 \cdot 10^{-16} \frac{E^7}{E_0^7} \frac{1}{r_0} \cdot \frac{1}{R[m] \cdot H[mm]} \int_{\lambda_{min}}^{\lambda_{max}} G_3\left(\frac{\lambda_c}{\lambda}\right) \cdot \mu_{resist}(\lambda) \cdot e^{-\mu_{resist}(\lambda) \cdot z} \cdot e^{-\sum_i \mu_i(\lambda) d_i} d\lambda[nm] \tag{3.4}$$

where:

$D(z)$	Absorbed dose [J/cm³] in depth z
E	Electron energy [GeV]
E_0	Rest mass electron [GeV]
r_0	Radius of curvature of bending magnet [m]
R	Distance source to scanner [m]
I	Electron current [A]
H	Scanning height [mm]
G_3	Universal spectral distribution function
λ_c	Characteristic wavelength of the source
$\mu_i(\lambda)$	Linear absorption coefficient of i-th material [1/μm]
d_i	Thickness of i-th absorber [μm]

TABLE 3.2

Comparison of Typical Exposure Dose Values for PMMA and SU-8 Resists

Property	PMMA Resist	SU-8 Resist
Top Dose [J/ccm³]	Maximum 20,000	Less than 100
Bottom Dose [J/ccm³]	Minimum 4,000	Minimum 15
Dose Ratio	< 5	< 7
Critical Dose [J/ccm³]	< 100	< 0.05

Besides resist performance, exposure costs are another critical factor, especially for commercial applications. Systematic studies have been performed comparing PMMA and SU-8 resist for x-ray lithography applications [42–44]. While key structure features, such as sidewall verticality and roughness are comparable, SU-8 is of superior sensitivity allowing patterning of millimeter–thick resist layers in only a few minutes (see Table 3.2).

It should be mentioned, however, that the extreme sensitivity of SU-8 requires thicker gold absorber structures to more completely block the radiation.

Another critical issue of fully cross-linked SU-8 resist is the inability to fully remove the cross-linked material [45], limiting the use of this resist predominantly to applications where the final product is made from SU-8.

3.4 High-Aspect-Ratio LIGA Structures

Examples of high-aspect structures made from PMMA and SU-8 are shown in Figures 3.9a through g. The examples also demonstrate typical LIGA properties such as smooth and vertical sidewalls, and arbitrary, two-dimensional geometry.

Besides the increased sensitivity, SU-8 also offers the option of building multilevel microstructures by performing the basic SU-8 process multiple times. Figure 3.9g shows an example of a three-layer structure fabricated by combined optical lithography and x-ray lithography, respectively.

An important feature of LIGA resist structures are vertical, smooth sidewalls. Early work performed at the Forschungszentrum Karlsruhe/Insitut für Mikrostrukturtechnik showed that LIGA sidewalls are nearly perfectly vertical, showing a slope error of only 0.04 μm per 100 μm of resist height [34]. This value has been confirmed in later experiments by other groups [46–48]. When using harder x-ray photons, for example from the CAMD wiggler source, this value has to be slightly corrected, to approximately 1μm per 100 μm of resist height [49], due to increased dose deposition from secondary radiation [50,51] in the shadowed resist areas, primarily due to larger penetration depth of high-energy x-ray photons and photoelectrons.

(a)

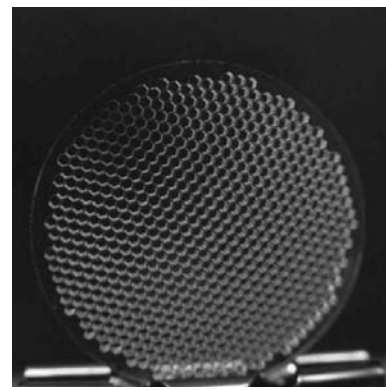

(b)

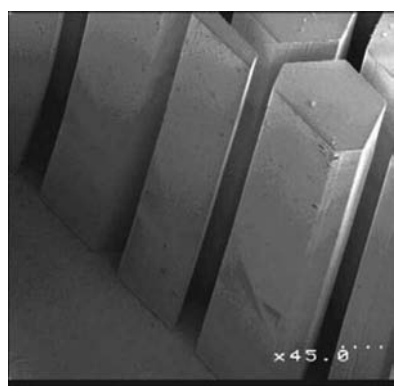

(c)

FIGURE 3.9
(a) Approximately 2.5 mm–tall gear patterned into PMMA. (b) Approximately 1.5 mm–tall free-standing PMMA mesh with approximately 150 μm–thick ridges. (c) Approximately 3 mm–tall posts in SU-8. The gap between adjacent posts is approximately 300 μm.

The contributions to any measured deviation from a perfectly vertical sidewall are manifold and include *engineering* as well as *fundamental* effects [52]. Inaccuracies in scanner motion during x-ray exposure, high but not perfect selectivity of the developer, or a sloped absorber sidewall profile are engineering effects related to the performance of the process and as such can be more readily controlled. The more fundamental limits are related to primary effects including natural divergence of the synchrotron light source, Fresnel diffraction at the absorber pattern and penetration depth of photo electrons into shaded areas [53] as well as secondary effects from fluorescence light produced by the mask and the substrate materials [54,55] and thermal effects [56] in the mask and resist [57].

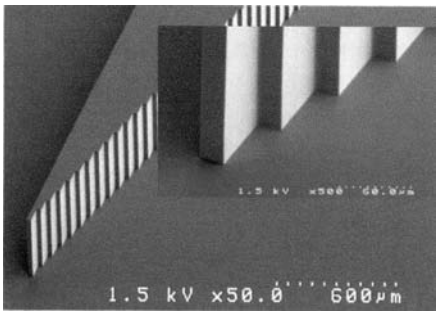

(d)

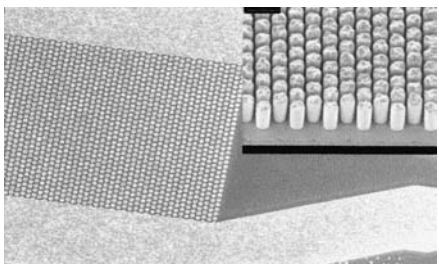

(e)

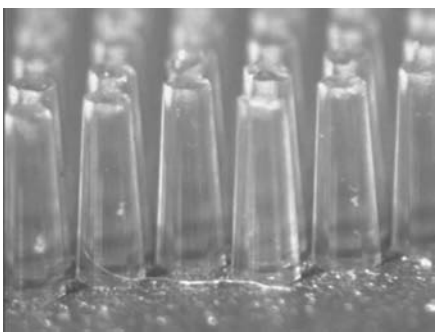

(f)

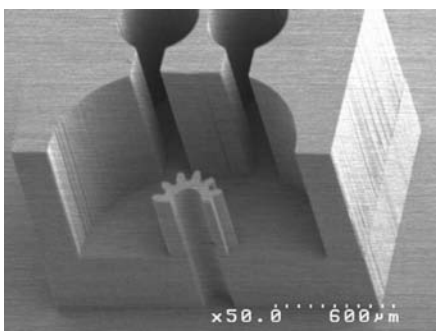

(g)

FIGURE 3.9 (continued)
(d) 20 µm grating pattern in SU-8 in 400 µm height; close-up illustrates high patterning accuracy at the substrate–resist interface.[13] (e) Fluid channel structure with approximately 5 µm–wide post pattern on a graphite substrate to provide a densely packed column. (f) 1 mm–tall conical posts in SU-8, achieved with 6x tilt-and-rotate exposures as an example for tapered sidewalls. (g) 3-level SU-8 structure fabricated by combined optical and x-ray lithography, total height is 1.5 mm, of a microengine.

By combining x-ray lithography with other microfabrication processes, multilevel and quasi-three-dimensional microstructures [58] are possible. One example involves using a sacrificial layer (titanium) and aligned x-ray lithography exposure to build acceleration sensors that are partly anchored to the substrate and partly released [59]. By performing this process on a complementary metal oxide semiconductor (CMOS) substrate, very compact acceleration sensors with minimum length of conductive wires connecting the sensor electrode with the underlying CMOS circuit have been built and successfully tested [60].

Development of tall, narrow microstructures is a challenging task. With developing times for millimeter-tall PMMA microstructures of several days, developer, developing procedures, and parameters have to be carefully chosen to ensure excellent structure properties, and systematic results are reported in a number of publications [61–64].

3.4.1 Electroplating of DXRL Microstructures

The electrodeposition of metals and alloys plays an important role in the fabrication of LIGA or UV-LIGA microstructures, for example, electrolytic gold deposition in the mask fabrication technology or nickel deposition for the production of mold inserts. Among metals and alloys, nickel and copper are two of the most commonly used in microfabrication. In this section, a very brief introduction to electroplating technology, specifically for plating of Ni, is given. Interested readers are encouraged to read the book by Schlesinger and Paunovic [65] and various publications in the LIGA field [66–68] for further information.

Electrodeposition, or electroplating, is a technology that deposits a functional surface layer on metals or metalized, nonconducting materials, for example, to enhance corrosion resistance or for decorative applications. In this process a solid metal surface is grown on a conductive cathode when a potential is applied between the anode and cathode inserted into a bath of metal salts [65]. The process requires strict control of several parameters, including the salt and buffer concentrations, pH, and temperature of the bath, to deposit the metal. Other conditions, such as the applied potential, bath current, pattern geometry, and rate of mixing in the bath, also affect the uniformity of the deposition.

3.4.1.1 Basic Principle of Electrodeposition

Electroplating is basically an electrochemical reaction induced by the current (or potential) applied between the two electrodes. The metal salts are dissolved into the electroplating solution (electrolyte). The current flowing through the plating tank is a flow of positive ions (electron in opposite direction), and it can be used to measure the reaction rate.

The anodic process is oxidation,

$$M \rightarrow M^{n+} + ne^{-}, \tag{3.5}$$

while a reduction reaction happens at the cathode:

$$M^{n+} + ne^{-} \rightarrow M. \tag{3.6}$$

If the current efficiencies at both the anode and cathode are assumed to be the same, there would be no change in mass of the metal ions. Figure 3.10 shows schematically a basic setup for electroplating. It consists of electrodes (anode cathode, and sometimes a reference, too), an aqueous-metal solution, and a DC or AC power supply.

To keep the plating solution clean, some type of filtration mechanism is occasionally used. Mechanical mixing of the solution enhancing plating uniformity is typically employed, too.

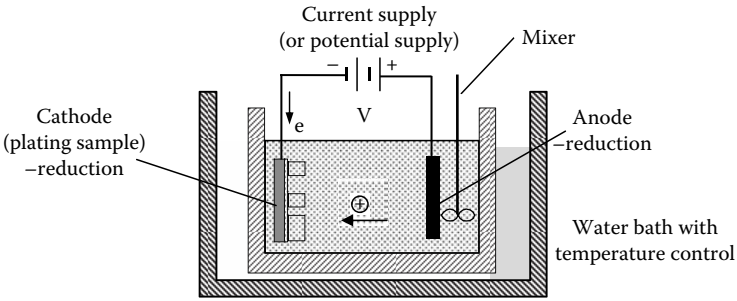

FIGURE 3.10
Schematic setup of an electroplating experiment.

The plating seed layer, which is normally a thin metal film deposited on the substrate, serves as the cathode. The anode is the metal from the plating ions. An electrical potential is applied across the electrodes, which are inserted into the tank filled with the electrolyte (salt plating solution with the targeted metal ions). A current flow is formed between the cathode and the anode and through the electrolyte solution. When the metal ions in the electrolyte obtain electrons from the cathode, they are reduced to nano-sized metal particles and deposit on the surface of the metal film coated on the substrate.

In LIGA or UV-LIGA, Ni is commonly electroplated because it has excellent electroplating properties. The aqueous-metal solution is made of nickel (Ni^{2+}), hydrogen (H^{+}), sulfate ions (SO_4^{2-}), and additives such as sodium lauryl sulfate ($CH_3(CH_2)_{11}OSO_3Na$). With an external electric field applied, nickel ions are attracted to the negatively biased cathode. The nickel ions that reach the cathode receive free electrons and are converted to metallic nickel at the cathode surface forming the electrodeposits. Simultaneously, nickel anodes produce ions in the plating solution by the electrochemical etching process. Hydrogen ions, which also gain electrons from the cathode, form bubbles of hydrogen gas. The formation of hydrogen gas is undesirable because it lowers the plating efficiency and the bubbles can obstruct the deposition of the intended electrodeposit [69].

3.4.1.1.1 Galvanostatic and Potentiostatic Plating

Galvanostatic plating is the process in which a constant current is supplied across the bath with no direct control of the bath potential. Potentiostatic plating is the process in which the potential across the electrodes is controlled at a required level. The galvanostatic plating technique is commonly used for electroplating processes with an established relationship between the current and overpotential. The advantage of this method is that it does not require complex electronics, such as an electrochemical potentiostat or a reference electrode. It is typically carried out using a heated bath, standard cathode, and a constant current power supply. Potentiostatic electroplating

is sometimes preferred in electroplating alloys or multilayer structures such as giant-magnetoresistive (GMR) film because mixed plating baths are commonly used and selective electroplating is achieved with controlled potentials across electrodes.

3.4.1.2 Electroplating Rate and Calculation of the Deposition Thickness

Theoretical calculation of electroplating rate and thickness could be performed using Faraday's law.

$$w = \frac{A_w}{F \cdot n_{el}} I \cdot t \tag{3.7}$$

where w is the amount of metal deposited at the cathode or dissolved at the anode in grams, A_w is the atomic weight of the metal to be plated, n_{el} is the number of electrons involved in the reaction, $F = 96487$ (C/mol) is Faraday's constant, I is the current flowing through the plating tank, and t is the electroplating time.

This calculation assumes that all of the current is effectively used in the deposition or dissolution of the metal. In practice, secondary electrochemical reactions may occur such as the reduction of hydrogen, which consume a small percentage of the current.

Therefore, the previous equation needs to be modified as:

$$w_{practical} = \eta \cdot \frac{A_w}{F \cdot n_{el}} I \cdot t, \tag{3.8}$$

where η is plating efficiency.

The thickness of electroplated metal can be calculated by considering the volume and density of the electroplated metals as follows,

$$w = \rho \cdot A \cdot h \tag{3.9}$$

where ρ is the density of plated metal, A is the area being electroplated, and h is the thickness of deposition. The deposit thickness can be determined as follows,

$$h = \eta \cdot \frac{A_w \cdot I \cdot t}{\rho \cdot A \cdot F \cdot n_{el}}. \tag{3.10}$$

and the electroplating rate can therefore be derived as,

$$\frac{dh}{dt} = \eta \cdot \frac{A_w \cdot I}{\rho \cdot A \cdot F \cdot n_{el}} = \eta \cdot \frac{A_w \cdot J}{\rho \cdot F \cdot n_{el}}, \tag{3.11}$$

where J is the current density. One of the most commonly electroplated metals is nickel. We therefore will use nickel as an example in our calculation here. The atomic weight of nickel is 58.69 g/mol, the number of electrons involved $n_{el} = 2$, and its mass density $\rho = 8.9 \text{g/cm}^3$. Using Faraday's constant, the thickness of electroplated nickel can be calculated as,

$$h[cm] = \frac{\eta \cdot A_w \cdot I \cdot t}{\rho \cdot A \cdot F \cdot n_{el}} = \eta \cdot \frac{58.69}{8.9 \times 96487 \times 2} \cdot \frac{I}{A} \cdot t = \frac{\eta}{29263} \cdot J \cdot t, \qquad (3.12)$$

where the unit for the current density J is Amperes per unit square centimeter and the time unit t is in seconds. If we assume cathode efficiency to be 95.5% and the current density chosen to be 10 mA/cm^2, the time to electroplate a thickness of 5 μm can be calculated to be about 25.5 minutes, and the time required for electroplating 50 μm of nickel film is about 255.4 minutes. If the electroplating current density is increased to about 50 mA/cm^2, then the time required to plate 50 μm–thick nickel film is about 51 minutes.

3.4.1.2.1 Surface Uniformity of Electroplated Metals

In general, the deposit thickness will not be perfectly uniform across the entire plated area. The electroplating uniformity is affected by factors such as nonuniform current distribution, the geometric factor, and the throwing power of the plating solution. The local current density affects the deposition rate and therefore the thickness of the metal deposition at that point.

There are several factors that affect the current density distribution on the plating base: (1) geometries of the plating base, (2) the location and orientation of the particular part relative to the anode, (3) and the position and the orientation in the plating bath. If a particular part of the sample is closer to the anode, the equivalent electrical resistance is obviously smaller, and the current density will be larger. The nonuniform current density consequently results in thicker deposition in prominences and less thick depositions in recessed areas. To obtain uniform electroplating, it is therefore critical to maintain a uniform current density across the entire seed layer. In microfabrication processes such as LIGA and UV-LIGA, microsized plating molds are normally prepared on the substrate so that only selected portions of the seed layer on the substrate are exposed to the electroplating solution as illustrated in Figure 3.11. As the template cavities on the substrate tend to have different size and geometry, it is inevitable that there will be nonuniform current distributions across the sample surface. This results in nonuniform electroplating across the sample surface. This has always been a challenging issue in microfabrication [70]. Frequently, shields are adopted to improve the uniformity of current density.

The throwing power of the plating solution also affects the electroplating uniformity. Metal distribution is influenced by cathode polarization, the cathode efficiency–current density relationship, and the electrical conductivity of

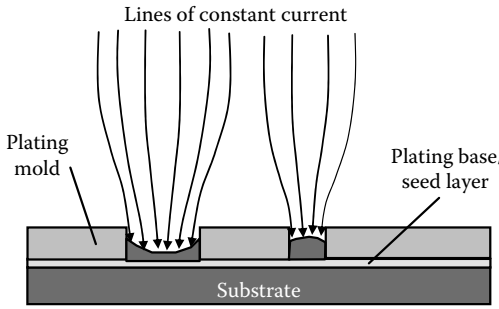

FIGURE 3.11
Nonuniform current density by masking material.

the solution [71]. Throwing power can be determined experimentally. A solution with high-throwing power is capable of depositing almost equal thicknesses on both recessed and prominent areas. In addition the throwing power can also be slightly improved by lowering the current density, increasing the electrical conductivity of the solution, increasing the anode-to-cathode distance, and raising the pH value and temperature.

3.4.2 Nickel Electroplating and Solutions

Because nickel is one of the most commonly electroplated metals in MEMS, especially in the LIGA fabrication process, we will again use it as the example. Generally, nickel sulfate solution (Watts solution) and nickel sulfamate solution are used for nickel plating. Typical composition of the solutions and plating parameters are summarized in Table 3.3.

Sulfate solution is most commonly used for decorative plating. Nickel sulfamate solution is used for electroplating in engineering applications. It offers high deposition rates, low residual stress, and good ductility. The disadvantage is the relatively higher cost in comparison with nickel sulfate solution. It is important to carefully maintain the solutions and continuously treat them for impurities.

TABLE 3.3

A Typical Composition and Operating Conditions for Nickel Sulfamate Solution

$NiSO_4 \cdot 6H_2O$ (Nickel Sulfate)	
$Ni(SO_3NH_2)_2$ (Nickel Sulfamate)	300–450 g/L
$NiCl_2 \cdot 6H_2O$ (Nickel Chloride)	0–30 g/L
$B(OH)_3$ (Boric Acid)	30–45 g/L
$CH_3(CH_2)_{11}OSO_3Na$ (Sodium Lauryl Sulfate)	1 g/L
Temperature	40–60
Agitation rate	200 rpm
pH	3.5–4.5
Current density	20–150 mA/cm^2
Deposition rate	25–85 μm/hr

For most of the MEMS applications, sulfamate solution is preferred. The nickel sulfamate is the primary source of nickel ions (Ni^{2+}). A potential problem with this solution is hydrolysis of nickel sulfamate, which produces sulfate and ammonium ions. These greatly increase the tensile stress of the deposit. To avoid hydrolysis of the nickel sulfamate it is important to maintain the temperature below 65°C and the pH above 3.0. Nickel chloride has a pronounced effect on stress and also causes anode corrosion. However, it also increases conductivity, thereby reducing voltage requirements, throwing power, and uniformity of coating thickness distribution. The major concern, however, is that chloride increases the internal stress of the electroplated nickel, which may have serious consequences for microfabricated structures. Low chloride content should be maintained for the minimum residual stress. A low concentration of nickel chloride, however, is still needed for satisfactory anode performance.

Boric acid in the bath serves as a buffer and helps to control the pH of the solution. Because the cathode efficiency (90 to 97%) is generally lower than the anode efficiency (close to 100%), the nickel ion concentration and the pH of the solution will slowly rise during the electroplating process. Regular additions of sulfuric acid (H_2SO_4) are therefore required to adjust the pH. Low boric acid concentrations may result in cracks in plated film. The recommended concentration depends on temperature, ranging from 30 g/L at 20°C to over 4 5g/L at 52°C [72]. High boric acid tends to salt out of solution at lower temperatures and is difficult to redissolve [73]. Surfactant (sodium lauryl sulfate) may also be added to lower the surface tension of the plating solution to avoid air and hydrogen bubbles clinging to the sample being plated. It may also affect corrosion performance [74].

3.4.3 Electroplating Quality and Influential Factors

Process quality control involves maintaining the concentrations of the main constituents within specified limits, and controlling current density, temperature, pH, agitation, and the purity of plating solutions.

3.4.3.1 Internal Stress

Existence of residual or internal stresses is a common problem with electroplated metals and alloys due to the effect of the electrocrystallization process or the codeposition of impurities (hydrogen, sulfur, etc.) [75], especially when thick layers of metal are plated as in fabrication of high-aspect-ratio microstructures (HARM). Lower residual stress can be achieved with sulfamate nickel solution in comparison with using nickel sulfate solution, which is more commonly used for decorative electroplating applications [76].

3.4.3.1.1 Current Density

As is evident from Equation 3.7, the current density J determines the electroplating rate. Higher current density produces a higher plating rate, but

has the disadvantage of higher residual stress and nonuniform electroplating thickness. Research has found that 20 to 50 mA/cm^2 can be a reasonably good plating current density. When the current density becomes higher than approximately 100 mA/cm^2, nonuniformity will appear. Electroplating with controlled pulse current is also widely used to reduce residual stresses.

Within normal operating limits (20 to 150 mA/cm^2), it has been reported that current density and temperature have little effect on the hardness and the structure of the deposits. On the other hand, current density has varying effects on stress. It may fluctuate from compressive to tensile, and the properties and characteristics of the deposit are also affected by current density. Increasing current density may cause a minor increase in tensile stress in a bath that is free of chloride.

3.4.3.1.2 Temperature

Temperature can influence the brightness range, throwing power, ductility, hardness, internal stress, and burning characteristics. Stress has a pronounced minimum at 50°C with value of about 13.8 MPa in tensile, increasing uniformly above and below 50°C. In general, ductility of the plated metals decreases rapidly as the bath temperature increases.

3.4.3.1.3 pH Value

The pH of the plating solutions significantly influences bath performance [77]. The pH can affect the bright plating range, cathode efficiency, effects of impurities, throwing power, stress, and the physical properties of the plated metal. In a sulfamate solution for nickel electroplating, the stress increases rapidly at pH values above 5.0 because of the codeposition of basic nickel salts. Hardness in the sulfamate solution is also affected by pH. If pH rises above pH 5.0, hardness increases and ductility decreases through codeposition of small amounts of basic nickel salts. It is therefore suggested that a pH range of around 4.0 (3.9 to 4.1) be maintained. In normal operating conditions the pH tended to rise and this was counteracted by the addition of dilute sulfuric acid.

3.4.3.1.4 Agitation

Agitation is important to dislodge hydrogen or air bubbles from the cathode surface, which might otherwise cause pitting. It is especially important for electroplating into small holes or microfeatures as commonly needed in microfabrication to enhance the movement of ions. Some researchers also have reported dramatically improved electroplating results in MEMS using megasonic agitation [77a]. Agitation also helps to maintain a uniform temperature in the plating bath.

3.4.3.1.5 Filtration

Continuous filtration is often needed to keep the plating solutions free of insoluble particles. They may be introduced through solid particles adhering

to the sample, additions of impure chemicals, corrosion of bath components, airborne particles, and so forth.

3.5 Molding of LIGA Microstructures

In the acronym LIGA, the *A* stands for *Abformung*, which is the German word for molding. It was foreseen from the very beginning of LIGA that replication via a molding process was the most viable means of commercialization and mass production. Besides being a fast, highly automated production process, molding also offers the advantage of a wide choice of materials including polymers, ceramics, and metals.

Replication of parts by molding is an "old" technology. There are a number of methods that come under the umbrella of molding. The processes most applicable to molding of high-aspect-ratio microstructures discussed in the course of this chapter are hot embossing (or thermoforming) and injection molding. Information regarding other common molding processes can be found in any modern plastic or polymer processing handbook [78].

Injection molding and hot embossing are thermal processes in which a thermoplastic polymer material is heated sufficiently beyond its softening temperature to effectively change its shape to that of the mold. In the case of injection molding, the polymer is melted from granular raw material and injected into a chamber containing the mold insert as shown in Figure 3.12a. Typically, the injection molding machine consists of a heated barrel (3) equipped with a reciprocating screw (2) usually driven by a hydraulic motor (6), which feeds the molten polymer from a hopper (1) into a temperature-controlled split cavity containing the micromold insert (5). Heated injection nozzles and distribution plates (4) enable optimized injection of the molded plastic into the cavity. The screw melts the polymer and also acts as a ram during the injection phase. The polymer melt is typically injected at several hundred atmospheres into the cavity with overall filling times of less than one second [79].

For hot embossing, preformed polymer sheets are compressed using a heated mold causing locally softening and deformation of the polymer sheet (see Figure 3.12b). The hot embossing or stamping process uses a heated press (platens (1) and (2) with guiding pistons (3)), into which an assembly of mold insert (4) and polymer sheet (5) is placed. Ramping up the temperature above the glass transition temperature (T_g) of the polymer and closing the press will allow pattern transfer from the mold insert into the polymer. Cooling down below T_g, opening the press, and taking out the structured polymer sheet, completes the fabrication cycle, which typically takes several minutes.

Both processes require a vacuum when molding tall, high-aspect-ratio microstructures, which enables proper filling of the mold with polymer and also prevents "burning" of the polymer with air compressed in the microcavities during the filling process.

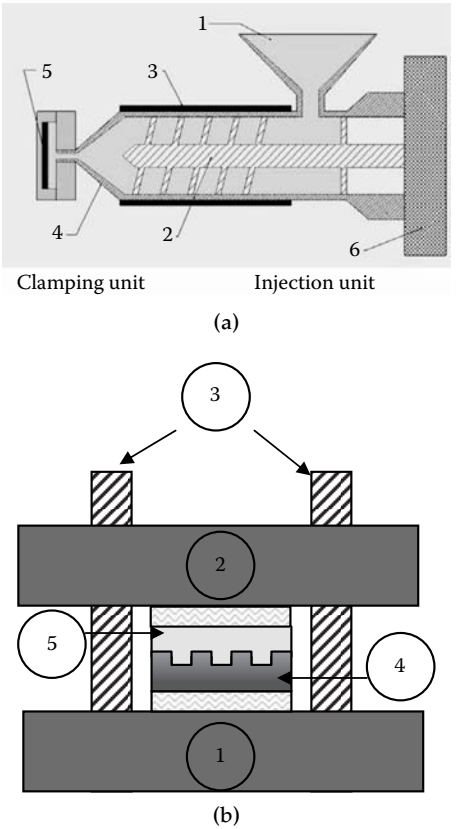

FIGURE 3.12
(a) Schematic of injection molding equipment and process (see text for details). (b) Schematic of the hot embossing process (see text for details).

There are a number of thermoplastic polymers that are routinely molded either by injection molding or hot embossing; however, the process for molding microstructures and especially high-aspect-ratio microstructures is quite different from conventional "macromolding." For most macroscale molding, the mold inserts are held at a constant temperature (isothermal process), usually below the glass transition temperature of the polymer. Micromolding almost always involves a variothermal process [80], in which the molds are also heated above the T_g of the polymer during the mold fill step and have to be cooled to below the glass transition temperature prior to the demolding step. High-quality transfer of a pattern into polymer sheets is contingent on choosing the correct set of embossing parameters, including molding temperature, molding force, molding rate (the rate of displacement of the molding tool during the compression stage), hold time, demolding temperature, and demolding rate. While all these parameters affect the quality of the molding, molding temperature and force are the two most significant ones as they ensure complete mold filling without excessive thermal or mechan-

ical load on the mold insert or molded part. Advanced processing equipment like the HEX 02 hot embossing machine from Jenoptik Mikrotechnik (Jenoptik Mikrotechnik, Jena, Germany) allows continuous control and measurement of all the above parameters during the molding process, thus resulting in a high degree of repeatability between process runs. Figure 3.13a shows the open vacuum chamber of the HEX 02 machine at CAMD and Figure 3.13b represents a typical displacement-versus-temperature curve measured during the embossing cycle of a PMMA sample [81,82].

This representation also provides good insight into the occurrences taking place during the embossing process. In the region marked $T << T_g$, the curve slopes downward because the expansion of the material and machine column displaces the force unit in the negative direction. The curve levels out in the region marked $T \sim T_g$, and starts rising as the polymer begins to soften slightly and starts conforming to the mold insert face. When $T > T_g$, the curve starts sloping upward as the polymer loses viscosity and is beginning to flow to the sides. This is the ideal zone for embossing the polymer because the polymer is sufficiently viscous to flow, but does not flow too freely yet. When $T >> T_g$, the polymer has almost liquefied and hence the curve slopes up sharply. At this point the polymer flows too freely and embossing in this zone yields poor results.

Both injection molding and hot embossing have their advantages and disadvantages, and a decision as to which process is used is often determined by the application and microstructure details. Injection molding is better suited for mass production of microparts as processing time is shorter and the process can be easily fully automated. However, aspect ratios are limited to somewhere around 20 [83] and features that are too small (< 50 μm) tend to break in the demolding step. Hot embossing is suitable for prototyping and small series fabrication of replicated microstructures with typical cycle times of 15 min [84], and smallest structures less than 10 μm wide have been successfully replicated [85]. As hot embossing is a relatively gentle process with low material flow and very slow processing rates, the produced parts exhibit lower internal stress, making them ideal for optical components [86–92] and molding of very high-aspect-ratio microstructures (up to 50 [83]).

Hot embossing is an additive process, in that the structure-forming material is deposited only in those areas constituting the microdevice structure. This is in contrast to bulk and surface micromachining where feature blanket deposition of the structural material is followed by an etching, subtractive process to realize the final device geometry. Similar to the silicon-based micromachining processes, hot embossing can also be combined with prestructured, fragile substrates like CMOS wafers using an aligned hot embossing process. The final result is an integrated, compact mechanical sensing and actuating device on top of signal controlling microelectronics [93–95].

Injection molding and hot embossing are well suited to combining production capability with a wide choice of engineering materials to meet the future demands of a variety of MEMS applications. While polymers are commonly used in research and are the preferred material for many bio-MEMS

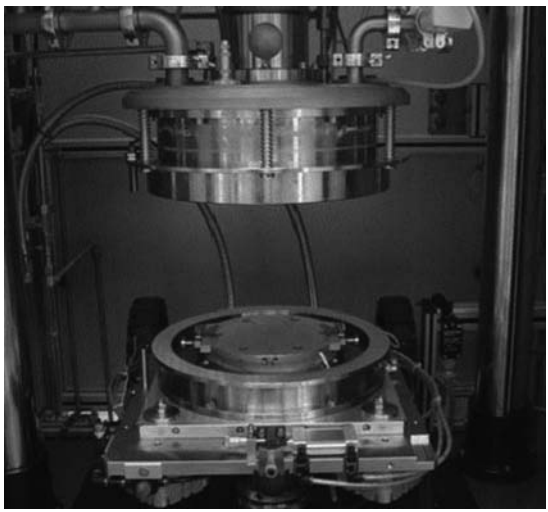

(a)

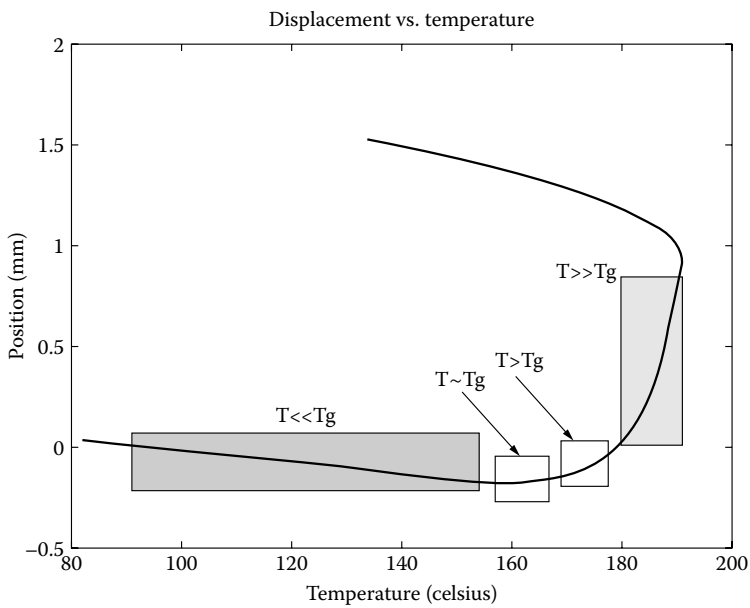

(b)

FIGURE 3.13
(a) Open vacuum chamber of the HEX 02 hot embossing machine at CAMD. (b) Displacement versus temperature curve measured during an embossing cycle (see text for details).

applications for producing cheap, disposable microfluidic chips [96–98], replicated microstructures in ceramic and metal for generally harsh environment applications or for devices with specific material properties, for example, piezoelectric functions [99], are also in demand [100,101]. Shaping

of metal microstructures typically uses the lost mold approach commonly applied for dental applications [102]. The process starts with a molded plastic part, which is embedded in a ceramic matrix. During the ceramic sintering process the polymer is evaporated (pyrolisis) and completely removed from the form. The cavity formed in the hard ceramic material is then heated and evacuated, followed by injection of the melted metal material, for example, using metal injection molding or centrifugal casting. In the final step the ceramic material is dissolved (lost mold) releasing the metallic microparts.

Patterning of ceramic microparts starts with making a fine, ideally nanosized ceramic powder of the desired ceramic material and thoroughly mixing it with a polymeric binder forming the so-called feedstock. The feedstock becomes the raw material for the subsequent replication process. The viscosity of the feedstock is determined by the particle load as well as the requirements of the replication process. For injection molding it has to be low enough to allow sufficient flow through the injection channels, while in hot embossing sheet material, so-called *green tape* allows the use of solid material with a high particle load, which will only flow into the mold cavities at elevated temperatures and high applied pressures during the embossing step. After shaping the feedstock, the polymeric binder material has to be removed at high temperatures (debinding) and the ceramic powder will be compacted in a final sinter step typically achieving 98% of the theoretical density. Along with this step goes material shrinkage of around 20% making it difficult to control the actual dimensions of the micrometer scale features [83].

3.6 Application of LIGA Microstructures

Since the early 1990s, precision LIGA microstructures have been designed and fabricated targeting applications in micro-optics, microfluidics, actuators, and sensors [103]. Some of these early ideas have matured to the point that commercial products have become available today. However, for many of these potential products, small volume production of only a few hundred or thousand parts is common practice, and scaling up of production volume remains a key challenge. Today's applications focus on life science and bio-MEMS [104], thermal management [105], microreactor technology [106], precision mechanics [6,107] and micro-optics [108,109]. Products developed benefit from both a wide range of available materials and extremely small and precise feature properties. The examples presented in the following paragraphs illustrate ongoing efforts at CAMD and collaborating partners, while other examples can be found in the literature [110–113].

3.6.1 Mold Insert Fabrication

One of the main applications is the fabrication of robust, high-quality mold inserts using an x-ray lithography–fabricated microstructure as a template. Two different approaches are realized as illustrated in Figures 3.14a and 3.14b [114]. Modification of these approaches, for example by using a prestructured substrate before performing the LIGA lithography process, are also commonly practiced and allow the fabrication of multilevel mold inserts [104,112].

Table 3.4 briefly summarizes the advantages and disadvantages of both approaches, and indicates that there is no standard process, but different choices taking into account the design and requirements of the application.

LIGA–fabricated mold inserts are typically made of electroplated nickel or nickel-iron alloys. These tools are very robust compared to silicon tools, however their quality and strength is largely dependent on the level of process control that is maintained during the electroforming step. Figure 3.15a shows the plated nickel "disc" still attached to the silicon substrate, while Figure 3.15b shows the front side after release from the silicon carrier.

Major challenges have been the overplating of large resist areas into which narrow fluidic channels have been patterned, and to reduce stress in the plated nickel to avoid or minimize bending of the substrate and the mold insert. While the latter aspect has been achieved through bath optimization as well as plating parameter adjustments, the uniform overplating is realized

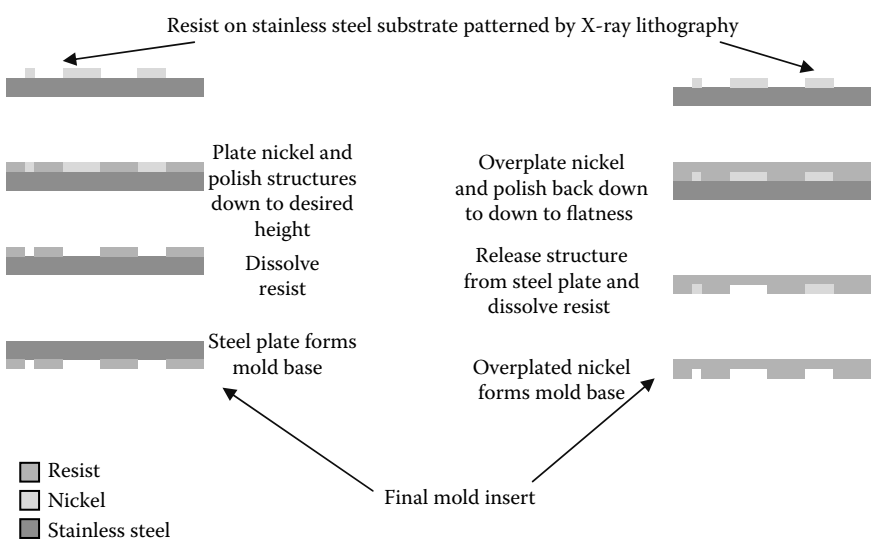

FIGURE 3.14
(Left) Fabrication of a steel-nickel mold insert suitable for larger LIGA structures. (Right) Fabrication of a nickel mold insert using the overplating approach also suitable for submicrometer LIGA structures.

TABLE 3.4

Advantages and Disadvantages of Mold Insert Fabrication Approaches

Plated-on Mold Insert	Overplated Mold Insert
Superior flatness because flatness is a function of the machined substrate	Flatness is dependent on stresses induced due to electroplating conditions
Lower robustness as the interface between the electroformed part and the substrate is typically a weak interface; this also limits the smallest feature size	Higher robustness because microscale features and mold base are formed monolithically; submicrometer structures can be successfully replicated from these mold inserts
Machined substrate serves the dual purpose of a fixture for attaching mold to molding machine	Separate fixture must be fabricated and machining is necessary in order to attach the electroformed mold to molding machine
Shorter electroplating time	Longer electroplating time; especially for large polymer areas, additional deposition of a seed layer is required to ensure somewhat uniform overplating

by depositing a thin gold film onto the structured resist providing a conducting surface once the plating up of the HARM pattern is completed. Figure 3.15b shows the thin gold film still on the actual nickel insert.

The growing interest in replicating nanometer-sized structures commonly referred to as nano-imprint-lithography (NIL) has initiated research into the molding of HAR submicrometer structures [115]. Figures 3.15c and 3.15d show an early example of CAMD efforts. In this case the insert was fabricated from an intermediate x-ray mask patterning an approximately 2 μm–thick PMMA resist applied onto a silicon substrate. The mold insert has been electroplated into these structures using the overplating approach. The final thickness of the insert is approximately 0.5 mm, similar to the shims used for CD/DVD molding. Successful replication using a HEX 02 hot embossing machine (Jenoptik GmbH, Germany) is demonstrated in Figure 3.15d showing the master structures on the insert (hexagon mesh) and the corresponding hexagonal posts replicated in PMMA.

3.6.2 Precision Parts by Direct LIGA

3.6.2.1 Safety-and-Arming Switch

In the United States, the MEMS Exchange [116] offers a large suite of MEMS fabrication services available through a number of providers. The CAMD service group is providing LIGA services for the MEMS Exchange and had the opportunity to fabricate prototype safe-and-arm switches for munitions. This project uses a direct LIGA approach combining x-ray lithography and nickel electroplating. Figure 3.16a shows details of the pattern including a 10 μm–wide spring structure on a graphite x-ray mask, while Figure 3.16b shows a total of 16 wafers with approximately 300 μm–tall nickel parts. Fabrication steps include x-ray lithography, electroplating of nickel, polishing of the

(a)

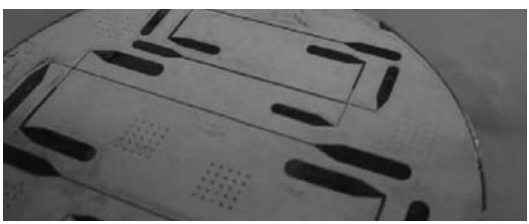

(b)

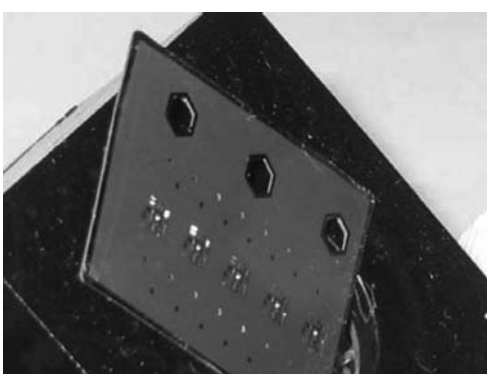

(c)

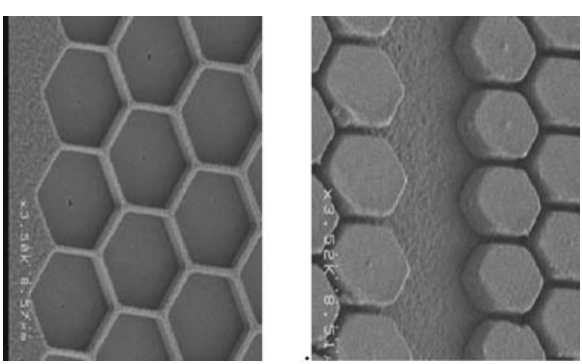

(d)

FIGURE 3.15
(a) Ni mold insert electroplated on a silicon substrate with microfluidic pattern. (b) Ni mold insert after release from the silicon substrate. (c) Overview of a nickel shim/mold insert with submicrometer features, (d) Hexagonal structures on mold insert (left) with smallest lateral dimensions of 1 μm and 2 μm height; molded posts in PMMA (right) [114a].

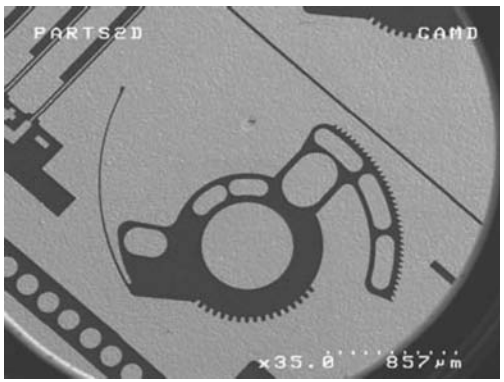

(a)

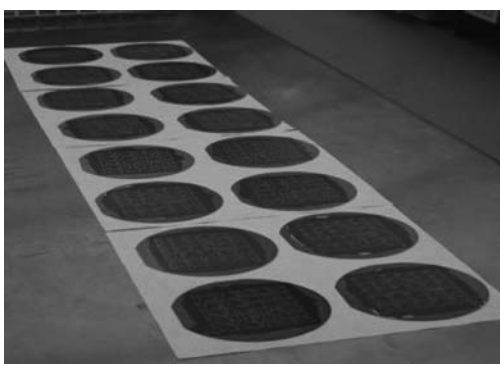

(b)

FIGURE 3.16
An x-ray mask and 16 identical 100 mm silicon wafers with 300 µm nickel structures still embedded in the PMMA template. (a) SEM picture of an x-ray mask showing a component with 10 µm critical dimension. (b) 16 wafers exposed under the same conditions with identically high yield results.

nickel surface, and resist removal. This semiproduction run illustrates that high-yield production using direct LIGA is viable.

3.6.2.2 Nanobarcodes

For biorecognition applications, Nanoplex [117] is interested in patterning 5 to 10 µm–thick PMMA resist templates with submicrometer, densely packed holes. These holes are used as templates to electrodeposit metal bar codes consisting of alternating thin metal layers of discrete height. In collaboration with the Institut für Mikrostruktur-technik/Forschungstram Karlsruhe (IMT/FZK), an intermediate x-ray mask was directly patterned on a silicon nitride membrane mask using a 100 keV electron beam writer. SEM images in Figures 3.17a through 3.17c illustrate the current fabrication capabilities for these microstructures. Figure 3.17c shows a reversed pattern of approximately 8 µm–tall PMMA posts patterned by soft x-ray lithography.

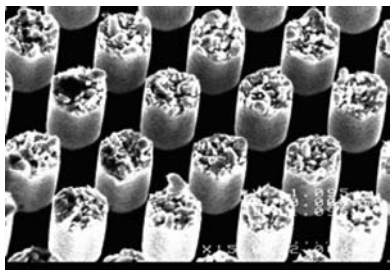

(a)

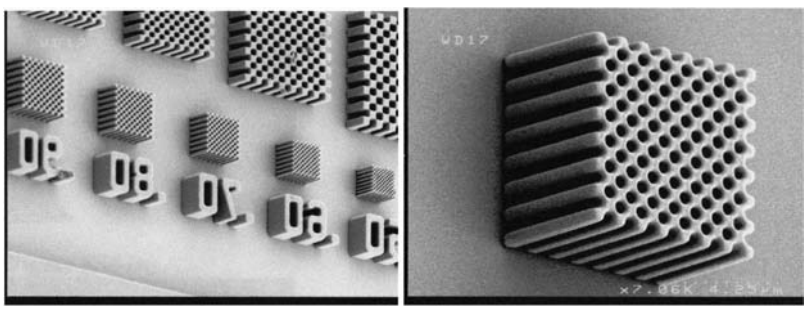

(b)

FIGURE 3.17
Gold mask structure and copied PMMA pattern for nanobarcode application. (a) Approximately 1 μm–wide gold posts in ~2-μm thick gold on intermediate x-ray mask. (b) Examples of test arrays of submicrometer holes patterned onto ~6-μm thick PMMA using soft x-ray lithography (left), close-up view of test field with ~0.6-μm wide holes (right).

3.6.2.3 Harmonic Drive® Microgears

Micromotion [118] is interested in receiving x-ray lithography–patterned resist templates in 550 μm and 1050 μm heights, respectively, for nickel-iron alloy electroplating and further assembly of Harmonic Drive® microgears. Harmonic Drive gear assemblies are perfectly suited for precision positioning applications. The backslash-free microgear trains consist of only six toothed wheels and are of interest for actuators in industrial robots, lens adjustment and optical switches in micro-optics, and microdosing pumps and surgical equipment in medicine [119]. In order to achieve the highest levels of performance, the gears have to be fabricated in nickel-iron alloy with very tight tolerances, nearly perfect vertical sidewalls (deviation from a perfect sidewall of less than 1 μm for a 1 millimeter–tall structure), good control of absolute dimensions (better than 1 μm), no defects, and in large numbers in a batch process.

In a close collaboration among BESSY [120], CAMD, and MRT GmbH [121] efforts have been focused on fabricating these gears with high yield and in high quality in PMMA and SU-8 resist. While achieving all requirements at the same time remains a major challenge and still requires process research and optimization, the current status is encouraging and sufficient to deliver

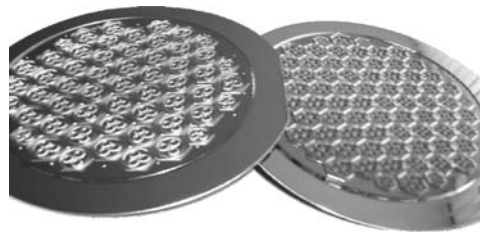

(a)

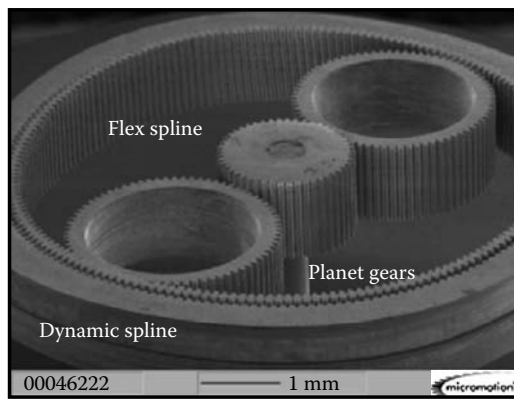

(b)

FIGURE 3.18
(a) Resist templates of SU-8 microgears ready for electroplating. (b) Assembled Harmonic Drive gear train from nickel-iron parts. (Photos courtesy of Micromotion.)

prototype structures to different customers. Figures 3.18 illustrate the actual accomplishments. The figure on the left shows x-ray lithography–patterned SU-8 structures (approximately 100 gear assemblies covering an area of 85 mm on a 100 mm silicon wafer) in 550 μm and 1050 μm thicknesses, respectively, ready for electroplating. The SEM picture to the right shows a completely assembled drive made from electroplated nickel-iron parts. A remaining challenge to achieving high-yield production involves tiny defects on the mask absorber structure resulting in imperfect gear and flexspline structures. The main reason for the defects is imperfections on the surface of the beryllium mask substrate and difficulties in performing the electroplating step there.

3.6.2.4 Polymer Chips for Bio-MEMS Applications

Replication techniques such as injection molding or hot embossing are crucial for many applications in bio-MEMS where cost and large numbers of fabricated devices are important. There are a number of groups and companies that have specialized in producing polymeric microfluidic chips with standard designs as well as supporting the fabrication of chips with customer-specific features [104,122–124]. Commonly used polymers include polymethyl-methacrylate (PMMA), polycarbonate (PC), polypropylene (PP), and

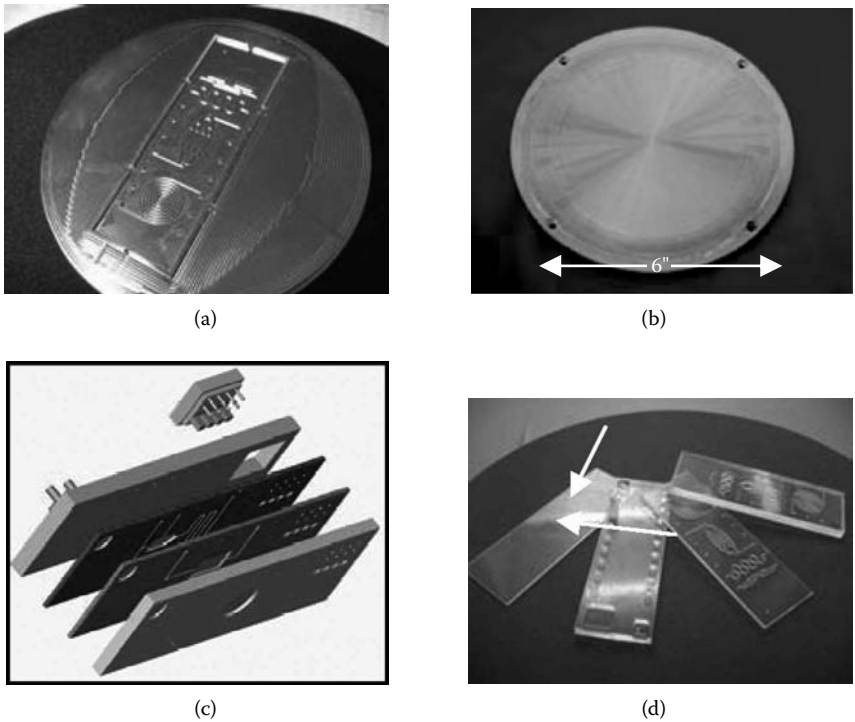

FIGURE 3.19
(a) Brass (left) and LIGA Ni (right) mold inserts with microfluidic structures. (c–d) Vertical fluidic stack concept (left) and molded fluidic chips in glass slide (1" × 3") format (right).

recently cyclic-olefine copolymer (COC). In collaboration with LSU's Center for BioModular Multi-Scale Systems [125] (CBM^2), the CAMD service staff routinely fabricates fluidic chips for bio-MEMS applications. Depending upon the needs, mold inserts are fabricated using micromachining, LIGA, or a combination of both processes (see Figures 3.19a and b). Replication of typical high-aspect-ratio structures is done by hot embossing, which is very suitable for these geometries and also best meets the demand for fast turnaround and the moderate number of chips typically needed for initial tests of a given design. One focus of the joint research efforts is combining multiple chips in a vertical stack [126] where each chip performs one specific operation only. Passive alignment of sealed chips and optimized fluid interconnects between them make execution of complex bioanalysis protocols easily possible (see Figures 3.19c and d).

3.6.2.5 Regenerators for Cryocoolers and Stirling Cycle Heat Engines

LIGA offers the possibility of producing small, well-defined features in tall structures, an important advantage for heat exchanger and cooling device applications. One example is a cryo-cooler, a device that removes heat from

an environment that needs to be maintained at cryogenic temperature. Regenerative heat engines and cryo-coolers use a regenerator to absorb and release energy at appropriate times within a process cycle. An example of a heat engine with a regenerator is a Stirling heat engine (described in any thermodynamics text [127]), which is basically a Stirling heat engine running in reverse. The regenerator typically consists of a porous solid matrix through which a gas flows cyclically back and forth. In one direction, energy is transferred from the gas into the solid matrix, while in the other direction the gas absorbs energy from the solid matrix. A regenerator functions best when the temperature difference between the solid and the gas at any position within the regenerator is minimal, the pressure drop of the gas across the regenerator is minimal, the axial conduction within the solid matrix in the flow direction is minimal, and the dead space (total volume associated with the pores in the regenerator) is small. In addition to these thermodynamic parameters, the regenerator should be made from a material that is strong and tough and resistant to damage from shock loads, compression, and other factors.

A typical regenerator design is shown in Figure 3.20a. The assembled device is basically a well-aligned stack of disks with each disk perforated with an array of tightly packed microchannels providing high porosity with minimized flow resistance and an extremely high heat transfer-to-volume ratio. In addition, alignment holes for pins are included in the design allowing for simple assembly of a stack of disks. Figure 3.20b shows a close-up view of a nickel regenerator with a unique involute design that minimizes axial conduction. The individual webs of each disk are about 14 μm wide, and each web is separated by a gap of 90 μm. The disks are around 250 μm thick and the regenerator consisted of a stack of 45 such disks. The disks are fabricated using a direct LIGA process combining x-ray lithography and electroplating of nickel. One complete disk is shown in Figure 3.20c together with a mounting jig. Currently, cooling tests are being conducted and initial results indicate improved performance.

In some very low temperature cryo-coolers (below 10 K), an additional parameter becomes important: the specific heat of the solid matrix [128]. At higher temperatures, the heat capacity of the solid is usually much greater than the heat capacity of the gas slug, which cycles back and forth within the regenerator. However, at extremely low temperatures, the specific heat of many materials asymptotically approaches a value of zero. In such a case, it is important to fabricate the solid matrix from a material with a nonzero heat capacity, for example, lead or a variety of rare earth metals. Figure 3.21a shows a nickel regenerator for another cryo-cooler design. In this case, each disk is approximately 200 μm thick. A close-up view of the hexagonal holes is shown in Figure 3.21b near one of the alignment holes. The hexagonal pores are 40 μm wide from flat to flat. Using the inverse pattern made from nickel or copper as a tool in an electric discharge machining (EDM) process, this design can also be transferred into rare earth material, such as erbium

(a)

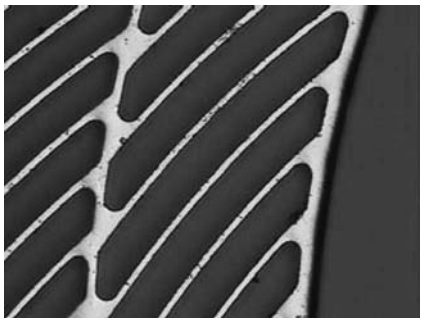

(b)

(c)

FIGURE 3.20
(a) A regenerator consisting of a stack of aligned, porous disks using pins. (b) Detail of a nickel regenerator disk; channel walls are 14 μm wide and 250 μm tall. (c) Single disk (approximately 1"Ø) and mounting jig. (Courtesy of International Mezzo Technologies, Inc., Baton Rouge, LA.)

(see Figure 3.21c). A stack of such disks can be used on the cold end of a very low-temperature cryo-cooler.

3.6.2.6 Examples of Precision Parts (HT Micro)

Commercial applications for deep x-ray lithography–based processing include several broad categories such as microfluidics, micromechanics, and micro-optics. Common to all the applications is the demand to mass produce precision, high-aspect-ratio geometries of millimeter-scale components with micrometer-sized features, while maintaining dimensional tolerances down to the submicrometer range and using materials suited for and compatible with a given application.

As an example, many biofluidic interfaces share these requirements. Figure 3.22a shows a 4-layer plastic component comprised entirely of PMMA and fabricated with deep x-ray lithography. Within this component are 12 channels

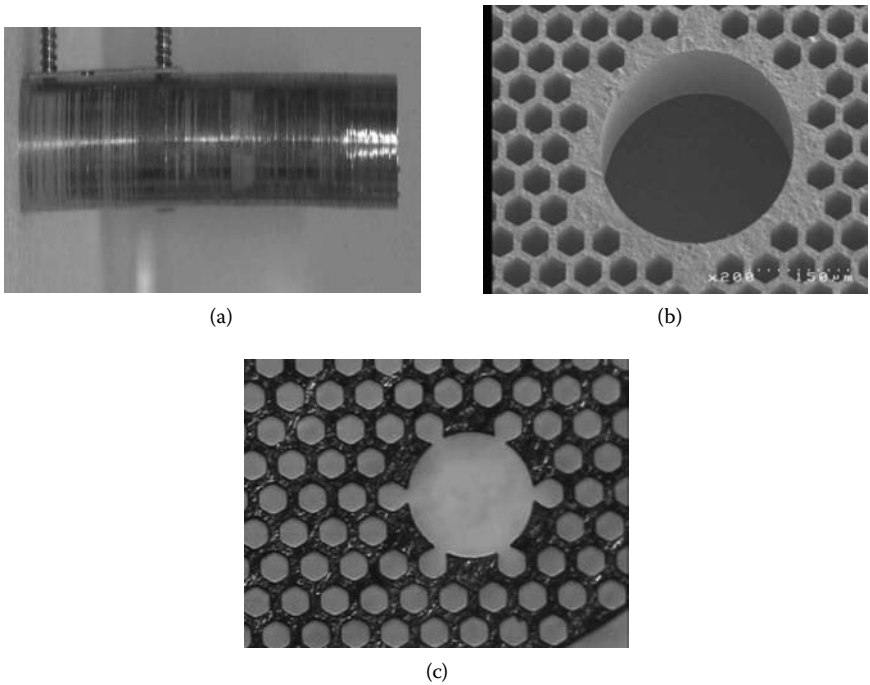

FIGURE 3.21
(a) Regenerator assembled from nickel disks; (b) close-up view of the pore structure of the nickel disk, and (c) disk patterned in erbium using micro-EDM. (Courtesy of International Mezzo Technologies, Inc., Baton Rouge, LA.)

that feed 12 reservoirs caged in by PMMA pillars, as shown in the detailed photographs in Figure 3.22b. The PMMA cage structures consist of rows of 30 μm–diameter cylindrical pillars with a height of 300 μm, which reside on 33 μm centers resulting in rows of 3 × 300 μm gaps. Another similar millimeter-sized biointerface structure with micron precision features is exhibited in Figure 3.22c. This particular component, also constructed with multilayer PMMA chips, contains features interfacing with three optical fibers (center) and intended to be used as an optical biosensor.

Another set of components, springs, combines precision patterning using deep x-ray lithography and electroplating of high-yield strength materials, such as NiFe alloys [129]. By precisely controlling the structure features, a simple spring-mass acceleration switch may be realized as shown in Figure 3.22d. The spiral spring supports a ring, which when accelerated, will contact the outer rim or top (not shown) and bottom shoulder at a predefined acceleration threshold.

The ability to maintain tolerances between high-aspect-ratio structures also aids considerably in the ability to batch fabricate microactuators where a small, micrometer-wide working gap can be maintained through a relatively

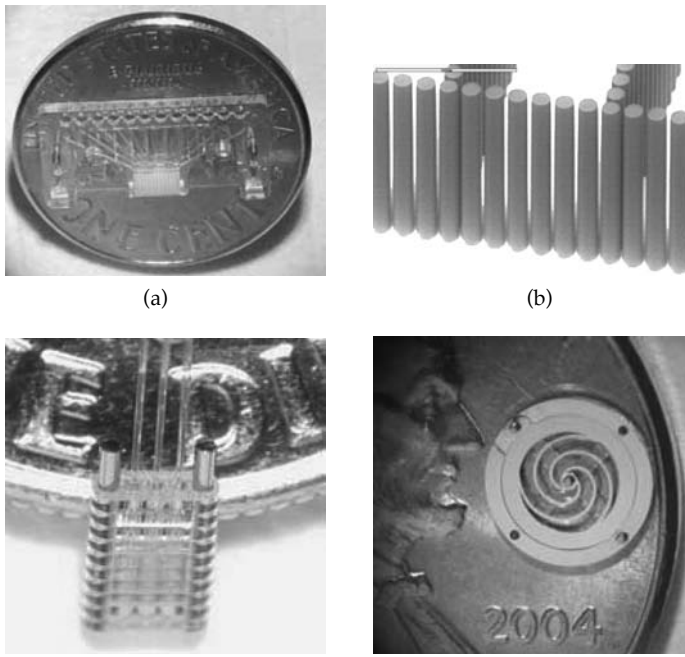

(a) (b)

(c) (d)

FIGURE 3.22
(a) and (b) PMMA fluidic chips with flow filter structures. (c) Optical biosensor with fibers. (d) Acceleration switch made in NiFe alloy. (Photos courtesy of HT MicroAnalytical, Inc.)

much larger thickness and overlap stroke dimensions of several hundred micrometers. Coupled with compliant springs, low frequency (20 Hz) resonators with several hundred-micrometers amplitudes may be fabricated. Such resonant actuators have been applied to generate structured light sources for use in miniature con-focal microscopes. Figure 3.23a shows a microscope developed at the University of Arizona that uses a deep x-ray lithography–defined "optical bench" for alignment and support of miniature optics as well as a resonant amplitude grating, which allows structured light into the microscope when illuminated from a light source [130]. The amplitude grating is shown supported by the center of the resonant actuator in Figure 3.23b, which also shows the electrostatic comb drive, which is capable of resonating the grating at a plus or minus 100 μm amplitude with 10 volts with quality factors at atmosphere of over 50. Figure 3.23c reveals a view of the left side of the microscope in Figure 3.23a where a conventional 1 mm–diameter glass objective lens is supported and clamped to the optical bench.

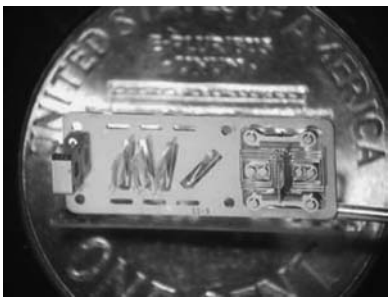

(a)

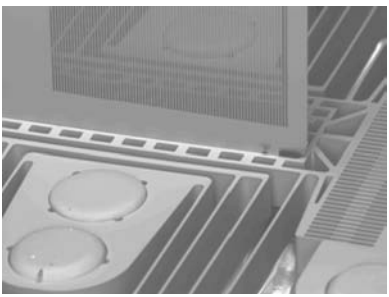

(b)

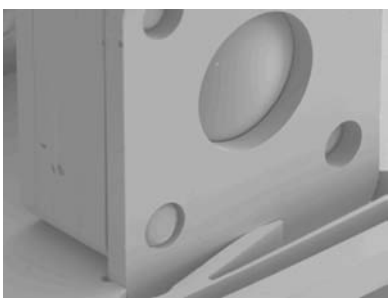

(c)

FIGURE 3.23
(a–c) Examples of a micro-optical bench with integrated electrostatic actuator (see text for details). (Photos courtesy of HT MicroAnalytical, Inc.)

3.7 Summary

In the past several years a number of prototype microsystems using LIGA microstructures have been fabricated, tested, and become ready for commercial use. While direct LIGA fabricated parts still struggle with high yield, high reproducibility production molding is a proven manufacturing process and higher volume, low-cost production is feasible and progressing. The main areas of application of LIGA microstructures include micro-optics, microfluidic, microactuators and sensors, chemical and biochemical processing, and precision microtools. Common to these areas is a need for high-aspect-ratio microstructures with arbitrary two-dimensional shape, extremely high precision, submicrometer structural details, smallest dimensions in the micrometer range, and structure heights ranging from some 10 μm up to several millimeters. The choice of a variety of engineering materials and the availability of suitable manufacturing processes offer unique advantages over silicon-based MEMS products, and will be a driving factor for future polymer, metal, and ceramic microparts.

Key advantages of LIGA-made microstructures are the inherent precision and the ability to cover lateral dimensions from submicrometer to millimeter sizes. These features make LIGA microstructures valuable for integrating assembly and packaging features into MEMS devices, and drastically minimizing the overall packaging effort, a huge cost factor in MEMS devices. The molding process especially can be flexibly combined, for example with Si-based microelectronics on the batch/wafer level, further improving system integration and high-yield production and reducing overall device assembly efforts. Research in LIGA is an ongoing, active field and a number of new ideas combined with novel materials prove that LIGA technologies still spark the interest and excitement of the research community. These efforts are often driven by concrete requirements for new MEMS applications from industrial partners. A remaining challenge for LIGA is the lack of standardized processes demanding reevaluation and optimization of process details for nearly every new microstructure. This also slows down the transition into commercial manufacturing.

In conclusion, LIGA technology has matured to the point that commercial applications have become possible and are being pursued. Applications including bio-MEMS and microfluidics have moderate structure requirements but need cost-effective production and dedicated materials to meet market demands. A number of alternative microfabrication technologies, including precision micromachining and micro-EDM are employed for mold insert fabrication, and molding becomes the manufacturing technology of choice for the microparts. A direct-LIGA approach combining x-ray lithography and electroplating is used for applications for microstructures with extreme precision and very high aspect ratios. Prototype fabrication of these structures can be satisfied but scaling-up production with high yield and high quality remains a challenge for the future.

Acknowledgment

Thank you to Prof. Wanjun Wang (LSU-ME department) for his support with the electroplating section and editing of the overall text, Proyag Datta (research associate at CAMD) for contributions to the molding chapter, and Jens Hammacher for his assistance in preparing some of the figures. I also appreciate contributions from Professor Kevin Kelly (LSU-ME department and founder, Mezzo International, Inc.) on LIGA applications for the regenerator and heat exchanger, and Dr. Todd Christenson, HT Micro Analytical, Inc., for commercial examples of LIGA structures in precision engineering and micro-optics. Last, but not least, I would like to acknowledge the many publications written by former and current colleagues and friends who are

using LIGA technologies in their MEMS research and whose work I have included in this chapter.

References

[1] Becker, E.W., Ehrfeld, W., Münchmeyer, D., Belz, H., Heuberger, A., Pongratz, S., Glashauser, W., Michel, H.J., and Siemens, R., Production of separation-nozzle systems for uranium enrichment by a combination of x-ray lithography and galvanoplastics, *Naturwissenschahften* 69 (1982), 520–523.

[2] Becker, E.W., Ehrfeld, W., Münchmeyer, D., Hagmann, P., and Maner, A.. Fabrication of microstructures with high aspect ratios and great structural heights by synchrotron radiation lithography, galvanoforming and plastic moulding (LIGA process), *Microelectronic Engineering* 4, (1986), 35–56.

[3] Kendall, D.L. and Shoultz, R.A., in *SPIE Handbook of Microlithography, Micromachining, and Microfabrication*, Vol. II, Rai-Choudhury, P., Ed. (1997), 41–98.

[4] Pang, S.W., in *SPIE Handbook of Microlithography, Micromachining, and Microfabrication*, Vol. II, Rai-Choudhury, P., Ed. (1997), 99–152.

[5] Hormes, J., Goettert, J., Lian, K., Desta, Y.M., and Jian, L., Materials for LiGA and LiGA-based Microsystems, *Nuclear Instruments and Methods in Physics Research, B* 199 (2003), 332–341.

[6] HT Micro, http://www.htmicro.com. Accessed August 14, 2006.

[7] Friedrich, C., Warrington, R., Bacher, W., Bauer, W., Coane, P., Göttert, J., Hanemann, T., Hausselt, J., Heckele, M., Knitter, R., Mohr, J., Piotter, V., Ritzhaupt-Kleissl, H.-J., and Ruprecht, R., in *SPIE Handbook of Microlithography, Micromachining, and Microfabrication*, Vol. II, Rai-Choudhury, P., Ed. (1997), 299–377.

[8] Hruby, J., LIGA technologies and applications, *MRS Bulletin* 26, 4 (2001), 337–340.

[9] Arendt, M., Meyer, P., Saile, V., and Schulz, J., Launching into a golden age (1)—marketing strategy for distributed LIGA-fabrication, *Proceedings of the 10th International Conference on Commercialization of Micro and Nano Systems (COMS 2005)*, Baden-Baden, August 21–25, 2005, MANCEF, Albuquerque, NM.

[10] Hahn, L., Meyer, P., Bade, K., Hein, H., Schulz, J., Löchel, B., Scheunemann, H.U., Schondelmaier, D., and Singleton, L. MODULIGA: The LIGA process as a modular production method-current standardization status in Germany, *Microsystems Technologies* 11 (2005) S.240–245.

[11] Malek, C.K. and Saile, V., Applications of LIGA technology to precision manufacturing of high-aspect-ratio micro-components and -systems: A review, *Microelectronics Journal* 35 (2004), S.131–143.

[12] Hruby, J.M., LIGA technologies and applications, *MRS Bulletin* 26, 4 (2001), 337–340.

[13] Jian, L., Desta, Y.M., Aigeldinger, G., Bednarzik, M., Goettert, J., Loechel, B., Jin, Y., Singh, V., Ahrens, G., Gruetzner, G., Ruhmann, R., and Degen, R., SU-8 based deep x-ray lithography/LIGA, *Proc. SPIE* (International Society for Optical Engineering) 4979 (2003), 394–401.

[14] Koch, E.E., Ed., *Handbook on Synchrotron Radiation*, Vols. 1–3, North-Holland, Amsterdam (1983).

[15] Advanced Light Source, list of synchrotron sources, http://www-als.lbl.gov/als/synchrotron_sources.html. Accessed August 14, 2006.
[16] More details on the properties of synchrotron radiation are available in the following sources: Saile, V., Properties of synchrotron radiation, in *Vorlesungsmanuskript of the 23. IFF-Ferienkurs*, Forschungszentrum Jülich (1992), 1.1–28; *Handbook on Synchrotron Radiation*, Vol. 1, edited by E.E. Koch, North-Holland, Amsterdam (1983).
[17] A good summary of the history of x-ray lithography for VLSI application is presented in the *IBM Journal of Research and Development* 37, 3 (1993), 287–474.
[18] Cerrina, F., X-ray lithography, in *SPIE Handbook of Microlithography, Micromachining, and Microfabrication*, Vol. I, Rai-Choudhury, P., Ed. (1997), 251–319.
[19] Kempson, V.C. et al., Experience of routine operation of Helios 1, *EPAC* (1994), 594–596.
[20] Ehrfeld, W.; Bley, P., Goetz, F., Mohr, J., Muechnmeyer, D., and Schelb, W., Progress in deep-etch synchrotron radiation lithography, *J. Vac. Sci. Technol. B* 6, 1 (1988), 178–182.
[21] Christenson, T., X-ray based fabrication, *Micro/Nano R&D Magazin*e 10, 10 (2005), 1–2.
[22] BESSY Anwenderzentrum, http://www.graphilox.de/azm/. Accessed August 14, 1996.
[23] ANKA GmbH, http://www.anka-online.de/english/index.html. Accessed August 14, 1996.
[24] IMT at Forschungszentrum Karlsruhe, http://www.fzk.de/imt/. Accessed August 14, 1996.
[25] For more details visit the CAMD homepage http://www.camd.lsu.edu/. Details about the LIGA activities are summarized under "Microfabrication"; technical details on beamlines and scanners are discussed under "Beamlines."
[26] Griffiths, S., Hruby, J., and Ting, A., The influence of feature sidewall tolerance on minimum absorber thickness for LIGA x-ray masks, *J. Micromech. Microeng*. 9 (1999), 353–361.
[27] Chen, Y., Kupka, R.K., Rousseaux, F., Carcenac, F., Decanini, D., Ravet, M.F., and Launois, H., 50 nm x-ray lithography using synchrotron radiation, *J. Vac. Sci. Technol. B* 12, 6 (1994), 3959–3964.
[28] Schomburg, W.K., Baving, H.J., and Bley, P., Ti-and Be-x-ray masks with alignment windows for the LIGA process, *Microelectronic Engineering* 13 (1991), 323–326.
[29] Klein, J., Guckel, H., Siddons, D.P., and Johnson, E.D., X-ray masks for very deep x-ray lithography, *Microsystems Technologies* 4 (1998), 70–73.
[30] Coane, P., Giasolli, R., Ledger, S., Lian. K., Ling, Z., and Göttert, J., Fabrication of HARM structures by deep x-ray lithography using graphite mask technology, *Microsystem Technologies* 6 (2000), 94–98.
[31] Desta, Y. et al., Fabrication of graphite masks for deep and ultra-deep x-ray lithography, *Proc. SPIE* (International Society for Optical Engineering) 4175, (2000).
[32] Desta, Y. et. al., X-ray masks for the LIGA process, HARMST 2003, Monterey, CA, June 2003.
[33] Wang, L., Desta, Y.M., Fettig, R.K., Goettert, J., Hein, H., Jakobs, P., and Schulz, J.. High resolution x-ray mask fabrication by a 100 keV electron-beam lithography system, *J. Micromech. Microeng*. 14 (2004), S.722–726.

[34] Mohr, J., Ehrfeld, W., and Münchmeyer, D., Analyse de Defektursachen und der strukturvebertragung bei der Roentgentiefenlithographie mit synchrotronstrahlung, KfK Report 4414, Forschungszentrum Karlsruhe (1988).
[35] Guckel, H. et al., U.S. patent # 5378583 (1995).
[36] Bernhardt, D., Fabrication and structure-analysis of ultra-tall HARM made in SU-8 and PMMA, master's thesis, Fachhochschule Gelsenkirchen, February 2004.
[37] Becnel, C., Desta, Y., and Kelly, K., Ultra-deep x-ray lithography of densely packed SU-8 features (parts I & II), *J. Micromech. Microeng*. 6 (2005), 1242.
[38] Schnabel, W., Polymer Degradation—Principles and Practical Applications, Hanser, Munich (1981).
[39] Levinson, H.J. and Arnold, W.H. Optical lithography, in *SPIE Handbook of Microlithography, Micromachining, and Microfabrication*, Vol. I Rai-Choudhury, P., Ed., (1997), 11–138, SPIE Press, Bellingham, WA.
[40] Meyer, P., Schulz, J., and Hahn L., DoseSim: Microsoft-Windows graphical user interface for using synchrotron x-ray exposure and subsequent development in the LIGA process, *Review of Scientific Instruments* 74 (2003), S.1113–1119.
[41] Maid, B., Ehrfeld, W., Hormes, J., Mohr, J., and Muechmeyer, D., *Adaptation of Spectral Distribution of Synchrotron Radiation to x-ray Depth Lithography,* KfK Report 4579 (1988), Forschungszentrum Karlsruhe, Karlsruhe, Germany.
[42] Jian, L., Desta, Y.M., Goettert, J., Multi-level microstructures and mold inserts fabricated with planar and oblique x-ray lithography of SU-8 negative photoresist, *Proc. SPIE* (International Society for Optical Engineering) 4557 (2001), 69–76.
[43] Reznikova, E.F., Mohr, J., and Hein, H. Deep photo-lithography characterization of SU-8 resist layers, *Microsystems Technologies* 11 (2005), 282–291.
[44] Goettert, J., Ahrens, G., Bednarzik, M., Degen, R., Desta, Y.M., Gruetzner, G., Jian, L., Loechel, B., Ruhmann, R., and Jin, Y., Cost effective fabrication of high precision microstructures using a direct-LIGA approach, Proc. COMS (2002), Ypsilanti, Michigan, September 2002.
[45] Dentinger, P.M., Clift, W.M., and Goods, S.H., Removal of SU-8 Photoresist for thick film application, *Microelectronic Engineering* 61–62 (2002), 993–1000.
[46] Feiertag, G., VDI Report 242, Röntgenticfenlithographische Mikrostruktur-fertigung, Düsseldorf (1996).
[47] Feiertag G., Ehrfeld, W., Lehr, H., Schmidt, A., and Schmidt, M., Accuracy of structure transfer in deep x-ray lithography, *J. Microelectronic Eng*. 35 (1997), 557–560.
[48] Feiertag, G., Ehrfeld, W., Lehr, H., Schmidt, A., and Schmidt, M., Calculation and experimental determination of the structure transfer accuracy in deep x-ray lithography, *J. Micromech. Microeng*. 7 (1998), 323–331.
[49] Aigeldinger, G., Implementation of an ultra deep x-ray lithography system at CAMD, Ph.D. thesis, University of Freiburg, 2001.
[50] Münchmeyer, D., Ehrfeld, W., and Becker, E.W., KfK Report 3732, Untersuchungen zur Abbildungenauigket der Röntgentiefen lithografie mit synchrotronstrah-lung bei der Hersellung Technischer Trennduesen, Forschungszentrum Karlsruhe (1984).
[51] Pantenburg, F.J. and Mohr, J., Influence of secondary effects on the structure quality in deep x-ray lithography, *Nuclear Instruments and Methods in Physics Research B* 97 (1995), 551–556.
[52] Griffiths, S.K., Fundamental limitations of LIGA x-ray lithography: Sidewall offset, slope and minimum feature size, *J. Micromech. Microeng*. 14 (2004), 999–1011.

[53] Zumaqué Diaz, H., Zur auflösungsreduzierenden sekundärstrahlung in der Röntgentiefenlithographie, Ph.D. thesis, University of Bonn BONN-IR-98-N, (1998).
[54] Pantenburg, F.J., Chlebek, J., El-Kholi, A., Huber, H.-L., Mohr, J., Oertel, H.K., and Schulz, J., Adhesion problems in deep-etch x-ray lithography by fluorescence radiation from the plating base; *Microelectronic Engineering* 23 (1994), 223–226.
[55] Griffiths, S.K. and Ting, A., The influence of x-ray fluorescence on LIGA sidewall tolerances, *Microsystems Technologies* 8 (2002), 120–128.
[56] Achenbach, S., Pantenburg, F.J., and Mohr, J., Numerical simulation of thermal distortions in deep and ultra deep x-ray lithography, *Microsystems Technologies* 9 (2003), 220–224.
[57] Achenbach, S., Pantenburg, F.J., and Mohr, J., *Optimization of the Process Conditions for the Fabrication of Microstructures by Ultra Dep X-Ray Lithography (UDXRL)*, FZKA Report 6576 (2000), Forschungszentrum, Karlsruhe, Germany.
[58] Tabata, O., You, H., Matsuzuka, N., Yamaji, T., Uemura, S., and Dama, I., Moving mask deep x-ray lithography system with multi stage for 3-D microfabrication, *Microsystem Technologies* 8 (2002), 93–98.
[59] Burbaum, C. and Mohr, J., *Herstellung von mikromechanischen Beschleunigungssensoren in LIGA-Technik*, KfK Report 4859 (1991), Forschungszentrum, Karlsruhe, Germany.
[60] Strohrmann, M., Mohr, J., and Schulz, J., *Intelligent Microsystem for Acceleration Measurement Based on LIGA Micromechanics*, FZKA Report 5561 (1995), Forschungszentrum, Karlsruhe, Germany.
[61] Zanghellini, J., El-Kholi, A., and Mohr, J., Development behavior of irradiated microstructures, *Microelectronic Engineering* 35 (1997), 409–412.
[62] Zanghellini, J., Achenbach, S., El-Kholi, A., Mohr, J., and Pantenburg, F.J., New development strategies for high aspect microstructures, *Microsystems Technologies* 4 (1998), 94–97.
[63] Nilson, R.H., Griffiths, S.K., and Ting, A., Modeling acoustic agitation for enhanced development of LIGA resists, *Microsystems Technologies* 9 (2002), 113–118.
[64] Griffiths, S.K., Crowell, J.A.W., Kistler, B.L., and Dryden, A.S., Dimensional errors in LIGA-produced metal structures due to thermal expansion and swelling of PMMA, *J. Micromech. Microeng.*, 8 (2004), 1548–1557.
[65] Schlesinger, M. and Paunovic, M., Eds., *Modern Electroplating*, John Wiley & Sons, New York (2000).
[66] Bacher, W., Bade, K., Leyendecker, K., Menz, W., Stark, W., and Thomes, A., Electrodeposition of microstructures: An important process in microsystem technology, in *Electrochemical Technology: Innovations and New Developments*, Masuko, N., Osaka, T., and Ito, Y., Eds., Kodansha, Tokio (1996), 159–189.
[67] Cho, H.S., Hemker, K.J., Lian, K., Goettert, J., and Dirras, G., Measured mechanical properties of LIGA Ni structures, *J. of Sensors and Actuators A* 103 (2003), 59–63.
[68] Yang, N.Y.C., Headley, T.J., Kelly, J.J., and Hruby, J.H., Metallurgy of high strength Ni-Mn microsystems fabricated by electrodeposition, *Scripta Materialia* 51 (2004), 761–766.
[69] Dukovic, J. and Tobias, C.W., Influence of attached bubbles on potential drop and current distribution at gas-evolving electrodes, *Journal of the Electrochemical Society* 134 (1987), 331–343.

[70] Romankiw, L.T. and O'Sullivan, E.J.M., Plating techniques, in *SPIE Handbook of Microlithography, Micromachining, and Microfabrication*, Vol. II, Rai-Choudhury, P., Ed. (1997), 197–298.
[71] Okinaka, Y. and Wolowodiuk, C., Cyanoaurate(III) formation and its effect on current efficiency in gold plating, *Journal of the Electrochemical Society* 128 (1981), 288–294.
[72] Baudrand, D.W. and Mandich, N.V., Troubleshooting electroplating installations: Nickel sulfamate plating system, *Plating and Surface Finishing* 89 (2002), 68–76.
[73] Tsuru, Y., Nomura, M., and Foulkes, F.R., Effects of boric acid on hydrogen evolution and internal stress in films deposited from a nickel sulfamate bath, *Journal of Applied Electrochemistry* 32 (2002), 629–634.
[74] Saito, T., Sato, E., Matsuoka, M., and Iwakura, C., Electroless deposition of Ni-B, Co-B and Ni-Co-B alloys using dimethylamineborane as a reducing agent, *Journal of Applied Electrochemistry* 28 (1998), 559–563.
[75] Okinaka, Y., Koch, F.B., Wolowodiuk, C., and Blessington, D.R., Left double quote polymer right double quote inclusions in cobalt-hardened electroplated gold, *Journal of the Electrochemical Society* 125 (1978), 1745–1750.
[76] Schlesinger, M. and Paunovic, M., *Electrochemical Engineering Principles*, Prentice Hall, Englewood Cliffs, New Jersey (1991).
[77] Mandich, N.V., pH, hydrogen evolution and their significance in electroplating operations, *Plating and Surface Finishing* 89 (2002), 54–58.
[78] Harper, C.A., Ed., *Modern Plastics Handbook*, McGraw Hill, New Delhi (2000).
[79] Matthew, H. and Naitove, M.H., Close up on Technology: Mold simulation mold analysis gets faster, easier, smarter, Plastics Technology, http://www.plasticstechnology.com/articles/200602cu1.html.
[80] Heckele, M. and Schomburg, K.W., Review on micro molding of thermoplastic polymers, *J. Micromech. Microeng.*, 14 (2004), R1–R14.
[81] Rowland, H.D., Polymer deformation and filling modes during microembossing, *J. Micromech. Microeng.* 14 (2004), 1625–1632.
[82] Schift, H. et al., Pattern formation in hot embossing of thin polymer films, *Nanotechnology* 12, 2 (2001), 173–177.
[83] Ruprecht, R., Bade, K., Bauer, W., Baumeister, G., Hanemann, T., Heckele, M., Holstein, N., Merz, L., Piotter, V., and Truckenmueller, R., *Micro Replication in Polymers, Metals, and Ceramics*, FZKA Report 6990 (2004), 95–102, Forschungszentrum, Karlsruhe, Germany.
[84] Worgull, M. and Heckele, M., New aspects of simulation in hot embossing, *Microsystem Technologies* 10, 5 (2004), 432–437.
[85] Michel, A., Ruprecht, R., Harmening, M., and Bacher, W., *Abformung von Mikrostrukturen auf prozessierten Wafern*, KfK Report 5171 (1993), Forschungszentrum, Karlsruhe, Germany.
[86] Otto, T. et al., Fabrication of micro optical components by high precision embossing, *Proc. SPIE (International Society for Optical Engineering)* 4179 (2000), 96–106.
[87] Heckele, M. and Bacher, W., FZKA Report 6080 (1998), 89–94, Forschungszentrum, Karlsruhe, Germany.
[88] Müller, A., Göttert, J., Mohr, J., and Rogner, A., *Microsystem Technologies* 2 (1996), 40–45.
[89] Larsson, O., Ohman, O., Billman, A., Lundbladh, L., Lindell, C., and Palmskog, G., *Proc. Transducer '97* (1997), 1415–1418, Forschungszentrum, Karlsruhe, Germany.

[90] Ruther, P., Gerlach, B., Göttert, J., Ilie, M., Mohr, J., Müller, A., and Ossmann, C., *Pure and Applied Optics* 6 (1997), 643–653.
[91] Kim, J.-H. and Neyer, A., *J. Opt. Commun.* 17 (1996), 172–178, Forschungszentrum, Karlsruhe, Germany.
[92] Müller, C. and Mohr, J., FZKA Report 5609, Forschungszentrum Karlsruhe (1995), Forschungszentrum, Karlsruhe, Germany.
[93] Both, A., Bacher, W., Heckele, M., and Ruprecht, R., *Herstellung beweglicher LIGA-Mikrostrukturen durch positionierte Abformung*, FZKA Report 5671 (1995), Forschungszentrum, Karlsruhe, Germany.
[94] Müller, K.-D., FZKA Report 6254, Forschungszentrum Karlsruhe (1999), Forschungszentrum, Karlsruhe, Germany.
[95] Strohrmann, M., Bley, P., Fromheim, O., and Mohr, J., *Sensors & Actuators A* 41–42 (1994), 426ff.
[96] Guber, A.E. et al., Microfluidic lab-on-a-chip systems based on polymers—fabrication and application, *Chemical Engineering Journal* 101, 1–3 (2004), 447–453.
[97] Kricka, L.J. et al., Fabrication of plastic microchips by hot embossing, *Lab on a Chip* 2, 1 (2002), 1–4.
[98] One example of a commercial microfluidic lab chip is the Caliper LabCard™. For more details see http://www.calipertech.com/.
[99] Fatikow, S., Microrobots take on microassembly tasks, *MST News* 22 (1997), 20–26.
[100] Woellmer, H., Precision casting of metal microparts, *FZKA Nachrichten*, 3–4 (1998), 237–242.
[101] Bauer, W. and Knitter, R., Shaping of ceramic microcomponents, *FZKA Nachrichten* 3–4 (1998), 243–250.
[102] Caesar, H.H., *Dental-Labor* 2 (1988), 189–193.
[103] *Management Project Microsystems Technologies (PMT)*, FZK Karlsruhe, FZKA Report 6080 (1998).
[104] Products for microfluidic, micro-optics, and life science applications are developed by Boehringer-Ingelheim within their microtechnology department (formerly microParts GmbH), http://www.boehringer-ingelheim.de/produkte/mikrosystemtechnik/microtechnology/index.jsp. Accessed August 14, 2006.
[105] Products for thermal management applications including heat exchangers, regenerators, and microreactor systems are developed by International Mezzo Systems, http://www.mezzotech.biz/about.html. Accessed August 14, 2006.
[106] Products for microreactor technology, life sciences, and micro-optics are developed and commercialized at the Institut fuer Mikrotechnik Mainz, http://www.imm-mainz.de/. Accessed August 14, 2006.
[107] Micromotion GmbH uses direct LIGA technology for fabricating miniaturized Harmonic Drive® Gear systems, http://www.mikrogetriebe.de/. Accessed August 14, 2006.
[108] Axsun Technologies offers LIGA services and produces miniaturized optical systems for sensor applications, http://www.axsun.com/. Accessed August 14, 2006.
[109] Polymicro represents a group of research institutes and industry members offering micro-optics components and systems made by replication techniques in polymers. http://www.polymicro-cc.com/site/. Accessed August 14, 2006.
[110] Bley, P., Goettert, J., Harmening, M., Himmelhaus, M., Menz, W., Mohr, J., Müller, C., and Wallrabe, U., The LIGA process for the fabrication of micromechanical and micro-optical vomponents, in *Micro System Technologies 91*, Reichl, H., Ed., Springer, Berlin (1991).

[111] Mohr, J., Goettert, J., Müller, A., Ruther, P., and Wengeling, K., Micro-optical and optomechanical systems fabricated by the LIGA technique, Photonics West '97, *Proc. SPIE* (International Society for Optical Engineering) 3008 (1997), 273–278.
[112] Müller, A., Goettert, J., and Mohr, J., LIGA microstructures on top of micromachined silicon wafers used to fabricate a micro-optical switch, *J. Micromech. Mircoeng.* 3 (1993), 158–160.
[113] Qi, S.Z., Liu, X.Z., Ford, S., Barrows, J., Thomas, G., Kelly, K., McCandless, A., Lian, K., Goettert, J., and Soper, S.A., Microfluidic devices fabricated in poly(methyl methacrylate) using hot-embossing with integrated sampling capillary and fiber optics for fluorescence detection, *Lab on a Chip* 2 (2002), 88–95.
[114] Bacher, W. et al., Fabrication of LIGA mold inserts, *Microsystem Technologies* 4, 3 (1998), 117–119.
[115] Datta, P. and Goettert, J., Methods for polymer hot embossing process development, in Book of Abstracts, HARMST05, June 10–13, 2005, Gyeongju, Korea, 256–257, accepted for publication in Microsystem Technologies.
[116] MEMS Exchange, http://www.mems-exchange.org. Accessed August 14, 2006.
[117] Nanoplex, http://www.nanoplextech.com/.
[118] Micromotion GmbH uses direct LIGA technology for fabricating miniaturized Harmonic Drive® Gear systems, http://www.mikrogetriebe.de/. Accessed August 14, 2006.
119. Degen, R. and Slatter, R., Hollow shaft micro servo actuators realized with the Micro†Harmonic†Drive®, *Proceedings ACTUATOR2002*, Bremen, June 2002.
[120] BESSY Anwenderzentrum, http://www.graphilox.de/azm/. Accessed August 14, 1996.
[121] MRT GmbH, http://www.microresist.de/. Accessed August 14, 2006.
[122] Solutions for lab-on-a-chip applications using COC polymer chips are offered by Thinxxs, Germany; for more information visit their webpage at http://www.thinxxs.com/.
[123] Solutions for microfluidic chips are available from microfluidic ChipShop; for details see their catalog at http://www.microfluidic-chipshop.com/index.php?pre_cat_open=209.
[124] Fluidic chips (LabCard) and fluidic handling system for analytical applications are offered by Micronics Inc; for more details see their webpage at http://www.micronics.net/. Accessed August 14, 2006.
[125] Homepage CBM² at http://www.lsu.edu/cbmm. Accessed August 14, 2006.
[126] Datta, P., Hammacher, J., Pease, M., Gurung, S., and Goettert, J., Development of an integrated polymer microfluidic stack, to be published in *Proc. iMEMS* 2006, Singapore, May 2006.
[127] Ackerman, R., *Cryogenic Regenerative Heat Exchangers*, Plenum Press, New York (1997).
[128] Radebaugh, R. Foundations of Cryocoolers, Short course presented at the 12th International Cryocooler Conference, MIT, Cambridge, MA, June 17, 2002.
[129] Schlossmacher, P., Yamasaki, T., Ehrlich, K., Bade, K., and Bacher, W., Production and characterization of Ni-based alloys for applications in microsystems technology, *FZKA Nachrichten* 30 Karlsruhe (1998), 207–214.

[130] Tkaczyk, T.S., Rogers, J.D., Rahman, M., Christenson, T.C., Gaalema, S., Dereniak, E.L., Richards-Kortum, R., and Descour, M.R., Multi-modal miniature microscope: 4M device for bio-imaging applications—an overview of the system, *Proc. SPIE* (International Society for Optical Engineering) 5959 (2005), 138–146.

[131] Rogers, J.D., Kärkkäinen, A., Tkaczyk, T.S., Rantala, J., and Descour, M.R., Realization of refractive micro-optics through grayscale lithographic patterning of photosensitive hybrid glass, *Opt. Express* 12 (2004), 1294–1303. http://www.opticsinfobase.org/abstarct.cfm?URI=oe-12-7-1294.

4

Nanoimprinting Technology for Biological Applications

Sunggook Park and Helmut Schift

CONTENTS

Nanoimprint lithography (NIL) is a low-cost and flexible patterning technique, which is particularly suitable to fabricating components for biological applications. Its unique advantage is that both topological and chemical surface patterns can be generated at the micro- and nanometer scale. This chapter presents an overview of NIL technology with the focus on the compatibility of materials and processes used for biological applications. Some examples will be given, such as how NIL can be employed to fabricate biodevices used to understand and manipulate biological events.

4.1 Introduction

Microsystem technologies opened up the development of a variety of biomicrosystems such as bio-MEMS, biochips, and lab-on-a-chip devices, and nanotechnologies are now attracting the interest of the research community as future key technologies in biological applications. They enable us to understand and manipulate fundamental biological processes and to improve the performance of modern medical devices [1,2]. This is because most biological events begin at the nanometer scale and thus control of the phenomena at this characteristic scale could lead to new devices with innovative and unprecedented properties, such as increased speed and sensitivity of assays. Several advanced patterning techniques allow production of arbitrary or periodic patterns with nanometer resolution,(such as electron beam lithography [EBL] and scanning probe lithography [SPM]); these have been used to study biological events occurring on the nanometer scale, such as the adhesion and signaling of cells on nanostructured substrates [3,4]. However, those techniques are serial methods with low throughput and do not meet the demands necessary for implementation in the development of new nanoscale medical devices because a large number of identical devices, often with large patterned areas, are needed for well-controlled experiments. This will allow screening and statistics that will reduce fatal errors in the functioning of the device, and hence in diagnoses and treatment of a certain disease [5]. Thus, the need to develop a high throughput and parallel patterning technique with nanometer resolution has emerged, and one of the most promising technologies, which is both flexible and easily accessible for patterning nanometer-scale features is nanoimprint lithography (NIL) [6–11].

NIL is a low-cost, scalable lithographic technique with sub–10 nm lateral resolution, which is able to pattern large-area micro- and nanostructures in one step. It is based on conformal molding of a mold (stamp) with a nanostructured relief into a resist film, instead of exposure using an optical mask, and was first proposed in 1995 by S.Y. Chou [6,7]. He demonstrated patterning of holes of 25 nm diameters in a poly(methyl methacrylate) (PMMA) film and subsequent fabrication of metal dots by metal deposition and lift-off, indicating the capability of this conformal molding technique in the production of patterns with lateral resolution far beyond the diffraction limit of optical lithography. Following his initiative, considerable efforts have been devoted to overcome the many challenges of NIL technology with the ultimate aim of implementing this technique in the semiconductor industry. Such efforts involve understanding of fundamentals related to the process, such as polymer flow behavior [12–20]; developing new and optimal material systems applicable to the NIL process [21,22]; overcoming the overlay issue [23,24]; fabricating reliable stamps with sub–100 nm features [25–28]; improving antisticking coating methods [29–31]; and commercializing NIL equipment with

full automation. New applications of the NIL technology have been exploited, mostly in areas where less stringent conditions than those for semiconductor production are required, as can be seen in optics and biological applications [32–56]. Progress in NIL technology is rapid. Readers who are interested in various aspects of NIL technology are referred to recent review papers and books [8–11]. This chapter will focus on NIL technology as a tool for identifying, locating, and manipulating events with biofunctional effects.

This chapter will be organized as follows: In Section 4.2, a general overview of NIL technology will be given, which includes an introduction to the NIL process, resist materials, polymer rheology during NIL, NIL stamp fabrication, and antisticking layer coating techniques. The focus in all cases will be on the applicability of those NIL components to biological applications. Then, some of recent research efforts on the fabrication of topological and chemical nanopatterns, whose main targets are in biological applications, will be presented in Section 4.3. Examples of topological nanopatterns and fabrication of elements in nanofluidic channels and engineering nanopores will be given, followed by examples of chemical patterning via NIL and its use in biofunctionalizing substrate surfaces. Finally, we will provide concluding remarks on the future development of NIL technology in conjunction with biological applications in Section 4.4.

4.2 Overview of NIL Technology

4.2.1 NIL Process

NIL is a simple method of patterning nanostructures by deforming a resist with a hard stamp (Figure 4.1). Even though several variations from the process originally reported by Chou et al. have been developed, all of them have a common feature. First, a resist is cast on a substrate. A hard stamp with desired nanostructures on its surface is then pressed into the resist, which forces the resist to flow into the cavities of the stamp. After conformal molding, the stamp is detached from the substrate. The pattern transfer is performed by homogeneously thinning down the residual resist using anisotropic reactive ion etching (RIE) until the compressed areas of the pattern are exposed to the substrate surface.

In selecting an adequate process among the NIL variants, it is necessary to consider all the requirements and restrictions imposed on materials, in-lab process capabilities, pre- and postprocesses, and compatibility with pursuing applications. The resist can be a thermoplastic, UV-curable polymer, or any other deformable materials. In case of a thermoplastic resist, the resist is heated above its glass transition temperature (T_g), and during imprinting a pressure in the range of 50 to 100 bars is applied against the thin polymer

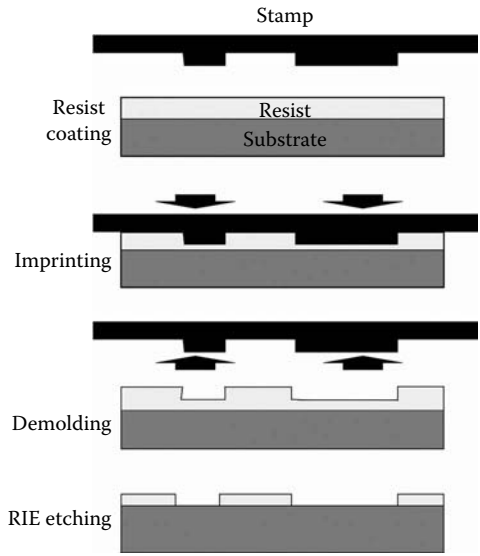

FIGURE 4.1
Process scheme of nanoimprint lithography including the window-opening process as the first step to subsequent pattern transfer.

film for a few minutes. Then the resist is hardened before demolding by cooling down below T_g. In case of a UV-curable polymer, a low viscous photo-curable organosilicon liquid is imprinted with a transparent mold and then hardened by curing upon UV irradiation through the mold (UV-NIL). The process takes place at room temperature and relatively low pressure. New process variants and hybrid approaches have also been developed. One example is the room-temperature NIL, in which a vapor of appropriate solvent is added during the process to reduce the T_g of the applied polymers allowing imprinting at or near room temperature [57]. In the laser-assisted direct imprint (LADI) process, a single excimer laser pulse is irradiated through a transparent mold and melts a thin surface layer of silicon during imprinting, which offers a rapid technique for patterning nanostructures in Si that does not require subsequent RIE [58].

NIL has proven to be very successful in patterning structures at the nanometer scale. Using NIL, the fabrication of an array of dots with 10 nm diameter and 40 nm pitch was demonstrated (Figure 4.2) [59], while line gratings of 5 nm line width and 14 nm pitch were fabricated using UV-NIL with a stamp made by selectively wet-etching $Al_{0.7}Ga_{0.3}As$ from a cleaved edge of a GaAs/$Al_{0.7}Ga_{0.3}As$ superlattice grown by molecular beam epitaxy [60]. As demonstrated, the ultimate resolution of NIL technology seems to be determined by the minimum feature size in the stamp, which is the driving force of the growing efforts in the area of biological and medical application because the length scale of sub–10 nm now attainable via NIL is on the same order as the size of molecules of current biological interest.

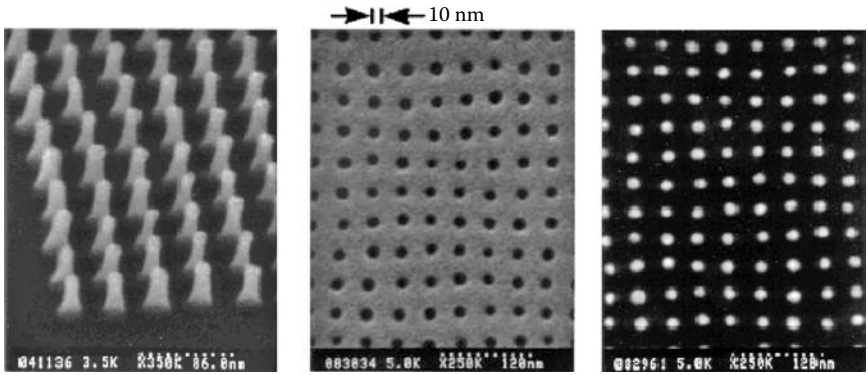

FIGURE 4.2
SEM micrographs of (a) a SiO_2 mold with 10 nm minimum diameter pillars with a 40 nm period, (b) 60 nm–deep holes imprinted into PMMA using the mold shown in (a), (c) metal dots formed by NIL and a lift-off process. (Reprinted with permission from S.Y. Chou, P.R. Krauss, W. Zhang, L. Guo, and L. Zhuang, *J. Vac. Sci. Technol. B* 15, 6 (1997) 2897, American Institute of Physics.)

4.2.2 Polymer Flow during NIL

The flow behavior of a resist during NIL is determined by the interplay of thermal and mechanical properties of the resist, the process parameters, and the geometries of the stamp structures. The most important thermal and mechanical properties of a resist are T_g, viscosity, and modulus. Basically, resists suitable for NIL are those that allow sufficient flow for conformal molding at the process temperature and pressure while during demolding a high modulus is desirable to ensure that the deformed polymer patterns sustain the detachment of the stamp without damage. During NIL, the temperature is normally held some 50 to 100°C above its T_g, which will allow the resist to easily flow into cavities of stamp structures due to decreased polymer viscosity. The viscosity of a resist is a strong function of the temperature, and the imprint time to the completion of the molding is proportional to the viscosity ($t \sim h$) [11]. In contrast to this, the pressure is a less important process parameter. Practically, a range of pressure that is high enough for the resist to flow but low enough to prevent any damage of the substrate and stamp is used without any complicated optimization. The reason is that most thermal and mechanical properties of resists are weak functions of pressure, and that it is difficult to control the pressure accurately because it varies with the geometries of the stamp. More important is its even distribution over the stamp surface, which determines how homogeneously the resist filling can take place. This is often achieved using an equilibration mechanism behind the stamp, such as an air cushion or an elastic stamp mattress.

The other important process parameter is the initial thickness of the resist [11,15]. The process time to mold a thin polymer layer can be reduced to a few seconds by using a high initial layer thickness. For thicker films, the squeezed polymer can flow more freely in the central plane of the film unaffected by the friction at the boundaries. However, the use of a high initial thickness usually results in an unacceptable residual layer thickness, which makes the pattern transfer extremely difficult. Ideally, no residual layer is desired for pattern transfer. On the other hand, an extremely thin initial resist might not be able to provide enough material to fill cavities in the stamp, not alone an impractically long imprinting time up to several tens of minutes. Finally, in optimizing the initial resist thickness, requirements with regard to the target application of the patterned surface need to be considered.

Stamp geometry, that is, the distribution of stamp cavities and protrusions on a stamp surface, also plays a significant role in the polymer deformation during NIL and thus should be considered in designing the stamp and the NIL process [11–15,19,20]. To date, only a few studies have been performed on polymer flow during NIL, and precise design rules concerning feature geometries are not known. However, one general rule on polymer filling is still available: The transport distances of the resist result in a remarkable difference in the filling of cavities according to their size and arrangement. The shorter the distances, the faster the filling of the stamp cavities under identical imprinting conditions. Thus, large, isolated features or gratings surrounded by a large space, as is often the case, are very challenging with respect to a complete filling. Even worse is that in such a case the stamp sinks down quickly in the center of the grating, whereas due to the slow squeeze flow in

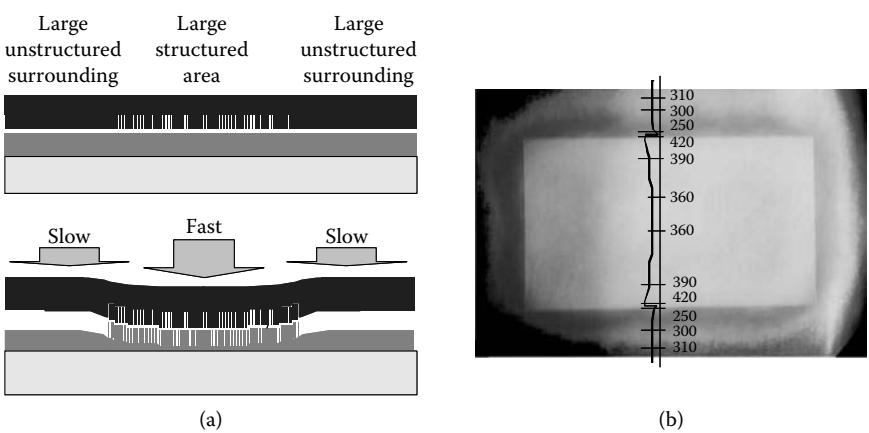

FIGURE 4.3
(a) Schematics representing bending of the stamp during NIL, which results from different sinking velocities due to the stamp geometry. (b) Optical micrograph of a grating with 400 nm period imprinted in PMMA. The structural area of 5 mm × 3 mm is located in the center of a full 4 inch Si wafer. Profilometric height measurement of a cross-section schematically represented in nm indicates large resist thickness variations near and within the grating due to the wafer bending.

the surrounding area, the polymer thickness stays almost constant. The different sinking velocities result in a local bending of the stamp during NIL, producing a residual layer with inhomogeneous thickness distribution (Figure 4.3). Thus, care must be taken with the amount of resist thinned down during the removal of the residual layer in order to ensure complete transfer of the structures.

The actual mechanism of the squeeze flow of a resist into a stamp cavity is a complex function of imprinting conditions [11,15,19,20]. The initial stage of the filling could occur in two different ways: the first beginning from the borders of the stamp cavity and the second filling from the center. Different initial filling behaviors were experimentally observed. A simulation study by Jeong et al. clearly indicates that the capillary force, surface tension, and width of the stamp groove are important factors determining the initial filling behavior (Figure 4.4) [19]. For large width, the resist initially fills the stamp cavity from the borders. When the feature width decreases, the deformation mode also changes. The simulation correctly predicts the flow behavior reported by Heyderman et al., which was attributed to capillary-driven flow rather than shear-thinning phenomena [15].

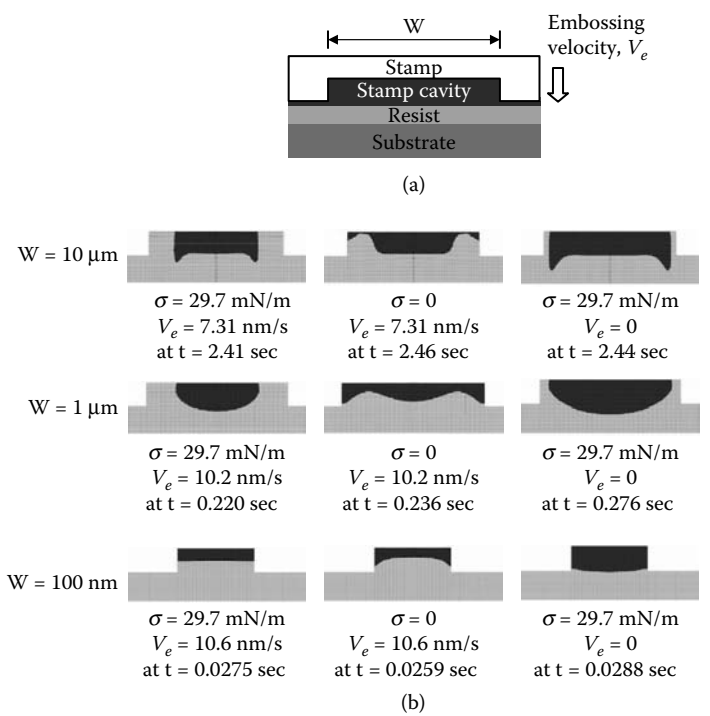

FIGURE 4.4
(a) The geometry of computation domain, and (b) simulated free surface shapes during the initial state of NIL for different geometries (W = 10 μm, 1 μm, and 100 nm), surface energy, and embossing velocities. (Courtesy of J.-H. Jeong, J.-H. Jeong, Y.-S. Choi, Y.-J Shin, J.-J. Lee, K.-T. Park, E.-S. Lee, and S.-R. Lee, *Fibers and Polymers* 3, 3 (2002) 113.)

4.2.3 Biocompatibility of the Resist

A variety of materials are applicable to the NIL process. NIL was initially developed as a patterning method in a thin film of thermoplastic polymer resist such as PMMA, a standard resist for high-resolution EBL. However, it has also proven to be a suitable method for patterning of thermo- and UV-curable polymers, small organic semiconducting materials, sol-gel materials, and even direct patterning into inorganic materials such as Si [6–17,22,36,37,58]. Thus, there is a relatively large degree of freedom in selecting appropriate resist materials applicable to the NIL process. Resists specially designed for NIL are also available. Those resists have been developed to improve performance of the molding process while still being suitable for microelectronics and MEMS systems, as well as for large-area patterning and electroplating processes. The requirements of resist for improving the molding process include a short response time either by heat or UV irradiation, lower molding temperature and pressure, increased mechanical strength once patterns are formed, higher uniformity, and better etch resistance for pattern transfer.

Apart from the abilities of conformal molding, another important criterion for biological applications is biocompatibility, particularly when the fabricated structures in the device are in direct contact with biological molecules that are diagnosed and manipulated. This is because the success of many medical devices is limited by the interaction of the device materials with the contacting biological molecules. Most of the NIL resists are known to be biocompatible. However, when a resist is used in a medical device, testing and evaluation of the device with specifically applied molecules has to be conducted. One example is a study performed by Bunk et al., where motilities of actin filament on various NIL resists and substrate materials were investigated after incubation with heavy meromyosin [4]. One group of resists (mrL-6000.1XP from Micro Resist and ZEP-520, an EBL resist) consistently exhibited high-quality motility of the actin filaments, while a second group (PMMA-200 and PMMA-950 with a molecular weight of 200 and 950 kg/mol, respectively, and mrI-9030 from Micro Resist) showed a low quality of motility with only a few smoothly moving filaments. Such information is very useful in the design of medical devices; the first set of resists are suitable polymers for the creation of myosin-binding tracks for motility, whereas resists in the second set would be useful for padding of areas where motility is unwanted. Based on these findings, grooves fabricated in a bilayer resist system with PMMA-950 and mrL-6000.1XP were found to be effective in prohibiting U-turns of the filaments, and to exhibit 20 times higher density of moving filaments in the grooves made of mrL-6000.1XP than on the surrounding PMMA.

Despite the importance of biocompatibility, information on the interactions between numerous biological molecules and NIL resists is still lacking and more efforts need to be devoted to this task. An alternative to overcome the problem related to this interaction is to modify the resist surface with a

molecule containing functionalities that give rise to desirable surface properties. This method of modifying surfaces is preferential because materials and process parameters for a standard NIL process can still be used while providing surface functionalities. However, compared to silicate or gold surfaces, chemical modification of polymer surfaces has not been well established and needs to be studied further.

4.2.4 Stamps with Nanostructures

As in any other molding-based technology, one of the most important requirements for NIL is to obtain reliable stamps with desired structures that can be repeatedly used without damage during demolding. Most stamps with nanoscale features have been fabricated via EBL in a resist, followed by RIE of the Si substrate by using the resist as a masking layer. With this method, single lines, small arrays of dots, or sparsely distributed structures as small as 10 nm can be made. EUV-Interference Lithography (EUV-IL) is another potential tool for fabricating NIL stamps with extremely small, periodic nanopatterns when combined with appropriate pattern transfer processes (Figure 4.5) [26,61]. Using a spatially coherent beam in the EUV energy range, high density, periodic patterns down to 32 nm pitch have been demonstrated [62]. When large-area diffraction gratings and small coherent EUV beams are used, patterning as large as 5 mm × 5 mm is possible. In particular, the stamp fabrication via EUV-IL has drawn interest in biological applications because an array of periodic patterns with sizes in the range of macromolecules, such as proteins, is very often required for purposes of sensing and isolating bioentities.

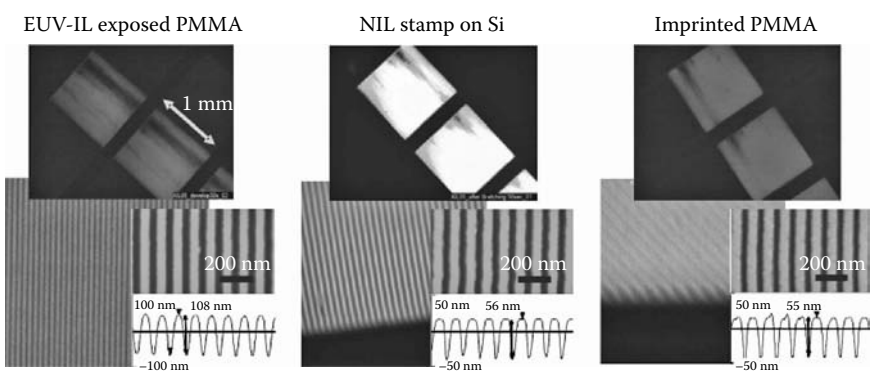

FIGURE 4.5
Dark field optical microscope, SEM, and AFM images: (a) for EUV-IL exposed PMMA, (b) after transferring the pattern into Si to be used as a NIL stamp, and (c) imprinted PMMA using the stamp shown in (b). The half pitch of the pattern is 50 nm and the area of patterns is 1 mm × 1 mm. (Reprinted with permission from S. Park, H. Schift, H.H. Solak, and J. Gobrecht, *J. of Vac. Sci. Technol. B* 22, 6 (2004) 3246, American Institute of Physics.)

While the ultimate lateral resolution of NIL depends on the minimum feature size in the stamp [8], actual success of imprinting often relies on stamp characteristics such as the geometry and aspect ratio of features, size of patterned areas, sidewall profile, and surface roughness. Those factors also have a significant role in determining the flow behavior of the resist. Thus all of them have to be taken into account beginning with stamp design and need to be controlled by carefully optimizing process parameters during stamp fabrication.

As stamp materials, Si wafers are well suited and most widely used because the thermal expansion coefficient of the stamp is often identical to the substrates to be structured, so that pattern distortion generated by a mismatch of the thermal expansion of stamp and substrate can be minimized. Another reason is the ease of access to standard semiconductor processing equipment in a cleanroom environment. Other materials, such as Ni, SiC, diamond, quartz, and even cross-linked polymers have been demonstrated as potential stamp materials [25,63–65]. Consideration in selecting appropriate stamp materials includes flexibility and mechanical strength, process temperature and pressure, and compatibility with other materials and applications. For example, when flexibility and robustness higher than those of Si is needed, Ni stamps fabricated using electroplating are more favorable. If the thermomechanical replication process does not exert high forces on the relief structure, then polymer resist hardened by light, heat, or by chemical initiation may support high temperatures and can be repeatedly used as NIL stamps [25]. However, the lifetime of polymeric molds is still low and good solutions for antisticking coatings have to be found.

4.2.5 Antiadhesive Layer Coating

An increase in the effective surface area by the presence of nanostructures increases adhesion between the stamp surface and the molded resist. This effect becomes significant as structures become complex and the aspect ratio increases. A low surface energy release layer on the stamp helps to improve the imprint quality, and it also increases the stamp's lifetime significantly by preventing surface contamination. Low adhesion and friction at structure sidewalls can only be assured if the stamp is fully covered with a durable antiadhesive layer that can resist the high temperatures and pressures of the NIL process.

Fluorinated trichlorosilanes are often used as antiadhesive layers for Si stamps due to its stable covalent anchoring to hydrated Si surfaces. Surfaces with extremely low surface energy can be achieved by the formation of a dense and fully bound film of silanes, cross-linked between the molecules by the formation of Si–O–Si bonds, which provide satisfactory results in many cases. Use of codeposition of fluorinated mono- and trichlorosilanes was reported to further improve the coating density by self-organization between the two silanes by end-capping the reactive trichloro-group by the

monochlorosilane [30,31]. The silane coating can be applied either in solution or in the gas phase. However, it should be noted that for stamps with features of the nanometer scale, the gas phase deposition is preferred to the solution-dipping method in order to prevent issues related to wetting into the small sized cavities.

A fluorinated silane coating can also be applied to stamp materials other than Si where silane chemistry is no longer valid. This possibility would greatly enhance the versatility of NIL technology. For Ni stamps, a preferred mold material for MEMS and microembossing applications, sputtered or plasma-polymerized teflon-like coatings have been used as release agents. However, such coatings are still less effective and less stable in the long term than Si stamps coated with fluorinated silanes. Recently it was found that the surface energy of a Ni surface coated with fluorinated silane molecules can be lowered dramatically by introducing a very thin layer of SiO_2 (approximately 10 nm) before the coating [29]. Because x-ray photoelectron spectroscopy on the differently treated surfaces indicates a similar amount of the silane molecules attached on the substrates, the decrease in the surface energy was attributed to the increase in the number of the silane molecules covalently bound to Ni surfaces by the deposition of a thin SiO_2 layer. This is also supported by simultaneous imprint tests with sinusoidal gratings of different coatings, where no failure appears for the coating with a SiO_2 interlayer.

4.3 NIL in Biological Applications

In the following we will present some examples of recent developments, where patterns fabricated via NIL were used in biological applications. The use of imprinted patterns can be divided into two categories: the use of surface topologies as a three-dimensional template and chemical contrast on the substrate surface. Surface topologies provide structures that allow integration of components in biomedical devices, such as channels in fluidic devices, detection components, and electrodes in biosensors. Surface roughness and increased adhesive area caused by the presence of surface topologies can also be used to constrain and control motion and growth of biological molecules. On the other hand, the chemical contrast points to an opportunity to control the functionalities of biorelevant events that include transmembrane and intracellular molecules, as well as protein distributions.

4.3.1 Nanofluidic Devices

Microfluidic devices have wide applications in liquid handling in biology and chemistry for manipulating samples in small quantities. The goals of further miniaturization of the fluidic channels are to increase speed and

sensitivity of assays and to enable studies of fluid transport and molecular behavior at extremely small dimensions [4,5,40,42]. For this purpose, NIL is a ready method of defining fluidic channels of the micro- and nanoscales at low cost. Apart from the formation of channels, there are also other aspects that need to be considered in designing a nanofluidic device, which include modifying surface functionalities, sealing of the channels, integration with other microstructures for feeding and detection of fluids, and so forth.

Modifying surface functionalities in the channels is an essential process in the realization of functioning micro- and nanofluidic devices. For example, in order to transport biological molecules within a device, it is necessary to confine their motion along the channel while the molecule should not be adsorbed by the channel walls or escape from the channels. In this regard, it is sometimes necessary to have surface functionalities of the channel walls be different from those on the channel track. Recently, Cheng et al. developed an effective method of achieving highly efficient guiding of microtubules transported by kinesin motors that are immobilized within polymer nanotracks created by NIL [41]. The nanoscale protein tracks constrained by polymer barriers made of a cyclized perfluoropolymer called CYTOP, prevent the gliding microtubules from swaying and compel them to approach the track edge at glancing angles, thus restraining them from moving out of the track. Furthermore, the surface of the CYTOP barriers are chemically modified to have protein-nonadhesive properties, which effectively prevent microtubules from either climbing up the barriers or randomly gliding over the top surface of the barriers.

The fabrication of nanofluidic channels is completed by sealing of the channel using either rigid or soft materials following NIL to produce high-resolution nanoscale templates. Despite the relative ease of constructing nanoscale structures via NIL, the sealing of these structures into functional nanofluidic devices presents great technical challenges. Taking advantage of the filling behavior of resist during NIL, Guo et al. developed a simple method of fabricating enclosed nanofluidic channels [10,40]. If a very thin polymer layer is used during imprinting, the displaced polymer will not be able to fill the trenches on the mold completely, therefore creating enclosed nanochannel features (Figure 4.6). The fabrication process can also be well controlled to give a predictable channel width and height. The channel width is determined by the feature sizes on the channel template used for imprinting. The channel height can be controlled by the depth of the template and the initial thickness of the polymer layer, as well as by adjusting the ratio of the ridge width to the trench width on the channel template. One of the biological applications has been illustrated by stretching genomic DNA in such nanochannel arrays. Over 90% stretching has been observed in nanochannels with a cross-section size of approximately 120 nm × 75 nm (Figure 4.7). Thus, nanofluidic channels could be used for studying the static as well as the dynamic behavior of DNA molecules in confined geometries.

Nanofluidics reduces the size of fluidic systems dramatically. However, it is not simply a matter of shrinking components. Another challenge is how to integrate those nanostructures with other components of micro- or even

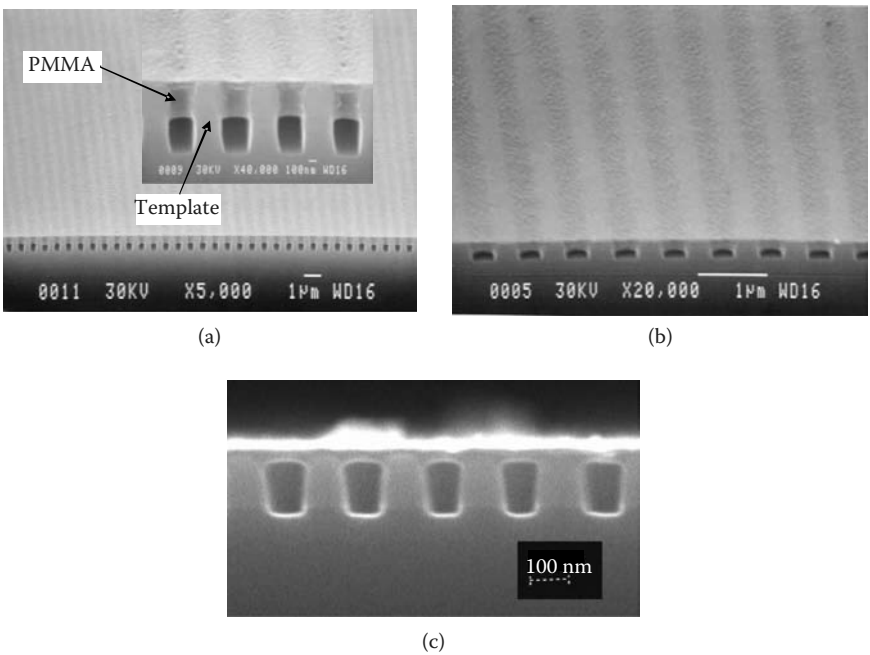

FIGURE 4.6
SEM micrographs of imprinted nanofluidic channels of various cross-sections. (a) 300 nm (width) × 500 nm (height) channels; inset shows a close-up view. (b) 300 nm × 140 nm channels. (c) 75 nm × 120 nm channels. (Reprinted with permission from L.J. Guo, X. Cheng, and C.-F. Chou, *Nano Letters* 4, 1 (2004) 69, American Chemical Society.)

macroscales that operate functions such as mixing, valving, reagent storage and reconstitution, thermal processing, and so forth. Although NIL has proven to be very successful in nanopatterning, especially in replicating periodic nanoscale features with uniform sizes, it still has limitations in producing both large and small features in various combinations and distributions, which is attributed to the rheological behavior of resists during NIL [10,11,13,15]. Several strategies have been developed to overcome this problem, such as an addition of auxiliary structures around the important patterns, lowering the process temperature and pressure, and combining NIL with photolithography [10,13,15]. However, due to the complexity of the rheological behavior during NIL, an individual strategy needs to be found depending on the geometries of the applied patterns and applications.

4.3.2 Engineering Nanopores

High-volume fabrication of perforated membranes has potential for any applications that require templates with nanoscale openings accessible from both sides. By placing biomembranes onto the artificial pores, actions such as separation, sensing, and drug delivery can be performed. Such membrane

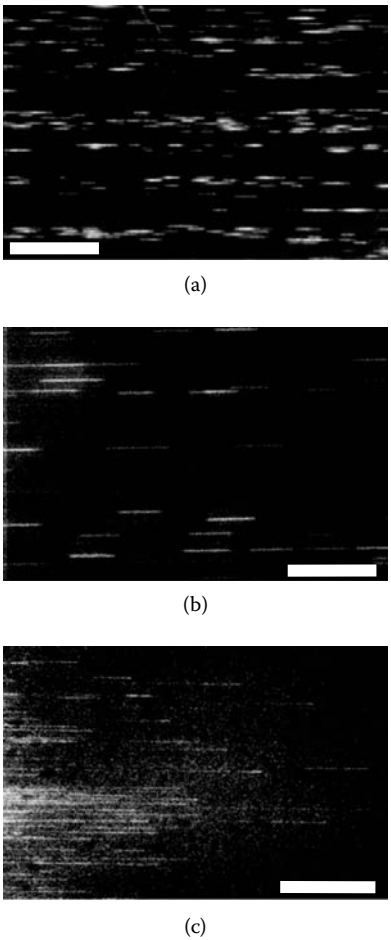

FIGURE 4.7
Fluorescent images showing the stretching of 103 kb–long T5 phage DNA in the imprinted nanofluidic channels. (a) In 300 nm wide and 700 nm height channels, DNA is stretched but to a lesser degree (approximately 15%). (b) In 300 nm × 500 nm channels, DNA is more stretched (30%). In 75 nm × 120 nm channels, DNA stretching reaches about 95%. The scale bar is 20 μm in (a) and (b), 50 μm in (c). (Reprinted with permission from L.J. Guo, X. Cheng, and C.-F. Chou, *Nano Letters* 4, 1 (2004) 69, American Chemical Society.)

structures can be found everywhere in nature, in particular in biological systems, as can be exemplified in transmembrane proteins.

A schematic diagram of the fabrication procedure for nanopore membranes is given in Figure 4.8a [53]. First, the nanopores are replicated by NIL in PMMA spin-coated on a $Si_3N_4/Si/Si_3N_4/Cr$ substrate. The Si_3N_4 on the reverse side of the substrate is prestructured with a square opening to be used as a mask for the final membrane production step. The Si_3N_4 on the front side of the substrate includes alignment marks to align the NIL stamps, so that the nanopores coincide with the membranes. Following imprinting,

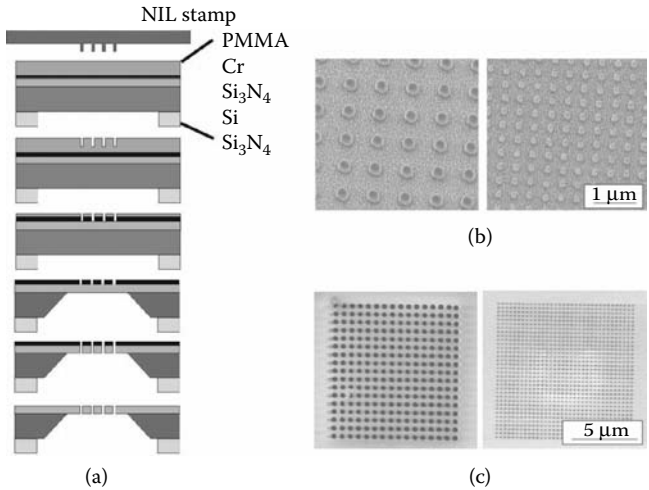

FIGURE 4.8
(a) Process scheme for the fabrication of Si_3N_4 nanopores using NIL. SEM micrographs (b) of the NIL stamps used for the nanopore fabrication and (c) of the corresponding nanopores. (Reprinted from L.J. Heyderman, B. Ketterer, D. Bächle, F. Glaus, B. Haas, H. Schift, K. Vogelsang, J. Gobrecht L. Tiefenauer, O. Dubochet, P. Surbled, and T. Hessler, *Microelectron. Eng*. 67–68 (2003) 208, with permission from Elsevier.)

the PMMA residual layer is removed using an O_2 RIE and the pores transferred into the Cr layer, which is again transferred into the Si_3N_4 using a CHF_3/O_2 plasma. The Si is etched in a KOH bath to reveal the Si_3N_4 membranes. Figures 4.8b and 4.8c show the NIL stamps and the fabricated nanopore membrane structures, respectively. Pores with diameters down to approximately 140 nm were achieved with this method. The pore diameter is basically defined by the size of the nanopillars in the stamp, which were generated using EBL. The slight difference in diameter between the stamp pillars and the resulting nanopores is in the range of 35 to 50 nm. This is surprisingly low considering any lateral movement during imprinting and any widening of the nanopores during the postprocesses. The wall slope can be changed from perpendicular to negative by changing the etch parameters, so allowing tailoring of the pore profile. The membranes were found to be stable. However, more work must be done before implementing those nanopore membrane structures in biological applications, such as load tests, liquid compatibility, biocompatibility, and functionalization of surfaces. For separation processes, it is also important to study the permeation rate and investigate methods for creating force gradients, such as pressure, concentration, electrical potential, and temperature differences.

4.3.3 Chemical Nanopatterning

In addition to the application of topological patterns, NIL may also play an important role in spatially controlling chemical functionality on a surface,

which has become a major challenge for electronic, optoelectronic, biological, and sensing applications [1–4,51,52]. In general, local modification of surface chemistry requires the process sequence of nanofabrication via a suitable patterning method, followed by selective localization of a molecule using chemistry known for its immobilization.

A simple method of fabricating chemical nanopatterns using NIL is based on its pattern transfer ability, which has shown sub–10 nm resolution in the generation of metal lift-off [59]. The process is schematically shown in Figure 4.9a. After the window opening by O_2 RIE, selective chemical modification of the substrate surface is achieved by deposition of a molecule with certain functionalities that need to be imposed on the local substrate surface areas. Finally, the chemical patterning will be completed by lift-off of the remaining resist using a solvent. The chemical modification can be performed either in the gas phase or by dipping in the solution. Figure 4.9b shows atomic/lateral force microscopy (AFM/LFM) images for chemical patterns with a mixture of fluorinated mono- and trichlorosilanes fabricated by the method described in Figure 4.9a. Periodic contrasts in topology, as well as friction force between areas of the silane molecules and the background, are clearly distinguished in the images. The smallest width for SiO_2 lines was 15 nm. The results clearly demonstrate the capability of NIL as a tool for the local modification of chemical functionalities on a surface in an unprecedented lateral resolution by combining with an appropriate surface chemistry.

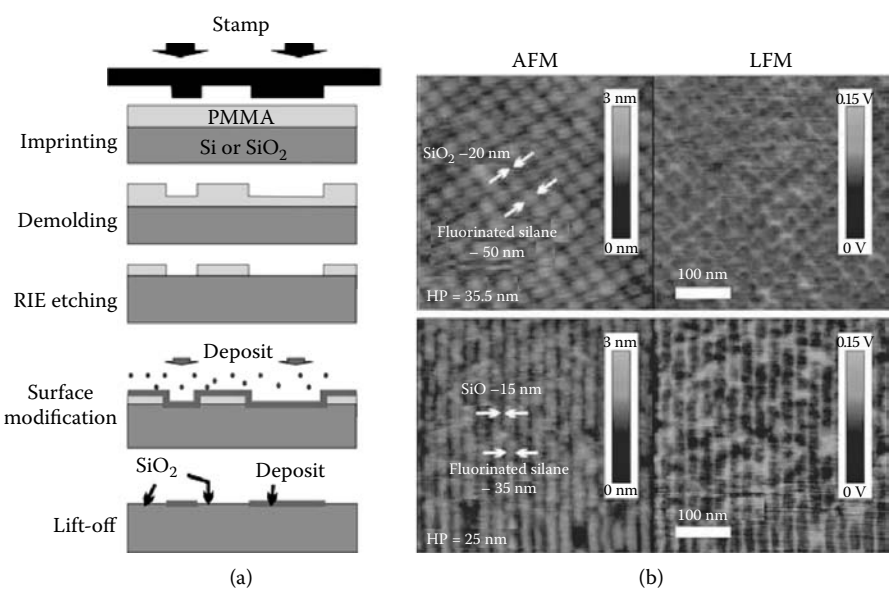

FIGURE 4.9
(a) Process schemes of fabricating chemical patterns via NIL and (b) AFM/LFM images for chemically patterned surfaces modified with a mixture of fluorinated mono- and trichlorosilanes.

Integrated biological applications often require a sequence of additional chemical bindings to the modified local surface functionalities. In such cases, a small amount of contamination could seriously damage the following process, and thus pure chemical contrast needs to be achieved to implement chemical nanopatterns in integrated devices. In order to reduce the level of impurities and inhomogeneities, care should be taken for each process involved. As the pattern size becomes smaller, and thus a smaller resist height is used, it is more difficult to achieve homogeneous thinning of the patterned resist for the window opening process due to inhomogeneous distribution of the residual layer thickness over the patterned areas. In addition, the possible diffusion of the molecules used for the surface modification into the resist necessitates additional topological contrast. Thus, in order to ensure homogeneous window opening and selective surface modification, the aspect ratio for the patterns has to be increased. In addition, a complete removal of resist during the lift-off, which is required to achieve clean chemical contrast, is not an easy task [7]. All the problems mentioned must be solved in order to implement NIL as a practical fabrication technology for high-resolution chemical patterns for various applications.

4.3.4 Protein Nanopatterning

For the development of integrated biodevices, such as biosensors and biochips, it is crucial to be capable of organizing bioactive materials on glass or semiconductor surfaces with micro- and nanometer resolution [1,2]. In particular, patterning of protein layers has been extensively investigated because integrated biodevices rely on the selectivity and sensitivity of receptor molecules, which bind selected analytes. The strategy of improving sensitivity goes toward miniaturization of the pattern size because it will help to improve the detection limits in those devices by increasing the density of the receptor elements [2].

The process of chemical patterning based on NIL (Figure 4.9a) can directly be used to create nanoscale patterns of various biological molecules. However, defining patterns of such molecules on surfaces is not a simple task considering the complex and fragile nature of those molecules. A critical requirement is the ability to avoid nonspecific bindings of proteins (or biomolecules in general). The uncontrolled presence of proteins on an array will most likely affect the outcome of the assay and thus bias the results. Therefore, the noninteractive areas of the pattern require special attention through designed surface chemistry in order to ensure a very low background signal.

Recently, two independent studies have demonstrated the patterning of bioactive proteins with nanoscale resolutions via NIL and local chemical modification using different methods of suppressing nonspecific protein bindings. The method exploited by Falconnet et al. combines NIL and molecular assembly patterning by lift-off (MAPL) [56]. The MAPL process was recently introduced as a technique for producing micropatterns via conventional photolithography and assembly of biofunctional PEG-graft

polyelectrolyte copolymers, such as cationic poly(L-lysine)-graft-poly(ethylene glycol) (PLL-g-PEG) on transparent negatively charged niobium oxide (Nb_2O_5)–coated glass slides. After achieving chemical contrast of PLL-g-PEG/PEG-biotin and Nb_2O_5, the Nb_2O_5 areas were rendered nonfouling by spontaneous adsorption of the nonfunctionalized PLL-g-PEG from an aqueous solution to inhibit nonspecific protein adsorption in the background (Figure 4.10a). In the final step, fluorescence-labeled alexa-488-conjugated streptavidin was adsorbed onto the biotin functionalized patterned surfaces. Scanning near-field optical microscopy (SNOM) was used to image the protein adsorption onto the 100 nm PLL-g-PEG/PEG-biotin stripes. Even though the fluorescent-labeled lines appear broader than the actual line width of the PLL-g-PEG/PEG-biotin stripes due to the resolution limit of SNOM of approximately 100 nm, the regular line pattern of 400 nm–periodicity is clearly recognized, verifying selective adsorption of the streptavidin.

The second approach developed by Guo et al. consists of nanoscale patterning via NIL and a fluoropolymer surface passivation [10,40]. In contrast to the chemical patterning process shown in Figure 4.9a, the local passivation to prevent nonspecific adsorption of biological molecules was done using CHF_3 RIE immediately after the window-opening step. In their study, patterns of selectively passivated Si surfaces are created using NIL, O_2 RIE, and deposition of a passivating $(CF_x)_n$ polymer, which prevents nonspecific adsorption of the biological molecules in the unpatterned regions. The template surface was then processed with a sequence of chemical modification steps, and an aminosilane monolayer, biotin, streptavidin, and ultimately a

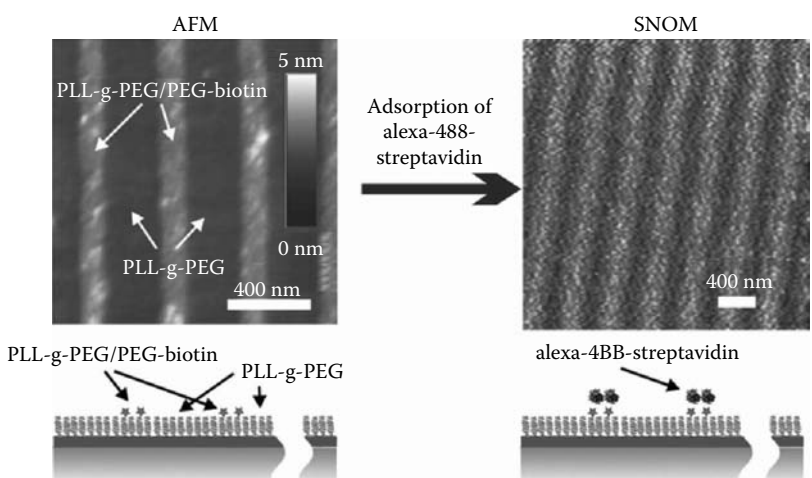

FIGURE 4.10
(a) AFM image for the chemical pattern of PLL-g-PEG/PEG-biotin after backfilling with PLL-g-PEG. (b) Scanning near-field optical microscope (SNOM) image after adsorption of a fluorescent labeled protein, alexa-488-streptavidin on the chemical pattern shown in (a). (Modified from D. Falconnet, D. Pasqui, S. Park, R. Eckert, H. Schift, J. Gobrecht, R. Barbucci, and Marcus Textor, *Nano Letters* 4, 19 (2004) 1909.)

protein target were bound subsequently. This technique results in a highly specific immobilization of a monolayer of biofunctional target protein in patterned areas, and less than 0.1% of a monolayer in surrounding regions. Successful patterning at the nanometer scale was verified using epifluorescence microscopy. In addition, the nanopatterned proteins processed using this method retained their biological functionality, as demonstrated by subsequent antigen binding on patterned antibodies.

4.4 Outlook

In many biological applications, surface patterns with topological or chemical contrast are required, and combinations thereof. Topological structures are fabricated in the form of channels, pillars, and pores for micro- and nanofluidic devices and nanoarrays. Biological active surface structures can be generated by chemical patterning. The patterning of nanostructures on a hard substrate material can be realized using NIL with relative ease, by using the imprinted polymer as a masking layer for pattern transfer. The direct chemical patterning of polymers, however, is more challenging because materials have to be found that allow both good processability and a stable binding of biofunctional molecules. Furthermore, the integration of the nanostructures into other larger-sized components remains to be solved. In microfluidic devices, for example, the integration of a sieve made from nanopillars into a fluidic microchannel requires a high-aspect-ratio nanostructuring capability. For this, several process aspects have to be improved—the ability to fabricate high-aspect ratio structures requires optimization of each process step including fabrication of high-quality stamps, improving antisticking layer coatings, controlled demolding, and so forth. Another challenge lies in in-plane alignment, which is practically limited to approximately 1 μm with commercially available NIL equipment. For example, in a sieve structure, a slight misalignment of the nanopillar pattern with respect to the microchannel could damage the overall device functioning dramatically. For that, efforts are needed to improve the alignment resolution as well as to find alternatives to conventional stamp fabrication, such as using nanoparticles and block copolymers as templates.

The driving force for new nanopatterning methods is the huge demand for low-cost disposable devices and fast prototyping of a large variety of assays. The NIL technology provides a flexible, low-cost, and biocompatible method for fabricating nanostructures and is still evolving very quickly. Its capability to pattern substrates by molding, without changing the chemical properties of the polymer, makes it possible to use a wide range of new materials with tailored chemical and biological properties. Even though there are still many key issues to be solved, NIL technology will play an important role in any biological applications that require topological and chemical patterns at the micro- and nanometer scale.

Acknowledgment

It is our great pleasure to thank many colleagues at the Paul Scherrer Institut (PSI) and Swiss Federal Institute of Technology (ETHZ) for their intensive collaboration and contribution to the results presented here. Particularly, thanks go to C. Padeste, H.H. Solak, L.J. Heyderman, K. Vogelsang, Professor J. Gobrecht (PSI), D. Falconnet, D. Pasqui, and Professor M. Textor (ETHZ). We would also like to thank Professor S.Y. Chou (Princeton University), Professor L.J. Guo (University of Michigan, Ann Harbor) and Dr. J.-H. Jeong (Korea Institute of Machinery & Materials) for allowing us to use their results for this chapter.

References

[1] C.M. Niemeyer and C.A. Mirkin, Eds., *Nanobiotechnology—Concepts, Applications and Perspectives*, Wiley-VCH Verlag GmbH & Co., Weinheim, 2004.
[2] A.S. Blawas and W.M. Reichert, Protein patterning, *Biomaterials* 19 (1998) 595.
[3] K.B. Lee, S.J. Park, C.A. Mirkin, J.C. Smith, and M. Mrksich, Protein nanoarrays generated by dip-pen nanolithography, *Science* 295 (2002) 1702.
[4] R. Bunk, J. Klinth, L. Montelius, I.A. Nicholls, R. Omling, S. Tagerud, and A. Mansson, Actomyosin motility on nanostructured surfaces, *Biochem. and Biophys. Res. Comm*. 301 (2003) 783.
[5] J.O. Tegenfeldt, C. Prinz, H. Cao, R.L. Huang, R.H. Austin, S.Y. Chou, E.C. Cox, and J. C. Sturm, Micro- and nanofluidics for DNA analysis, *Anal. Bioanal. Chem*. 378 (2004) 1678.
[6] S.Y. Chou, P.R. Krauss, and P.J. Renstrom, Imprint of sub-25 nm vias and trenches in polymers, *Appl. Phys. Lett*. 67, 21, (1995) 3114.
[7] S.Y. Chou, P.R. Krauss, and P.J. Renstrom, Imprint lithography with 25-nanometer resolution, *Science* 272 (1996) 85.
[8] C.M. Sotomayor Torres, S. Zankovych, J. Seekamp, A.P. Kam, C. Clavijo Cedeno, T. Hoffmann, J. Ahopelto, F. Reuther, K. Pfeiffer, G. Bleidiessel, G. Gruetzner, M.V. Maximov, and B. Heidari, Nanoimprint lithography: an alternative nanofabrication approach, *Mater. Sci. and Eng*. C23 (2003) 23.
[9] S. Zankovych, T. Hoffmann, J. Seekamp, J.-U. Bruch, and C.M. Sotomayor Torres, Nanoimprint lithography: challenges and prospects, *Nanotechnology* 12 (2001) 91.
[10] L.J. Guo, Recent progress in nanoimprint technology and its applications, *J. Phys. D: Appl. Phys*. 37 (2004) R123.
[11] C.M. Sotomayor Torres, Ed., *Alternative Lithography: Unleashing the Potentials of Nanotechnology*, Kluwer, Boston, MA, 2003.
[12] H. Schift, L.J. Heyderman, and J. Gobrecht, Efficient replication of nanostructured surfaces, *Chimia* 56 (2002) 543.
[13] H. Schift, S. Park, and J. Gobrecht, Nano-imprint—molding resists for lithography, *J. Photopolym. Sci. Technol*. 16, 3 (2003) 435.

[14] H. Schift, L .J. Heyderman, M. Auf der Maur, and J. Gobrecht, Pattern formation in hot embossing of thin polymer films, *Nanotechnology* 12 (2001) 173.
[15] L. J. Heyderman, H. Schift, C. David, J. Gobrecht, and T. Schweizer, Flow behaviour of thin polymer films used for hot embossing lithography, *Microelectron. Eng*. 54 (2000) 229.
[16] H. Schift, C. David, M. Gabriel, J. Gobrecht, L.J. Heyderman, W. Kaiser, S. Köppel, and L. Scandella, Nanoreplication in polymers using hot embossing and injection molding, *Microelectron. Eng*. 53 (2000) 171.
[17] H. Schift, C. David, J. Gobrecht, A. D'Amore, D. Simoneta, W. Kaiser, and M. Gabriel, Quantitative analysis of the molding of nanostructures, *J. Vac. Sci. Technol. B* 18 (2000) 3564.
[18] H.-C. Scheer and H. Schulz, A contribution to the flow behaviour of thin polymer films during hot embossing lithography, *Microelectron. Eng*. 56 (2001) 311–332.
[19] J.-H. Jeong, Y.-S. Choi, Y.-J Shin, J.-J. Lee, K.-T. Park, E.-S. Lee, and S.-R. Lee, Flow behavior at the embossing stage of nanoimprint lithography, *Fibers and Polymers* 3**,** 3 (2002) 113.
[20] H.D. Rowland and W.P. King, Polymer deformation and filling modes during microembossing, *J. Micromech. Microeng*. 14 (2004) 1625.
[21] K. Pfeiffer, G. Bleidiessel, G. Gruetzner, H. Schulz, T. Hoffmann, H.-C. Scheer, C. M. Sotomayor Torres, and J. Ahopelto, Suitability of new polymer materials with adjustable glass temperature for nano-imprinting, *Microelectron. Eng.* 46 (1999) 431.
[22] K. Pfeiffer, F. Reuther, M. Fink, G. Gruetzner, P. Carlberg, I. Maximov, L. Montelius, J. Seekamp, S. Zankovych, C. M. Sotomayor-Torres, H. Schulz, and H.-C. Scheer, A comparison of thermally and photochemically cross-linked polymers for nanoimprinting, *Microelectron. Eng*. 67–68 (2003) 266.
[23] W. Zhang and S.Y. Chou, Multilevel nanoimprint lithography with submicron alignment over 4 in. Si wafers, *Appl. Phys. Lett*. 79**,** 6 (2001) 845.
[24] A. Lebib, Y. Chen, J. Bourneix, F. Carcenac, E. Cambril, L. Couraud, and H. Launois, Nanoimprint lithography for a large area pattern replication, *Microelectron. Eng*. 46 (1999) 431.
[25] K. Pfeiffer, M. Fink, G. Ahrens, G. Gruetzner, F. Reuther, J. Seekamp, S. Zankovych, C. M. Sotomayor Torres, I. Maximov, M. Beck, M. Graczyk, L. Montelius, H. Schulz, H. -C. Scheer, and F. Steingrueber, Polymer stamps for nanoimprinting, *Microelectron. Eng*. 61–62 (2002) 393.
[26] S. Park, H. Schift, H.H. Solak, and J. Gobrecht, Stamps for nanoimprint lithography by EUV interference lithography, *J. of Vac. Sci. Technol. B* 22, 6 (2004) 3246.
[27] Z. Yu and S.Y. Chou, Triangular profile imprint molds in nanograting fabrication, *Nano Letters* 4**,** 2 (2004) 341.
[28] Z. Yu, L. Chen, W. Wu, H. Ge, and S.Y. Chou, Fabrication of nanoscale gratings with reduced line edge roughness using nanoimprint lithography, *J. Vac. Sci. Technol. B* 21, 5 (2003) 2089.
[29] S. Park, H. Schift, C. Padeste, B. Schnyder, R. Kötz, and J. Gobrecht, Anti-adhesive layers on nickel stamps for nanoimprint lithography, *Microelectron. Eng*. 73–74 (2004) 196.
[30] S. Park, H. Schift, C. Padeste, A. Scheybal, T. Jung, B. Schnyder, R. Kötz, and J. Gobrecht, Improved anti-adhesive coating for nanoimprint lithography by co-evaporation of tri- and monochlorosilanes, *Mat. Res. Soc. Proc*. EXS-2 (2004) 37.

[31] H. Schift, S. Saxer, S. Park, C. Padeste, U. Pieles, and J. Gobrecht, Controlled co-evaporation of silanes for nanoimprint stamps, *Nanotechnology* 16 (2005) S171–175.
[32] W. Wu, B. Cui, X. Sun, W. Zhang, L. Zhuang, L. Kong, and S.Y. Chou, Large area high density quantized magnetic disks fabricated using nanoimprint lithography, *J. Vac. Sci. Technol. B* 16**,** 6 (1998) 3825.
[33] J. Wang, S. Schablitsky, Z. Yu, W. Wu, and S.Y. Chou, Fabrication of a new broadband waveguide polarizer with a double-layer 190 nm period metal-gratings using nanoimprint lithography, *J. Vac. Sci. Technol. B* 1**7,** 6 (1999) 2957.
[34] Z. Yu, S.J. Schablitsky, and S.Y. Chou, Nanoscale GaAs metal-semiconductor-metal photodetectors fabricated using nanoimprint lithography, *Appl. Phys. Lett*. 74, 16 (1999) 2381.
[35] L. Guo, P.R. Krauss, and S.Y. Chou, Nanoscale silicon field effect transistors fabricated using imprint lithography, *Appl. Phys. Lett*. 71, 13 (1997) 1881.
[36] J. Wang, X. Sun, L. Chen, and S.Y. Chou, Direct nanoimprint of submicron organic light-emitting structures, *Appl. Phys. Lett*. 75, 18 (1999) 2767.
[37] M.D. Austin and S.Y. Chou, Fabrication of 70 nm channel length polymer organic thin-film transistors using nanoimprint lithography, *Appl. Phys. Lett*. 81, 23 (2002) 4431.
[38] C. Chao and L.J. Guo, Polymer microring resonators fabricated by nanoimprint technique, *J. Vac. Sci. Technol. B* 20, 6 (2002) 2862.
[39] J.D. Hoff, L.-J. Cheng, E. Meyhofer, L.J. Guo, and A.J. Hunt, Nanoscale protein patterning by imprint lithography, *Nano Letters* 4, 5 (2004) 853.
[40] L.J. Guo, X. Cheng, and C.-F. Chou, Fabrication of size-controllable nanofluidic channels by nanoimprinting and its application for DNA stretching, *Nano Letters* 4, 1 (2004) 69.
[41] L.-J. Cheng, M.-T. Kao, E. Meyhofer, and L.J. Guo, Highly efficient guiding of microtubule transport with imprinted CYTOP nanotracks, *Small* 1, 4 (2005) 409.
[42] J.O. Tegenfeldt, C. Prinz, H. Cao, R.L. Huang, R.H. Austin, S.Y. Chou, E.C. Cox, and J.C. Sturm, Micro- and nanofluidics for DNA analysis, *Anal. Bioanal. Chem*. 378 (2004) 1678.
[43] T. Martensson, P. Carlberg, M. Borgstrom, L. Montelius, W. Seifert, and L. Samuelson, Nanowire arrays defined by nanoimprint lithography, *Nano Letters* 4, 4 (2004) 699.
[44] M. Behl, J. Seekamp, S. Zankovych, C.M. Sotomayor Torres, R. Zentel, and J. Ahopelto, Towards plastic electronics: patterning semiconducting polymers by nanoimprint lithography, *Adv. Mater.* 14**,** 8 (2002) 588.
[45] I. Martini, J. Dechow, M. Kamp, A. Forchel, and J. Koeth, GaAs field effect transistors fabricated by imprint lithography, *Microelectron. Eng*. 60, 3–4 (2002) 451.
[46] A. P. Kam, J. Seekamp, V. Solovyev, C. Clavijo Cedeño, A. Goldschmidt, and C. M. Sotomayor Torres, Nanoimprinted organic field-effect transistors: fabrication, transfer mechanism and solvent effects on device characteristics, *Microelectron. Eng*. 73–74 (2004) 809.
[47] N. Kehagias, S. Zankovych, A. Goldschmidt, R. Kian, M. Zelsmann, C.M. Sotomayor Torres, K. Pfeiffer, G. Ahrens, and G. Gruetzner, Embedded polymer waveguides: design and fabrication approaches, *Superlattices and Microstructures* 36, 1–3 (2004) 201.
[48] N. Bogdanski, H. Schulz, M. Wissen, H.-C. Scheer, J. Zajadacz, and K. Zimmer, 3D-Hot embossing of undercut structures—an approach to micro-zippers, *Microelectron. Eng*. 73–74 (2004) 190.

[49] M. Beck, F. Persson, P. Carlberg, M. Graczyk, I. Maximov, T. G. I. Ling, and L. Montelius, Nanoelectrochemical transducers for (bio-) chemical sensor applications fabricated by nanoimprint lithography, *Microelectron. Eng*. 73–74 (2004) 837.
[50] H. Schift, R.W. Jaszewski, C. David, and J. Gobrecht, Nanostructuring of polymers and fabrication of interdigitated electrodes by hot embossing lithography, *Microelectron. Eng*. 46 (1999) 121.
[51] H. Schift, L.J. Heyderman, C. Padeste, and J. Gobrecht, Chemical nano-patterning using hot embossing lithography, *Microelectron. Eng*. 61–62 (2002) 423.
[52] S. Park, H. Schift, C. Padeste, and J. Gobrecht, Nanostructuring of anti-adhesive layer by hot embossing lithography, *Microelectron. Eng*. 67–68 (2003) 252.
[53] L.J. Heyderman, B. Ketterer, D. Bächle, F. Glaus, B. Haas, H. Schift, K. Vogelsang, J. Gobrecht L. Tiefenauer, O. Dubochet, P. Surbled, and T. Hessler, High volume fabrication of customised nanopore membrane chips, *Microelectron. Eng*. 67–68 (2003) 208.
[54] L. J. Heyderman, H. Schift, C. David, B. Ketterer, M. Auf der Maur, and J. Gobrecht, Nanofabrication using hot embossing lithography and electroforming, *Microelectron. Eng*. 57–58 (2001) 375.
[55] H. Schift, J. Söchtig, M. Rossi, and S. Westenhöfer, Replicated high precision micro-optical insert elements for optical bench arrangements, *SPIE Proc*. (International Society for Optical Engineering) 3513 (1998) 122.
[56] D. Falconnet, D. Pasqui, S. Park, R. Eckert, H. Schift, J. Gobrecht, R. Barbucci, and Marcus Textor, A novel approach to produce protein nanopatterns by combining nanoimprint lithography and molecular self-assembly, *Nano Letters* 4, 19 (2004) 1909.
[57] D.-Y. Khang, H. Yoon, and H.H. Lee, Room temperature imprint lithography, *Advanced Materials* 13, 10 (2001) 749.
[58] S.Y. Chou, C. Keimel, and J. Gu, Ultrafast and direct imprint of nanostructures in silicon, *Nature* 417 (2002) 835.
[59] S.Y. Chou, P.R. Krauss, W. Zhang, L. Guo, and L. Zhuang, Sub-10 nm imprint lithography and applications, *J. Vac. Sci. Technol. B* 15, 6 (1997) 2897.
[60] M.D. Austin, H. Ge, W. Wu, M. Li, Z. Yu, D. Wasserman, S.A. Lyon, and S.Y. Chou, Fabrication of 5 nm linewidth and 14 nm pitch features by nanoimprint lithography, *Appl. Phys. Lett* 84, 26 (2004) 5299.
[61] H.H. Solak, C. David, J. Gobrecht, V. Golovkina, F. Cerrina, S.O. Kim, and P.F. Nealey, Sub-50 nm period patterns with EUV interference lithography, *Microelectron. Eng*. 67–68 (2003) 56.
[62] H.H. Solak, Nanolithography with coherent extreme ultraviolet light, *J. Phys.D: Appl. Phys.* 39 (2006) R171.
[63] Y. Hirai, S. Harada, S. Isaka, M. Kobayash, and Y. Tananka, Nano-imprint lithography using replicated mold by electroforming, *Jpn. J. Appl. Phys. Part 1* 41, 6B (2002) 4186.
[64] Y. Hirai, S. Yoshida, N. Takagi, Y. Tanaka, H. Yabe, K. Sasaki, H. Sumitani, and K. Yamamoto, High aspect pattern fabrication by nano imprint lithography using fine diamond mold, *Jpn. J. Appl. Phys. Part 1* 42, 6B (2003) 3863.
[65] S.W. Pang, T. Tamamura, M. Nakao, A. Ozawa, and H. Masuda, Direct nanoprinting on Al substrate using SiC mold, *J. Vac. Sci. Technol. B* 16 (1998) 1145.

5

Hot Embossing for Lab-on-a-Chip Applications

Ian Papautsky

CONTENTS

5.1 Introduction

Polymer microfabrication has become a popular alternative to the established silicon and glass-based microelectromechanical system (MEMS) fabrication technologies, particularly for microfluidic and lab-on-a-chip applications [1]. MEMS technologies are revolutionizing chemical and biomedical applications, and have enabled the fabrication of biochips with microchannels for applications such as electrophoresis [2–4], polymerase chain reaction (PCR) [5,6], electrical field flow fractionation [7,8], gas chromatography [9,10], liquid

chromatography [11,12], and DNA separation techniques [13,14]. Such microscale total analysis systems (μTAS) or lab-on-a-chip (LOC) [15] perform functions of large analytical devices in small, often disposable units. They rely primarily on microscale fluid flow as these systems must contain elements for the acquisition, pretreatment, separation, posttreatment, and detection of samples.

Earlier biochips were fabricated in either silicon [6,9–12] or glass [2–4] using technologies developed primarily in the microelectronics industry. A number of microfluidic devices for various applications, especially in biotechnology, were fabricated by defining the features using standard photolithography. This was followed by etching the substrates using chemicals or plasma and then sealing with a cover plate. Glass and oxidized silicon possess a negative charge and support electroosmotic flow, which is a desirable surface characteristic. Glass systems have proven to be successful especially when applied to separating and sequencing DNA [16]. Silicon and glass were popular as substrate materials primarily because of the existing and established microfabrication methods for microelectronic devices.

However, established silicon and glass processing methods exhibit limitations due to the complex fabrication procedures, geometrical design restrictions, and costs involved. The need for high-aspect-ratio features for various life science applications also posed a serious problem with the existing microfabrication technologies in silicon and glass. Polymers as substrate material offer a solution to these challenges and lend themselves to the mass fabrication of microfluidic devices.

Polymers offer several major advantages that are not immediately available in silicon and glass, including a wide range of material characteristics, biochemical compatibility, ease of processing and prototyping, and lower costs [29]. These characteristics make polymers the most promising substrate materials for applications in the life sciences. Replication technologies (hot embossing, injection molding, and casting) are well suited for these applications because the principles behind these processes are already well established in the macroscale world. A number of microfluidic systems have been recently demonstrated in polymers for biomedical applications, including miniaturized electrophoresis chips [16–18], microfluidic mixers [19–21], pumps and valves [22], devices for cell or protein patterning [23,24], and microfluidic switches [25]. Becker et al. [29] summarized the advantages of using polymers for microfluidics to include: (a) a wide range of available material properties and surface chemistries that permit application-specific substrate optimization; (b) suitable microfabrication technologies for a large variety of geometries (rectangular, rounded, high aspect ratio, etc.); (c) low conductivity for electrokinetic pumping or electrophoretic applications; (d) low material cost, which is key for disposable devices or high-volume production; and (e) ease of manufacturing due to replication-based fabrication.

In addition to the inherent material properties, the rapid growth of polymers in applications involving chemistry and biology is also due to the

application of established replication technologies. These include hot embossing [1,17,18,29,36], injection molding [29,36,54], and methods of rapid prototyping like casting [15,16,19,20,29] and laser micromachining [24,26–29]. Injection molding is one of the most well known technologies where polymer pellets are melted in a heated screw and injected at high pressure against the tool to replicate features. The process can be automated and used to rapidly fabricate LOCs, but is limited by the tool materials and the availability of appropriate substrate polymers. Casting is an inexpensive but slower technique for fabricating microfluidic LOCs in elastomers, where the elastomer precursor and the curing agent are mixed at a fixed ratio and poured over the template. The system is thermally cured, allowing the elastomer to be peeled off once it sets. The most prominent elastomer is polydimethylsiloxane (PDMS), and the casting template can be fabricated by conventional micromachining techniques [16]. Laser ablation is a direct technique in which the energy of a laser pulse is used to break bonds in a polymer molecule and to remove the decomposed polymer fragments from the ablation region [24,29,30]. However, the interaction of the laser light and the polymer material induces surface modifications compared to the untreated material [29,30].

Hot embossing is a reasonably fast and moderately expensive technique used to replicate microfluidic LOCs in thermoplastics. It is a straightforward process, schematically represented in Figure 5.1, where the polymer and the master are heated above the glass transition temperature (or softening point) of the thermoplastic and a controlled force is applied under vacuum. The assembly is then cooled below the glass transition temperatures and they are de-embossed. Though the process cannot be fully automated, it is widely used to replicate microstructures on thermoplastics due to low startup costs and ease of fabrication. Hot embossing offers the advantage of a relatively simpler replication process with few variable parameters and high structural accuracy, and is therefore well suited for a wide range of microfluidic LOC applications from rapid prototyping to high-volume mass fabrication [17].

In this chapter, we will limit ourselves to hot embossing for microfluidic lab-on-a-chip applications. Other microfluidic devices, such as pumps and valves, have been purposefully omitted. The same holds true for a number of other polymer microfabrication technologies that have also been applied to fabrication of microfluidic devices, such as injection molding, casting, and laser ablation.

FIGURE 5.1
Hot embossing process flow.

5.2 Polymers

5.2.1 Material Properties

Polymers are macromolecular substances comprised of thousands of monomeric units. Polymers are formed from either only one monomer or a variety of monomers (copolymers). In most cases, polymers are amorphous with chain lengths varying throughout the bulk material. Thus, polymers do not have an exactly defined melting temperature. Instead, a melting interval exists referred to as the glass transition temperature (T_g), in which the viscosity changes substantially and the material becomes a viscous mass. Many polymers solidify after cooling under the T_g, resulting in a solid phase that is hard and brittle.

In hot embossing, T_g is one the most critical parameters. If the temperature is increased above T_g, the material becomes viscous and can be molded or embossed. For demolding or de-embossing, the material is cooled below T_g. This is an important step because geometric stability of the embossed component can suffer due to relaxation during the demolding and the resulting entropy elasticity. Softeners can be added to polymers to lower the glass transition temperature, but this decreases hardness and increases elasticity and impact strength of the material. Plasticizers added during the polymerization process increase the T_g.

Polymers can be broadly classified into three groups according to the interconnection of the monomer units in the polymer chain, which will substantially affect their properties and thus the embossing behavior. The first group is the *thermoplastic polymers*, which consist of unlinked or weakly linked linear chain molecules. Above the glass transition temperature, these materials become plastic and can be molded into specific shapes, which they retain once cooled below T_g. Thermoplastics are commonly used in hot embossing; polymethylmethacrylate (PMMA) and polycarbonate (PC) are the most commonly used thermoplastics. The second group is the *elastomeric polymers*, which also contain weakly cross-linked polymer chains. Under an applied stress, molecular chains can be stretched to a high extent, but relax and return to the original state once the external force is removed. Elastomers do not melt before reaching the decomposition temperature and are typically processed by casting. Polydimethylsiloxane (PDMS) is one of the most popular elastomers. The third category is the *duroplastic polymers* (also known as *thermoset polymers*), which contain heavily cross-linked polymer chains and therefore do not easily change shape. These materials have to be cast into the final shape, and are harder and more brittle than thermoplastics.

Hot embossing has very specific constraints with regard to the material properties of polymers. Glass transition temperature and thermal expansion coefficient are the most critical parameters to successful replication. As already mentioned, the glass transition temperature is the temperature range where a rigid glassy polymer material softens. Thermoplastics that contain very long polymer chains with strong intermolecular interactions do not melt

and flow, but remain soft until they decompose. Thermal expansion coefficient refers to a change in length or volume resulting from a specified change in temperature. This parameter is important not only in hot embossing fabrication, but also in the microchannel sealing process where different materials are thermally bonded. Other parameters that must be considered include adsorption and transparency at desired wavelengths and autofluorescence when using optical detection; gas permeability when working with cells; chemical resistance when using nonaqueous solutions; electrical insulating properties and thermal dissipation when working with electroosmotic flows; and analyte adsorption, surface properties, and biocompatibility.

5.2.2 Polymethylmethacrylate and Polycarbonate

The majority of the hot embossing work to date, particularly in microfluidic and bio-MEMS applications, has been performed in PMMA (also known as Plexiglas or Lucite). PC (also known as Lexan, GE or Makrolon, Bayer) is another popular polymer material. Both of these materials offer high optical clarity above 400 nm [38] and have a long history as biomedical materials. PMMA is available in a broad range of molecular weights and is a well-known e-beam resist. It is a thermoplastic polymer with a relatively low T_g of 106°C, which makes it better suited for hot embossing than PC (T_g = 150°C). Other physical properties of the two materials, such as the density, elasticity modulus, thermal conductivity, and water absorption, are quite similar. The refractive index of PC is 1.586 [31], higher than that of PMMA, making PC a good material for applications that use optical detection. Material properties of PMMA and PC are summarized in Table 5.1. Both materials exhibit excellent chemical resistance to weak acids, but suffer from poor

TABLE 5.1

Basic Material Properties of Embossing Polymer Materials

Property	PMMA	PC	PS	PP	COC
Density (g m^{-3})	1.17–1.20	1.20	1.05	0.896–0.915	1.01–1.02
Glass Transition Temperature, T_g (°C)	106	150	80–100	0–10	138
Elasticity Modulus (GPa)	3.1–3.3	2.0–2.4	3	1.1–1.6	3.1
Linear Thermal Expansion Coefficient (10^{-6} K^{-1})	70–90	65	70	100–200	60
Thermal Conductivity (W m^{-1} K^{-1})	0.186	0.192–0.21	0.18	0.22	0.16
Tensile strength (MPa)	48–76	62.1–65.5	40	40	66
Water absorption (%)	0.3–0.4	0.35	0.05	0.02	<0.01
Refractive Index	1.49	1.586	1.51	1.51	1.53

Source: Data compiled from Mark, J.E., *Polymer Data Handbook*, Oxford University Press, New York, 1999; Harper, C.A., *Modern Plastics Handbook,* McGraw-Hill, New York, 2000; Becker, H. and Gartner, C., *Electrophoresis,* 21, 12, 2000; Becker, H. and Heim, U., *Sensors and Actuators A*, 83, 130–135, 2000; Topas® Grade 5013 data sheet; and Ticona Inc., www.ticona.com.

TABLE 5.2

Chemical Resistance of Common Embossing Polymer Materials

	PMMA	PC	PS	PP	COC
Aldehydes		0	–	+	+
Alcohols, aliphatic		–	+	+	+
Esters	–	–	–	0	
Ethers		–	–	-	
Ketones	–	–	–	0	+
Aliphatic Hydrocarbons	0	–	–	+	
Aromatic Hydrocarbons	0	–	–	0	
Halogenated Hydrocarbons		–	–	0	
Acids, weak/diluted	+	+	+	+	+
Acids, strong/concentrated	–	–	+ (except HNO_3)	+	+
Acids, oxidizing	0	–	–	0	
Bases weak	+	–	+	+	+
Bases strong	–	–	+	+	+

+ = excellent chemical resistance; plastic not damaged after continuous contact with the substance. The plastic may remain resistant for years.

0 = good/limited chemical resistance; continuous contact causes slight damage, which may be partially reversible (softening, swelling, reduction of mechanical strength, discoloration).

– = low chemical resistance; continuous contact causes immediate damage to the plastic (reduction of mechanical strength, deformation, discoloration, cracks, dissolution, risk of breakage).

Source: Compiled from Mark, J.E., *Polymer Data Handbook*, Oxford University Press, New York, 1999; Becker, H. and Gartner, C., *Electrophoresis*, 21, 12, 2000; Weast, R. C. and Astle, M. J., *CRC Handbook of Chemistry and Physics*, 60th ed., CRC Press, Boca Raton, FL, 1979; Becker, H. and Locascia, L. E., *Talanta*, 56, 267, 2002; and Topas® Grade 5013 data sheet, Ticona Inc., www.ticona.com.

resistance to strong acids, strong and weak bases, and most organic solvents. Chemical resistances of these polymers are summarized in Table 5.2.

Other thermoplastic materials have been used in hot embossing due to the interest in developing microdevices that offer higher operating temperatures, superior chemical resistance, or enhanced optical properties. In many microfluidic applications, the polymer material forms the window of detection, and thus potential changes in refractive index of different plastics may be important. Other polymer materials that have been used in hot embossing include polystyrene (PS), polyamide (PA), polybutyleneterephthalate (PBT), polyoxymethylene (POM), polypropylene (PP), polyphenylene ether (PPE), and polysulfone (PSU), and polyetherketone (PEEK). Table 5.1 lists material properties of some common polymers that are critical in hot embossing [32,33], while chemical resistances of these polymers are given in Table 5.2 [34].

5.2.3 Cyclic Olefin Copolymer

Cyclic olefin copolymer (COC) or Topas by Ticona [35] is a relatively new polymer material that has been gaining popularity due to its excellent physical

and chemical properties [29,36,37]. COC is a thermoplastic copolymer consisting of ethylene and bicyclic olefin (norbornene) monomers. Due to the olefinic characteristics, COC has a good chemical resistance to hydrolysis, acids and bases, and most organic polar solvents such as acetone, methanol, and isopropyl alcohol. However, it is soluble in nonpolar organic solvents including toluene and naphtha.

COC is transparent to light with wavelengths above 300 nm and has higher transparency in visible and near ultraviolet regions than PMMA [37,38]. Figure 5.2 compares the UV transmittance characteristics of COC with PMMA and PC. Further, the refractive index of COC is 1.53 at 589 nm, higher than that of PMMA. Thus, COC has excellent optical properties, making COC ideally suited for fluorescence-based biochemical analysis and bio-optical applications.

The water absorption of COC is less than 0.01%, and for comparison the water absorption of PMMA is 0.3 to 0.4%, an order of magnitude higher [29]. COC has the elasticity modulus of 3.1 GPa and density of 1.01 to 1.02 g/m^3 [31], which are comparable to the properties of PMMA (E = 3.1 to 3.3 GPa and ρ = 1.17 to 1.20 g/m^3 [29,31]). By having lower density than PMMA,

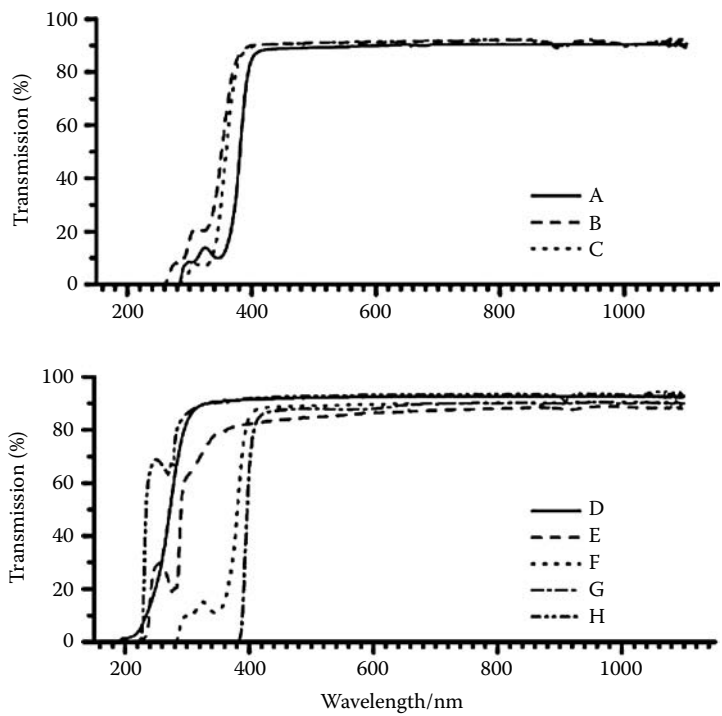

FIGURE 5.2
Transmission spectra of COC, PMMA, PC, PDMS, and glass. Top: A, 0.25-mm thick PMMA; B, 3-mm thick PMMA; C, 5-mm thick PMMA. Bottom: D, 1-mm thick BoroFloat glass; E, 1-mm thick COC; F, 0.25-mm thick PC; G, 2-mm thick PC; H, 1-mm thick PDMS. (From Piruska, A. et al., *Lab on a Chip*, 5, 1348, 2005. With permission.)

COC is easier to emboss. Overall, based on its material properties, COC is ideally suited for hot embossing fabrication of microfluidic chips and devices, especially if signal detection is performed spectroscopically [35–37].

5.3 Master Fabrication

The underlying principle of hot embossing is the replication of a microfabricated master, which represents the negative (inverse) structure of the desired polymer structure. Thus, microfabrication is only necessary one time for the fabrication of this master structure, which then can be replicated many times into the polymer substrate. This offers substantial cost advantages and freedom of design because the master can be fabricated with a large number of different microfabrication technologies.

The success of hot embossing is completely dependent on the master, also called the tool, because any surface defect will be replicated faithfully in the polymer. Thus, hot embossing has specific constraints with regard to masters that must be considered. First, because the master needs to be removed from the desired polymer structure, undercuts cannot be tolerated. Second, fidelity of the replication and master lifetime depend strongly on the surface quality of the master. Generally, smoother master surfaces result in lower frictional forces during de-embossing. Roughness values below 100 nm RMS are necessary for reliable, high-quality replication [29].

The tool material should not form any kind of chemical or physical bond during replication. Release agents, which are commonly used on the macroscale to help release molds of complex structures, are typically not suitable for microfluidic devices. This is because such agents may modify the polymer surface or diffuse into the polymer matrix, and thus adversely affect biological samples. Further, release agents tend to increase the autofluorescence of the polymer, making the device less compatible with fluorescent-based detection schemes commonly employed in microfluidic devices.

There are a number of methods used to fabricate tools. These methods can be broadly classified into four categories: traditional micromachining methods (e.g., milling), bulk micromachining (e.g., wet or dry etching of Si), surface micromachining (e.g., nickel electroplating of photoresist or LIGA molds), and mold micromachining (e.g., PDMS or polyester tools). Surface morphology, adhesion properties to the thermoplastic, lifetime, feature sizes, and costs are the critical factors to be considered in master fabrication.

5.3.1 Micromachining Methods

Modern micromachining technologies, such as sawing, cutting, and computerized numerically controlled (CNC) milling, are capable of producing tools

with structures on the order of a few tens of micrometers. One key advantage of these techniques is the wide range of materials that can be machined, particularly stainless steel, which cannot be processed with other microfabrication techniques but offers excellent tool lifetimes. Another advantage lies in the fact that there is no photolithography step, which in turn eliminates the need to fabricate a mask and thus can substantially shorten the tool development time. Relatively simple geometries with straight walls are a good fit for these techniques.

However, high-aspect structures (height vs. width ratio greater than 2), very deep holes, or very small structures (less than 10 μm) cannot be fabricated. Further, with surface roughness around several μm, these techniques typically do not produce smooth surface finish. CNC machining of materials such as stainless steel yields tools with a very long lifetime. However, it is mostly used for large features, often greater than 50 μm, with tolerances around 10 μm [1], and is limited by difficulties in machining complex designs. Because the entire tool is fabricated in the same material, any adhesion problem between the substrate and features is entirely avoided. However, results in a long lifetime, but all of these prototyping fabrication processes are labor intensive and slow.

5.3.2 Bulk Micromachining

In bulk micromachining, the master is created by etching the substrate wafer, typically silicon. Silicon is a very good material for use as an embossing tool [29,39]. It has a high modulus of elasticity and high thermal conductivity—two material properties that are highly desirable in a hot embossing tool. In addition, there is a large variety of silicon microfabrication techniques. To make a silicon master, a drawing of the microfluidic channels is first created using CAD software, and the image is transferred to a photomask. A silicon wafer is coated with a masking material such as silicon dioxide or silicon nitride, and then coated with a layer of photoresist. The process is schematically illustrated in Figure 5.3. Following UV exposure, the photoresist is developed revealing the transferred image. The image is then transferred to the exposed masking layer by etching in a solution of hydrofluoric acid (HF). The exposed silicon is then etched anisotropically using potassium hydroxide (KOH), tetramethylammonium hydroxide (TMAH), or ethylenediaminepyrocatechol (EDP). If silicon with a crystallographic orientation of <100> is used, the resulting microstructure has a trapezoidal shape, with wall angle off 54.74°. The slant in the wall allows a good mold release and the surface roughness of well-oriented wet-etched silicon wafers is excellent [40–42]. The height and the width of the tool features are controlled by the amount of time the wafer is etched. In the final step, the mask layer is stripped using an HF solution.

Dry etching methods, such as reactive ion etching (RIE) and the Bosch process (for a review, see [43]) can be used to fabricate deep structures with

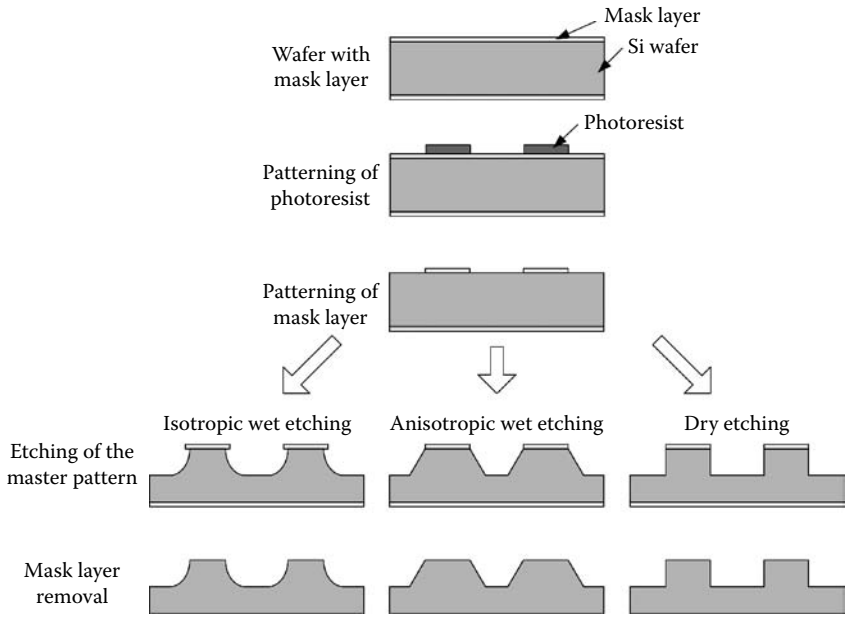

FIGURE 5.3
Bulk micromachining of silicon masters.

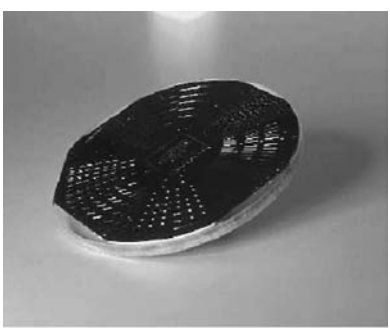

FIGURE 5.4
Photograph of a silicon master anodically bonded to a glass wafer. (From Alonso-Amigo, M.G., *J. Assoc. Lab. Auto.*, 5, 96, 2000.)

vertical sidewalls. However, scalloping or high surface roughness due to non-optimized or fast etches can limit the desirable depth of structures resulting in poor de-embossing characteristics. Typical depths range from 10 to 40 μm.

Although silicon masters are simple to fabricate and offer good resolution and surface properties, they suffer from a number of disadvantages. A common problem of these masters is that they may be too fragile for typical hot embossing pressures and may need some form of reinforcement. Silicon wafers can be reinforced by anodic bonding to glass wafers [44]. A sample silicon master reinforced with a 5 mm–thick glass wafer is shown in Figure 5.4.

However, such masters suffer from reductions in durability and lifetime. Silicon masters may also potentially adhere to polymers due to their surface chemistry, which would reduce the number of possible replication cycles. Finally, to fabricate some silicon masters, specialized equipment is necessary to perform DRIE (deep reactive ion etching), which may not be available at all research laboratories. For greater master durability and replication performance, the surface micromachined masters are used.

5.3.3 Surface Micromachining

In surface micromachining, the master is created by first patterning a mold on the wafer surface, followed by electroplating nickel, and finally removing the mold producing the nickel master. This is the most commonly used method for making masters in hot embossing. It is popular because nickel tools offer high surface smoothness, long lifetimes, and the ability to replicate small- and high-aspect-ratio features.

There are two reincarnations of this method. The first method uses a silicon or glass wafer as a substrate material [45,46], while the second method uses a nickel plate [37,49]. The first process is schematically illustrated in Figure 5.5a. A silicon or glass wafer is coated by evaporation or sputtering with a conducting electroplating seed layer (approximately 100 nm) such as Ni or Cu or Au. A thin layer (approximately 50 nm) of Ti or Cr is used to enhance adhesion of the conducting layer to the silicon substrate. The wafer is then coated with a layer of photoresist, which is subsequently exposed to UV light. The photoresist is then developed so that the areas to be electroplated are free of resist. The wafer is placed into a nickel galvanic bath, where due to the migration of metal ions between the electrolyte and the seed layer, nickel is deposited in the photoresist structure.

Low-stress nickel films can be deposited from a nickel sulfamate galvanic solution. Such solutions are commercially available (e.g., Technics, Inc.) or can be mixed (e.g., 375 g of nickel sulfamate, 7.5 g nickel bromide, and 37.5 g boric acid per 1 L of deionized water [51,52]). Electrodeposition is performed at around 50°C to reduce stress, with current density on the order of 20 mA/cm^2 [51,52]. Plating is allowed to proceed long enough for the metal to grow higher than the resist and form the master base. To ensure that the plating takes place on top of the photoresist, a thin layer of seed metal can be sputtered on the top surface. Following metal deposition, the resist and seed layers can be dissolved and the resulting metal structure can be used for hot embossing.

In the second method, schematically illustrated in Figure 5.5b, photoresist is deposited and patterned on a nickel plate instead of a silicon wafer. Electroplating is performed using the same conditions as described above until nickel completely fills all microstructures and grows above the photoresist. In this method, it is necessary to mechanically machine the nickel

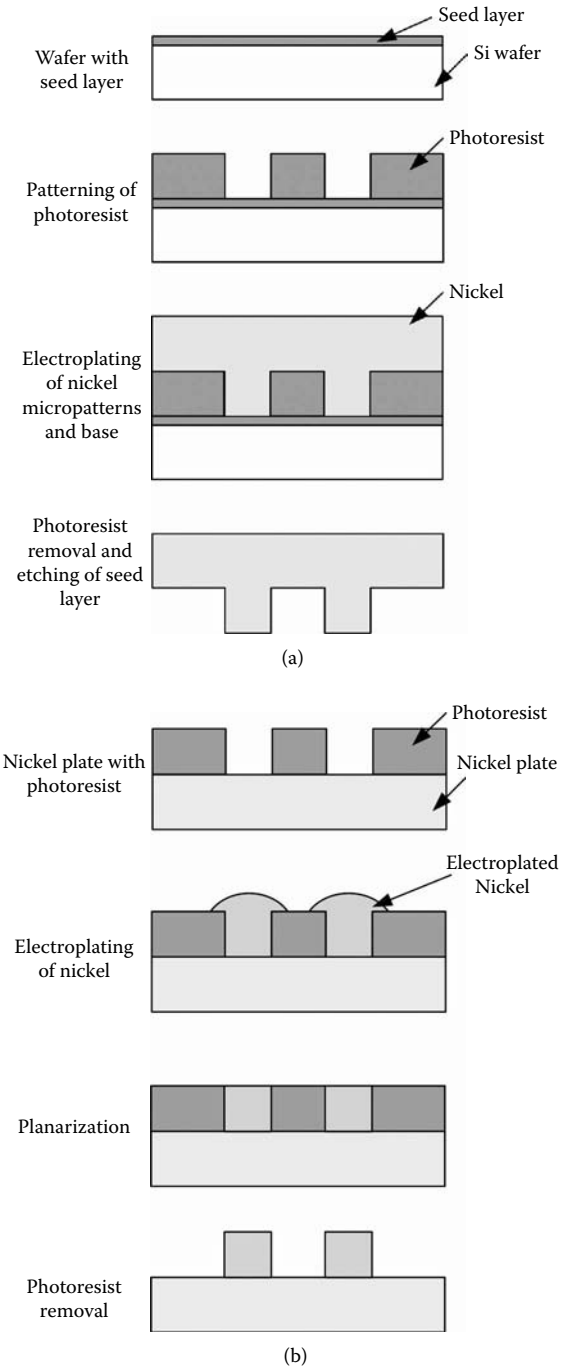

FIGURE 5.5
Fabrication of surface micromachined masters by photolithography and nickel electroplating using a silicon wafer as a substrate (a) and a nickel plate as a substrate (b).

microstructures to the desired height and polish prior to embossing. The photoresist is stripped off to complete the fabrication process.

The height of the metal structure depends on the height of the photoresist mold. Positive thick photoresists allow structural heights on the order of 10 to 40 μm (e.g., Clariant AZ P4620). Thicker structures, up to 1 mm, can be obtained using negative thick photoresist (MicroChem SU-8). X-ray LIGA (German for Lithographie, Glavanoformung, Abformnung) [47] is a well-established technique, where PMMA resist layers are exposed with synchrotron radiation, and can yield high-aspect-ratio structures and molds thicker than 1 mm.

The electroplating method produces master surfaces with very low roughness (about 10 nm RMS for LIGA). Further, nickel tools have good surface chemistry for most polymers. However, there are a number of drawbacks. One is the slow growth rate of nickel in the electroplating process, typically between 10 and 100 μm/hr. Another is the high stress levels in thick nickel films, which tend to deform the master. Electroplating baths can also exhibit a radial dependency of the growth rate, which can result in a different height of the nickel structure in the middle and at the rim of a nickel wafer. Finally, electroplating features of substantially different dimensions may be challenging. Smaller features will have a higher current density and thus will exhibit a higher growth rate, resulting in a different height of smaller and larger nickel structures.

Smoothness of the wall surface depends strongly on the quality of the mask used during photolithography. A high-resolution transparency can be used as an alternative to the traditional chrome-coated glass, if the features are greater than 20 μm [48,49,60]. Figure 5.6 compares structural features made by UV lithography of SU-8. The one developed from a chromium-coated mask shows much better feature shape and surface smoothness compared to that developed from a transparency mask. The latter, however, is much less expensive.

Conventional lithography, x-ray, or UV LIGA followed by electroplating nickel or nickel alloys on silicon or nickel substrates are common techniques of fabricating tools with very small and complex features [1,17,29,50]. The electroplated nickel surface can be very smooth and can have good surface chemistry with many polymers [29]. However, electroplating of tall, high-aspect-ratio structures has to be done for a very long time [51,52], and increasing the current density to speed up the process typically increases stress levels.

In addition to stress, poor adhesion to the substrate seed layers and non-uniform deposition are the other issues to be considered in electroplating. X-ray LIGA offers a potential solution in fabricating tools with very small, complex features and high-aspect-ratio structures [29,53], but is highly limited by the restricted availability and high cost associated with the synchrotron radiation sources. Replication tools with aspect ratios of some ten to 600 can be fabricated using LIGA, and the lifetime of these mold inserts was reported to be as high as 1000 cycles [54]. The surface roughness of the tools was reported to be as low as 10 nm [29].

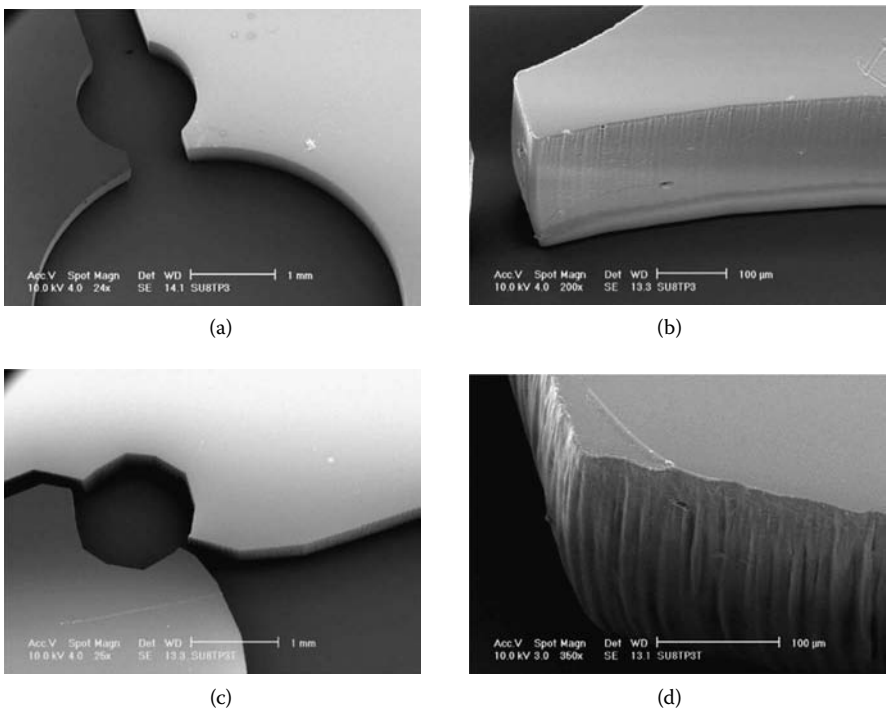

FIGURE 5.6
SEMs of SU-8 structural features developed from a chromium-coated mask (a) and sidewall close-up (b) and a transparency mask (c) and sidewall close-up (d). (From Lee, L.J. et al., *Biomedical Microdevices*, 3, 339, 2001.)

5.4 Hot Embossing

The microfabrication process of hot embossing is rather straightforward [55]. Once an embossing master is fabricated, it is mounted inside the embossing system together with a planar polymer substrate. An embossing machine, schematically illustrated in Figure 5.7, mainly consists of a force frame that delivers the embossing force. The embossing tool and the planar polymer substrate are mounted on heating plates, which are used for thermal cycling. The plates may also contain cooling channels, which are used to reticulate high heat–capacity oil during the cooling phase to permit rapid active cooling.

5.4.1 Conventional Hot Embossing Process

There are three basic steps in hot embossing, schematically represented in Figure 5.8. At the beginning of the embossing cycle, the master and polymer

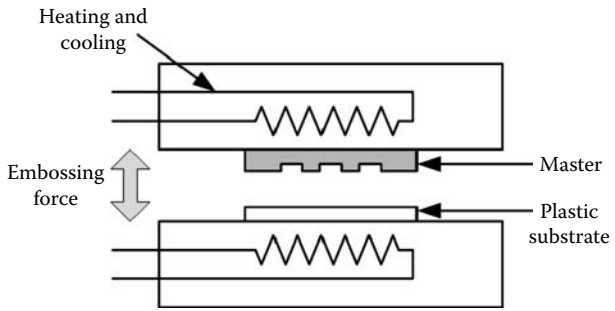

FIGURE 5.7
Schematic diagram of the hot embossing machine. (Adapted from Becker, H. and Gartner, C., *Electrophoresis*, 21, 12, 2000.)

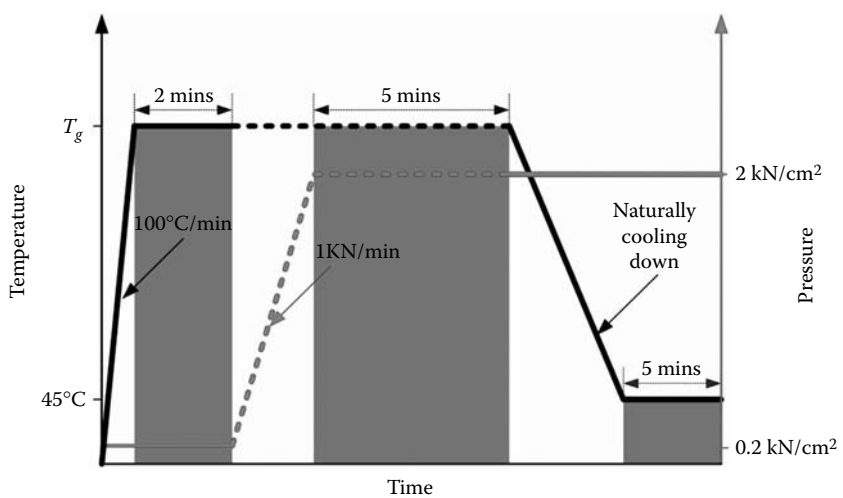

FIGURE 5.8
Graphical representation of the temperature and force program in a typical hot embossing process.

substrate are heated independently in a vacuum chamber at approximately 75 mTorr to a temperature just above the T_g of the polymer. For most thermoplastics, this temperature is typically on the order of 100 to 180°C (see Table 5.1). A vacuum is needed to prevent trapping of air in microstructures and to remove water vapor driven out from the polymer substrate during the process. The vacuum also increases the lifetime of metal masters by preventing corrosion at elevated temperatures. For most applications, the master and the substrate are heated to the same temperature. However, it is possible to independently control each heating plate to attain optimum embossing results.

In the second step, the master is brought into contact with the substrate and then embossed with a controlled force. Typical embossing pressures are on the order of 0.5 to 2 kN/cm². While applying the embossing pressure,

the master-substrate sandwich is cooled to just below T_g. In order to minimize thermally induced stress in the material and replication errors due to mismatch in thermal expansion coefficients of the master and the substrate, the temperature differential in the thermal cycle should be as small as possible. Typical values of the thermal expansion coefficient of polymers are on the order of 7×10^5 K^{-1}, while silicon is approximately 2.5×10^6 K^{-1} and nickel is around 1.3×10^5 K^{-1}.

In the final step, the embossed substrate is cooled to a temperature below the T_g, where the plastic material transitions back to the rigid state. After reaching this lower cycle temperature, the embossing master is mechanically separated from the polymer substrate, which now contains the desired microfeatures. This is usually the most critical step due to the large forces that act on the polymer structure. This is particularly true for microstructures with vertical sidewalls and high aspect ratios. The overall cycle time of the embossing process is typically 1 to 10 min.

For every design, however, the process conditions vary slightly. Geometry of the structures is an important factor that includes feature size, aspect ratio, radius of curvature, and whether the structure is freestanding or connected, and can significantly influence the process parameters. Layout properties of the design, such as the distribution of large and small features over the wafer area and the total wafer area to be processed, also must be considered.

5.4.2 Examples of Embossed Structures

An example of a microchannel structure fabricated in PMMA using hot embossing is shown in Figure 5.9. The microchannels are 50 μm wide and

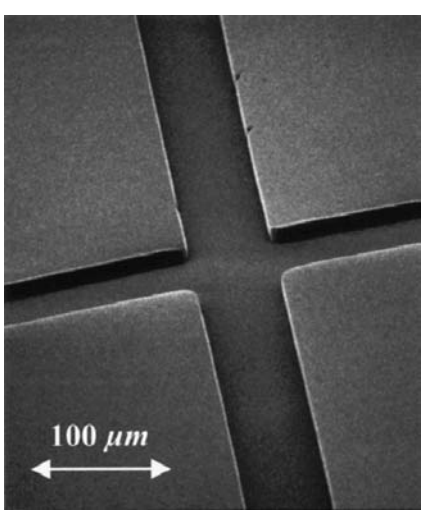

FIGURE 5.9
SEM of an intersection of two 50 μm–wide and 11 μm–deep microchannels embossed in PMMA. (From Studer, V., Pepin, A., and Chen, Y., *Appl. Phys. Lett.*, 80, 3614, 2002.)

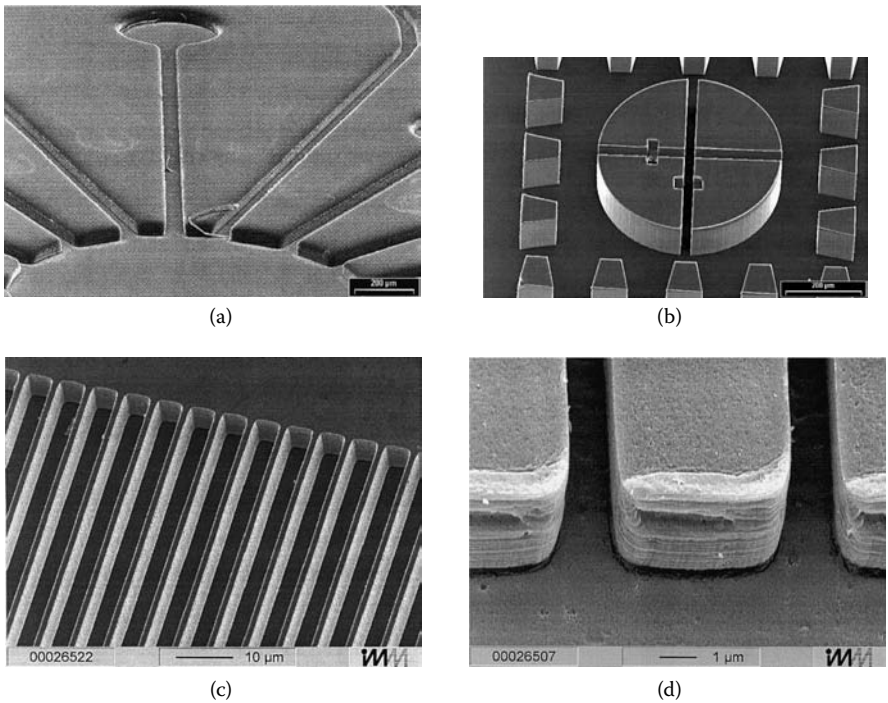

FIGURE 5.10
Examples of embossing tools and structures. SEMs of (a) a microchannel array of a flow cytometry system in PC fabricated with a silicon RIE-tool, (b) a high aspect ratio test structure embossed in PC using a master fabricated with LIGA and nickel electroplating, (c) a silicon tool for a two-dimensional channel array for 2D-capillary electrophoresis, and (d) the replicated PMMA structure. (From Becker, H. and Heim, U., *Sensors and Actuators A,* 83, 130–135, 2000.)

11 µm deep [56]. The fabricated microfluidic structure shows excellent replication capabilities and well-defined shapes, exhibiting very low surface roughness of less than 5 nm. The microchannel intersection illustrates the high surface quality and vertical sidewalls of an RIE etched silicon master.

Microstructures can be replicated in a wide range of shapes and aspect ratios. An SEM of a microchannel array of a flow cytometry system embossed in PC using an RIE etched silicon master [65] is shown in Figure 5.10a. Small micrometer sized channels (50 µm × 50 µm in cross-section) and large hundreds of micrometers reservoirs can be replicated equally well. Figure 5.10b illustrates the high aspect ratio capabilities of the process. The test structure was embossed in PC using a master fabricated with LIGA and nickel electroplating [57,65]. Channel in the circular middle structure has an aspect ration of 7, and is 20 µm wide and 140 µm deep. An advanced silicon etch process can also be used to generate high aspect ratio masters [65]. Figure 5.10c illustrates a silicon tool for a two-dimensional channel array for 2D-capillary electrophoresis. The ridges are 0.8 µm wide and 5 µm high with a 5 µm pitch. The resulting sub-micrometer channel array pattern replicated in PMMA is shown in Figure 5.10d.

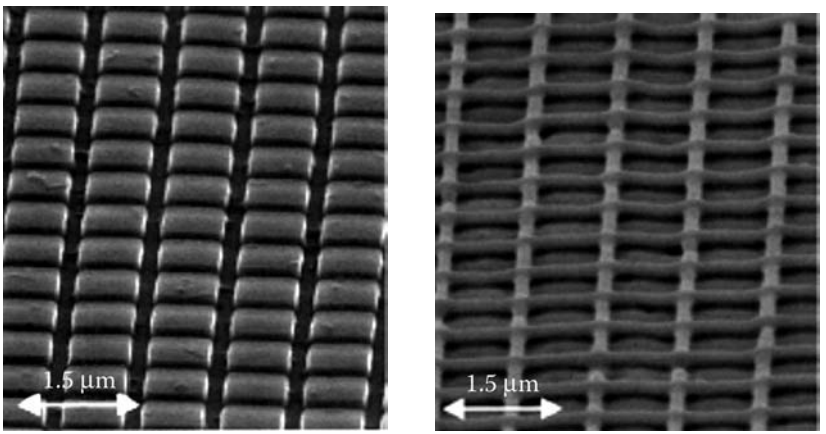

FIGURE 5.11
SEMs of (a) a silicon master and (b) the resulting PMMA structure. Features are 150 nm wide and 200 nm deep at 1 μm spacing. (From Studer, V., Pepin, A., and Chen, Y., *Appl. Phys. Lett.*, 80, 3614, 2002.)

High structural resolution and density are achievable with hot embossing. Figure 5.11 shows SEM images of a grid pattern of approximately 150 nm-wide trenches spaced at 1 μm [56]. Depth of the silicon master fabricated with the advanced silicon etch process and height of the resulting PMMA structures is 200 nm.

5.4.3 Hot Embossing with Polymer Masters

Recently, polymer masters have been demonstrated for embossing plastics. Microstructures formed in negative resist SU-8 on silicon can be used directly as a tool for replicating parts in PC and PP [59]. However, the lifetime of these tools was very short, only a few replications, due to the poor adhesion of SU-8 to the underlying base substrate during de-embossing. Alternatively, photoresist (AZP 4620 or SU-8) can be used to define a template for casting polydimethylsiloxane (PDMS) to form the embossing tool. The process is schematically illustrated in Figure 5.12. Figure 5.13 shows examples of such PDMS masters and the embossed microstructures in PMMA and COC [60–62]. Both large and small features can be replicated using this technique. For example, the PDMS master in Figure 5.13 is 90 μm thick with an array of 150 μm–wide features at 250 μm center-to-center spacing. The PMMA structure is 250 μm deep, containing an array of 600 μm–wide microchannels at 1 mm center-to-center spacing. Figure 5.13 also shows a 5 μm–thick PDMS master with 10 μm–wide ridges at 10 μm side-to-side spacing, and a 20 μm–deep COC pattern with 30 μm–wide channels at 10 μm side-to-side spacing.

The use of PDMS tools can also be extended to fabrication of multilayered structures. This is schematically shown in Figure 5.14. The process involves

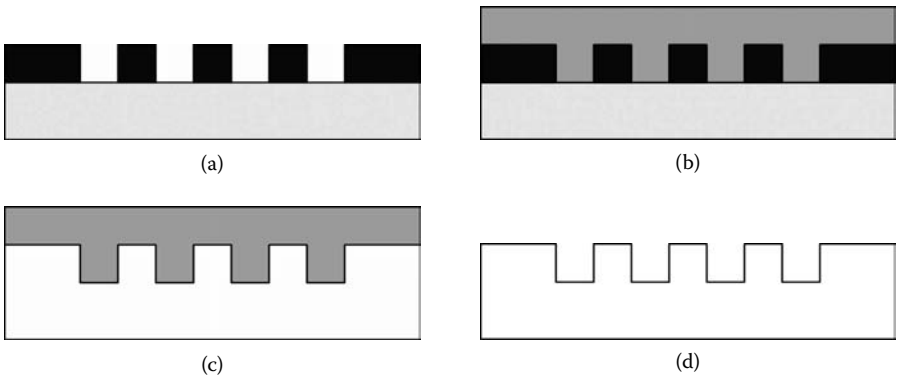

FIGURE 5.12
Schematic diagram illustrating hot embossing using a PDMS tool: (a) photolithographically define AZP 4620 layer on a silicon substrate, (b) cast PDMS, (c) use PDMS tool to emboss COC, and (d) embossed COC substrate.

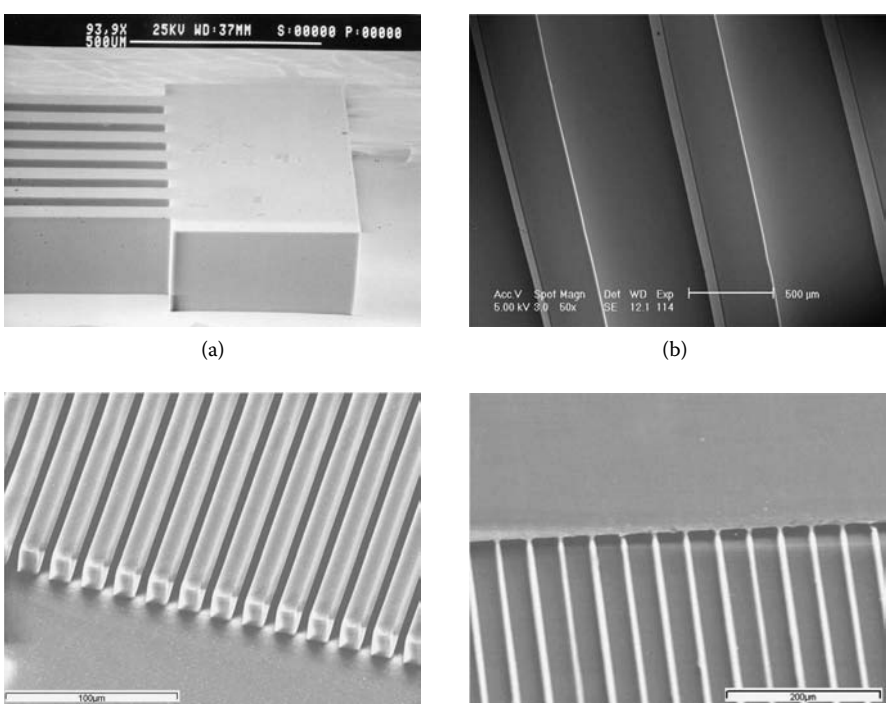

FIGURE 5.13
SEM images of PDMS masters and embossed structures. (a) A 90 µm–thick PDMS master containing an array of 150 µm–wide features with 250 µm center-to-center spacing. (b) A 250 µm–deep PMMA structure containing an array of 600 µm–wide microchannels with 1 mm center-to-center spacing. (c) A 5 µm–thick PDMS master containing 10 µm–wide ridges with 10 µm side-to-side spacing. (d) A 20 µm–deep COC pattern containing 30 µm–wide channels with 10 µm side-to-side spacing.

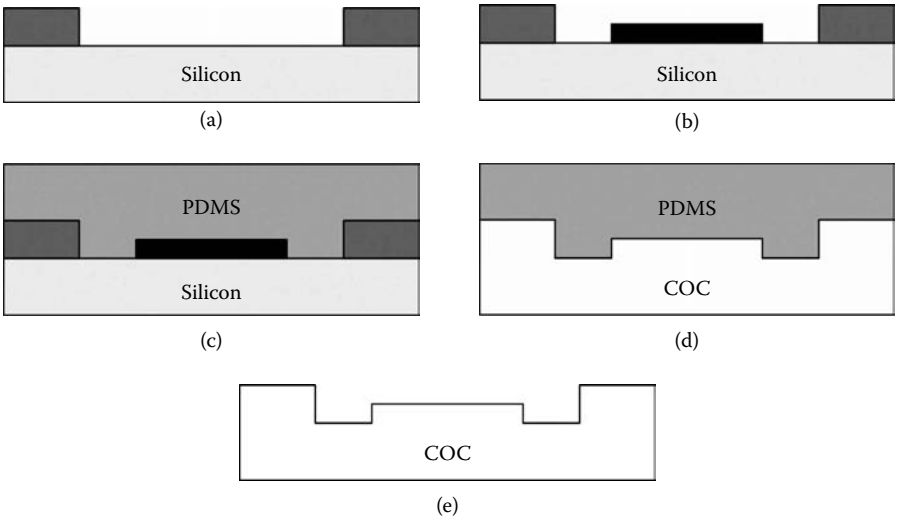

FIGURE 5.14
Schematic diagram illustrating fabrication of a multilayered structure: (a) pattern SU-8 layer on a silicon substrate to define the outer strucure, (b) pattern AZP 4620 layer to define the inner structure, (c) cast PDMS, (d) use PDMS tool to emboss COC, (e) embossed COC substrate.

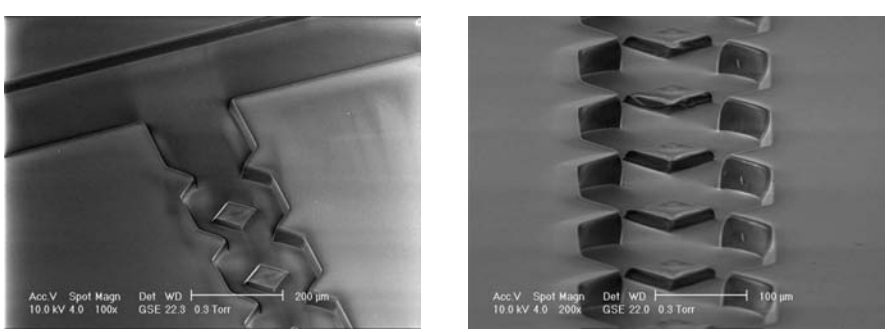

(a) (b)

FIGURE 5.15
SEM images of the micromixer embossed in COC, illustrating the (a) input and (b) channel regions. The 55 µm–high mixing channel is 200 µm at the widest point and 100 µm at the narrowest. The diamond obstructions are 15 µm in height and 100 µm in width.

an additional lithography step using AZP 4620 photoresist. A passive micromixer fabricated using this process is shown in Figure 5.15. The mixing channel width is 200 µm at the widest point and 100 µm at the narrowest, with diamond obstructions 100 µm in width. Channel height is 55 µm with 15 µm–high obstructions. Although this process can be successfully used to fabricate multilayered structures, the greatest difficulty is the patterning of AZP 4620 diamonds within the existing SU-8 channels.

TABLE 5.3

Comparison of Embossing Tool Properties

Property	Nickel	Silicon	PDMS (Sylgard® 184)
Density (g m^{-3})	8.90	2.32	0.970
Young's Modulus (MPa)	200,000	47,000	0.36–0.87
Thermal Expansion Coefficient at 25°C (10^6 K^{-1})	13.4	2.49	310
Thermal Conductivity (W m^{-1} K^{-1})	90.7	124	0.18
Poisson's Ratio	0.31	0.28 for (100) plane	0.5

Source: Data for nickel and silicon are from Lide, D.R. *CRC Handbook of Chemistry and Physics*, CRC Press, Boca Raton, FL, 2003. Data for PDMS are from Sylgard 184 Silicone Elastomer data sheet, Dow Corning, Inc., 2003, www.dowcorning.com.

When depositing a second layer of photoresist over the channels, a meniscus forms between the channel walls, leaving a concave surface. This rounded surface causes the UV light to diffract away from the features causing an uneven exposure, leading to sloped sidewalls on the features. Further, adhesion of the AZP 4620 to the preprocessed silicon surface is very poor following SU-8 processing.

Mechanical properties of PDMS affect the hot embossing process. PDMS masters are not as strong as those of nickel or silicon discussed earlier, and have a much lower Young's modulus [63,64] (Table 5.3). Thus, embossing pressure is very important. PDMS has a higher thermal expansion, and will expand and deform considerably more than conventional tools. Thus optimizing temperature is equally important in order to reduce discrepancies in replication. Overall, the use of PDMS masters can substantially reduce the time, complexity, and costs involved in fabricating prototype microfluidic chips, but limits the master lifetime to approximately 20 cycles.

5.5 Conclusions

Polymer fabrication of microfluidic devices using hot embossing is a young filed that shows enormous growth. One of the driving forces behind this field is the commercialization of microfluidics with medical and pharmaceutical applications, which demand a high number of low-cost, disposable devices. Further, the field of bio-MEMS is moving away from its fabrication roots in microelectronics, and is developing fabrication technologies better suited for applications in the life sciences [65,66].

References

1. Becker, H., Heim, U., and Rotting, O., The fabrication of polymer high aspect ratio structures with hot embossing for microfluidic applications, *Proc. SPIE* (International Society for Optical Engineering), 3877, 74, 1999.
2. Nakanishi, H., et al., Fabrication of Electrophoresis devices on quartz and glass substrates using a bonding with HF solution, in *Proc. IEEE Workshop on Micro Electro Mechanical Systems*, Nagoya, Japan, January 26–30, 1997, 299–304.
3. Effenhauser, C.S., Manz, A., and Widmer, M.H. Glass chips for high speed capillary electrophoresis separation with submicrometer plate heights, *Anal. Chem*., 65, 2637, 1993.
4. Fan, Z.H. and Harrison, D.J., Micromachining of capillary electrophoresis injectors and separators on glass chips and evaluation of flow at capillary interconnections, *Anal. Chem*., 66, 177, 1994.
5. Northrup, M.A., et al., A MEMS-based miniature DNA analysis system, in *Proc. Transducers '95*, Stockholm, Sweden, June 25–29, 1995, 764–767.
6. Wilding, P., Shoffner, M.A. and Kircka, L.J., Manipulation and flow of biological fluids in straight channels micromachined in silicon, *Clin. Chem.*, 40, 1815, 1994.
7. Gale, B.K., Caldwell, K.D. and Frazier, A.B., A micromachined electrical field flow fractionation system, *Trans. Biomed. Eng*., 45, 1459, 1998.
8. Edwards, T.L., Gale, B.K., and Frazier, A.B., Micromachined thermal field flow fractionation system, in *Proc. Transducers '99*, Sendai, Japan, June 7–10, 1999, 742–745.
9. Terry, S.C., Jerman, J.H. and Angell, J.B. A gas chromatographic air analyzer fabricated on a silicone wafer, *Trans. Electron Devices*, ED-26, 1880, 1979.
10. Reston R.R. and Kolesar, E.S. Silicon-micromachined gas chromatography system used to separate and detect ammonia and nitrogen dioxide—part I: design, fabrication, and integration of gas chromatography system, *J. Microelectromechanics. Syst*., 3, 134, 1994.
11. Ocvirk, G. et al., Integration of a micro liquid chromatography onto a silicon chip, in *Proc. Transducers '95*, Stockholm Sweden, June 25–29, 1995, 756–759.
12. Manz, A., et al., Design of an open-tubular column liquid chromatograph using silicon chip technology, *Sensors and Actuators*, B1, 249, 1990.
13. Clark, S.M. and Mathies, R.A., High-speed parallel separation of DNA restriction fragments using capillary array electrophoresis, *Anal. Biochem*., 215, 163, 1993.
14. Han, J. and Craighead, H.G., Entropic trapping and sieving of long DNA molecules in a nanofluidic channel, *J. Vac. Sci. Tech*., 17, 2142, 1999.
15. Duffy, D.C. et al., Rapid prototyping of microfluidic systems in poly(dimethylsiloxane), *Anal. Chem.*, 70, 4974, 1998.
16. McDonald, J.C. et al., Fabrication of microfluidic systems in poly(dimethylsiloxane), *Electrophoresis,* 21, 27, 2000.
17. Becker, H. and Dietz, W., Microfluidic devices for μ-TAS applications fabricated by polymer hot embossing, *Proc. SPIE,* 3515, 177, 1998.
18. Wabuyele, M.B. et al., Single molecule detection of double-stranded DNA in polymethylmethacrylate and polycarbonate microfluidic devices, *Electrophoresis,* 22, 3939, 2001.

19. Beebe, D.J. et al., Passive mixing in microchannels: fabrication and flow experiments, *Mec. Ind*., 2, 343, 2001.
20. Stroock, A.D. et al., Chaotic mixers for microchannels, *Science*, 295, 647, 2002.
21. Rohr, T. et al., Porous polymer monoliths: simple and efficient mixers prepared by direct polymerization in the channels of microfluidic chips, *Electrophoresis,* 22, 3959, 2001.
22. Tamanaha, C.R., Whitman, L.J., and Colton, R.J., Hybrid macro-micro fluidics system for a chip-based biosensor, *J. Micromech. Microeng*., 12, N7, 2002.
23. Delamarche, E. et al., Patterned delivery of immunoglobulins to surfaces using microfluidic networks, *Science,* 276, 779, 1997.
24. Duncan, A.C. et al., Laser microfabricated model surfaces for controlled cell growth, *Biosensors & Bioelectronics,* 17, 413, 2002.
25. Duffy, D.C. et al., Rapid prototyping of microfluidic switches in poly(dimethyl siloxane) and their actuation by electro-osmotic flow, *J. Micromech. Microeng*., 9, 211, 1999.
26. Klank, H., Kutter, J.P., and Geschke, O., CO_2-laser micromachining and back-end processing for rapid production of PMMA-based microfluidic systems, *Lab on a Chip*, 2, 242, 2002.
27. Zhang, Y. et al., High aspect ratio micromachining of polymers with an ultrafast laser, *Appl. Surface Sci*., 186, 345–351, 2002.
28. Kancharla V.J. and Chen, S., Fabrication of biodegradable polymeric microdevices using laser micromachining, *Biomedical Microdevices*, 4, 105–109, 2002.
29. Becker, H. and Gartner, C., Polymer microfabrication methods for microfluidic analytical applications, *Electrophoresis,* 21, 12, 2000.
30. Roberts, M.A., UV laser machined polymer substrates for the development of microdiagnostic systems, *Anal. Chem.,* 69, 2035, 1997.
31. Mark, J.E., *Polymer Data Handbook*, Oxford University Press, New York, 1999.
32. Kaplan, W.A., *Modern Plastics Encyclopedia*, McGraw-Hill, New York, 1998.
33. Harper, C.A., *Modern Plastics Handbook*, McGraw-Hill, New York, 2000.
34. Weast, R.C. and Astle, M.J., *CRC Handbook of Chemistry and Physics*, 60th ed., CRC Press, Boca Raton, FL, 1979.
35. Topas® Grade 5013 data sheet, Ticona Inc., www.ticona.com.
36. Rotting, O. et al., Polymer microfabrication technologies, *Microsyst. Technol*., 8, 32, 2002.
37. Ahn, C.H. et al., Disposable smart lab on a chip for point of care clinical diagnostics, *Proc. IEEE*, 92, 154, 2004.
38. Piruska, A. et al., The autofluorescence of plastic materials and chips under laser irradiation, *Lab on a Chip*, 5, 1348, 2005.
39. Lin, L., Shia, T.K., and Chiu, C.-J., Silicon-processed plastic micropyramids for brightness enhancement applications, *J. Micromech. Microeng.,* 10, 395, 2000.
40. Martynova, L. et al., Fabrication of plastic microfluid channels by imprinting methods, *Anal. Chem.,* 69, 4783, 1997.
41. McComrick, R.M. et al., Microchannel electrophoretic separations of DNA in injection molded plastic substrates,*Anal. Chem*., 69, 2626, 1997.
42. Becker H. and Heim U., Silicon as tool material for polymer hot embossing, *Proc. MEMS '99*, Orlando, FL 1999, 228–231.
43. Jansen, H.V. et al., A survey on the reactive ion etching of silicon in microtechnology, *J. Micromech. Microeng*., 6, 14, 1996.
44. Alonso-Amigo, M.G., Polymer microfabrication for microarrays, microreactors, and microfluidics, *J. Assoc. Lab. Auto*., 5, 96, 2000.

45. Lorenz, H. et al., SU-8: A low-cost negative resist for MEMS, *J. Micromech. Microeng.*, 7, 121, 1997.
46. Bifano, T.G., Fawcett, H.E., and Brierden, P.A., Precision manufacture of optical disc master stampers, *Precision Engineering*, 20, 53, 1997.
47. Becker, E.W. et al., Fabrication of microstructures with high aspect ratios and great structural heights by synchrotron radiation lithography, galvanoforming and plastic moulding (LIGA process), *Microelectronics Engineering*, 4, 35, 1986.
48. Becker, H. and Locascio, L.E., Polymer microfluidic devices, *Talanta*, 56, 267, 2002.
49. Lee, L.J. et al., Design and fabrication of CD-like microfluidic platform for diagnostics: polymer-based microfabrication, *Biomedical Microdevices,* 3, 339, 2001.
50. Puntambekar, A. et al., Fixed-volume metering microdispenser module, *Lab on a Chip,* 2, 213, 2002.
51. Brazzle, J.D., Papautsky, I., and Frazier, A.B., Hollow metallic micromachined needle arrays, *Biomedical Microdevices,* 2, 197, 2000.
52. Papautsky, I. et al., Low temperature IC compatible process for fabricating surface-micromachined metallic microchannels, *J. Microelectromech. Syst.*, 7, 267, 1998.
53. van Kan, J.A. et al., Micromachining using focused high energy ion beams: deep ion beam lithography, *Nuclear Instruments and Methods in Physics B,* 148, 1085, 1999.
54. Piotter V. et al., Injection molding and related techniques for fabrication of microstructures, *Microsyst. Techn.* 3, 129–133, 1997.
55. Heckele, M., Bacher, W., and Muller, K.D., Hot embossing—the molding technique for plastic microstructures, *Microsystem Techol.*, 4, 122, 1998.
56. Studer, V., Pepin, A., and Chen, Y., Nanoembossing of thermoplastic polymers for microfluidic applications, *Appl. Phys. Lett.*, 80, 3614, 2002.
57. Becker, H., Heim, U., and Rotting, O., The fabrication of polymer high aspect ratio structures with hot embossing for microfluidic applications, *Proc. SPIE* (International Society for Optical Engineering), 3877, 74, 1999.
58. Wabuyele, M.B., et al., Single molecule detection of double-stranded DNA in poly(methylmethacrylate) and polycarbonate microfluidic devices, *Electrophoresis*, 22, 3939, 2001.
59. Edwards, T.L. et al., Rapid micromold tooling for injection molding microfluidic components, *Sensors and Materials,* 14, 167, 2002.
60. Narasimhan, J. and Papautsky, I., Polymer embossing tools for rapid prototyping of plastic microfluidic devices, *J. Micromech. Microeng.*, 14, 96, 2004.
61. Narasimhan, J., Polymer embossing tools for rapid prototyping of plastic microfluidic devices, M.S. Thesis, University of Cincinnati, Cincinnati, OH, 2003.
62. Lee, J.-H. et al., Rapid prototyping of plastic microfluidic devices in COC, *Proc. SPIE* (International Society for Optical Engineering), 5718, 82, 2005.
63. Lide, D.R. *CRC Handbook of Chemistry and Physics*, CRC Press, Boca Raton, FL, 2003.
64. Sylgard 184 Silicone Elastomer data sheet, Dow Corning, Inc., 2003, www.dowcorning.com.
65. Becker, H. and Heim, U., Hot embossing as a method for the fabrication of polymer high aspect ratio structures, *Sensors and Actuators A*, 83, 130–135, 2000.
66. Becker, H. and Deitz, W., Microfluidic devices for μ-TAS applications fabricated by polymer hot embossing, *Proc. SPIE* (International Society for Optical Engineering), 3515, 177, 1998.

Part II

Microfluidic Devices and Components for Bio-MEMS

6

Micropump Applications in Bio-MEMS

Jeffrey D. Zahn

CONTENTS

6.1 Introduction

Batch-fabricated microfluidic platforms that can mimic conventional sample handling techniques performed in hospitals and laboratories hold great potential to enable both research and healthcare advances. Such miniaturized diagnostic devices have been termed micro total analysis systems (μTAS) or biochips, and combine sensing mechanisms (physical, optical, electrical, or chemical) with microfluidics. Such autonomous platforms have attracted considerable research interest due to the opportunity for fabricating a highly integrated system able to perform all necessary processing steps required for the specific application. While microfluidics promises to have an impact in many research fields, one of the more attractive applications of microfluidics has been in biomedical and life science diagnostics [1]. μTAS applications are attractive because of the potential of such systems to allow faster analysis of biological material, as well as reducing the amount of reagent required for processing steps. In addition, miniaturization of such systems can result in higher repeatability and precision of analysis, lower power consumption, and the potential to create portable diagnostic tools for on-site analysis. These advantages result not only in time and cost savings for diagnostic tests, but can also be life saving in time-critical environments such as critical medical diagnostics or biowarfare pathogen detection. A major research thrust in microfluidics has been the development of autonomous platforms for allowing controlled microscale fluid transport allowing fluid flow rates ranging from nl/hrs to μl/min within compact fluid-handling and delivery systems—micropumps [2,3].

Micropumps are a desired component of bio-MEMS and microfluidic devices because of their wide application in surgery, drug delivery, drug discovery, and rapid diagnosis and treatment of disease. Micropumps may be coupled with other microfluidic devices such as microfilters for particle [4] or molecular filtration [5], microflow sensors for flow measurements [6], micromixers [7] for analyte and reactant dosing and reaction engineering, microneedles [8] and microdispensers [9] for precise fluid delivery, and microseparators [10] for biological component separations.

Micropumps have been the focus of extensive research efforts and a large variety of micropumps have been realized. These pumps have been designed from an array of operating principles, which will be discussed below. The most commonly exploited principles are mechanical actuation (piezoelectric, electrostatic, pneumatic, thermopneumatic) or nonmechanical actuation (electrokinetic, surface tension driven). Because most biological processes occur in a saline environment, the micropumps presented here will be primarily concerned with liquid micropumps capable of handling biological fluids even though other types of micropumps (gaseous, low dielectric material, etc.) have also been developed.

6.2 Background

In order to design and fabricate micropumps it is necessary to understand how fluids behave on the microscale [11]. The basic physics of transport phenomena do not change as the transition from macroscale to microscale systems is made because the continuum hypothesis is still valid at the size scales of these devices. However, a different realm of the physics becomes important as surface forces dominate over body and inertial forces. As characteristic length scales decrease (such as the width of a fluid flow channel), the surface forces decrease proportional to the square of the length scale. The body forces, however, decrease as the cube of the characteristic length. Therefore, a tenfold decrease in channel dimensions leads to a tenfold increase in the surface-to-volume ratio of the channel. This means that although surface forces decrease by one hundredfold, the volume forces decrease a full one thousandfold. Therefore, the surface forces become 10 times more important relative to the body forces. The main consequence of miniaturization is that surface forces, such as friction and surface tension, become proportionally more significant than body forces, such as inertial and gravitational forces. Thus in this region, pressure forces are equally dissipated by drag forces on the fluid with relatively little inertia. Due to the unique planar processing techniques utilized in microfabrication, flows are generally constrained in a microchannel so that fluid flows within the plane of the channel.

The Reynolds number illustrates the relative importance of the inertial to the viscous forces of the flow and is defined as

$$\mathrm{Re} = \frac{\rho U L}{\mu} \tag{6.1}$$

where ρ is the density of the fluid, U is the mean flow velocity, L is the characteristic length scale of the flow, and μ is the viscosity of the fluid. As the characteristic length scale of the device decreases, so does the Reynolds number.

For an incompressible Newtonian fluid, the conservation of mass may be written as

$$\bar{\nabla} \bullet \bar{u} = 0 \tag{6.2}$$

It is useful to nondimensionalize the flow parameter to illustrate the importance of the Reynolds number in determining the flow regime. Here the velocity, u, is nondimensionalized to a characteristic velocity, U_C, such as the

mean flow velocity; lengths are nondimensionalized to a characteristic length, L_C, such as a channel hydraulic diameter; time is nondimensionalized to a characteristic time scale of the flow, T_C; and pressure is nondimensionalized to a characteristic pressure

$$\left(\frac{\mu U_c}{L_C}\right).$$

The nondimensional Navier-Stokes equation may be written as follows

$$\mathrm{Re}\left[\frac{1}{St}\frac{\partial \bar{u}}{\partial t} + \bar{u} \bullet \bar{\nabla}\bar{u}\right] = -\bar{\nabla}p + \bar{\nabla}^2\bar{u} \tag{6.3}$$

where St is the Strouhal number

$$St = \frac{T_C}{\left(L_C / U_C\right)} \tag{6.4}$$

where T_c is a characteristic time scale of the transient fluid behavior.

In the case of microscale phenomena related to fluid flows, the characteristic length scale is on the order of microns. Thus, the Reynolds number is usually on the order of 1 or less.[1] For most microfluidic problems, the flow is assumed to be in a quasi-steady state, so that the flow is either steady or slowly changing so that the Strouhal is equal to 1. Then as the Reynolds number becomes small ($Re \ll 1$, $Re/St \ll 1$), the inertial terms become negligible compared to the viscous forces.

Thus, the left-hand terms of Equation 6.3 disappear relative to the right-hand terms, and the viscous force balances the pressure force, which is known as the creeping flow limit [12].

$$\bar{\nabla}p = \bar{\nabla}^2\bar{u} \tag{6.5}$$

A physical interpretation of Equation 6.3 is that the left-hand terms correspond to body or inertial forces of the fluid and the right-most term is a surface viscous term through which the fluid transmits shear on a boundary. As the characteristic length scale of a flow decreases, the volume of the fluid in the channel decreases so there is less mass through which body forces may act. At the same time, the relative surface area of the flow geometry increases leading to greater surface forces, which become more dominant in

[1] Water-filled (ρ = 1000 Kg/m^3, μ = 0.001 Pa-s) channel with a hydraulic diameter (L) of 0.0001 m, traveling at an average velocity (U) of 0.01 m/s).

determining the flow mechanics. Equation 6.5 is merely a mathematical representation of this effect.

A few interesting conclusions may be drawn from Equation 6.5. Because it is a linear equation, all flows in the creeping flow limit are kinematically reversible. This means that if fluid is displaced by some forward actuation stroke, such as a moving piston in a micropump, and the reverse stroke is in exactly the opposite direction, then all fluid will return to its original position at the end of the cycle with zero net fluid motion. Thus, one of the challenges in designing micropumps is designing a flow asymmetry in order to produce a net pumping motion.

Equation 6.5 may be analytically solved for a wide variety of flow geometries. Because most microchannels are etched into a substrate, the fluid channels run within the plane of the wafer. One common type of geometry that is fabricated is the rectangular microchannel. Here fully developed flow in the laminar regime for an x-directed velocity profile in a rectangular duct with y and z cross-sections is considered. The simplest geometry is plane Poiseuille flow. In this case, the channel width, $2b$, is much larger than the channel depth, $2a$. With $b>>a$, the x-directed velocity profile may be taken as independent of the channel width. The flow profile may then be approximated by plane Poiseuille flow [13].

$$v_x = \frac{a^2}{2\mu}\left(-\frac{dP}{dx}\right)\left[1-\left(\frac{y}{a}\right)^2\right]. \tag{6.6}$$

Integrating over the cross-sectional area gives the approximate flow rate

$$Q = \frac{4ba^3}{3\mu}\left(-\frac{dP}{dx}\right). \tag{6.7}$$

If the width and depth are approximately the same size, ($a \approx b$), then the flow profile may be solved by separation of the variables

$$v_x = \frac{16a^2}{\mu\pi^3}\left(-\frac{dP}{dx}\right)\sum_{i=1,3,5\ldots}^{\infty}(-1)^{(i-1)/2}\left[1-\frac{\cosh\left(i\pi z/2a\right)}{\cosh\left(i\pi b/2a\right)}\right]\frac{\cos\left(i\pi y/2a\right)}{i^3} \tag{6.8}$$

$$-a \le y \le a$$
$$-b \le z \le b \tag{6.8}$$

where $2a$ is the length of one of the walls and $2b$ is the length of the other wall. Integrating this profile across y and z gives the average flow rate, Q as

$$Q = \frac{4ba^3}{3\mu}\left(-\frac{dP}{dx}\right)\left[1 - \frac{192a}{\pi^5 b}\sum_{i=1,3,5...}^{\infty}\frac{\tanh\left(i\pi b / 2a\right)}{i^5}\right]. \quad (6.9)$$

The average velocity, U, is $Q/(4ab)$.

Many micropumps are fabricated as stacked, bonded substrates and fluid may flow through the different layers. In this case, the flow profiles may be very complex and may only be solved using computational methods.

6.3 Fabrication Processes

The devices discussed in this chapter are all fabricated using techniques adapted from the electronic circuit processing industry. Each step in producing a device requires either material addition, removal, or substrate bonding. However, to discuss these techniques in depth is beyond the scope of this work, and is the basis of many stand-alone texts [14,15] and may be referenced as needed. Therefore, this discussion will provide a summary overview of the most commonly employed techniques.

The first step in producing a micropump is patterning a substrate (usually silicon, glass, or plastic) using photolithography. Here, a photosensitive material, photoresist, is added onto a substrate and patterned by optical lithography. By shining long-wavelength ultraviolet (LWUV) light through a patterned photomask, the photoresist is selectively exposed and developed to transfer a pattern from the mask onto the substrate. This procedure is analogous to printing a photograph with the photomask serving as the negative and the photoresist serving as photographic paper. This technique can reproducibly pattern features smaller than one micron. The major advantages of optical lithography are the ability to miniaturize devices and produce many identical devices in parallel at tremendous cost savings per device.

Material addition using adaptive techniques may be accomplished by a variety of methods. The most common methods for depositing thin films onto a substrate are by chemical vapor deposition or physical vapor deposition. In addition, polymeric materials may be deposited by spin casting in a manner similar to spinning photoresist onto a substrate.

Chemical vapor deposition requires gaseous reactants to be introduced into a reactor system. Once in the reactor, a chemical reaction occurs leaving a solid film on the substrate. Common CVD reactors utilize low-pressure chemical vapor deposition (LPCVD) systems in which silicon-containing gases are introduced into a heated reaction tube to produce thin films of polycrystalline silicon, silicon dioxide, and silicon nitride. Films may also be deposited using plasma-enhanced chemical vapor deposition (PECVD), in which reactions are promoted by ionizing reactant gases in a plasma, so

lower deposition temperatures are usually required. PECVD may also be used for depositing polymer films from fluorocarbon precursors.

Physical vapor deposition refers to the direct physical addition of material from a source. Direct evaporation of material under a vacuum produces a uniform material layer on a substrate. Thermal evaporation is used in materials with a low melting temperature, while e-beam evaporation is used for materials with higher melting temperatures. Sputtering is achieved by bombarding a target material with energetic inert gas atoms within a plasma. The target atoms are *sputtered* off the surface by momentum transfer and pass through the chamber until they deposit on the substrate surface.

Material removal is accomplished by etching processes. This is the most common way of producing microchannels as a lithographically defined pattern is etched into a substrate. Thus, most microchannels are three-dimensional projections of a two-dimensional lithographically defined pattern, which is why most microchannels are defined within the plane of the substrate. The most commonly employed etching processes are wet etching and plasma etching. In wet etching the patterned substrate is placed in a chemical etch bath. Wet etching is usually isotropic (i.e., the etch rate is the same in all directions) and produces curved sidewalls. However, there are etchants, such as potassium hydroxide (KOH), ethylene diamine pyrocatechol (EDP), and tetra-methyl ammonium-hydroxide (TMAH), which selectively etch along silicon crystal planes to produce anisotropic etched profiles.

Plasma or dry etching may also be isotropic or anisotropic depending on the plasma source and reactor configuration. One of the more popular dry etching techniques is deep reactive ion etching (DRIE) [16]. In DRIE a directed etch step is cycled with a sidewall passivation step to produce very-high-aspect sidewall structures in silicon. The advantages of DRIE over other etching techniques is very good sidewall and dimensional control, fast etch rates, and good etch repeatability.

Polymer microchannel fabrication is often accomplished by molding or embossing techniques. A popular technique for prototyping is the use of soft lithography [17,18] or molding of poly-dimethylsiloxane (PDMS) against a thick photoresist master. A photoresist master is created by standard lithographic techniques and a liquid PDMS precursor solution with a curing agent is poured over the master. Due to the low surface tension of the PDMS solution, it readily flows and takes the shape of the master. The PDMS then cures and is peeled off as a negative impression of the master pattern. Other polymeric materials such as polyurethane, polycarbonate, PMMA, and so forth may also be micromachined by hot embossing against a negative master.

One of the critical fabrication processes for creating micropumps is bonding and sealing of devices. Direct silicon wafer bonding may be accomplished by high-temperature fusion bonding techniques, while glass–silicon bonding may be accomplished by anodic bonding [19], in which a high potential is placed across the wafer stack at an elevated temperature. Glass–glass [10] and polymeric bonding may be accomplished by heating the materials to

their glass transition temperature and allowing the material to reflow and bond. Polymeric materials, especially PDMS, may also be bonded to glass or to itself by exposing the surface to an oxygen plasma [20] or corona discharge. This treatment causes the surface to become reactive, promoting covalent bonding of substrates.

Due to the planar processing and wafer bonding techniques utilized to create micropumps, most devices are shown as cross-sectional diagrams. These types of diagrams illustrate the different wafer layers and any specific features along the depth of the device. This cutaway view allows individual pump components (actuation membranes, valves, etc.) to be highlighted and shows how the components work together to create the final micropump.

6.4 Mechanical Micropumps

6.4.1 Actuation Sources

All mechanical micropumps require an actuation source to provide a mechanical stroke cycle. Mechanical actuation usually involves coupling mechanical deformation of a moving boundary to an increase or decrease in the fluid pressure to drive flow. Actuators that perform this function may be classified as either external or integrated actuators (Figure 6.1). Some examples of mechanical pumps requiring an actuation source are positive displacement pumps, fixed-geometry rectification pumps, and peristaltic pumps.

6.4.1.1 External Actuators

External actuators are classified as such because they are not integrated into the device by micromachining. They require either external components or coupling to the micropump. Because these actuators tend to be larger than the microfluidic components, they increase the total size of the micropump. However, these actuators have the advantage of being capable of producing large forces and stroke displacement.

6.4.1.2 Electromagnetic Actuation

Electromagnetic actuation works in a similar manner to a solenoid valve in the form of an electromagnet (Figure 6.1a). An energized solenoid coil produces a magnetic field, which produces a force on a ferromagnetic plunger. The plunger is coupled to a membrane so that when the coil is de-energized the plunger returns to its original position. This is a fairly large structure due to the size of the solenoid coil. However, large strokes can be achieved and may be tailored by the coil current and number of wire turns within the coil.

6.4.1.3 Piezoelectric Actuation

Piezoelectric actuation has been accomplished by coupling the displacement generated in a piezoelectric material to pump membrane displacement (Figure 6.1b). In a piezoelectric material such as lead zirconate titanate (PZT), an applied voltage produces a strain and mechanical deformation. The piezoelectric element may be a piezoelectric disk which is glued directly onto the pump membrane. A disk-style actuator has a fast response time and large

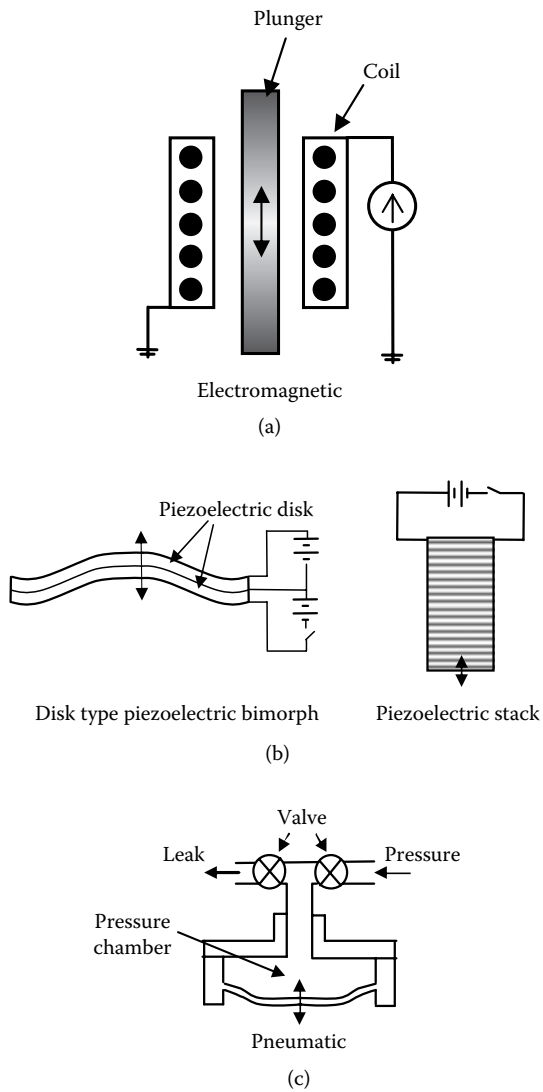

FIGURE 6.1
Actuation sources based upon (a) electromagnetic actuation, (b) piezoelectric actuation, (c) pneumatic actuation.

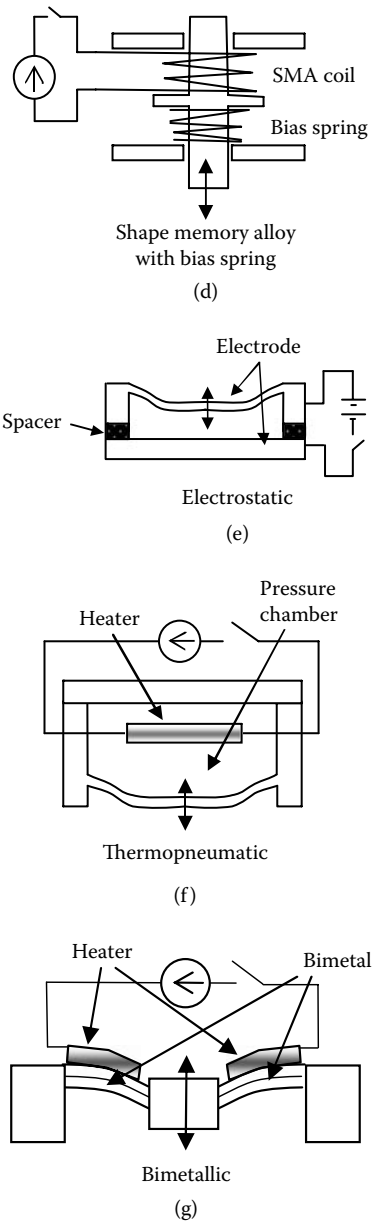

FIGURE 6.1 (CONTINUED)
Actuation sources based upon (d) shape memory alloy (SMA), (e) electrostatic actuation, (f) thermopneumatic actuation, and (g) bimetallic thermal actuation. (Adapted from Shoji, S. and Esashi, M., *Journal of Micromechanics and Microengineering,* 4, 157–171, 1994.)

stroke displacement but the pump pressure is relatively small. Greater pressure may be obtained by using a piezoelectric stack actuator with a tradeoff in stroke displacement and response time.

6.4.1.4 Pneumatic Actuation

Pneumatic actuation uses a high-pressure gas source that is coupled to the pump membrane (Figure 6.1c). Within a pneumatic chamber the gas pressure is controlled through the use of two solenoid valves, which may either open to pressurize or close to depressurize the pump chamber. The advantage of pneumatic actuation is that very large pressures may be generated. The disadvantages are the requirement of a pressurized gas source, and the response time is limited by the speed at which the solenoid valves open and close.

6.4.1.5 Shape Memory Alloy

Shape memory alloys (SMA) may be used as actuation sources by coupling the SMA with a bias spring (Figure 6.1d). The SMA is initially shaped and memorized into an expanded coil. The coil is compressed when placed into the actuator. When the SMA temperature is raised to the critical memory temperature by running a current through the coil, the coil expands and produces a force on the actuation membrane. As the coil cools, a bias spring produces an opposite force, which compresses the coil back to its initial state. By cycling coil expansion and compression a pump stroke is obtained.

6.4.1.6 Integrated Actuators

Integrated actuators are micromachined as a pump component during the microfabrication process. Because they are produced during the fabrication process, integrated actuators usually exhibit a fast response time and better force coupling to the pump. However, producing integrated actuators usually adds complexity to the microfabrication process.

6.4.1.7 Electrostatic Actuation

Electrostatic actuation is based on capacitive charging of two parallel electrodes; a fixed electrode and a movable electrode in an electric field (Figure 6.1e). As the electrodes charge, a force pulls on the moveable electrode to deform the pumping membrane. This actuation method generally has very low power consumption, but the electrode displacement is usually very small because with constant applied voltage, the force is inversely proportional to the square of the electrode spacing.

6.4.1.8 Thermopneumatic Actuation

Thermopneumatic actuation is based on gas expansion within a sealed actuation chamber (Figure 6.1f) to deform a pump membrane. Thermopneumatic actuation may be produced either by gas expansion or liquid-vapor phase change (boiling) due to resistive heating or direct electrolysis of water to produce oxygen and hydrogen gas bubbles. Thermal bubble generation may also be used directly within a microchannel as bubble expansion acts as a

piston to displace fluid. This actuation mechanism produces very large forces and stroke volumes. However, resistive heating for thermopneumatic actuation requires a large amount of energy.

6.4.1.9 Bimetallic Thermal Actuation

Bimetallic actuation is based on thermomechanical actuation due to differences in the thermal expansion coefficient of two layers of material (Figure 6.1g). When the structure is heated by resistive power, dissipation in each material causes expansion and the difference in expansion in the two materials causes deformation. The actuator displacement depends, in an approximately linear manner, on the temperature change, which may be well controlled by the power dissipated within the structure.

6.4.2 Positive Displacement Pumps

Positive displacement micropumps move fluid through the use of a mechanical actuation source. They are designed to maximize pump pressure and stroke volume, and minimize dead volume. In addition, it is desirable for the pumps to be self-priming and bubble purging [21].

The actuation source is usually placed within a pump chamber with a moving membrane boundary [22]. The actuator usually acts to deform a membrane causing a stroke-volume change, ΔV, within the pumping chamber, with an initial volume, V_O. This may be considered a cycling between a supply phase, where the diaphragm stroke increases the pump chamber volume and a pump phase where the diaphragm reduces the chamber volume. The compression ratio of the pump is defined as

$$\varepsilon = \frac{\Delta V}{V_O} \tag{6.10}$$

and most positive displacement micropumps function at high pressure with a small compression ratio due to the small membrane displacements obtained from the actuation source.

The deformation of the pump membrane is usually a reversible stroke due to cyclic actuation between the supply and pump phases. Due to the kinematic reversibility of viscous-dominated flows, it is necessary to rectify the flow in one direction by integrating check valves into the micropump (Figure 6.2). Check valves are designed to have a smaller flow resistance in the forward flow direction than the reverse flow direction. Thus by cycling pump actuation within a pump stroke, a net pumping action is achieved. When the pump membrane is displaced upward (supply mode) it creates a negative pressure within the pump chamber. This draws fluid in through an inlet check valve, and flow is restricted from entering the pump chamber from the outlet by the outlet check valve. When the pump membrane is relaxed (pump mode) it creates a positive

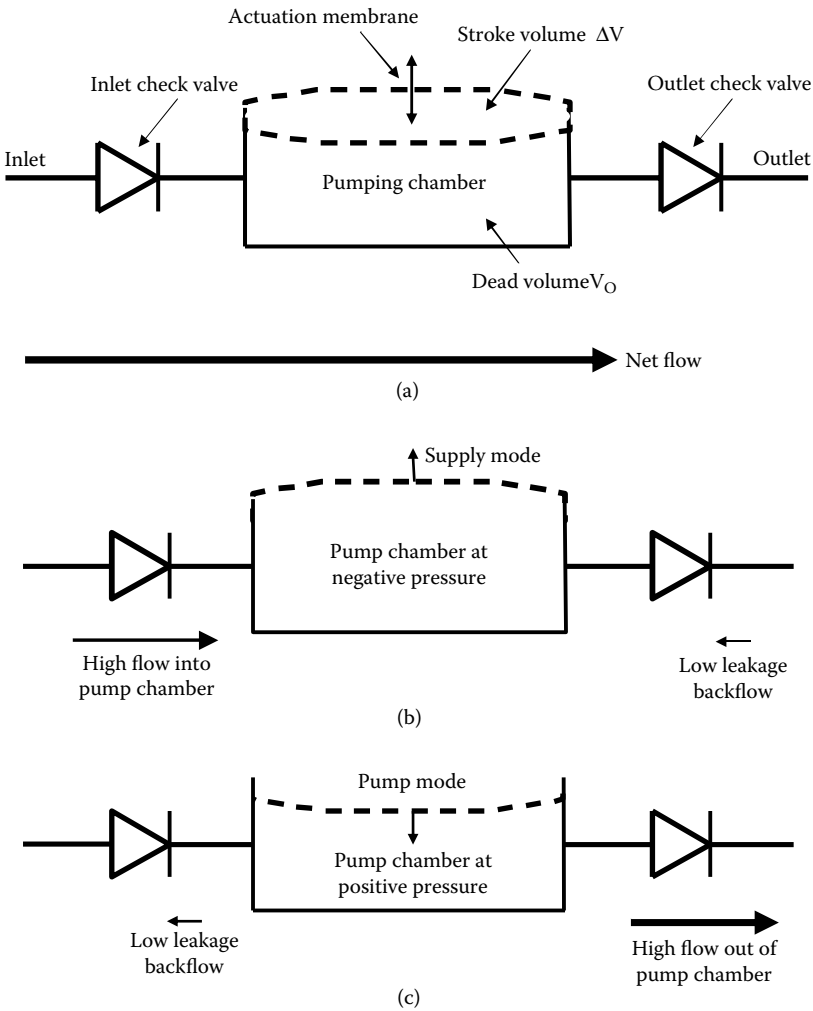

FIGURE 6.2
(a) Structure of a positive displacement pump consisting of a pump chamber with a pump membrane and two check valves. Schematic of one pump cycle during the pump (b) upstroke and (c) downstroke. (From Richter, M., Linnemann, R., and Woias, P., *Sensors and Actuators A* 68, 480–486, 1998.)

pressure within the pump chamber, which now opens the outlet check valve and closes the inlet check valve so within one pump stroke, a fluid volume of ΔV would be displaced if the check valves have 100% flow rectification.

6.4.2.1 Positive Displacement Pumps with Integrated Check Valves

In order to achieve a fast pumping rate, passive check valves are used within the pump structure to limit the pump response time, thus allowing a high

stroke frequency. In order to design an appropriate check valve, the compression ratio must be

$$\varepsilon > \kappa \left| \Delta P_{valve} \right| \tag{6.11}$$

where κ is the compressibility of the liquid (0.5×10^8 m^2/N for water) and ΔP_{valve} is the pressure required to open the valve. Most liquid micropumps can easily meet this requirement. However, it is also preferable to design check-valves that require very little pressure to open the valve. The valve performance may be further characterized by its ability to rectify flow given by the rectification factor

$$R = \frac{Q_{forward}}{Q_{backward}} \tag{6.12}$$

where Q is the flow rate and the subscript refers to the open (forward) and closed (backward) valve states.

Several design examples of positive displacement micropumps with integrated check valves are shown in Figure 6.3. Figure 6.3g shows a planar thermopneumatic micropump where the pressure generated by the growth and collapse of a bubble acts as a piston to drive flow. These pumps are realized using a variety of check-valve designs including ring diaphragm valves (Figures 6.3a, 6.3f), disc valves (Figures 6.3b, 6.3c, and 6.3d), and cantilevered check valves (Figures 6.3e and 6.3g).

6.4.3 Fixed-Geometry Rectification Micropumps

One of the drawbacks to positive displacement pumps with integrated check valves is the complicated fabrication protocols required to produce them. Fixed-geometry pumps are much simpler to produce because they require no moving check valves. They achieve flow rectification by proper microchannel design in order to rectify flow in one direction. They are based upon either diffuser or nozzle pumps [34,35,36] or the use of Tesla-type [37,38] fixed-geometry valves (Figure 6.4). Proper microchannel design adds a geometric flow resistance asymmetry so the physical structure of the microchannel rectifies the flow. A diffuser valve consists of a diverging geometry, while the nozzle geometry consists of a converging geometry. The fixed-geometry valve acts as both a diffuser and nozzle element due to the reversible actuation stroke. In the case of a diffuser- or nozzle-type fixed-geometry valve, flow through the expansion during the positive actuation stroke has a smaller resistance than the backflow through the nozzle during the negative stroke.

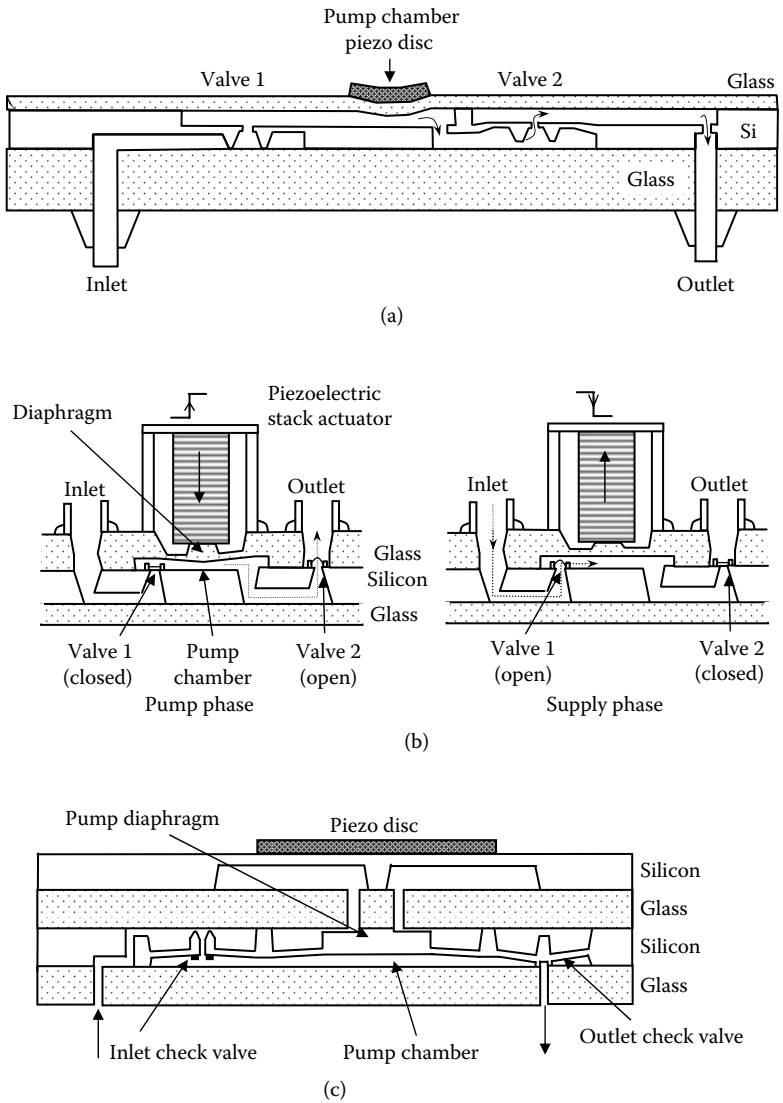

FIGURE 6.3
Schematic of positive displacement check valve pumps. (a) Piezoelectric actuation with a ring mesa check valve. (Adapted from Van Lintel, H.T.G., van den Pol, F.C.M., and Bouwstra, S.A., *Sensors and Actuators* 15, 153–167, 1988.) (b) Piezoelectric stack actuation with disc valves in pump and supply mode. (Adapted from Shoji, S., Nakagawa, S., and Eashi, M., *Sensors and Actuators A* 21–23, 189–192, 1990.) (c) Piezoelectric actuation with disc valves. (Adapted from Maillefer, D. et al., *Proceedings of the 12th IEEE International Workshop on Micro-Electromechanical Systems MEMS '99*, Orlando, FL, January, 17–21, 541–546, 1999; and Maillefer, D. et al., *Proceedings of the 14th IEEE International Workshop on Micro-Electromechanical Systems MEMS '01*, Interlaken, Switzerland, January, 21–25, 413–417, 2001.)

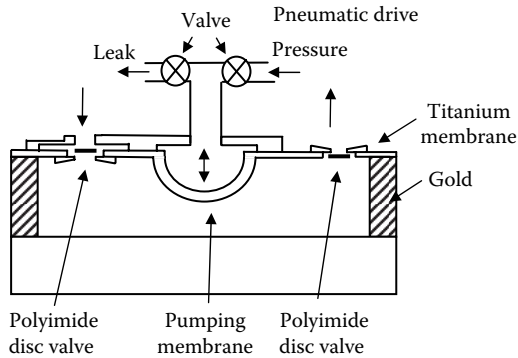

(d)

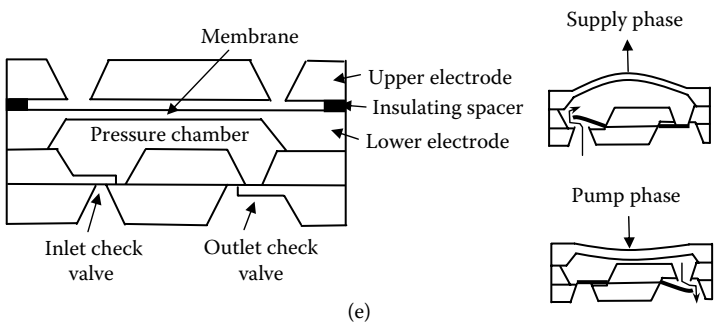

(e)

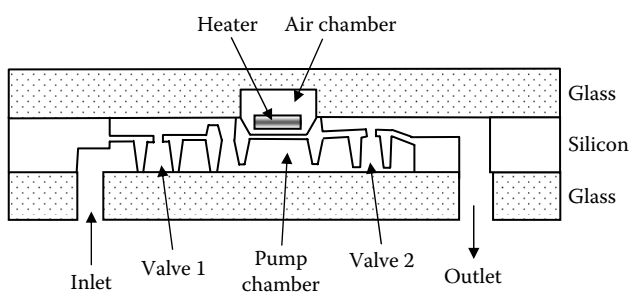

(f)

FIGURE 6.3 (CONTINUED)
Schematic of positive displacement check valve pumps. (d) Pneumatic actuation with disc valves. (Adapted from Rapp, R. et al., *Sensors and Actuators A* 40, 57–61, 1994.) (e) Electrostatic actuation with cantilever valves. (Adapted from Zengerle, R., Richter, A., and Sandmaier, H., *Proceedings of the 5th IEEE International Workshop on Micro-Electromechanical Systems MEMS '92*, Travemünde, Germany, February, 4–7, 19–24, 1992.) (f) Thermopneumatic actuation with ring mesa valves. (Adapted from Lammerink, T.S.J., Elwenspock, M., and Fluitman, J.H.J., *Proceedings of the 6th IEEE International Workshop on Micro-Electromechanical Systems MEMS '93*, Ft. Lauderdale, FL, February, 7–10, 254–259, 1993.)

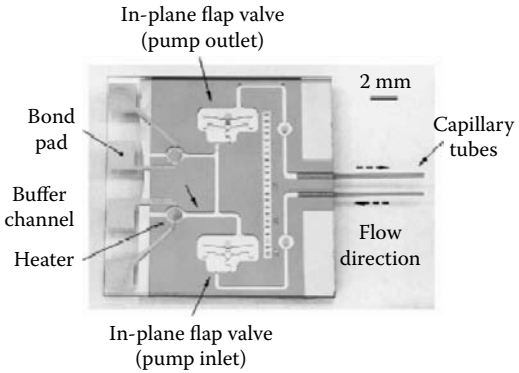

FIGURE 6.3 (CONTINUED)
Schematic of positive displacement check valve pumps. (g) Planar thermopneumatic actuation with cantilever valves. (From Zimmermann, S. et al., *Proceedings of the 17th IEEE International Workshop on Micro-Electromechanical Systems MEMS '04*, Maastricht, The Netherlands, January, 25–29, 462–465, 2004.)

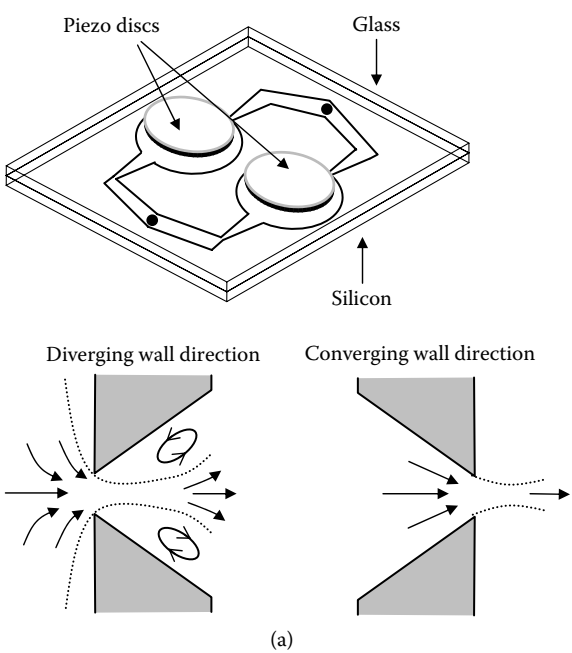

FIGURE 6.4
Fixed-geometry positive displacement pumps. (a) Diffuser or nozzle micropump. (Adapted from Stemme, E. and Stemme, G., *Sensors and Actuators A* 39, 159–167, 1993.)

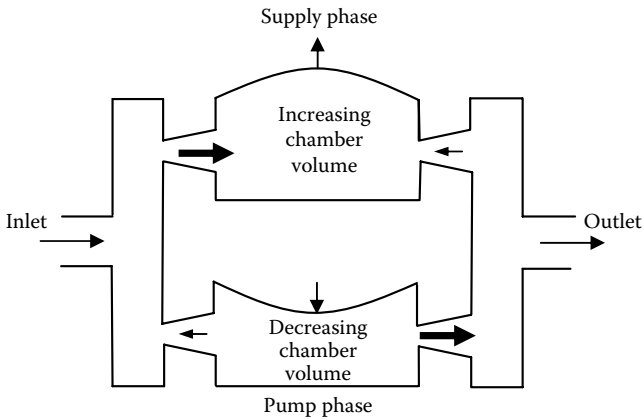

(b)

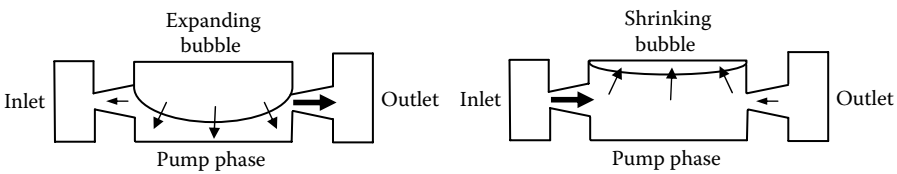

(c)

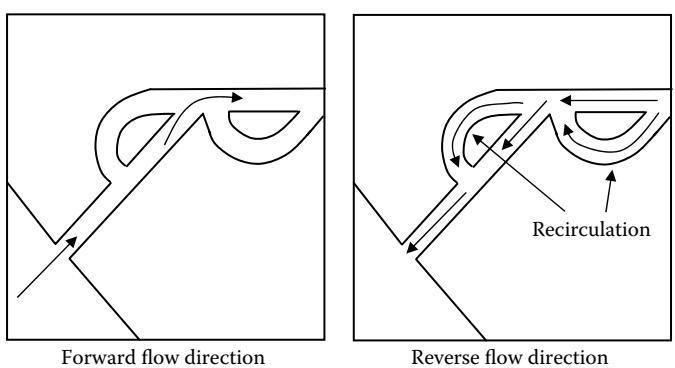

(d)

FIGURE 6.4 (CONTINUED)
Fixed-geometry positive displacement pumps. (b) Double pump chamber operated in an antiphase (push–pull) mode. (Adapted from Olsson, A. et al., *Journal of Micro Electromechanical Systems* 6, 2, 161–166, 1997.) (c) Diffuser or nozzle micropump utilizing thermopneumatic actuation. (Adapted from Tsai, J.H. and Lin, L., *Proceedings of the 14th IEEE International Workshop on Micro-Electromechanical Systems MEMS '01*, Interlaken, Switzerland, January, 21–25, 135–140, 2001.) (d) Tesla-style fixed-geometry valves. (Adapted from Forster, F. et al., Design, *Proceedings of the ASME Fluids Engineering Division, IMECE '95*, San Francisco, CA, November 12–17, 234, 39–44, 1995.)

This is because flow through the expansion causes the flow to decelerate with a resulting increase in pressure. This in turn promotes a turbulent boundary layer between a central jet and the sidewall. Flow in the opposite direction through the nozzle element will remain laminar and thus have a higher flow resistance. As a result, flow out of the diffuser element will have less pressure loss than flow back through the nozzle element. When the actuation membrane is pulsed, a net forward flow is produced.

A Tesla valve acts in a similar manner. The Tesla valve consists of a bifurcating loop that connects two parts of a microchannel. As fluid flows in the forward direction, most of the fluid flow is through the main microchannel. In the opposite flow direction, the bifurcating geometry of the loop region causes fluid flow in the loop region instead of through the main channel. This extra flow through the loop region increases the pressure drop in the backflow mode.

A measure of the efficiency of fixed-valve micropumps is based on the fluid diodicity, η, defined as [37]

$$\eta = \frac{\Delta P_{forward}}{\Delta P_{reverse}} \tag{6.13}$$

where

$$\Delta P = \zeta \frac{\rho u^2}{2} \tag{6.14}$$

and ζ is the loss coefficient and u is the characteristic velocity of the flow. The loss coefficient is different depending on whether the flow is in the forward or reverse direction. Once the diodicity of the fixed-geometry valve is known, the pump flow rate may be estimated as [33]

$$Q = 2\Delta V f \frac{\sqrt{\eta} - 1}{\sqrt{\eta} + 1} \tag{6.15}$$

where f is the membrane actuation frequency and ΔV is the pump stroke volume. Diffuser or nozzle elements have been reported to have diodicities ranging from 1 to 5, while Tesla valves have been reported to have a diodicity of 1.2 at a Reynolds number of 130 [37].

One of the drawbacks to fixed-valve micropumps is that they rely on strong inertial forces in very small channels where viscosity makes obtaining high Reynolds numbers difficult. A relatively high Reynolds number and flow rate are required to obtain a high level of fluid diodicity. For example, the

fluid diodicity of a Tesla type microvalve drops to 1.02 as the Reynolds number is decreased to 60.

6.4.4 Peristaltic Pumps

Peristaltic pumps are based upon using a series of actuation membranes to displace volume in the desired flow direction. By cycling membrane displacement, a peristaltic motion and volume displacement may be achieved. Each actuation membrane acts to displace volume for forward pumping and as a valve to rectify flow. Because the actuation membranes act with both volume displacement and valving functions, it is desirable to design peristaltic pumps with a compression ratio as close to 1 as possible so that each actuation membrane acts digitally to either completely open or completely block the microchannel.

Peristaltic micropumps therefore require at least three actuation membranes in series to obtain a nonreversible pump stroke. One advantage of peristaltic micropumping is that the flow direction is based upon the sequence of membrane actuation. Therefore, peristaltic micropumps are bidirectional pumps producing flow in either a forward direction using one actuation sequence or reversing the flow direction by reversing the actuation sequence.

A typical actuation sequence is shown in Figure 6.5a [39] for a three-stage piezoelectric-actuated peristaltic pump. The actuation membranes are labeled 1, 2, and 3 referring to the actuation membranes from the right to the left. The actuation membranes are normally closed and actuation of the piezoelectric disc causes the actuation membrane to lift. Thus, the membrane can be in one of two positions where the 0 position is the nonactuated (closed) membrane position and the 1 position is the open position. A convention is chosen so each membrane is individually referenced from membranes 1 through 3 so the sequence (1,0,1) refers to membrane 1 and 3 in the open sequence and membrane 2 in the closed sequence. A six-stage peristaltic motion is required to displace one actuation membrane stroke volume, ΔV. Initially, all three membranes are in the closed position (0,0,0). The first step in the sequence is to actuate membrane one to pull a stroke volume ΔV into the number one position (1,0,0). Next the number two membrane is actuated to displace the stroke volume forward one position (1,1,0). At this point, two stroke volumes, $2\Delta V$, have been displaced forward. The number 1 membrane is allowed to relax causing backflow of one stroke volume (0,1,0). Now membrane 3 is actuated pulling in one stroke volume from the outlet (0,1,1). Membrane two is allowed to relax displacing the fluid forward (0,0,1). Finally, membrane 3 is relaxed (0,0,0) and fluid is displaced forward. At the end of this sequence the net effect is that one stroke volume, ΔV, has been propelled through the device. The flow rate through this pump depends on

the stroke volume as well as the frequency at which the membrane sequence is produced.

$$Q = \Delta V f \tag{6.16}$$

Using this sequencing, bidirectional fluid flow rates up to 500 µl/min have been achieved at an actuation rate of 100 Hz.

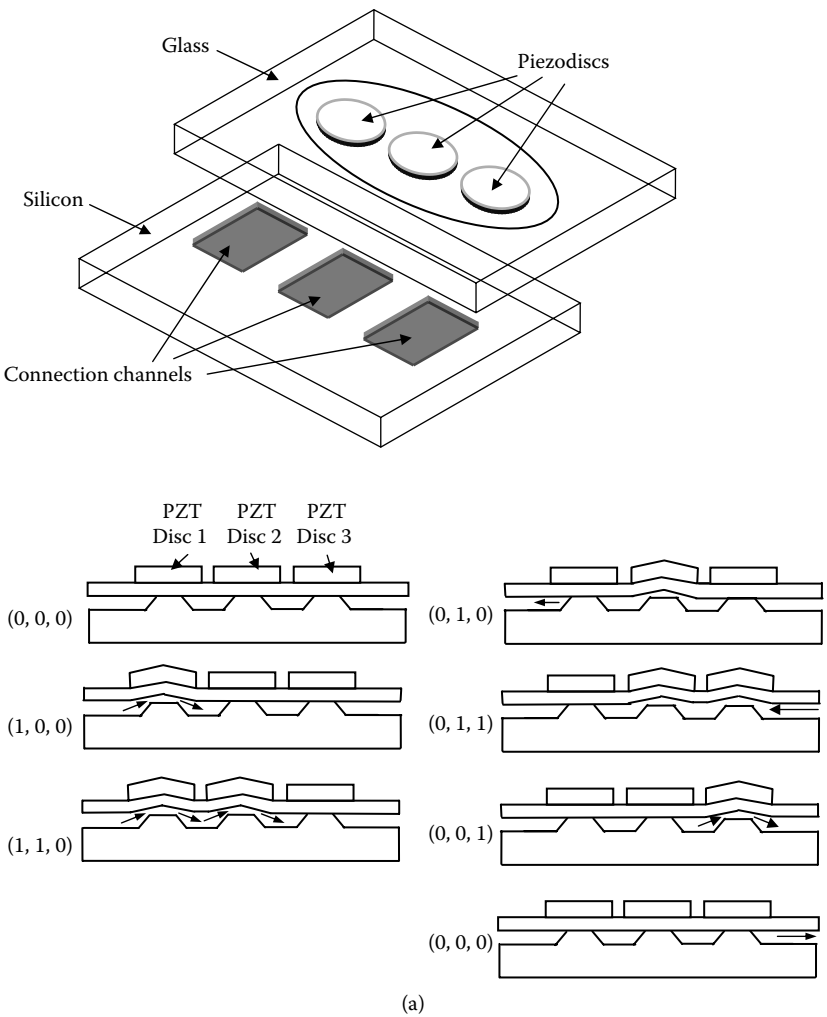

FIGURE 6.5
(a) Piezoelectric actuated peristaltic micropump and pump sequence for displacing one stroke volume ΔV. For reverse pumping the actuation sequence should be reversed. (Adapted from Husband, B. et al., *Microelectronic Engineering* 73–74, 858–863, 2004.)

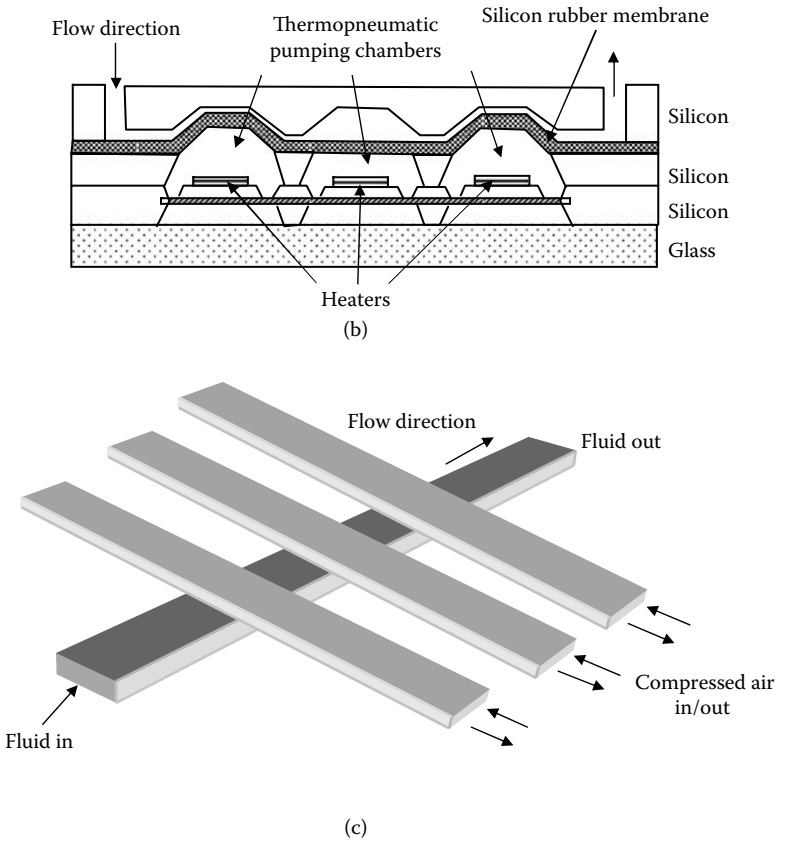

FIGURE 6.5 (CONTINUED)
(b) Thermopneumatic actuated peristaltic micropump. (Adapted from Grosjean, C. and Tai, Y.C., *Proceedings of the 10th International Conference on Solid-State Sensors and Actuators, Transducers '99*, Sendai, Japan, June, 7–10, 1776–1779, 1999.) (c) Pneumatic actuated peristaltic micropump. (Adapted from Unger, M.A. et al., *Science* 288, 113–116, 2000.)

In addition to piezoelectric actuation [39], peristaltic pumps have been realized with similar actuation sequencing using thermopneumatic actuation where liquid boiling displaces a silicone rubber membrane (Figure 6.5b [40]) and pneumatic actuation (Figure 6.5c [41,42]) where compressed air is used to compress a silicone rubber microchannel.

6.4.5 Acoustic Streaming

Acoustic streaming has also been utilized for micropump applications. Pumping is achieved by using interdigitated piezoelectric transducers (IDT) to produce a mechanical traveling wave such as a flexural plate wave (FPW) (Figure 6.6a) [4,43–45]. Pumping is achieved by using two sinusoidal electric drives, which are 90° out of phase with each other (Figure 6.6b, c). The offset

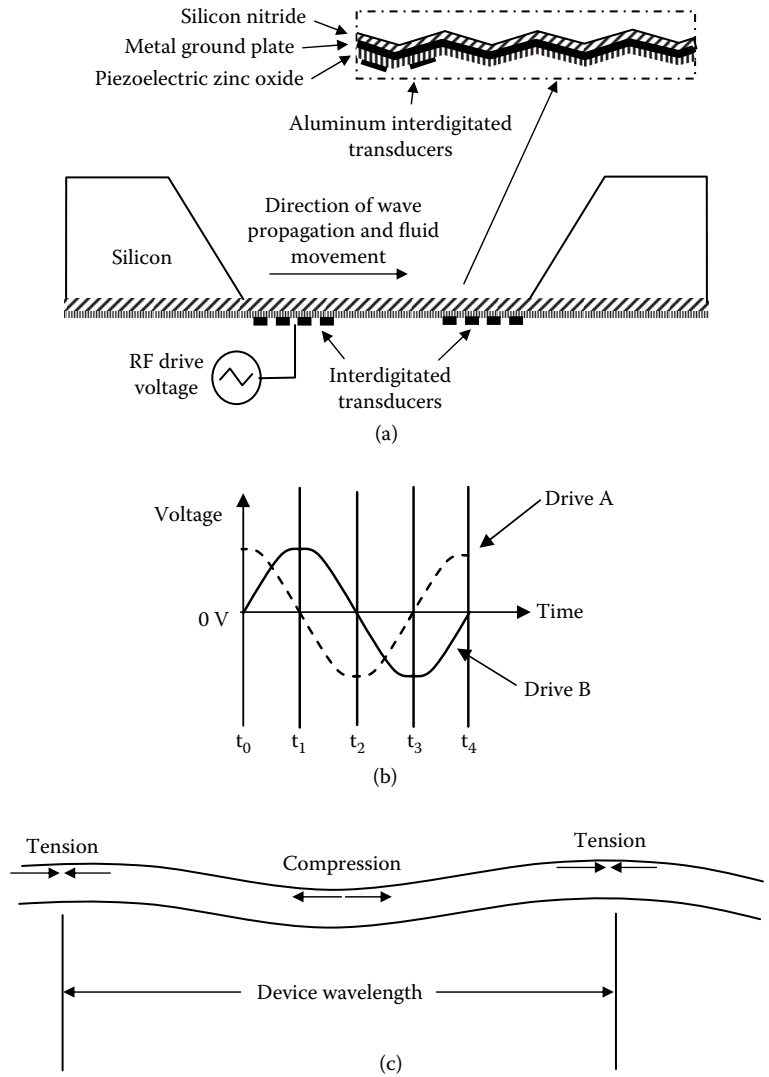

FIGURE 6.6
(a) Cross-sectional view of a flexural plate wave micropump based on interdigitated transducers. (Adapted from Moroney, R. M., White, R.M., and Howe, R.T., *App. Phys. Letters* 59, 774–776, 1991; Moroney, R. M., White, R.M., and Howe, R.T., *Proceedings of IEEE Ultrasonics Symposium*, Honolulu, HI, December, 4–7, 355–358, 1990; and Bradley, C.E., Bustillo, J.M., and White, R.M., *Proceedings of IEEE Ultrasonics Symposium*, Seattle, WA, November, 7–10, 505–510, 1995.) (b) Unidirectional wave generation using two sinusoidal inputs 90° out of phase. (c) Tension and compression of the FPW device at time t_4. The arrows show the electrodes under tension or compression.

of the fingers determines the FPW wavelength and constructive and destructive interference cause the acoustic wave to stream in one direction. This mechanical wave produces a directional shear at the boundary with flow produced from momentum transport into the bulk fluid.

6.5 Nonmechanical Micropumps

Nonmechanical micropumps convert nonmechanical energy into kinetic energy of the fluid. Nonmechanical micropumps based upon electrokinetic pumping, electrowetting, and surface tension gradients have been demonstrated.

6.5.1 Electroosmotic Flow Micropumps

Electroosmotic flow (EOF) pumping is a subset of electrokinetic phenomena related to the movement of electric charges in an applied electric field. Charge movement, in turn, produces a shear on the surrounding fluid to produce flow [46–48]. Electroosmotic pumps are used in small channels without a need for high pressures and may be combined with electrophoresis in bioanalytical separations. Most solid surfaces develop a spontaneous electrical double layer (EDL) when immersed in an electrolyte solution [49,50]. When an electrolyte is brought into contact with a solid surface, the surface develops an electric charge. Countercharges from the electrolyte associate with these surface charges to form a strongly associated charge layer known as the Stern layer. However, the Stern layer does not completely shield the surface charge and so a more weakly associated diffuse layer of countercharges forms adjacent to the Stern layer. The Stern layer is relatively immobile while the charges in the diffuse layer are free to move. These two features are know as the electrical double layer, which is a local region close to the solid surface where charge neutrality is not maintained. The electric double layer is modeled by a Boltzmann distribution where the potential close to the wall is approximately given as

$$\phi = \phi_w \left(1 - e^{-\frac{z}{L_D}} \right) \tag{6.17}$$

where ϕ_w is the wall potential, z is the coordinate perpendicular to the wall, and L_D is the electrical double layer (Debye length) length given by

$$L_D = \sqrt{\frac{\varepsilon kT}{q^2 \left(\sum z_i^2 C_{ibulk} \right)}} \tag{6.18}$$

where q is the electric charge, ε is the medium permittivity, k is Boltzmann's constant, T is the absolute temperature, z_i is the valence of species I, and C_{ibulk} is the bulk concentration of species i. In practice, the EDL thickness may range from approximately 1 μm in pure water down to 0.3 nm in a 1 molar salt solution.

When a microchannel is produced from an insulating material such as glass or plastic, the surface becomes negatively charged when filled with an aqueous solution. Because the microchannel is insulating, a tangential electric field may be applied down the length of the channel to produce an electroosmotic flow. In the presence of the electric field, positively charged ions will move toward the negatively charged cathode, and the negatively charge ions will move toward the positively charged anode. In the bulk region of the microchannel, charge neutrality is maintained so there is no net charge movement. However, in the electric double layer, the diffuse layer will move within the electric field. These ions in turn will drag fluid with them and produce a shear. Thus in the absence of a pressure gradient, electroosmotic flows may be modeled by modifying the Navier-Stokes equation to reflect the balance of the coulombic force density and viscous dissipation. The coulombic force density may be further modified by applying Poisson's equation.

$$\mu\bar{\nabla}^2\bar{u} = -\rho_E\bar{E} = \varepsilon\bar{E}\bar{\nabla}^2\phi \ . \tag{6.19}$$

Here $\rho_f = -\varepsilon\nabla\phi$ is the total free charge density, ϕ is the scalar electric potential and E is the applied electric field along the channel. It may also be approximately shown that

$$\phi_w = \frac{\sigma_w L_D}{\varepsilon} \tag{6.20}$$

where σ_w is the wall charge per unit area. Combining Equations 6.17, 6.19, and 6.20 and applying a no-slip boundary condition, the velocity profile in an electroosmotic flow (Figure 6.7) is

$$U = \frac{\sigma_w L_D E}{\mu}\left(1 - e^{-\frac{z}{L_D}}\right) . \tag{6.21}$$

If the Debye length is small compared to the channel diameter, a plug flow profile is obtained.

$$U \cong \frac{\sigma_w L_D E}{\mu} \tag{6.22}$$

It should be noted that the free flow velocity is proportional to the wall surface charge and Debye length. Because σ_w is a property of the microchannel material it must be experimentally determined. However, the free flow velocity may be tailored by controlling wall charge per unit area (determined by microchannel material selection), Debye length (determined by solution components and ionic strength), and applied electric field.

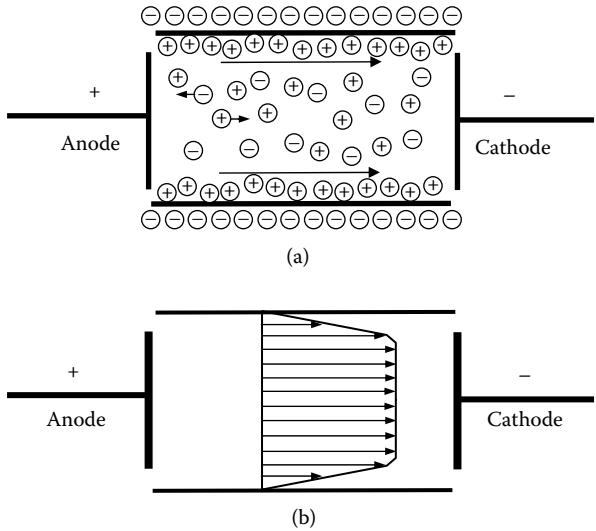

FIGURE 6.7
(a) Charge distribution with surface charge on the microchannel boundary. (b) Electroosmotic flow field. (Adapted from Manz, A. et al., *J. Micromach. Microeng.* 4, 257–265, 1994; Chen, C.H. et al., *Proceedings of the ASME Fluids Engineering Division, IMECE '00*, Orlando, FL, November, 5–10, 523–528, 2000; and Chen, C.H. and Santiago, J.G., *Journal of Micro Electromechanical Systems* 11, 6, 672–683, 2002.)

6.5.2 Electrowetting

On the microscale, surface tension may be used as an effective actuator for micropump applications. Surface tension–driven pumps require the movement along a fluid-fluid interface to produce a shear in order to drive flow. Electrowetting is based upon a change in the liquid–solid surface tension by charging the electrical double layer at an electrode surface. The change in surface tension may be related by Lippman's equation [51]

$$\gamma = \gamma_o - \frac{1}{2} CV^2 \tag{6.23}$$

where γ_o is the surface tension when no potential is applied and C is the capacitance per unit area charged to voltage V. The water contact angle may modeled as a function of the bias using Young's equation and Lippman-Young's equation.

$$\gamma_{SA} = \gamma_{SG} - \gamma_{AG} \cos\theta \tag{6.24}$$

$$\cos\theta = \cos\theta_o + \frac{1}{\gamma_{AG}} \frac{1}{2} CV^2 \tag{6.25}$$

where γ_{SA} is the surface tension between the solid and aqueous phases, γ_{SG} is the surface tension between the solid and gas phases, γ_{AG} is the tension between the aqueous and gas phases, is the contact angle, and θ is the contact angle with no bias voltage. If a dielectric covers the electrode, as the electrode is biased the aqueous phase will induce an electric double layer to charge a capacitor. A pressure can be generated as the change in contact angle

$$\Delta P = P_A - P_G = \frac{\gamma_{AG}}{d}\left(\cos\theta - \cos\theta_o\right) \tag{6.26}$$

where d is the diameter of the fluid channel. Substituting Equation 6.25 into 6.26 yields

$$\Delta P = \frac{1}{2d}CV^2 = \frac{k\varepsilon_o V^2}{2dt} \tag{6.27}$$

where k is the aqueous dielectric constant of the insulator and t is the thickness of the dielectric. Thus, as the electrode is biased, a double layer will initially charge at the gas–liquid interface. This will provide a force so that the aqueous layer will displace the gaseous phase to move to the surface of the electrode. Electrowetting phenomena have been used extensively for droplet manipulation [51–52] (Figure 6.8) with droplet splitting and merging for controlled chemical reactions recently demonstrated [53]. It has also been used as an actuation mechanism for a positive displacement pump [54].

6.5.3 Marangoni Pumps

The Marangoni effect is based on producing a nonuniform surface tension at a gas–liquid interface. The interfacial stress condition at an interface is given by

$$\left\|T_{ij}n_j\right\| + \gamma\left(\nabla\cdot\vec{n}\right)n_i + \nabla\gamma = 0 \tag{6.28}$$

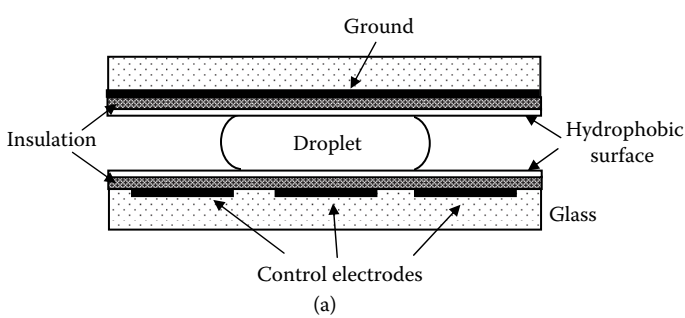

FIGURE 6.8
Droplet manipulation using electrowetting. (a) Schematic of an electrowetting on insulator device. (Adapted from Lee, J. et al., *Sensors and Actuators A* 9, 259–268, 2002.)

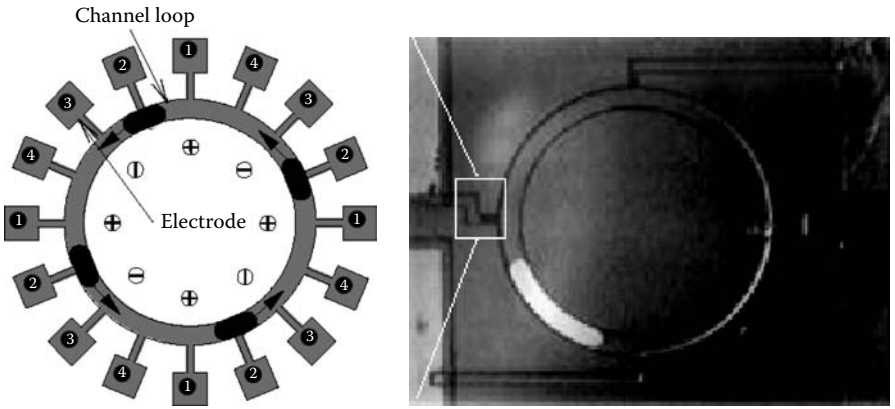

(b)

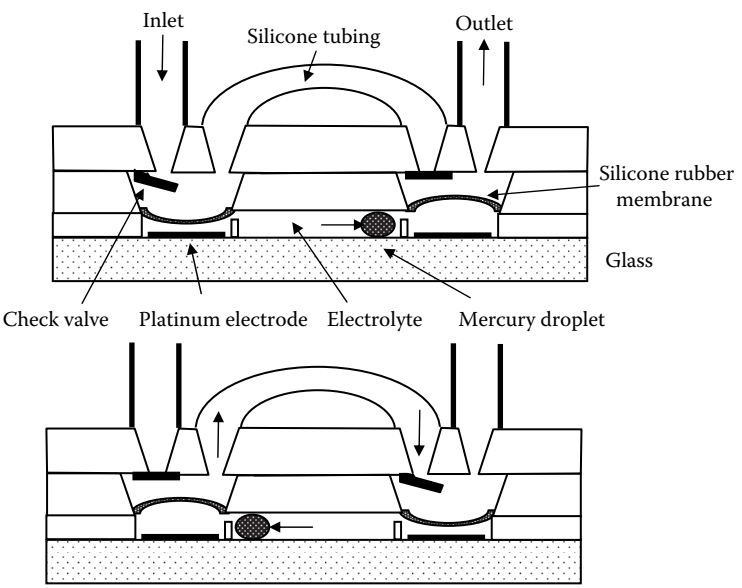

(c)

FIGURE 6.8 (CONTINUED)
Droplet manipulation using electrowetting. (b) A rotary liquid micromotor. (From Lee, J. and Kim, C.J., Surface Tension Driven Microactuation Based on Continuous Electrowetting (CEW), *Journal of Microelectromechanical Systems* 9, 2, 171–180, 2000.) (c) Schematic of a positive displacement pump using electrowetting as an actuation source. (Adapted from Yun, K.S. et al., *Proceedings of the 14th IEEE International Workshop on Micro-Electromechanical Systems MEMS '01*, Interlaken, Switzerland, January, 21–25, 487–490, 2001.)

where T_{ij} is the stress tensor and γ is the space varying interfacial tension between the phases. When the surface tension varies along the interface, a force is exerted parallel to the interface toward the larger surface tension. This interfacial motion produces a shear on the interface, which pumps liquid

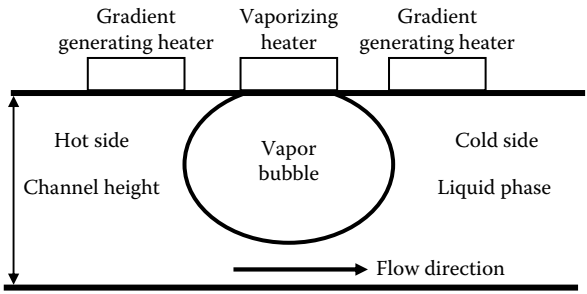

FIGURE 6.9
Surface tension–driven Marangoni micropump. (Adapted from Debar, M. and Liepmann, D., *Proceedings of the 15th IEEE International Workshop on Micro-Electromechanical Systems MEMS '02*, Las Vegas, NV, January, 20–24, 109–112, 2002; and Chen, Z. et al., *Analytical Chemistry* 76, 3707–3715, 2004.)

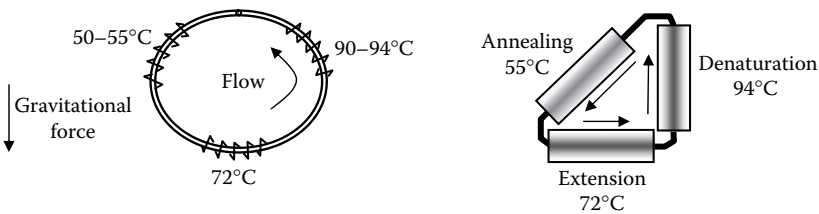

FIGURE 6.10
A buoyancy–driven thermocycling loop. (Adapted from Chen, Z. et al. *ASME Fluids Engineering Division IMECE '04*, CD-ROM IMECE 2004–62303, ASME, New York, NY.)

through momentum transport. Because surface tension is a strong function of temperature, decreasing as temperature rises, a surface tension gradient may be produced by placing a bubble in a temperature gradient to produce flow. The temperature gradient is produced using three heaters; a central heater that creates a vapor bubble through resistive dissipation and two side heaters whose heat fluxes (resistive dissipation rate) differ to produce a temperature gradient across the vapor bubble. Flow is then induced toward the cooler side (higher surface tension side) of the vapor bubble [55]. This is also known as the thermocapillary effect (Figure 6.9).

6.5.4 Buoyancy-Driven Flows

Fluid density differences may also use the gravitational body force to drive fluid flows. This has been accomplished by constructing a microfluidic circulation loop with integrated heaters along the channels (Figure 6.10). Each heater maintains a leg of the channel at a different temperature. Because fluid density is a strong function of temperature, when the loop is aligned within the gravitational field, fluid circulation occurs [56,57] with the warmest (least dense) fluid rising to the top of the loop and the coolest (most

dense) fluid settling, setting up a thermosyphon. This is analogous to free convection currents occurring in a heated house. By constraining the channel temperatures at 94°C, 72°C, and 55°C, continuous thermocycling of fluid temperatures used to drive polymerase chain reaction DNA amplification was demonstrated [55].

6.6 Conclusions

Miniaturized fluid handling and analysis systems propel fluids through a variety of methods. Although, many different varieties of micropumps have been designed, fabricated, and tested utilizing mechanical actuations or deriving flow from unique fluid physical properties, micropumps have only begun to penetrate the industrial market. There are still opportunities for micropump optimization, closer integration with biological assays, and parallelization of micropumps for multiplexed assays. Combined with advances in biosensors, μTAS will drive biological research, healthcare advances, and biological discoveries over the coming decades.

References

[1] Manz, A., Graber, N., and Widmer, H.M., Miniaturized Total Chemical Analysis Systems: A Novel Concept for Chemical Sensing, *Sensors and Actuators B*, 1, 244–248 1990.

[2] Shoji, S. and Esashi, M., Microflow Devices and Systems, *Journal of Micromechanics and Microengineering*, 4, 157–171, 1994.

[3] Gravesen, P., Brandebjerg, J., and Jensen, O.S., Microfluidics—A Review, *Journal of Micromechanics and Microengineering* 3, 168–182, 1993.

[4] Caton, P.F. and White, R.M., MEMS Microfilter with Acoustic Cleaning, *Proceedings of the 14th IEEE International Workshop on Micro-Electromechanical Systems MEMS '01*, Interlaken Switzerland, January 21–25, 479–482, 2001. IEEE, Piscataway, NJ.

[5] Desai, T.A. et al., Nanopore Technology for Biomedical Applications, *Biomedical Microdevices* 2, 1, 11–40, 1999.

[6] Nguyen, N.T. et al., Integrated Thermal Flow Sensor for In-Situ Measurement and Control of Acoustic Streaming in Flexural-Plate-Wave Pumps, *Sensors and Actuators A* 79, 2, 115–121, 2000.

[7] Deshmukh, A.A., Liepmann, D., and Pisano A.P., Continuous Micromixer with Pusatile Micropumps, *Proceedings 2000 Solid State Sensor and Actuator Workshop*, Hilton Head, SC., June 4–8, 73–76, 2000. Transducers Research Foundation, San Diego, CA.

[8] Zahn, J.D. et al., Continuous on Chip Micropumping for Microneedle Enhanced Drug Delivery, *Biomedical Microdevices* 6, 3, 183–190 2004.

[9] Luginbuhl, P. et al., Micromachined Injector for DNA Mass Spectrometry, *Proceedings of Transducers '99 The 10th International Conference on Solid-State Sensors and Actuators*, Sendai Japan, June 7–10, 1130–1133, 1999. Institute of Physics Publ., Philadelphia, PA.
[10] Simpson, P.C., Woolley, A.T., and Mathies, R.T., Microfabrication Technology for the Production of Capillary Array Electrophoresis Chips, *Biomedical Microdevices* 1, 1, 7–25, 1998.
[11] Brody, J.P. et al., Biotechnology at Low Reynolds Numbers, *Biophysical Journal* 71, 3430–3441, 1996.
[12] Leal, G., *Laminar Flow and Convective Transport Processes. Scaling Principles and Asymptotic Analysis*, Butterworth-Heinemann, Boston, MA, 1992.
[13] White, F.M., *Viscous Fluid Flow*, 2nd ed., McGraw-Hill Book Company, New York, 1991.
[14] Madou, M.J., *Fundamentals of Microfabrication: The Science of Miniaturization*, 2nd ed. CRC Press, Boca Raton, FL, 2002.
[15] Jaeger, R.C., *Modular Series on Solid State Devices Volume V. Introduction to Microelectronic Fabrication*, Addison-Wesley Publishing Co., Reading, MA, 1993.
[16] Bhardwaj, J. K. and Ashraf, H., Advanced Silicon Etching Using High Density Plasmas, *Proceedings of the Micromachining and Microfabrication Technology of the International SPIE*, Austin, TX, October 23–24, V. 2639, 224–233, 1995. SPIE, Bellingham, WA.
[17] Xia, Y. and Whitesides, G.M., Soft Lithography. *Annu. Rev. Mater. Sci*. 28, 153–184, 1998.
[18] Duffy, D. et. al., Rapid Prototyping of Microfluidic Systems in Poly(dimethylsiloxane), *Analytical Chemistry* 70, 23, 4974–4984, 1998.
[19] Wallis G.D. and Pomerantz D.I., Field Assisted Glass–Metal Sealing, *J. Appl. Phys*. 40 3946–3948, 1969.
[20] Mittal, L.K., *Polymer Surface Modification: Relevance to Adhesion*, VSP, Uthrecht, The Netherlands, 1996.
[21] Linnemann, R. et. al., A Self-Priming and Bubble-Tolerant Silicon Micropump for Liquids and Gases, *Proceedings of the 11th IEEE International Workshop on Micro-Electromechanical Systems MEMS '98*, Heidelberg, Germany, January, 25–29, 532–537, 1998. IEEE, Piscataway, NJ.
[22] Richter, M., Linnemann, R., and Woias, P., Robust Design of Gas and Liquid Micropumps, *Sensors and Actuators A* 68, 480–486, 1998.
[23] Van Lintel, H.T.G., van den Pol, F.C.M., and Bouwstra, S., A Piezoelectric Micropump Based on Micromachining in Silicon, *Sensors and Actuators* 15, 153–167, 1988.
[24] Shoji, S., Nakagawa, S., and Eashi, M., Micropump and Sample Injector for Integrated Chemical Analyzing Systems, *Sensors and Actuators A* 21–23, 189–192, 1990.
[25] Maillefer, D. et al., A High-Performance Silicon Micropump for an Implantable Drug Delivery System, *Proceedings of the 12th IEEE International Workshop on Micro-Electromechanical Systems MEMS '99*, Orlando, FL, January, 17–21, 541–546, 1999. IEEE, Piscataway, NJ.
[26] Maillefer, D. et al., A High-Performance Silicon Micropump for Disposable Drug Delivery Systems, *Proceedings of the 14th IEEE International Workshop on Micro-Electromechanical Systems MEMS '01*, Interlaken, Switzerland, January, 21–25, 413–417, 2001. IEEE, Piscataway, NJ.

[27] Schabmueller, C.G.J. et al., Self-Aligning Gas/Liquid Micropump, *J. Micromech. Microeng*. 12, 420–424, 2002.
[28] Rapp, R. et al., LIGA Micropump for Gases and Liquids, *Sensors and Actuators A* 40, 57–61, 1994.
[29] Zengerle, R., Richter, A., and Sandmaier, H., A Micro Membrane Pump with Electrostatic Actuation, *Proceedings of the 5th IEEE International Workshop on Micro-Electromechanical Systems MEMS '92*, Travemünde, Germany, February, 4–7, 19–24, 1992. IEEE, Piscataway, NJ.
[30] Bourouina, T., Bosseboeuf, A., and Grandchamp, J.P., Design and Simulation of an Electrostatic Micropump for Drug Delivery Applications, *J. Micromech. Microeng*. 7, 186–188, 1997.
[31] Lammerink, T.S.J., Elwenspock, M., and Fluitman, J.H.J., Integrated Micro-Liquid Dosing System, *Proceedings of the 6th IEEE International Workshop on Micro-Electromechanical Systems MEMS '93*, Ft. Lauderdale, FL, February, 7–10, 254–259, 1993. IEEE, Piscataway, NJ.
[32] Zimmermann, S. et al., A Planar Micropump Utilizing Thermopneumatic Actuation and In-Plane Flap Valves, *Proceedings of the 17th IEEE International Workshop on Micro-Electromechanical Systems MEMS '04*, Maastricht, The Netherlands, January, 25–29, 462–465, 2004. IEEE, Piscataway, NJ.
[33] Bustgens, B. et al., Micropump Manufactured by Thermoplastic Molding, *Proceedings of the 7th IEEE International Workshop on Micro-Electromechanical Systems MEMS '94*, Oiso, Japan, January, 25–28, 18–21, 1994. IEEE, Piscataway, NJ.
[34] Stemme, E. and Stemme, G., A Valveless Diffuser/Nozzle Based Fluid Pump, *Sensors and Actuators A* 39, 159–167, 1993.
[35] Olsson, A. et al., Micromachined Flat Walled Valveless Diffuser Pumps, *Journal of Micro Electromechanical Systems* 6, 2, 161–166, 1997.
[36] Tsai, J.H. and Lin, L., A Thermal Bubble Actuated Micro Nozzle-Diffuser Pump, *Proceedings of the 14th IEEE International Workshop on Micro-Electromechanical Systems MEMS '01*, Interlaken, Switzerland, January, 21–25, 135–140, 2001. IEEE, Piscataway, NJ.
[37] Forster, F. et al., Design, Fabrication and Testing of Fixed Valve Micropumps, *Proceedings of the ASME Fluids Engineering Division, IMECE '95*, San Francisco, CA, November 12–17, 234, 39–44, 1995. ASME, New York, NY.
[38] Bardell, R.L. et al., Designing High Performance Micropumps Based on No Moving Parts Valves, *Proceedings of the Microelectromechanical Systems Division, IMECE, '97*, Dallas, TX, November, 16–21, 47–53, 1997. ASME, New York, NY.
[39] Husband, B. et al., Novel Actuation of an Integrated Peristaltic Micropump, *Microelectronic Engineering* 73–74, 858–863, 2004.
[40] Grosjean, C. and Tai, Y.C., A Thermopneumatic Peristaltic Micropump, *Proceedings of the 10th International Conference on Solid-State Sensors and Actuators, Transducers '99*, Sendai, Japan, June, 7–10, 1776–1779, 1999. Institute of Physics Publ., Philadelphia, PA.
[41] Unger, M.A. et al., Monolithic Microfabricated Valves and Pumps by Multilayer Soft Lithography, *Science* 288, 113–116, 2000.
[42] Hong, J. W. et al., A Nanoliter Scale Nucleic Acid Processors with Parallel Architecture, *Nature Biotechnology* 22, 435–439, 2004.
[43] Moroney, R. M., White, R.M., and Howe, R.T., Microtransport Induced by Ultrasonic Lamb Waves, *App. Phys. Letters* 59, 774–776, 1991.

[44] Moroney, R. M., White, R.M., and Howe, R.T., Fluid Motion Produced by Ultrasonic Lamb Waves, *Proceedings of IEEE Ultrasonics Symposium*, Honolulu, HI, December, 4–7, 355–358, 1990. IEEE, Piscataway, NJ.

[45] Bradley, C.E., Bustillo, J.M., and White, R.M., Flow Measurements in a Micromachined Flow System with Integral Acoustic Pumping, *Proceedings of IEEE Ultrasonics Symposium*, Seattle, WA, November, 7–10, 505–510, 1995. IEEE, Piscataway, NJ.

[46] Manz, A. et al., Electroosmotic Pumping and Electrophoretic Separations for Miniaturized Chemical Analysis Systems, *J. Micromach. Microeng.* 4, 257–265, 1994.

[47] Chen, C.H. et al., Development of a Planar Electrokinetic Micropump, *Proceedings of the ASME Fluids Engineering Division, IMECE '00*, Orlando, FL, November, 5–10, 523–528, 2000. ASME, New York, NY.

[48] Chen, C.H. and Santiago, J.G., A Planar Electroosmotic Micropump, *Journal of Micro Electromechanical Systems* 11, 6, 672–683, 2002.

[49] Probstein, R.F., *Physicochemical Hydrodynamics*, 2nd ed., Wiley, New York, 1994.

[50] Senturia, S.D., *Microsystem Design*, Kluwer Academic Publishers, Boston, MA, 2001.

[51] Lee, J. et al., Electrowetting and Electrowetting-on-Insulator for Microscale Liquid Handling, *Sensors and Actuators A* 9, 259–268, 2002.

[52] Lee, J. and Kim, C.J., Surface Tension Driven Microactuation Based on Continuous Electrowetting (CEW), *Journal of Microelectromechanical Systems* 9, 2, 171–180, 2000.

[53] Cho, S.K., Moon, H., and Kim, C.J., Creating, Transporting, Cutting and Merging Liquid Droplets by Electrowetting-Based Actuation for Digital Microfluidic Circuits, *Journal of Microelectromechanical Systems* 12, 1, 70–80, 2003.

[54] Yun, K.S. et al., A Micropump Driven by Continuous Electrowetting Actuation for Low Voltage and Low Power Operations, *Proceedings of the 14th IEEE International Workshop on Micro-Electromechanical Systems MEMS '01*, Interlaken, Switzerland, January, 21–25, 487–490, 2001. IEEE, Piscataway, NJ.

[55] Debar, M. and Liepmann, D., Fabrication and Performance Testing of a Steady Thermocapillary Pump with No Moving Parts, *Proceedings of the 15th IEEE International Workshop on Micro-Electromechanical Systems MEMS '02*, Las Vegas, NV, January, 20–24, 109–112, 2002.

[56] Chen, Z. et al., Thermosyphon-Based PCR Reactor: Experiment and Modeling, *Analytical Chemistry* 76, 3707–3715, 2004.

[57] Chen, Z. et al., Buoyancy Driven Microfluidics, *Proceedings of the ASME Fluids Engineering Division IMECE '04*, CDROM IMECE2004-62303, 2004. ASME, New York, NY.

7

Micromixers

D. E. Nikitopoulos and A. Maha

CONTENTS

7.1 Introduction

The topic of mixing on the microscale has been at the forefront of research and development efforts over roughly the last fifteen years since the technological thrust toward miniaturization of fluidic systems began. Mixing is of significant importance to realizing lab-on-a-chip microscale reactors and bioanalysis systems because the reactions carried out on the micro- or even nanoscale in such devices require the on-chip mixing of samples and reagents. Typical application class examples are thermal-cycling reactors for the popular polymerization chain reaction (PCR)[1,2] and the Ligase chain reaction (LCR)[3] as well as other similar applications. Fully integrated microfluidic chips performing such reactions require modestly fast mixing in batch mode, should the mixing be performed on-chip. This is so because the

bottleneck in terms of temporal performance usually lies with the thermal cycling reactions themselves, and because a specific volume of mixture is usually needed to be produced. In such an application, the emphasis would be shifted toward low levels of the resource used to drive the chip, that is, low pressure if the device is pressure driven or low voltage if the device is electrokinetically driven. This requirement can be critical for reactions such as PCR and LDR sequences where several levels of on-chip mixing are necessary, and even more so if the chips are multiplexed. A second example application area of microscale mixers is to perform continuous flow fast-reaction kinetics experiments. In this case mixing must be faster than reaction rates with timescales down to microseconds. In contrast with the previous application area, the emphasis is on localized mixing with very small timescales and batch volume delivery is not a necessity. Low levels of the driving force to operate the chip are desired, but can be sacrificed in exchange for speed, so long as the chip is not structurally compromised. Yet another possible performance requirement of microscale mixers could demand longer-term continuous production, in which case the emphasis would be on maximizing the mixture flow rate delivered, while keeping the driving force for delivery at low levels. An application that would require such performance would be *in situ*, designer drug delivery, whereby a particular drug cocktail would be synthesized on-chip from constituents at proportions specific to a particular patient, and directly delivered at the point of care.

The primary concentration of this chapter is going to be on pressure-driven batch micromixers for applications such as the first example above and possibly the third one. Nevertheless, we will review micromixers developed for the second application class as well as others. After discussing the basics and providing an overview of the micromixing literature, we will discuss the important performance parameters of micromixers, which are meant to be integrated on microfluidic chips such as those used to perform thermal-cycling reactions (e.g., PCR, LDR). We will then outline a methodology for designing optimized, simple, passive, batch-production, pressure-driven micromixers for such applications.

7.2 Some Basic Considerations

It is very well known from the most fundamental considerations that on the microscale mixing is driven by diffusion, and that diffusion processes are inherently slow. This is particularly true in the applications of interest where binary mass diffusion coefficients are significantly low on the order of $D_{12} = 10^{10}$–10^{11} m^2/s or less. On a macroscale, mixing can be made more effective through turbulent transport, which reduces transport timescales by orders of magnitude relative to diffusive ones, and is commonplace in many systems of everyday and industrial use (e.g., internal combustion engines, gas turbine

combustion systems, chemical reactors, etc.). Turbulent flows are characterized by large Reynolds numbers, $\mathrm{Re} = UD/\nu$, where, U, is a velocity scale representative of the process, D is a length scale and, ν is the kinematic viscosity (or momentum diffusion coefficient) of the fluid. In microfluidic systems the length scales are of micron order (e.g., ranging from 1 mm to 500 mm), and because in bioanalytical applications the fluids are predominantly aqueous solutions, the kinematic viscosity is on the order of $10^6\,\mathrm{m}^2/\mathrm{s}$. The transition Reynolds number from laminar to turbulent flow is approximately 2300 for ducts and channels, so in order to have the benefit of fully developed turbulent flow, the Reynolds number ought to be higher than that. The critical Reynolds numbers for other flows, such as jets and free shear layers, are also on the order of several hundreds. If one wishes to generate turbulent flow (e.g., $\mathrm{Re} = 5000$) in a microchannel 100 μm by 100 μm in cross-section, one requires a velocity of approximately 48m/s. At this velocity the pressure drop in the channel is more than 4 atmospheres per millimeter of length, which is prohibitive. Other than examining the feasibility of turbulent microflow, the example brings forth the fact that in addition to the requirement of rapid and effective mixing, one has to be vigilant with respect to the required pressure to drive the microfluidic chip. High pressure requirements are undesirable because they require on-chip, micropumping devices able of sustaining them, which at present do not exist. In addition they impose higher loads on microfluidic chip components and make it more prone to leakage if not breakage and/or debonding of bonded surfaces. Increasing the microchannel cross-section alleviates the high pressure requirement, but increases the volume of the device. Nevertheless, in the above example, if one uses a 500 μm by 500 μm channel, the pressure drop per unit length of channel for the same Reynolds number is reduced by two orders of magnitude, but the volume of the channel is increased by a factor of 25. Larger chip volume translates into larger amounts of samples and reagents and to some extent negates part of the advantage of reducing bioanalytical processes to the microscale. The example highlights the fact that chip volume is yet another parameter one needs to be vigilant about. In conclusion, turbulent flow on the microscale for the benefit of achieving effective mixing is not out of the question, but its usefulness is limited because of pressure drop and chip-volume constraints. It is perhaps not surprising that to the extent of the author's awareness, the highest Reynolds number reported for the operation of a micromixer in the micromixing literature is laminar (500),[4] well below the transition to turbulence value, with still a rather high pressure drop of approximately 0.47 atmospheres per millimeter of length. This mixer was a simple T-junction type fabricated in silicon and covered by Pyrex glass. It should be noted that in Wong et al.,[4] very fast mixing was demonstrated at this value of the Reynolds number caused by instability in the shear layer formed at the interface of the mixed streams in a low-aspect-ratio channel (0.5) with a hydraulic diameter of 67 μm, but required a pressure of almost 5.5 atmospheres, which is its major operational drawback.

In the absence of turbulent transport, the only recourse to achieving effective mixing is the reduction of the molecular diffusion length. This follows from basic dimensional considerations because the time required to achieve full mixing is the diffusive time, $t_D = \delta_D^2 / D_{12}$, necessary for the concentration signal to traverse a length, δ_D. When the mass diffusion coefficient is very small ($<O$ [10^{-10} m^2/s]) the only way to cut down on the mixing time is to reduce this diffusion length. Almost all efforts to improve mixing performance on the microscale strive to achieve this by employing a wide variety of means. For example, the so-called lamination micromixers[5] pursue the creation of several alternating narrow layers of the compounds to be mixed, so as to cut down on the diffusion length; micromixers based on chaotic advection (chaotic stirring)[6,7,8] pursue the same goal by kinematically folding the interfaces between the compounds multiple times; a broad variety of micromixers achieve the same through the use of time-varying external perturbations or exploiting instability mechanisms.

Much like other devices, micromixers are traditionally classified as active or passive depending on whether or not an external energy source is used other than that driving the flow through the device. Although active mixers may effectively provide rapid mixing, it cannot be denied that the additional mechanical and electronic devices, both on- and off-chip, often add undesirable complexity. These additional devices need extra energy, space, and if on-chip, may also be difficult to fabricate and integrate to form a cost-effective and compact lab-on-a-chip. Additionally, electrical fields and heat sometimes generated by active control may damage biological samples.[9] Different methods and substrates have been used to fabricate both active and passive micromixers, but it is generally agreed that passive mixers are most often easier to fabricate and simpler in design than active mixers. This is more so for pressure-driven devices than electrically driven ones.

Several reviews of micromixers have appeared, especially during recent years, and we will mention a few. A brief review of passive and active micromixers can be found in Campbell and Grzybowski[10] who also provide a tabulated assessment of performance and manufacturing complexity of a few mixers, but focus their discussion on self-assembled magnetic micromixers. Passive micromixers were recently reviewed in Hardt et al.[11] A more comprehensive and nicely illustrated review of a broad variety of both passive and active mixers available in the literature is presented in Nguyen and Wu[5] and will not be duplicated herein. However, an overview with representative examples of micromixers from each class will be given here for the benefit of the reader. An overview will be given for passive, active and multiphase flow mixers, the former organized in terms of the driving force used to generate the main flow through the device, as appropriate. The last category (multiphase) is discussed separately, although it contains micromixers from both of the other categories, in order to emphasize that the related devices involve an auxiliary passive fluid and moving interfaces.

7.3 Passive Micromixers

In passive mixers, no external energy source is required as an input for enhancing the mixing mechanism. We will discuss these micromixers dividing them into two groups based on the driving force: pressure driven and electrically driven.

7.3.1 Pressure-Driven Passive Micromixers

It is worth mentioning a few mixers that are not identified as veritable micromixers because they were not realized on microchips, but used concentric capillaries combined with a microsphere blockage to force the mixed fluids through an annular gap on the order of 10 mm. Such are those of Regenfuss et al.[12] and the later improvement upon it by Shastry et al.,[13] who achieved full mixing in continuous flow after a few decades of microseconds operating at high Reynolds numbers (Re of approximately 1000 to 1700) and pressures on the order of 5 atmospheres.

One of the earliest efforts to achieve rapid mixing on the microscale for the purpose of emulsifying immiscible fluids was reported by Schwesinger et al.[14] and revisited with improvements by Mahe et al.[15] In the original work, Schwesinger et al.[14] designed and demonstrated a two-layer microchip mixer in silicon, which successfully produced emulsions by successively layering the fluids in microchannels of a triangular cross-section and typical size of 150 to 200 μm. This was achieved by splitting and recombining the mixing channels several times on two levels, so as to proliferate alternating layers of the different fluids in the channel cross-section. This concept and design can also be effectively used for mixing rather than emulsification, and in such application the layering succeeds in reducing the diffusion length by a factor of 2^n if the original stream is split and recombined n times. This early design is a good candidate for integration with other microfluidic devices. The main complexity in the micromanufacturing process, other than what is standard when utilizing silicon technology, is the need for alignment of the two chip layers.

In one of the pioneering works on microscale on-chip mixers, Knight et al.[16] demonstrated very rapid local mixing on a silicon chip taking advantage of hydrodynamic focusing through the use of a single 10 μm–wide mixing channel of unitary aspect ratio fed by three tributaries in a cross (Ψ) configuration. The middle one was shaped as a nozzle terminating in a 5:1 aspect ratio exit, with the intent of further facilitating the rapid formation of a narrower middle diffusion layer. Satisfying requirements imposed for studies of chemical kinetics, the hydrodynamic focusing, Ψ-junction, mixer of Knight et al.[16] generated very rapid (O[μs]) local mixing of very small volumes (O[nL]) at supply pressures as high as 3 atmospheres. The authors examined in detail the effect of the supply pressure ratio, the optimum value

of which is specific to their mixer configuration, and reduced dead time by a factor of approximately eight relative to the previously mentioned capillary-based mixers, by optimizing focusing. The hydrodynamic focusing concept was used with equal success by Pabit and Hagen,[17] who employed coaxial, UV-transparent, fused silica capillaries (20 μm ID in 100 mm ID) to achieve off-chip rapid mixing for fast kinetic studies using UV-excited fluorescence probes. The hydrodynamic focusing effect also contributed to efficient solvent extraction by Hibara et al.,[18] who generated a multilayer flow of miscible and immiscible fluids in 70 μm–wide channels of low aspect ratio (0.43) using a focusing Ψ-junction configuration in combination with a downstream Ψ-junction one. Although achieving rapid mixing was not their objective, their simple, single-manufacturing-layer, glass device, could be operated as a micromixer. A Ψ-junction mixer realized in silicon and featuring a contraction upstream and an expansion downstream of the mixing channel was developed by Veenstra et al.[19] With a modest aspect ratio (2), they achieved improved mixing at a low Reynolds number (0.23) and essentially provided an indication of how an increased aspect ratio can reduce mixing time or reduce pressure drop. Y-junction micromixers have been successfully employed by Wu et al.[20] to study nonlinear diffusive mixing in microchannels. Interested in gas mixing, Gobby et al.[21] performed numerical simulations at low Reynolds numbers studying the characteristics of Ψ- and T-junction micromixers with and without throttling downstream of the mixing point. They concluded that mixing in gases is improved with throttling and with modest increases in mixing channel aspect ratio (3). A two-wafer, multistream (10) mixer with a contraction into a high-aspect-ratio (8) mixing channel was developed by Floyd et al.[22] on a silicon chip through the use of deep reactive ion etching (DRIE). This mixer, which was integrated with a heat exchanger and a probing region to perform infrared transmission kinetics studies of liquid reactions, yielded fully mixed product in a few tens of milliseconds at a modestly high Reynolds number (97). Considering that the estimated pressure drop is very modest, this type of mixer is promising for bio-analytical applications, although the two-wafer alignment and costly DRIE requirement in its manufacture cannot be overlooked. Various two- and three-stream high-aspect-ratio (6) micromixers were evaluated through numerical simulations by Maha et al.[23] in terms of pressure drop and mixing performance for batch operation. It was shown that a combination of high-aspect-ratio narrow channels combined with hydrodynamic focusing and an optimization design scheme for batch mixture production can reduce mixture production time by an order of magnitude for a fixed pressure drop requirement, or reduce pressure drop by several orders of magnitude for a fixed mixture production time relative to unitary aspect ratio counterpart mixers. This was demonstrated experimentally by Maha[24] for such micromixers hot embossed on polymethylmethacrylate (PMMA) and polycarbonate (PC) polymers using micromilled brass mold inserts. The simple manufacturing process, capacity for inexpensive mass production and integrability of such polymer mixers make them very good candidates for

integration into disposable polymer microchips to perform a variety of bioassays. A very low aspect ratio (0.012), Ψ-junction glass micromixer was developed by Holden et al.[25] to simultaneously produce mixtures of quasi-continuously varying concentrations. This was elegantly achieved by an array of exit channels connected with their entrances arranged diagonally over the span of the mixing channel. Up to eleven discretely different concentrations were produced simultaneously. A tilted UV lithography technique was used by Yang et al.[26] to fabricate a micromixer on SU-8 incorporating opposing arrays of staggered spatially distributed impinging microjets in a T-junction mixer channel. This novel and rare three-dimensional mixer on a single layer is readily integrable on SU-8 chips.

A number of micromixers have been designed and realized incorporating passive elements, which can generate secondary flows, to fold the fluid interfaces and improve local diffusional mixing by cutting down the diffusion length. Introduction of such elements also results in a pressure drop overhead because of increased dissipation. So it is useful to put the relevant designs in this perspective when evaluating their performance, if pressure drop information is available, which is rarely the case. Most of the micromixers incorporating secondary flow–generating elements can be viewed as stirring devices often involving chaotic advection mechanisms.

It is well known that bends in channels generate secondary flows at modestly high, to high Reynolds numbers in the laminar regime. This has been employed by several investigators and mixers with bends have been used in integrated chips.[27] The same principle, augmented by elastic-fluid instabilities, was also demonstrated to be effective in improving mixing on the microscale by Pathak et al.[28] for non-Newtonian fluids in low-aspect-ratio serpentine microchannels. Arrays of modest-aspect-ratio (2) single-level, serpentine (zigzag) microchannels combined with simple Ψ-junction mixers were introduced and used by Kamidate et al.,[29] and more recently by Lin et al.,[30] to successfully generate, in a predictable manner, dynamically controlled spatial and temporal concentration gradients on glass-covered polydimethylsiloxane (PDMS) microchips embossed using silicon mold inserts. A numerical study by Mengeaud et al.[31] indicates that successive bends in serpentine (zigzag) channels improve mixing at high Reynolds numbers ($O[10^2]$), and that increasing the number of bends per unit length of channel while holding its width constant, can be detrimental to the mixing enhancement. Their results should be put in perspective of the fact that their simulations were two-dimensional, while in such flows 3-dimensional effects could be substantial. A passive, single-layer micromixer incorporating complex Tesla structures has been demonstrated by Hong et al.[32] in a cyclo-olefin-copolymer (COC), low-aspect-ratio (0.45) microchannel fed by a T-junction. The structures are essentially a combination of a serpentine channel with curved walls and wedgelike obstacles. Improved mixing was realized with this device and attributed to Coanda effects in the curved parts of the channel requiring a modest Reynolds number (6), which is the lowest among the single-layer passive microchannel mixers with bends.

Three-dimensional (two-level), serpentine, microchannels of low aspect ratio (0.5) fed by a T-junction were introduced by Liu et al.,[33] who demonstrated faster and more complete mixing at modestly high Reynolds numbers (up to 75) compared to single-level serpentine and straight channel counterparts. Standard silicon manufacturing technology was used to realize the 3-dimensional design, which required a two-wafer process and resulted in channels of trapezoidal cross-sections. A similar 3-dimensional two-layer design, realized in PDMS by Park et al.,[34] also incorporated rounded channel walls to induce rotation in addition to the bend-induced secondary flows and a splitting and recombination scheme similar to that of Schwesinger et al.[14] This design realized improved mixing performance for Reynolds numbers in the 1 to 50 range. A multilevel 3-dimensional micromixing device of vascular tortuosity was developed and demonstrated by Therriault et al.[35] incorporated the effects of bends and flow splitting and recombination on numerous levels, and displayed significant mixing effectiveness improvement over a broad Reynolds number range (greater than 1). This improvement was shown to increase almost exponentially with the Reynolds number. Putting the added complexity of a multiple layer process aside and the potentially increased dead volume, the two- and multilayer designs mentioned in this paragraph could be good candidates for batch production micromixers.

Improved mixing has also been realized through the use of grooved channels as generators of secondary flows. In one of the earliest works, Stroock et al.[36] took advantage of chaotic advection generated by secondary flows in low-aspect-ratio (0.35) microchannels bearing angled or herringbone-patterned grooves on the bottom surface and demonstrated significant mixing improvement relative to the ungrooved channel baseline. Their glass-covered, Y-junction mixer microchannels were embossed in PDMS using a mold insert fabricated by a two-layer photolithography process on SU-8. About the same time, Johnson et al.[37] also demonstrated mixing improvements in low-aspect-ratio (0.43) T-junction mixer microchannels stamped in polycarbonate (PC) with laser-ablated angled grooves on their bottom surface. A computational parametric study was conducted by Wang et al.[38] on the performance of grooved mixing channels; they concluded that the minimum length to generate a single recirculation in the channel depends exponentially on the groove aspect ratio and is relative independent of velocity. In an other numerical study, Liu et al.[39] revealed that at low Reynolds numbers (1), both the 3-dimensional serpentine channel mixer (e.g., as in Liu et al.[33]) and the one employing a herringbone groove pattern on the channel wall (e.g., as in Stroock et al.[36]) perform comparably, while at a higher Reynolds number (10) the serpentine design maintains its performance while the one with the herringbone grooves does not. Nevertheless, added manufacturing complexity and added dead volume notwithstanding, grooved channels have been proven to be effective means for enhancing mixing on the microscale in low-aspect-ratio microchannels at low to modest Reynolds numbers. They could

be promising for integration into multifunction biochips especially if manufactured successfully on various biocompatible materials.

The potential of attaining improved mixing by placing obstacles in microchannels has also been explored. While it is well known that at very low Reynolds numbers obstacles cannot generate secondary flows such as recirculations, it is possible to achieve this at higher Reynolds numbers. This was also shown in a numerical study by Wang et al.,[40] who investigated the effect on mixing due to various arrangements of cylindrical obstacles in a microchannel. An effective micromixer incorporating staggered cylindrical obstacles in a mixing chamber was demonstrated by Lin et al.[41] on a silicon chip generating fluid streams of high Reynolds numbers (approximately 380). A ceramic cross-junction microchannel mixer with sidewall obstacles was demonstrated also at high Reynolds numbers (greater than 100) by Wong et al.[42] This configuration produces essentially a serpentine channel and the benefits are predominantly due to the successive bends. Micromixers employing obstacles can be realized with relative ease using single-layer or wafer manufacturing processes, yet the high Reynolds number requirements imply high operating pressures, which is the major drawback of this approach.

Swirl chambers have also been employed on the microscale to achieve effective mixing. The multi-inlet design of Böhm et al,[43] realized in a glass-covered silicon chip using two wafers and DRIE is an early example of this type. It was a very effective mixing device, but required very high pressures (15 atmospheres) and a costly manufacturing process. Recently Lin et al.[44] simulated and demonstrated a multi-inlet swirl-chamber micromixer with performance at low Reynolds numbers (less than 20) realized in a multilayer silicon chip. Swirl-chamber mixers can be effective micromixing devices, but in general they require multilayer manufacturing, high pressures, and increased volume.

A combination of a microvalve and chamber design was realized by Voldman et al.[45] to provide both mixing and valving action on a glass-covered silicone chip. This was micromanufactured in two silicon wafers, one of which incorporated a cantilevered flap-valve element, and required DRIE. This dual-function device, which performed reasonably well in terms of mixing time for batch applications, could also be used as an active mixer with improved performance by pulsing the supply of the valved fluid.

7.3.2 Electrically Driven Passive Micromixers

In addition to pressure-driven flows, electrically driven flows are very well suited for application in microfluidic devices that handle biological samples and perform biological assays. A number of such passive micromixing devices have been realized thus far. A design combining the effects of electroosmotic flow, convective effects due to bends, and flow-stream splitting and recombination has been realized on a quartz wafer by He et al.[46] Voltages on the order of KVolts were applied to produce velocities of order 0.3 mm/s and

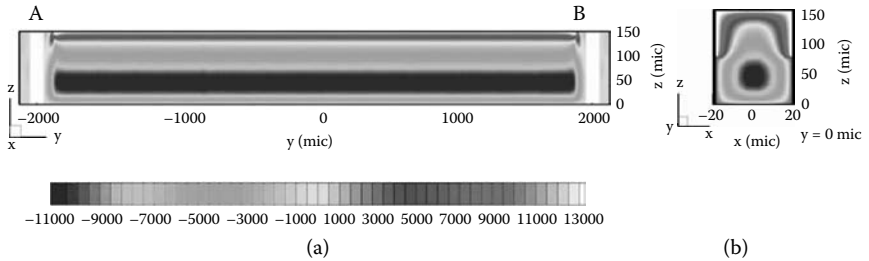

FIGURE 7.1
Main velocity component contours in chamber electroosmotic micromixer (a) streamwise midplane, $x = 0$ μm; (b) cross-flow midplane, $y = 0$ μm.

mixing performance was improved by approximately an order of magnitude relative to a reference Y-junction electroosmotically driven mixing channel. A variety of chamber-based electroosmotic mixers were proposed by Yager et al.[47] relying on recirculations generated by pressure gradients imposed by the conservation of mass. The simplest realization of the device involves a microscale mixing channel with electrodes (A and B) at each end as in Figure 7.1a. When a potential difference is applied between electrodes A and B, the fluid will be set into motion near the wall region with a velocity in proportion to the electroosmotic mobility of the wall material. Because the ends of the mixing channel (between A and B) cannot be penetrated by the flow, conservation of mass will dictate a flow inside the core of the cross-section in the opposite direction to that near the walls. Thus a recirculating flow will be established within the mixing channel with shear layers in the proximity of the walls. This is shown in the numerical simulation results of Figure 7.1[48] for a channel incorporating material nonhomogeneity. The upper part of the channel has a different elecroosmotic mobility than the lower part. The resulting recirculating flow field is shown in Figure 7.1 where it is clearly visible that the fluid is moving in one direction in the proximity of the wall, while it is moving in the opposite direction in the core. Because of the unequal mobility of the top and bottom parts of the channel, flow is not symmetrical with respect to all the geometrical axes of symmetry. The near wall velocity is higher on the top half compared to the bottom half, and as a result the return velocity is higher in the lower part of the core. Consequently, the shear layers on the top half and bottom half are of unequal strengths. The top-to-bottom asymmetry will be absent if the channel has homogeneous mobility. This flow is effective in mixing because it folds material lines multiple times in a short period of time, depending on the potential difference level (88 volts in this example). Figure 7.2 illustrates this stretching and folding of material lines caused by the recirculating flow, which is responsible for the effective mixing function. A plug of liquid with a substantially low mass diffusion coefficient ($1.2\ 10^{-10}$ m^2/sec) is mixed with a second liquid to form approximately 40 nL of a 2.78% mixture in less than one second. This illustrates the effectiveness of this type mixer.

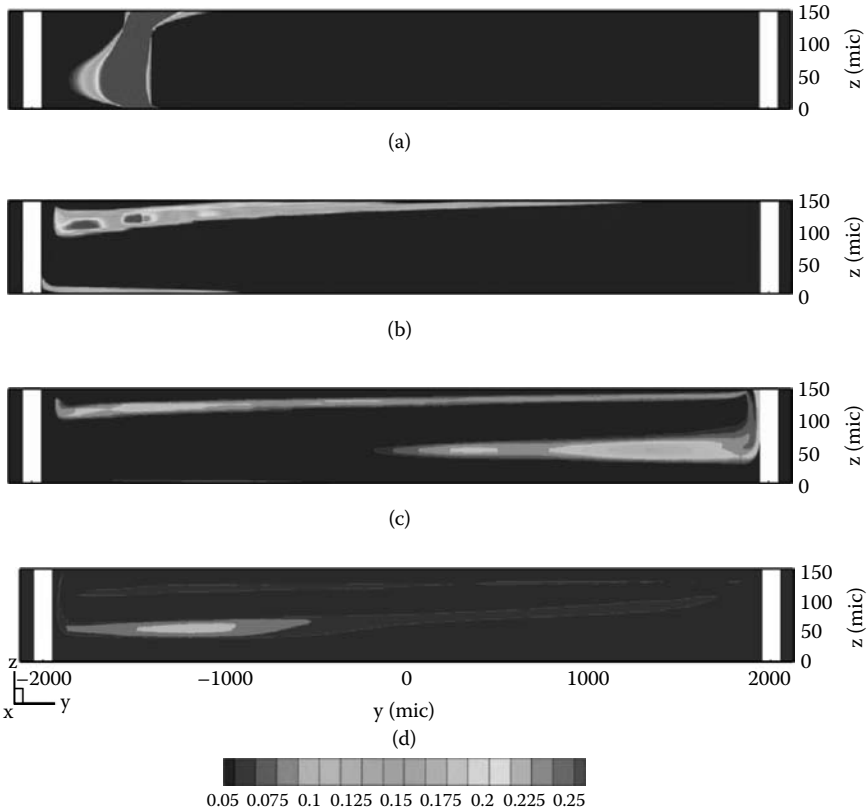

FIGURE 7.2
Concentration contours in chamber electroosmotic micromixer on streamwise midplane, x = 0 μm (a) t = 10 μs, (b) t = 200 μs, (c) t = 500 μs, (d) t = 780 ms; mass diffusion coefficient is 1.2 10^{-6} cm^2/s and 2.78% mixture.

Based on the analytical work of Ajdari,[49] recent technological advances in microfabrication have enabled the development of a variety of complex microscale charge patterns on material surfaces (e.g., see Stroock et al.[50]). This ability has motivated a number of efforts to explore electroosmotic passive micromixers based on inhomogeneous surface-charge distribution in microchannels. These generate secondary flows much like geometrical nonhomogeneous patterns do in pressure-driven flows. Numerical predictions by Erickson and Li[51] on an electroosmotically driven T-junction microchannel mixer with alternating surface-charge (or zeta potential) sign on its side walls demonstrated that mixing can indeed be improved in this manner. Similar simulations on a broader variety of surface-charge patterns were conducted by Qian and Bau,[52] who also demonstrated how chaotic advection and associated mixing benefits can be generated in such heterogeneously charged devices. Another numerical study by Hong et al.[53] demonstrated improved mixing using angled and herringbone patterns of

inhomogeneous surface-charge distributions based on the grooved channel configurations used by Stroock et al.[36] in a counterpart pressure-driven flow. T-junction mixers with inhomogeneous surface-charge distributions have been successfully demonstrated on a microchip by Wu and Liu[54] in a low-aspect-ratio (0.3) PDMS microchannel on a silicon substrate by implanting patterned electrodes into the silicon substrate. Applying voltage of alternating signs to successive electrodes generated a nonuniform charge distribution on the bottom wall of the channel, resulting in secondary flows during operation and improved mixing performance. Glass T-junction micromixers with various heterogeneous zeta potential patterns in very low aspect- ratio microchannels (0.04) have been manufactured by Biddiss et al.[55] They used soft lithography techniques to chemically pattern the glass microchannel bottom surface. Both physical realizations[54,55] of this very interesting concept achieved significant mixing enhancement relative to their homogeneous counterparts. Widespread practical usage in integrated chips of these types of enhanced micromixers may be hampered by the manufacturing process complexity and the durability and shelf life of surface modification when the latter is the chosen method of introducing surface-charge nonuniformity. Much like many electrokinetically driven devices, these micromixers are limited to very low flow rates dictated by the requirement of keeping the driving voltages low.

Secondary flows associated with electrohydrodynamic (EHD) instability generated by conductivity gradients in the working fluid have also been shown through simulation and experimentation to enhance mixing by Lin et al.[56] and could be promising for a practical mixing device of fluids with inherent or imposed conductivity gradients in the practical environment. Coupled electrorotation of latex microspheres has been proposed and demonstrated by Wilson et al.[57] on a glass chip with two electrodes separated by a PDMS wedge, and although intrusive, may be promising for inducing fast local mixing in microfluidic environments.

7.4 Active Micromixers

Active micromixers can be classified according to the type of external force or energy used to actively improve the mixing process. A broad variety of excitation forces have been used, including pressure pulsations, electrical, magnetic, capillary, thermal, and acoustic. The earliest pulsed-flow/pressure micromixer was introduced by Evans et al.[58] It was a chamber design realized on silicon with a quartz cover. The actuation was provided by thermally driven bubble valves/pumps powered by integrated polysilicon heaters. Although complex and with a sizeable dead volume, this device is the first to incorporate the idea of improved mixing through chaotic-advection-inducing flow

pulsations. The same idea has since been considered in a variety of microchannel mixers. An early example was that of Volpert et al.[59] Following their work, pressure pulsations were also used by Deshmukh et al.,[60] who employed a low-aspect-ratio (approximately 0.2) mixer microchannel with a T-junction fabricated in silicon using DRIE. An integrated planar micropump was used to pulse the flow in the mixing channel dividing the mixed liquids into small serial segments and making the mixing process independent of convection. A similar device, with a cross-junction and without integrated pumping, was presented by Lee et al.[61] and was also fabricated in silicon using DRIE.

The chaotic-advection behavior and associated mixing enhancement of pulsed flow cross-junction mixers have been studied theoretically by Lee,[62] while Niu and Lee[63] analyzed a multi-cross-junction variant. Pulsations are in general introduced through the side channels of the cross-junction(s). Glasgow and Aubry[64] demonstrated numerically and experimentally the merits of flow pulsation in a T-junction microchannel mixer. Analysis and realization of pulsed flow T-junction micromixers has been presented more recently by Tabeling et al.[65] Their micromixer was realized with glass and PDMS technology and utilized an on-chip microhydraulic actuation system based on microvalves introduced by Unger et al.,[66] fabricated using their soft lithography technique. A multi-side-channel (as in Unger et al.[66]), pulsed flow T-junction mixer was analyzed and evaluated by Bottausci et al.[67] They concluded that the multiple side-channel design performs better than the single side-channel one when the pulsations introduced through the side channels are out of phase. A swirl-chamber mixer micromilled in PMMA was proposed by Chung et al.[9] in which the swirling of the fluids was achieved by forward and backward pumping. The mixing chamber was fitted with two opposing channels of unit aspect ratio tangent to the circular chamber. Simulation indicated up to a twofold mixing improvement compared to that in a straight channel at rather high, yet laminar, Reynolds numbers (20 to 400). In general, the majority of the pulsed flow and pressure micromixers are continuous-flow devices and have been shown to improve mixing compared to their steady-state counterparts leading to shorter mixing-channel lengths for Reynolds numbers of order one or less. When considering such micromixers for applications, this improvement should be put in perspective of the added complexity, not so much in terms of manufacturing processes, but that resulting from the need for pressure actuation.

Electrical excitation has also been used as an alternative to pressure pulsations toward improving mixing on the microscale by inducing unsteady secondary flows and chaotic advection. One of the earliest micromixers utilizing unsteady electrical fields was that of Lee et al.[61] They demonstrated a pressure-driven, continuous-flow device with periodic electrical excitation introduced in a chamber on the flow path. They used a combination of silicon and SU-8 technology to manufacture this low-aspect-ratio (approximately 0.13) active

mixer. They took advantage of dielectophoretic forces induced by the inhomogeneous electrical field to improve mixing of dielectric microparticles. Shortly after, Oddy et al.[68] presented electrical active mixers based on electrokinetic instability excited by sinusoidal oscillations of the electrical filed. They evaluated a glass-covered PDMS cross-junction mixer and a chamber cross-junction one very similar to that of Lee et al.[61] in Borofloat glass. The main flow in both these low-aspect-ratio (0.1 to 0.33) micromixers could be either pressure or electrically driven. Their measurements proved the concept that substantial improvement in mixing can be achieved through the exploitation of electrokinetic instability by applying AC voltages of a few kVolts at frequencies of a few Hz. A T-junction active mixer with an array of electrodes installed on either side of a unit aspect ratio, mixing channel was successfully demonstrated by El Moctar et al.[69] Unsteady mixing-enhancing flow is generated due to EHD instability under the application of steady electrical fields for fluids that have different electrical properties. This pressure-driven device can also be operated as an active one by applying an unsteady electrical field, which further improves mixing performance at low Reynolds numbers (approximately 0.02). A Ψ-junction and ring-chamber combination active mixer has been simulated by Chen et al.,[70] and realized by Zhang et al.,[71] on a silicon chip with integrated heavily doped silicon electrodes. Unsteady electrical fields imposed in the ring chamber generate secondary flows, which improve mixing as shown in the simulation results. The device can be pressure or electrokinetically driven. More recently, Shin et al.[72] conducted an experimental study of an electrically driven and actuated cross-junction, microchannel mixer realized on glass. Under a steady driving voltage of a few hundred volts, they observed instability developing along the focused middle stream with a frequency of a few Hz. Under unsteady conditions with tens of volts peak-to-peak amplitude, they showed modest mixing enhancement at frequencies around the first harmonic of the natural instability mode. Active electrically excited micromixers are attractive for low-flow-rate applications and do not involve fabrication and operational technological complexity superior to that required for their passive counterparts, other than an AC generator. Indeed, they are easier to manufacture than passive mixers employing nonhomogeneous charge distributions on microchannel walls. They have the standard operational drawbacks of electrically driven microfluidic devices.

Magnetic actuation has also been exploited to produce better micromixing performance. The principle of using magnetohydrodynamic (MHD) forcing to improve mixing on the microscale was nicely demonstrated by Solomon et al.[73] They performed experiments comparing long-range chaotic mixing of miscible and immiscible impurities in a time-periodic flow by producing an alternating magnetic field that generated alternating vortex structures due to MHD instability. Chaotic advection created by magnetic forces inducing mixing on flows carrying magnetic microbeads has been demonstrated by Suzuki and Ho[74] and Suzuki et al.[75] on a low-aspect-ratio serpentine microchannel with a T-junction and an integrated array of copper electrodes normal to the channel length. A glass-covered SU-8 channel was created on a silicon substrate in which the

conductors were embedded. This design succeeded in rapidly dispersing magnetic microbeads at very low Reynolds numbers (approximately 0.01). Very good performance in mixing using magnetic microbeads was achieved by Rida et al.[76] on a micromixer realized in polymethylmethacrylate (PMMA) with integrated ferromagnetic permalloy layers to focus the magnetic field generated by an external electromagnet. In a rather rare design involving moving parts, Lu et al.[77] and Ryu et al.[78] developed micromixer chips with PDMS or Parylene Ψ-junction microchannels with an integrated permalloy bar rotor on a silicon substrate. When the microrotor was rotated by an external rotating magnetic field, it could act both as a mechanical stirrer and a pumping impeller.

7.5 Multiphase Micromixers

Multiphase flow has also been considered to improve mixing performance. The main advantage emanating from the use of two or more phases is the reduction of the volume of the working fluid through the use of an immiscible gas or liquid buffer. Smaller mixed volumes imply smaller diffusion lengths and therefore faster mixing. One of the earliest two-phase micromixers was developed by Hosokawa et al.,[79,80] who succeeded in manipulating and mixing very small (pL-nL) droplets of liquids on a microfluidic chip through pneumatic action. To achieve this they utilized an array of venting microchannels with ultrahydrophobic surfaces to contain the liquid through capillary pressure. A series of elegant and well-documented parametric studies (e.g., Song et al.[81] and Bringer et al.[82]) demonstrated the advantages of effectively mixing small volumes of several reagents by chaotic advection generated in a pressure-driven, liquid–liquid periodic plug/slug two-phase flow in microchannels with and without bends. Chaotic advection was generated by secondary flows, which develop due to shear in droplets when they are pushed through low-aspect-ratio microchannels. This effect was enhanced by the presence of randomly placed bends in the microchannels. This method requires an auxiliary immiscible and inert fluid in order to create and transport the plugs of mixture; it has reported mixing times as low as submillisecond and utilizes a relatively simple and easy-to-manufacture chip. It is well suited for chemical kinetics and biochemical assays provided that the auxiliary fluid does not affect them. Integration with reactor and thermal cycler modules could be challenging because of the utilization of a two-phase flow system.

Small droplet manipulation through the exploitation of electrowetting phenomena was used to achieve fast mixing by Fowler et al.[83] They demonstrated the potential of this concept to perform fast mixing on a glass chip requiring a multilayer manufacturing process. Other than the reduced size of the droplets, the mechanisms responsible for mixing enhancement are the secondary flows generated inside the droplet as it is moved (rolled) in the chip chamber by capillary forces generated by periodically varied electrowetting actuation.

The same electrowetting principles were used in a more recent experimental study by Paik et al.,[84] who illustrated the flow patterns and enhanced mixing inside millimeter-sized droplets and used an immiscible liquid (silicone oil) rather than a gas buffer between droplets. Small-volume liquid manipulation and enhanced mixing using electrowetting phenomena is restricted to polarizable or conductive liquids only. Thermocapillary phenomena have also been considered recently for both active and passive mixing microdevices requiring chemical patterning of substrates to control surface energy for containment of the liquids and the embedding of microheating elements. For a review and theoretical aspects of this still nascent approach we refer the reader to Darhuber et al.[85]

7.6 Performance Metrics for Microscale Mixer Design and Evaluation

A plethora of micromixer designs has been demonstrated and to various degrees evaluated in the literature in terms of performance. The majority of the relevant works have given emphasis on the extent of mixing, or mixing efficiency, defined in various ways; the mixing time; and the associated volume. The latter two often depend on the accepted value of the former, and this is often a source of inconsistency for the performance evaluation bottom line. For example, if the extent of mixing or mixing efficiency decided as a base is shifted from 70% with respect to the fully mixed composition to a 90% value, the resulting mixing time for a diffusion-driven channel mixer could easily be tripled. Furthermore, the mixing time may have a different significance depending on the mixer function for a given application. For example, if kinetic studies are the object (e.g., as in Knight et al.[16] and Bringer et al.[82]), where local very rapid mixing is required for very small volumes, the mixing time would be the time required to attain the desired mixing efficiency for the desired small volume locally, measured from the moment the compounds come in contact. For a batch-production micromixer as needed for a PCR[1,2,86] or LDR[3] application, the mixing time is that required for the production of a specified batch volume mixed to the desired extent. The difference between these two applications is subtle but important in defining this very important metric. So, in evaluating micromixing solutions, consistency in the definition of performance metrics and target values as they pertain to a specific application class is very important in deciding which solution is best suited for the application needs.

One of the primary performance metrics, which as pointed out above relates to others, is one that indicates the extent of mixing or mixing efficiency. While there are various ways in which this has been defined in the literature, we will introduce one of the more popular definitions as introduced by Erickson and Li[51] and is given in Equation 7.1:

$$\varepsilon = \left(1 - \frac{\int_{A_e} |c - c_\infty| \, dA}{\sum_i \int_{A_i} |c_i - c_\infty| \, dA} \right) \tag{7.1}$$

where A_e is the area of the exit, or a relevant segment of it; A_i is the area of the inlet of the mixing region; c is the local value of the concentration; c_i is the concentration of the the ith incoming stream inside the mixing channel; and c_∞ is the mixture steady-state concentration. This definition of efficiency is most adequate when applied locally. For a batch or continuous production micromixer, what really matters is the rate at which the mixed product is produced at the delivery end of the mixer. Thus, for such mixers, it is important to evaluate the mixing efficiencies in terms of mass fluxes instead of concentrations. This is necessary because it is possible to have two different mixers with the same inlet conditions and exit average concentrations, yet with different velocity profiles across the exit. In such cases, these mixers will produce mixed product at different rates depending on the distribution of the concentration relative to the distribution of the velocity. Therefore, it would be more appropriate to evaluate the mixing efficiency on the basis of the following definition introduced by Maha et al.[23]:

$$\eta = \left(1 - \frac{\int_{A_e} \rho U |c - c_\infty| \, dA}{\sum_i \int_{A_i} \rho_i U_i |c_i - c_\infty| \, dA} \right) \tag{7.2}$$

where U and r are the local velocity and density, respectively, of the mixture, and U_i and r_i are the velocity and density of the fluid of the ith layer. Both of these definitions can obviously be easily used in numerical simulations of micromixers. The same is not true when carrying out experimental performance evaluations of micromixers, especially if three-dimensional effects are involved. The first one can be implemented in an experiment at steady state, or nearly so, if confocal microscopy is used (see, e.g., Knight et al.[16] and Stroock et al.[36]) to conduct the evaluation. If three-dimensional effects are not strong, then line-of-sight averaging observations, such as those obtained from standard fluorescence microscopy, can also be validly used by replacing the area average in Equation 7.1 by a line average.[38] The definition of Equation 7.2 also requires velocity measurement over the mixer cross-section, which is a more challenging proposition. The differences between the definition of Equation 7.1 and Equation 7.2 are discussed for diffusion-driven, passive mixers of various types in Maha et al.[23,24] and illustrated in Figure 7.3. Differences on the order of 5 percentage points are observed, which, as expected, are gradually eliminated as the mixture

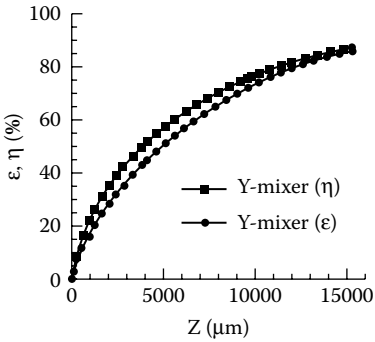

FIGURE 7.3
Comparison of two mixing efficiency definitions obtained through numerical simulations in a standard Y-junction microchannel mixer at 1:1 volumetric flow rate ratio. (Adapted from Maha, A. et al., *Proceedings of SPIE*, 2004, 5345, 183–193.)

approaches a fully mixed state. Such differences can be more substantial in mixers with either passively or actively induced secondary flows. In the case of diffusion-driven mixing discussed here, the use of the definition of Equation 7.1 provides conservative estimates (see Figure 7.3), and thus lends credibility to experimental evaluations of such mixers, which have made use of it.

The above definitions are given for steady flows but also apply for unsteady flows with the understanding that the integrals would then be over time as well as area elements. In the case of unsteady flows, an efficiency in terms of time-averaged quantities would not be sufficient and a measure of the second moment, for example of the concentration, would also be necessary to reflect the intensity of the fluctuations about the time-averaged values.

When the appropriate definition of mixing efficiency is used, and subject to the specific requirement regarding its value, the mixing time (also appropriately defined for the application as mentioned previously), the pressure drop and the volume of the device are important metrics of performance for a microscale mixer. Of these, only the first is specific to the micromixer, while the other two are, in general, metrics of performance for any microfluidic device. The pressure drop in combination with the volumetric flow rate of the fluid in the device reflects on the magnitude of the power required to drive the flow in the device, and it is specific to pressure-driven, microfluidic chips. In the laminar microfluidic environment, the pressure drop along a microchannel is a linear function of the volumetric flow rate, and thus the power requirement is in general quadratic with flow rate. A large variety of microfluidic devices and microscale mixers are driven electrokinetically. In this case, the power input to drive the device is electrical with the applied potential (voltage) difference and the electrical current drawn determining its magnitude. Theoretically, the magnitude of the required voltage to sustain a desired mean velocity of fluid or charged species is proportional to the length of the channel, just like pressure drop is in pressure-driven flows. So, long channels in electrokinetically driven flow

translate into high voltages, which are undesirable, just as high pressures are in pressure-driven flow.

Other metrics of significant practical relevance are manufacturing and operational complexity, which ultimately translate to cost, biocompatibility of materials and process residuals, shelf life (particularly when surface treatments are applied), potential of clogging during operation, and integrability. The last one is important because micromixers are more likely to be needed as an integral part of a microfluidic biochip, whose primary function is other than mixing, and ought to be designed with that in mind. Some of these practically important attributes understandably tend to be overlooked in individual scientific articles in terms of detailed and comparative assessment. Naturally it is up to the designer and the user to decide what tradeoffs to accept.

In addition to high efficiency, minimal mixing time, low pressure loss, and small volume, it is obviously desirable that the microscale mixer of choice involve a low level of manufacturing complexity, low manufacturing cost, easy mass production, excellent biocompatibility of materials used, and a *point-and-shoot* operational complexity with low fowling propensity. Many of these attributes are coupled and their tolerated levels are application dependent. In general, simplicity in the manufacturing process implies low cost. So, when evaluating mixer concepts for integrated devices, multistep or multilayer processes and associated alignment and assembly are less desirable. This criterion often places active devices in a dimmer light because these require in general more complex manufacturing processes as well as additional excitation input, even though in many cases other performance metrics are substantially improved. The same can be said for passive mixers requiring multilevel manufacturing processes. Because of these and other similar considerations, it would be useful if a baseline of a readily feasible and simple micromixer could be established against which other more complex ones can be compared and put in perspective. This could facilitate both the designer and the user in deciding if added complexity is warranted. Few will argue that a microchannel-based, diffusion-driven mixer is one of the simplest. In the following section, an easy-to-use design and optimization procedure will be given for such a mixer with batch production specifically in mind. Although a pressure-driven mixer will be considered, extension to an electroosmotically driven one can be easily made. A somewhat more general case will be considered involving multiple layers of fluids to be mixed and an assessment of the influence of design parameters on performance will be made.

7.7 Design Methodology for Optimal Diffusion-Based Micromixers for Batch Production Applications

As discussed in previous sections, if batch delivery of mixed product is required at the outlet port of the mixer, the relevant mixture production time

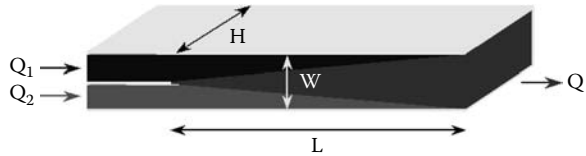

FIGURE 7.4
Two-layer mixing channel.

is not the raw diffusion time but the time it takes for the mixer to deliver the required volume of fluid and is still measured from the moment the constituents come in contact with each other. It should be noted that there might be time overhead associated with the delivery of the mixture constituents to the point of contact, and in a batch delivery micromixer it ought to be taken into account. Although this time overhead could be influenced by the particular microscale mixer design, it is reasonable not to include it in the tally because it may be constrained by other aspects of the microfluidic chip functionality and the macro–micro interface.

So, for a simple two-compound, batch delivery, microscale mixer consisting of a channel with a width, w, height, H, and length, L, (see Figure 7.4) the estimate of the mixture production time, t_M, will have two contributions. One is $t_D = \delta_D^2 / D_{12}$, the diffusion time associated with an appropriate diffusion length, δ_D, and the other is the time, t_P, required to produce the desired volume, V, of mixture. The latter is then dictated by the total volumetric flow rate, Q, since $t_P = V/Q$. Thus the estimate of the mixture production time is:

$$t_M = t_D + t_P = \frac{\delta_D^2}{D_{12}} + \frac{V}{Q} = \left[\frac{\delta_D}{w}\right]^2 \frac{w^2}{D_{12}} + \frac{V}{Q} \tag{7.3}$$

In a microchannel mixer where two or more alternating flow stream layers are introduced into the mixing channel by means of tributary channels, such as in Knight et al.[16] (3 tributaries or layers), Hibara et al.[18] (2 and 3 tributaries or layers), or Floyd et al.[22] (10 tributaries or layers), the relevant diffusion length is a fraction of the total width of the mixer channel and also depends on the flow rate of each merging stream. In general, it is safe to select $\delta_D = w_{s\max}/2$, where w_{smax}, is the width of the widest internal stream layer or twice the width of the widest wall-bounded layer, whichever two is largest. Consequently, the estimate of the mixture production time becomes:

$$t_M = \frac{1}{4}\phi^2 \frac{w^2}{D_{12}} + \frac{V}{Q}, \tag{7.4}$$

where $\phi = \dfrac{w_{s\max}}{w}$ is defined as the diffusion width fraction.

The constituents must be fully mixed by the time they reach the exit of the mixing channel, therefore the diffusion time, t_D, together with the volumetric flow rate, Q, define the estimate of the necessary length of the mixer channel:

$$L = t_D \frac{Q}{Hw} = \frac{\delta_D^2}{D_{12}} \frac{Q}{Hw} = \left[\frac{\delta_D}{w}\right]^2 \frac{Q}{AR\, D_{12}} = \frac{1}{4}\phi^2 \frac{Q}{AR\, D_{12}}, \tag{7.5}$$

where AR is the channel aspect ratio defined as the ratio of its height (depth) over its width, $AR = H/w$. In terms of the mixer application here, we will operate under the premise that the layers of the fluids are parallel to the height (depth) of the channel. In general, the aspect ratio is going to be viewed as the ratio of the rectangular channel cross-section dimension in a direction parallel to the mixed fluids layer, over the dimension normal to the fluid layers as portrayed in Figure 7.4.

It is worth pointing out that w_{smax} is not necessarily the geometrical width of a tributary channel. In fact, the widths of the tributary channels are relatively irrelevant, as is the average velocity of the fluids in these tributaries. If the flow is steady and laminar, the initial widths of fluid streams in the mixing channel are solely determined by the flow rates in the tributaries. This is so for two reasons. The first has to do with the fact that in most cases of pressure-driven microfluidic devices, the flow Reynolds number is low and the flows are laminar without instabilities. For low Reynolds numbers where viscosity is a dominant or at least a significant factor, momentum discontinuities, such as those created when streams from tributary channels merge into one, are smoothed out fairly quickly, that is, the length over which the resulting flow assumes a fully developed velocity profile (known as the entrance or development length) is short. For example, in the case of flow entering a tube with an initially uniform (or nearly so) velocity profile, the entrance length is known (see White[87]) to be, to a very good approximation, $0.06\mathrm{Re}D_h$, with, D_h, the hydraulic diameter defined as $D_h = 4A/P$, where A, is the channel cross-sectional area and P the wetted perimeter. Thus, it is evident that for modest Reynolds numbers (say less than 10) the entrance length is a fraction of the hydraulic diameter, or by extension, any length scale associated with the cross-section of the channel. The second reason has to do with the fact that mass diffusion in the applications of interest here is substantially lower than momentum diffusion as reflected by the Schmidt number, $Sc = \nu/D_{12}$, which is usually on the order of 10^3 to 10^5. This means that momentum discontinuities are smoothed out by molecular action much faster than concentration discontinuities. Thus in steady laminar flow, the flow of multiple merging streams fed into a single channel by tributaries becomes fully developed while the fluid streams themselves are for all practical purposes still unmixed. Therefore, the widths of the various streams in the mixing channel are determined by the initial flow rate of each distinct fluid in the original tributary. This fact is simply illustrated in Figure 7.5,

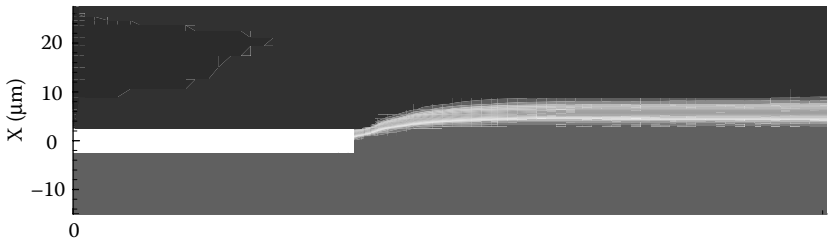

FIGURE 7.5
Merging of two streams of miscible fluids in a mixing channel 42.5 μm wide and 150 μm high. The upper fluid channel has an entrance width of 25, while the lower fluid channel has a 12.5-μm entrance width. The flow rate of each stream is equal to 37.5 nL/s. The binary mass diffusion coefficient is $D_{12} = 1.2\ 10^{-10}$ m^2/s, the Schmidt number is Sc = 8300 and the Reynolds number in the mixing channel is Re = 0.78.

where the merging of two aqueous solution streams (blue and red) originating from tributary channels of unequal widths, with unequal average velocities but equal flow rates, merge into a single channel. It is evident in Figure 7.5 that in spite of the initially different average velocities and tributary channel widths, the width of each fluid stream in the mixing channel after the development region is equal to one-half of the mixing channel width as dictated by the equality of the merging stream flow rates and the symmetry of the velocity profile for fully developed laminar flow in a rectangular duct. It can also be seen that the flow development length is a fraction of the mixing channel width and that the interface between streams is still relatively sharp by the end of the flow development region.

This illustration assumes that the fluids mixed have equal viscosities and densities, which is approximately the case in many bioanalytical applications utilizing dilute aqueous solutions. If the fluids mixed have disparate properties, the above illustration and the estimates that will follow can still be made, but the applicable solutions are somewhat more complicated. The above observation facilitates the estimation of the value of, ϕ, which is necessary for the design of a multistream or multilayer, diffusion-driven, microchannel mixer. For a two-stream or two-layer mixer with the constituents fed at equal flow rates, the value of ϕ is obviously unity and corresponds to the optimum operating point of this type of mixer in terms of the proportion between the incoming flow rates, which is 1:1. Any other proportion would increase ϕ and by virtue of Equation 7.4 and Equation 7.5 would also increase the mixture production time and mixing channel length, respectively. This indicates that in order to attain optimum performance, a layered mixer must be operated at flow rates with specific proportions. For multistream layered mixers that mix two fluids, A and B, it is easy to see that in order to best exploit the reduction of the diffusion length through layering, the minimum value of ϕ must be $\phi_{\min} = 1/(n-1)$, where n is the number of layers. The ratio of volumetric flow rates of the two compounds can then be written as

$$\psi_n = \frac{Q_A}{Q_B} = \frac{\sum_{j}^{even} Q_j}{\sum_{i}^{odd} Q_i}, \tag{7.6}$$

where the even-indexed flow rates are of fluid *A* and the odd-indexed ones of fluid *B*. The magnitude of each flow rate, Q_k, of layer *k* must be appropriate in order for the thickness of the layer to be equal to the optimum value, $\phi_{\min} = 1/(n-1)$, if the layer is not wall-bound and $\phi_{\min}/2 = 1/2(n-1)$, if the layer is wall-bound. Also, because of the symmetry of the velocity profile in the channel, it is obvious that if the number of tributaries feeding the mixing channel is even, the optimum flow rate ratio will always be $\psi_{o2k} = 1$. For an odd number of tributaries (and layers) the flow rate ratio is going to be a function of the channel aspect ratio $\psi_{o2k-1}(AR)$. The optimum individual flow rates and flow rate ratio can be estimated using the semi-analytical theoretical solution for laminar flow in rectangular channels (e.g., see White[89]). In order to facilitate the design of multistream channel-based diffusional mixers, the dependence of the optimum flow rate ratio, ψ_o, on the channel aspect ratio for various multistream or multilayer microchannel mixers is shown in Figure 7.6. As the number of streams is increased, the sensitivity of ψ_o to aspect ratio is reduced and its value moves toward unity. Starting at modest channel aspect ratios, ψ_o approaches an almost fixed value. For a 3-layer mixer, which has appeared frequently in the literature, the optimum value of ψ_o for channels with aspect ratios 3 and above is approximately 2.2.

Also as a design aid, tabulated values of the individual stream flow rates, as percentages of the total produced mixture flow rate, are given in Table 7.1 for 3-, 4-, and 5-layer channel mixers and for various channel aspect

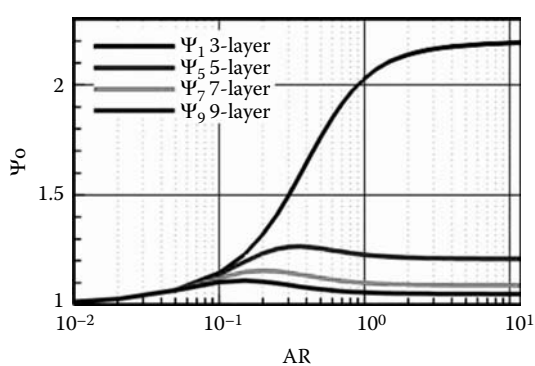

FIGURE 7.6
Flow rate ratios for optimum performance of some multistream layer microchannel mixers as function of channel aspect ratio. For an even number of streams or layers $\psi_o = 1$.

TABLE 7.1

Individual Stream or Layer Volumetric Flow Rates in % of Total Mixture Volumetric Flow Rate for Optimum Performance of Some Multistream Layer Microchannel Mixers and Their Dependence on Channel Aspect Ratio

Type	ψ_o	AR	Q_1(%)	Q_2(%)	Q_3(%)	Q_4(%)	Q_5(%)
3-layer	1.14	1/10	23.3	53.4	23.3	N/A	N/A
	1.41	1/4	20.7	58.5	20.7	N/A	N/A
	1.76	1/2	18.1	63.8	18.1	N/A	N/A
	2.03	1	16.5	67	16.5	N/A	N/A
	2.14	2	15.9	68.1	15.9	N/A	N/A
	2.18	4	15.7	68.5	15.7	N/A	N/A
	2.19	10	15.7	68.7	15.7	N/A	N/A
4-layer	1.00	1/10	14.4	35.6	35.6	14.4	N/A
	1.00	1/4	11.6	38.4	38.4	11.6	N/A
	1.00	1/2	9.3	40.7	40.7	9.3	N/A
	1.00	1	8.1	41.9	41.9	8.1	N/A
	1.00	2	7.6	42.4	42.4	7.6	N/A
	1.00	4	7.5	42.5	42.5	7.5	N/A
	1.00	10	7.4	42.6	42.6	7.4	N/A
5-layer	1.14	1/10	10	26.6	26.7	26.6	10
	1.25	1/4	7.4	27.8	29.5	27.8	7.4
	1.26	1/2	5.7	27.8	33	27.8	5.7
	1.23	1	4.8	27.5	35.4	27.5	4.8
	1.21	2	4.5	27.4	36.3	27.4	4.5
	1.21	4	4.4	27.4	36.5	27.4	4.4
	1.21	10	4.3	27.4	36.6	27.4	4.3

ratios. The aspect-ratio dependence of these flow rates is also weakened at higher aspect ratios.

These theoretical optimum volumetric flow-rate proportions for various multistream and multilayer microchannel mixers are needed for the appropriate selection and design of such devices for a given application. As mentioned previously, in order to complete the design of a diffusion-driven micromixer of this type, one needs to also specify its dimensions, the operating flow rate, and the pressure drop. There are two ways to approach the design issue:

1. Determine a design that will produce the desired volume, *V*, with a minimum mixture production time for a specified acceptable pressure loss in the device, or
2. Determine a design that will produce the desired volume, *V*, while incurring a minimum pressure loss for a specified acceptable mixture production time.

Equation 7.4 and Equation 7.5 provide the simple basis for identifying the appropriate design together with the relationship between pressure loss

($-\Delta p$) and total mixture flow rate, Q, for the flow in the mixing channel. This relationship can be simply expressed as:

$$Q = \frac{\left(-\Delta p\right) w^4}{12 L_M \mu} g(AR) , \tag{7.7}$$

where $g(AR)$ is a function of the aspect ratio alone.

In order to cast the analysis in a more general context, it is useful to identify the relevant scales for all the variables. These are given in Table 7.2.

In the pressure scale, ρ is the density of the fluid(s). The length scale can be viewed as the side of a cube whose volume is the desired mixture volume while the time scale represents the order of magnitude of the diffusion time necessary to mix statically in a cubic chamber with the prescribed volume. For example, if the volume of an aqueous mixture is 10 nL and the binary mass diffusion coefficient of the compounds is on the order of 10^{-10} m^2/s, the length scale would be 215 μm and the time scale 464 s. The diffusive time scale is actually one quarter of this. The scales for the volumetric flow rate and pressure would be 21.5 pL and 0.02 Pa, respectively.

Applying this scaling to Equation 7.4, Equation 7.5, and Equation 7.7 and eliminating the mixing length, L, from the last one we obtain:

$$t_M = \phi^2 \frac{w^2}{4} + \frac{1}{Q} \tag{7.8}$$

$$L = \frac{1}{4} \phi^2 \frac{Q}{AR} \tag{7.9}$$

$$Q^2 = Sc \frac{\left(-\Delta p\right) w^4}{3\phi^2} AR\, g(AR) \tag{7.10}$$

TABLE 7.2

Definition of Scales

Quantity	**Scale**
Length	$\sqrt[3]{V}$
Time	$\sqrt[3]{V^2} / D_{12}$
Volumetric Flow Rate	$D_{12} \sqrt[3]{V}$
Pressure	$\rho(\nu / \sqrt[3]{V})^2$

The optimization condition that satisfies both approaches (1 and 2) above is:

$$Q = \frac{4}{\phi^2 w^2} \tag{7.11}$$

In physical terms, this states that the optimum mixer design and operating point is that for which the diffusion time is equal to the production time. This applies for both possible usages where either the mixture is delivered to an interconnected module (e.g., incubator, thermocycler, etc.) or that for which the mixing channel itself also accommodates the next process (e.g., incubation, thermocycling, etc.). The latter usage, when applicable, substantially reduces the volume of the microfluidic chip, which is highly desirable. The volume for the optimum mixing channel is identical with the volume of mixture desired. If the mixer is not operated at the optimum volumetric flow ratio and stream volumetric flow rate proportions, the factor ϕ will be other than the ideal one ($1/(n-1)$) and can be estimated from the chosen values of these operational parameters. Based on the above optimum condition (Equation 7.11) and Equation 7.8, Equation 7.9, and Equation 7.10, one can calculate all geometric (w_o, L_o) and operational (Q_o, t_{Mo} or $[-\Delta p_o]$) parameters for the multilayer, batch production, microchannel diffusion mixer for an aspect ratio of choice.

Summarizing at this point, the reader is reminded that there are optimum choices to be made on two levels:

1. in terms of the optimum volumetric flow rate ratio(s), and then
2. in terms of the geometry and the other operational parameters.

As an example, results are presented as a design guide here for the popular 3-layer mixer (Ψ-junction or cross-junction), including off-optimum operation in terms of volumetric flow rate ratio(s) in the range of $0.1<\Psi<10$. The optimum mixer parameters can be read from the series of Figures 7.7, 7.8, 7.9, and 7.10, with the aid of Figures 7.11 and 7.6. The former have been built so that the effect of the aspect ratio is scaled out for $AR \geq 0.5$, as evidenced by the almost common trend for all aspect ratios for which results are shown. Results for $AR = 0.1$ are also included in each figure to illustrate that this scaling does not hold as one moves to lower aspect ratios. Subject to this constraint, the effect of the aspect ratio is carried by the factor, f_{AR}, which can be looked up from Figure 7.11. Then, for a chosen channel aspect ratio, Figure 7.7 can be used to determine the optimum (minimum) mixture production time in case of approach (1) or the optimum (minimum) mixer pressure loss in case of approach (1). Having done that, one can use the remaining figures to determine the corresponding length of the mixing channel, L_o, from Figure 7.8, the appropriate mixture flow rate, Q_o, from Figure 7.9, and the appropriate mixing channel width, w_o, from Figure 7.10. The

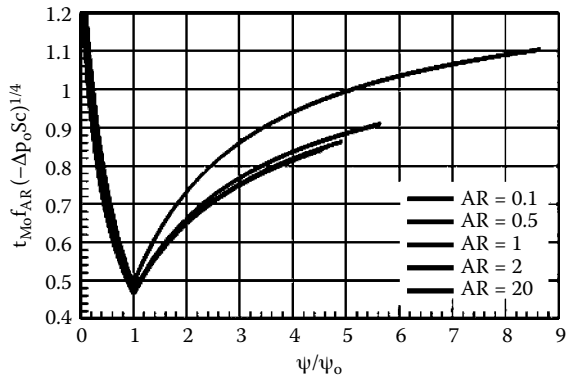

FIGURE 7.7
Scaled optimum mixture production time as a function of the flow rate ratio for the cross-junction or Ψ-junction (3 tributaries) microchannel mixer.

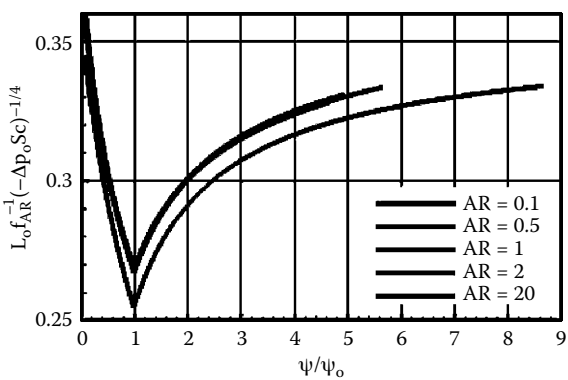

FIGURE 7.8
Scaled optimum mixing-channel length as a function of the flow rate ratio for the cross-junction or Ψ-junction (3 tributaries) microchannel mixer.

physical values of these variables are obtained by reversing the scaling, using the scales in Table 7.2.

In terms of the optimum mixture production time, Figure 7.7 indicates that the departure from optimum performance caused by a nonoptimum value of the volumetric flow rate ratio, ψ, is less significant if this value is larger than the optimum one. This corresponds to a higher flow rate than optimum for the middle stream of the 3-layer mixer, and it is so because the flow velocities are higher in the core of the cross-section and an increase in flow rate does not cause as strong a change in the width of the stream. The significant effect of the aspect ratio is illustrated if we consider the variation of the factor, f_{AR}. To put it in perspective, one is reminded that most micromixers in the literature are demonstrated in channels with low aspect ratios, very often less than 0.5. This is so because the overwhelming majority of the

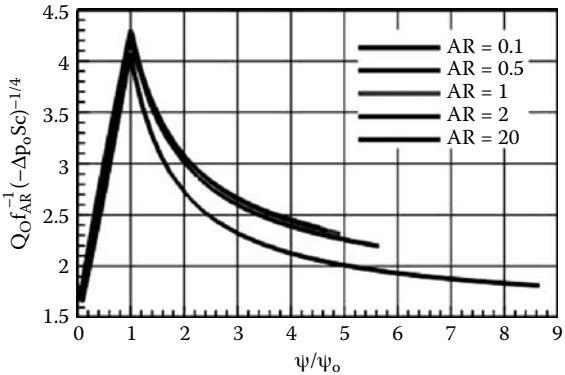

FIGURE 7.9
Scaled optimum operating volumetric flow rate as a function of the flow rate ratio for the cross-junction or Ψ-junction (3 tributaries) microchannel mixer.

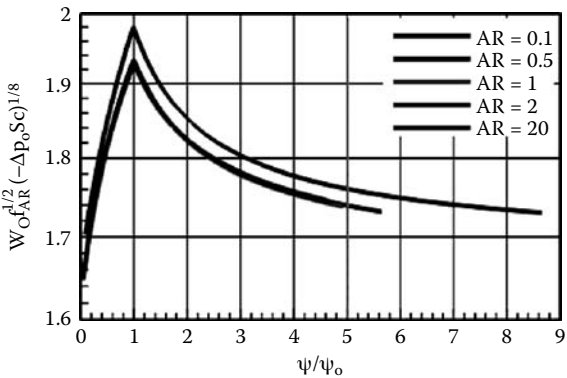

FIGURE 7.10
Scaled optimum mixing-channel width as a function of the flow rate ratio for the cross-junction or Ψ-junction (3 tributaries) microchannel mixer.

mixers in the literature that are manufactured on a single wafer, and most of those manufactured with multiple wafers, have been realized using either silicon and glass technology or soft lithography and PDMS. Neither of these easily accommodates high aspect ratios, while other polymer-based technologies do. So, at the reference aspect ratio value of 0.5, f_{AR} is approximately 0.5. In contrast, the value of f_{AR} corresponding to an aspect ratio of 8 is approximately 2.75 (see Figure 7.11). This indicates that the optimum mixture production time can be reduced by more than half an order of magnitude simply by moving to a higher channel aspect ratio. The value of aspect ratio 8 for this comparison was chosen because it has been used in a multilayer mixer manufactured in silicon using DRIE.[22] For applications where the pressure loss is the critical factor rather than the mixture production time, the advantage of using high-aspect-ratio channels is more spectacular

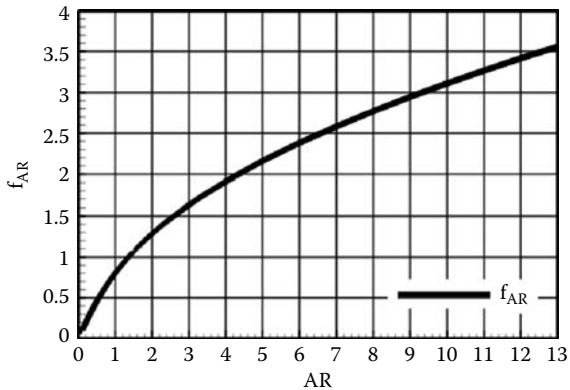

FIGURE 7.11
Aspect ratio factor based on analytical solution for laminar flow in channels of rectangular cross-section (White[89]).

because, as seen in the abscissa of Figure 7.7, the pressure loss for the optimum solution decreases with a factor $f_{AR}{}^4$ as the aspect ratio is increased. So, in terms of the previous example, the optimum mixer realized in a readily achievable channel of aspect ratio 8 involves a pressure loss that is three orders of magnitude lower than that corresponding to the equivalent optimum mixer realized in a channel of aspect ratio 0.5.

Although higher aspect ratios (as high as 50) are possible in silicon, based on the depths achieved through DRIE at channel widths as small as 5 μm (see, for example, McAuley et al.[88]). In polymers such as polymethylmethacrylate (PMMA), polycarbonate (PC), or cyclo-olefin-copolymer (COC), even higher aspect ratios can be achieved via LIGA at widths of order 10 μm (see Chapter 3 by J. Goettert in this book), while aspect ratios of order 10 to 15 at widths of order 10 mm are routinely achievable using either LIGA, UV-LIGA, or micromilling with hot embossing (see Maha et al.[24]) in polymers. Therefore, the improvements from the use of high-aspect-ratio channels can be significantly more substantial than the above example indicates. To better illustrate the benefits of using high-aspect-ratio microchannels in diffusion-driven mixers, some representative estimates of parameters are given in Table 7.3 with the highest aspect ratios chosen to be well within present capabilities with presently available micromanufacturing technologies. One observation that can be made by looking at these numbers is that there is a point of diminishing returns in terms of the potential benefits of increasing the channel aspect ratio, which is indicated by the trend of the factor, f_{AR}, in Figure 7.11, which at high aspect ratio values increases only with the square root of this parameter. It should also be noted that these estimates are based on simple theory and are probably conservative in terms of mixture production time or pressure loss because the implicit assumption was that mixing is "complete." In practice, an acceptable mixing efficiency for most applications can be 90% and the values of these parameters would

TABLE 7.3

Various Theoretical Optimal 3-Stream Layer Mixer Geometries and Operating Conditions

#	V (nL)	AR	–Dp (kPa)	t_M (s)	w (mm)	L (mm)	Q (nL/s)
1	50	15	10	0.42	20	8.4	240
2	50	10	10	0.51	22	10.2	195
3	50	6	10	0.67	25	13	149
4	50	2	10	1.24	34	21	81
5	50	1	10	1.98	43	26	51
6	50	0.5	10	3.5	58	30	29
7	50	0.2	10	8.2	89	32	12
8	50	10	$4.5\ 10^{-3}$	3.5	58	1.5	28

be lower than those indicated by this simple calculation. It should be noted that the simple methodology used here ignores three-dimensional effects and related local Peclet number variations. Therefore, quantitative results may be less than accurate when strong three-dimensional effects are present (e.g., in the mixing channel entrance region). Nevertheless, the methodology is adequate for first "back-of-the-envelope" estimates.

The three-stream layer, channel-based, diffusion-driven, two-fluid, micromixer, the optimum design of which was addressed here as an example, is the simplest possible configuration that can be realized on a single wafer (be it silicon, glass, or polymer) with two inlets and one outlet. If it is manufactured taking advantage of state-of-the-art capabilities in combining high aspect ratios and reduced channel width, it can perform significantly well in terms of mixture production time and/or pressure losses for batch mixture production. It can be considered as a baseline to assess the relative benefits of using more complex passive or active designs. Furthermore, many passive and active schemes applied to microchannels are also applicable at high aspect ratios, in which case the baseline optimum performance can naturally be improved. The methodology presented here can also be easily extended to electroosmotically driven micromixers of the same type as the pressure driven one dealt with herein.

References

1. Hashimoto, M., Chen, P.-C., Mitchell, M.W., Nikitopoulos, D.E., Soper, S.A., and Murphy, M.C., 2004, Rapid PCR in a continuous flow device, *Lab on a Chip*, 4(6), 638–645.
2. Chen, J., Wabuyele, M., Chen, H., Patterson, D., Hupert, M., Shadpour, H., Nikitopoulos, D. E., and Soper, S.A., 2005, Electrokinetically synchronized polymerase chain reaction microchip fabricated in polycarbonate, *Journal of Analytical Chemistry*, **77**, 658–666.

3. Barrett, D.O., Maha, A., Wang, Y., Soper, S.A., Nikitopoulos, D.E., and Murphy, M.C., 2004, Design of a microfabricated device for the Ligase detection reaction (LDR), Paper IMECE2004-62111, ASME International Mechanical Engineering Congress and RD&D Expo.
4. Wong, S. H., Ward, M.C.L., and Wharton, C.W., 2004, Micro T-mixer as a rapid mixing micromixer, *Sensors Actuators B*, 100, 365–385.
5. Nguyen, N.-T. and Wu, Z., 2005, Micromixers—a review, *Journal of Micromechanics and Microengineering*, 15, R1–R16.
6. Aref, H., 1984, Stirring by chaotic advection, *Journal of Fluid Mechanics*, 143, 1–21.
7. Ottino, J. M., 1989, *The Kinematics of Mixing: Stretching, Chaos, and Transport*, Cambridge University Press, Cambridge, U.K.
8. Streamler, M.A., Haselton, F.R., and Aref, H., 2004, Designing for chaos: applications of chaotic advection at the microscale, *Philosophical Transactions of the Royal Society of London A*, 362, 1019–1036.
9. Chung, Y.C., Hsu, Y.L., Jen, C.P., Lu, M.C., and Lin, Y.C., 2004, Design of passive mixers utilizing microfluidic self-circulation in the mixing chamber, *Lab on a Chip*, 4(1), 70–77.
10. Campbell, C.J. and Grzybowski, B.A., 2003, Microfluidic mixers: from microfabricated to self-assembling devices, *Philosophical Transactions of the Royal Society of London A*, 362, 1069–1086.
11. Hardt, S., Drese, K.S., Hesse, V., and Schönfeld, F., 2005, Review: passive micromixers for applications in the microreactor and μTAS fields, *Microfluidics and Nanofluidics*, 1(2), 108–118.
12. Regenfuss, P., Clegg, R.M., Fulwyler, M.J., Barrantes, F.J., and Jovin, T.M., 1985, Mixing liquids in microseconds, *Rev. Sci. Instrum.*, 56, 283–290.
13. Shastry, M.C.R., Luck, S.D., and Roder, H., 1998, A continuous-flow capillary Mixing method to monitor reactions on the microsecond time scale, *Biophysical Journal*, 74, 2714–2721.
14. Schwesinger, N., Frank, T., and Wurmus, H., 1996, A modular microfluid system with an integrated micromixer, *Journal of Micromechanics and Microengineering*, 6, 99–102.
15. Mahe, C., Tranchant, J.F., Tromeur, M., and Schwesinger, N., 2003, Emulsions on demand using microstructured devices, *Proceedings of SPIE*, 4982, 290–296.
16. Knight, J.B., Vishwanath A., Brody, J.P., and Austin, R.H., 1998, Hydrodynamic focusing on a silicon chip: mixing nanoliters in microseconds, *Physical Review Letters*, 80(17), 3863–3866.
17. Pabit, A. and Hagen, S.J., 2002, Laminar-flow fluid mixer for fast fluorescence kinetics studies, *Biophysical Journal*, 83, 2872–2878.
18. Hibara, A., Tokesh, M., Uchiyama, K., Hasimoto, H., and Kitamori, T., 2001, Integrated multilayer flow system on a microchip, The Japan Society for Analytical Chemistry, *Analytical Sciences*, 17, 89–93.
19. Veenstra, T.T., Lammerink, T.S.J., Elwenspoek, M.C., and Berg, A.V.D., 1999, Characterization method for a new diffusion mixer applicable in micro flow injection analysis systems, *Journal of Micromechanics and Microengineering*, 9, 199–202.
20. Wu, Z., Nguyen, N.T., and Huang, X.Y., 2004, Non-linear diffusive mixing in microchannels: theory and experiments, *Journal of Micromechanics and Microengineering*, 14, 604–611.

21. Gobby, D., Angeli, P., and Gavriilidis, A., 2001, Mixing characteristics of T-type microfluidic mixers, *Journal of Micromechanics and Microengineering*, 11, 126–132.
22. Floyd, T.M., Schmidt, M.A., and Jensen, K.F., 2001, A silicon microchip for infrared transmission kinetics studies of rapid homogeneous liquid reactions, in *Micro Total Analysis Systems*, Ramsey, J.M. et al., Eds., 277–279.
23. Maha, A., Barrett, D.O., Nikitopoulos, D.E., Soper, S.A., and Murphy, M.C., Simulation and design of micro-mixers for microfluidic devices, *Proceedings of SPIE*, 24–29 January 2004, San Jose, CA, Vol. 5345, 183–193.
24. Maha, A., 2005, Simulations and experimental analysis of high-aspect-ratio diffusive micromixers, MSc thesis, Louisiana State University.
25. Holden, M., Kumar, S., and Castellana, E.T., 2003, Generating fixed concentration arrays in a microfluidic device, *Sensors and Actuators B*, 92, 199–207.
26. Yang, R., Williams, J.D., and Wang, W., 2004, A rapid micro-mixer/reactor based on arrays of spatially impinging micro-jets, *Journal of Micromechanics and. Microengineering*, 14, 1345–1351.
27. Kamidate, T., Kaide, T., Tani, H., Makino, E., and Shibata, T., 2001, Effect of mixing modes on chemiluminiscent detection of epinephrine with lucigenin by an FIA system fabricated on a microchip, *Analytical Sciences*, 17, 951–955.
28. Pathak, J.A., Ross, D., and Migler, K.B., 2004, Elastic flow instability, curved streamlines, and mixing in microfluidic flows, *Physics of Fluids*, 16(11), 4028–4034.
29. Jeon, N.L., Dertinger, S.K.W., Chiu, D.T., Choi, I.S., Stroock, A.D., and Whitesides, G.M., 2000, Generation of solution and surface gradients using microfluidic systems, *Langmuir*, 16, 8311–8316.
30. Lin, F., Saadi, W., Rhee, S.W., Wang, S-J, Mittal, S., and Jeon, N.L., 2004, Generation of dynamic temporal and spatial concentration gradients using microfluidic devices, *Lab on a Chip*, 4, 164–167.
31. Mengeaud, V., Josserand, J., and Girault, H., 2002, Mixing processes in a zigzag microchannel: finite element simulations and optical study, *Analytical Chemistry*, 74, 4279–4286.
32. Hong, C.C., Choi, J.W., and Ahn, C. H., 2004, A novel in-plane microfluidic mixer with modified Tesla structure, *Lab on a Chip*, 4, 109–113.
33. Liu, R.H., Stremler, M.A., Sharp, K.V., Olsen, M.G., Santiago, J.G., Adrian, R.J., Aref, H., and Beebe, D.J., 2000, Passive mixing in a three-dimensional serpentine microchannel, *Journal of Micro-Electromechanical Systems*, 9(2), 190–197.
34. Park, S.J., Kim, J.K., Park, J., Chung, S., Chung, C. and Chang, J.K., 2004, Rapid three-dimensional passive rotation micromixer using the breakup process, *Journal of Micromechanics and Microengineering*, 14, 6–14.
35. Therriault, D., White, S.R., and Lewis, J.A., 2003, Chaotic mixing in three-dimensional micro vascular networks fabricated by direct-write assembly, *Nature Materials*, 2, 265–271.
36. Stroock, A.D., Dertinger, S.K.W., Ajdari, A., Mezic, I., Stone, H.A., and Whitesides, G.M., 2002, Chaotic mixer for microchannels, *Science*, 295, 647–651.
37. Johnson, T.J., Ross, D., and Lacascio, L.E., 2002, Rapid microfluidic mixing, *Analytical Chemistry*, 74, 45–51.
38. Wang, H., Iovenitti, P., Harvey, E., and Masood, S., 2003, Numerical investigation of mixing in microchannels with patterned grooves, *Journal of Micromechanics and Microengineering*, 13, 801–808.
39. Liu, Y.Z., Kim, B.J., and Sung, H.J., 2004, Two-fluid mixing in a microchannel, *International Journal of Heat and Fluid Flow*, 25(6), 986–995.

40. Wang, H., Iovenetti, P., Harvey, E. and Masood, S., 2002, Optimizing layout of obstacles for enhanced mixing in microchannels, *Smart Materials and Structures*, 11, 662–667.
41. Lin, Y., Gerfen, G.J., Rousseau, D.L., and Yeh, S.R., 2003, Ultrafast microfluidic mixer and freeze-quenching device, *Analytical Chemistry*, 75(20), 5381–5386.
42. Wong, S.H., Bryant, P., Ward, M.C.L., and Wharton, C., 2003, Investigation of mixing in a cross-shaped micromixer with static mixing elements for reaction kinetics studies, *Sensors Actuators B*, 95, 414–424.
43. Böhm, S., Greiner, K., Schlautmann, S., de Vries, S., and van den Berg, A., 2001, A rapid vortex micromixer for studying high-speed chemical reactions, *Proceedings Micro Total Analysis Systems (μTAS)*, 25–27.
44. Lin, C-H, Tsai, C-H, Fu, L-M, 2005, A rapid three-dimensional vortex micromixer utilizing self-rotating effects under low Reynolds number conditions, *Journal of Micromechanics and. Microengineering*, 15, 935–943.
45. Voldman, J., Gray, M.L., and Schmidt, M.A., 2000, An integrated liquid mixer/valve, *Journal of Micro-Electromechanical Systems*, 9(3), 295–302.
46. He, B., Burke, B.J., Zhang, X., Zhang, R., and Regnier, F.E., 2001, A picoliter-volume mixer for microfluidic analytical systems, *Analytical Chemistry*, 73(9), 1942–1947.
47. Yager, P., Holl, M.R., Kamholz, A., Cabrera, C., and Macounova, K., 2002, Meso- and microfluidic continuous flow and stopped flow electroosmotic mixer, U.S. Patent No. US6,482,306B1.
48. Rani, S. and Nikitopoulos, D.E., 2006, Numerical simulation of electroosmotically driven chamber mixers, manuscript in progress.
49. Ajdari, A., 1995, Electro-osmosis on inhomogeneously charged surfaces, *Physical Review Letters*, 75, 755–758.
50. Stroock, A.D., Weck, M., Chiu, D.T., Huck, W.T.S., Kenis, P.J.A., Ismagilov, R.F., and Whitesides, G.M. 2000, Patterning electro-osmotic flow with patterned surface charge, *Physical Review Letters*, 84(15), 3314–3317.
51. Erickson, D. and Li, D., 2002, Influence of surface heterogeneity on electrokinetically driven microfluidic mixing, *Langmuir*, 18, 1883–1892.
52. Qian, S. and Bau, H.H., 2002, A chaotic electroosmotic stirrer, *Analytical Chemistry*, 74, 3616–3625.
53. Hong, S., Thiffeault, J. L., Frechette, L., and Modi, V., 2003, Numerical study of mixing in microchannels with patterned zeta potential surfaces, ASME Paper IMECE2003-41912.
54. Wu, H-Y. and Liu, C-H., 2003, A novel electrokinetic micromixer, IEEE *Transducers '03*, Proceedings 12th International Conference on Solid State Sensors, Actuators and Microsystems, Boston.
55. Biddiss, E., Erickson, D., and Li, D., 2004, Heterogeneous surface charge enhanced micromixing for electrokinetic flows, *Analytical Chemistry*, 76, 3208–3213.
56. Lin, H., Storey, B.D., Oddy, M.C., Chen, C-H., and Santiago, J., 2004, Instability of electrokinetic flows with conductivity gradients, *Physics of Fluids*, 16(6), 1922–1935.
57. Wilson, C.F., Wallace, M.I., Morishima K., Simpson, G.J., and Zare. R.N., 2002, Coupled electrorotation of polymer microspheres for microfluidic sensing and mixing, *Analytical Chemistry*, 74, 5099–5104.
58. Evans, J., Liepmann, D., and Pisano, A.P., 1997, Planar laminar mixer, *Proceedings IEEE 1997*, 96–101.

59. Volpert, M., Meinhart, C.D., Mezic, I., and Dahleh, M., 1999, An actively controlled micromixer, *Proceedings ASME International Mechanical Engineering Congress & Exposition*, Nashville, TN, 483–487.
60. Deshmukh, A.A., Liepmann, D., and Pisano, A.P., 2001, Characterization of a micro-mixing, pumping, and valving system, *Proceedings Transducers 2001, 11th International Conference on Solid-State Sensors and Actuators*, Munich, Germany, 779–782.
61. Lee, Y.K., Deval, J., Tabeling, P., and Ho, C.H., 2001, Chaotic mixing in electrokinetically and pressure driven microflows, *MEMS 2001 IEEE International Conference*, 483–486.
62. Lee, Y-K, 2002, Lyapunov exponents of a micro chaotic mixer, *International Journal of Nonlinear Sciences and Numerical Simulation*, 3(3–4), 561–564.
63. Niu, X. and Lee, Y.K., 2003, Efficient spatial-temporal chaotic mixing in microchannels, *Journal of Micromechanics and Microengineering*, 13, 454–462.
64. Glasgow, I. and Aubry, N., 2003, Enhancement of microfluidic mixing using time pulsing, *Lab on a Chip*, 3, 114–120.
65. Tabeling, P., Chabert, M., Dodge, A., Jullien, C., and Okkels, F., 2004, Chaotic mixing in cross-channel micromixers, *Philosophical Transactions of the Royal Society of London A*, 362, 987–1000.
66. Unger, M.A., Chou, H.P., Thorsen, T., Scherer, A., and Quake, S.R., 2000, Monolithic microfabricated valves and pumps by multilayer soft lithography, *Science*, 288, 113–116.
67. Bottausci, F., Mezic, I., Meinhart, C.D., and Cardonne, C., 2004, Mixing in the shear superposition micromixer: three-dimensional analysis, *Philosophical Transactions of the Royal Society of London A*, 362, 1001–1018.
68. Oddy, M.H., Santiago, J.G., and Mikkelsen, J.C., 2001, Electrokinetic instability micromixing, *Analytical Chemistry*, 73, 5822–5832.
69. El Moctar, A.O., Aubry, N., and Batton, J., 2003, Electro–hydrodynamic microfluidic mixer, *Lab on a Chip*, 3, 273–280.
70. Chen, H., Zhang, Y., Mezic, I., Meinhart, C., and Petzold, L., 2003, Numerical simulation of and electroosmotic micromixer, ASME Paper IMECE2003-55017.
71. Zhang, Y., Follman, D., Chen, H., Mezic, I., Meinhart, C., Petzold, L., and McDonald, N. C., 2003, Design and fabrication of a ring electrokinetic chaotic micromixer (RECM) with integrated electrodes, ASME Paper IMECE2003-44005.
72. Shin, S.M., Kang, I.S., and Cho, Y.-K., 2005, Mixing enhancement by using electrokinetic instability under time-periodic electric field, *Journal of Micromechanical Microengineering*, 15, 455–462.
73. Solomon, T.H., Tomas S., and Warner, J.L., 1996, Role of lobes in chaotic mixing of miscible and immiscible impurities, *Physical Review Letters*, **77**(13), 2862–2865.
74. Suzuki, H. and Ho, C.M., 2002, A magnetic force driven chaotic micro-mixer, IEEE MEMS 2002, 40–43.
75. Suzuki, H., Kasagi, N., and Ho, C.M., 2003, Chaotic mixing of magnetic beads in micro cell separator, *Proceedings of 3rd International Symposium of Turbulence and Shear Flow Phenomena*, 817–822.
76. Rida, A., Lehnert, T., and Gijs, M.A.M., 2003, Microfluidic mixer using magnetic beads, *7th International Conference on Miniaturized Chemical and Biochemical Analysis Systems*, Squaw Valley, California.
77. Lu, L.H., Ryu K.S., and Liu, C., 2002, A magnetic microstirrer and array for microfluidic mixing, *Journal of Micro-Electromechanical Systems*, 11(5), 462–469.

78. Ryu, K.S., Shaikh, K., Goluch, E., Fan, Z., and Liu, C., 2004, Micro magnetic stir-bar mixer integrated with parylene microfluidic channels, *Lab on a Chip*, 4, 608–613.
79. Hosokawa, K., Fujii, T., and Endo, I., 1999a, Droplet-based nano/picoliter mixer using hydrophobic microcapillary vent, IEEE Paper 0-7863-5194-0.
80. Hosokawa, K., Fujii, T., and Endo, I., 1999b, Handling of picoliter liquid samples in a poly(dimethylsiloxane)-based microfluidic device, *Analytical Chemistry,* 71(20), 4781–4785.
81. Song, H., Bringer, M.R., Tice, J.D., Gerdts, C.J., and Ismagilov, R.F., 2003, Experimental test of scaling of mixing by chaotic advection in droplets moving through microfluidic channels, *Applied Physics Letters*, 83 (22), 4664–4666.
82. Bringer, M.R., Gerdts, C.J., Song, H., Tice, J.D., and Ismagilov, R.F., 2004, Microfluidic systems for chemical kinectics that rely on chaotic mixing in droplets, *Philosophical Transactions of the Royal Society of London A*, 362, 1087–1104.
83. Fowler, J., Moon, H., and Kim, C.-J., 2002, Enhancement of mixing by droplet-based microfluidics, IEEE Paper 0-7803-7185, 97–100.
84. Paik, P., Pamula, V.K., Pollack, M.G., and Fair, R.B., 2003, Electrowetting-based droplet mixers for microfluidic systems, *Lab on a Chip*, 3, 28–33.
85. Darhuber, A.A., Chen, J.Z., Davis, J.M., and Troian, S.M., 2004, A study of mixing in thermocapillary flows on micropatterned surfaces, *Philosophical Transactions of the Royal Society of London A*, 362, 1037–1058.
86. Mitchell, M., Liu, X.W., Bejat, Y., Ford, M.S., Nikitopoulos, D.E., Soper, S.A., and Murphy, M.C., Modeling and validation of a molded polycarbonate continuous flow polymerase chain reaction device, in *MicroFluidics, Bio-MEMS, and Medical Microsystems*, Becker, H. and Wolas, P., Eds., Society of Photo-optical Instrumentation Engineers (SPIE), 4982, 2002, 83–98.
87. White, F.M., *Fluid Mechanics*, 1986, McGraw-Hill, New York.
88. McAuley, S.A., Ashraf, H., Atabo, L., Chambers, A., Hall, S., Hopkins, J., and Nicholls, G., 2001, Silicon micromachining using a high density plasma source, *Journal of Physics D: Applied Physics*, 34, 2769–2774.
89. White, F.M., 1974, *Viscous Fluid Flow,* McGraw-Hill, New York.

8

Microfabricated Devices for Sample Extraction, Concentrations, and Related Sample Processing Technologies

Gang Chen and Yuehe Lin

CONTENTS

8.1 Introduction

During the past decade, microfluidic analytical systems fabricated on silica, glass, and polymer microchips have undergone explosive growth. Much attention has been paid to capillary electrophoresis (CE) microchips owing to their high degree of integration, portability, minimal solvent and reagent consumption, high performance, and speed [1–3]. These microchip analysis systems hold considerable promise for applications such as environmental monitoring, biomedical and pharmaceutical analysis, clinical diagnostics, and forensic investigations. Many microfluidic systems were produced on glass substrates using standard photolithographic techniques [3–5], whereas some polymer chips were fabricated based on techniques such as *in situ* polymerization [6], laser ablation [7], imprinting [8], and injection molding [9].

As with other analytical techniques, sample introduction and sample pretreatments are extremely important. The analytical procedures based on microelectromechanical systems (MEMS) devices and systems starts with a sampling step. The sample usually undergoes some kind of sample preparation or pretreatment step before being submitted to the actual analysis. This step may involve extracting the sample from its matrix, removing large matrix components from the sample, masking or removing interference species, derivatizing the sample to make it detectable, or performing a sample preconcentration step. Once the sample has been prepared, it is subjected to analysis, at which time the presence of the analyte of interest is ascertained and its concentration often quantified. This chemical information is then converted to an electronic signal during the data-acquisition step.

The aim of lab-on-a-chip devices is to integrate the components for sample pretreatment (including sample extraction, sample concentration, and sample derivertization), sample introduction, separation, and detection on a microfabricated chip made of glass, silica, and polymers. The integration of sample pretreatment into microfluidic devices is still a challenging task when attempting to achieve true miniaturized total analysis systems (μ-TAS). The challenge is made more complex by the enormous variation in samples to be analyzed. Moreover, the pretreatment technique must be compatible with the coupled microdevice in terms of time, reagent, and power consumption, as well as sample volume. This chapter provides a thorough overview of the developments in this field to date.

8.2 Sample Extraction and Concentrations

In most cases, real samples are not suitable for direct analysis for a number of reasons. For example, samples contain large organic or inorganic particles

that must be removed from the sample matrix to prevent disruption of fluid handling by fouling or blockage of the analytical system. The biological sample is often contained within a cell and must be removed by means of a cell membrane rupture technique. Usually the analytes in biological and environmental samples are only available in trace amounts, and detection of a signal over the background noise becomes difficult although highly sensitive detection techniques have been employed. The sample needs to be separated from a complex background matrix in an initial purification step. Extracting and preconcentrating a sample before analysis can alleviate the sensitivity demands placed on the detector by concentrating available analyte molecules into a smaller volume for enhanced detection. Many applications therefore require some form of sample preconcentration before analysis to ensure that trace amounts of analytes can be reproducibly quantified. Physiological samples present a particular challenge because analytes are often present at submicromolar levels. To counteract lower detection sensitivity, a number of solution-based, online preconcentration techniques have been developed for electrokinetic separation.

8.2.1 Solid-Phase Extraction Techniques on Microchips

In general, solid-phase extraction (SPE) refers to processes where the analyte is retained by an appropriate solid stationary phase and subsequently eluted in a more concentrated form. It includes the isolation of analytes from an interfering sample matrix and sample preconcentration. A perhaps somewhat arbitrary division of SPE methods into two categories, termed nonselective and selective, has been made. This reflects the degree of selectivity of the surface layers used for sample extraction. In the first case, surfaces adsorbing a wide range of compounds were used, whereas in the latter, selectivity was imparted to the surface by immobilizing very bioactive species.

Nakagawa et al. [10] fabricated a simple microchip device for DNA extraction based on electrostatic interactions between surface amine groups and DNA. The microchannel was fabricated on a silicon wafer by photolithography and modified with amine groups on the surface. The amount of DNA captured in the microchip increased, depending on surface amine density. Furthermore, DNA extraction from whole blood, using an amine-coated microchip, was examined. The quantification of DNA and proteins in a washing or eluting fraction indicates that proteins were removed at washing steps, and only DNA was effectively eluted by changing the alkalinity of the buffer. The performance of a polymerase chain reaction (PCR) for the eluted fraction indicates that DNA extracted from whole blood was well purified using an amine-coated microchip.

A high-efficiency DNA extraction microchip was designed by Chung et al. [11] to extract DNA from lysed cells using immobilized beads and the solution flowing back and forth. This chip was able to increase the extraction efficiency two-fold when there was no serum. When serum existed in the

solution, the extraction efficiency of immobilized beads was 88-fold higher than that of free beads. The extraction efficiency of the microchip was tested under different conditions and numbers of *E. coli* cells. This study indicated that DNA could be efficiently extracted, even when the number of bacterial cells was smaller. This microfluidic extraction chip could find potential applications in genomic studies where the samples are limited.

Wolfe et al. [12] developed a silica-based, solid-phase extraction system suitable for incorporation into a microchip platform (μ-TAS) that would find utility in a variety of genetic analysis protocols, including DNA sequencing. The extraction procedure used is based on adsorption of the DNA onto bare silica. The procedure involves three steps: (1) DNA adsorption in the presence of a chaotropic salt, (2) removal of contaminants with an alcohol and water solution, and (3) elution of the adsorbed DNA in a small volume of buffer suitable for PCR amplification. Multiple approaches for incorporating this protocol into a microchip were examined with regard to extraction efficiency, reproducibility, stability, and the potential to provide PCR-amplifiable DNA. This method allowed nanogram quantities of DNA to be extracted and eluted in less than 25 min, with the DNA obtained in the elution buffer fraction. Evaluation of the eluted DNA indicated that it was of suitable quality to be subsequently amplified by PCR.

For DNA purification to be functionally integrated into the microchip for high-throughput DNA analysis, Tian et al. [13] developed a miniaturized purification process that could be easily adapted to the microchip format. In this study, they evaluated the effectiveness of a variety of silica resins for miniaturized DNA purification and gauged the potential usefulness for on-chip solid-phase extraction. A micro-solid-phase extraction device containing only nanograms of silica resin is shown to be effective for adsorbing and desorbing DNA in the program-nanogram mass range. Fluorescence spectroscopy, as well as capillary electrophoresis with laser-induced fluorescence detection, were employed to analyze DNA recovered from solid-phase resins, whereas the PCR was used to evaluate the amplifiable nature of the eluted DNA. They demonstrated that DNA can be directly recovered from white blood cells with an efficiency of roughly 70%, whereas greater than 80% of the protein was removed with a 500 nl bed volume μ-SPE process, which took less than 10 min. With a capacity in the range of 10 to 30 ng/mg of silica resin, it was shown that the DNA extracted from white blood cells, cultured cancer cells, and even whole blood on the low microliter scale is suitable for direct PCR amplification. The miniaturized format as well as the rapid time frame for DNA extraction is compatible with fast electrophoresis on microfabricated chips. Lander's group also demonstrated a microchip solid-phase extraction method for purifying DNA from biological samples, such as blood [14]. Silica beads were packed into glass microchips, and the beads were immobilized with sol-gel to provide a stable and reproducible solid phase onto which DNA could be adsorbed. Optimization of the DNA loading conditions established a higher DNA recovery at pH 6.1 than at 7.6. This lower pH also allowed for the flow rate to be increased, resulting in a

decrease in extraction time from 25 min to less than 15 min. Using this procedure, template genomic DNA from human whole blood was purified on the microchip platform with the only sample preparation being mixing of the blood with a load buffer before loading on the microchip device. Comparison between the microchip SPE procedure and a commercial microcentrifuge method showed that comparable amounts of PCR-amplifiable DNA could be isolated from cultures of Salmonella typhimurium. The greatest potential of the microchip SPE device was illustrated by purifying DNA from spores from the vaccine strain of Bacillus anthracis where eventual integration of SPE and PCR and separation on a single microdevice could potentially enable complete detection of the infectious agent in less than 30 min.

Maruyama et al. [15] fabricated a three-phase flow, water/n-heptane/water microchannel on a glass microchip that was used as a liquid membrane to separate metal ions. Surface modification of the microchannel by octadecylsilane groups induced spontaneous phase separation of the three-phase flow in the microfluidic device, which allows control of interfacial contact time and off-chip analysis using a conventional analytical apparatus. Before selectively transporting a metal ion through the liquid membrane in the microchannel, the forward and backward extraction of yttrium and zinc ions was investigated in a two-phase flow on a microfluidic device using 2-ethylhexyl phosphonic acid mono-2-ethylhexyl ester (commercial name, PC-88A) as an extractant. The extraction conditions (contact time of the two phases, pH, extractant concentration) in the microfluidic device were examined. These investigations demonstrated that the conventional methodology for solvent extraction of metal ions is applicable to solvent extraction in a microchannel. Finally, the three-phase flow was employed in the microchannel as a liquid membrane, and the selective transport of Y ions through the liquid membrane was observed. This was the first time that a targeted metal ion was selectively separated from an aqueous feed solution into a receiving phase within a few seconds by employing a liquid membrane formed in a microfluidic device.

Tokeshi et al. [16] reported a newly designed microchannel for solvent extraction fabricated in a quartz glass chip and applied to solvent extraction of a Co-2-nitroso-5-dimethylaminophenol complex. The aqueous solution of the Co complex and toluene were introduced into the microchannel, and the Co complex extracted in toluene was detected by thermal lens microscopy (TLM). The Co complex was quickly extracted into toluene when the flow was stopped. The observed extraction time, about 50 s, was almost equivalent to the value calculated using the diffusion distance and diffusion coefficient. The dependence of the TLM signal on the concentration of the Co complex showed good linearity in the range of 1.10^{7} to 1.10^{6} M. Kutter et al. [17] created a microfabricated device with C18-coated channels used to demonstrate on-chip solid-phase extraction. Sample solutions containing a neutral dye were enriched and eluted in less than 4 min. Distinct elution peaks with good signal-to-noise ratios were obtained even for highly diluted samples.

The gain in concentration estimated from the enrichment and elution volumes was 80-fold.

8.2.2 Field Amplification Stacking Techniques on Microchips

Field amplification stacking (FAS) in conventional capillary systems was first mentioned by Mikkers et al. [18] and was intensively studied [19–22]. It has been used on microchips for stacking analytes [23] and for stacking a full column's worth of sample [24, 25]. Sample preconcentration is achieved by generating a high electrical field within an injected sample plug that rapidly drives and stacks sample ions at the ends of that plug. This field amplification is created when the sample is dissolved in a buffer that has a much lower conductivity than the running buffer used for electrophoresis separation. Higher preconcentration efficiencies require a larger amount of sample to be introduced into the microsystem. Full-column stacking techniques using polarity reversal offer this possibility at the price of increased analysis time (1 to 2 min, typically). Li et al. [24] used such a device to preconcentrate trace-level protein digests as preparation for quadrupole time-of-flight mass spectrometry. When the entire channel between the sample reservoir and the on-chip nanoelectrospray emitter was filled with sample solution, the polarity was reversed to remove the sample matrix whereas the analyte stacked at the boundary of the running buffer. The progress of matrix removal could be followed by current monitoring until only a small amount of buffer was left in the channel. Finally, the preconcentrated sample zone was pumped by the electroosmotic flow (EOF) into the electrospray emitter for mass spectrometry (MS) analysis. The concentration detection limit could be enhanced from 3- to 50-fold for different peptides. A different configuration was used by Lichtenberg et al. [23] for full-column stacking of fluorescently labeled amino acids combined with on-chip CE for separation. The design consists of a 55 to 170 mm–long, folded stacking channel connected to a 40 mm–long separation channel. In this way, high-efficiency stacking of a large sample volume could be combined with rapid separation in a short CE column. The stacking channel and the stacking itself were filled in 90 s, whereas the separation took only 35 s. The signal gain was found to be nearly linear with stacking channel lengths from 55 to 170 mm, yielding 60- to 95-fold increases.

8.2.3 Field-Amplified Injection on Microchips

Jacobson and Ramsey [26] and Kutter et al. [27] have investigated field-amplified injection (FAI) techniques on microchips extensively. Although FAS works for both negatively and positively charged ions, FAI has an electrophoretic bias depending on the direction of EOF. In this case, positive ions are stacked at the sample–buffer interface during the injection process. FAI can be easily implemented using the time-based, gated injection methods proposed by Jacobson et al. [28]. FAI yielded a concentration enhancement

for dansylated amino acids of up to 13.8-fold. Separations using stacked injection had efficiencies of 22,000 to 29,000 theoretical plates, which made them only 60 to 70% as efficient as CE on the same devices. In combination with postcolumn complexation for detection, FAI was also used to preconcentrate inorganic cations before microchip CE [27], employing the same procedure as described above. The stacked injection mode improved the signal by a factor of 16, which corresponded to extrapolated detection limits of 18 ppb for calcium and 0.5 ppb for magnesium.

8.2.4 Stacking of Neutral Analytes

At philosophical pH ranges, some analytes, such as glucose, are neutral. Methods like FAS or FAI mentioned above are applicable to positively or negatively charged analytes only. Methods for stacking neutral analytes for separation by micellar electrokinetic chromatography in fused silica capillaries have also been investigated. One approach, termed *sweeping*, involves the injection of an analyte zone into a column of separation buffer containing a pseudostationary phase (micelles). Upon application of the electric field, the micelles are swept through the analyte zone, collecting analyte and resulting in a unique focusing effect. More importantly, charged species could also be preconcentrated in this way. In a recent report, sensitivity increases approaching 1,000,000-fold have been achieved [29]. Though not yet applied to microchips, it is clear that the use of this technique could be enormously advantageous for the less sensitive detection methods integrated into microfluidic devices.

8.2.5 Isotachophoresis for Sample Preconcentration

Isotachophoresis (ITP) extends the stacking concept of FAS to ternary buffer systems and can be used for both sample preconcentration and as an analytical technique. In the case of ITP, the sample is injected between a leading and a terminating buffer electrolyte, LE and TE, respectively. Upon application of the separation voltage, the sample constituents are separated over a given time into distinct zones located between LE and TE in order of descending mobilities in the separation channels. Once this steady state is reached, the boundaries between sample zones are very sharp because of a self-focusing mechanism. The concentration in the sample zones is equal to the concentration of the leading buffer. Therefore, a preconcentration or dilution can be tailored by adapting the LE composition. Kaniansky et al. [30] realized various ITP configurations on a poly(methyl methacrylate) (PMMA) chip with two coupled separation columns and on-chip conductivity detectors. One application involving a combination of sample pretreatment by ITP and separation by CE involved the analysis of low concentration constituents (10 μM each of nitrite, phosphate, and fluoride) in a model mixture containing high background concentrations of ions such as chloride (600 μM) and sulfate (800 μM). A sample fraction containing the microconstituents could be

extracted from the steady-state ITP zone system and electrophoretically transferred into the second column for CE separation. Another polymer microfluidic device for the ITP separation of metal cations, fabricated with silicone rubber by casting, has recently been reported [31]. Similarly, detection was performed using an integrated single-electrode conductivity detector, indicating the utility of this less sensitive detection technique when used together with a preconcentration method like ITP. The separation of a sample containing a mixture of the four metal ions, lithium, lanthanum, dysprosium, and ytterbium, was reproducibly achieved using these devices. The miniaturized separations were achieved in less than 600 s, which is less than half the time taken for conventional capillary-electrophoresis separations.

8.3 Derivatization of Samples

Usually an ultraviolet detector, laser-induced laser detector, or electrochemical detector is coupled with the microfluidic system for high sensitivity detection. Unfortunately, none of these methods is universal, that is to say, not all analytes can be detected by a single detection technique because some analytes are not active for a chosen detection method. Sometimes sample derivatization is necessary before detection. This involves the chemical transformation of the analyte to render it detectable by the detection system employed. In biochemical assays on microchips, specific or nonspecific labeling of biomolecules with fluorescent labels is a common technique. A significant number of examples of sample derivatization exist in chip-based analysis to facilitate small-volume detection, particularly by fluorescence. Based on the fact that some analytes cannot be detected by the detector employed, they have to be derivatized before detection. Off-chip, precolumn, or postcolumn derivatization are commonly used. In addition, the sample preparation and preconcentration are important when analyzing environmental samples (concentrations in trace amounts) with microchip CE, which is generally known not to be as sensitive as classical chromatographic methods.

8.3.1 Labeling and Complexation on Microchips

Nowadays, fluorescence detection continues to be the method employed for chip-based analysis, as it has superior sensitivity and is ideally suited to the ultrasmall volume (pl) analysis and the detection of single molecules. Unfortunately, most species are not intrinsically fluorescent and so must be covalently labeled with a fluorescent tag. Generally these tagging reactions are carried out manually before the separation is done, which leads to additional preparative tasks and the requirement for comparatively large sample volumes. In addition, total analysis times are drastically increased consider-

ing the labeling times. For instance, the labeling reaction beforehand took several hours, whereas the first reported separations of fluorescein isothiocyanate (FITC)-labeled amino acids took only a few seconds [32]. Fluorescent labeling reactions that are kinetically very fast for aminated species do exist, opening up the possibility of online tagging directly before or after analysis by separation. This type of application is ideal for a chip-based approach because low dead-volume connections between microchannels minimize band broadening due to mixing with the reagent. Besides, covalent fluorescent labeling, noncovalent fluorescent labeling, complexation, and chemiluminescence are available for postcolumn (postseparation) tagging of species. Flow-injection analysis–type methods have been integrated into microfluidic devices to convert inorganic, ionic species to colored molecules detectable by absorbance, fluorescence, or other optical detection methods. In this case, no electrophoresis separations are carried out.

8.3.2 Postcolumn Reactors for Derivatization

The first successful example of on-chip labeling reactions was a postcolumn fluorescent tagging of amino acids using o-phthaldialdehyde (OPA) [33]. This particular label was chosen because of its rapid reaction kinetics. The planar glass device consisted of a typical microchip CE structure with an additional side channel intersecting with the separation channel 6 mm after the injection cross (the chip consisted of an injection channel and a separation channel that crossed each other) via this side channel; the labeling reagent was pumped into contact with the separated analyte zones. The reaction took place downstream, followed by fluorescence detection at 351.1 nm using an argon-ion laser. Band broadening due to adding reagent at the entrance of the reaction column was studied by injecting rhodamine B plugs into the system and comparing peak shapes before and after the mixing point. This additional band broadening was attributed to the different migration speeds at which already labeled and unlabeled analytes migrated in the channel. Although the kinetics of the labeling reaction were relatively fast (the reaction half-time is 4 s), analyte bands spread in the reaction column. Harrison et al. [34] worked on postcolumn reactors using the same sample and label combination as Jacobson et al. Initially they encountered comparably low separation efficiencies using a design with the separation and reaction channels laid out in a straight line. However, a closer analysis of the band-broadening source led to an improved design and operation conditions, which allowed separations having theoretical plate numbers, N, of over 83,000 [35]. The authors proposed two reasons for band broadening: (1) the analyte band spread because of different mobilities of labeled and unlabeled species during the reaction, as in Jacobson et al. [33]; (2) differences in electroosmotic velocity caused by mismatched pH or ionic strength in running the CE buffer and labeling streams caused Poiseuille flow profiles and distorted the bands further [36]. In an early configuration similar to that in

Fluri et al. [35], the labeling reagent stream was directly introduced into the reaction channel in a perpendicular, head-on manner. This confined the label to a narrow zone at one side of the channel and increased the time necessary for diffusive mixing [38]. In a later design, the label and separation channels intersected in a Y configuration, ensuring fast diffusive mixing of sample and reagent flows. The second important issue, namely the mismatch in electroosmotic mobilities of the different liquids, could be verified by changing the pH of the labeling reagent. In addition, glass microchips, integrating chemical derivatization reactions, electrophoretic separations, and amperometric detection, have been developed by Wang et al. [37]. The performance of the new integrated microfabricated devices is demonstrated for rapid on-chip measurements of amino acids utilizing precolumn reactions of amino acids to generate electroactive derivatives that are separated electrophoretically and detected at the end-column electrochemical detector. The influence of the sample-to-reagent mixing ratio, reagent concentrations, driving voltage, detection potential, and other variables is explored. The integrated microsystem offers a rapid (6 min) simultaneous measurement of eight amino acids, down to the 2.5 MM (5 fmol) level, with linearity up to the 0.2 mM level examined, and good reproducibility (RSD) 2.2 to 2.7%). The integrated microfabricated device expands the scope of on-chip electrochemical detection to electroactive analytes and holds promise of being a powerful analytical tool.

8.3.3 Precolumn Reactor Derivatization

OPA has also been used as the labeling reagent for precolumn labeling of amino acids on a microchip [38]. The amino acid sample was mixed with the labeling reagent including OPA in a 1 nl reaction chamber before it was injected into the 15.4 mm separation column by time-based, gated injection with 1.8% relative standard deviation (RSD) in the peak area. The series combination of reaction chamber and separation channel created a direct dependence of the reaction time for each particular analyte based on its electrophoretic mobility. Fluorescent labeling of amino acids before off-chip high-performance liquid chromatography (HPLC) separation has been proposed using 4-fluoro-7-nitrobenzofurazan (NBD-F) as the fluorophore [39]. The labeling reaction requires the sample-NBD-F mixture to be heated to 60°C for 2 min, which is achieved in a 100 mm–long, 50 μl–volume reaction channel in a silicon–glass sandwich structure. Integrated Cr–Pt resistors heated the chip at a rate of 2°C s^{1} up to 90°C, consuming 2 W. The temperature could also be monitored by integrated resistive sensors. Postcolumn reactors for complexation fluorescent tagging are not the only technique for making ions of interest visible for optical detection methods. Using the same chip structure as in those used by Jacobson et al. [33], calcium and magnesium were labeled after separation using 8-hydroxyquinoline-5-sulfonic acid (HQS) to form a fluorescent complex [40]. Fluorescence is maximal at an excitation

around 390 nm and pH 8, conditions that could be met by using an argon-ion laser and a borate buffer system. A fourfold decrease in signal intensity between offline and online complexation could be observed, which was easily compensated for by field-amplified stacking and injection. Liu et al. [41] combined on-chip CE with postcolumn complexation using a fluorogenic dye, NanoOrange, to detect proteins by laser-induced fluorescence. An advantage of NanoOrange is the short reaction half-life of only 110 ms for noncovalent binding to the hydrophobic regions of proteins (compared with 12 s for OPA). The labeling rate is therefore within the range for a diffusion-limited reaction, leading to plate heights of 10 to 20 μm. Wang et. al. [42] have developed a novel lab-on-a-chip protocol generating two electrophoretic peaks for a single analyte, based on the coupling of two different precolumn enzymatic reactions of the same substrate followed by electrophoretic separation of the reaction products. Such operation is illustrated for the measurement of glucose in connection with the corresponding glucose oxidase (GOx) and glucose dehydrogenase (GDH) reactions. The precolumn enzymatic reactions generate hydrogen peroxide and NADH species, which are separated (based on their different charges) and detected at the end-column amperometric detector. The peak-to-current ratio can be used for confirming the peak identity, estimating the peak purity, addressing comigrating interferences, and deviations from linearity. A driving voltage of 2000 V results in peroxide and NADH migration times of 93 and 260 s, respectively. Factors influencing the unique dual glucose response are examined and optimized. The concept can be extended to different target analytes based on the coupling of two precolumn reactions with electrophoretic separation of the reaction products.

8.3.4 Postcolumn Reactors for Chemiluminescence on Microchips

A different derivatization technique for biomolecules integrated on-chip is chemiluminescence detection, based on the horseradish peroxidase (HRP)–catalyzed reaction of luminol with peroxide in a postcolumn scheme [43]. The device used for this experiment is the same as described in Fluri et al. [35], with the added feature of a sputter-deposited aluminum mirror on the backside of the detection zone of some devices for increased concentration sensitivity. Luminol (5 mM) was added to the separation buffer itself, whereas 1.5% peroxide was mixed with the analyte bands after separation at the Y-shaped intersection before detection. The initial optimization of the detector setup showed a 1.6-fold improvement in detection limits for fluorescein-labeled HRP from 171 nM down to 105 nM when using the mirror. Depending on the injection technique used, the separation efficiency was determined to be 1000 to 5800 theoretical plates, a value in general sufficient for the immunoassay application of the device. A direct immunoassay of mouse immunoglobulin G (IgG) using a fragment of the HRP-conjugate of goat antimouse IgG was demonstrated for a concentration range from 0 to 60μg mL^{1}, by injecting the sample after off-chip immunological reaction.

8.3.5 Miniaturized Flow Injection Analysis (μFIA)

Wet chemical methods have been integrated into micromachined fluidic systems. One pioneer example focused on the analysis of phosphate using the molybdenum blue method to form a blue-colored phosphate complex allowing easy detection by absorbance [44, 45]. The microfluidic system was three-dimensional in nature, consisting of a number of silicon chips (23 × 23 mm) stacked on top of one another. The regular arrangement of through-holes around the chip perimeter ensured the passage of liquid between layers. This example was interesting in that it was the first to use silicon-based micropumps for controlling liquid fluid within a valveless system. A more recent example of μFIA is based on three-layer, glass-silicon-glass devices, containing an integrated optical cuvette etched through the silicon chip [46]. The device was developed to analyze ammonia in waste and drinking waters, using the Berthelot reaction to convert ammonia through reaction with phenol to a blue indophenol dye. In this case, syringe pumps were used to control the flows in the chip. An all-glass version of the three-layer chips for this application has also been reported [47]. EOF-driven μFIA systems based on glass have also been used for phosphate analysis by the molybdenum blue method [48], as well as analysis of other inorganic analytes [49].

8.4 Microfabricated Dialysis Devices

8.4.1 Microfabricated Single-Stage Microdialysis Device for Fast Desalting of Biological Samples

Electrospray ionization (ESI)-MS is amenable to analysis of nearly the entire range of biomolecules, and the use of mild ionization conditions allows noncovalent associations to be directly detected. However, sample matrix interference (generally due to low molecular weight salts) presents a major limitation to the use of ESI-MS for analyzing large biopolymers. Biological samples extracted under physiological conditions typically contain significant concentrations of nonvolatile solvents and salts (e.g., sodium chloride), and other reagents are often added to stabilize samples or to maintain their enzymatic activity. The presence of small to moderate amounts of salts will not only affect electrospray stability, but may also significantly reduce the detected ion signals because of both the suppression of ionization and the formation of multiple sodium adduct species. Low signal-to-noise ratios in the mass spectra and poor reproducibility due to excessive adduction can result in inaccurate mass assignments, and in severe cases, even preclude spectrum interpretation. Although online liquid chromatography (LC)/MS can tolerate small to moderate amounts of salt, and desalting columns are commercially available, they are not suitable for many ESI-MS experiments where samples may precipitate on the column or interact with the solvent,

or when very high salt concentrations are present. Direct ESI-MS of biological samples often relies upon centrifugation or offline microdialysis for desalting. Such a batch cleanup process can be time-consuming (taking several hours) and may suffer from adverse effects, such as sample losses during each step due to protein aggregation or precipitation on the filtering media. When only a small amount of sample is available, these effects can become even more pronounced. If noncovalent associations are of interest, slow desalting steps are more likely to result in denaturation or complex dissociation in solution.

A microdialysis approach has been used to address complex biological samples [50–52]. This approach employs a small microdialysis tube through which the sample flows in conjunction with a countercurrent flow of a suitable buffer. The dialyzed samples can be directly interfaced with the ESI source at a flow rate of approximately 2 to 5 μL/min. Although the microdialysis approach has demonstrated great promise for efficient sample cleanup capability, dialysis fibers less than the 200 μm diameter size used in our earlier work are not yet available, and this factor contributed to the minimum useful flow rates and sample processing times achieved previously. It is clear that miniaturizing the approach will not only further increase its speed, flexibility, and robustness, but also allow the use of lower rates and result in enhanced sensitivity. Recently we reported on a microfabricated microdialysis device constructed for this purpose and demonstrated its desalting efficiency for protein samples [53].

Figure 8.1 shows the structure of the single-stage microdialysis device. The sample and buffer channels were machined directly into the polycarbonate chip (30 × 30 × 6 mm) using a laser micromachining system. The sample channel was 160 μm wide, 60 μm deep, and 11 cm long. The buffer channel was 500 μm wide, 250 μm deep, and 12 cm long. A Spectra/Por Biotech 1.1 dialysis membrane with a molecular weight cutoff (MWCO) of 8000 was sandwiched between the chips. Figure 8.1b shows a photograph of the overlapping sample and buffer channels after aligning the microchannel dialysis chips.

The microfabricated dialysis device can be used in the online mode for direct ESI-MS analysis and has been evaluated for this purpose using the arrangement shown in Figure 8.2. High voltage was applied to the metal syringe needle used for buffer delivery and provided electrical contact through the buffer and sample solution. In this arrangement, the ESI emitter was a short piece of silica capillary (4 to 6 cm, 200 μm o.d. × 100 μm i.d.) fixed to the chip through a standard fitting. A 5 μM horse heart myoglobin solution in a complex matrix consisting of 500 mM of NaCl, 100 mM of Tris, and 10 mM of ethylenediaminetetraacetic acid (EDTA) was studied as an example. Figure 8.3a shows a mass spectrum obtained for this solution by direct infusion with the microspray ESI source. No protein charge state envelope was evident, and the spectrum was complicated by undesired peaks due to Tris and EDTA (commonly used in protein sample preparation). Online microdialysis was carried out using a dialysis buffer solution containing 10 mM of NH_4OAc and 1% (v/v) acetic acid at a flow rate of

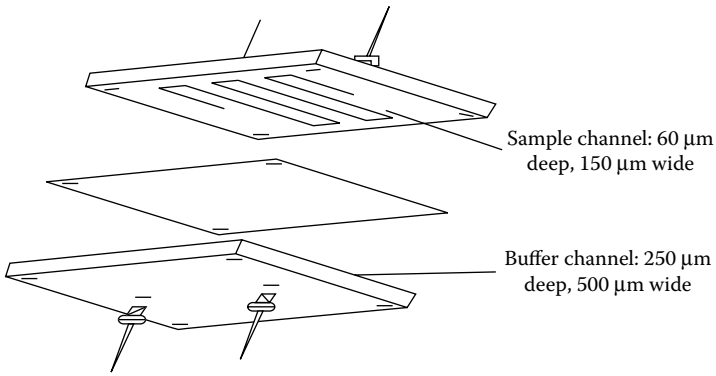

(a)

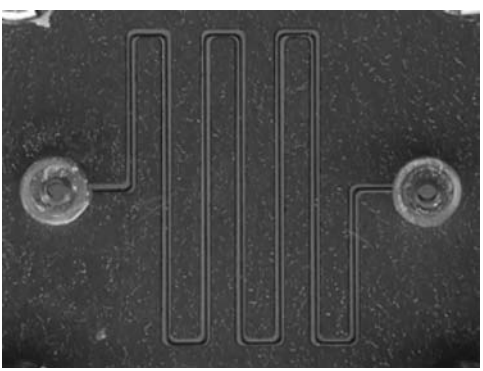

(b)

FIGURE 8.1
Schematic diagram of microfabricated single-stage microdialysis device (a) and photo of overlapping sample and buffer channels after alignment of the microchannel device (b). (Reprinted with permission from Xu, N. et al., *Anal. Chem.*, 70, 3553, 1998. Copyright 1998 American Chemical Society.)

100 µl/min, while the sample was introduced at a flow rate of 0.5 µl/min. As shown in Figure 8.3b, effective desalting was achieved. Multiple charge states from 19+ to 10+ of denatured myoglobin were clearly resolved, and the interference peaks from the Tris and EDTA were greatly diminished. The S/N was increased by a factor of more than 40 compared to that obtained without desalting.

With the current design, the total volume of the sample serpentine channel is only 1 µl, and the actual dialysis time for the sample, that is, the time the sample spent inside the microdialysis channels, was approximately 2 min at a sample flow rate of 0.5 µL/min. The effectiveness of the cleanup can be ascribed to the size difference between the sample channel and the buffer channel, and the fact that the cleanest sample solution is effectively exposed to the cleanest dialysis buffer because of its countercurrent flow. For effective

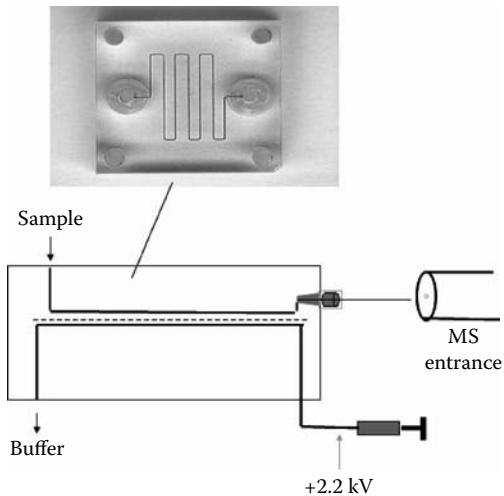

FIGURE 8.2
Schematic representation of the setup of the microfabricated device for online ESI-MS analysis. The top panel shows a photograph of the sample channel chip. (Reprinted with permission from Xu, N. et al., *Anal. Chem.*, 70, 3553, 1998. Copyright 1998 American Chemical Society.)

desalting, it has been found that air bubbles trapped inside the sample channels need to be forced out before the dialysis occurs. The sample loss during the dialysis is minimal because of the short residence time in the microdialysis channel and the fact that the analytes are above the MWCO of the chosen membrane. The Spectra/Por Biotech 1.1 membrane used for this work has a high tolerance to acidic solvents, such as 90% acetic acid and organic solvents (e.g., 90% methanol), thus providing versatility in applying the microfabricated dialysis device.

8.4.2 Microfabrcated Dual-Stage Microdialysis Device for Rapid Fractionation and Cleanup of Complex Biological Samples

As discussed previously, a single-stage microdialysis device can be used for rapid and efficient desalting of biological samples. More recently, we developed a microfabricated dual-stage microdialysis device for fast and efficient fractionation and cleanup of complex biological samples (i.e., cellular extracts) [54].

Figure 8.4 shows the structure and flow diagram of the dual-stage microdialysis device. The sample channel (60 μm deep, 150 μm wide) was machined directly into the polymer chip (30 × 30 × 6 mm) by using multiple parallel laser passes. A 500 μm–wide buffer channel was machined from 225 μm–thick polyimide with a silicone adhesive on one side. The adhesive was used to attach the buffer channel to a flat polymer chip. Two microdialysis membranes are sandwiched between three polymer chips with microfabricated serpentine channels. This novel design makes the dual-stage microdialysis device highly compact and rugged, eliminating the need for tubing to connect the two

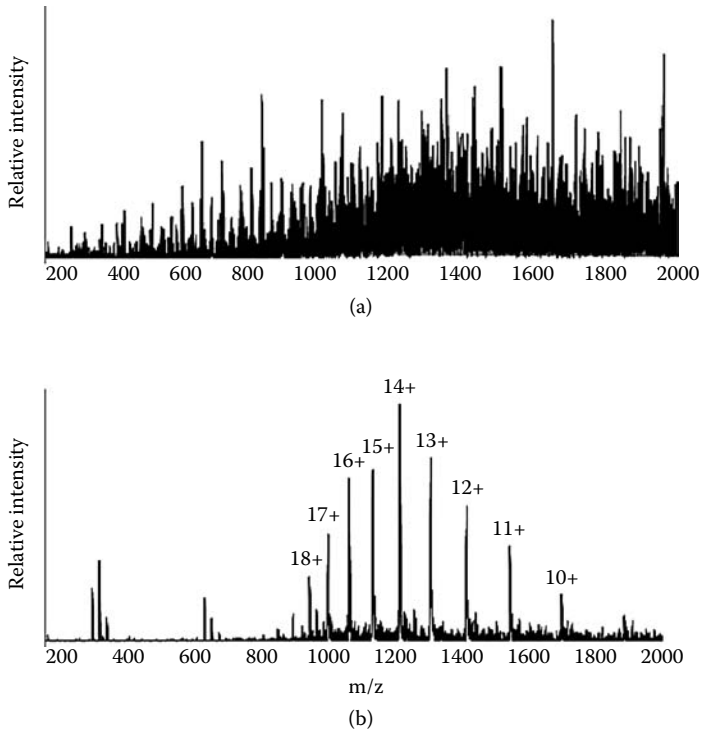

FIGURE 8.3
(a) ESI-mass spectrum of 5 μM horse heart myoglobin in 500 mM of NaCl, 100 mM of Tris, and 10 mM of EDTA by direct infusion; (b) ESI mass spectrum of previous myoglobin sample after online microdialysis using 10 mM of NH_4OAc and 1% acetic acid as a dialysis buffer. (Reprinted with permission from Xu, N. et al., *Anal. Chem.*, 70, 3553, 1998. Copyright 1998 American Chemical Society.)

stages of the microdialysis units. The fluid channels were designed to make the raw sample flow in a microchannel along one side of the first stage membrane so that a portion of sample flows through the membrane and enters the second stage. This partial flow in the first stage provides a mechanism for sweeping out cellular residues in the sample channel and results in a reduced possibility of membrane clotting. Alternatively, the sample channel outlet (b) can be completely sealed if the lifetime of the membrane is not of concern. The sample flow rate entering the second stage of the device can be adjusted by controlling the flow rate at the outlet (b) by throttling the sample flow through fused silica tubing of various lengths and inner diameters. The sample entering the second stage of the device is stripped of the small molecules and salts by a dialysis buffer flowing in a microchannel on the opposite side of the second-stage membrane.

A protein mixture consisting of 30 μM of bovine serum albumin (BSA), 8 μM of cytochrome c, and 2.4 μM of ubiquitin in 10 mM phosphate buffer

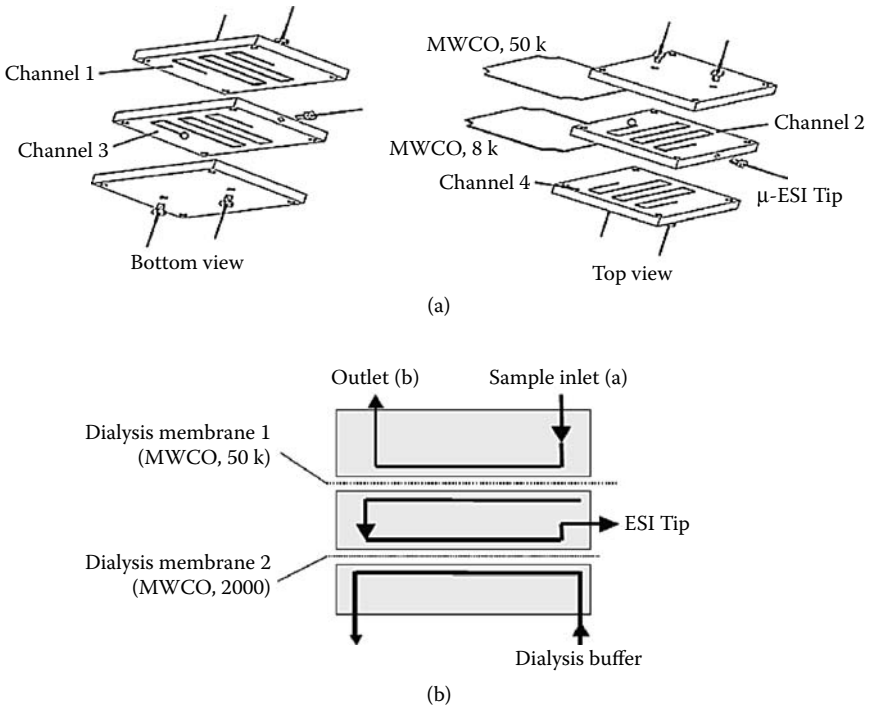

FIGURE 8.4
(a) Exploded view showing construction of the microfabricated dual-stage microdialysis device. (b) Flow diagram of the device showing sample inlet, buffer inlet, and microelectrospray tip. (Reprinted with permission from Xiang, F. et al., *Anal. Chem.*, 71, 1485, 1999. Copyright 1999 American Chemical Society.)

saline PBS was used to evaluate the performance of the dual-stage microdialysis device. A 50 kDa MWCO membrane and an 8 kDa MWCO membrane were used in the first- and second-stage microdialysis, respectively. The sample was injected at 0.5 μL/min, and the cleanup buffer at 10 μL/min. As shown in Figure 8.5a, direct infusion of the protein mixture produced no useful ESI-MS spectrum. ESI-MS performance is well known to be poor for such solutions, presumably due to the excess BSA and NaCl. After the online dual dialysis in the microfabricated device, the spectrum in Figure 8.5b clearly showed peaks from cytochrome c, ubiquitin, and removal of the unresolved envelope of peaks at higher m/z. The improvement in spectral quality using the dual-stage microdialysis device enabled us to effectively assign peaks and accurately determine molecular weights.

For analyzing complex biological samples, initial sample fractionation and cleanup can simplify analytical procedures. Online dual dialysis using the microfabricated device is a fast and efficient means of achieving this. The molecular weight range selected for analysis by dual microdialysis can be controlled by selecting appropriate MWCO membranes at both stages.

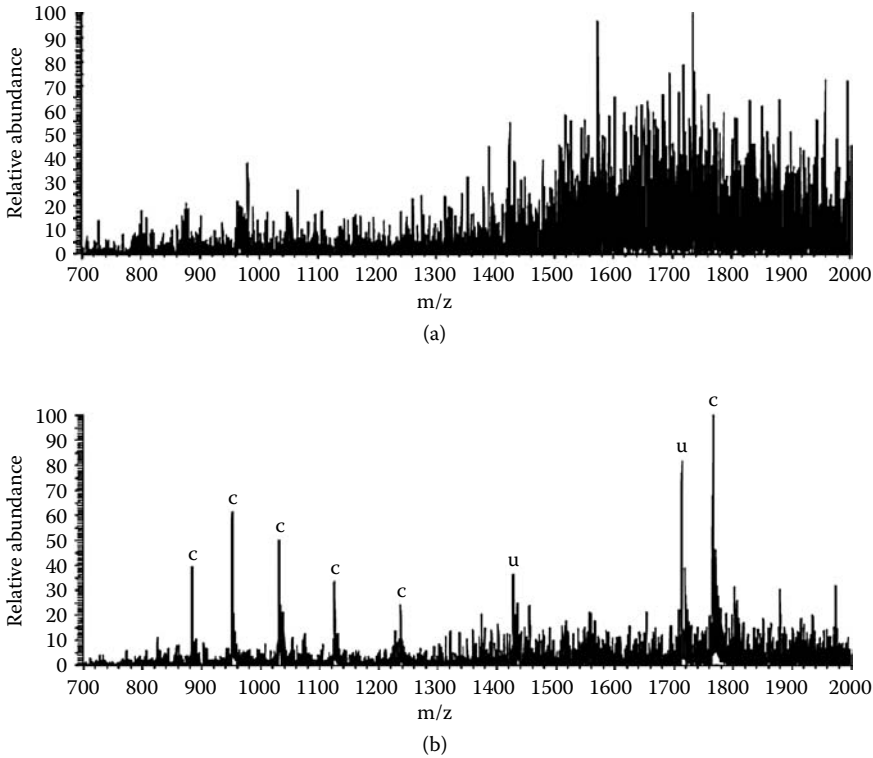

FIGURE 8.5
ESI-MS spectra of a protein mixture consisting of 30 μM of bovine serum albumin, 8 μM of cytochrome c, and 2.4 μM of ubiquitin in 0.01 M of PBS. (a) Sample directly infused without passing through the dual-microdialysis device; (b) sample passed by the dual microdialysis device. Identities of the peaks: u, ubiquitin; c, cytochrome *c*. (Reprinted with permission from Xiang, F. et al., *Anal. Chem.*, 71, 1485, 1999. Copyright 1999 American Chemical Society.)

8.4.3 Application to Complex Cellular Samples

The analysis of cellular extracts and other complex biological samples is of great interest for many purposes, including biotechnology, pathogen detection, medical research, bioremediation, and clinical applications. However, such analysis will require that complex samples be readily separated, fractionated, or cleaned up to the point where useful mass spectra can be obtained. Interferences from both high-molecular-weight and low-molecular-weight components constitute limitations for the direct use of ESI-MS to analyze target biomolecules in such complex systems.

The use of the microfabricated dual-stage microdialysis device for sample processing is attractive because of its ruggedness, its potential for extension to multichannel devices, and its feasibility in greatly increasing the speed and care of automation. To evaluate the processing efficiency of the microfabricated dialysis device, an *E. coli* lysate with a total protein concentration

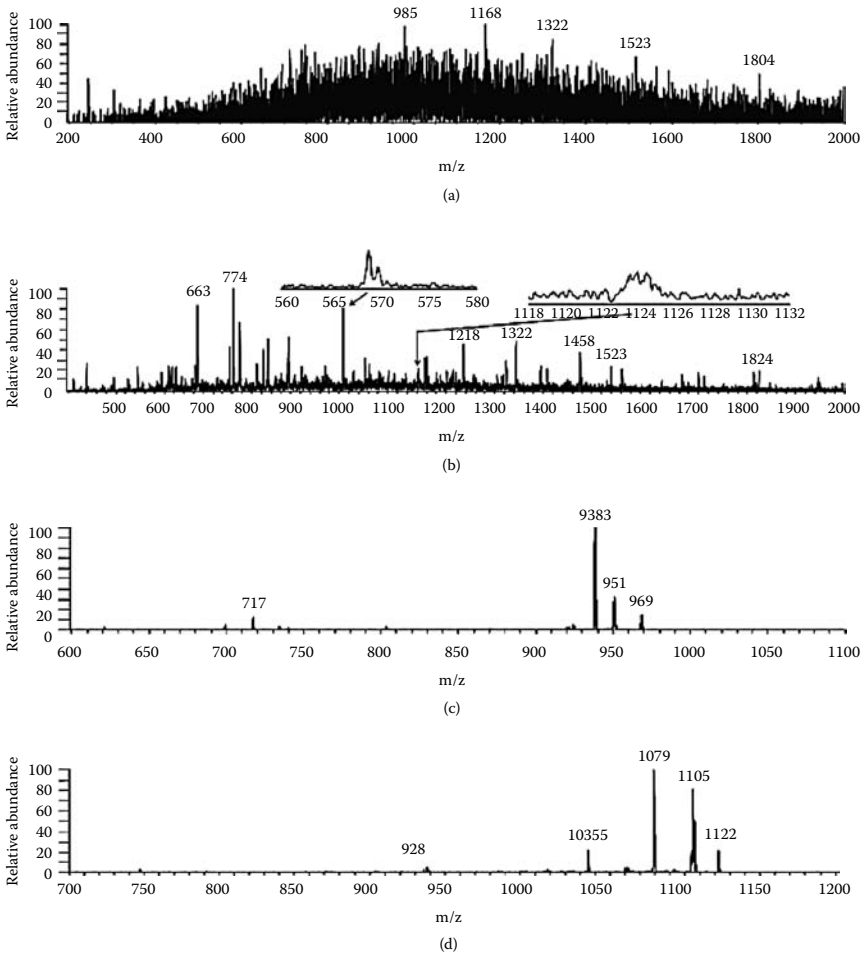

FIGURE 8.6
ESI-MS spectra for an *E. coli* cell lysate. (a) Spectrum obtained from the sample directly infused without passing through the dual microdialysis device; (b) spectrum obtained using online dual microdialysis sample processing; two expanded views show detail of peaks at m/z 969 and 1124; (c) CID spectrum of m/z 969 at a relative collision energy of 35%; (d) CID spectrum of m/z 1124 at a relative collision energy of 35%. (Reprinted with permission from Xiang, F. et al., *Anal. Chem.*, 71, 1485, 1999. Copyright 1999 American Chemical Society).

of approximately 1 mg/mL was analyzed by ESI-MS before and after the dual dialysis. Direct infusion of the crude cell lysate produced the spectrum shown in Figure 8.6a. The spectrum is largely uninterpretable because of the complex components, the high concentration of NaCl, and the consequently low signal-to-noise ratio. After passing the sample through the dual-stage microdialysis device with a 50 kDa (MWCO) membrane in the first stage and a 8-kDa (MWCO) membrane in the second stage, a large improvement in spectral quality was observed (Figure 8.6b). An approximately 20-fold increase of signal-to-noise ratio was obtained. The characteristic peaks

from major cellular components are readily discernible in the spectrum and provide the basis for further MS/MS experiments [55]. Lower flow rates with ESI-MS provide greater sensitivity. With the current device, online ESI-MS can be conducted at a few hundred nL/min, more than an order of magnitude reduction compared to the previous dual-stage dialysis system [56]. Another feature of the current device is the reduced dead volume achieved by eliminating connection tubing between the two stages. These features should allow faster analysis of smaller samples. MS/MS of distinctive ions provides a potential basis for identification (i.e., serving as biomarkers) of microorganisms. Figures 8.6c and d show two MS/MS spectra of m/z 969 and 1124 ions in the expanded views of Figure 8.6b. The spectra in Figures 8.6c and d show an average of 38 scans and present an excellent signal-to-noise ratio. Using a flow rate of 200 nL/min, only 16 μL of the sample was consumed for MS/MS data acquisition of 40 cellular components. The distinctive MS/MS spectral patterns can be used to identify mass spectrometric–detected species useful as biomarkers, which then provide a basis for confident identification of microorganisms. The results presented also demonstrate the application of this for detecting bacteriophage MS2 in the presence of a large excess of *E. coli*.

8.5 Conclusions

It is clear that the integration of the components for the sample pretreatment on microfluidic devices represents one of the remaining bottlenecks in achieving true μ-TAS. The challenge is made more complex by the enormous variation in samples to be analyzed. More importantly, the pretreatment technique employed has to be compatible with the analysis device to which it is coupled in terms of time, reagent, and power and sample consumption. As this review shows, however, significant progress has been made, especially in recent years, driven largely by developments in the life sciences. An exponential increase in papers dealing with this subject is to be expected in the next couple of years.

Acknowledgments

The work performed at Pacific Northwest National Laboratory (PNNL) was supported by a Laboratory Directed Research and Development Program, Strategic Environmental Research and Development Program (Project # CU 1297), U.S. Department of Energy (DOE)-Environmental Management Science Program, and National Institutes of Health (NIH)/1R01 ES010976-01A2.

PNNL is operated by Battelle for DOE under Contract DE-AC05-76RL01830. The work performed at Fudan University was supported by the High-Tech Research and Development (863) Program of China (Grant No. 2004AA639740), the National Nature Science Foundation of China (Grant No. 20405002), and the Nature Science Foundation of Shanghai (Grant No. 2004ZR14015).

References

[1] Verpoorte, E., Microfluidic chips for clinical and forensic analysis, *Electrophoresis*, 23, 677, 2002.
[2] Reyes, D.R. et al., Micro total analysis systems. 1. Introduction, theory, and technology. , *Anal. Chem.*, 74, 2623, 2002.
[3] Wang, J., Chen, G., and Chatrathi, M.P., Microchip capillary electrophoresis coupled with a boron-doped diamond electrode-based electrochemical detector, *Anal. Chem.*, 75, 935, 2003.
[4] Harrison, J.D. et al., Capillary electrophoresis and sample injection systems integrated on a planar glass chip, *Anal. Chem.*, 64, 1926, 1992.
[5] Jacobson, S.C. et al., High-speed separations on a microchip, *Anal. Chem.*, 66, 1114, 1994.
[6] Chen, Z.F. et al., Fabrication and characterization of poly(methyl methacrylate) microchannel by in-situ polymerization method with novel metal template, *Electrophoresis*, 24, 3246, 2003.
[7] Roberts, M.A. et al., UV laser machined polymer substrates for the development of microdiagnostic systems, *Anal. Chem.*, 69, 2035, 1997.
[8] Martynova, L. et al., Fabrication of plastic microfluid channels by imprinting methods, *Anal. Chem.*, 69, 4783, 1997.
[9] McCormick, R.M. et al., Microchannel electrophoretic separations of DNA in injection-molded plastic substrates, *Anal. Chem.*, 69, 2626, 1997.
[10] Nakagawa, T., Fabrication of amino silane-coated microchip for DNA extraction from whole blood., *J Biotechnol.*116(2), 105, 2005.
[11] Chung, Y.C. et al., Microfluidic chip for high efficiency DNA extraction, *Lab on a Chip*, 4(2), 141, 2004.
[12] Wolfe, K.A. et al., Toward a microchip-based solid-phase extraction method for isolation of nucleic acids, *Electrophoresis*, 23(5), 727, 2002.
[13] Tian, H.J., Huhmer, A.F.R., and Landers, J.P., Evaluation of silica resins for the direct and efficient extraction of DNA from complex biological matrices in a miniaturized format, *Anal. Biochem.*, 283(2), 175, 2000.
[14] Breadmore, M.C. et al., Microchip-based purification of DNA from biological samples, *Anal. Chem.*, 75(8), 1880, 2003.
[15] Maruyama, T. et al., Liquid membrane operations in a microfluidic device for selective separation of metal ions, *Anal. Chem.*, 76(15), 4495, 2004.
[16] Tokeshi, M., Minagawa, T., and Kitamori, T., Acceleration of an enzymatic reaction in a microchip, *J. Chromatogr. A.*, 894(1–2), 19, 2000.
[17] Kutter, J.P., Jacobson, S.C., and Ramsey, J.M., Integration of a microextraction system: solvent extraction of Co-2-Nitroso-5-dimethylaminophenol complex on a microchip, *J. Microcol. Sep.* 12(2), 93, 2000.

[18] Mikkers, F.E.P., Everearts, F.M., and Verheggen, T.P.E.M., High-performance zone. Electrophoresis, *J. Chromatogr.,* 169, 11, 1979.
[19] Burgi, D.S. and Chien, R.L., Application and limits of sample stacking in capillary electrophoresis, *Meth. Mol. Biol.*, 52, 211, 1996.
[20] Chien, R.L. and Burgi, D.S., Sensitivity enhancement for capillary electrophoresis, *Anal. Chem.*, 64, 489A, 1992.
[21] Burgi, D.S. and Chien, R.-L., Field amplified sample stacking: optimization in sample stacking for high-performance capillary electrophoresis, *Anal. Chem.*, 63, 2042, 1991.
[22] Chien, R.-L. and Helmer, J.C., *Anal. Chem.*, 63, 1354, 1991.
[23] Lichtenberg, J. Verpoorte, E., and de Rooij, N.F., Sample preconcentration by field amplification stacking for microchip-based capillary electrophoresis, *Electrophoresis*, 22, 258, 2001.
[24] Li, J. et al., Rapid and sensitive separation of trace level protein digests using microfabricated devices coupled to a quadrupole—time-of-flight mass spectrometer, *Electrophoresis*, 21, 198, 2000.
[25] Herr, A.E. et al., Electroosmotic capillary flow with nonuniform zeta potential, *Anal. Chem.*, 72, 1053, 2000.
[26] Jacobson, S.C. and Ramsey, J.M., Microchip electrophoresis with sample stacking, *Electrophoresis*, 16, 481, 1995.
[27] Kutter, J.P. et al., Determination of metal cations in microchip electrophoresis using on-chip complexation and sample stacking, *J. Microcolumn. Sep.*, 10, 313, 1998.
[28] Jacobson, S.C. et al., Effects of column geometry on the performance of microchip electrophoresis devices, *Anal. Chem.*, 66, 1107, 1994.
[29] Quirino, J.P. and Terabe, S., Approaching a million fold sensitivity increase in capillary electrophoresis with direct ultraviolet detection: cation selective exhaustive injection and sweeping, *Anal. Chem.*, 72, 1023, 2000.
[30] Kaniansky, D. et al., Capillary electrophoresis separations on a planar chip with the column-coupling configuration of the separation channels, *Anal. Chem.,* 72, 3596, 2000.
[31] Prest, J.E. et al., Determination of metal cations on miniaturised planar polymeric separation devices using isotachophoresis with integrated conductivity detection, *Analyst,* 126, 433, 2001.
[32] Effenhauser, C.S., Manz, A., and Widmer, H.M., Glass chips for high-speed capillary electrophoresis separations with submicrometer plate heights, *Anal. Chem.*, 65, 2637, 1993.
[33] Jacobson, S.C. et al., Microchip capillary electrophoresis with an integrated postcolumn reactor, *Anal. Chem.*, 66, 3472, 1994.
[34] Harrison, D.J. et al., Integrated electrophoresis systems for biochemical analyses, in *Proceedings of the IEEE Solid-State Sensor and Actuator Workshop*, Hilton Head Island, SC, IEEE Electron Devices Society, 1994, 21.
[35] Fluri, K. et al., Integrated capillary electrophoresis devices with an efficient postcolumn reactor in planar quartz and glass chips, *Anal. Chem.,* 68, 4285, 1996.
[36] Seiler, K. et al., Electroosmotic pumping and valveless control of fluid flow, *Anal. Chem.,* 66, 3485, 1994.
[37] Wang, J. et al., Micromachined separation chips with a precolumn reactor and end-column electrochemical detector, *Anal. Chem.* 2000, 72, 5774–5778.
[38] Jacobson, S.C. et al., Precolumn reactions with electrophoretic analysis integrated on a microchip, *Anal. Chem.*, 66, 4127, 1994.

[39] Eijkel, J.C.T. et al., Micromachined heated chemical reactor for pre-column derivatization, *J. Chromatogr.,* 815, 265, 1998.
[40] Swaile, D.F. and Sepaniak, M.J., Determination of metal ions by capillary zone electrophoresis using on-column chelation, *Anal. Chem.,* 63, 179, 1991.
[42] Liu, Y.J. et al., Electrophoretic separation of proteins on a microchip with noncovalent, postcolumn labeling, *Anal. Chem.,* 72, 4608, 2000.
[42] Wang, J. et al., Glucose biochip: dual analyte response in connection to two pre-column enzymatic reactions, *Analyst,* 2001, 126, 1203–1206
[43] Mangru, S.D. and Harrison, D.J., Microchip-based capillary electrophoresis and affinity electrophoresis, *Electrophoresis,* 19, 2301, 1998.
[44] Verpoorte, E.M.J. et al., Silicon-based chemical microsensors and microsystems, *Interfacial Des. Chem. Sensing,* 561, 244, 1994.
[45] Verpoorte, E.M.J. et al., 3-dimensional micro-flow manifolds for miniaturized chemical-analysis systems, *J. Micromech. Microeng,.* 4, 246, 1994.
[46] Daridon, A. et al., Chemical sensing using an integrated microfluidic system based on colorimetrics: a comparative kinetic study of the Bertholet reaction for ammonia determination in microfluidic systems, *Sens. Actuators B*, 76, 235, 2001.
[47] Daridon, A. et al., Multi-layer microfluidic glass chips for microanalytical applications, *Fresenius J. Anal. Chem.,* 371, 261, 2001.
[48] Doku, G.N. and Haswell, S.J., Further studies into the development of micro FIA (m FIA) system based on electroosomotic flow for the determination of phosphate as orthophosphate, *Anal. Chim. Acta,* 382, 1, 1999.
[49] Haswell, S.J., Development and operating characteristics of micro flow injection analysis systems based on electroosmotic flow, *Analyst*, 122, R1, 1997.
[50] Wu, Q., Liu, C.L., and Smith, R.D., On-line microdialysis desalting for electrospray ionization mass spectrometry of proteins and peptides, *Rapid Commun. Mass Spectrom.* 10, 835, 1996.
[51] Liu, C. et al., On-line microdialysis sample cleanup for electrospray ionization mass spectrometry of nucleic acid samples, *Anal. Chem.* 68, 3295, 1996.
[52] Muddiman, D.C. et al., Characterization of PCR products from bacilli using electrospray ionization FTICR mass spectrometry, *Anal. Chem.*, 68, 3705, 1996.
[53] Xu, N. et al., A microfabricated dialysis device for sample cleanup in electrospray ionization mass spectrometry, *Anal. Chem.*, 70, 3553, 1998.
[54] Xiang, F. et al., An integrated microfabricated device for dual-microdialysis and on-line ESI ion trap mass spectrometry for analysis of complex biological samples, *Anal. Chem.,* 71, 1485, 1999.
[55] Xiang, F. et al., Characterization of microorganisms and biomarker development from Global ESI-MS/MS analyses of cell lysates, *Anal. Chem.*, 72, 2475, 2000.
[56] Liu, C. et al., On line dual microdialysis with ESI-MS for direct analysis of complex biological samples and microorganism lysates, *Anal. Chem.*, 70, 1797, 1998.

9

Bio-MEMS Devices in Cell Manipulation: Microflow Cytometry and Applications

Choongho Yu and Li Shi

CONTENTS

9.1 Conventional Cytometers

Flow cytometers are widely used for rapidly analyzing large populations of cells and other particulate or molecular analytes that have been captured on the surface of carrier particles. The analysis speed is in the range of 10^5 to 10^6 particles per minute. In addition, particles can be sorted based on their distinct dielectric or fluorescence properties. These capabilities have made flow cytometers indispensable in bioindustrial research and clinical diagnostic applications for the last 40 years [1–4].

Two of the key components of a typical cytometer are the hydrodynamic focusing system and the optical detection system. The hydrodynamic focusing system uses a high-speed sheath fluid medium to focus particles in a

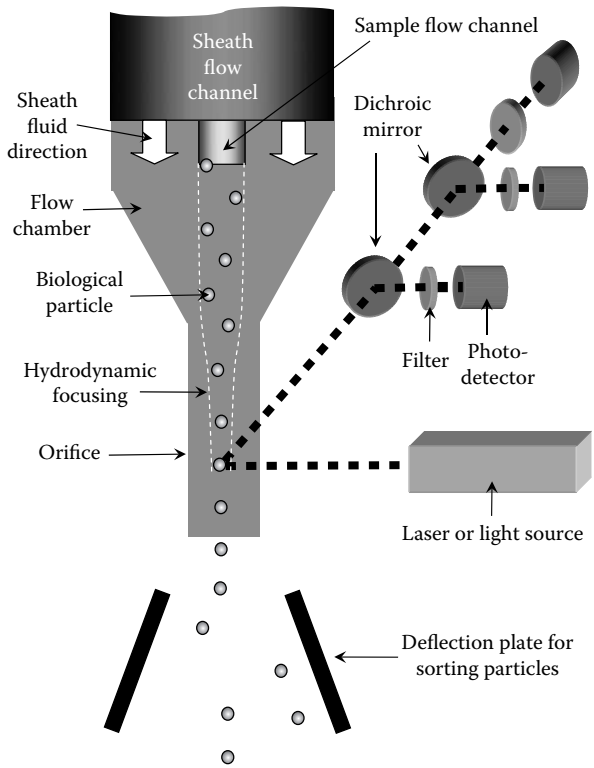

FIGURE 9.1
Schematic of a conventional flow cytometer (not to scale).

fluid suspension within the focal point of the optical detection system. In practice, the sheath fluid is injected into a flow chamber at a high speed and particles are focused into a tight stream of 10 to 25 μm in diameter established within a 50 to 300 μm–diameter flow channel. In addition, the sheath fluid medium prevents impurities or agglomerated clusters from clogging the channel. The hydrodynamic focusing system consists of a tapered flow chamber with a smaller diameter flow channel or an orifice at the end, as schematically shown in Figure 9.1. In detail, the sample and sheath fluids are simultaneously supplied through two concentric fluidic channels by using a mechanical pump. The pressurized sheath fluid pushes the particle suspended in the sample fluid to the center of the chamber and the orifice. By the time the particle reaches the optical detection region, the particle stream is tightly focused within the focal point of the excitation source. The particle trajectory in this so-called hydrodynamic focusing channel is represented by the white dotted line in Figure 9.1.

In order to confine the particle stream within the focal point of the excitation optics during the entire measurement, the fluid flow should be in the laminar

flow regime, where the sample and sheath fluids rarely mix together. In this flow regime, once the stream is stabilized, the particle tends to stay on the same path in the fluidic channel. The flow in the channel is laminar when the Reynolds number (*Re*) is less than approximately 2300. The Reynolds number is defined as $Re \equiv \rho u D/\mu$, where ρ, u, μ, and D are the density, velocity, dynamic viscosity of fluid, and the diameter of the channel, respectively. For example, the density and the dynamic viscosity of water-based solutions are on the order of 10^3 kg/m^3 and 10^3 N·s/m^2, respectively. The diameter of the channel is often less than 500 μm in conventional cytometers. Therefore, the flow in a cytometer is usually in the laminar regime unless the fluid velocity is faster than a few meters per second. Figure 9.2 shows a flow of ink focused by sheath fluid in the laminar regime. It can be seen that the core and sheath fluids are clearly separated.

In general, flows in microfluidic devices are usually laminar flows, in which mixing is limited by the slow nature of molecular diffusion. While there have been significant efforts to enhance mixing in microfluidic channels, the slow mixing process in microchannels is a very attractive feature for cytometry applications. Moreover, this feature allows one to integrate a sorting mechanism with a focusing channel because it is relatively easy to switch the flow direction without disturbing the particle streams, as will be discussed in a subsequent section.

Another key component of a flow cytometer is the optical system that excites fluorescently labeled particles and detects photons of selected wavelengths. The particle trajectory is coincident with the focus of one or more illumination sources and detectors that are used to determine the light scattering and fluorescence properties of individual particles. Because the fluorescence or scattering signal is much weaker than the excitation, it is important to align various optical components including dichroic mirrors, filters, and photodetectors in order to maximize the signal-to-noise ratio. The excitation light can consist of one or more wavelengths depending on the type or number of light sources. Xenon and mercury lamps generate polychromatic incoherent lights that require complicated optics for filtering and focusing. They are inherently

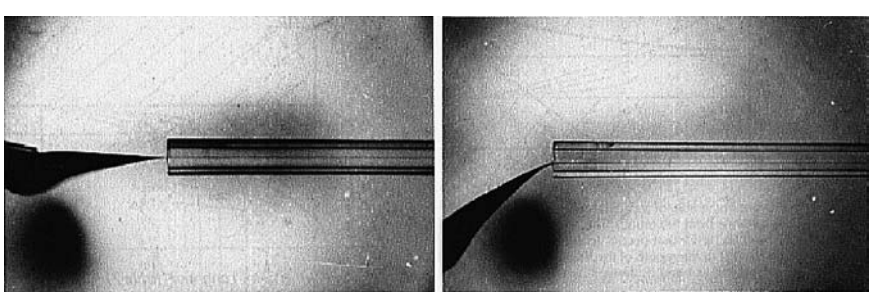

FIGURE 9.2
Photographs of a stream of hydrodynamically focused ink along the center of the tube in the laminar flow regime. The ink flows from the left to the right. (From Melamed, M. R., Lindmo, T., and Mendelsohn, M. L., *Flow Cytometry and Sorting*, Copyright © Wiley, New York, 1991. Reprinted with permission of Wiley-Liss, Inc.)

inferior to monochromatic and coherent laser lights, which are often used for conventional cytometry applications. However, lasers often consume a lot of power and are much larger than microfludic devices. It is also difficult to fabricate solid-state lasers and microfluidic channels on the same chip. Hence, it has been challenging to integrate lasers with microfluidic devices, and this integration has been a topic of active research.

For optical detection, biological particles are stained by fluorochromes. Different particles can be selectively stained with different types of fluorochromes with different excitation and emission spectra, enabling one to distinguish different cells or determine particle properties. Additionally, the light scattering pattern of a particle depends on the particle shape. Forward-angle light scattering (FALS) detection at an angle of about 0.5 to 5° can be used for measuring the cell size, and side-angle light scattering (SALS) detection at an angle of about 15 to 150° can be used for measuring internal granularity and surface roughness. The combination of FALS and SALS can be used to discriminate dead and viable cells [1,3]. Dichroic mirrors installed at a 45° angle to the path of an incident beam can be used to separate the excitation and fluorescence spectra into two different optical paths, one deflected and one transmitted, as shown in Figure 9.1. The deflected or transmitted light can be further filtered by using a band-pass filter prior to detection by a sensitive photodetector. The low intensity of the fluorescence signal requires the use of photomultiplier tubes (PMTs) with a high gain and excellent signal-to-noise ratio. Because PMTs are bulky, it is rather difficult to integrate them with a microfluidic device. As a comparison, photodiodes such as p-i-n (PIN) or avalanche photodiodes (APDs) can be made more compact than PMTs.

Conventional cytometers are equipped with a particle sorter at the end of the orifice as shown in Figure 9.1. Small droplets of the particle suspension are formed by the application of controlled vibration at the end of the orifice. Under the influence of an electric or magnetic field originating from the deflection plates, the particles with different dielectric or magnetic properties are deflected toward different paths and subsequently collected by different containers. It is rather difficult to miniaturize this sorting mechanism due to the difficulty in breaking the suspension into droplets in a microfluidic device.

9.2 Microflow Cytometers

Hydrodynamic focusing and optical detection systems make conventional cytometers complex, large, and expensive. First, the hydrodynamic particle focusing mechanism requires a complicated system for controlling the proper flow rates of the sheath and sample flows. In addition, a reservoir is required for the sheath flow medium, which also has to be supplied and kept free of

dust and bacteria. The optical system, moreover, is large, expensive, and prone to misalignment from electrical drift, thermal expansion, and vibration. As a result, the system requires constant alignment and preventive maintenance by skilled personnel. This prevents the wide use of cytometers outside core facilities or laboratories for detecting pathogens, human disease, hazardous species, and many other biological particles.

The recent development of microelectromechanical systems (MEMS) technologies has provided a possible solution to the aforementioned problems of conventional cytometers. Because of their small size, MEMS devices can effectively handle micron-size biological cells and can be fabricated in large volumes at low costs. In addition, they offer other potential benefits such as portability, low power consumption, disposability, ease of operation, simplicity, small sample and sheath fluid volumes, and on-chip integration of electronic circuitry. If all optical components including light sources, detectors, lenses, and filters can be integrated with a microfluidic device on the same chip, the device would not require frequent alignment and maintenance and would be much more robust and easier to operate than conventional cytometers. Furthermore, a microflow cytometer can be used as a module or a component of other medical diagnosis devices or micro total analysis systems. Because of these potential benefits of miniaturized cytometers, there have been many attempts to fabricate microflow cytometers using MEMS fabrication techniques.

Efforts to miniaturize a flow cytometer can be categorized into three different groups: (1) the development of a microfluidic system for particle focusing, (2) the integration of a detection system, and (3) the development of a micro cell sorter and counter, as discussed in the following.

9.2.1 Particle Focusing Systems

One of the essential functions of the cytometer is to focus the particles within the focal point of a detection system. Various approaches to the miniaturization of the focusing mechanism have been investigated. These approaches are based on pressurized sheath liquid or air flows, electrokinetic flows, small constriction, or dielectrophoresis. Some of them require a sheath fluid as in a conventional cytometer, while the sheath fluid is eliminated in some other approaches.

9.2.1.1 Hydrodynamic Focusing

The conventional hydrodynamic focusing mechanism is miniaturized in several microcytometer designs. One of the very first versions of a small-scale sheath and sample flow chamber was reported by Miyake et al. [5]. In this work, small fluidic channels were carved on three thin metal sheets. Glass pieces were bonded with the metal pieces to form the flow channel that allowed optical access to the particles inside the channel. Sobek et al. [6]

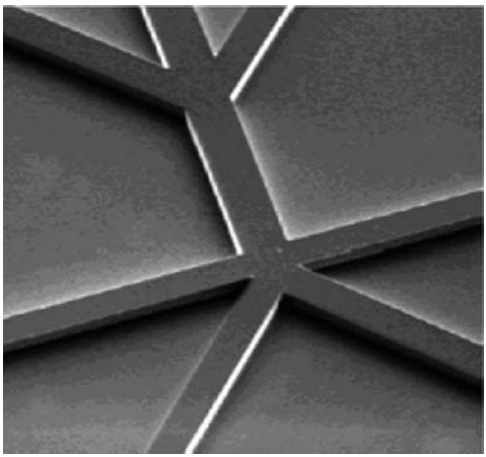

FIGURE 9.3
SEM of an etched Si mold for soft lithograpahy patterning of a PDMS hydrodynamic focusing microchannel. The channel is 7.6 μm deep and 25 μm wide. (From Dittrich P. S. and Schwille, P., *Anal. Chem.*, 75, 5767, 2003. Reprinted with permission from American Chemical Society.)

fabricated a hexagonal fluidic channel using multiple etching and bonding procedures. A hypodermic needle was used for injecting the sample fluid, and optical waveguides were fabricated for detecting the fluorescence signal. A simpler microflow chamber based on a silicon micromachining process was reported by Hodder et al. [7]. In their design, one sample and two sheath flow channels were created with the use of anisotropic etching of a silicon wafer. A similar configuration of the three separated fluidic channels is shown in the upper portion of Figure 9.3. When the three fluidic channels were merged into one, hydrodynamic focusing in the lateral direction occurred. The channel height was 50 μm and the width of the channel ranged from 150 to 580 μm. For optical measurements, a glass cover was bonded with the etched silicon wafer by anodic bonding to complete a trapezoid-shaped channel. A similar focusing system made of a glass wafer was reported by Lee et al. [8].

Recently, other new MEMS materials, such as plastics or polymers instead of commonly used silicon and glass wafers, have been employed to fabricate microflow cytometers. Plastic and polymer materials have become a popular choice in bio-MEMS applications because the fabrication process is simple and the materials are transparent, biocompatible, low in cost, and disposable. However, some properties of polymers and plastics are inferior to those of glass and silicon. For example, they often emit fluorescence at a wavelength close to the signal from particular analytes. Thus, one needs to be careful in selecting a fluorochrome for use in a polymeric fluidic channel. In addition, they are less resistive to heat and chemicals than glass or silicon. In some applications, the polymer surface needs to be treated in order to prevent unwanted surface reactions with molecules in the flow. Additionally, their electrical breakdown voltage is often not high enough to allow for electrokinetically driven flows.

Conventional silicon micromachining procedures are used for the fabrication of the molds for soft lithography patterning of polymer-based microcytometers. Figure 9.3 shows a scanning electron micrograph (SEM) of the mold of an upstanding channel patterned on a silicon wafer [9]. One of the upper three branches is for the sample flow. while the other two are for the sheath flow. The middle and lower branches are for particle sorting. The microfluidic channel was made of an intaglio on a solidified poly dimethylsiloxane (PDMS) layer, which was formed from liquid phase PDMS poured on the mold. Lee et al. [10] used quartz to fabricate the template for imprinting patterns on a polymethylmethacrylate (PMMA) layer. Figure 9.4 shows a two-dimensional (2D) hydrodynamic focusing channel using this so-called hot embossing method. The sample and sheath flows can be injected into the three separate channels shown on the left of the image. The middle channel was for the sample flow, and the upper and lower channels were for the sheath flow. Similar 2D liquid sheath fluid systems for hydrodynamic focusing were developed by Tung et al. [11] and Kruger et al. [12].

Yang et al. [13] used a thick SU-8 negative photoresist to create a three-dimensional (3D) hydrodynamic focusing channel. They tilted the direction of exposure for cross-linking the resist so as to form the slanted focusing chamber shown in Figure 9.5a. A suspended hole and sidewalls for injecting sample and sheath fluid were formed in subsequent exposures, as shown in Figures 9.5 b and c. Note that the exposed portions of a negative photoresist were cross-linked and became hardened.

The aforementioned designs require a large amount of liquid sheath fluid, which is difficult to accommodate in a microcytometer. Huh et al. [14] replaced the liquid sheath medium with air to eliminate the large sheath liquid reservoirs, that is, 250 to 1000 mL for 1 mL biological samples. They

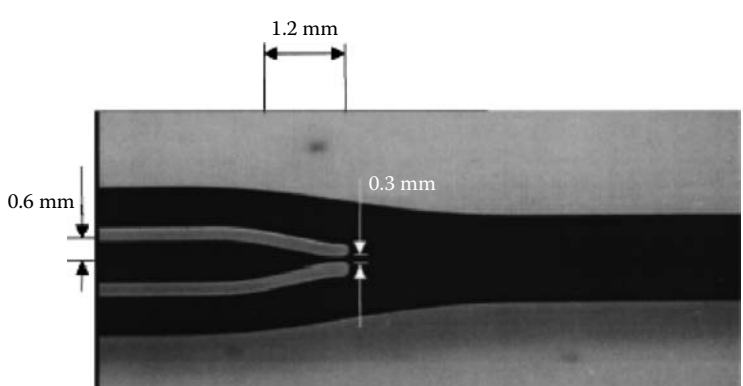

FIGURE 9.4
Photograph of a microfluidic focusing chamber fabricated by using the hot embossing method. The depth of the channel is around 40 μm. (From Lee, G.-B., Hung, C.-I., Ke, B.-J., Huang, G.-R., Hwei, B.-H., and Lai, H.-F., *ASME J. of Fluids Engineering*, 123, 672, 2001. Reprinted with permission from ASME.)

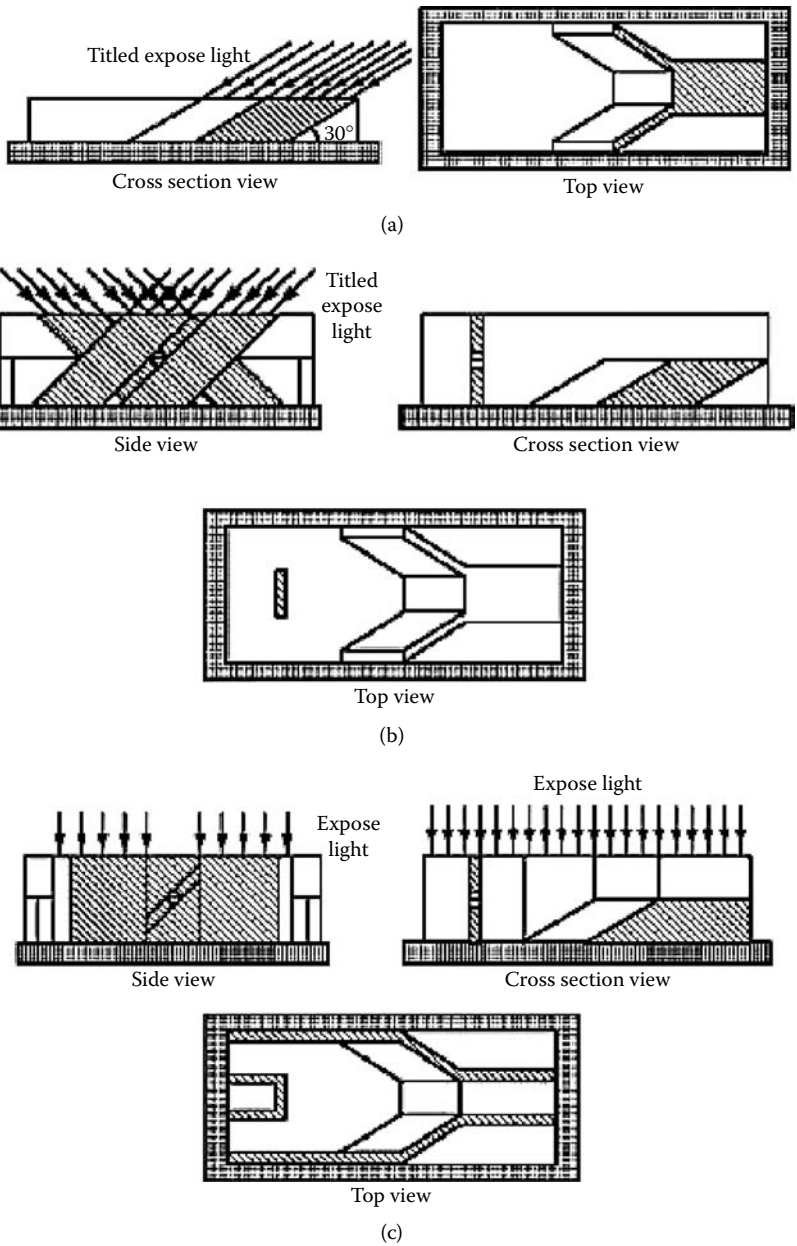

FIGURE 9.5
Fabrication process of a 3D hydrodynamic focusing channel made of SU-8 negative photoresist. (a) A slanted flow chamber was formed with the use of a 30° tilted exposure from the substrate. (b) A suspended injector nozzle at the center of the sample fluid channel was formed after subsequent exposure at a 45° tilted angle. (c) The sidewalls of the focusing chamber were finalized after a vertical exposure. (From Yang, R., Feeback, D. L., and Wang, W., *Sensors Actuators A*, 118, 259, 2005. Reprinted with permission from Elsevier.)

demonstrated that stable focusing could be achieved with the use of compressed air as a sheath fluid in a microfluidic channel.

A mechanical pump is often required in a hydrodynamic focusing system to deliver the high-speed sheath fluid. However, the miniaturization of the fluid pump has remained a challenging task. Alternative approaches to the pressure-driven sheath flow have been investigated. In one approach, electric manipulation of biological particles was employed by Schrum et al. [15]. In their work, electrokinetically driven sheath fluid was used to focus the sample flow, and the mechanical pump was replaced with a high voltage power supply. As shown in the photo images of Figure 9.6 (obtained using a time-integrated charge coupled device [CCD] camera), the sample fluid was focused laterally. The two sheath flow channels were perpendicular to the sample and waste flow channel in order to maximize the focusing capability near the junction. High voltages in the range of 10^2 to 10^3 V were used to drive the sheath fluid. The application of this approach is limited by the susceptibility of biological cells to the high electric field. Fu et al. [16] and Jacobson et al. [17] also reported the use of electrokinetic flows with similar designs.

9.2.1.2 Small Constriction

Except for Huh et al.'s work with an air sheath flow, the aforementioned microcytometer based on the hydrodynamic focusing approach required a

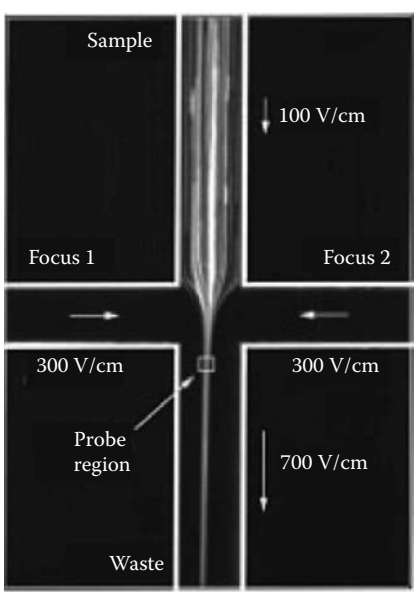

FIGURE 9.6
An electrokinetic focusing microfluidic channel. The sample fluid was focused by introducing the sheath fluids in a direction perpendicular to the sample flow. (From Schrum, D. P., Culbertson, C. T., Jacobson, S. C., and Ramsey, J. M., *Anal. Chem.*, 71, 4173, 1999. Reprinted with permission of the American Chemical Society.)

large sheath fluid reservoir, which needs to be kept free of dust and bacteria in addition to a complicated fluidic control system for ensuring proper rates of the fluid medium. To address these problems, microcytometers without the need of a sheath flow have been developed. One of the approaches was to use a small constriction to focus the sample flow. For example, Altendorf et al. [18] used a small V-groove constriction as the focusing channel without using a sheath flow. The V-groove channel was 15 μm deep and 20 to 25 μm wide, and was made by anisotropic etching of a silicon wafer. Gawad et al. [19] fabricated 40 μm–wide and 20 μm–deep rectangular-shaped channel that was used for impedance detection of the particles with high signal-to-noise ratio. The small channel sizes in these designs require careful sample preparation in order to prevent channel clogging.

9.2.1.3 Dielectrophoretic Focusing

Recently, dielectrophoresis focusing has been investigated to replace the hydrodynamic focusing mechanism or a small constriction design in order to eliminate the sheath flow and prevent channel clogging. In dielectrophoresis, a nonuniform AC electric field induces a dipole moment in a charge-neutral particle, causing the particle to move toward a region of maximum or minimum electric field strength [20]. A dielectrophoretic force $\vec{F}$, acting on a spherical particle of radius r, subjected to an AC electric field $\vec{E}$ of angular frequency ω, can be calculated as [21]

$$\vec{F} = 2\pi\varepsilon_m r^3 \,\mathrm{Re}[f(\varepsilon_p^*, \varepsilon_m^*)]\nabla \vec{E}_{rms}^2 \tag{9.1}$$

The subscripts m, p, and rms stand for medium, particle, and root-mean-square value, respectively. The term ε_i^* is the complex permittivity of the indexed material, which is defined as

$$\varepsilon_i^* = \varepsilon_i - j\sigma_i / \omega \tag{9.2}$$

where ε and σ are the permittivity and electrical conductivity, and $j = \sqrt{-1}$.

For a spherical homogeneous particle with ohmic loss, the expression $f(\varepsilon_p^*, \varepsilon_m^*)$, referred as the Clausius–Mossotti factor, is defined as

$$f(\varepsilon_p^*, \varepsilon_m^*) = \frac{\varepsilon_p^* - \varepsilon_m^*}{\varepsilon_p^* + 2\varepsilon_m^*} = \frac{\varepsilon_p - \varepsilon_m - j(\sigma_p - \sigma_m)/\omega}{\varepsilon_p + 2\varepsilon_m - j(\sigma_p + 2\sigma_m)/\omega} \tag{9.3}$$

At frequencies well above and below $\tau_{MW}^{-1} = (\sigma_p + 2\sigma_m)/(\varepsilon_p + \varepsilon_m)$, the real component of the Clausius–Mossotti factor becomes independent of the frequency of the electric field [22], that is,

$$\mathrm{Re}[f(\varepsilon_p^*, \varepsilon_m^*)] \rightarrow \begin{cases} \dfrac{\sigma_p - \sigma_m}{\sigma_p + 2\sigma_m}, & \text{for } \omega\tau_{MW} << 1 \\ \dfrac{\varepsilon_p - \varepsilon_m}{\varepsilon_p + 2\varepsilon_m}, & \text{for } \omega\tau_{MW} >> 1 \end{cases} \tag{9.4}$$

On the other hand, the Clausius–Mossotti factor for a heterogeneous particle, such as a biological cell, deviates from Equation 9.3 due to the different polarizability of the particle. For instance, eukaryotic cells, which contain a nucleus and other organelles suspended in a semifluid medium called the cytosol, are enclosed by outer membranes. Those layered spherical particles can be modeled using an effective complex permittivity. For the particle that has a single outer shell of thickness d, the complex permittivity of the particle in Equation 9.3 can be substituted by the effective complex permittivity described as [22]

$$\varepsilon_{p,eff}^* = \varepsilon_s^* \left[\frac{\left(\dfrac{r}{r-d}\right)^3 + 2\left(\dfrac{\varepsilon_{\text{int}}^* - \varepsilon_s^*}{\varepsilon_{\text{int}}^* + 2\varepsilon_s^*}\right)}{\left(\dfrac{r}{r-d}\right)^3 - \left(\dfrac{\varepsilon_{\text{int}}^* - \varepsilon_s^*}{\varepsilon_{\text{int}}^* + 2\varepsilon_s^*}\right)} \right] \tag{9.5}$$

where ε_s^* and $\varepsilon_{\text{int}}^*$ are the complex permittivity of the shell and that of the cell interior, respectively. In the case of $d << r$, which holds for most of the cells without a cell wall, such as mammalian cells, ε_s^* in Equation 9.5 can be calculated as

$$\varepsilon_s^* = C_s^* d = \left(C_s - \frac{jG_s}{\omega}\right) d \tag{9.6}$$

where C_s^*, C_s, and G_s are the complex specific capacitance, specific capacitance, and specific conductance of the shell, respectively.

As shown in Equation 9.1, the dielectrophoretic force depends on the properties of the particle and the medium as well as the amplitude of the applied electric field. The force is attractive or repulsive depending on the sign of the real component of the Clausius–Mossotti factor, which is a function of the frequency of the electric field as well as the dielectric properties of the particle and the suspending medium. Figure 9.7 shows the dielectrophoretic force acting on particles in a nonuniform electric field in a 2D space. When particles are attracted to or repelled from regions of high electric field strength, the phenomenon is respectively called positive or negative dielectrophoresis.

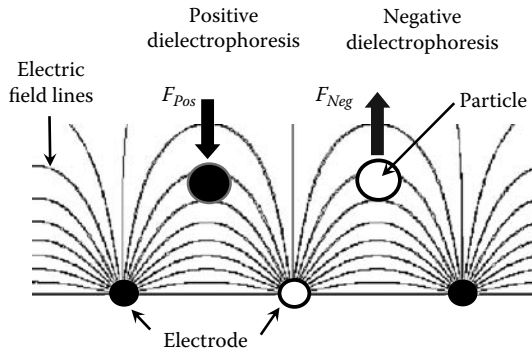

FIGURE 9.7
A schematic diagram showing the positive and negative dielectrophoretic forces exerted on particles in a nonuniform electric field. (From Yu, C., Vykoukal, J., Vykoukal, D., Schwartz, J., Shi, L., and Gascoyne, P.R.C., *J. Microelectromech. Syst.* 14, 480, 2005. Reprinted with permission from IEEE.)

At the so-called crossover frequency, $\mathrm{Re}[f(\varepsilon_p^*, \varepsilon_m^*)]$ is 0, thereby the dielectrophoretic force acting on the particle is zero. At frequencies above the crossover frequency, $\mathrm{Re}[f(\varepsilon_p^*, \varepsilon_m^*)]$ is often positive for mammalian cells with a maximum value of 1, whereas at frequencies below the crossover frequency, $\mathrm{Re}[f(\varepsilon_p^*, \varepsilon_m^*)]$ has a minimum value of 0.5. The dielectric properties of the particle are affected by several factors including the particle type, membrane structure, internal organization, and in the case of cells, viability.

To estimate the frequency range for negative and positive dielectrophoresis, one can calculate the Clausius–Mossotti factors as a function of the frequency of the applied voltage. For example, the factor for a homogeneous particle like latex beads can be calculated by using Equation 9.3. The permittivities of the bead and the medium used in the calculation were $2.5\varepsilon_0$ and $80\varepsilon_0$, where ε_0 is the permittivity of free space. The conductivity of the latex beads can be calculated as $\sigma_p = \sigma_{p,bulk} + 2K_s / r$, where $\sigma_{p,bulk}$ and K_s are the bulk conductivity and surface conductance of the latex bead. The bulk conductivity is approximately zero and the typical value of the K_s is on the order of 1 nS [23,24]. The Clausius–Mossotti factor is negative regardless of the frequency, as shown in case a in Figure 9.8, unless the medium conductivity is much lower than the typical value used for a flow cytometer, as shown in case c in Figure 9.8.

For heterogeneous particles such as biological cells, the single-shell model with effective permittivity, that is, Equations 9.5 and 9.6, is often used. Although some of the cells have multiple shells and complex organelles, the single-shell model is frequently used with averaged dielectric properties of the shell and the cell interior due to difficulties in finding the property of each element in a single cell. Figure 9.9 shows the Clausius–Mossotti factor as a function of the frequency of the applied voltage for different dielectric properties of a biological cell. The dielectric properties of the membrane of HL-60 leukemia cells [25] and the typical dielectric properties of the interior of a blood cell [26] were used for the calculation of case a in Figure 9.9. Within the typical

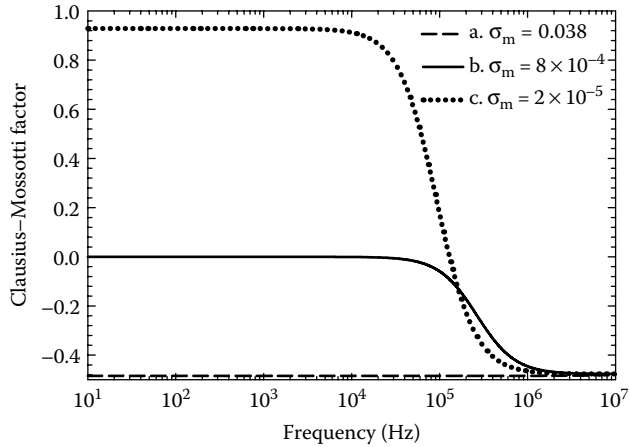

FIGURE 9.8
The Clausius–Mossotti factor for a 10 μm–diameter latex bead as a function of the frequency of the applied voltage for the different dielectric properties of the medium and the bead. The permittivity and conductivity of the bead are $2.5\varepsilon_0$ and 8×10^4 S/m, ε_0 is the permittivity of free space. The unit of σ_m is S/m. (From Yu, C., Vykoukal, J., Vykoukal, D., Schwartz, J., Shi, L., and Gascoyne, P.R.C., *J. Microelectromech. Syst.* 14, 480, 2005. Reprinted with permission from IEEE.)

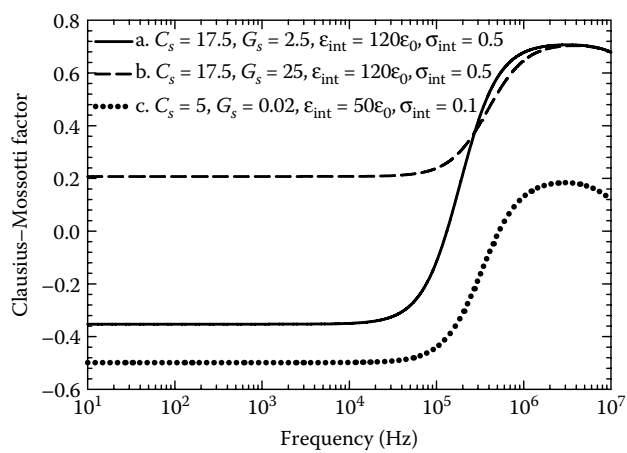

FIGURE 9.9
The Clausius–Mossotti factor as a function of the frequency of the applied voltage for different dielectric properties of a 10 μm–diameter biological cell. ε_{int} and σ_{int} are the permittivity and the electrical conductivity of the cell interior. The units of C_s, G_s, and σ_{int} are mF/m², kS/m², and S/m, respectively. The thickness of the membrane is 5 nm. The permittivity and conductivity of the medium are $80\varepsilon_0$ and 0.056 S/m, respectively. (From Yu, C., Vykoukal, J., Vykoukal, D., Schwartz, J., Shi, L., and Gascoyne, P.R.C., *J. Microelectromech. Syst.* 14, 480, 2005. Reprinted with permission from IEEE.)

range of the dielectric properties of biological cells [27], negative dielectrophoresis is expected at frequencies below about 100 kHz. At high frequencies above 100 kHz, the dielectrophoretic force is determined by the frequency-

dependent complex permittivities, and thus strongly depends on the frequency. At low frequencies, on the other hand, the conductivities dominate the Clausius–Mossotti factor. In a living cell, the conductivity of the plasma membrane is several orders of magnitude smaller than that of the cell interior [28]. Depending on the conductivity of the medium and that of the cell interior, either positive or negative dielectrophoresis is achieved. For instance, when the medium conductivity is on the same order of or one order of magnitude smaller than that of the cell interior, the large difference between the conductivity of the membrane and that of the suspending medium can result in the maximum negative value of the Clausius–Mossotti factor. In other words, a large negative force weakly depending on the frequency can be expected at frequencies below 100 kHz, unless the membrane conductance is assumed to be much higher than the range of 20 to 2000 S/m^2 of a typical biological cell [27], as in case b of Figure 9.9. Note that a very low frequency close to DC needs to be avoided in order to prevent hydrolysis of the medium.

As discussed later in this chapter, negative dielectrophoresis has been employed in microflow cytometers. In order to optimize dielectrophoretic focusing regardless of the particle type and structure, one needs to operate the microcytometer in a regime where the repulsive dielectrophoretic force is maximized. This can be achieved by using a frequency well below the crossover value and a voltage below the threshold for which cell damaging by the electric field occurs.

Cui et al. [29] developed a cytometer based on traveling wave dielectrophoresis (twDEP) that moves particles to the optical detection region by applying an AC electric field generated from an array of electrodes. A small channel size is needed in this design because of the lack of a focusing mechanism. Additionally, the traveling speed of particles, approximately 13 μm/s, is lower than the speed of up to a few m/s in a conventional cytometer.

Fiedler et al. [30] and Morgan et al. [31] used a pair of funnel-shaped microelectrodes, which are marked as E in Figure 9.10, patterned on the top and bottom of a fluidic channel for focusing micron- and nanometer-size particles via negative dielectrophoresis. Cheung et al. [32] reported a similar design to focus particles for impedance spectroscopy. In these designs, an AC electric field was applied between the two identical funnel-shaped electrodes, one patterned on the top and the other on the bottom of the channel. The particles were repelled by the electric field away from the electrodes and focused gradually toward the center of the channel. The focusing was achieved using negative DEP force without the need of a sheath fluid or a narrow channel width. Nevertheless, the channel heights of these designs need to be as small as 30 μm to obtain a large electric field gradient, and thus a sufficiently large focusing force at an applied voltage below the threshold for cell damage.

Similar small channel heights have also been used in 2D hydrodynamic focusing channels. Figure 9.11 shows a cross-sectional area of such a channel formed by fusion bonding of two etched glass wafers [33]. Note that the channel height was only a few times larger than the typical size of a cell in order to ensure vertical focusing. However, channel clogging can be

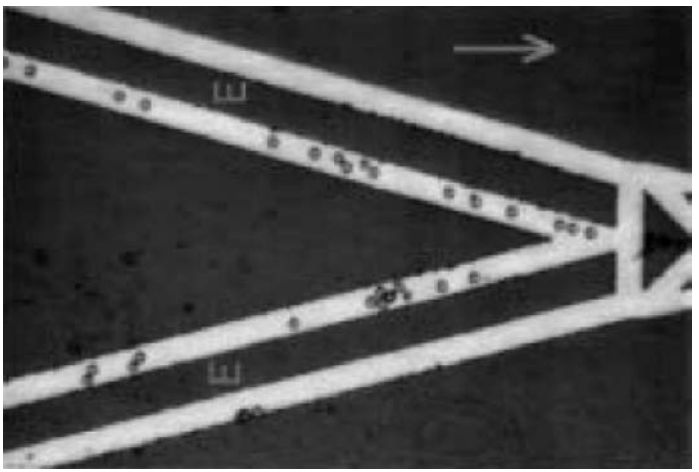

FIGURE 9.10
Photograph of a pair of funnel-shaped electrodes patterned on the bottom of a microchannel. The dark areas marked as E are electrodes and the flow direction is indicated by the arrow. The width of the exit gap of the particles is 35 μm and the channel height is 30 μm. (From Fiedler, S., Shirley, S. G., Schnelle, T., and Fuhr, G., *Anal. Chem.*, 70, 1909, 1998. Reprinted with permission of the American Chemical Society.)

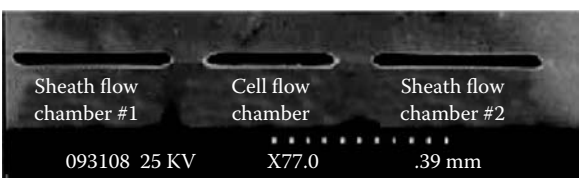

FIGURE 9.11
Cross-section view of a typical micromachined flow cytometer. (From Lin, C.-H., and Lee, G.-B., *J. Micromech. Microeng.* 13, 447, 2003. Reprinted with permission from IOP Pupl.)

problematic for the small channel height in either the hydrodynamic focusing or DEP focusing channels.

There have been a few attempts to develop 3D focusing channels employing dielectrophoresis. Lin et al. [34] combined hydrodynamic focusing and dielectrophoretic focusing to focus particles in both the lateral and vertical directions. They fabricated electrodes on the top and bottom walls at the downstream part of the hydrodynamic focusing channel. The particles were focused in the lateral direction using the hydrodynamic focusing mechanism and in the vertical direction using negative dielectrophoresis.

Yu et al. [35] explored the use of dielectrophoresis to obtain 3D focusing without the use of hydrodynamic focusing. They designed a ring-shaped microelectrode array to focus biological particles using negative dielectrophoresis, as shown in Figure 9.12. Particles are directed toward the center of the microchannel from all directions by negative dielectrophoretic force generated by the fringing field from the ring-shaped microelectrodes patterned

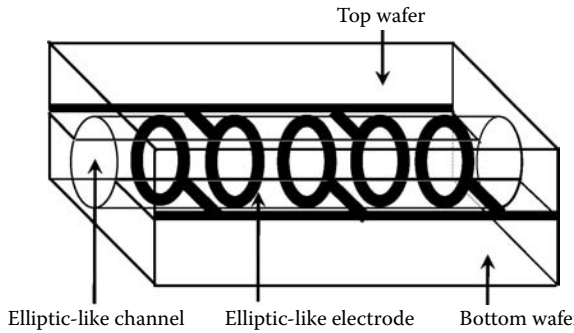

FIGURE 9.12
A schematic diagram of a microfluidic channel with an array of interdigitated ring-shaped microelectrodes patterned on the circumference of the channel for dielectrophoretic particle focusing. (From Yu, C., Vykoukal, J., Vykoukal, D., Schwartz, J., Shi, L., and Gascoyne, P.R.C., *J. Microelectromech. Syst.* 14, 480, 2005. Reprinted with permission from IEEE.)

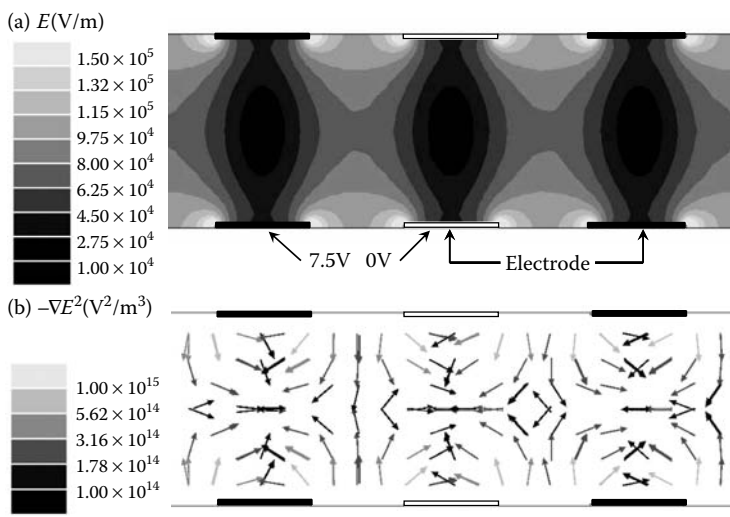

FIGURE 9.13
(a) Calculation results of the magnitude of the electric field (E) in a cross-section of the 100 μm–diameter channel when a DC voltage of 7.5 V is applied to the black electrodes and the white electrodes are grounded. The permittivity and conductivity of the fluid in the channel are 80 ε_0 and 0.056 S/m. The field strength is represented by the gray-scale bar. (b) The calculation results of the $-\nabla E^2$ vector field. The vector points toward the center of the channel. The magnitude of $-\nabla E^2$ is represented by the gray-scale bar. (From Yu, C., Vykoukal, J., Vykoukal, D., Schwartz, J., Shi, L., and Gascoyne, P.R.C., *J. Microelectromech. Syst.* 14, 480, 2005. Reprinted with permission from IEEE.)

on the circumference of an elliptic-like channel. In this configuration, the electric field strength gradually changes in the radial direction of the channel with the region of the minimum field gradient located at the center of the channel. Figure 9.13a shows the magnitude of the electric field (E) in a cross-section along the longitudinal direction of the 100 μm–diameter channel when

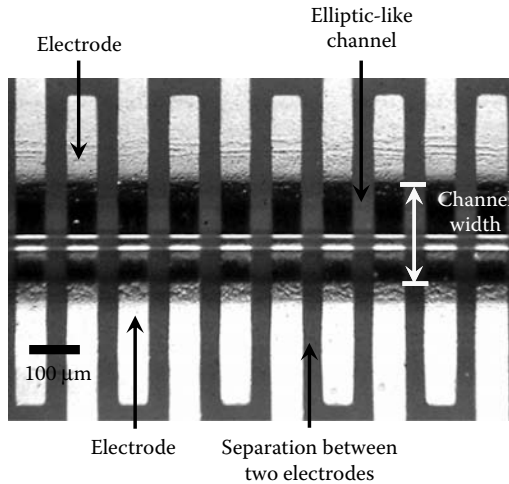

FIGURE 9.14
A photograph of the elliptic-like channel with the Au/Cr electrode array. (From Yu, C., Vykoukal, J., Vykoukal, D., Schwartz, J., Shi, L., and Gascoyne, P.R.C., *J. Microelectromech. Syst.* 14, 480, 2005. Reprinted with permission from IEEE.)

a DC voltage of 7.5 V is applied to one of the two sets of the interdigitated ring-shaped electrodes and the adjacent set is grounded. Figure 9.13b shows the $-\nabla E^2$ vector field. Because the dielectrophoretic force is proportional to the product of the Clausius–Mossotti factor and ∇E^2 as described in Equation 9.1, the force is parallel to the direction of the $-\nabla E^2$ vector field when the real part of the Clausius–Mossotti factor is negative. The minima of the magnitude of the electric field were found to be at the center of the channel, where particles were focused by negative dielectrophoresis. Figure 9.14 shows a photograph of the bottom half of the dielectrophoretic focusing channel etched into a glass wafer. Two of these etched glass wafers were thermally bonded together to create the elliptic-like channel shown in Figure 9.12. An AC voltage is applied between adjacent electrode rings on the channel wall. This design allows a large channel diameter of about 100 μm to prevent clogging.

The width of the focusing stream was measured when the amplitude of the applied voltage was varied from 0 to 20 V at three different frequencies, 10, 30, and 100 kHz. The results were shown for polystyrene beads and human leukemia cells in Figure 9.15. Although the width of the particle streams at the three different frequencies varies in the low voltage range, it steadily decreases with the applied voltages at any specific frequency. At 15 $V_{p\text{-}p}$, the cells were focused within 10 to 15 μm, sufficiently small for cytometry applications. On the other hand, at voltages below 5 V, the dielectrophoretic force was too weak to hold the particles at the center of the channel because the dielectrophoretic force falls exponentially with the distance from the edges of the electrodes [36].

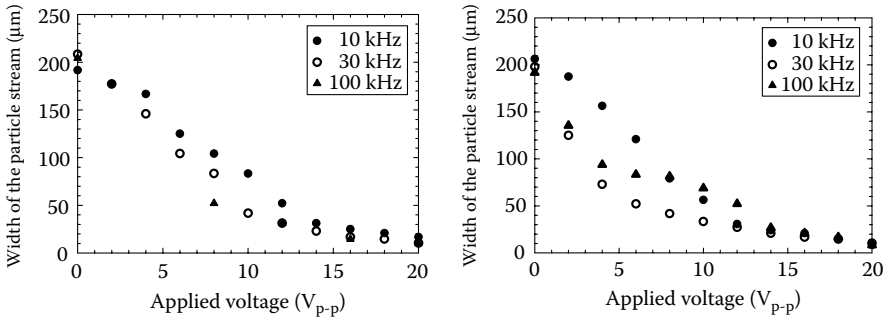

FIGURE 9.15
The width of a flow stream of microbeads (left) and human leukemia cells (right) as a function of the applied voltage at different frequencies. (From Yu, C., Vykoukal, J., Vykoukal, D., Schwartz, J., Shi, L., and Gascoyne, P.R.C., *J. Microelectromech. Syst.* 14, 480, 2005. Reprinted with permission from IEEE.)

To verify that the particle was indeed focused by a negative dielectrophoretic force, they varied the frequency of the applied AC voltage and observed that the latex beads could not be focused when the frequency was 200 Hz at a medium conductivity of 2×10^{-5} S/m. This observation agrees with their calculation results shown in case c of Figure 9.8 that the dielectrophoretic force is positive at this frequency and cannot be used to focus the latex beads. Additionally, they found that the leukemia cells cannot be focused at a frequency much higher than 100 kHz, indicating that the Clausius–Mossotti factor becomes positive or close to zero at high frequencies, in agreement with case a of Figure 9.9. The frequency dependence would suggest that the focusing observed for the beads and cells at the frequency window of 10 to 100 kHz was not due to other effects such as Joule heating of the medium. In addition, the temperature rise due to Joule heating could be estimated as $\Delta T \approx \sigma V_{rms}^2 / k$ [37], where σ and k are the electrical conductivity and the thermal conductivity of the medium, respectively. For $\sigma = 0.038$ S/m, $V_{rms} = 5.3$ V, $k = 0.6$ J m^{-1}s^{-1}K^{-1}, the temperature rise is on the order of 2°C. This small temperature rise was not sufficient to focus particles via thermally induced fluid flow.

At a voltage of 15 V_{p-p}, they did not observe signatures indicating cell damage. According to the investigation by Forster et al. [38] and Muller et al. [39] on the effect of an electric field on cell viability, yeast cells were not damaged by exposure in an electric field of up to approximately 7×10^5 V/m. At an applied voltage of 15 V_{pp}, the maximum voltage difference between the two adjacent electrodes in the focusing channel is 7.5 V. As shown in Figure 9.13a, the field strength is below 7×10^5 V/m at most part of the channel when a voltage of 7.5 V is applied. Thus, the field strength is expected to be below the threshold for damaging the cell. Additionally, Wang et al. [40] found that an accumulation of electrochemically generated peroxide in the suspending medium by an electric field could account for cell damage,

but can be eliminated by the addition of catalase to the suspending medium. In the fluidic device of Yu et al. [35], the medium is continually refreshed and thereby the peroxide accumulation would be negligible. In the focusing channel, furthermore, the cells were moved away from the high field region very quickly into the center with the minimum field strength. Hence, cells can be focused at a voltage of about 15 $V_{p\text{-}p}$ without being damaged.

9.2.2 Detection Systems

Microorganisms can be detected with the use of a variety of methods including optical, electrochemical, impedance, piezoelectric, and acoustic methods [41]. Schwarz et al. [42] have reviewed spectroscopic and electrochemical detection methods in microsystems, including fluorescence, absorbance, chemiluminescence, amperometry, and conductometry. Depending on the application, different methods have their own advantages.

9.2.2.1 Optical Detection

The common detection method for flow cytometry is optical detection of light scattering and fluorescence. In the fluorescence detection approach, different cells are selectively stained with different fluorescent dyes. The excitation must be narrowly focused on the particle stream in order to increase the signal-to-noise ratio. Because the fluorescence intensity is often several orders of magnitude smaller than the excitation intensity, one or more dichroic and band-pass filters are used to reduce the scattered and excitation lights that reach the detector. To increase the signal-to-noise ratio further, the fluorescent light needs to be focused into the detection zone of a photodetector, which needs to be highly sensitive. A PMT is often used as the detector due to its high sensitivity. Ideally, all optical components, including light sources, filters, lenses, and photodetectors, should be self-aligned and integrated on-chip with the microflow focusing channel.

These stringent requirements make it difficult to miniaturize the optical detection system and integrate it with microflow focusing channel. To date, the miniaturization and integration of the complex optical systems is one of the key challenges for developing microflow cytometers, as well as other lab-on-a-chip devices or micro total analysis systems.

Despite these challenges, an optical detection scheme has been used in several microcytometer designs because the optical properties of biological particles are well established for cytometry applications. Ideally, with the optical components integrated directly with the microflow focusing channel, the optical component does not need frequent alignment and maintenance. In several efforts toward achieving this goal, off-the-shelf optical components were assembled with microfluidic focusing channels [15,18,29,43]. On the other hand, there have also been intense efforts toward the miniaturization and on-chip integration of these components. For example, small laser diodes

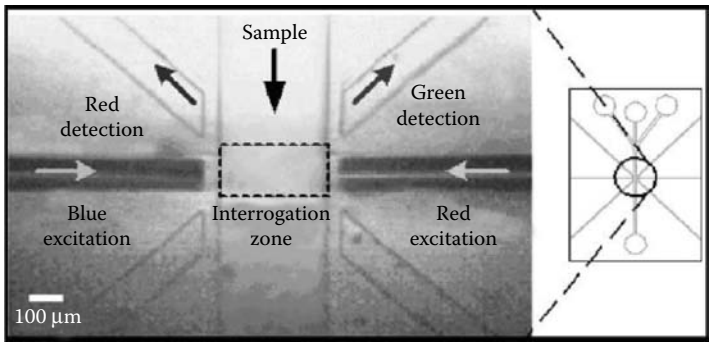

FIGURE 9.16
A microfluidic channel with multiple embedded optical fibers for two-color excitation and detection. (From Tung, Y.-C., Zhang, M., Lin, C.-T., Kurabayashi, K., and Skerlos, S. J., *Sensors Actuators B*, 98, 356, 2004. Reprinted with permission of Elsevier.)

or light emitting diodes (LEDs) were mounted or fabricated on the microfluidic channel to serve as the excitation source in the experiments by Tung et al. [11], Kruger et al. [12], Cui et al. [29], and Chabinyc et al. [44]. For transmitting the excitation or fluorescence signals, optical fibers were embedded near the microfluidic channel. Alternatively, optical wave guides incorporated with optical fibers were also used to achieve this goal. [8,16,33,34,44–46]. For optical waveguides, spin-on-glass (SOG)/SU-8 photoresist [8] or silicon nitride/silicon oxide [6,47] can be used. Additionally, Grosse et al. [48] fabricated optical leaky wave guides on a glass wafer, and Camou et al. [49] fabricated PDMS 2D optical lenses near microfluidic channels in order to improve the the signal-to-noise ratio of fluorescence spectroscopy. Figure 9.16 shows an integrated optical detection system developed by Tung et al. [11] In this system, optical fibers were inserted into prefabricated grooves close to the optical detection region. They demonstrated the feasibility of two-color excitation and detection in a single interrogation zone.

In addition to the miniaturization of the light source, the PMT that was often used in a large-scale cytometer was replaced with a miniaturized and inexpensive PIN photodiode or APD in a few microcytometer developments. Tung et al. [11] used a lock-in detection method to improve the signal-to-noise ratio of the PIN detector. To achieve high sensitivity, Kruger et al. [12] and Chabinyc et al. [44] integrated APD with microfluidic devices with optical filter coatings or a colored polycarbonate filter.

9.2.2.2 Impedance Detection

Cell properties can also be analyzed with the use of an impedance detection system integrated with a microflow cytometer. The impedance detection scheme is based on the Coulter counter principle [50]. In this approach, the impedance of a medium is monitored when a particle stream flows through the detection zone. The recorded impedance signal is used for cell counting

and size measurements. This technique is much less complicated than the optical detection method because it does not require cell modification, such as tagging fluorescence markers or antibodies. It is also much easier to miniaturize the impedance detection mechanism than the optical detection method. However, impedance detection is generally slow and the density of cells needs to be low.

Ayliffe et al. [51] were able to distinguish different cell types using an electric impedance measurement technique in a microfluidic device. In their experiment, cells were flowed through a 10 μm–wide and 4 μm–high channel with protruding electrodes on the two sidewalls of the channel filled with electrically conducting liquid. In this electrode configuration, a change of the electrical resistance in the liquid-filled capillary can be detected as a particle passes through the channel. Gawad et al. [19] used an array of electrodes patterned on the bottom of the channel to perform impedance spectroscopy. They demonstrated that their microcytometer could be used to distinguish erythrocytes from ghost cells. Cheung et al. [32] patterned electrodes on the top and bottom of the channel for sizing the biological particles with the use of impedance spectroscopy as shown in Figure 9.17. In these two latter designs, the impedance values measured by two sets of electrodes were compared. When one cell is between one pair of electrodes with no intervening cell between the other pair of electrodes, the difference in the impedance of the suspending fluid can be detected. In order to ensure only one cell passing through the detection region at a time, the density of the cell needs to be low.

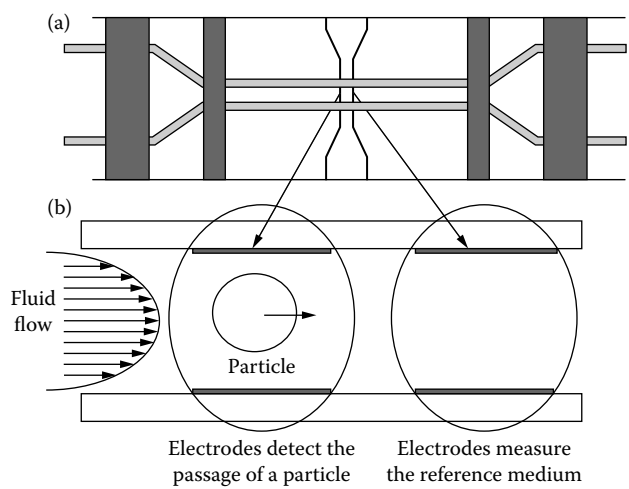

FIGURE 9.17
Top (a) and side (b) views of the measurement channel of the microfabricated impedance spectroscopy. The impedance of two pairs of electrodes are compared when a particle passes through one of the interrogation regions as shown in (b). (From Cheung, K., Gawad, S., and Renaud, P., in *Proc. IEEE Microelectromechanical Systems (MEMS)*, 2004, 343. Reprinted with permission from IEEE.)

9.2.3 Sorting and Counting

A particle sorter or counter can be added to the focusing and detection channel of the microflow cytometer. Fiedler et al. [30] used dielectrophoresis to sort biological particles, while Fu et al. [52,53] fabricated fluorescence-activated cell sorter. Alternatively, a similar concept of the conventional cell sorter shown in Figure 9.1 can be exploited in microcytometers. For example, additional fluidic channels can be fabricated at the downstream of the particle focusing channel to replace the deflection plates of a conventional large-scale cytometer. As demonstrated by Dittrich et al. [9] in Figure 9.18, the horizontal fluidic channels were used to deflect the particle stream. The end of the main flow channel can be separated into two or more paths for collecting different types of particles. The flow was driven by using a mechanical pump [12] or by using an electrokinetic flow [9,16]. The switching speed of an electrokinetic flow is usually faster than that of a pressure-driven flow, although a high voltage is required for the operation. Some other sorters can potentially be integrated with a microflow cytometer. Carlson et al. [54] have reported a different blood cell sorter made of a lattice of channels. Cells can also be sorted and trapped within a cage created by negative dielectrophoresis from an electric field generated by electroplated metal posts [55].

On the other hand, particles can also be counted with the use of an optical or impedance detection method. For example, Altendorf et al. [18] used an external optical system to count different blood cells by measuring the intensity of small- and large-angle scattering. In a different work, two parallel optical fibers for excitation and detection were embedded close to the fluidic channel. The scattered light was monitored as the particles flowed across the optical path [16].

Cell counting has been realized with the use of a Coulter counter by recording the peaks in the recorded impedance signal. In a Coulter counter,

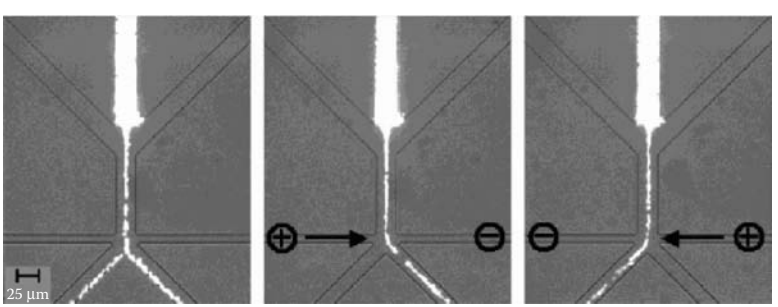

FIGURE 9.18
Photograph of an electrokinetic sorting device showing particle streams before the switching fluid was injected (the left panel), after the switching fluid was injected from the left (the middle panel), and from the right (the right panel) to the main stream. (From Dittrich P. S. and Schwille, P., *Anal. Chem.*, 75, 5767, 2003. Reprinted with permission of the American Chemical Society.)

the signal depends on the particle size and dielectric properties, and the signal-to-noise ratio increases as the channel size decreases. In order to maximize the impedance signal, Koch et al. [56] reduced the size of the detection channel and used a particle filter in front of the channel in order to avoid sample clogging. A detailed description of the resistive-pulse sensing method can be found in Bayley et al. [57].

9.3 Summary

This chapter discusses the miniaturization of flow cytometers for analyzing biological particles. Many attempts have been made to miniaturize the conventional hydrodynamic focusing method and also to utilize dielectrophoretic focusing for use in a microflow cytometer. Three-dimensional focusing has been achieved by using a 3D design of a hydrodynamic focusing microchannel fabricated using a soft photolithography–based process, by combining hydrodynamic focusing with dielectrophoresis focusing, and by using a dielectrophoretic focusing channel with an array of ring-shaped electrodes patterned on the elliptic channel wall.

One of the major challenges to the fabrication of a microcytometer is the miniaturization and on-chip integration of the optical detection system. There have been attempts to replace bulky and complex light sources and optical components with miniaturized LEDs, integrated waveguides and optical fibers, and compact PINs or APDs. The success of this approach critically depends on the future advancement of optical MEMS research. Meanwhile, micro cell sorters and counters based on the Coulter counter principle have been demonstrated and used successfully in microflow cytometers.

Although many of the microcytometer designs bear similarity to conventional large-scale systems, new approaches such as dielectrophoresis have received increasing attention. The further development in the research described in this chapter can potentially lead to highly effective, portable, and low-cost microcytometers, which can be used as a stand-alone device as well as a module in a micro total analysis system.

References

[1] Shapiro, H.M., *Practical Flow Cytometry*, Wiley, New York, 1995.
[2] Melamed, M.R., Lindmo, T., and Mendelsohn, M.L., *Flow Cytometry and Sorting*, Wiley, New York, 1991.
[3] Watson, J.V., *Introduction to Flow Cytometry*, Cambridge University Press, Cambridge, U.K., 1991.

[4] Ormerod, M.G., *Flow Cytometry*, Oxford University Press, New York, 2000.
[5] Miyake, R., Ohki, H., Yamazaki, I., and Yabe, R., A development of micro sheath flow chamber, in *Proc. IEEE Microelectromechanical Systems (MEMS)*, 1991, 265.
[6] Sobek, D., Young, A.M., Gray, M.L., and Senturia, S.D., A microfabricated flow chamber for optical measurements in fluids, in *Proc. IEEE*, 2, 1993, 219.
[7] Hodder, P.S., Blankenstein, G., and Ruzicka, J., Microfabricated flow chamber for fluorescence-based chemistries and stopped-flow injection cytometry, *Analyst*, 122, 883, 1997.
[8] Lee, G.-B., Lin, C.-H., and Chang, G.-L., Micro flow cytometers with buried SU-8/SOG optical waveguides, *Sensors Actuators A,* 104, 165, 2003.
[9] Dittrich P.S. and Schwille, P., An integrated microfluidic system for reaction, high-sensitivity detection, and sorting of fluorescent cells and particles, *Anal. Chem.*, 75, 5767, 2003.
[10] Lee, G.-B., Hung, C.-I., Ke, B.-J., Huang, G.-R., Hwei, B.-H., and Lai, H.-F., Hydrodynamic focusing for a micromachined flow cytometer, *ASME J. of Fluids Engineering*, 123, 672, 2001.
[11] Tung, Y.-C., Zhang, M., Lin, C.-T., Kurabayashi, K., and Skerlos, S.J., PDMS-based opto-fluidic micro flow cytometer with two-color, multi-angle fluorescence detection capability using PIN photodiodes, *Sensors Actuators B,* 98, 356, 2004.
[12] Kruger, J., Singh, K., O'Neill, A., Jackson, C., Morrison, A., and O'Brien, P., Development of a microfluidic device for fluorescence activated cell sorting, *J. of Micromechanics and Microengineering,* 12, 486, 2002.
[13] Yang, R., Feeback, D.L., and Wang, W., Microfabrication and test of a three-dimensional polymer hydro-focusing unit for flow cytometry applications, *Sensors Actuators A*, 118, 259, 2005.
[14] Huh, D., Tung, Y.-C., Wei, H.-H., Growtherg, J.B., Skerlos, S.J., Kurabayashi, K., and Takayama, S., Use of air-liquid two-phase flow in hydrophobic microfluidic channels for disposable flow cytometers, *Biomedical Microdevices*, 4, 141, 2002.
[15] Schrum, D.P., Culbertson, C.T., Jacobson, S.C., and Ramsey, J.M., Microchip flow cytometry using electrokinetic focusing, *Anal. Chem.*, 71, 4173, 1999.
[16] Fu, L.-M., Yang, R.-J., Lin, C.-H., Pan, Y.-J., and Lee, G.-B., Electrokinetically driven micro flow cytometers with integrated fiber optics for on-line cell/particle detection, *Analytica Chimica Acta*, 507, 163, 2004.
[17] Jacobson S.C. and Ramsey J.M., Electrokinetic focusing in microfabricated channel structures, *Anal. Chem.*, 69, 3212, 1997.
[18] Altendorf, E., Zebert, D., Holl, M., and Yager, P., Differential blood cell counts obtained using a microchannel based flow cytometer, in *Proc. IEEE Int. Conf. on Solid-State Sensors and Actuators*, Chicago, IL, 1997, 531.
[19] Gawad, S., Schildb, L., and Renauda, Ph., Micromachined impedance spectroscopy flow cytometer for cell analysis and particle sizing, *Lab on a Chip*, 1, 76, 2001.
[20] Pohl, H.A., *Dielectrophoresis*, Cambridge University Press, London, U.K., 1978, chap. 1.
[21] Wang, X.-B., Huang, Y., Becker, F.F., and Gascoyne, P.R.C., A unified theory of dielectrophoresis and traveling wave dielectrophoresis, *J. Phys. D: Appl. Phys.*, 27, 1571, 1994.
[22] Jones, T.B., *Electromechanics of Particles*, Cambridge University Press, New York, 1995, chaps. 2 and 3.

[23] Arnold, W.M., Schwan, H.P., and Zimmermann, U., Surface conductance and other properties of latex particles measured by electrorotation, *J. Phys. Chem.*, 91, 5093, 1987.

[24] Morgan, H., Hughes, M.P., and Green, N.G., Separation of submicron bioparticles by dielectrophoresis, *Biophys. J.*, 77, 516, 1999.

[25] Wang, X., Becker, F.F., and Gascoyne, P.R.C., Membrane dielectric changes indicate induced apoptosis in HL-60 cells more sensitively than surface phosphatidylserine expression or DNA fragmentation, *Biochim. Biophys. Acta*, 1564, 412, 2002.

[26] Yang, J., Huang, Y., Wang, X., Wang, X.-B., Becker, F.F., and Gascoyne, P.R.C., Dielectric properties of human Leukocyte subpopulations determined by electrorotation as a cell separation criterion, *Biophys. J.*, 76, 3307, 1999.

[27] Gascoyne, P.R.C., Becker, F.F., and Wang, X.-B., Numerical analysis of the influence of experimental conditions on the accuracy of dielectric parameters derived from electrorotation measurements, *Bioelectrochem. Bioenerg.*, 36, 115, 1995.

[28] Gascoyne, P.R.C., Wang, X.-B., Huang, Y., and Becker, F.F., Dielectrophoretic separation of cancer cells from blood, *IEEE Trans. Ind. Appl.*, 33, 670, 1997.

[29] Cui, L., Zhang, T., and Morgan, H., Optical particle detection integrated in a dielectrophoretic lab-on-a-chip, *J. Micromech. Microeng.*, 12 ,7, 2002.

[30] Fiedler, S., Shirley, S.G., Schnelle, T., and Fuhr, G., Dielectrophoretic sorting of particles and cells in a microsystem, *Anal. Chem.*, 70, 1909, 1998.

[31] Morgan, H., Holmes D., and Green, N.G., 3D focusing of nanoparticles in microfluidic channels, in *Proc. IEE Nanobiotechnol.*, 150, 76, 2003.

[32] Cheung, K., Gawad, S., and Renaud, P., Microfluidic impedance spectroscopy flow cytometer: particle size calibration, in *Proc. IEEE Microelectromech. Sys. (MEMS)*, 2004, 343.

[33] Lin, C.-H. and Lee, G.-B., Micromachined flow cytometers with embedded etched optic fibers for optical detection, *J. Micromech. Microeng.* 13, 447, 2003.

[34] Lin, C.-H., Lee, G.-B., Fu, L.-M., and Hwey, B.-H., Vertical focusing device utilizing dielectrophoretic force and its application on microflow cytometer, *J. Microelectromech. Sys.*, 13, 923, 2004.

[35] Yu, C., Vykoukal, J., Vykoukal, D., Schwartz, J., Shi, L., and Gascoyne, P.R.C., A three-dimensional dielectrophoretic particle focusing channel for micro-cytometry applications, *J. Microelectromech. Sys.*, 14, 480, 2005.

[36] Wang, X.-B., Vykoukal, J., Becker, F.F., and Gascoyne, P.R.C., Separation of polystyrene microbeads using dielectrophoretic/gravitational field-flow-fractionation, *Biophys. J.*, 74, 2689, 1998.

[37] Ramos, A., Morgan, H., Green, N.G., and Castellanos, A., AC electrokinetics: a review of forces in microelectrode structures, *J. Phys. D: Appl. Phys.*, 31, 2338, 1998.

[38] Forster, E., and Emeis, C.C., Quantitative studies on the viability of yeast protoplasts following dielectrophoresis, *FEMS Microbiology Letters*, 26, 65, 1985.

[39] Muller, T., Pfennig, A., Klein, P., Gradl, G., Jager, M., and Schnelle, T., The potential of dielectrophoresis for single-cell experiments, *IEEE Eng. Med. Biol. Mag.*, November/December 2003, 51.

[40] Wang, X., Yang, J., and Gascoyne, P.R.C., Role of peroxide in AC electrical field exposure effects on Friend murine erythroleukemia cells during dielectrophoretic manipulations, *Biochim. Biophys. Acta*, 1426, 53, 1999.

[41] Gruden, C., Skerlos, S., and Adriaens, P., Flow cytometry for microbial sensing in environmental sustainability applications: current status and future prospects, *FEMS Microbiol. Ecol.*, 49, 37, 2004.
[42] Schwarz, M.A. and Hauser, P.C., Recent developments in detection methods for microfabricated analytical devices, *Lab on a Chip*, 1, 1, 2001.
[43] Byun, I., Kim, W., and Park, S., A micro flow cell cytometry based on MEMS technologies using silicon and optical fibers, *J. Mater. Sci.*, 38, 4603, 2003.
[44] Chabinyc, M.L., Chiu, D.T., McDonald, J.C., Stroock, A.D., Christian, J.F., Karger, A.M., and Whitesides, G.M., An integrated fluorescence detection system in poly(dimethylsiloxane) for microfluidic applications, *Anal. Chem.*, 73, 4491, 2001.
[45] Kanda, M., Nakata, M., Osoegawa, M., Niwa, S., Yamashita, T., Suzuki, S., and Murayama, K., Flow cytometer using a fiber optic detection system, in *Proc. SPIE,* 4260, 2001, 155.
[46] Qi, S., Liu, X., Ford, S., Barrows, J., Thomas, G., Kelly, K., McCandless, A., Lian, K., Goettert, J., and Soper, S.A., Microfluidic devices fabricated in poly (methyl methacrylate) using hot-embossing with integrated sampling capillary and fiber optics fluorescence detection, *Lab on a Chip*, 2, 88, 2002.
[47] Kutter, J., P., Mogensen, K.B., Friis, P., Jorgensen, A.M., Petersen, J.N., Telleman, P., and Hubner, J., Integration of waveguides for optical detection in microfabricated analytical devices, in *Proc. SPIE,* 4177, 2000, 98.
[48] Grosse, A., Grewe, M., and Fouckhardt, H., Deep wet etching of fused silica glass for hollow capillary optical leaky waveguides in microfluidic devices, *J. Micromech. Microeng.*, 11, 257, 2001.
[49] Camou, S., Fujita, H., and Fujii, T., PDMS 2D optical lens integrated with microfluidic channels: principle and characterization, *Lab on a Chip,* 3, 40, 2003.
[50] Coulter W.H., High speed automatic blood cell counter and cell size analyzer, in *Proc. Natl. Electronics Conf.*, 12, 1956, 1034.
[51] Ayliffe, E., H., Frazier, A.B., and Rabbitt, R.D., Electric impedance spectroscopy using microchannels with integrated metal electrodes, *J. Microelectromech. Sys.*, 8, 1, 1999.
[52] Fu, A.Y., Chou, H.P., Spence, C., Arnold, F.H., and Quake, S.R., An integrated microfabricated cell sorter, *Anal. Chem.*, 74, 2451, 2002.
[53] Fu, A.Y., Spence, C., Scherer, A., Arnold, F.H., and Quake, S.R., A microfabricated fluorescence-activated cell sorter, *Nature Biotechnol.*, 17, 1109, 1999.
[54] Carlson, R.H., Gabel, C.V., Chan, S.S., Austin, R.H., Brody, J.P., and Winkelman, J.W., Self-sorting of white blood cells in a lattice, *Phys. Rev. Lett.*, 79, 11, 1997.
[55] Voldman, J., Martha L., Gray, M.T., and Martin A.S., A Microfabrication-Based Dynamic Array Cytometer, *Anal. Chem.*, 74, 3984, 2002.
[56] Koch, M., Evans, A.G.R., and Brunnschweiler, A., Design and fabrication of a micromachined coulter counter, *J. Micromech. Microeng.* 9, 159, 1999.
[57] Bayley, H. and Martin, C.R., Resistive-pulse sensings from microbes to molecules, *Chem. Rev.*, 100, 2575, 2000.

Part III

Sensing Technologies for Bio-MEMS Applications

10

Coupling Electrochemical Detection with Microchip Capillary Electrophoresis

Carlos D. García and Charles S. Henry

CONTENTS

10.1 Introduction

Laboratory-on-a-chip (LOC) or μ-total analysis systems (μTAS) are some of the names given to a novel class of analytical tools that emphasize miniaturization and integration of function to enhance device performance.[1] Because these devices can contain a wide range of different sample pretreatment and analysis methods on a single monolithic structure, the final goal of most μTAS devices is to integrate an entire laboratory onto a single microchip. Since the initial report describing a gas chromatography column fabricated on a silicon wafer,[2] an enormous number of papers have been published showing the capabilities of microdevices. Some of the advantages of μTAS over conventional bench-top systems include custom design, reduced consumption of reagents and sample, lower waste generation, and increased analysis speed and portability.

Much of the initial research in μTAS devices has focused on the use of capillary electrophoresis (CE). CE is very attractive for miniaturized devices because it offers high separation efficiency, low cost, fast analysis, and minimal waste generation. An additional advantage of CE is the simplicity of the required instrumentation. In CE, the separation takes place inside a capillary (ID < 100μm) filled with an electrolyte solution. When a potential is applied at the extremes of the capillary, ions migrate based on their electrophoretic mobility. The electrophoretic mobility of an ion depends on its charge-to-mass ratio, the magnitude of the applied potential and the electrolytic solution conditions (viscosity, pH, and ionic strength). Bulk flow is also generated inside the capillaries by a process referred as electroosmotic flow (EOF). EOF occurs as a result of the formation of a charged ionic double layer at the capillary–buffer interface when a potential is applied to the extremes of the capillary. As a result of the applied potential, the double layer moves and carries the bulk solution through the capillary.[3] This flow mechanism requires no moving parts and therefore can be easily miniaturized. Microchip CE combines most of the advantages of CE with sample handling capabilities, custom design, portability, low power requirements, and (sometimes) similar analytical performance. Microchip CE also allows high separation speed, minimum sample consumption, low analysis cost, and automation.

Many modes of detection have been employed to monitor separations on microchip CE devices but for many reasons, the most commonly used detection method is laser-induced fluorescence (LIF).[4] However, the cost of optical instrumentation, the frequent need for analyte derivatization, and the limited portability of LIF have led to a significant interest in electrochemical detection (ECD) as an attractive alternative for detection for microchip CE.

In this chapter, an introduction to microchip CE with electrochemical detection (CE-ECD) is provided. First, motivations for coupling microchip CE-ECD and early developments in the field are presented. This is followed by

two sections on instrument development and electrode configurations. The remaining portion of the chapter focuses on detection waveforms and applications of microchip CE-ECD. It is worth mentioning that additional material containing valuable information about different aspects of microchip CE,[5] microchip CE-ECD,[6–17] detection for microfluidic systems,[18,19] and microfabrication[20,21] can also be found in previously presented material.

10.2 Motivations for Electrochemical Detection

Electrochemical detection (ECD) offers great promise for μTAS. ECD can be used with many different assay types, ranging from CE to DNA and protein arrays. Furthermore, ECD features include remarkable mass sensitivity (approaching that of fluorescence), inherent miniaturization of both the detector and control instrumentation, independence from sample turbidity, optical path length, or substrate clarity, low cost, minimal power demands, and high compatibility with advanced micromachining and microfabrication technologies.[15] In addition, ECD does not scale linearly with decreasing electrode size, a limitation in most optical methods. Therefore, it is easier to miniaturize the detection elements and still maintain a significant signal level. Furthermore, with the use of microfabrication, it is possible to integrate multiple electrodes into a single microchip, thus improving the ability to perform more selective and more sensitive detection modes. Finally, electrodes for detection can be fabricated at the same time as electrodes for driving the electrophoresis, making the overall microfabrication process very efficient.

10.3 Historical Development

Capillary electrophoresis (CE) was developed as a powerful tool for the separation of biomolecules and credit is normally given to Jorgenson and Lukacs for the initial report of the modern version of this technique.[22] CE has evolved from these humble beginnings showing separation of proteins in an open tube to include a vast array of different analytes and methodologies. For an extensive introduction to CE, it is recommended that readers consult the excellent review presented by Righetti.[23]

Initial CE research used optical detection methods such as UV absorbance during the first years of development. It was not long, however, before other methods of detection began to appear. Ewing is generally credited with the first report of electrochemical detection coupled with conventional CE.[24] While not the main focus of the current manuscript, it is worth considering this initial development because many of the same problems faced in the

development of conventional CE-ECD are also faced in the development of microchip CE-ECD. In the initial work of Wallingford and Ewing, a 75 μm fused silica capillary was used, and a carbon fiber working electrode was aligned at the exit of the capillary. The major obstacle faced in this work was trying to measure a nA signal in the presence of the large background current (μA) generated by the separation potential. To overcome this problem, the authors used a current decoupler. Decouplers provide a ground for the separation current prior to the working electrode, but do not significantly impede flow. In this first example of CE-ECD, a small section of the fused silica was etched with HF, leaving a porous conductive joint. It was soon recognized by Ewing and others that a simple approach to decoupling the separation and detection currents was to use capillaries with smaller inner diameters (approximately 25 μm) and place the electrode just outside the capillary exit. Ewing was also able to couple ECD with micellar electrokinetic chromatography (MEKC) to separate neutral compounds.[25]

The development of microchip CE-ECD, like the development of conventional CE-ECD did not take place until several years after the first report of microchip CE by Manz et. al.[26] Again, it was Ewing's group that reported the first microfabricated device for CE-ECD.[27] In this device, an electrode array was fabricated at the end of a wide, shallow, continuous electrophoretic separation channel. Shortly after the publication of this work, Mathies's group published the first example of microchip CE-ECD in what is now considered the conventional format with a cross-shaped microchannel pattern.[28] Their basic chip design is shown in Figure 10.1. In their design, Pt electrodes were fabricated on a glass microchip after etching channels. Upon sealing of a top piece of glass to complete the channel, the first microchip CE-ECD system with integrated electrodes was realized. Using this system, they were able to separate dopamine, epinephrine, and catechol as well as DNA fragments from two different bacterial systems. For DNA, the authors adopted an indirect detection mode using Fe-$(phen)_3^{2+}$ in the background buffer. Upon intercalation to DNA, the Fe-$(phen)_3^{2+}$ could no longer be detected giving a negative signal. These original papers on microchip CE-ECD set the stage for what has now become a growing and active field of research and development in μTAS.

10.4 Instrumental Development

One advantage of using electrochemical detection with microchip CE is the ability to miniaturize the associated instrumentation for both the electrophoresis and detection. Furthermore, because all of the components are electronic, it should be possible to construct a small rugged system for point-of-measurement applications. Several research groups have demonstrated the ability to generate small portable analyzers and high-voltage power supplies.

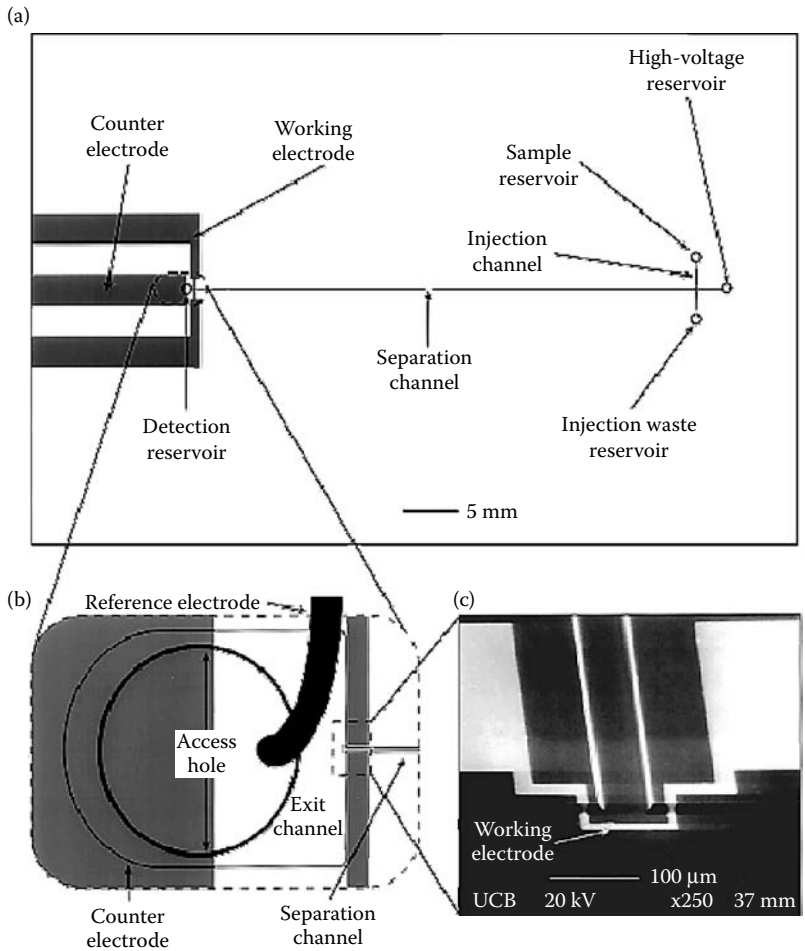

FIGURE 10.1
Capillary electrophoresis chip with integrated electrochemical detection first produced by Mathies's group. (a) Overall chip layout. (b) Schematic drawing of the alignment of the reference electrode relative to the access hole and working electrodes. (c) Scanning electron microscope image showing the working electrode alignment in a final device. (Reprinted from Woolley, A.T., Lao, K., Glazer, A.N., and Mathies, R.A., *Anal. Chem.* 1998, 70(4), 684–688. With permission.)

The first example of a miniaturized and integrated microchip CE-ECD system was published by Martin and coworkers.[29] In their system, the detection electrodes were placed directly in the channel, and the working electrode was controlled with an electrically isolated potentiostat. The use of an in-channel electrode significantly reduced the peak skew and thus the ability to resolve more peaks. Furthermore, the electrically isolated potentiostat prevented the electrophoresis voltage from interfering with the potentiostat. A second example of miniaturizing instrumentation was published by Baldwin's group.[30] In their work, the authors integrated both the potentiostat for

electrochemical detection and the high-voltage power supply for controlling electrophoresis. A battery-powered potentiostat was used to isolate the interfering separation current, allowing the ECD of cotechol and dopomine. The combined system was an amazing 4 in. × 6 in. × 1 in. and weighed only 350 g. A third example of miniaturizing the instrumentation for microchip CE-ECD was published by Garcia and coworkers.[31] In this work, a simple 3-channel power supply with integrated analog controls was constructed. The power supply could be operated in any of the three standard injection modes: gated, pinched, or hydrodynamic. The system could operate from either battery or AC power sources and had a battery lifetime of two hours for continuous operation. The final example of a miniaturized integrated microchip CE-ECD system was published by Jiang and coworkers.[32] In their example, a miniaturized potentiostat was produced that fit in a card that was 3.6 × 5.0 cm. A high-voltage power supply was also generated that could produce up to 4000 V and perform either gated or pinched injection.

10.5 Electrode Configurations

The second key element in developing an effective electrochemical detector is the interface between the microchip and the electrode. To date, there have been two popular methods for coupling, which we will refer to here as off-chip detection and microfabricated electrodes. In the off-chip electrode configuration, the electrodes are separate from, but aligned to, the microchip. With microfabricated electrodes, the electrodes are produced using micromachining techniques and are contained on the same microchip as the electrophoresis system. Finally, there has been recent interest in the development of other electrode configurations, that integrate electrodes as part of the microchip but do not use micromachining methods for construction. This section will present the major types of electrode configurations and their advantages and disadvantages.

10.5.1 Off-Chip Detection

The first two electrode configurations reported for microchip CE-ECD used microfabricated electrodes, however off-chip electrodes quickly became the most popular approach because they could be made with existing electrodes and required significantly less microfabrication time and expertise. Much of the earlier work in this field was pioneered by Wang's group.[33,34] Wang's group used a simple X-positioner as shown in Figure 10.2a to align an electrode with the end of a glass microchip that had been cut to expose the separation channel. A simple Teflon spacer provided constant spacing between the working electrode and the outlet of the channel. Using this configuration, Wang's group

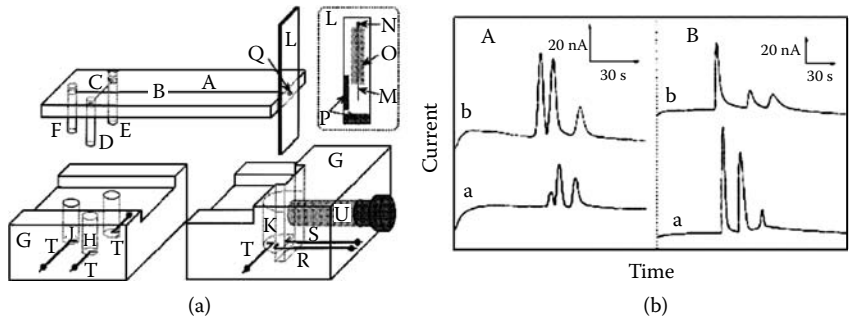

FIGURE 10.2
(a) Schematic drawing of the alignment system initially developed by Wang's group for microchip CE-ECD. (Reprinted from Wang, J., Tian, B., and Sahlin, E., *Anal. Chem.* 1999, 71(23), 5436–5440. With permission.) (b) Electropherograms showing the comparison of glass and PMMA microchips used for the separation of different compounds. (Reprinted from Wang, J., Pumera, M., Chatrathi, M.P., Escarpa, A., Konrad, R., Griebel, A., Dorner, W., and Lowe, H., *Electrophoresis* 2002, 23(4), 596–601. With permission.)

was able to demonstrate several important separations and modes of detection including amperometry and voltammetry. An example of one of these separations is shown in Figure 10.2b from a report detailing the comparison of glass and poly(methylmethacrylate) (PMMA) microchips for CE-ECD.[35] The major advantages of off-chip electrodes include excellent electrode stability and a wide range of electrode materials, including chemically modified electrodes. The major disadvantages of off-chip electrodes include tedious or manual electrode alignment and limits to the number of working electrodes that can be used simultaneously. The remainder of this section provides examples of different types of off-chip detection configurations.

In addition to the work of Wang's group, several other examples of microchip CE-ECD using off-chip electrode configurations have been published. One example of this was a simple design for electrode alignment published by Zeng and coworkers.[36] In their system, a traditional microelectrode was used for detection and aligned using a simple X-positioner. The positioner was integrated as part of the microchip holder to simplify device alignment and use. With this system and a carbon-fiber electrode, they were able to achieve a detection limit of 240 nM for dopamine, and showed nice separations of several catecholamine neurotransmitters. A second interesting example of using off-chip electrodes for detection was published by Coltro and coworkers.[37] In their example, microchips were made by printing the pattern on transparencies followed by thermal sealing of two layers of the polyester material. The toner used in the printing process served as the spacer to form the channel. Electrodes for these devices were made by patterning the metal layer present on a compact disk, making the overall system very inexpensive and easy to assemble in laboratories without microfabrication equipment. A final interesting example of off-chip electrode alignment systems was published by Bao and coworkers.[38] In their

report, a simple X-Y-Z positioner was used to hold the electrode in close proximity to the outlet of the microchip. Using this system, it was feasible to switch between electrodes of different materials. Several other interesting examples of off-chip electrode configurations have been published, which readers are encouraged to investigate as well.[39,40]

10.5.2 Microfabricated Electrodes

Microfabrication provides the ability to generate large numbers of well-defined electrodes on planar surfaces. It was for this reason that both Ewing's and Mathies's groups took this approach when they developed the first microchip CE-ECD systems. Microfabricated electrodes also have the advantage of being produced using many of the same methods that are used for fabrication of the channels for electrophoresis. The major advantages of microfabricated electrodes include ease of fabrication using existing microfabrication methods, production of electrode arrays for multielectrode detection, and integration of electrodes as part of the microchip. The major disadvantages of microfabricated electrodes include the cost of fabrication relative to off-chip electrodes, a limited number of electrode materials that can be used, and longevity of the electrodes under electrophoresis conditions. Furthermore, it is difficult to fabricate multiple electrodes from different materials in a single microchip without significantly increasing the fabrication time and complexity. The remaining portion of this section details examples of microfabricated electrodes coupled with microchip CE.

Numerous examples of microchip CE-ECD systems using integrated electrodes have been published in recent years. The following highlights some examples of this approach but is by no means exhaustive. Instead, we hope to highlight several good examples of how this approach can be used to perform microchip CE-ECD. One example of integrated electrodes was published by Baldwin's group.[41,42] In their approach, electrodes for both detection and electrophoresis were integrated on one substrate, along with the microchannels. As can be observed in Figure 10.3, one unique aspect of their approach was the use of recessed channels to contain the electrodes. Electrodes were fabricated in channels that were recessed in the glass prior to sealing the microchip, facilitating the ability to form very good seals around the electrodes. A second interesting example of microchip CE-ECD that used traditional micromachining methods was reported by S. Lunte's group.[43] In this effort, dual Au electrodes were fabricated on a glass substrate and then a poly(dimethylsiloxane) (PDMS) substrate containing the channels was sealed on top of the electrodes. The use of dual electrodes provides an additional degree of selectivity based on relative oxidation and reduction potentials. For example, in the separation of a mixture of tyrosine, 5-hydroxyindole-3-acetic acid, and catechol, only catechol is reversibly oxidized and gives a peak at the second electrode. Lunte's group also extended this work to integrate electrodes directly in the channel, as discussed above in Section 10.4.[29]

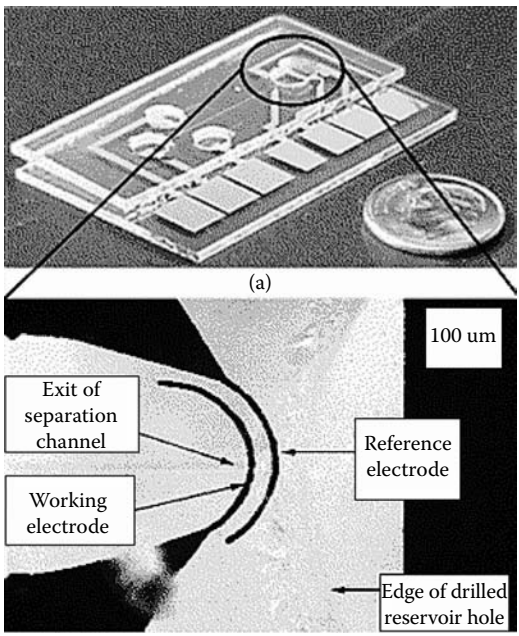

FIGURE 10.3
Photographs of (a) entire CE/ED microchip and (b) magnified (30×) top view of the ED cell and electrodes. (Reprinted from Keynton, R.S., Roussel, T.J., Crain, M.M., Jackson, D.J., Franco, D.B., Naber, J.F., Walsh, K.M., and Baldwin, R.P., *Anal. Chim. Acta* 2004, 507(1), 95–105. With permission.)

In addition to traditional microfabrication methods, several groups have demonstrated hybrid methods for microchip CE-ECD. Osborne and C. Lunte were among the first to report the use of a decoupler to improve detection limits with microchip CE-ECD.[44] More discussion of decouplers will be provided later in this chapter. Using this configuration, the authors achieved detection limits as low as 25 nM. A second example of using hybrid microfabrication techniques to produce CE-ECD microchips was reported by Manica and Ewing.[45] In their approach, a Au-coated glass plate was patterned by inking the metal with a permanent marker followed by etching of the exposed Au and Cr. Finally, the ink was removed with a simple acetone rinse. The electrophoresis channel was made from PDMS and sealed directly over the electrode pattern. Using this approach, the authors were able to achieve detection limits of 648 nM for dopamine.

10.5.3 Other Electrode Configurations

In addition to the two main categories of electrodes used with microchip CE-ECD, several groups have demonstrated alternative electrode configurations that are interesting with respect to the current discussion. In these cases,

the authors have sought to maintain the portability of microchip CE-ECD by integrating the electrodes as part of the microchip without using microfabrication techniques for their creation. This approach has several advantages. First, a wider variety of electrode materials and chemically modified electrodes can be coupled to microchip CE. Second, multielectrode detection systems can be made without the use of extensive cleanroom systems.

The first example of this approach was presented by the Lunte group when they demonstrated the alignment of a Pt wire at the exit of a capillary channel made from a low-temperature, co-fired ceramic microchip.[46] While this work demonstrated the principle, several later reports showing the integration of carbon-fiber and carbon-paste electrodes provided better performance. Carbon is an attractive electrode material for detection of biological molecules because it resists electrode fouling. Carbon electrodes cannot be produced using traditional microfabrication methods, leaving an important gap in electrode materials. In the work of Lunte, an additional channel was fabricated in one piece of the material, and an electrode was aligned prior to final assembly of the system.[47,48] Hauser's group published a similar report[64] using metallic wires at roughly the same time as the work of Lunte's group. In their design, the end of the separation capillary was etched to a conical shape and a traditional microelectrode aligned in the opening. They were able to demonstrate the use of several different electrode materials, including copper, and the electrodes were integrated as part of the microchip and demonstrated the ability to detect a wide range of analytes, including catecholamines, phenolic compounds, carbohydrates, and amino acids.

Another approach to fabrication of carbon electrodes was recently demonstrated by Martin's group. In their approach, a PDMS channel of the electrode pattern was produced and reversibly sealed to a glass substrate. Carbon ink diluted with solvent to reduce the viscosity, was pushed through the channel and then the solvent driven off in a heating step. The PDMS was removed leaving behind a trace of the carbon. The resulting microelectrodes were 6 μm high on average and possessed very good electrochemical behavior. The author was able to demonstrate the use of the electrodes in both a flow injection mode as well as with electrophoresis using an integrated thin-film Pd decoupler to provide a sensitive, stable electrode system. The authors also showed the ability to increase selectivity of the electrodes using a Nafion® coating on the electrodes.

A final approach to the fabrication of electrode systems using integrated microwires was recently reported by Garcia et al. and Liu et al.[49,50] Building on the previous work of Hauser and Lunte, this system integrated solid metal wires into the microchip. Unlike the work of Lunte, however, the electrodes were placed directly in the flowing stream by incorporating the electrode alignment channel in the same PDMS layer as the separation channels.[49] The system has proven to be easy to fabricate, generates very low detection limits, and can be adapted to many different electrode configurations. In many ways, the design provides the advantages of both off-chip and microfabricated electrodes without many of the disadvantages inherent in both of these

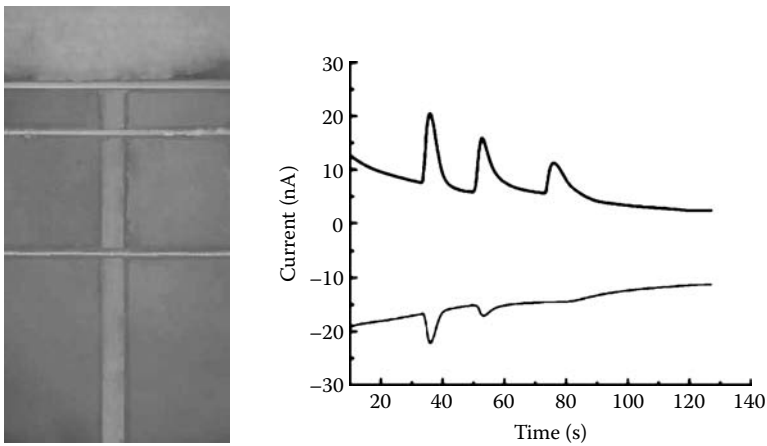

FIGURE 10.4
Picture of a microchip containing a single Pd electrode and two Au electrodes as well as an electropherogram obtained for dopamine, catechol, and ascorbic acid operating in dual electrode detection mode. (Courtesy of Vickers, J.A. and Henry, C.S., Unpublished data.)

configurations. For example, the electrode alignment results in the generation of a high collection efficiency (up to 90% depending on electrode size) that provides detection limits as low as 100 nM in a nondecoupled detection scenario. A second advantage of the system is the use of solid metal electrodes. The electrodes provided enough chemical stability to be used for pulsed amperometric detection (PAD) thus opening the door to detecting alcohols, carbohydrates, amines, and thiols.[3,31,49,51–56] Finally, the design permitted the inclusion of multiple electrodes made from different materials.[50] Figure 10.4 shows a picture of a microchip containing a single Pd electrode and two Au electrodes as well as an electropherogram obtained for dopamine, catechol, and ascorbic acid operating in dual electrode detection mode.[57] Dopamine and catechol have reversible electrochemistry and therefore give a reduction peak at the second electrode. Ascorbic acid does not have reversible electrochemistry and therefore only gives a peak at the oxidizing electrode. In this case, the Pd electrode serves as a decoupler and allows detection limits to be reduced to 5 nM for dopamine.[57]

10.6 Detection Modes

10.6.1 Amperometry

Many modes of electrochemical detection have been used with microchips. Among others, the most common is DC amperometry or simply amperometry. In *amperometry*, a constant potential is applied to the detection electrode

and the current is followed as a function of time. This is the simplest electrochemical technique that can be applied for detection of readily electroactive compounds, and the required instrumentation is rather simple, inexpensive, and can be integrated with the power supply used for the separation (see Section 10.4). A final advantage of amperometric detection is the ability to reach extremely low detection limits. The use of a constant potential reduces the background current caused by double-layer charging, and thus detection limits in the low nM range can be achieved. Amperometry also has several disadvantages. The two most significant disadvantages are (1) the low number of naturally electrochemically active compounds, and (2) electrode fouling resulting in loss of signal.

Because of the instrumental simplicity of amperometric detection, it has been widely applied in bioanalysis.[37,41,58–62] One of the most common applications has been analysis of catecholamines. Catecholamines are a major class of neurotransmitters that are also readily electrochemically active. Neurotransmitters also serve as model compounds for comparing new microchip CE-ECD designs with existing systems. For example, a microdisk electrode operating in amperometric mode was used to evaluate a microchip that utilized hydrodynamic injection instead of one of the electrically controlled injection techniques.[39] Using this system, the authors were able to show low relative standard deviations (5%) and detection limits in the low μM range. Ascorbic acid, noradrenaline, and L-dopa were used as the model analytes in this study, again because these compounds are all easily detected using amperometry.

In addition to the use of amperometry for characterization of new microchips, it has also been applied to a variety of real-world applications. Hauser and Schwarz used a microchip CE-ECD system with amperometric detection for the chiral separation and detection of the enantiomers of adrenaline, noradrenaline, ephedrine, and pseudoephedrine.[63] Detection was carried out with a new two-electrode amperometric detector, eliminating the need for individual counter and reference electrodes. A similar concept, using the amperometric working and electrophoretic ground electrodes only was also presented. The latter serves as a counter and pseudoreference as well, and was applied to the determination of neurotransmitters, ascorbic acid, phenols, carbohydrates, and amino acids on gold, platinum, or copper working electrodes.[64] Chiral separations are particularly important in the characterization of pharmaceuticals. Amperometric detection has also been used for the detection of DNA.[65] In this example, DNA fragments were detected using both an electroactive intercalating dye (iron phenanthroline) and ferrocene-labeled primers.

One other interesting example of the use of amperometric detection was recently reported by Nyholm's group.[58] A potentiostatless detection scheme was presented based on the use of a microband array of two gold electrodes positioned in the proximity of the capillary outlet. The induced potential difference between the two electrodes was recorded as a function of the applied separation high voltage and the dependence of the electrochemically

generated current on the high-voltage field, and the concentration of $Fe(CN)_6^4/Fe(CN)_6^3$ was investigated. The results showed that plots of the generated current versus the CE separation voltage have the same shape as cyclic voltammograms obtained with the same electrodes in a traditional potentiostatic setup and that the current is proportional to the concentration of the redox couple. As a decoupling device is not needed, the described potentiostatless approach significantly simplifies the instrumental setup for amperometric detection.[66] Other contributions from the same group were also published.[17,67,68]

10.6.2 Pulsed Electrochemical Detection

As stated before, one problem with amperometry is electrode fouling. Electrodes are fouled by the accumulation of adsorbed cabonaceus material, causing a significant decrease in signal as well as transient instability in the signal. Several strategies have been suggested to overcome problems associated with electrode fouling. Among other approaches,[69–71] a potential waveform referred to as *pulsed electrochemical detection* (PED) can be applied. PED uses a potential pulse applied to a noble metal (Au or Pt) electrode to remove adsorbed materials. Two main forms of PED exist: pulsed amperometric detection (PAD) and integrated pulsed amperometric detection (iPAD). In PAD, a high positive potential is applied in order to clean the electrode surface, followed by a negative potential step to reactivate the electrode surface. A third potential is then applied for detection of the target analytes at a clean electrode surface. In iPAD, a triangular waveform is applied to the electrode and the current is integrated over this waveform, followed by the application of a high positive potential and a negative regenerating potential. PAD is particularly useful when the analyte lacks a strongly absorbing chromophore, when the analyte is not electrochemically active under other techniques, or when rapid electrode fouling occurs. iPAD is better for analytes that adsorb to the surface during the detection step including amines and thiols.

The first report of PAD on an electrophoretic microchip was presented by Fanguy and Henry in 2002.[72] Under optimized detection conditions, glucose, maltose, and xylose were detected. Later, the separation and detection of underivatized carbohydrates, amino acids, and sulfur-containing antibiotics was described by Garcia and Henry.[49] In that report, the separation and injection potentials, buffer pH and composition, injection time, and PAD parameters were studied. Later, a solution with higher pH (compared to the running buffer) was used at the waste reservoir in order to improve the detection performance while maintaining good separation by using a lower electrolyte pH.[53] As a proof of this concept, the separation of glucosamine and glucose was performed at pH 7.1, while the detection was performed at pH 11.0, mimicking the use of postcolumn pH modification used in HPLC-ECD (high performance liquid chromatography, electrochemical detection).

It was also observed that when sodium dodecyl sulfate (SDS) was added, not only a stabilization of the EOF but also an improvement in the electrochemical signal of about 30%, was achieved. The compatibility of higher concentrations of SDS (up to 40 mM) with PAD was also demonstrated. The separation and detection of catechins (natural antioxidants) were performed in less than 2 minutes and successfully compared with HPLC-UV.[55]

iPAD has also been used with microchip CE-ECD. iPAD achieves a much lower baseline stabilization time in comparison to PAD. Carbohydrates such as glucose, mannose, sucrose, maltose, glucosamine, lactose, maltotriose, and galactose were analyzed by PAD and iPAD. The electrochemical response and migration times were studied as functions of buffer concentration, pH, and the concentration of SDS.[54] Results showed that both iPAD and PAD are affected in a similar manner by changes in solution conditions. For both detection methods, the highest electrochemical responses were obtained using lower electrolyte concentrations (4 mM), higher pH values (12.2), and a moderate level of SDS (0.8 mM). Other microelectrode applications of pulsed electrochemical detection were recently reviewed by LaCourse.[73]

10.6.3 Conductivity

CE offers several advantages with respect to ion chromatography in the analysis of ions. Costs of column hardware and required eluent chemicals are lower, separation times can be incredibly short (less than 1 min), and the sample injection volume (which is required for a quantitative analysis in CE) can be as low as 10 fL. Additionally, conductivity detection is intrinsically simpler than optical methods in terms of hardware, as UV lamps, monochromators, focusing optics, and photodetectors are not required. Conductivity detection can be considered a universal detection method with the possibility of direct as well as indirect measurement of the analyte's response signal.[74] It is also worth noting two articles by Kuban and Hauser regarding the fundamental aspects of contactless conductivity detection for CE.[75,76]

There are two general modes of conductivity detection that have been adapted to microchip CE—contact and contactless. Contact conductivity detection utilizes electrodes that are in direct contact with the background electrolyte. Contactless detection isolates the detection electrodes from the solution through an insulator. Contact conductivity has the advantage of lower detection limits, but contactless detection has the advantage of being able to place the electrodes anywhere along the separation channel. For more information on the fundamentals behind both detection modes, the readers are directed to an excellent review published by Guijt and coworkers.[14]

Contact conductivity detection has been reported by several groups. Liu and coworkers demonstrated the use of contact conductivity detection to monitor mixing of solutions in a microfluidic device.[77] The conductivity detector in this case showed the ability to follow the concentration of two buffers that were mixing in a separation channel and has the potential to

help control reactions in bio-MEMS and μTAS devices. Several other examples of contact conductivity detection have been published. Organic molecules (amino acids, peptides, proteins, oligonucleotides) were separated and detected with an on-column contact conductivity detector fabricated in PMMA.[78] The detector consisted of a pair of Pt wires (127 μm diameter) with an end-to-end spacing of approximately 20 μm and situated within the fluidic channel. Reverse-phase ion pair microcapillary electrochromatography coupled with a similar detector was also used to separate and detect double-stranded DNA fragments.[79] A group of 22 organic and inorganic acids expected in wines was also separated and detected on a PMMA chip with integrated conductivity detection.[80]

Despite the sensitivity advantages of contact conductivity detection, it is contactless detection that has begun to dominate the field of microchip CE with conductivity detection.[60,81–89] One interesting approach for contactless conductivity detection for microchip-CE was presented by Verpoorte et al.[90] The detector integrates easily with well-known microfabrication techniques for glass-based microfluidic devices. Platinum electrodes are structured in recesses in-plane with the microchannel network after glass etching, which allows precise positioning and batch fabrication of the electrodes. A thin glass wall of 10 to 15 μm separates the electrodes and the buffer electrolyte in the separation channel to achieve the electrical insulation necessary for contactless operation. Another contactless conductivity microchip detector is based on placing two planar sensing aluminum film electrodes, and was presented by Wang et al.[91] In that report, the separation of 7 inorganic explosive residues (cations and anions) was achieved using the same microchannel and run buffer. The addition of 18-crown-6 ether was used to improve the separation of potassium and ammonium ions. The possibility of using a high-voltage contactless conductivity detection for lab-on-a-chip devices was demonstrated by P. Hauser's lab.[92] The same group studied the effects of the cell geometry and operating parameters on the performance of an external contactless conductivity detector[93] and used microchip-CE and conductivity detection to analyze inorganic and organic ions;[94] amino acids;[95] mixtures of underivatized sulfonates, carboxylates, amino acids, sugars, sweeteners, and catecholamines;[96] and other biochemically relevant species such as immunoglobulin G, down to 0.4 nM.[97]

A passive electrochemical detection principle that can be applied to capillary electrophoresis was also presented.[98] The separation electrical field is used to generate a potential difference between two electrodes located along the channel. For constant-current electrophoresis, the generated signal is proportional to the resistance of the solution passing between the two electrodes. Contrary to conductivity detectors that are AC driven and need to be decoupled from the separation field, the passive detection directly takes advantage of the separation field. The signal is simply measured by a high-impedance voltmeter. The detection concept has been validated by numerical simulations showing how the magnitude of the signal is related to the ratio between the electrode distance and the length of the sample plug. As a proof

of the principle, this detection concept has been demonstrated by the electrophoretic separation of three alkali ions on a polymer microchip. Based on preliminary results, a detection limit of 20 μM and a dynamic range of up to 3 orders of magnitude have been achieved.

A microscale continuous ion exchanger based on two liquid streams flowing in parallel was presented by Kuban, Dasgupta, and Morris.[99] The ion exchange reaction occurs through diffusional transfer of molecules between the ion exchanger phase and the eluent phase and is applied for conductivity suppression. Using either a liquid or a solid ion exchanger, the detection of various inorganic cations including heavy metals is possible. A similar system using vertically stratified flows in microchannels was also presented describing computational simulations and applications to solvent extraction and ion exchange.[100]

Isotachophoresis (ITP) is a well-known electrophoretic separation technique for qualitative and quantitative analysis of ionic compounds based on differences in the effective electrophoretic mobilities of the ions. ITP can be used as a separation technique itself, but can also be considered as an ideal preconcentration technique when it is coupled with CZE (capillary zone electrophoresis) or HPLC. In this regard, Grab et al. described the design, fabrication and use of new microanalytical devices based on PMMA.[101] The devices are fabricated by hot embossing and are sealed with a thin plexiglas cover plate which contains platinum electrodes for contact conductivity detection and power supply. Two different chip designs were introduced to demonstrate the advantages of the manufacturing procedure and the use of PMMA as a substrate material. The channel system on the chips is equipped with two sample loops with different volumes to take advantage of the high sample loadability and the enrichment qualities of ITP. Later, the performance of different electrode geometries (thin-film platinum) was studied considering the influence of the width of the electrodes and their positioning relative to the separation channel.[102] The same year, Bodor et. al. reported the use of CZE coupled online with ITP sample pretreatment (ITP-CZE) on a PMMA chip and on-column conductivity detection.[103] The sensor was used to detect bromate in drinking water up to a 20 nM (2.5 ppb) limit of detection. Prest et. al. applied ITP to the analysis of inorganic arsenic species using both miniaturized planar polymer separation devices and capillary-scale devices. Limits of detection of 2 and 5 mg/L for arsenic (V) and arsenic (III), respectively, have been achieved with the miniaturized device. A similar device was also applied for the analysis of amino acids using glycolate as the leading ion. Addition of magnesium to the leading electrolyte as a counter species was found to improve the separations.[104] ITP was also combined with CZE and applied for the detection of nitrite, phosphate, and fluoride (each at 10 μM) accompanied by matrix constituents (sulfate and chloride) at considerably higher concentrations.[105] This concept (called column switching) was then applied in a feasibility study to perform sample cleanup and separate malate, malonate, tartrate, and citrate.[106]

10.6.4 Other Electrochemical Detection Modes

Microfluidic chip devices are shown to be attractive platforms for performing microscale voltammetric analysis and for integrating voltammetric procedures with on-chip chemical reactions and fluid manipulations. Wang and coworkers recorded linear-sweep, square-wave, and adsorptive-stripping voltammograms while electrokinetically driving the sample through the microchannels.[107] According to the authors, the adaptation of voltammetric techniques to microfluidic chip operation required an assessment of the effect of relevant experimental variables, particularly the high voltage used for driving the electroosmotic flow, upon the background current, potential window, and size or potential of the voltammetric signal. Rapid square-wave voltammetry and flow injection operation allowed a detection limit of 2 pmol of 2,4,6-trinitrotoluene.

The detection of native carbohydrates at planar copper electrodes was reported using a PDMS microchip and sinusoidal voltammetry. This technique utilizes information in the frequency domain to achieve sensitive detection through either of two approaches—maximization of signal or minimization of noise—and detection limits of less than 200 amol were reported for glucose and sucrose.[108] The performance of this technique was also compared to constant potential amperometry. Sinusoidal voltammetry was found to be roughly an order of magnitude more sensitive than amperometry, with calculated mass detection limits of 12 and 15 amol for dopamine and isoproterenol, respectively.[109]

Potentiometric detection is based on electrode-bearing membranes, which are semipermeable to certain ions only, leading to a charge separation and thus the buildup of a measurable potential, which follows the Nernst equation. Potentiometry is rarely used in separation methods but is promising for certain classes of analytes that can only, with difficulty, be quantified by more standard methods [7,110]

10.7 Dual Electrochemical Detection and ECD Coupled to Other Detection Modes

As CE has been reduced to the microchip scale, separation times have been significantly reduced meaning peak overlap can become a real problem. One way to overcome the reduced resolution is to use detectors that are more selective.[111] In ECD, one way selectivity can be achieved is through the use of dual electrode detectors. Dual electrode detectors can apply two different potentials (typically one oxidizing and one reducing) to detect compounds that comigrate out of the column. In the case presented by Lai et al.,[111] the first electrode typically oxidizes compounds coming out of the channel. The second electrode then reduces any compounds that have a

reversible electrochemical mechanism. An example of dual electrode detection is shown in Figure 10.4 and was also discussed in Section 10.5.3. The first carbon-based, dual-electrode detector for microchip CE was reported in 2001. A PDMS layer containing separation and injection channels was sealed to another PDMS layer containing carbon-fiber working electrodes. End-channel amperometric detection was employed and the performance of the chip was evaluated using catechol. The response was found to be linear between 1 and 600 μM with an experimentally determined limit of detection (LOD) of 500 nM.[48] A prototype that includes all necessary electrodes on-chip and utilizes miniaturized CE- and ED-supporting electronics was reported by Balwin's group.[41] State-of-the-art design and modeling tools and novel microfabrication procedures were used to create recessed platinum electrodes with complex geometries and the CE/ED device from two patterned ultra-flat glass substrates.

Wang also presented a microchip with dual conductivity and amperometric detection.[112] The combination of a contactless conductivity detector with an end-column thick-film amperometric detector greatly enhances the sample characterization to offer simultaneous measurements of both ionic and electroactive species, improved reproducibility, and confirmation of peak identity. The combination of amperometric and fluorescence detection was reported by Lapos, Manica, and Ewing.[113] The combination allows the analysis of a wider spectrum of compounds per separation, leading to higher throughput and enabling resolution of two neutral analytes, NBD-arginine and catechol. In addition, insight into the detection and separation mechanisms is realized. Differences in migration time and peak widths between the two detectors are compared, providing a better understanding of detector alignment. By the use of an internal standard (active in only one of the detection modes) reproducibility has been improved. This dual detection method was applied to normalize unknown peak mobilities in a cerebral spinal fluid sample.

10.8 Decouplers

One of the problems associated with microchip CE-ECD is the noise introduced by the separation current in the detection circuit. In order to solve this problem using conventional CE, a crack created right before the detection point was performed. The purpose was to allow the majority of the separation current to flow though the crack and minimize its effect on the detection current. Due to the possibility of customizing the design at the microchip scale, a wide variety of designs have been proposed for microchip CE-ECD. All decouplers have in common the ability to provide an electrical ground point in the channel prior to the detection electrode without stopping electroosmotic flow.

The first decoupler was published by Hubert Girault's group and consisted of a series of small laser-etched holes in a polymer microchip.[111,114–116] More recently, the use of Pd electrodes for decoupling has been reported.[117] The decoupling electrode as well as the working electrodes, were thermally evaporated onto a plastic chip and oriented vertically across the separation channel. After the sample zones flow over the Pd decoupler, their electrochemical response is measured at downstream electrodes. Because the electrodes are on the separation channel, the electrode channel alignment is no longer a problem. In addition, a platinized pseudoreference electrode has been used as a decoupler to offer a stable potential in electrochemical detection generating a limit of detection for dopamine of 0.125 μM.[118] The development of a cellulose acetate decoupler for on-column electrochemical detection in microchip capillary electrophoresis was presented by Osbourn and Lunte.[44] The capillary-based, laser-etched decoupler was translated to the planar format to isolate the detector circuit from the separation circuit. The decoupler was constructed by aligning a series of holes (30 μm) through the cover plate of the microchip with the separation channel, and casting a thin film of cellulose acetate within the holes. The decoupler shows excellent isolation of the detection circuit for separation currents up to 60 μA, with noise levels at or below 1 pA at a carbon-fiber electrode. Detection limits of 25 nM were achieved for dopamine. According to the authors, this decoupler combines excellent mechanical stability, effective shunting of high separation currents, and ease of manufacture.[44] A method of integrating a carbon microelectrode with a microfabricated palladium decoupler for use in microchip CE was detailed by Kovarik et. al.[119] The manner in which the working electrode is made did not add additional etching or lithographic steps to the fabrication of the glass electrode plate. The hybrid poly(dimethylsiloxane) and glass device was characterized with fluorescence microscopy and by monitoring a CE-based separation of dopamine. Hydrodynamic voltammograms exhibited diffusion-limited currents occurring at potentials above +1.0 V. It was also shown that the half-wave potential did not shift as the separation potential is changed, as is the case in nondecoupled systems.

10.9 Electrode Materials and Designs

The proper selection of the electrode material is one of the many ways of optimizing selectivity, stability, and sensitivity in microchip CE-ECD. The electrode material will also define the potential window to be used for detection. Working electrodes for microchips have been fabricated using a wide variety of materials. The choice of material is, however, largely determined by the type of electrode being used. In the following section, we classify electrodes according to metallic electrodes and carbon electrodes (carbon, carbon paste, carbon nanotubes, and diamond electrodes).

10.9.1 Thin-Film Metallic Electrodes

Many applications have been published using metallic thin-film electrodes. The main advantage for their application in microchip CE-ECD is the relatively simple procedure required to fabricate the films (chemical vapor deposition or photolithography),[70,109,111,120,121] relatively good stability (when amperometry is used), ease of alignment with respect to the separation channel, variety of metals available, the ability to integrate electrode arrays, and a very well-controlled surface area. On the other side, delamination (when the electrode is exposed to redox cycles) and the possibility of inducing a potential difference (within the detection electrode) as a consequence of the applied separation potential are the main drawbacks of these electrodes. In general, three materials have been used for thin film electrodes: Au, Pt, and Cu. Pd has also been used, but has found much more of an application as a decoupler (see Section 10.8).

Numerous examples of thin-film electrodes have been published for a variety of important bioanalytical applications. A CE chip-based detection system with a downstream gold-coated carbon electrode, presented by Wang and coworkers, was used for the simultaneous measurements of glucose, ascorbic acid, acetaminophen, and uric acid,[122] glucose and ethanol,[123] and later for the determination of creatine, creatinine, *p*-aminohippuric acid, and uric acid.[124] The design was based on the use of a screen-printed carbon electrode[125] with a silver contact printed also on a ceramic substrate. The active working electrode area (0.30 mm × 2.50 mm) was defined by a layer of insulator. The carbon working electrode area was then coated with a gold film, prepared by applying a pulse waveform (square-wave pulse potential between 0.2 and +0.75V, vs. Ag/AgCl), with a pulse width of 0.6 s for 20 min in a solution containing 300 ppm of Au(III), 0.1M NaCl, and 1.5% (w/v) HCl. The detector was also applied to develop an electrochemical immunoassay protocol, based on the use of a ferrocene redox label.[126] The use of a redox tracer offers the advantages of simplified protocol, wider linear range, higher stability, and higher separation efficiency compared to an analogous use of enzyme tags. The direct mouse-immunoglobulin G (IgG) assay and the competitive 3,3',5-triiodo-L-thyronine (T_3) version were accomplished within less than 150 s, and offer minimum detectable concentrations of 2.5×10^{12} and 1×10^{6} g/mL, respectively. Other examples of applications of thick-film amperometric detectors to microchip CE were recently presented.[127]

The second common metallic type of electrodes can generally be referred to as solid electrodes. Solid electrodes are comprised of a pure material and are typically adapted from a traditional electrochemical measurement.[38,108,116,128–130] One of the main advantages of solid electrodes is that the surface can be regenerated by polishing (mechanical or chemical) without affecting the electrode performance. A PDMS and glass microchip with an off-chip platinum working electrode was presented by Fanguy and Henry[131] reporting a limit of detection for dopamine and uric acid of 1 μM. Once characterized, the system was used to measure the concentration of uric acid

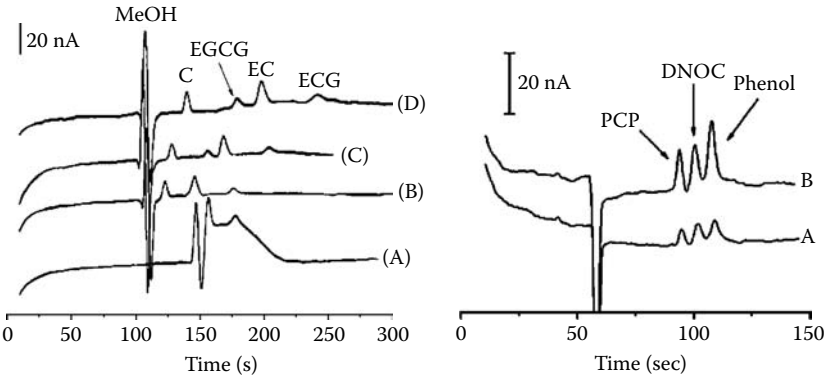

FIGURE 10.5
(Left) Effect of the surfactant concentration on the separation of catechin (C), epigallocatechin gallate (EGCG), epicatecatechin (EC) and epicatechin gallate (ECG). (a) No SDS added to the BGE, (b) 10 mM SDS, (c) 20 mM SDS and (d) 30 mM SDS. (Reprinted from Hompesch, R.W., Garcia, C.D., Weiss, D.J., Vivanco, J.M., and Henry, C.S., *Analyst* 2005, 130(5), 694–700. With permission.) (Right) Separation and PAD of phenols using the PDMS microchip. (a) 22.5 μM phenol, 13.1 μM pentachlorophenol, and 8.3 μM 4,6- dinitro-o-cresol. (b) 67.7 μM phenol, 39.4 μM pentachlorophenol, and 25.0 μM 4,6-dinitro-o-cresol. Reprinted from Ding, Y. and Garcia, C.D., *Analyst* 2006, 131(2), 208–214. With permission.)

in a dilute urine sample in less than 30 s. A three-dimensional positioner was used to align the electrode and the channel outlet. Both total homocysteine (tHcy) and protein-bound homocysteine (pbHcy) in plasma were detected by end-column and off-column amperometric detection using a Au/Hg wire microelectrode. The detection limit for homocysteine was 500 nM and the response was linear between 1 and 100 μM.[129] A number of other papers reported the use of solid metallic electrodes (gold or platinum) for coupling EC with microchip CE.[63,64,132–134] It is worth noting the novelty of the design presented by Garcia and Henry (described in Section 10.5.3) for the integration of gold wires with PDMS chips.[3,31,49,52–55] Examples of these results are included in Figure 10.5.

10.9.2 Carbon Electrodes

Carbon has been well established for many years as an electrode material. It is mechanically and thermally stable, impermeable to gases, and fluids, and chemically resistant to a broad range of solvents. In addition, the low cost, great applicability, and low background currents over a wide potential range have driven years of research, particularly in electroanalysis.[69] The primary advantage of carbon electrodes, however, lies in their resistance to fouling by organic redox couples.[48] Carbon electrodes can be used for many runs without fouling, while metal electrodes require periodic electrochemical cleaning.

The advantages of carbon electrodes were combined with a microfluidic device for conducting enzyme immunoassays. The lab-on-a-chip protocol

integrates precolumn reactions of alkaline phosphatase–labeled antibody (anti-mouse IgG) with the antigen (mouse IgG), followed by electrophoretic separation of the free antibody and antibody-antigen complex. The separation is followed by a postcolumn reaction of the enzyme tracer with the 4-aminophenyl phosphate substrate and subsequent amperometric detection of the liberated 4-aminophenol product. A remarkably low detection limit of 2.5×10^{16} g/mL (2aM) was obtained for the mouse IgG model analyte.[135] Aromatic amino acids (tyrosine, 5-hydroxytryptophan, tryptophan, *p*-aminobenzoic acid, and *m*-aminobenzoic acid) were also separated and detected using carbon surfaces.[136] In this case, the working electrode was a thick-film carbon-strip electrode positioned opposite the outlet of the separation channel.

Multistrand carbon-fiber microdisk electrodes were constructed with 6 μm O. carbon fibers. A bundle (about 30 to 40 fibers) of 30 mm–long carbon fibers were carefully inserted into a 20 mm length × 250 μm ID and 375 μm OD fused-silica capillary, from one terminal (connection terminal) of the capillary until the fibers protruded from the other end of the capillary. Epoxy, copper wire, and mercury were used to allow electrical contact. After curing, the capillary was cut to a disk, polished with abrasive paper, and cleaned ultrasonically. The microdisk electrode was inserted into the orientating bore on the chip, moving toward the separation channel along the groove under the bottom of the detection cell until a desired distance (20 to 50 μm) between the disk surface of the electrode and the channel exit.[137] Carbon fibers,[138] a sol-gel-derived carbon composite,[139] carbon ink,[140] and pyrolyzed photoresist carbon films[141] are additional examples of the analytical performance of carbon electrodes.

The first reported use of a carbon-paste electrochemical detector for microchip capillary electrophoresis (CE) was described by Martin et al. A PDMS microchip CE device was constructed by reversibly sealing a PDMS layer containing separation and injection channels to a separate PDMS layer that contained carbon-paste working electrodes. End-channel amperometric detection with a single electrode was used to detect amino acids derivatized with naphthalene dicarboxaldehyde. Two electrodes were placed in series for dual electrode detection. This approach was also demonstrated for the detection of copper(II) peptide complexes. A major advantage of carbon paste is that catalysts can be easily incorporated into the electrode. Carbon paste that was chemically modified with cobalt phthalocyanine was used for the detection of thiols following a CE separation. These devices illustrate the potential for an easily constructed microchip CE system with a carbon-based detector that exhibits adjustable selectivity.[142]

Carbon nanotubes have begun to attract enormous interest in electrochemistry because of their small size and good electrochemical properties. The vast majority of studies thus far have used ensembles of carbon nanotubes and nanostructure macroscopic electrodes either with randomly dispersed nanotubes or with aligned carbon nanotubes.[143–146] The resultant nanotube-modified electrodes have most frequently been used for electroanalytical purposes such as the development of biosensors. The carbon nanotube

(CNT)-modified electrode also allows CE amperometric detection at significantly lower operating potentials and yields substantially enhanced signal-to-noise characteristics. Such advantages were illustrated in connection with several classes of hydrazine, phenol, purine, and amino acids and tyrosine.[147] Although some advantages of the use of CNT are clear, the reported detection limits for catechol and dopamine were still 7 and 8 μM, respectively. Carbon nanotube electrodes have also been demonstrated to be highly useful as detectors in flow injection analysis and standard capillary electrophoresis.[148,149]

Thin films of highly boron-doped diamond (BDD) have also recently received increasing attention as new electrode materials for electrochemical applications. Such material exhibits attractive electrochemical properties, including low and stable background currents, a wide potential window in aqueous media, high resistance to deactivation via analyte fouling, and long-term stability. Based on these unique features, several groups have reported on the favorable analytical performance of diamond electrodes in various electroanalytical measurements of biologically and environmentally important compounds.[120,121,150] A chemically vapor-deposited boron-doped diamond (BDD) film band electrode was used for end-column amperometric detection (Figure 10.6). The favorable performance of the diamond electrode microchip detector was indicated from comparison to a commonly used thick-film carbon detector. The diamond electrode offered enhanced sensitivity, lower noise levels, and sharper peaks for several groups of important analytes (nitroaromatic explosives, organophosphate nerve agents, phenols).[120,121,150]

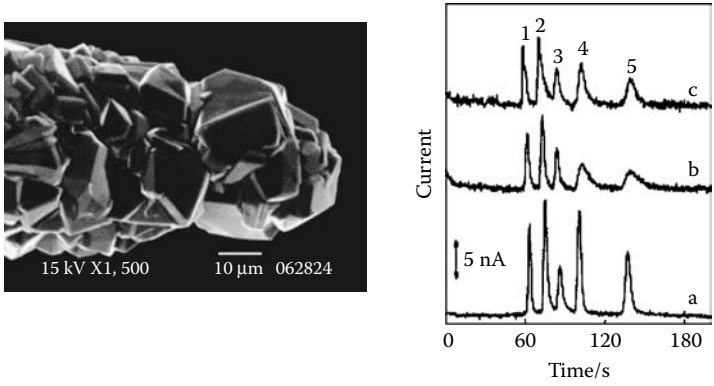

FIGURE 10.6
(Left) SEM image of a BDD microfiber electrode on a tungsten wire. (Right) Electropherograms of five aromatic amines, detected with boron-doped diamond (a), screen-printed carbon (b), and glassy carbon (c) electrodes. Sample mixture: 50 μM 4-aminophenol (1), 50 μM 1,2-phenylenediamine (2), 50 μM 2-aminonaphthalene (3), 100 μM 2-chloroaniline (4), and 100 μM o-aminobenzoic acid (5). Operation conditions: separation buffer solution, 30 mM acetate buffer (pH 4.5); separation voltage, +1500 V; injection voltage, +2000 V for 1 s; working potential, +1.1 V (a), +0.9 V (b), +0.9 V (c) (with respect to Ag/AgCl wire). (Reprinted from Einaga, Y., Sato, R., Olivia, H., Shin, D., Ivandini, T.A., and Fujishima, A., *Electrochim. Acta* 2004, 49(22–23), 3989. With permission.)

10.10 Conclusions and Future Directions

A large number of publications have been presented in recent years focusing on microchip CE-ECD. More and more groups are recognizing the great potential of electroanalytical techniques, particularly coupled to microchip CE. Among others, conductivity and amperometry are the most reported techniques due to their universality and simplicity. Other detection techniques, such as pulsed amperometric detection or dual detection schemes require more complex instrumentation and characterization, but also show significant potential for future applications. Conventional electrode materials such as gold or platinum are still used by most research groups but the introduction of carbon electrodes in the paste, diamond, and nanotube forms is very promising in terms of future analytical applications. The detection limit is still a problem to be solved in microchip CE-EC. Although great progress has been shown, typical detection limits are in the low μM to high nM range. To increase either the collection efficiency or the capacity of handling larger samples in order to work with real samples below the nM range is one of the future challenges in the area. Certainly, the future direction and limits of this technology are unpredictable, however it is a great pleasure to see that novel ideas are being published every day in the literature.

Acknowledgments

Carlos Garcia thanks The University of Texas at San Antonio and the San Antonio Area Foundation for financial support. In addition, the authors would like to thank Scott Martin and Jonathon Vickers for input on this chapter. Financial support for a portion of the work shown here was provided by the Department of Energy.

References

1. Manz, A., Graber, N., and Widmer, H.M., Miniaturized total chemical analysis systems: a novel concept for chemical sensing. *Sens. Actuators, B* 1990, B1, 244–248.
2. Terry, S.C., Jerman, J.H., and Angell, J.B., A gas chromatograph air analyzer fabricated on a silicon wafer. *IEEE Trans. Electron. Devices* 1979, ED-26, 1880.
3. Garcia, C.D., Engling, G., Herckes, P., Collett, J.L., Jr., and Henry, C.S., Determination of levoglucosan from smoke samples using microchip capillary electrophoresis with pulsed amperometric detection. *Environ. Sci. Technol.* 2005, 39(2), 618–623.

4. Johnson, M.E. and Landers, J.P., Fundamentals and practice for ultrasensitive laser-induced fluorescence detection in microanalytical systems. *Electrophoresis* 2004, 25(21–22), 3513–3527.
5. Bruin, G.J., Recent developments in electrokinetically driven analysis on microfabricated devices. *Electrophoresis* 2000, 21(18), 3931–3951.
6. Lacher, N.A., Garrison, K.E., Martin, R.S., and Lunte, S.M., Microchip capillary electrophoresis/electrochemistry. *Electrophoresis* 2001, 22(12), 2526–2536.
7. Tanyanyiwa, J., Leuthardt, S., and Hauser, P.C., Conductimetric and potentiometric detection in conventional and microchip capillary electrophoresis. *Electrophoresis* 2002, 23(21), 3659–3666.
8. Wang, J., Portable electrochemical systems. *TrAC. Anal. Chem.* 2002, 21(4), 226–232.
9. Vandaveer, W.R.I.V., Pasas, S.A., Martin, R.S., and Lunte, S.M., Recent developments in amperometric detection for microchip capillary electrophoresis. *Electrophoresis* 2002, 23 (21), 3667–3677.
10. Rossier, J., Reymond, F., and Michel, P.E., Polymer microfluidic chips for electrochemical and biochemical analyses. *Electrophoresis* 2002, 23 (6), 858–867.
11. Holland, L.A. and Leigh, A.M., Amperometric and voltammetric detection for capillary electrophoresis. *Electrophoresis* 2002, 23(21), 3649–3658.
12. Ehrfeld, W., Electrochemistry and microsystems. *Electrochim. Acta* 2003, 48 (20–22), 2857.
13. Liu, Y., Garcia, C.D., and Henry, C.S., Recent progress in the development of micro-TAS for clinical analysis. *Analyst* 2003, 128(8), 1002–1008.
14. Guijt, R.M., Evenhuis, C.J., Macka, M., and Haddad, P.R., Conductivity detection for conventional and miniaturised capillary electrophoresis systems. *Electrophoresis* 2004, 25(23–24), 4032–4057.
15. Wang, J., Electrochemical detection for capillary electrophoresis microchips: a review. *Electroanalysis* 2005, 17(13), 1133–1140.
16. Garcia, C.D. and Henry, C.S., Coupling capillary electrophoresis with pulsed amperometric detection. *Electroanalysis* 2005, 17(13), 1125–1131.
17. Nyholm, L., Electrochemical techniques for lab-on-a-chip applications. *Analyst* 2005, 130(5), 599–605.
18. Mogensen, K.B., Klank, H., and Kutter, J.P., Recent developments in detection for microfluidic systems. *Electrophoresis* 2004, 25(21–22), 3498–3512.
19. Vilkner, T., Jansek, D., and Manz, A., Micro total analysis systems: recent developments. *Anal. Chem.* 2004, 76(12), 3373–3386.
20. Becker, H. and Locascio, L., Polymer microfluidic devices. *Talanta* 2002, 56(2), 267–287.
21. Henry, C.S., *Microchip Capillary Electrophoresis: Methods and Protocols*. Humana Press, Totowa, NJ, 2005.
22. Jorgenson, J.W. and Lukacs, K.D., Zone electrophoresis in open-tubular glass-capillaries. *Anal. Chem.* 1981, 53(8), 1298–1302.
23. Righetti, P.G., Electrophoresis: the march of pennies, the march of dimes. *J. Chromatogr. A* 2005, 1079(1–2), 24.
24. Wallingford, R.A. and Ewing, A.G., Capillary zone electrophoresis with electrochemical detection. *Anal. Chem.* 1987, 59(14), 1762–1766.
25. Wallingford, R.A. and Ewing, A.G., Amperometric detection of catechols in capillary zone electrophoresis with normal and micellar solutions. *Anal. Chem.* 1988, 60(3), 258–263.

26. Manz, A., Harrison, D.J., Verpoorte, E.M.J., Fettinger, J.C., Paulus, A., Luedi, H., and Widmer, H.M., Planar chips technology for miniaturization and integration of separation techniques into monitoring systems. Capillary electrophoresis on a chip. *J. Chromatogr.* 1992, 593(1–2), 253–258.
27. Gavin, P.F. and Ewing, A.G., Continuous separations with microfabricated electrophoresis-electrochemical array detection. *J. Am. Chem. Soc*. 1996, 118(37), 8932–8936.
28. Woolley, A.T., Lao, K., Glazer, A.N., and Mathies, R.A., Capillary electrophoresis chips with integrated electrochemical detection. *Anal. Chem.* 1998, 70(4), 684–688.
29. Martin, R.S., Ratzlaff, K.L., Huynh, B.H., and Lunte, S.M., In-channel electrochemical detection for microchip capillary electrophoresis using an electrically isolated potentiostat. *Anal. Chem.* 2002, 74(5), 1136–1143.
30. Jackson, D.J., Naber, J.F., Roussel, T.J., Jr., Crain, M.M., Walsh, K.M., Keynton, R.S., and Baldwin, R.P., Portable high-voltage power supply and electrochemical detection circuits for microchip capillary electrophoresis. *Anal.Chem.*2003, 75(14), 3643–3649.
31. Garcia, C.D., Liu, Y., Anderson, P., and Henry, C.S., Versatile 3-channel high-voltage power supply for microchip capillary electrophoresis. *Lab Chip* 2003, 3(4), 331–335.
32. Jiang, L., Lu, Y., Dai, Z., Xie, M., and Lin, B., Mini-electrochemical detector for microchip electrophoresis. *Lab on a Chip* 2005, 5(9), 930–934.
33. Wang, J., Tian, B., and Sahlin, E., Micromachined electrophoresis chips with thick-film electrochemical detectors. *Anal. Chem.* 1999, 71(23), 5436 –5440.
34. Wang, J., Chatrathi, M.P., and Tian, B., Micromachined separation chips with a precolumn reactor and end-column electrochemical detector. *Anal. Chem.* 2000, 72(23), 5774–5778.
35. Wang, J., Pumera, M., Chatrathi, M.P., Escarpa, A., Konrad, R., Griebel, A., Dorner, W., and Lowe, H., Towards disposable lab-on-a-chip: poly(methylmethacrylate) microchip electrophoresis device with electrochemical detection. *Electrophoresis* 2002, 23(4), 596–601.
36. Zeng, Y., Chen, H., Pang, D.W., Wang, Z.L., and Cheng, J.K., Microchip capillary electrophoresis with electrochemical detection. *Anal. Chem.* 2002, 74(10), 2441–2445.
37. Coltro, W.K., da Silva, J.A., da Silva, H.D., Richter, E.M., Furlan, R., Angnes, L., do Lago, C.L., Mazo, L.H., and Carrilho, E., Electrophoresis microchip fabricated by a direct-printing process with end-channel amperometric detection. *Electrophoresis* 2004, 25(21–22), 3832–3839.
38. Bao, N., Xu, J.-J., Dou, Y.-H., Cai, Y., Chen, H.-Y., and Xia, X.-H., Electrochemical detector for microchip electrophoresis of poly(dimethylsiloxane) with a three-dimensional adjustor. *J. Chromatogr. A* 2004, 1041(1–2), 245.
39. Backofen, U., Matysik, F.M., and Lunte, C.E., A chip-based electrophoresis system with electrochemical detection and hydrodynamic injection. *Anal. Chem.* 2002, 74(16), 4054–4059.
40. Vandaveer, W.R.I.V., Pasas-Farmer, S.A., Fischer, D.J., Frankenfeld, C.N., and Lunte, S.M., Recent developments in electrochemical detection for microchip capillary electrophoresis. *Electrophoresis* 2004, 25(21–22), 3528–3549.
41. Keynton, R.S., Roussel, T.J., Crain, M.M., Jackson, D.J., Franco, D.B., Naber, J.F., Walsh, K.M., and Baldwin, R.P., Design and development of microfabricated capillary electrophoresis devices with electrochemical detection. *Anal. Chim. Acta* 2004, 507(1), 95–105.

42. Baldwin, R.P., Roussel, T.J., Jr., Crain, M.M., Bathlagunda, V., Jackson, D.J., Gullapalli, J., Conklin, J.A., Pai, R., Naber, J.F., Walsh, K.M., and Keynton, R.S., Fully integrated on-chip electrochemical detection for capillary electrophoresis in a microfabricated device. *Anal. Chem.* 2002, 74(15), 3690–3697.
43. Martin, R.S., Gawron, A.J., and Lunte, S.M., Dual-electrode electrochemical detection for poly(dimethylsiloxane)-fabricated capillary electrophoresis microchips. *Anal. Chem.* 2000, 72(14), 3196–3202.
44. Osbourn, D.M. and Lunte, C.E., On-Column Electrochemical Detection for Microchip Capillary Electrophoresis. *Anal. Chem.* 2003, 75(11), 2510–2514.
45. Manica, D.P. and Ewing, A.G., Prototyping disposable electrophoresis microchips with electrochemical detection using rapid marker masking and laminar flow etching. *Electrophoresis* 2002, 23(21), 3735–3743.
46. Henry, C.S., Zhong, M., Lunte, S.M., Kim, M., Bau, H., and Santiago, J.J., Ceramic microchips for capillary electrophoresis-electrochemistry. *Anal. Comm.* 1999, 36(8), 305–307.
47. Gawron, A.J., Martin, R.S., and Lunte, S.M., Microchip electrophoretic separation systems for biomedical and pharmaceutical analysis. *Eur. J. Pharm. Sci.* 2001, 14(1), 1–12.
48. Gawron, A.J., Martin, R.S., and Lunte, S.M., Fabrication and evaluation of a carbon-based dual-electrode detector for poly(dimethylsiloxane) electrophoresis chips. *Electrophoresis* 2001, 22(2), 242–248.
49. Garcia, C.D. and Henry, C.S., Direct determination of carbohydrates, amino acids and antibiotics by microchip electrophoresis with pulsed amperometric detection. *Anal. Chem.* 2003, 75(18), 4778–4783.
50. Liu, Y., Vickers, J.A., and Henry, C.S., Simple and sensitive electrode design for microchip electrophoresis/electrochemistry. *Anal. Chem.* 2004, 76(5), 1513–1517.
51. Garcia, C.D., Dressen, B.M., Henderson, A., and Henry, C.S., Comparison of surfactants for dynamic surface modification of poly(dimethylsiloxane) microchips. *Electrophoresis* 2005, 26, 703–709.
52. Garcia, C.D. and Henry, C.S., Direct detection of renal function markers using microchip CE with pulsed electrochemical detection. *Analyst* 2004, 129(7), 579–584.
53. Garcia, C.D. and Henry, C.S., Enhanced determination of glucose by microchip electrophoresis with pulsed amperometric detection. *Anal. Chim. Acta* 2004, 508(1), 1–9.
54. Garcia, C.D. and Henry, C.S., Comparison of pulsed electrochemical detection modes coupled with microchip capillary electrophoresis. *Electroanalysis* 2005, 17(3), 223–229.
55. Hompesch, R.W., Garcia, C.D., Weiss, D.J., Vivanco, J.M., and Henry, C.S., Analysis of natural flavonoids by microchip-micellar electrokinetic chromatography with pulsed amperometric detection. *Analyst* 2005, 130(5), 694–700.
56. Ding, Y. and Garcia, C.D., Pulsed amperometric detection with poly(dimethylsiloxane)–fabricated capillary electrophoresis microchips for the determination of EPA priority pollutants. *Analyst* 2006, 131(3), 208–214.
57. Vickers, J.A. and Henry, C.S., Unpublished data.
58. Klett, O., Nischang, I., and Nyholm, L., Deviceless decoupled electrochemical detection of catecholamines in capillary electrophoresis using gold microband array electrodes. *Electrophoresis* 2002, 23(21), 3678–3682.
59. Schwarz, M.A., Enzyme-catalyzed amperometric oxidation of neurotransmitters in chip-capillary electrophoresis. *Electrophoresis* 2004, 25(12), 1916–1922.

60. Muck, A., Jr., Wang, J., Jacobs, M., Chen, G., Chatrathi, M.P., Jurka, V., Vyborny, Z., Spillman, S.D., Sridharan, G., and Schoning, M.J., Fabrication of poly(methyl methacrylate) microfluidic chips by atmospheric molding. *Anal. Chem.* 2004, 76(8), 2290–2297.
61. He, F.Y., Liu, A.L., Yuan, J.H., Coltro, W.K., Carrilho, E., and Xia, X.H., Electrokinetic control of fluid in plastified laser-printed poly(ethylene terephthalate)-toner microchips. *Anal. Bioanal. Chem.* 2005, 382(1), 192–197.
62. Schoning, M.J., Jacobs, M., Muck, A., Knobbe, D.T., Wang, J., Chatrathi, M., and Spillmann, S., Amperometric PDMS/glass capillary electrophoresis-based biosensor microchip for catechol and dopamine detection. *Sens. Actuators, B* 2005, 108(1–2), 688.
63. Schwarz, M.A. and Hauser, P.C., Rapid chiral on-chip separation with simplified amperometric detection. *J. Chromatogr. A* 2001, 928(2), 225–232.
64. Schwarz, M.A., Galliker, B., Fluri, K., Kappes, T., and Hauser, P.C., A two-electrode configuration for simplified amperometric detection in a microfabricated electrophoretic separation device. *Analyst* 2001, 126(2), 147–151.
65. Ertl, P., Emrich, C.A., Singhal, P., and Mathies, R.A., Capillary electrophoresis chips with a sheath-flow supported electrochemical detection system. *Anal. Chem.* 2004, 76(13), 3749–3755.
66. Klett, O. and Nyholm, L., Separation high voltage field driven on-chip amperometric detection in capillary electrophoresis. *Anal. Chem.* 2003, 75(6), 1245–1250.
67. Bjorefors, F., Strandman, C., and Nyholm, L., Electrochemical detection based on redox cycling using interdigitated microarray electrodes at mL/min flow rates. *Electroanalysis* 2000, 12(4), 255–261.
68. Klett, O., Bjorefors, F., and Nyholm, L., Elimination of high-voltage field effects in end column electrochemical detection in capillary electrophoresis by use of on-chip microband electrodes. *Anal. Chem.* 2001, 73(8), 1909–1915.
69. Garcia, C.D., De Pauli, C.P., and Ortiz, P.I., Electrochemical characterization of glassy carbon electrodes modified by resol mixtures. *J. Electroanal. Chem.* 2001, 510(1–2), 115–119.
70. Manica, D.P., Mitsumori, Y., and Ewing, A.G., Characterization of electrode fouling and surface regeneration for a platinum electrode on an electrophoresis microchip. *Anal. Chem.* 2003, 75(17), 4572–4577.
71. Johnson, D.C. and LaCourse, W.R., Pulsed electrochemical detection at Nobel metal electrodes in LC. *Electroanalysis* 1992, 4, 367–380.
72. Fanguy, J.C. and Henry, C.S., Pulsed amperometric detection of carbohydrates on an electrophoretic microchip. *Analyst* 2002, 127(8), 1021–1023.
73. LaCourse, W.R. and Modi, S.J., Microelectrode applications of pulsed electrochemical detection. *Electroanalysis* 2005, 17(13), 1141–1152.
74. Zemann, A.J., Conductivity detection in capillary electrophoresis. *TrAC. Anal. Chem.* 2001, 20(6–7), 346.
75. Kuban, P. and Hauser, P.C., Fundamental aspects of contactless conductivity detection for capillary electrophoresis. Part I: Frequency behavior and cell geometry. *Electrophoresis* 2004, 25(20), 3387–3397.
76. Kuban, P. and Hauser, P.C., Fundamental aspects of contactless conductivity detection for capillary electrophoresis. Part II: Signal-to-noise ratio and stray capacitance. *Electrophoresis* 2004, 25(20), 3398–3405.
77. Liu, Y., Wipf, D.O., and Henry, C.S., Conductivity detection for monitoring mixing reactions in microfluidic devices. *Analyst* 2001, 126(8), 1248–1251.

78. Galloway, M., Stryjewski, W., Henry, A., Ford, S.M., Llopis, S., McCarley, R.L., and Soper, S.A., Contact conductivity detection in poly(methyl methacylate)-based microfluidic devices for analysis of mono- and polyanionic molecules. *Anal. Chem.* 2002, 74(10), 2407–2415.
79. Galloway, M. and Soper, S.A., Contact conductivity detection of polymerase chain reaction products analyzed by reverse-phase ion pair microcapillary electrochromatography. *Electrophoresis* 2002, 23(21), 3760–3768.
80. Masar, M., Poliakova, K., Dankova, M., Kaniansky, D., and Stanislawski, B., Determination of organic acids in wine by zone electrophoresis on a chip with conductivity detection. *J. Sep. Sci.* 2005, 28(9–10), 905–914.
81. Guijt, R.M., Baltussen, E., van der Steen, G., Schasfoort, R.B., Schlautmann, S., Billiet, H.A., Frank, J., van Dedem, G.W., and van den Berg, A., New approaches for fabrication of microfluidic capillary electrophoresis devices with on-chip conductivity detection. *Electrophoresis* 2001, 22(2), 235–241.
82. Guijt, R.M., Baltussen, E., van der Steen, G., Frank, H., Billiet, H., Schalkhammer, T., Laugere, F., Vellekoop, M., Berthold, A., Sarro, L., and van Dedem, G.W., Capillary electrophoresis with on-chip four-electrode capacitively coupled conductivity detection for application in bioanalysis. *Electrophoresis* 2001, 22(12), 2537–2541.
83. Laugere, F., Lubking, G.W., Berthold, A., Bastemeijer, J., and Vellekoop, M.J., Downscaling aspects of a conductivity detector for application in on-chip capillary electrophoresis. *Sens. Actuators, A* 2001, 92(1–3), 109.
84. Laugere, F., Lubking, G.W., Bastemeijer, J., and Vellekoop, M.J., Design of an electronic interface for capacitively coupled four-electrode conductivity detection in capillary electrophoresis microchip. *Sens. Actuators, B* 2002, 83(1–3), 104.
85. Wang, J., Pumera, M., Collins, G.E., and Mulchandani, A., Measurements of chemical warfare agent degradation products using an electrophoresis microchip with contactless conductivity detector. *Anal. Chem.* 2002, 74(23), 6121–6125.
86. Pumera, M., Wang, J., Opekar, F., Jelinek, I., Feldman, J., Lowe, H., and Hardt, S., Contactless conductivity detector for microchip capillary electrophoresis. *Anal. Chem.* 2002, 74(9), 1968–1971.
87. Wang, J. and Pumera, M., Nonaqueous electrophoresis microchip separations: conductivity detection in UV-absorbing solvents. *Anal. Chem.* 2003, 75(2), 341–345.
88. Laugere, F., Guijt, R.M., Bastemeijer, J., van der Steen, G., Berthold, A., Baltussen, E., Sarro, P., van Dedem, G.W., Vellekoop, M., and Bosschet, A., On-chip contactless four-electrode conductivity detection for capillary electrophoresis devices. *Anal. Chem.* 2003, 75(2), 306–312.
89. Vogt, O., Pfister, M., Marggraf, U., Neyer, A., Hergenroder, R., and Jacob, P., A new two-chip concept for continuous measurements on PMMA-microchips. *Lab Chip* 2005, 5(2), 205–211.
90. Lichtenberg, J., De Rooij, N.F., and Verpoorte, E., A microchip electrophoresis system with integrated in-plane electrodes for contactless conductivity detection. *Electrophoresis* 2002, 23(21), 3769–3780.
91. Wang, J., Pumera, M., Collins, G., Opekar, F., and Jelinek, I., A chip-based capillary electrophoresis-contactless conductivity microsystem for fast measurements of low-explosive ionic components. *Analyst* 2002, 127(6), 719–723.
92. Tanyanyiwa, J. and Hauser, P.C., High-voltage capacitively coupled contactless conductivity detection for microchip capillary electrophoresis. *Anal. Chem.* 2002, 74(24), 6378–6382.

93. Kuban, P. and Hauser, P.C., Effects of the cell geometry and operating parameters on the performance of an external contactless conductivity detector for microchip electrophoresis. *Lab Chip* 2005, 5(4), 407–415.
94. Kuban, P. and Hauser, P.C., Application of an external contactless conductivity detector for the analysis of beverages by microchip capillary electrophoresis. *Electrophoresis* 2005, 26(16), 3169–3178.
95. Tanyanyiwa, J., Abad-Villar, E.M., Fernández-Abedul, M.T., Costa-García, A., Hoffmann, W., Guber, A.E., Herrmann, D., Gerlach, A., Gottschlich, N., and Hauser, P.C., High-voltage contactless conductivity-detection for lab-on-chip devices using external electrodes on the holder. *Analyst* 2003, 128(8), 1019–1022.
96. Tanyanyiwa, J., Abad-Villar, E.M., and Hauser, P.C., Contactless conductivity detection of selected organic ions in on-chip electrophoresis. *Electrophoresis* 2004, 25(6), 903–908.
97. Abad-Villar, E.M., Kuban, P., and Hauser, P.C., Determination of biochemical species on electrophoresis chips with an external contactless conductivity detector. *Electrophoresis* 2005, 26(19), 3609–3614.
98. Bai, X., Wu, Z., Josserand, J., Jensen, H., Schafer, H., and Girault, H.H., Passive conductivity detection for capillary electrophoresis. *Anal Chem* 2004, 76(11), 3126–3131.
99. Kuban, P., Dasgupta, P.K., and Morris, K.A., Microscale continuous ion exchanger. *Anal. Chem.* 2002, 74(21), 5667–5675.
100. Kuban, P., Berg, J., and Dasgupta, P.K., Vertically stratified flows in microchannels. Computational simulations and applications to solvent extraction and ion exchange. *Anal. Chem.* 2003, 75(14), 3549–3556.
101. Grab, B., Neyer, A., Johnck, M., Siepe, D., Eisenbeib, F., Weber, G., and Hergenroder, R., A new PMMA-microchip device for isotachophoresis with integrated conductivity detector. *Sens. Actuators, B* 2001, 72(3), 249.
102. Grab, B., Siepe, D., Neyer, A., and Hergenroder, R., Comparison of different conductivity detector geometries on an isotachophoresis PMMA-microchip. *Fresenius J. Anal. Chem.* 2001, 371(2), 228–233.
103. Bodor, R., Kaniansky, D., Masar, M., Silleova, K., and Stanislawski, B., Determination of bromate in drinking water by zone electrophoresis-isotachophoresis on a column-coupling chip with conductivity detection. *Electrophoresis* 2002, 23(20), 3630–3637.
104. Prest, J.E., Baldock, S.J., Fielden, P.R., Goddard, N.J., and Treves Brown, B.J., Analysis of amino acids by miniaturised isotachophoresis. *J. Chromatogr. A* 2004, 1051(1–2), 221.
105. Kaniansky, D., Masar, M., Bielcikova, J., Ivanyi, F., Eisenbeiss, F., Stanislawski, B., Grass, B., Neyer, A., and Johnck, M., Capillary electrophoresis separations on a planar chip with the column-coupling configuration of the separation channels. *Anal. Chem.* 2000, 72(15), 3596–3604.
106. Kaniansky, D., Masar, M., Dankova, M., Bodor, R., Rakocyova, R., Pilna, M., Johnck, M., Stanislawski, B., and Kajan, S., Column switching in zone electrophoresis on a chip. *J. Chromatogr. A* 2004, 1051(1–2), 33.
107. Wang, J., Polsky, R., Tian, B., and Chatrathi, M.P., Voltammetry on microfluidic chip platforms. *Anal. Chem.* 2000, 72(21), 5285–5289.
108. Hebert, N.E., Kuhr, W.G., and Brazill, S.A., Microchip capillary electrophoresis coupled to sinusoidal voltammetry for the detection of native carbohydrates. *Electrophoresis* 2002, 23(21), 3750–3759.

109. Hebert, N.E., Kuhr, W.G., and Brazill, S.A., A microchip electrophoresis device with integrated electrochemical detection: a direct comparison of constant potential amperometry and sinusoidal voltammetry. *Anal. Chem.* 2003, 75(14), 3301–3307.
110. Yu, R.-Q., Zhang, Z.-R., and Shen, G.-L., Potentiometric sensors: aspects of the recent development. *Sens. Actuators B* 2000, 65(1–3), 150.
111. Lai, C.-C.J., Chen, C.-h., and Ko, F.-H., In-channel dual-electrode amperometric detection in electrophoretic chips with a palladium film decoupler. *J. Chromatogr. A* 2004, 1023(1), 143.
112. Wang, J. and Pumera, M., Dual conductivity/amperometric detection system for microchip capillary electrophoresis. *Anal. Chem.* 2002, 74(23), 5919–5923.
113. Lapos, J.A., Manica, D.P., and Ewing, A.G., Dual fluorescence and electrochemical detection on an electrophoresis microchip. *Anal. Chem.* 2002, 74(14), 3348–3353.
114. Rossier, J.S., Ferrigno, R., and Girault, H.H., Electrophoresis with electrochemical detection in a polymer microdevice. *J. Electroanal. Chem.* 2000, 492(1), 15–22.
115. Lacher, N.A., Lunte, S.M., and Martin, R.S., Development of a microfabricated palladium decoupler/electrochemical detector for microchip capillary electrophoresis using a hybrid glass/poly(dimethylsiloxane) device. *Anal. Chem.* 2004, 76(9), 2482–2491.
116. Du, Y., Yan, J., Zhou, W., Yang, X., and Wang, E., Direct electrochemical detection of glucose in human plasma on capillary electrophoresis microchips. *Electrophoresis* 2004, 25(21–22), 3853–3859.
117. Chen, D., Hsu, F.L., Zhan, D.Z., and Chen, C., Palladium film decoupler for amperometric detection in electrophoresis chips. *Anal. Chem.* 2001, 73(4), 758–762.
118. Wu, C.C., Wu, R.G., Huang, J.G., Lin, Y.C., and Hsien-Chang, C., Three-electrode electrochemical detector and platinum film decoupler integrated with a capillary electrophoresis microchip for amperometric detection. *Anal. Chem.* 2003, 75(4), 947–952.
119. Kovarik, M.L., Li, M.W., and Martin, R.S., Integration of a carbon microelectrode with a microfabricated palladium decoupler for use in microchip capillary electrophoresis/electrochemistry. *Electrophoresis* 2005, 26(1), 202–210.
120. Shin, D., Tryk, D.A., Fujishima, A., Jr., A.M., Chen, G., and Wang, J., Microchip capillary electrophoresis with a boron-doped diamond electrochemical detector for analysis of aromatic amines. *Electrophoresis* 2004, 25(17), 3017–3023.
121. Einaga, Y., Sato, R., Olivia, H., Shin, D., Ivandini, T.A., and Fujishima, A., Modified diamond electrodes for electrolysis and electroanalysis applications. *Electrochim. Acta* 2004, 49(22–23), 3989.
122. Wang, J., Chatrathi, M.P., Tian, B., and Polsky, R., Microfabricated electrophoresis chips for simultaneous bioassays of glucose, uric acid, ascorbic acid, and acetaminophen. *Anal. Chem.* 2000, 72(11), 2514–2518.
123. Wang, J., Chatrathi, M.P., and Tian, B., Microseparation chips for performing multienzymatic dehydrogenase/oxidase assays: simultaneous electrochemical measurement of ethanol and glucose. *Anal. Chem.* 2001, 73(6), 1296–1300.
124. Wang, J. and Chatrathi, M.P., Microfabricated electrophoresis chip for bioassay of renal markers. *Anal. Chem.* 2003, 75(3), 525–529.
125. Wang, J., Tian, B., and Sahlin, E., Integrated electrophoresis chips/amperometric detection with sputtered gold working electrodes. *Anal. Chem.* 1999, 71, 3901–3904.

126. Wang, J., Ibanez, A., and Chatrathi, M.P., Microchip-based amperometric immunoassays using redox tracers. *Electrophoresis* 2002, 23(21), 3744–3749.
127. Pumera, M., Wang, J., Lowe, H., and Hardt, S., Poly(methylmethacrylate) microchip electrophoresis device with thick-film amperometric detector: towards fully disposable lab-on-a-chip. *J. Assoc. Lab. Auto.* 2002, 7(2), 73.
128. Lee, H.-L. and Chen, S.-C., Microchip capillary electrophoresis with amperometric detection for several carbohydrates. *Talanta* 2004, 64(1), 210.
129. Pasas, S.A., Lacher, N.A., Davies, M.I., and Lunte, S.M., Detection of homocysteine by conventional and microchip capillary electrophoresis/electrochemistry. *Electrophoresis* 2002, 23(5), 759–766.
130. Wang, J., Ibanez, A., and Chatrathi, M.P., On-chip integration of enzyme and immunoassays: simultaneous measurements of insulin and glucose. *J. Am. Chem. Soc.* 2003, 125(28), 8444–8445.
131. Fanguy, J.C. and Henry, C.S., The analysis of uric acid in urine using microchip capillary electrophoresis with electrochemical detection. *Electrophoresis* 2002, 23(5), 767–773.
132. He, F.Y., Liu, A.L., and Xia, X.H., Poly(dimethylsiloxane) microchip capillary electrophoresis with electrochemical detection for rapid measurement of acetaminophen and its hydrolysate. *Anal. Bioanal. Chem.* 2004, 379(7–8), 1062–1067.
133. Yin, X.-B., Kang, J., Fang, L., Yang, X., and Wang, E., Short-capillary electrophoresis with electrochemiluminescence detection using porous etched joint for fast analysis of lidocaine and ofloxacin. *J. Chromatogr. A* 2004, 1055(1–2), 223.
134. Castano-Alvarez, M. and Fernandez-Abedul, M.T., Costa-Garcia, A., Poly(methylmethacrylate) and Topas capillary electrophoresis microchip performance with electrochemical detection. *Electrophoresis* 2005, 26(16), 3160–3168.
135. Wang, J., Ibanez, A., Chatrathi, M.P., and Escarpa, A., Electrochemical enzyme immunoassays on microchip platforms. *Anal. Chem.* 2001, 73(21), 5323–5327.
136. Wang, J. and Chen, G., Microchip capillary electrophoresis with electrochemical detector for fast measurements of aromatic amino acids. *Talanta* 2003, 60(6), 1239–1244.
137. Wang, Y. and Chen, H., Integrated capillary electrophoresis amperometric detection microchip with replaceable microdisk working electrode: II. Influence of channel cross-sectional area on the separation and detection of dopamine and catechol. *J. Chromatogr. A* 2005, 1080(2), 192.
138. Woods, L.A. and Ewing, A.G., Etched electrochemical detection for electrophoresis in nanometer inner diameter capillaries. *ChemPhysChem* 2003, 4(2), 207–211.
139. Sun, X., Yan, J., Yang, X., and Wang, E., Electrochemical detector based on sol-gel-derived carbon composite material for capillary electrophoresis microchips. *Electrophoresis* 2004, 25(20), 3455–3460.
140. Wang, J., Chatrathi, M.P., and Tian, B., Capillary electrophoresis microchips with thick-film amperometric detectors: separation and detection of phenolic compounds. *Anal. Chim. Acta* 2000, 416(1), 9.
141. Hebert, N.E., Snyder, B., McCreery, R.L., Kuhr, W.G., and Brazill, S.A., Performance of pyrolyzed photoresist carbon films in a microchip capillary electrophoresis device with sinusoidal voltammetric detection. *Anal. Chem.* 2003, 75(16), 4265–4271.
142. Martin, R.S., Gawron, A.J., Fogarty, B.A., Regan, F.B., Dempsey, E., and Lunte, S.M., Carbon paste-based electrochemical detectors for microchip capillary electrophoresis/electrochemistry. *Analyst* 2001, 126(3), 277–280.

143. Lin, Y., Taylor, S., Li, H., Fernando, K.A.S., Qu, L., Wang, W., Gu, L., Zhou, B., and Sun, Y.-P., Advances toward bioapplications of carbon nanotubes. *J. Mater. Chem.* 2004, 14(4), 527–541.
144. Karajanagi, S.S., Vertegel, A.A., Kane, R.S., and Dordick, J.S., Structure and function of enzymes adsorbed onto single-walled carbon nanotubes. *Langmuir* 2004, 20(26), 11594–11599.
145. Cai, C. and Chen, J., Direct electron transfer of glucose oxidase promoted by carbon nanotubes. *Anal. Biochem.* 2004, 332(1), 75–83.
146. Gooding, J.J., Nanostructuring electrodes with carbon nanotubes: a review on electrochemistry and applications for sensing. *Electrochim. Acta* 2005, 50(15), 3049.
147. Wang, J., Chen, G., Chatrathi, M.P., and Musameh, M., Capillary electrophoresis microchip with a carbon nanotube-modified electrochemical detector. *Anal. Chem.* 2004, 76(2), 298–302.
148. Chicharro, M., Sanchez, A., Zapardiel, A., Rubianes, M.D., and Rivas, G., Capillary electrophoresis of neurotransmitters with amperometric detection at melanin-type polymer-modified carbon electrodes. *Anal. Chem. Acta* 2004, 523, 185–191.
149. Deo, R.P. and Wang, J., Electrochemical detection of carbohydrates at carbon-nanotube modified glassy-carbon electrodes. *Electrochem. Commun.* 2004, 6(3), 284–287.
150. Wang, J., Chen, G., Chatrathi, M.P., Fujishima, A., Tryk, D.A., and Shin, D., Microchip capillary electrophoresis coupled with a boron-doped diamond electrode-based electrochemical detector. *Anal. Chem.* 2003, 75(4), 935–939.

11

Culture-Based Biochip for Rapid Detection of Environmental Mycobacteria

Ian Papautsky and Daniel Oerther

CONTENTS

11.1 Introduction

To environmental engineers, microorganisms are important for a number of reasons. First and foremost, pathogenic microorganisms represent a threat to public health and must be eliminated from potable water. Some biocatalytic microorganisms are used in bioprocesses to remove toxic pollutants (i.e., bioremediation) and thus should be encouraged to thrive. Yet others are nuisance microorganisms that upset the steady-state performance of bioprocesses. For environmental engineers, mycobacteria represent all three types. For instance, *Gordonia* (formerly *Nocardia*) *amarae* have been shown to

be a causative agent for the formation of filamentous nuisance biological foam (e.g., nocardiafoam) on the surfaces of aeration basins, secondary clarifiers, and anaerobic digesters in municipal sewage treatment around the world [1–3]. The problem of nocardiafoam has been studied for more than thirty years, and the estimated total accumulative cost of incidences of nocardiafoam disrupting the acceptable performance of sewage treatment plants is on the order of $1 billion.

Perhaps most notable of all mycobacteria are the pathogens *Mycobacterium tuberculosis* (i.e., the etiological agent of the disease tuberculosis [TB]) and *Mycobacterium leprae* (i.e., the etiological agent of the disease leprosy). Although TB was nearly eradicated during the 20th century, occurrence of the illness is rising, with more than two million annual deaths attributed to TB, especially in less developed countries—the largest number of deaths attributed to a single organism. This resurgence of TB is significantly more dangerous because the widespread use of antibiotics over the past fifty years has lead to the emergence of *Mycobacterium* demonstrating multiple-antibiotic resistance [4]. Furthermore, with the outbreak of human immuno virus (HIV)–induced acquired immunodeficiency syndrome (AIDS) in the industrialized world beginning in the 1980s, the infection of immunocompromised individuals with opportunistic pathogens belonging to the *Mycobacterium avium* complex (MAC) has risen dramatically [5,6]. Although a historically well-known opportunistic pathogen, MACs generally do not infect individuals with healthy immune systems. Instead, individuals suffering from HIV infection, patients on a regimen of immunosuppressant medication, as well as children and the elderly are the most commonly infected individuals. Because MAC infection primarily occurs due to oral ingestion, with inhalation as a secondary route, and because MACs are ubiquitous in nature, the United States Environmental Protect Agency (EPA) listed MACs as one of ten microbiological agents of interest on the Drinking Water Contaminant Candidate List (CCL) released in 1998 [7,8].

Mycobacteria are slim, rod-shaped microorganisms approximately 1–10 μm in size [9] with a high guanine plus cytosine content of DNA (high G+C Gram positive bacteria). These microorganisms are characterized by the presence of unique lipids called mycolic acids on the cell surface. Mycolic acid, found only in mycobacteria, is a group of complex branched-chain hydroxyl lipids that is covalently bound to the peptidoglycan of the mycobacterial wall. Mycolic acids make the mycobacterial cell surface hydrophobic and limit the maximum growth rate of the microorganisms. The mycobacteria include six distinct genera: *Corynebacterium*, *Gordonia*, *Mycobacterium*, *Nocardia*, *Rhodococcus*, and *Tsukamurella*. A recent review is available online [10].

The traditional methods of identifying and monitoring mycobacteria in environmental samples include direct observation using microscopy, often coupled with staining procedures or cultivation on semiselective media [11–13]. Although these traditional methods have been used successfully to track mycobacteria in a variety of environmental samples, they suffer a number of limitations. For example, direct observation using microscopy

requires significant training to recognize staining properties and the morphology of individual populations of microorganisms. Furthermore, it is accepted that the staining properties and morphology of microbial populations can change dramatically depending upon the environmental conditions experienced by the microorganisms. Thus, the robust nature of direct observation using microscopy can be questioned. Traditional cultivation of mycobacteria can require 3 to 5 weeks for the growth of colonies on agar surfaces. Obviously, such a turnaround time for an assay is extensive and cannot be classified as rapid by practical standards.

Recently, significant efforts have been invested in the development of molecular biology–based assays to identify and enumerate mycobacteria in environmental samples. Antibody stains [14–16], fluorescence *in situ* hybridization (FISH) targeting 16S ribosomal ribonucleic acid (16S rRNA) [14,17–20], and fatty acid methyl ester (FAME) analysis [21] have been demonstrated successfully, as well as commercial kits such as AccuProbe from Gen-Probe [22] and the COBAS AMPLICOR system from Roche [23]. An important strength of these methods is the ability to identify bacteria without cultivation. However, molecular biology–based techniques often lack the ability to distinguish between living and dead organisms, do not generate cultures that may be assayed subsequently for additional phenotypic traits, and are yet to be integrated into a user-friendly format. These drawbacks have caused cultivation to remain the primary means of screening for mycobacteria in clinical and environmental samples.

To improve culture-based techniques for monitoring specific microbial populations in environmental samples, we have developed a novel approach using microfabrication to create devices to rapidly screen for mycobacteria. Rather than using molecular biology–based assays to identify mycobacteria, we have miniaturized the culture-based assay to rapidly identify individual microbial populations adhered to a semiselective surface material inside a microfluidic biochip. Here we describe the development of this culture-based biochip and the application of this approach to rapid detection of mycobacteria in samples removed from a municipal activated sludge sewage treatment system.

11.2 Culture-Based Approach

The culture-based biochip function is schematically illustrated in Figure 11.1. Microorganisms in the environment are often present in multispecies populations arranged in flocs or biofilms. A sample collected from the environment (e.g., an activated sludge sewage treatment system) is first processed using chemical or physical procedures to disaggregate the microorganisms to release single, planktonic cells. The cell suspension is then incubated with

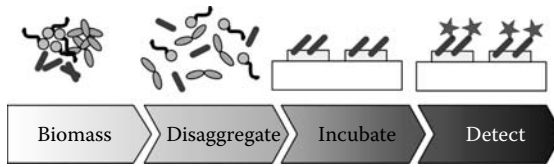

FIGURE 11.1
Culture-based biochip approach to detection of mycobacteria.

a culture-based biochip using available selective culturing conditions to isolate specific microbial populations from a mixture of microorganisms.

The biochip detects mycobacteria using selective culturing conditions based on the hydrophobic properties and the paraffinophilic nature of mycobacteria [11]. As mentioned earlier, one defining characteristic of mycobacteria is the presence of mycolic acid in cell walls. This unique hydrophobic cell envelope permits mycobacteria to preferentially adhere to hydrophobic surfaces such as long-chain saturated aliphatic hydrocarbons (e.g., paraffin) [24]. Another defining characteristic of mycobacteria is the presence of a paraffinase enzyme that allows mycobacteria to utilize paraffin as a carbon source. Thus, mycobacteria can be selectively isolated on paraffin surfaces, which serve as a baiting layer, providing both a hydrophobic surface and a carbon source. The use of this specialized metabolic trait to selectively isolate mycobacteria from environmental samples was first described by Sohngen in 1913 [25] for the selective isolation of *Mycobacterium* spp. and *Nocarida* spp. from soil using paraffin-coated rods. During the past fifteen years, Ollar and coworkers [11] expanded upon these initial studies by developing a paraffin bating technique for selective isolation of mycobacteria from clinical samples. On the biochip surface, target microorganisms become embedded and grow, while nontarget microorganisms are removed by washing. Following this semiselective culturing, target microorganisms are visualized using microscopy coupled with staining.

The primary advantages of the culture-based biochip are speed and specificity. Because microscopy is used to visualize microbial populations, the technique can be performed rapidly without the need for extensive growth of colonies of bacteria. Furthermore, by using an appropriate selective culturing condition, the specificity of the technique can be decided a priori. As described above and discussed extensively in the literature [11], paraffin is a suitable selective culturing surface for environmental mycobacteria. Ultimately, a microfluidic device containing an array of different culture media regions to simultaneously track multiple microbial populations in an environmental sample can be envisioned.

A microfluidic biochip for detection of mycobacteria is illustrated in Figure 11.2. It consists of a microchannel containing paraffin islands used for bating and culturing bacteria. The chip is formed by two plastic wafers, with one wafer containing a trench fabricated with hot embossing. Fabrication of the biochip is conceptually simple and is similar to the fabrication of conventional plastic biochips (see [29] for review). However, there are three main

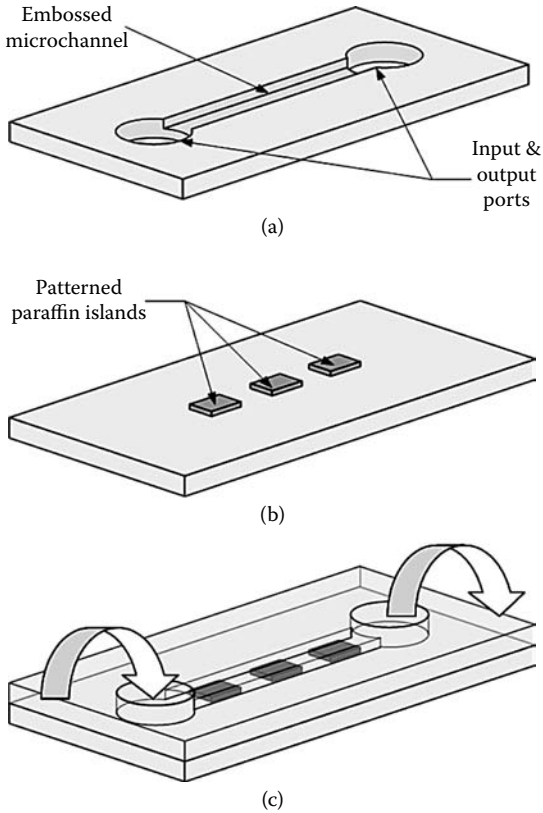

FIGURE 11.2
Schematic diagram of the culture-based microfluidic biochip for detection of mycobacteria. One substrate contains a microfluidic channel (a), while another substrate contains paraffin patterns (b). Two substrates are bonded together to complete the device (c). Arrows indicate the direction of sample flow into and out of the chip.

challenges to miniaturizing this technology: (1) paraffin must be depositing in uniform films of controlled thickness and patterned into detection islands, (2) microorganisms must adhere to and proliferate on the paraffin surfaces, and (3) microfluidic biochip channels containing paraffin patterns must be sealed at low temperature to ensure that paraffin patterns remain unchanged. Each of these challenges is discussed in detail below.

11.3 Paraffin Deposition and Patterning

11.3.1 Paraffins

Paraffin is a common name for a group of saturated hydrocarbons, typically consisting of a mixture of alkanes of different chain lengths. The general

chemical formula for paraffin is C_nH_{2n+2}, where *n* is greater than about 10. There are two hydrogen atoms bonded to each carbon atom of the chain plus an additional hydrogen atom bonded to each end of the chain. These saturated hydrocarbons contain only single bonds and can be arranged in simple straight chains (normal paraffins) or branched chains (isoparaffins). Most of the natural paraffins are normal paraffins, while isoparaffins are frequently produced in refinery processes. Longer-chain paraffins are major constituents of waxes. In most cases, the term *paraffin* refers specifically to normal alkanes.

Normal paraffins are named according to the number of carbon atoms in the chain. Table 11.1 summarizes the names and chemical formulas for several paraffins. The increased length of the carbon chains increases the molar weight, resulting in higher melting temperatures. The large selection of paraffins with different chain lengths means a wide range of melting temperatures. Figure 11.3 illustrates this range for paraffins with 15 to 70 carbon atoms.

Paraffins are characterized by very low chemical reactivity with nearly all materials. The term *paraffin* means chemically inactive, derived from Latin *para affinis* meaning "lacking affinity" or "lacking reactivity." Like most polymeric

TABLE 11.1

Summary of Normal Paraffins

n	Name	Formula
10	*n*-Decane	$CH_3(CH_2)_8CH_3$
15	*n*-Pentadecane	$CH_3(CH_2)_{13}CH_3$
20	*n*-Eicosane	$CH_3(CH_2)_{18}CH_3$
30	*n*-Triacontane	$CH_3(CH_2)_{28}CH_3$
40	*n*-Tetracontane	$CH_3(CH_2)_{38}CH_3$
50	*n*-Pentacontane	$CH_3(CH_2)_{48}CH_3$

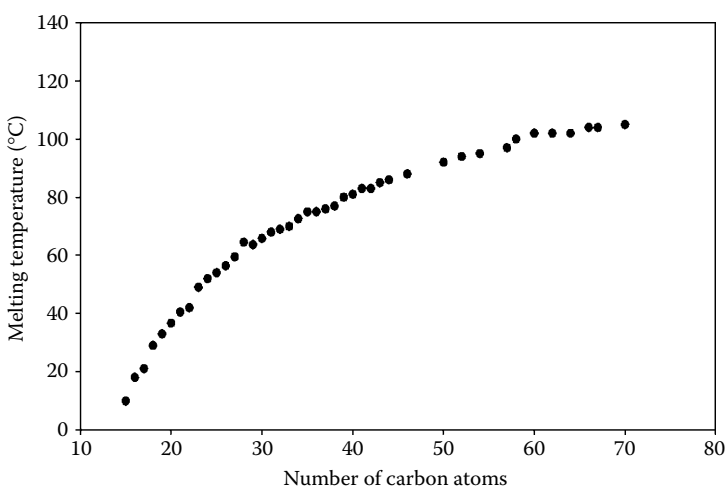

FIGURE 11.3
Variation of paraffin melting temperature based on carbon chain length.

materials, paraffins exhibit low thermal and electrical conductivities, which accounts for their excellent insulating properties. Unlike many other polymeric materials, paraffins are stable throughout phase change cycles because no chemical reactions occur during the thermal energy storage process.

On the macroscale, paraffins are used for a number of applications. Beyond the common use in candle making, paraffins are used in candies or to coat fruits in order to make them look shiny. Although these food-grade paraffins are edible, they are nondigestible and pass right through the body without being broken down. Another common use of paraffins is in preparing specimens for histology in medical and biological applications. In the automotive industry, paraffins have been used as thermostats, and more recently paraffin actuators have been used in positioning systems [30,31] and endoscopic surgical instruments [32].

There has been little reported on using paraffins in microfabrication. One example is the recent work by Mastrangelo and coworkers [33–35], who used paraffin as a working substance in thermally activated microactuators and microfluidic valves. These solid-liquid phase-change devices were fabricated by encapsulating a thin layer of paraffin with paralene. Two paraffins were used in that work: bonding wax from Logitech (bulk melting temperature T_m = 72°C) and *n*-hexatriacontane (C36, T_m = 75°C). These paraffins were thermally evaporated into 9 μm–thick layers and patterned with 20:80 sccm CF_4:O_2 plasma (100 nm/min at 200 W [34]).

Another recent example of paraffin application in microfabrication is the demonstration of thermally activated microactuators and valves by Klintberg and coworkers [36,37]. These devices were fabricated by encapsulating paraffin wax from Sigma-Aldrich (bulk melting temperature T_m = 44 to 46°C) using conventional silicon bulk micromachining [36] or hot embossing of polycarbonate [37]. However, unlike the work by Mastrangelo et al., paraffin was deposited into the prefabricated components, which was accomplished by pumping molten paraffin with a syringelike piston. In order to keep paraffin liquid during filling, the entire system was kept inside a 68°C oven.

For applications in bacteria culturing, microorganisms are sensitive to the complexity of paraffin chains. Mycobacteria exhibit good growth on paraffins with 12 to 23 carbon atoms, with some microorganisms using paraffins up to C40 [24]. On the other hand, poor growth occurs on paraffins with chains of less than 12 carbon atoms or more than 40. Thus, for paraffin baking, pure, relatively short-chain, low-melting temperature paraffins are needed. Consequently, despite the recent examples of paraffin deposition on the microscale discussed above, new approaches to paraffin deposition and patterning are needed.

11.3.2 Paraffin Deposition

In this work, TissuePrep Embedding Media paraffin (T565-2, Fisher Scientific), which exhibits a melting temperature of 55 to 57°C and thus contains

chains about 23 to 25 carbon atoms long, was liquefied and deposited onto clean 18 mm–diameter glass wafers (12-546, Fisher Scientific) using spin coating. Analogous to the traditional photolithographic photoresist polymers, a solvent was used to liquefy paraffin. A number of solvents can be used to dissolve paraffin, including xylene, carbon tetrachloride, acetone, hexane, and butanol [38]. For this application, the choice of solvent must include an appreciation for the impacts of the residual solvent upon the microorganisms. Thus, it is important that any residual solvent remaining in the film does not adversely affect bacterial colonization and proliferation on the microfabricated paraffin surfaces. Xylene and carbon tetrachloride chemically interact with paraffin chains on contact and are toxic to bacteria. Acetone, hexane, and butanol do not interact with paraffin chains and are soluble in paraffin to various degrees [38].

Paraffin and butanol were mixed in defined ratios using a water bath at 70°C. After spin coating, the molten paraffin solidified as it cooled, and the butanol was evaporated by placing the wafers onto a leveled hotplate at 40°C for 2 hours. Using this process, uniform paraffin films of different thickness were successfully deposited and patterned on the surface of 18 mm–diameter glass wafers (Figure 11.4a). The challenge to depositing paraffin was to deposit a uniform film on a glass wafer before the molten paraffin solidified during spin coating. Although paraffin can also be liquefied using a head gun or a high-intensity halogen lamp placed immediately over the glass wafer, it solidifies rapidly and produces inconsistent, chunky layers.

Using paraffin–butanol solutions of different concentrations (0 to 80% butanol by volume) and different spin-coating parameters (1000 to 9000 rpm), paraffin films of any desired thickness from 10 μm to 70 μm can be deposited. Figure 11.5 illustrates the dependence of paraffin film thickness on deposition rpm and solvent concentration. The data were collected by patterning trenches in paraffin film and scanning with a surface profilometer. The data clearly show that increasing the concentration of butanol yields thinner films. This result is consistent with our expectations because increasing butanol content produces films of lower viscosity.

11.3.3 Paraffin Patterning

Paraffin layers were patterned using dry etching. A 20 μm–thick layer of AZ4620 photoresist (Clariant Corp.) was used as a masking layer. Due to the low melting point of paraffin, the photoresist soft bake time was modified to 2 hours on a 40°C hotplate. The resist was exposed and developed in AZ400K developer (Clariant Corp) diluted with water at the ratio of 1:3.5 as normal. The paraffin layer was etched with a mixture of O_2 and CF_4 plasma at 50 W and 20 sccm total flow. The remaining masking AZ4620 photoresist

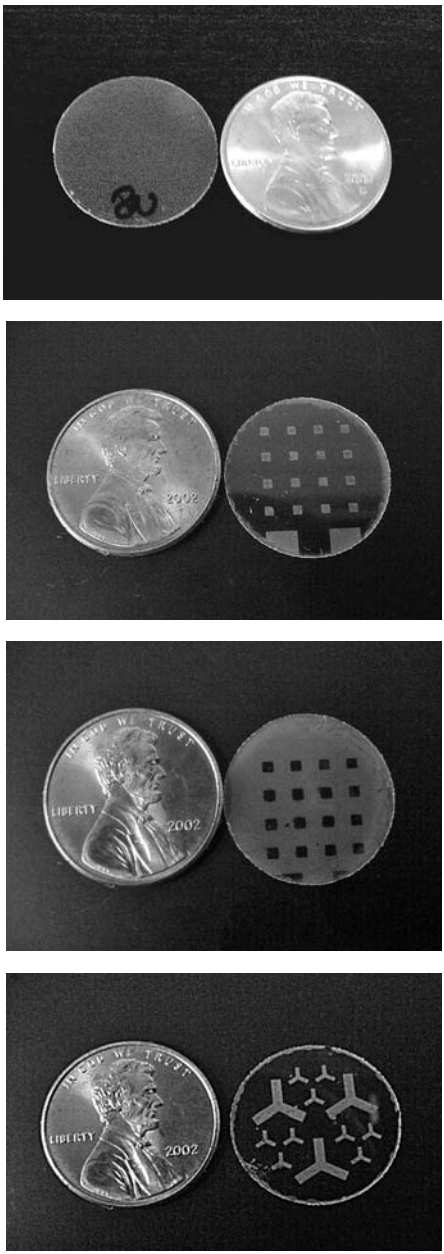

FIGURE 11.4
(a) Photograph of a 18 mm–diameter glass wafer with a 30 μm–thick layer of paraffin. Light-field (b) and dark-field (c) 30 μm–thick paraffin patterns are 750 μm square at 1.5 mm spacing. (d) Y-shaped 30 μm–thick paraffin patterns have characteristic dimensions of 250 μm (smaller patterns) and 1000 μm (larger patterns).

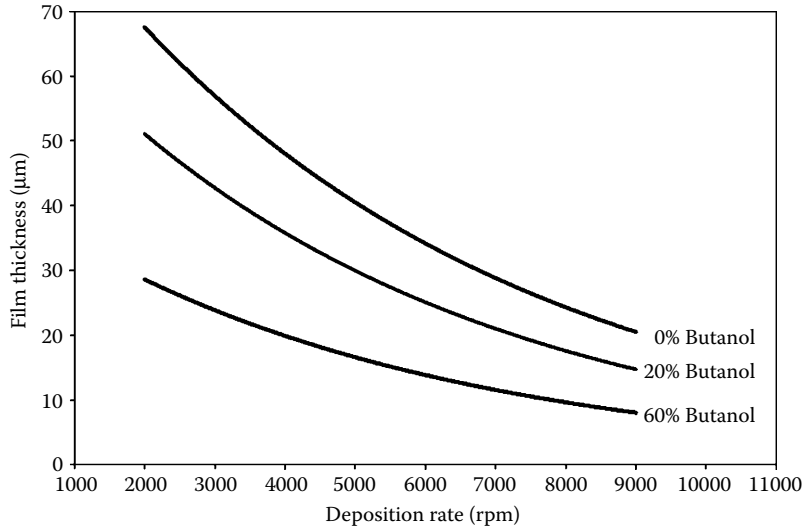

FIGURE 11.5
Dependence of paraffin film thickness on deposition rate and solvent concentration.

was stripped using a flood UV exposure followed by a treatment in undiluted AZ400K developer. The patterns used in this work included 4×4 arrays of 750 μm squares at 1.5 mm spacing, and arrays of Y-shaped patterns with characteristic dimensions of 250 μm (smaller patterns) and 1000 μm (larger patterns). Figure 11.4 illustrates these patterns in both light-field and dark-field in a 30 μm–thick paraffin film.

One of the key challenges to paraffin patterning was to find an appropriate photoresist. Due to the hydrophobic nature of paraffin, conventional photoresists exhibited poor adhesion (e.g., Shipley 1818 or Clariant AZ1500). Paraffin has a low surface tension, with a contact angle measured to be approximately $109° \pm 1°$. Adhesion promoters, such as hexamethyldisilazane (HMDS), showed only marginal improvement in adhesion. Thick photoresist AZ4620 from Clariant Corp., on the other hand, adhered to paraffin. We believe that this is due to the combination of a higher viscosity of this thick photoresist as compared with the conventional photoresists and the *n*-butyl acetate solvent, which has a lower surface energy and thus a higher contact angle. The contact angle of AZ4620 photoresist was measured to be approximately $89° \pm 2°$. Through experimentation, we found that the deposition speed used for the thick photoresist needed to be at least 4000 rpm in order to produce a deposit with minimal edge bead. While the edge bead is easily removed with acetone in conventional microfabrication processing, acetone cannot be used in our process as it attacks paraffin.

In dry etching, the addition of CF_4 was necessary because paraffin was found to exhibit a very low etch rate in pure oxygen plasma. Thus, 3 to 40% CF_4 was added to O_2. Affects of the CF_4-to-O_2 ratio and other fluorine containing gases,

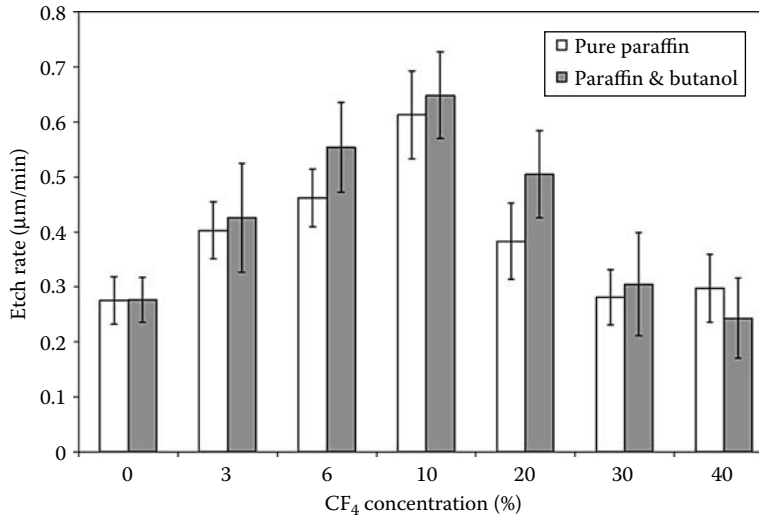

FIGURE 11.6
Dependence of pure paraffin and paraffin with butanol etch rates on the ratio of O_2 and CF_4. Error bars show one standard deviation.

such as CHF_3 and SF_6, were investigated by dry etching arrays of squares in paraffin film and scanning with a surface profilometer to determine the etch rate. From Figure 11.6, it is clear that the etch rate reaches a maximum of approximately 0.6 µm/min when the CF_4 percentage is approximately 10%. We suggest that this is due to the fact that supplementing pure O_2 plasma with fluorine-containing gases, such as CF_4, increases the oxygen atom concentration, which increases the etch rate of polymers, as recently reported [39]. If the ratio of O_2 to CF_4 is increased further and additional fluorine atoms react with paraffin, the rate of a competing reaction that generates nonvolatile products is expected to increase. We believe that this increase in nonvolatile products will prevent the reaction between O_2 and paraffin and thereby reduce the etch rate. The etch rate of paraffin films containing butanol was found to be higher than that of pure paraffin (Figure 11.6), peaking at approximately 0.65 µm/min at 10% CF_4. While the reason for this increased rate is not clear, one possible explanation is that the film containing butanol is less dense than the pure paraffin film due to butanol evaporation after soft baking. With respect to other fluorine-containing gases, CF_4 proved to be the most effective additive (Figure 11.7).

The contact angle of paraffin films before and after patterning were measured to check surface properties. These measurements were important for two reasons. First, O_2 plasma is commonly used to modify surface properties of polymers resulting in significantly lower contact angles [40–42]. Second, our detection approach relies on the hydrophobicity of the paraffin layer to selectively adsorb hydrophobic microorganisms from samples. Thus, changes to phobicity of the paraffin layer will have a direct effect on the

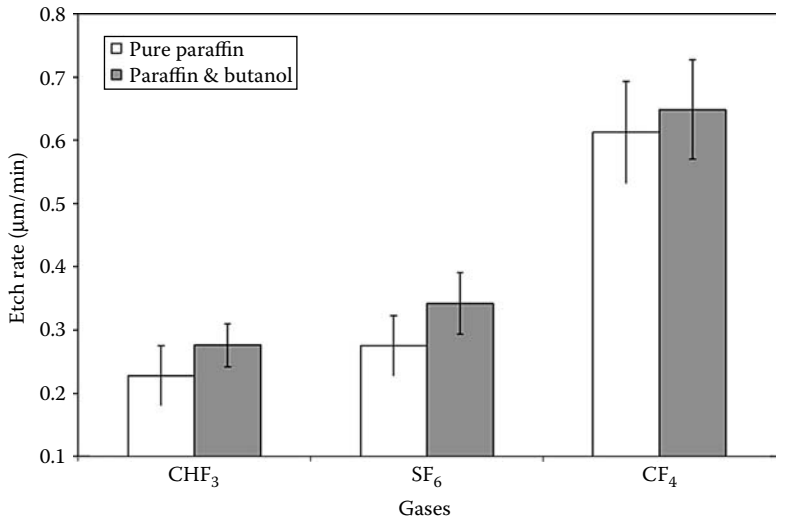

FIGURE 11.7
Etch rate comparison between 10% CHF_3, 10% SF_6, and 10% CF_4 for pure paraffin and paraffin with butanol. Error bars show one standard deviation.

performance of our device. As mentioned earlier, the pure paraffin contact angle was measured to be approximately 109° ± 1°. Contact angle measurements were performed using a contact angle analyzer (FTA 125, First Ten Angstroms, Inc.). Paraffin films containing butanol exhibited slightly higher contact angles, measured to be approximately 114° ± 5°, due to butanol having a lower surface tension. Following photoresist processing and dry etching, the contact angle of paraffin films reduced to 101° ± 2° for pure paraffin and to 107° ± 5° for paraffin-butanol mixtures. Tracking the contact angle over a period of three days after patterning showed virtually no change, 98° ± 5° for pure paraffin and 110° ± 5° for paraffin-butanol mixtures. These findings are consistent with the observations of others that the O_2 plasma surface modification effect is only temporary and lasts anywhere from several minutes to several hours, depending on the processing parameters [41,42]. In our case, contact angle data indicate that the hydrophobicity of the paraffin surface is not affected by the plasma and photoresist processing. Further, it may be possible to store patterned paraffin surfaces for at least several days, and possibly weeks or even longer without adverse effects on the surface hydrophobicity.

The results presented in this chapter demonstrate that paraffin can be successfully patterned using a variety of methods. In future research, the patterns of the paraffin surface will be further modified to include additional materials to either discourage the growth of specific populations of mycobacteria (i.e., through the incorporation of antibiotics) or to encourage the growth of specific populations of mycobacteria (i.e., through the incorporation of additional growth substrates such as polycyclic aromatic hydrocarbons).

Thus, the successful patterning of the paraffin surface is an important result suggesting that future research is needed to create an array of different types of modified patterned paraffin surfaces in a single device to simultaneously screen for a wide variety of specific populations of mycobacteria.

11.4 Testing of Paraffin Surfaces with Microorganisms

Concurrent with the development of a patterned paraffin surface, testing with microorganisms was performed to verify that the ability of the paraffin to selectively isolate mycobacteria was maintained [28]. Thus, we challenged the paraffin surfaces using pure cultures of target and nontarget microorganisms. Pure cultures of target microorganisms included four representative mycobacteria, namely, *Mycobacterium fortuitum*, *Tsukamurella pauromycobacterium*, *Rhodococcus equi*, and *Gordonia amarae*. Pure cultures of *Escherichia coli* (gamma-subclass proteobacteria), *Bacillus subtilis* (Gram positive), and *Paenibacillus polymyxa* (Gram positive) were tested as negative controls. The cultures were grown in commercially available Middelbrook medium for mycobacteria (Difco Laboratories, Detroit, MI) or Luria Bertani medium for all other microorganisms (10 g tryptone, 5 g yeast extract, and 10 g NaCl per liter H_2O, at a pH of 7) from stock cultures maintained at 4°C on 1.5% agar plates prepared with Middelbrook (for mycobacteria) or Luria Bertani media. Batch cultures of microorganisms were centrifuged at 10,000 g for 10 min, and resuspended in Czapek broth (3 g $NaNO_3$, 1 g K_2HPO_4, 0.5 g $MgSO_4$-H_2O, 0.5 g KCl, and 0.01 g $FeSO_4$ per liter H_2O) in 50 mL conical tubes. The concentration of biomass for each test was determined according to the procedure for volatile suspended solids (VSS) as reported in Standard Methods for the Examination of Water and Wastewater [43]. Paraffin-coated wafers were placed inside 50 mL conical tubes, and the cultures were incubated aerobically at 20°C for two hours. The paraffin-coated wafers were removed from the 50 mL conical tubes, rinsed twice in distilled, deionized water, and then each paraffin-coated wafer was stained with fresh 4′,6-diamidino-2-phenylindole dihydrochloride (DAPI) staining solution (100 mM Tris HCl [pH 7.2], 0.9 M NaCl, and 25 mg DAPI l-1 H_2O) for 2 min, rinsed with distilled, deionized water, and rapidly air dried. Fluorescent DAPI staining of microorganisms on the paraffin surfaces was visualized using an upright epifluorescence microscope (Nikon model E-600, Melville, NY) equipped with a digital CCD camera (Spot Advanced RT Monochrome, Diagnostic Instruments, Sterling Heights, MI). Digital images were captured and exported for analysis with MetaMorph Imaging software (version 4.6r1, Universal Imaging Corp., Downingtown PA). All paraffin surfaces were examined at 40× magnification and an average of ten random microscope fields (images) were collected from each chip to ensure a total count of at least 250 objects from each paraffin surface. Semiautomated image analysis

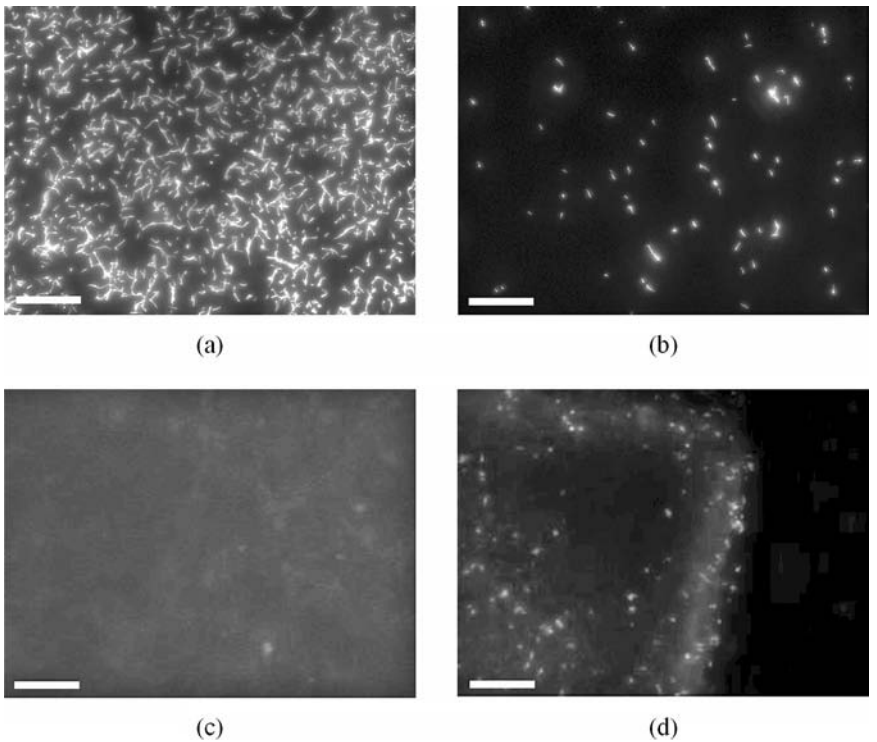

FIGURE 11.8
Pure cultures of a target microorganism *G. amarae* at low (a), and high (b) surface coverage, and (c) nontarget bacteria *E. coli* after 2 hrs of incubation. (d) Pure cultures of a target microorganism *G. amarae* after 2 hrs of incubation on a 750 μm square paraffin pattern. Organisms are DAPI stained (40× magnification, the size of the bar is 10 mm).

included manual thresholding with and without the use of the unsharp mask for enhanced edge detection of objects, followed by integrated morphometry analysis of a suite of parameters.

Figure 11.8 shows the results of a 2-hour incubation of a paraffin-coated substrate with a pure culture of *G. amarae* at high and low surface coverage or a pure culture of *E. coli*. Cells of the target microorganism can be seen on the paraffin surface, whereas only minimal cellular debris is visualized on the substrate incubated with the nontarget microorganism. Figure 11.8d illustrates the results of a 2-hour incubation of the patterned paraffin surface with a pure culture of *G. amarae*. The microorganisms are clearly confined to the patterned paraffin area (a corner of the 750 μm square pattern is shown). This qualitative screening approach was used repeatedly with target (*M. fortuitum*, *T. pauromycobacteriuim*, *R. equi*, and *G. amarae*) and nontarget (*E. coli*, *B. subtilis*, and *P. polymyxa*) microorganisms throughout the development of the prototype biochip.

Figure 11.9 provides summary data for the calibration experiment with four target and three nontarget microorganisms. As expected, no significant

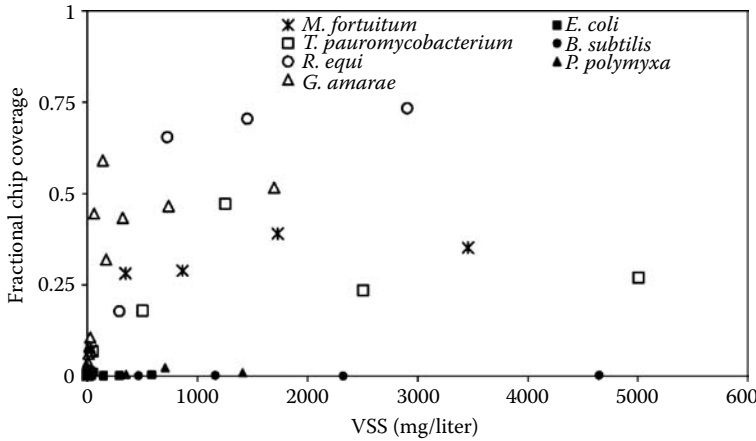

FIGURE 11.9
Relationship between the concentration of target microorganisms in solution and the percentage surface coverage of replicated biochips.

binding to the surface of the device was observed as the concentration of nontarget microorganisms was increased. For target microorganisms, the relationship between the percentage surface coverage and the concentration of biomass in the sample appeared to follow a rectangular hyperbola that is characteristic of surface sorption phenomena (i.e., as the concentration of biomass in the sample was increased, the percentage surface coverage increased to a maximum.) This result suggests that multiple target microorganisms appear to behave in a similar manner with an increase in the percentage of paraffin surface coverage, concurrent with an increase in the biomass in the sample. The maximum percentage surface coverage appears to depend upon the identity of the target microorganism. Further, the sensitivity of the paraffin surface to detect changes in the concentration of biomass in a sample is greatest for the lowest concentrations of biomass. In practical terms, this means that the biochip would be expected to perform best for the quantification of biomass in an environmental sample when the concentration of target microorganisms is less than approximately 100 mg VSS/liter. Although the concentrations of mycobacteria tested in these experiments are relevant for certain environmental samples, namely samples collected from wastewater treatment plants or to monitor bioremediation of soils, the concentrations we examined in this work were significantly higher than typically encountered in drinking water. Therefore, future research is needed to evaluate if our biochip approach can be used to monitor for mycobacteria in samples of drinking water in addition to samples of wastewater.

Finally, the specificity of the paraffin surfaces was tested by combining an excess of biomass from nontarget microorganisms with biomass from target microorganisms and incubating the mixture with prototype biochips. As shown in Figure 11.10a, we were successful in detecting *T. pauromycobacterium*

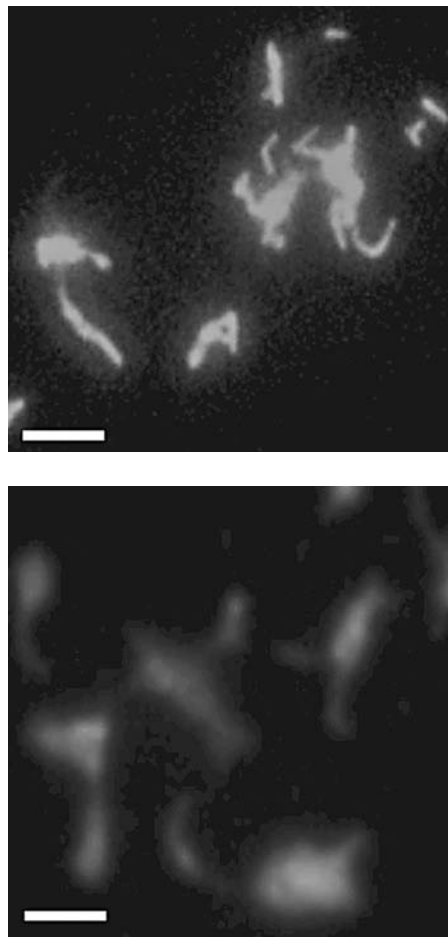

FIGURE 11.10
(a) Detection of *T. pauromycobacterium* from a mixture containing *E. coli*, *B. subtilis*, and *T. pauromycobacterium* after 2 hrs of incubation. (b) Mycobacteria detected following 2 hrs of incubation in samples of sewage sludge from the Mill Creek Wastewater Treatment Plant in Cincinnati, Ohio. Organisms are DAPI stained (100× magnification, the size of the bar is 4 μm).

from a mixture containing approximately 1000 mg VSS/liter of *E. coli* (nontarget), approximately 1000 mg VSS/liter of *B. subtilis* (nontarget), and approximately 50 mg VSS/liter of *T. pauromycobacterium* after 2 hours of incubation. Alternative mixtures of target and nontarget microorganisms showed similar results (data not shown). These results strongly point to the high specificity of the paraffin surfaces to selectively identify target microorganisms in the presence of an abundance of nontarget microorganisms.

To challenge the paraffin surfaces with a real environmental sample, grab samples of mixed liquor were collected from the aeration basins of the Mill Creek Wastewater Treatment plant operated by the Greater Cincinnati Metropolitan Sewer District, transported on ice to laboratories at the University of Cincinnati,

and analyzed within one hour of collection. Paraffin-coated substrates were incubated with the activated sludge sample, and cells were found to adhere to the surface (Figure 11.10b). A careful examination of the morphology and staining characteristics of the adhered microorganisms according to standard procedures [11,12] indicated that the microorganisms were members of the gram positive mycobacteria. This result demonstrates that the culture-based biochip technology outlined in Figure 11.1 is suitable to screen for mycobacteria in environmental samples collected from a municipal sewage treatment plant.

11.5 Microfluidic Culture-Based Biochip

To integrate the culture-based detection of mycobacteria with a microfluidic platform, paraffin islands were formed inside a cyclic olefin copolymer (COC) microchannel for bating and culturing bacteria. COC is a relatively new thermoplastic polymer that has been gaining popularity due to its excellent physical and chemical properties [44–46]. COC is more chemically inert than most thermoplastics, exhibits very low (less than 0.01%) water absorption, and has excellent optical properties making it ideally suited for fluorescence-based analyses [46,47].

The general concept of the microfluidic biochip was schematically illustrated in Figure 11.2. The chip is formed by two plastic wafers: one wafer containing a trench formed with hot embossing, the other containing paraffin islands. The fabrication sequence has three key three steps (Figure 11.11). First, paraffin was deposited and patterned on a COC substrate. As discussed previously, Tissue Prep paraffin can be successfully deposited and patterned on glass substrates by spin coating and dry etching. The same approach can be used to deposit paraffin on COC substrates. Next, a microchannel was formed in a second COC substrate using hot embossing. The hot embossing is rather straightforward and was discussed in detail in Chapter 5. Finally, the biochip was completed by adhesively bonding the two COC substrates.

11.5.1 Microchannel Fabrication

Microchannels in COC wafers were formed by hot embossing using soft PDMS embossing tools. Details of PDMS tool fabrication and performance are given elsewhere [51]. The process is briefly described as follows. Initially, a 3 in. silicon wafer was RCA cleaned and kept in an oven at 120°C for 30 min to remove moisture. A 110 μm–thick SU-8 (2075, MicroChem Corp.) mold was formed using standard methods. Many investigators [52–56] have optimized SU-8 processing for different applications involving various aspect ratios and feature sizes. Quick oxygen plasma was used to clean up surfaces from any remaining SU-8 residue. Prior to casting PDMS, the SU-8 surface was treated with CHF_3 plasma to enhance separation of the PDMS film from the SU-8 mold.

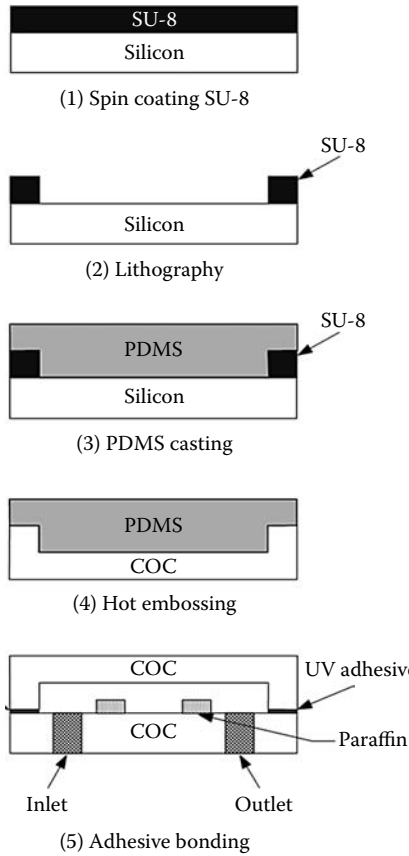

FIGURE 11.11
Schematic diagram of the microfluidic biochip fabrication.

PDMS elastomer precursor and the curing agent (Sylgard 184, Dow Corning) were well mixed at the ratio of 10:1 and poured onto the silicon surface with the SU-8 mold. The mixture was degassed inside a vacuum chamber for about 30 min and cured on a leveled, flat hot plate at 60°C for 3 hours. The flatness and proper leveling of the hot plate are critical to ensure that the PDMS film thickness is uniform. The cured PDMS was then peeled off with care from the SU-8 mold.

The embossing machine used in this work had a movable top hot plate and a stationary bottom hot plate on which the PDMS mold and blank COC wafer were placed. A vacuum pump was connected to the machine to provide a high vacuum during the entire embossing cycle. The PDMS mold and COC wafer were heated together to a temperature of 165°C, which is about 40°C above the glass transition temperature of COC. The vacuum was used to prevent formation of air bubbles during the embossing process. After the mold-polymer sandwich reached the temperature, the system was allowed to rest at that temperature for 5 min to make sure that all the materials inside the chamber reached the desired

temperature. Then a uniform, controlled force of 4.45 kN with a ramping speed of 1 kN/min was applied by lowering the bottom plate and holding it against the bottom stationary hot plate for 10 min. The system was cooled down to room temperature, at which point the force was released. The mold-polymer sandwich was then de-embossed manually by peeling the PDMS tool off the COC wafer. Inlet and outlet ports were drilled in the COC wafer with the microfluidic channel and the device was completed using adhesive bonding.

11.5.2 Adhesive Bonding

Due to presence of paraffin patterns on one of the COC wafers, conventional adhesive bonding by spin coating could not be used. Further, polymer fusion bonding could not be used because of the low melting temperature of paraffin (55 to 57 °C). Thus, a new stamping approach was developed to adhesively bond the COC wafers. Overall, the process resembles micro contact printing (μCP), and is illustrated in Figure 11.12. In this approach, a blank

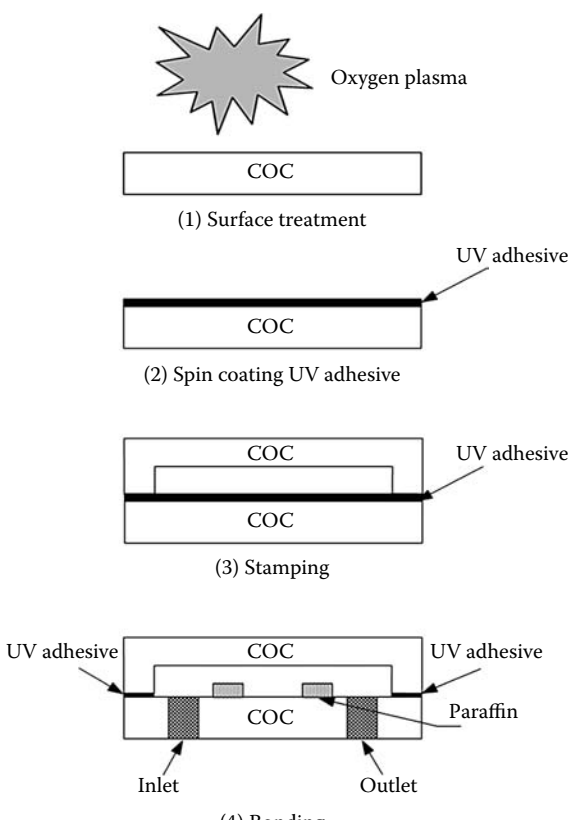

FIGURE 11.12
Schematic diagram of adhesive bonding approach using stamping.

COC wafer was first treated with quick oxygen plasma (50 W, 30 sec, 25 sccm) to make the surface hydrophilic in order to enhance spreading of the adhesive. The COC substrate with microfluidic channel was also treated with oxygen plasma to enhance the adhesive transfer. Loctite 3001 UV-cured adhesive was spin coated on a wafer at 2000 rpm for 20 sec. Low-viscosity UC-cured adhesive (100 cp) was used in this work because high-viscosity adhesives (e.g., Loctite 3301, 5000 cp) introduced air bubbles during processing and required degassing. A COC wafer containing embossed microchannels was briefly contacted on the surface of this wafer such that UV adhesive was transferred. An aligner was used to align and bond the embossed COC wafer, now containing UV-cured adhesive on its surface, with the paraffin-patterned wafer.

11.5.3 Challenging Biochip with Mycobacteria

The microfluidic culture-based biochips fabricated in this work are shown in Figure 11.13. The device was formed from 1 mm–thick, approximately 2 cm × 3 cm COC substrates. The microchannels are 1 mm in width, 15 mm in length, and 110 μm in height, while input and output ports are 600 μm in diameter. The three paraffin islands inside the microchannel are spaced at 2 mm, each being 800 μm wide, 1.5 mm long, and 5 μm thick, spaced at 2 mm.

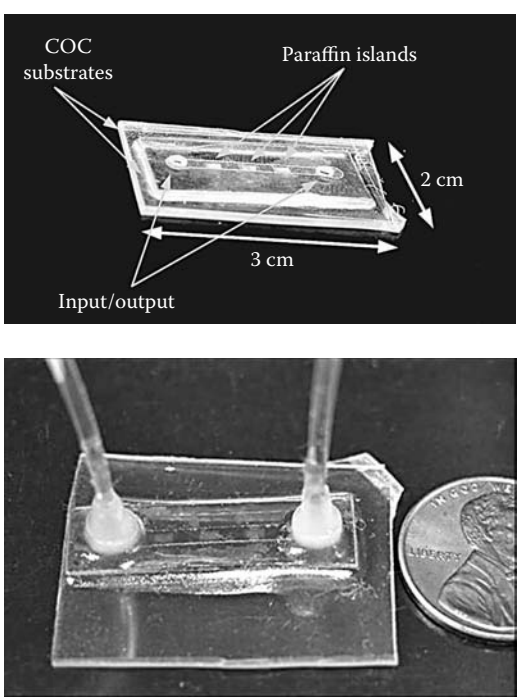

FIGURE 11.13
Photographs of the completed culture-based biochips for environmental monitoring.

The device was packaged with commercial HPLC connectors (e.g., Upchurch Scientific, Inc.) using 5000 cP UV-cured adhesive. A syringe pump (KDS 101, KD Scientific Inc.) was used to operate the biochip.

To demonstrate detection of mycobacteria in environmental samples in a robust, rapid, and easy-to-use fashion, biochips were incubated with a variety of biological samples. The culturing and detection procedures discussed earlier were used. The results showed target microorganisms binding to paraffin in the device in a predictable manner, with nontarget microorganisms not exhibiting significant adhesion. Representative results are shown in Figure 11.14. For example, panels b and c show the results of challenging the biochip with a mixture of a pure culture of *G. amarae* and nontarget *E. coli* following a 30-min incubation. Cells of the target organism can be clearly observed on the surface, while only cell debris is present on surfaces incubated with the nontarget microorganism. Figure 11.14, panels d and e, show results of a 2-hour incubation of a biochip with a pure culture of *G. amarae*. Once again, cells of the target microorganism can be clearly seen on the paraffin surface, whereas only minimal cellular debris is visualized off the paraffin surface. Because the paraffin islands and microfluidic channels were both fabricated using a transparency mask (printed using an inkjet printer at 1200 dpi), the edges of paraffin islands are not very smooth and appear wavy.

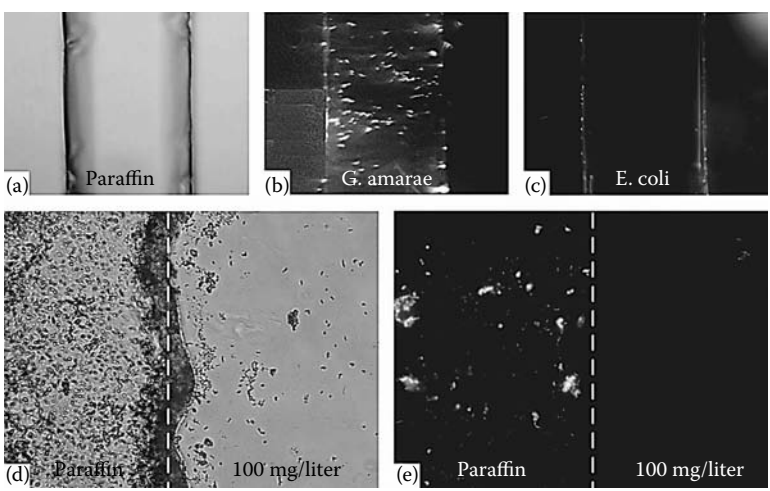

FIGURE 11.14
Representative results of challenging culture-based biochip with a pure culture of *G. amarae*. (a) Bright field image at 10× magnification illustrating a paraffin island inside a microfluidic channel prior to biochip operation. (b–c) Epifluorescence images at 10× of the paraffin island illustrating detection of target microorganism *G. amarae* and lack of interference from nontarget microorganism *E. coli* following 30 min of incubation. Bright field (d) and epifluorescence (e) images at 40× of the paraffin surface illustrating the detection of individual cells of *G. amarae*. All microorganisms were stained with DAPI.

11.6 Conclusions

Micromachining technologies have been used to fabricate paraffin substrates for culture-based detection of mycobacteria in environmental samples. A new method of depositing paraffin was demonstrated, permitting us to successfully deposit uniform paraffin films ranging from 10 to 70 μm in thickness. Dry etching techniques were demonstrated to be effective in patterning paraffin films. The developed culture-based biochip is capable of detecting pure cultures of target microorganisms in as little as 2 hours as compared to 3 weeks for a conventional assay in the presence of a 100-fold excess of nontarget microorganisms. Such a biochip to selectively culture mycolic acid containing actinomycetes from environmental samples will improve screening for mycobacteria to protect public health as well as screening for nocardiafoams to reduce the costs associated with treating nocardiafoam at sewage treatment plants. In the long term, we expect to develop an array-based technology for rapidly and specifically identifying, enumerating, and characterizing mycobacteria to protect drinking water, to monitor the success of petroleum bioremediation, and to identify the cause of filamentous foaming on the surfaces of sewage treatment plants.

Acknowledgments

The authors gratefully acknowledge support from the National Science Foundation (BES0116912 and BES0428600) and Emerging Concepts, Inc. The authors are also grateful to the Greater Cincinnati Metropolitan Sewer District for access to the Mill Creek Wastewater Treatment Plant.

References

[1] Pitt, P. and Jenkins, D. Res., Causes and control of nocardia in activated sludge, *J. Water Pollution Control Federation* 62, 143, 1990.

[2] Seviour, E., Williams, C., Seviour, R., Soddell, J., and Lindrea, K., Survey of filamentous bacterial populations from foaming activated sludge plants in eastern states of Australia, *Water Research*, 24, 493–498, 1990.

[3] Soddell, J. and Seviour, R., Microbiology of foaming in activated sludge plants—a review, *J. Appl. Bacteriol.*, 69, 145, 1990.

[4] McCormick, J.B., Epidemiology of emerging/re-emerging antimicrobial-resistant bacterial pathogens, *Curr. Opin. Microbiol.*, 1, 125–129, 1998.

[5] Horsburgh, C.R., *In vitro* and *in vivo* antimycobacterial activities of a new quinolone, *New Engl. J. Med.*, 324, 1332–1338, 1991.

[6] Nightingale, S.D. et al., Incidence of mycobacterium avium-intracellular complex bacteremia in human immunodeficiency virus-positive patients, *J. Infect. Dis.*, 165, 1082–1085, 1992.
[7] *Safe Drinking Water Act: Contaminant Candidate List*, U.S. Environmental Protection Agency, http://www.epa.gov/OGWDW/ccl/cclfs.html
[8] Federal Register notice about the Contaminant Candidate List, U.S. Environmental Protection Agency, http://www.epa.gov/safewater/ccl/ccl_fr.html
[9] K. J. Ryan, *Sherris Medical Microbiology*, 3rd Ed. Norwalk, CT: Appleton & Lange, 1994.
[10] M. Dworkin, M., Ed., The Prokaryotes: An Evolving Electronic Resource for the Microbiology Community, http://141.150.157.117:8080/prokPUB/index.htm
[11] Ollar, R. and Connell, N. *Molecular Mycobacteriology*, New York, Marcel Dekker, 1999.
[12] Jenkins, D., Richards, M., and Daigger, G., *Manual on the Causes and Control of Filamentous Bulking and Foaming*, 2nd Ed., Boca Raton, FL, Lewis Publisher, 1993.
[13] Eikelboom, D., *Process Control of Activated Sludge Plants by Microscopic Investigation*, London, U.K., International Water Association, 2000.
[14] Oerther, D., de los Reyes III, F., Hernandez, M., and Raskin, L., Simultaneous application of oligonucleotide probes and an antibody stain for in situ detection of gordona spp, *FEMS Microbiology Ecology*, 29, 129–136, 1999.
[15] Iwahori, K., Miyata, N., Morisada, S., and Suzuki, N., Rapid detection of Nocardia amarae in the activated sludge process using enzyme-linked immunosorbent assay (ELISA), *J. Biosci. Bioeng.*, 89, 469–473, 2000.
[16] Iwahori, K. et al., Production of anti-Gordonia amarae mycolic acid polyclonal antibody for detection of mycolic acid-containing bacteria in activated sludge foam, *J. Biosci. Bioeng.*, 92, 417, 2001.
[17] de los Reyes, F., Ritter, W., and Raskin, L., Group-specific small-subunit rRNA hybridization probes to characterize filamentous foaming in activated sludge systems, *Appl. Environ. Microbiol.*, 63, 1107–1117, 1997.
[18] Schuppler, M., Wagner, M., Schon, G., and Gobel, U., *Microbiology*, 144, 249, 1998.
[19] de los Reyes III, F. et al., Characterization of filamentous foaming in activated sludge systems using oligonucleotide hybridization probes and antibody probes, *Water Sci. Tech.*, 37, 485–493, 1998.
[20] de los Reyes, M. et al., Identification and quantification of Gordona amarae strains in activated sludge systems using comparative rRNA sequence analysis and phylogenetic hybridization probes, *Water Sci. Tech.*, 37, 521–525, 1998.
[21] Cha, D., Fuhrmann, J., Kim, D., and Golt., C. *Water Res.*, 33, 1964, 1999.
[22] AccuProbe® Culture Identification Tests, Gen-Proge, Inc., http://www.gen-probe.com/prod_serv/mycobac_accuprobe.asp
[23] Roche Molecular Diagnostics, http://www.roche-diagnostics.com/ba_rmd/rmd_products_mycobateria.html
[24] Soddell, J. and Seviour, R., *Water Sci. Tech.*, 34, 113–118, 1996.
[25] Sohngen, N., Benzen, petroleum, paraffinol, und paraffin als kohlenstoff und engiequelle fur mikroben, *Zbl. Bakt. Hyg. Abt.* II, 37, 595–609, 1913.
[26] Jing, G., Eluru, H., Polaczyk, A., Kinkle, B., Oerther, D., and Papautsky, I., Culture-based detection of mycobacteria in environmental samples, *J. Micromech. Microeng.*, 15, 270–276, 2005.
[27] Jing, G., Hollis, G., Eluru, H., Polaczyk, A., Kinkle, B., Oerther, D., and Papautsky, I., Developing rapid detection of mycobacteria using microwaves, *Analyst*, 129, 963–969, 2004.

[28] Polaczyk, A., Kinkle, B., Papautsky, I., and Oerther, D., Culture-based MEMS device to track *Gordonia* in activated sludge, *Environ. Sci. Technol.*, 40, 2269–2274, 2006.
[29] Becker, H. and Locascio, L.E., Polymer microfluidic devices, *Talanta*, 56, 267, 2002.
[30] Dowen, D.E., Design and implementation of paraffin based micro-positioning actuator, *Proc. SPIE*, 3132, 127–134, 1997.
[31] Tibbitts, S.F., High-output paraffin linear motors: utilization in adaptive systems, *Proc. SPIE*, 1543, 388–426, 1991.
[32] Kabei, N. et al., Thermal-expansion type microactuator using paraffin as expansive material, *Trans. JSME, Part C.*, 62, 4624–4629, 1997.
[33] Carlen, E.T. and Mastrangelo, C.H., Electrothermally activated paraffin microactuators, *J. Microelectromech. Syst.*, 11, 167–174, 2002.
[34] Selvaganapathy, P., Carlen, E.T., and Mastrangelo, C.H., Electrothermally actuated inline microfluidic valve, *Sensors and Actuators A*, 104, 275–282, 2003.
[35] Carlen, E.T. and Mastrangelo, C.H., Surface micromachined thermally actuated microvalve, *J. Microelectromech. Syst.*, 11, 408–420, 2002.
[36] Klintberg, L., Karlsson, M., Stenmark, L., and Thornell, G., A thermally activated paraffin-based actuator for gas-flow control in a satellite electrical propulsion system, *Sensors and Actuators A*, 105, 237–246, 2003.
[37] Klintberg, L., Svedberg, M., Nikolajeff, F., and Thornell, G., Fabrication of a paraffin actuator using hot embossing of polycarbonate, *Sensors and Actuators A*, 103, 307–316, 2003.
[38] Plomp, M., van Hoof, P.J.C.M., and van Enckevort, W.J.P., AFM-induced melt growth on n-paraffin crystals, *Surface Science*, 448, 231–249, 2000.
[39] D'Agostino, R., *Plasma Deposition, Treatment, and Etching of Polymers*, Boston, MA, Academic Press, 1990.
[40] Jo, B., Van Lerberghe, L., Motsegood, K., and Beebe, D., *J. Microelectromech. Syst.*, 9, 76, 2000.
[41] Morra, M., Occhiello, E., Marola, R., Garbassi, F., Humphrey, P., and Johnson, D., On the aging of oxygen plasma-treated polydimethylsiloxane surfaces, *Colloid Interface Sci.*, 137, 11–24, 1990.
[42] Lee, J., Park, C., and Whitesides, G., Solvent compatibility of poly(dimethylsiloxane)-based microfluidic devices, *Anal. Chem.*, 75, 6544–6554, 2003.
[43] Clesceri, L., Asn, A., and Eaton, A., *Standard Methods for Examination of Water & Wastewater*, 20th ed, Washington, DC, APHA/AWWA/WEF, 1999.
[44] Becker, H. and Gartner, C., Polymer microfabrication methods for microfluidic analytical applications, *Electrophoresis*, 21, 12, 2000.
[45] Rotting, O. et al., Polymer microfabrication technologies, *Microsyst. Technol.*, 8, 32, 2002.
[46] Ahn, C.H. et al., Disposable smart lab on a chip for point of care clinical diagnostics, *Proc. IEEE*, 92, 154, 2004.
[47] Piruska, A. et al., The autofluorescence of plastic materials and chips under laser irradiation, *Lab Chip*, submitted, 2005.
[48] Puntambekar, A., Choi, J.-W., Ahn, C. H., Kim, S., and Makhijani, V., Fixed-volume metering microdispenser module, *Lab Chip*, 2, 213–218, 2002.
[49] Divakar, R., Butler, D., and Papautsky, I., Room temperature low-cost UV-cured adhesive bonding for microfluidic biochips, in *Proc. Micro-Total Analysis Systems (μTAS 2001)*, Monterey, CA, 21–25, October, 2001.

[50] Huang, Z., Sanders, J.C., Dunsmor, C., Ahmadzadeh, H., and Landers, J.P., A method for UV-bonding in the fabrication of a glass electrophoretic microchips, *Electrophoresis*, 22, 3924–3929, 2001.
[51] Narasimhan, J. and Papautsky, I., Polymer embossing tools for rapid prototyping of plastic microfluidic devices, *J. Micromech. Microeng*., 14, 96, 2004.
[52] Loechel, B., Thick-layer resists for surface micromachining, *J. Micromech. Microeng*., 10**,** 108–111, 2000.
[53] Brien, J. et al., Advanced photoresist technologies for microsystems, *J. Micromech. Microeng*., 11**,** 353–358, 2001.
[54] Juncker, D. et al., Soft and rigid two-level microfluidic networks for patterning surfaces, *J. Micromech. Microeng*., 11**,** 532–541, 2001.
[55] Zhang, J., Tan, K., and Gong, H.,Characterization of the polymerization of SU-8 photoresist and its applications in micro-electro-mechanical systems (MEMS), *Polymer Testing*, 20**,** 693–701, 2001.
[56] Lorenz, H. et al., SU-8: A low-cost negative resist for MEMS, *J. Micromech. Microeng*., 7, 121–124, 1997.

12

MEMS for Drug Delivery

Kabseog Kim and Jeong-Bong Lee

CONTENTS

12.1 Introduction

There are many routes by which drugs can be delivered into the body. These routes include oral (drugs taken by mouth), injections, nasal (sprayed into nose), inhalation (breathed into the lungs), rectal (injection into the rectum), cutaneous (applied on the skin), and transdermal (delivery through the skin). Injections can be further divided into intravenous (injection into a vein), intramuscular (injection into a muscle), intrathecal (injection into the space around the spinal cord), and subcutaneous (injection beneath the skin). Each drug delivery route has specific advantages and disadvantages, and the route greatly impacts the therapeutic efficacy of the delivered drug inside the body.

The oral route is the most common way to deliver drugs into the body. However, it should be noted that the popularity of oral drug administration is not because it is effective, but because it is convenient. Compared to the

majority of the other methods, oral drug administration is the simplest and the least expensive method. In addition, it is also often the safest method for most drugs. However, conventional oral drug delivery is not an ideal route for the delivery of many drugs, especially newly available protein- or peptide-based drugs developed through biotechnology. The orally administered drug is partially absorbed in the mouth and stomach, although most of the drug is absorbed from the small intestine. The drug passes through the liver before it is transported via the bloodstream to its target site. Most drugs are degraded in the gastrointestinal tract by digestive enzymes or eliminated by the liver.

The most common alternative route to oral drug delivery is injection. Although injection would be an effective way to deliver large-molecule drugs into the body in large quantities, it has inherent problems, such as invasiveness (needles cause pain and tissue damage) and it is difficult to achieve a sustained, controlled release of the drug. In addition, this method is relatively expensive because medical professionals need to administer drugs in most cases.

Recently, there have been many studies on new drug delivery methods using emerging micro- and nanotechnologies with goals of overcoming these limitations. This chapter presents a survey of these newly proposed drug delivery methods using MEMS (microelectromechanical systems) techniques. The vast majority of the MEMS for drug delivery work are dedicated to the development of microneedles for minimally invasive transdermal drug delivery. Various materials and microfabrication processes used for the realization of various kinds of microneedles are surveyed, and methods for modeling mechanical robustness of microneedles are described. The development of microreservoir devices (using MEMS techniques) that contain drugs and deliver them via the oral route or via an intravenous injection is also discussed. The last section is devoted to a discussion of biocompatibility and biofouling issues in MEMS devices for drug delivery applications.

12.2 Human Skin and Microneedles

Hypodermic syringes with a hollow pointed needle have been one of the most commonly used body fluid extraction, vaccination, and medication devices since their invention by C. Pravaz and A. Wood in the 1850s [1]. While there have been many variations in materials and methods of providing safety, the hypodermic syringe design has changed very little since its first use. Conventional hypodermic needles create fear of injection-related pain among patients, and there has been increasing concern regarding the transmission of bloodborne pathogens such as HIV (human immunodeficiency virus) and hepatitis to healthcare workers by accidental needle stick injuries [2].

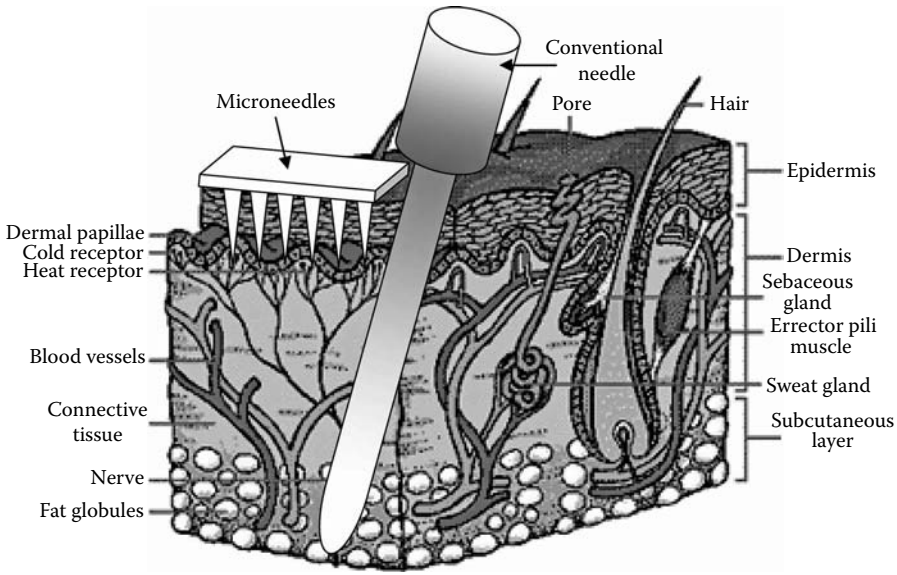

FIGURE 12.1
A schematic diagram of a cross-section of human skin with a microneedle array and a conventional needle. (From Australian College of Dermatologists. With permission.)

Figure 12.1 shows a schematic diagram of a cross-section of human skin. Human skin is composed of three layers: epidermis, dermis, and subcutaneous tissue. The outermost layer of the epidermis is stratum corneum (10 to approximately 15 μm thick), a layer of dead cells, which is a protective diffusion barrier layer preventing the loss of body fluids and blocking the entry of external materials into the body. Sensory fibers in the cutaneous nerves detect external stimuli such as temperature, pressure, and those causing pain, and generate signals that are relayed through a nerve pathway to the brain. Sensory fibers and blood vessels reach to the dermis layer in the skin. The pain associated with an injection using a hypodermic syringe is due to the fact that the needle is large and penetrates deep into the skin with excessive contact with these sensory fibers. The smallest needle typically used for insulin injection for diabetes is a 31-gauge needle which is 254 μm in outer diameter.

With the advances in MEMS technology, it is possible to make microneedles that are long enough to penetrate the epidermis, but short enough not to penetrate deep into the dermis layer and farther down in the subcutaneous tissue for minimally invasive transdermal drug delivery and body fluid sampling. Moreover, microneedles and microneedle arrays can be used as stand-alone devices as well as a part of more sophisticated *smart* biological detection and delivery systems in which microneedles are integrated with microfluidics and biosensors or microelectronics.

There have been many investigations on a variety of microneedles that allow precise control of the delivery depth and rate of the sophisticated gene and drugs. Both in-plane and out-of-plane microneedles made of various materials, including single crystal silicon, polysilicon, metals, and polymers, have been investigated. Various fabrication techniques, from a simple single-step process to a complex sequence of multiple fabrication steps and various shapes of microneedles in both solid and hollow forms have been studied.

12.3 In-Plane Silicon Microneedles

Although it was not intended for drug delivery, development of in-plane microneedles can be traced back to the work of Dr. Wise on neural probes at the University of Michigan in the 1980s [4]. An implantable ten-channel microelectrode recording array with an on-chip signal-processing smart probe was fabricated (Figure 12.2) for the long-term recording of neural biopotentials and as a basis for closed-loop neural prostheses. The probe is 4.7 mm long, 15 μm thick, and has a shank that tapers from 160 μm near the base to less than 15 μm near the tip. A one-dimensional array of microneural probes [5], and much more sophisticated microassembled, two-dimensional array [6] have been developed since that time.

In-plane microneedles have been under development since the early 1990s beginning at the University of California at Berkeley with Dr. Pisano's group. A combination of surface- and bulk-micromachining techniques was used to fabricate hollow, in-plane microneedles in 1 to 6 mm lengths with fully enclosed channels formed of silicon nitride (Figure 12.3) [7,8]. The channels are 9 μm in height and have one of two widths, 30 or 50 μm. Access to the channels is provided at their shank and distal ends through 40 μm square apertures in the overlying silicon nitride layer. Polysilicon microheaters were integrated to generate bubbles, which can be used as a micropump. Because it is complementary metal oxide semiconductor (CMOS) compatible, it has great possibilities for integration with electronics to realize *smart* microneedles. Polysilicon microneedles have also been made with a two-wafer polysilicon micromolding process, referred to as polymolding, which has the potential to be much more cost-effective because the silicon micromolds are reusable (Figure 12.4) [9,10].

Silicon dioxide has also been investigated as a viable material for microneedles by Dr. Fujita's group at the University of Tokyo. Chun et al. have used the deep reactive ion etching (DRIE) technique to define an array of deep holes in silicon and oxidize it to form hollow silicon dioxide microcapillaries [11]. Oka et al. have also fabricated SiO_2 hollow microneedles, which mimic a jagged mosquito's needle [12].

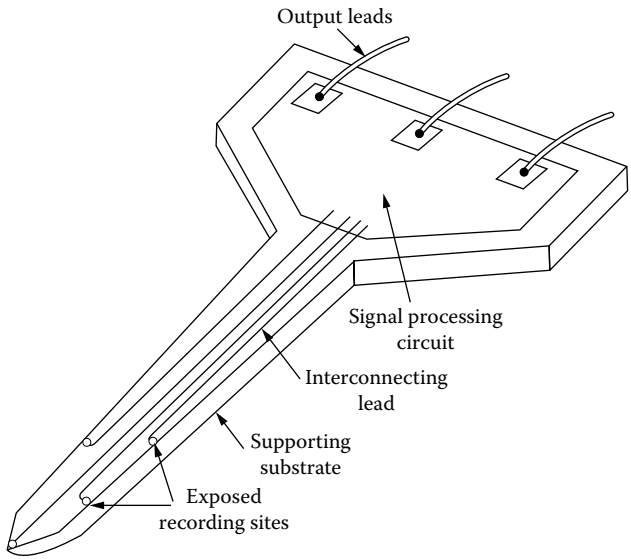

(a)

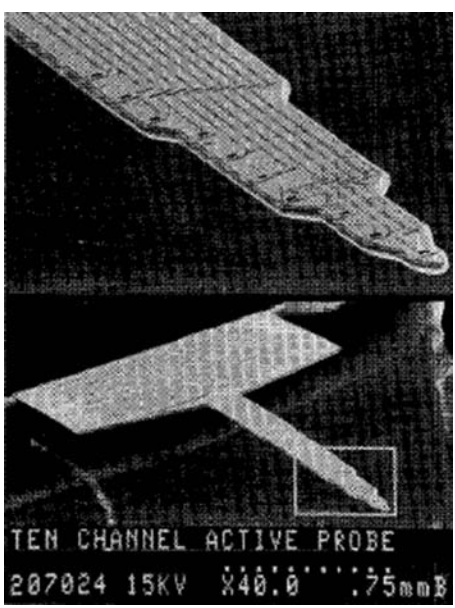

(b)

FIGURE 12.2
(a) Schematic diagram and (b) SEM images of an in-plane micro neural probe. (From K. Najafi and K. Wise, *IEEE J. Solid-State Circuits*, 21, 1035–1044, 1986. With permission.)

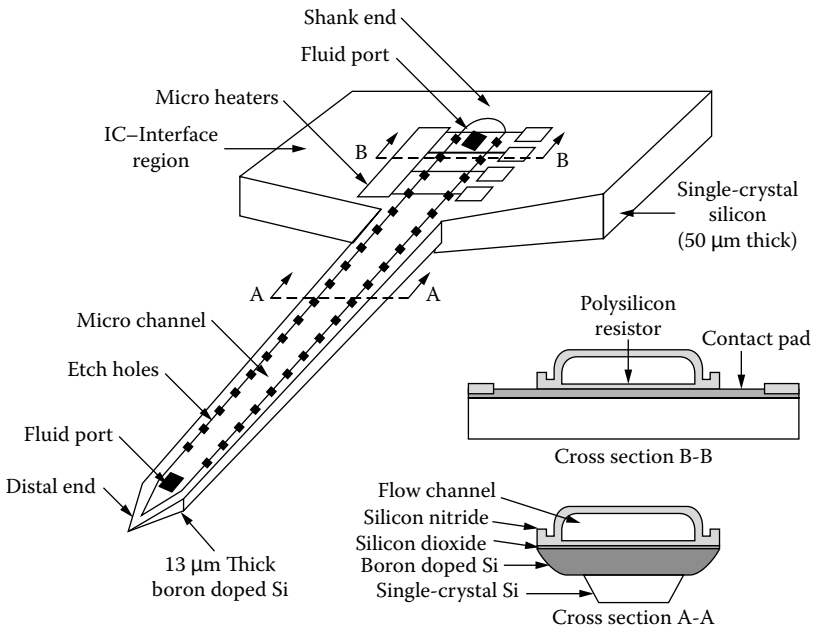

(a)

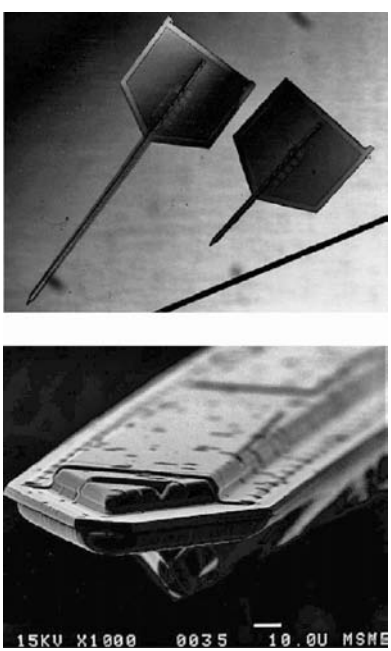

(b)

FIGURE 12.3
(a) Schematic diagrams and (b) SEM images of silicon processed in-plane microneedles (From L. Lin and A. Pisano, *J. Microelectromechanical Systems*, 8, 78–84, 1999. With permission).

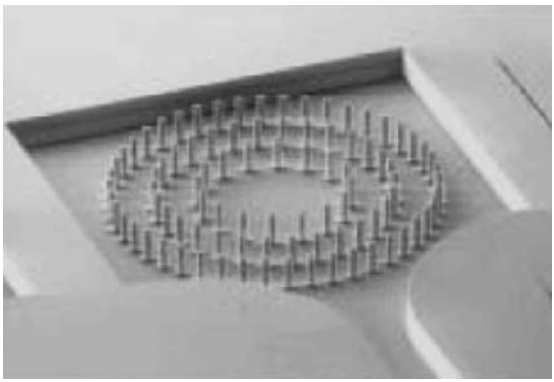

(a)

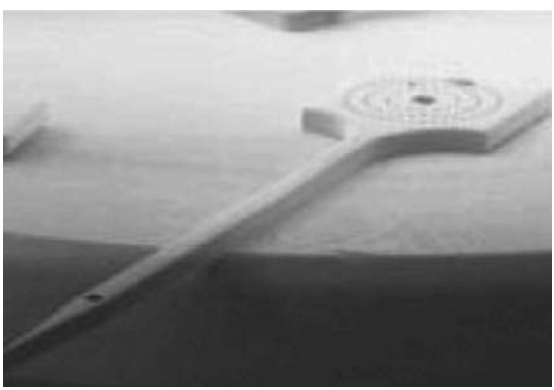

(b)

FIGURE 12.4
(a) SEM of a microneedle mold. (b) SEM of a polysilicon hypodermic microneedle fabricated by polymolding technique. (From J. Zahn, N. Talbot, D. Liepmann, and A. Pisano, *Biomedical Microdevices*, 2, 295–303, 2000. With permission.)

12.4 In-Plane Metallic Microneedles

Electroplated metals were also investigated as materials for microneedles by Dr. B. Frazier's group at Georgia Tech. Chandrasekaran et al. demonstrated surface micromachined, in-plane, hollow metallic hypodermic microneedles and microneedle arrays using electroplated palladium, palladium alloys, and nickel (Figure 12.5) [13–15]. These metallic microneedles feature complex tip geometries, microbarbs, mechanical penetration stops, and multiple fluid output ports. The fluid-coupled microneedles were packaged in a standard luer-lock fitting using UV-curable epoxy.

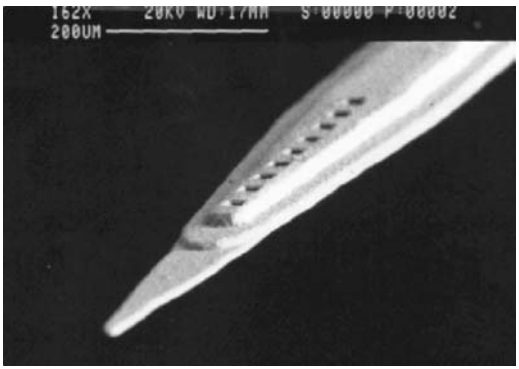

(a)

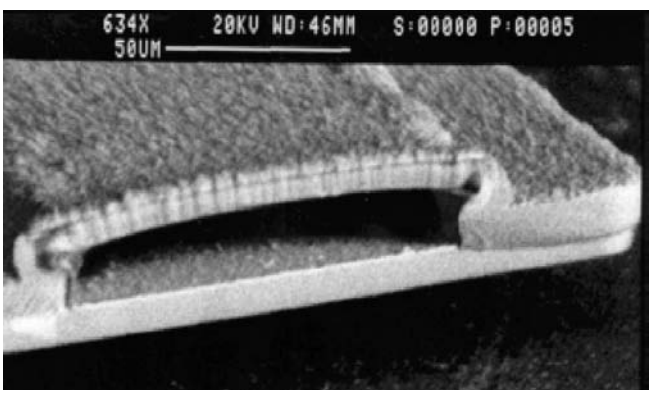

(b)

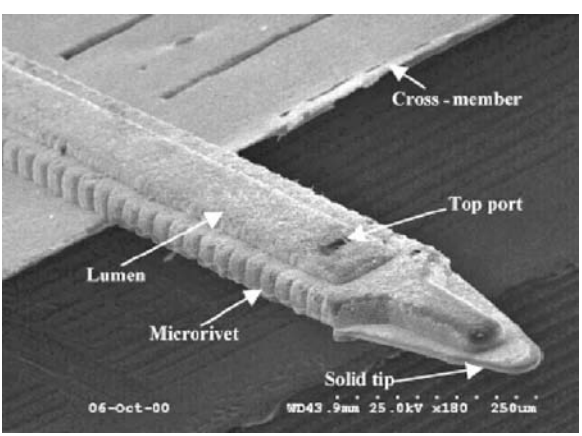

(c)

FIGURE 12.5
SEM photomicrographs of surface micromachined microneedles: (a) a metallic microneedle with multiple output ports, (b) cross-section of the microneedle showing its microchannel, (c) a sophisticatedly designed single microneedle with a shaft length of 500 μm.

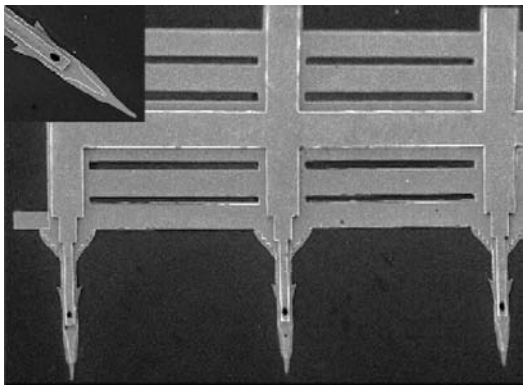

(d)

FIGURE 12.5 (continued)
SEM photomicrographs of surface micromachined microneedles: (d) an array of the microneedles with a center-to-center distance of 2 mm. (From S. Chandrasekaran, J. Brazzle and B. Frazier, *J. of Microelectromechanical Systems*, 12, 289–295, 2003, and S. Chandrasekaran and B. Frazier, *J. of Microelectromechanical Systems*, 12, 281–288, 2003. With permission.)

12.5 Out-of-Plane Silicon Microneedles

One of the major issues with respect to in-plane microneedles is their limited density. This is due to the fact that only a one-dimensional array of microneedles can be microfabricated in a wafer. In order to achieve two-dimensional arrays of microneedles, a complex microassembly process similar to one demonstrated by Bai et al. [6] would be needed. With the typical microneedle inner diameters of 10 to 100 μm, the limited density of the microneedles may become an issue when delivering a large amount of a drug or in blood analysis applications, which typically require a fair amount of blood. In addition, shear stress created by the tissue during insertion may cause mechanical fracture for the single microneedle or one-dimensional array of long microneedles. The out-of-plane microneedle array appears to be a viable option for addressing the aforementioned issues because many microneedles can be microfabricated in a wafer and the two-dimensional arrays are less prone to fracturing when exposed to shear forces during penetration.

The first demonstrated out-of-plane microdevices for drug and gene delivery are sharp solid silicon structures [16,17]. Dizon et al. realized an array of sharp solid silicon structures using a conventional anisotropic silicon wet etching technique [16]. The timed wet etching using a square mask and fast-etching (411) planes was used to realize approximately 80 μm high and very sharp (with a tip radius of curvature less than 0.1 μm) solid silicon structures (Figure 12.6a). An array of such sharp solid silicon micropiercing structures has been coated with specific genes, which have been successfully transferred

(a)

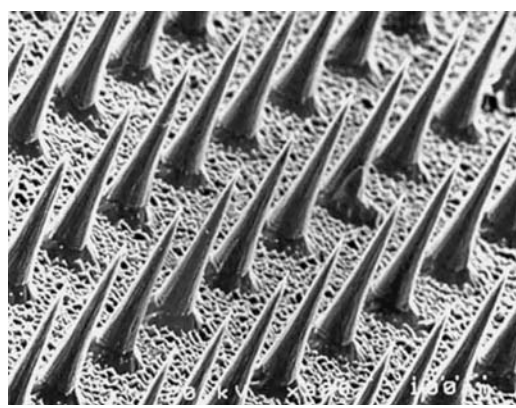

(b)

FIGURE 12.6
SEM images of (a) a wet etched sharp solid silicon microstructure. (From R. Dizon, H. Han, A. Russell, and M. Reed, *J. Microelectromech. Syst.*, 2, 151–159, 1993, with permission). (b) An array of dry etched sharp solid silicon microneedles. (From S. Henry, D. McAllister, M. Allen, and M. Prausnitz, *J. Pharm. Sci.*, 87, 922–925, 1998, with permission).

into plant and animal cells. The anisotropic silicon dry etching technique using SF_6 and O_2 plasma has also been used to realize an array of sharp solid silicon microstructures with a height of 150 μm (Figure 12.6b) [17]. The ratio between SF_6 and O_2 can be used to control the tapered angle of the etched silicon microstructure. Henry et al. [17] used such a solid microneedle array to pierce human skin and demonstrate the increased permeability of human skin by up to four orders of magnitude *in vitro*.

In order to realize three-dimensional out-of-plane hollow silicon microneedles, multiple lithography steps and a combination of wet and dry etching and deposition techniques have been used. Stoeber and Liepmann have fabricated arrays of out-of-plane, sharp, and hollow single-crystal silicon microneedles with a combination of isotropic and anisotropic etching techniques (Figure 12.7) [18].

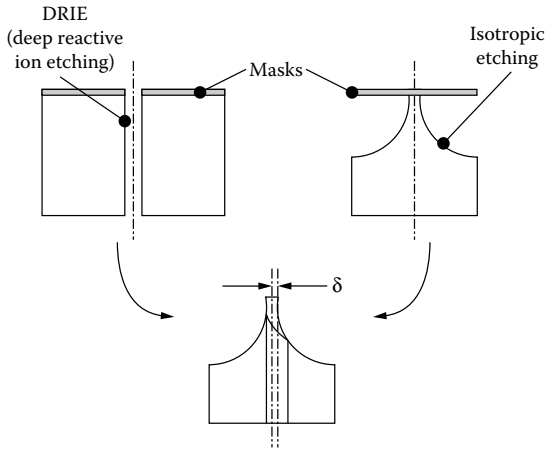

(a)

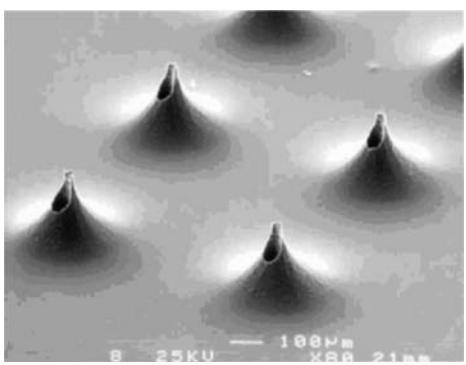

(b)

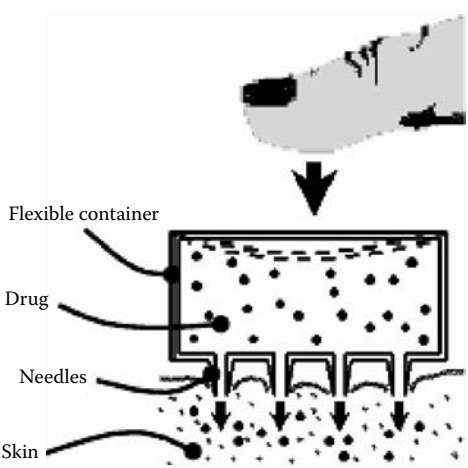

(c)

FIGURE 12.7
(a) Fabrication sequence, (b) SEM image of an array of pointed hollow silicon microneedles with a height of 200 μm and a channel diameter of 40 μm, and (c) a conceptual schematic diagram of a disposable MEMS syringe. (From B. Stoeber and D. Liepmann, Design, fabrication and testing of a MEMS syringe, in *Solid-State Sensors, Actuator and Microsystems Workshop*, Hilton Head Island, South Carolina, June 2–6, 2002. With permission.)

An array of needle channels through the substrate were defined using the DRIE process, which was followed by an isotropic etching process with a small offset of the center lines resulting in a microneedle with a sharp tip on the circumference of its shaft. They further demonstrated a disposable syringe that has a hollow microneedle array with a flexible polydimethyl siloxane (PDMS) container for drug storage.

Griss and Stemme demonstrated an array of hollow, out-of-plane silicon microneedles with openings in the shaft of the microneedles using three steps of dry etching (Figure 12.8) [19]. This particular microneedle was developed with

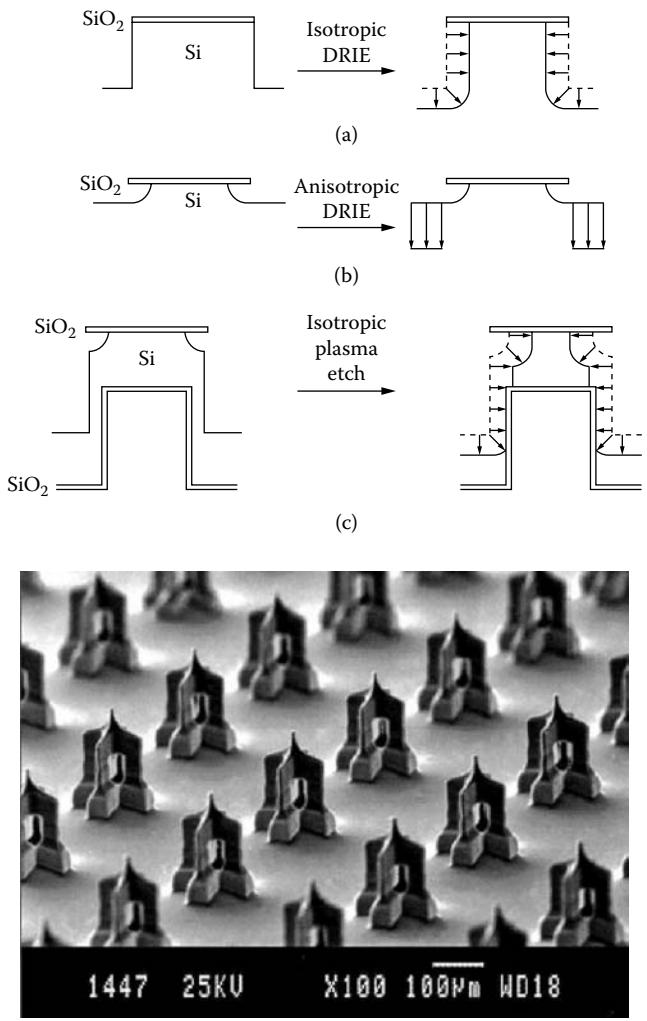

FIGURE 12.8
(Top) Three-step fabrication sequence, (Bottom) SEM image of side-opened, out-of-plane hollow silicon microneedles. (From P. Griss and G. Stemme, *J. of Microelectromechanical Systems*, 12, 296–301, 2003. With permission.)

a goal of achieving low flow resistance, high structural strength, a large area of drug exposure to the tissue, and a low risk of clogging. The size and position of the side flow channel openings were defined by RIE process parameters.

Gardeniers et al. demonstrated an array of hollow sharp silicon microneedles using a sequence of DRIE, anisotropic wet etching, and conformal thin film deposition steps (Figure 12.9) [20]. The thick black line in the Figure

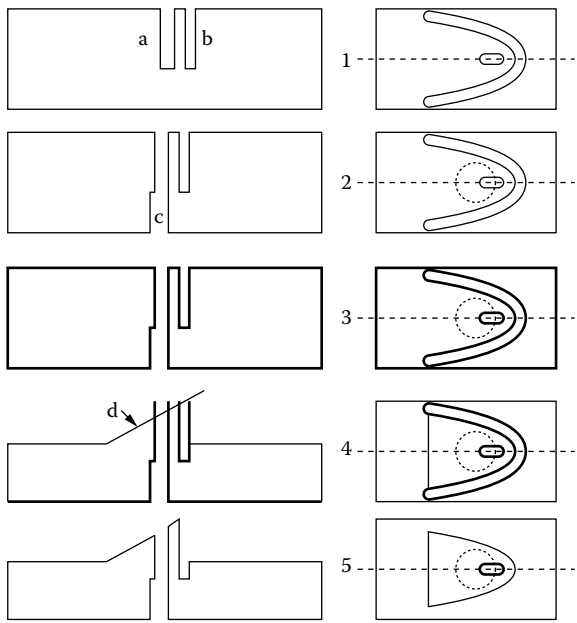

(a)

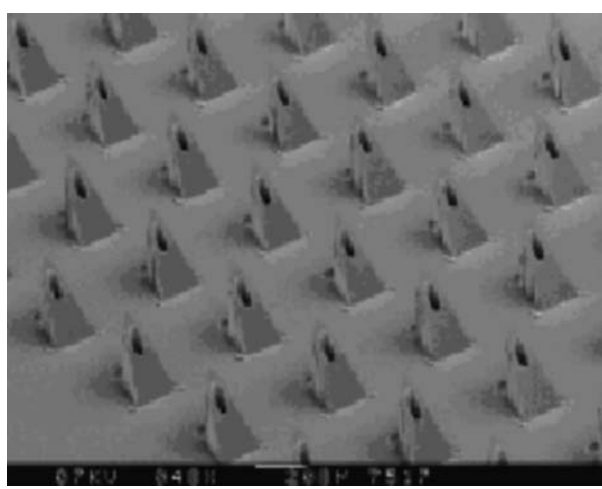

(b)

FIGURE 12.9
(a) Microneedle fabrication sequence; (b) SEM images of 350 μm–high triangular silicon microneedles. (From H. Gardeniers, R. Luttge, E. Berenschot, M. de Boer, S. Yeshurun, M. Hefetz, R. Oever, and A. Berg, *J. of Microelectromechanical Systems*, 12, 855–862, 2003. With permission.)

(c)

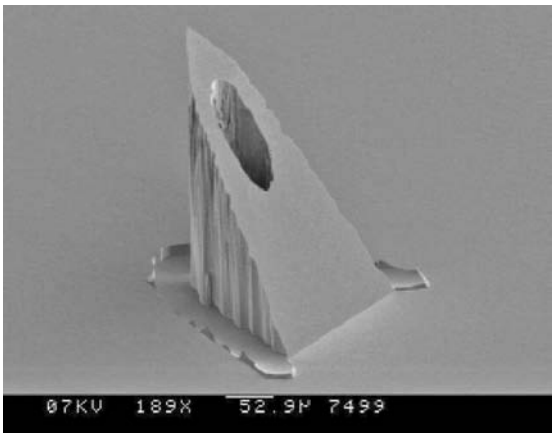

(d)

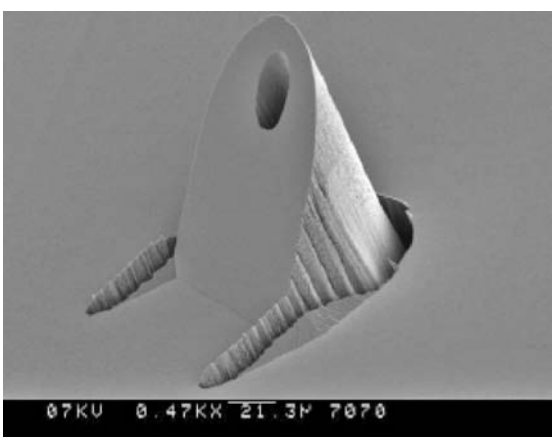

FIGURE 12.9 (continued)
(c,d) SEM images of 350 μm–high triangular silicon microneedles. (From H. Gardeniers, R. Luttge, E. Berenschot, M. de Boer, S. Yeshurun, M. Hefetz, R. Oever, and A. Berg, *J. of Microelectromechanical Systems*, 12, 855–862, 2003. With permission.)

12.9a represents a silicon nitride coating, which is used as a protection layer during KOH etching.

Mukerjee et al. produced different needle shapes by changing the relative position of the central bore hole to the shaft of the microneedles by a combination of DRIE, diamond blade circular sawing, and isotropic etching [21].

12.6 Out-of-Plane Metallic and Polymeric Microneedles

Along with out-of-plane silicon microneedles, there have been several investigations with respect to development of out-of-plane metallic microneedles

using electroplated metals. McAllister et al. demonstrated three-dimensional tapered-shaft and straight-shaft hollow metallic microneedles as shown in Figure 12.10 [22]. The straight-shaft microneedles were fabricated by electroplating through cylindrically defined SU-8 holes. For the tapered needles, a relatively complex combination of the SU-8 mold and the anisotropically etched sharp solid Si mold insert [17] and electroplating technique were used. The SU-8 was later etched from the top surface to form the tip opening by O_2/CHF_3 plasma and the SU-8 mold was fully etched away to release the metallic microneedles. Similar tapered metallic microneedles were demonstrated by Davis et al. using excimer and infrared laser micromachining [23]. In this approach, both the metal and polymer molds were drilled to form tapered conical holes by controlling the energy distribution of the laser beam, then conformal electroplating was carried out on these drilled molds to fabricate the metallic microneedles.

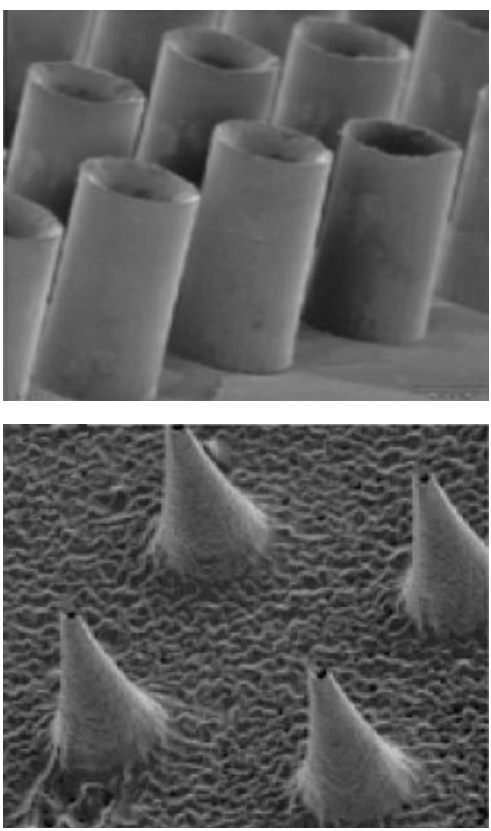

(a)

(b)

FIGURE 12.10
SEM photomicrographs of metallic microneedle arrays: (a) NiFe microtubes 200 μm in height and 80 and 40 μm in outer and inner diameter, respectively; (b) 150 μm–tall, hollow NiFe microneedles using an SU-8 mold of a silicon mold insert. (From D. McAllister, F. Cros, S. Davis, L. Matta, M. Prausnitz, M. Allen, *Dig. Transducers'99, Int. Conf. Solid-State Sensors and Actuators*, 1098–1101, 1999. With permission.)

Recently, Kim et al. demonstrated a tapered hollow metallic microneedle array using a relatively simple backside exposure of the SU-8 process [24]. An SU-8 mesa was formed on a glass substrate and another SU-8 layer, which was spun on top of the SU-8 mesa, was exposed through the backside of the glass substrate (Figure 12.11a). An array of SU-8 tapered pillar structures with angles between 3.1 and approximately 5° on top of the SU-8 mesa was formed. Conformal electrodeposition of metal was carried out, followed by mechanical polishing using a planarized polymeric layer. All organic layers were then removed to create a metallic hollow microneedle array with a fluidic reservoir on the back side. Both 200 μm– and 400 μm–tall, 10 by 10 arrays of metallic microneedles with inner diameters of the tip between 33.6 and approximately 101 μm, and wall thicknesses of 10 to approximately 20 μm were fabricated (Figure 12.11b). A polymeric microfluidic interconnector assembly was designed to have one male interconnector that directly fits into the fluidic reservoir (3 × 3 mm) of the microneedle array at one end, and another male interconnector that provides external fluidic interconnection to tubing (1/16 in. inner diameter) at the other end. Liquid transfer testing was carried out (Figure 12.11c) and the measured flow rate was approximately 72.5 nl/s-kPa.

As one of useful and cheap materials in MEMS applications, polymers have also been utilized to fabricate three-dimensional microneedle arrays. Moon and Lee demonstrated polymeric, hollow, out-of-plane microneedle arrays using a modified LIGA process [25]. The fabrication process consists of a vertical deep x-ray exposure and a successive inclined deep x-ray exposure, as shown in Figure 12.12. The first vertical exposure makes a triangular column array with a needle conduit through a deep x-ray mask. The triangular column array is shaped into the microneedle array by the second inclined x-ray exposure without additional mask alignment. Changing the inclined angle and the gap between the mask and PMMA (polymethyl-methacrylate) substrate, different types of microneedle arrays are fabricated. Although the microneedle is made of PMMA, a polymer, the three-dimensional tip is sharp, and mechanically robust enough to pierce the skin without fracturing.

12.7 Mechanical Robustness of the Microneedles

Microneedles made of brittle materials such as silicon have a high risk of catastrophic microneedle fracture during insertion. As an approach to solving this problem, Stupar and Pisano proposed parylene laminated silicon needles, parylene needles, and parylene needles with silicon tips [26]. It was found that fabricated parylene-coated silicon microneedles were strong enough to withstand significant bending moments.

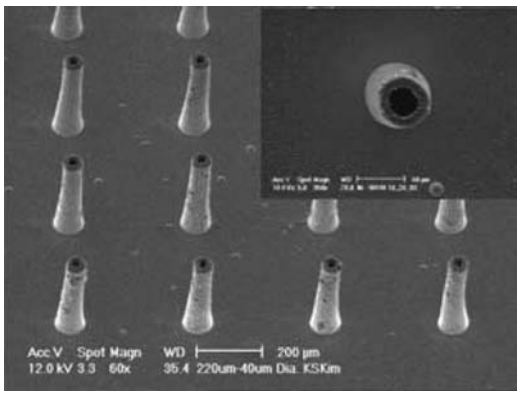

(a)

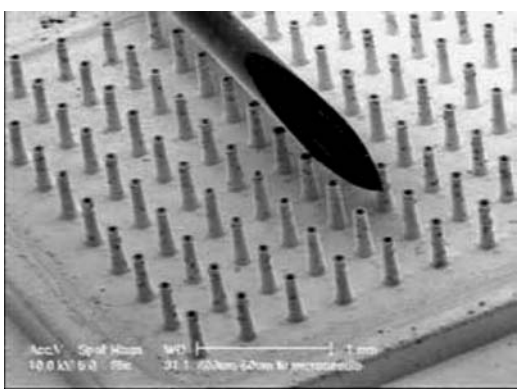

(b)

(c)

FIGURE 12.11
(a) Backside exposure of SU-8 through glass substrate and conformal electroplating process for simple tapered three-dimensional metallic microneedle array fabrication, (b) SEM photomicrograph of a 400 μm–tall tapered hollow metallic microneedle array in comparison with a conventional stainless steel needle. (From Kabseog Kim, D. Park, H. Lu, K-H. Kim, J.B. Lee, *J. Micromechanics and Microengineering*, 14, 597–603, 2004. With permission.). (c) An optical photomicrograph of successful liquid transfer through the microneedle array.

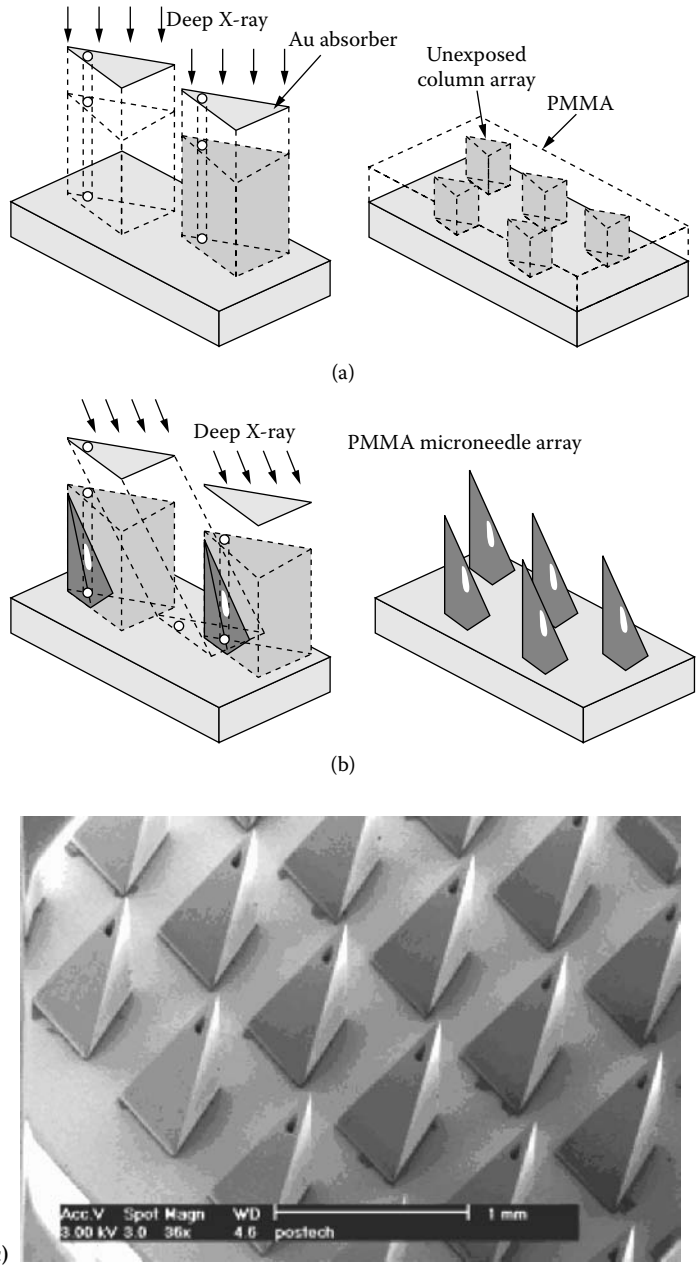

FIGURE 12.12
(a) and (b) Fabrication sequence of a PMMA microneedle array using the dual deep x-ray exposure process, (c) SEM of an array of sharp and long shank out-of-plane PMMA microneedles. (From S. Moon and S. Lee, *J. Micromechanics and Microengineering*, 15, 903–911, 2005. With permission.)

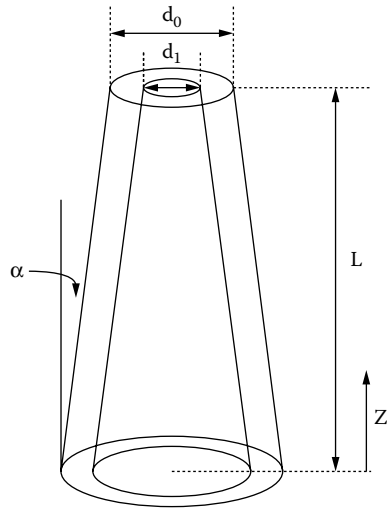

FIGURE 12.13
A schematic diagram of the hollow truncated cone column.

In order to predict the force of fracture of hollow microneedles, Kim et al. developed analytic solutions of the critical buckling of arbitrarily angled, truncated, hollow, cone-shaped columns (Figure 12.13) [24]. The critical buckling load (P_{cr}) for a fixed-free truncated cone column is given by:

$$P_{cr} = \frac{E}{80\pi L^2}\left[\begin{array}{l} \dfrac{5\pi^4}{16}\left(d_o^4 - d_i^4\right) + \left(5\pi^2 + \dfrac{5}{4}\pi^4\right)\left(d_o^3 - d_i^3\right)L\tan\alpha \\ + \left(15\pi^2 + \dfrac{5}{2}\pi^4\right)\left(d_o^2 - d_i^2\right)L^2\tan\alpha^2 \\ + \left(-120 + 30\pi^2 + \dfrac{5}{2}\pi^4\right)\left(d_o - d_i\right)L^3\tan\alpha^3 \end{array}\right], \qquad (12.1)$$

where d_0 and d_i are outer and inner diameters of the cone column, α is the taper angle, and L is the length of the microneedle. It was found that a single 400 μm–tall hollow cylindrical microneedle made of electroplated nickel with a wall thickness of 20 μm, a tapered angle of 3.08°, and a tip inner diameter of 33.6 μm has a critical buckling force of 1.8 N. This analytic solution can be used to create square or rectangular cross-sectioned column structures with proper modifications.

Recently, Davis et al. carried out comprehensive experimental and theoretical studies on the insertion and fracture forces of the microneedles [27]. It was found that insertion forces vary linearly with the interfacial area of the needle tip. Measured insertion forces were low (0.1–3 N) enough so that

the microneedle can be inserted into the skin by hand. A thin-shelled analytical model was used in this study to predict the fracture force. As expected, the fracture force was found to increase with increasing wall thickness, wall angle, and needle tip radius.

12.8 Microreservoir Devices for Drug Delivery

Although the majority of the MEMS work on drug delivery is on the development of microneedles, there has been another interesting approach for drug delivery using MEMS technology. The device is called a microreservoir and as the name suggests, it has a reservoir that contains a single dose of a drug, and the reservoir is covered by a lid. Depending on the size, the device can be surgically implanted, orally ingested, or injected into the body, and the lid of the reservoir is broken in a controlled manner to release the desired dosage of drug.

The first such device was reported by Santini et al. [28]. An array of microreservoirs was defined by crystallographic anisotropic bulk micromachining of silicon, and each microreservoir had a volume that could be filled with approximately 25 nl of drug (Figure 12.14). The microreservoirs were sealed with a very thin (0.3 μm–thick) gold membrane anode. When an appropriate electric potential is applied between the gold membrane anode and the cathode in the presence of chloride ion, the gold membrane is dissolved by its reaction with the chloride ion by forming soluble gold–chloride complexes. Because the device is scalable, large and small reservoirs with single or multiple drugs can be stored.

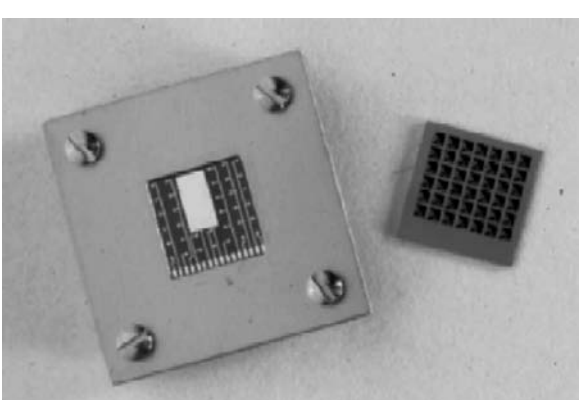

FIGURE 12.14
Silicon bulk micromachined microreservoir device for drug delivery. (From R. Shawgo, A. Grayson, Y. Li, and M. Cima, *Current Opinion in Solid State and Material Science*, 6, 329–334, 2002. With permission.)

A good introductory article on the microreservoir drug delivery device was published in an *IEEE Spectrum* [30]. When packaged with a power source and control electronics, the device is the size of a pacemaker. The device can be surgically implanted in the body and used for long-term controlled drug release. Specific reservoirs can be manually opened on demand by an external signal. It is also possible to make the microreservoir device ingestible; each membrane has a different thickness to be dissolved sequentially so that the drug can be released in a certain period of time.

A completely plastic microreservoir drug delivery system that does not require an electrical power source was reported by Su and Lin [31]. The device as shown in Figure 12.15 has an osmotic actuator on a substrate, which is bonded with a patterned PDMS to form a reservoir, a microfluidic channel, and a delivery port. Because this device uses water flow induced by osmosis as actuation mechanism [32], it does not require electrical power source.

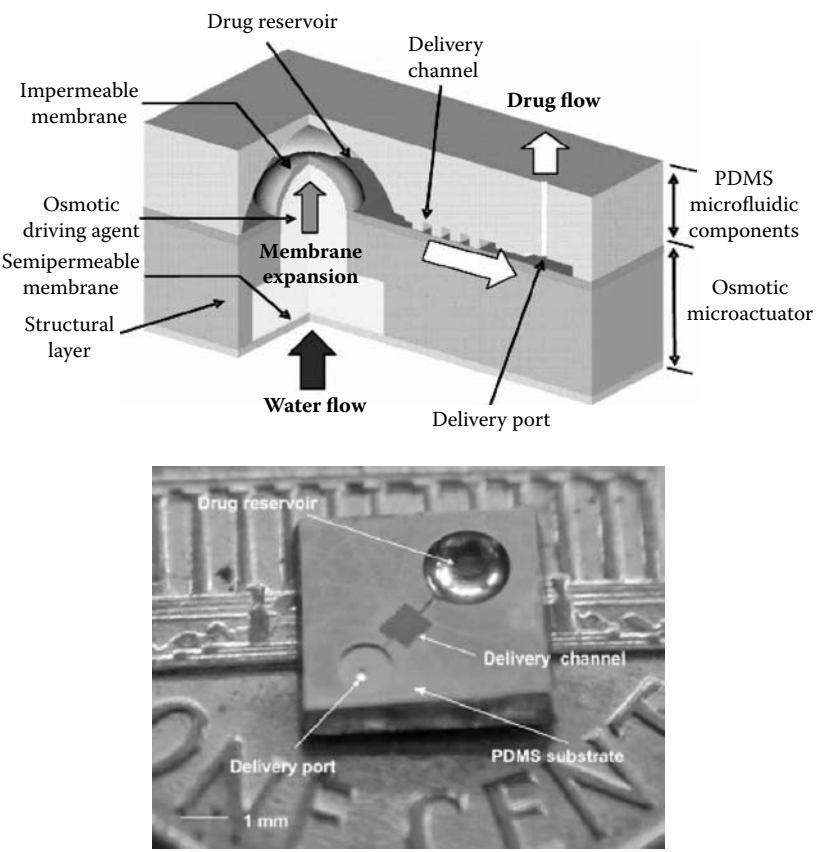

FIGURE 12.15
A water-powered drug delivery system. (From Y. Su and L. Lin, *J. Microelectromechanical Systems*, 13, 75–82, 2004. With permission.)

Since the drug delivery rate and drug storage reservoir volume are controllable, this device can be used both for quick drug release as well as long-term drug release.

12.9 Biocompatibility and Biofouling of MEMS Drug Delivery Devices

Biocompatibility of materials used in devices for *in vivo* applications is of paramount importance. Voskerician et al. carried out a comprehensive study on the biocompatibility and biofouling of common materials used for MEMS drug delivery devices including gold, silicon nitride, silicon dioxide, silicon, and SU-8 photoresist [33]. The material under test was placed into a stainless steel cage and the cage was implanted subcutaneously. The cage was periodically checked, the exudates in the cage were sampled, and leukocyte concentration was measured to determine the biocompatibility of the implanted material. It was determined that the responses of all of these materials, and that of the empty cage, were not much different, which let us draw the conclusion that all of the tested materials are biocompatible.

In addition, *in vivo* biofouling, which is measured as an undesirable accumulation of microorganisms on the implanted artificial surfaces, was also studied by scanning electron micrography. It was determined that gold, silicon nitride, silicon dioxide, and even SU-8 generate very low accumulations of microorganisms. In fact, gold is biocompatible, less prone to biofouling, and known for its corrosion resistance in many solutions over the entire pH range, making it an ideal coating material for *in vivo* MEMS devices.

However, silicon showed a much higher density of adherent cells in the biofouling test. This result shows that drug delivery MEMS devices made of silicon must be coated with biofouling-proof materials, such as silicon dioxide or silicon nitride, to be used in *in vivo* applications.

References

[1] R. McGrew and M. McGrew, *Encyclopedia of Medical History*, McGraw Hill, New York, 1985.

[2] J. Jagger, E. Hunt, J. Brand-Elnaggar, and R. Person, Rates of needle-stick injury caused by various devices in a university hospital, *New England J. of Medicine*, 319, 284–288, 1988.

[3] Australian College of Dermatologists, http://www.dermcoll.asn.au.

[4] K. Najafi and K. Wise, An implantable multielectrode array with on-chip signal processing, *IEEE J. Solid-State Circuits*, 21, 1035–1044, 1986.

[5] J. Chen, K. Wise, J. Hetke, and S. Bledsoe, A multichannel neural probe for selective chemical delivery at the cellular level, *IEEE Trans. Biomed. Eng.*, 44, 760–769, 1997.
[6] Q. Bai, K. Wise, and D. Anderson, A high-yield microassembly structure for three dimensional microelectrode arrays, *IEEE Trans. Biomed. Eng.*, 47, 281–289, 2000.
[7] L. Lin, A. Pisano, and R. Muller, Silicon processed microneedles, in *Dig. Transducers'93, Int. Conf. Solid-State Sensors and Actuators*, 237–240, 1993.
[8] L. Lin and A. Pisano, Silicon processed microneedles, *J. Microelectromechanical Systems*, 8, 78–84, 1999.
[9] N. Talbot and A. Pisano, Polymolding: two wafer polysilicon micromolding of closed flow passage for microneedles and microfluidic devices, *Solid State Sensor and Actuator Workshop Hilton Head*, 265–268, 1998.
[10] J. Zahn, N. Talbot, D. Liepmann, and A. Pisano, Microfabricated polysilicon microneedles for minimally invasive biomedical devices, *Biomedical Microdevices*, 2, 295–303, 2000.
[11] K. Chun, G. Hashiguchi, H. Toshioyoshi, B. Pioufle, J. Ishikawa, Y. Murakami, E. Tamiya, Y. Kikuchi, and H. Fujita, DNA injection into cell conglomerates by micromachined hollow microcapillary arrays, in *Dig. Transducers'99, Int. Conf. Solid-State Sensors and Actuators*, 41–47, 1999.
[12] K. Oka, S. Aoyagi, Y. Arai, Y. Isono, G. Hashiguchi, and H. Fujita, Fabrication of a microneedle for a trace blood test, *Sensors and Actuators A*, 97–98, 478–485, 2002.
[13] J. Brazzle, I. Papautsky, and B. Frazier, Hollow metallic micromachined needle arrays, *J. Micro Biomed. Devices*, 2, 197–205, 2000.
[14] S. Chandrasekaran, J. Brazzle and B. Frazier, Surface micromachined metallic microneedles, *J. of Microelectromechanical Systems*, 12, 289–295, 2003.
[15] S. Chandrasekaran and B. Frazier, Characterization of surface micromachined metallic microneedles, *J. of Microelectromechanical Systems*, 12, 281–288, 2003.
[16] R. Dizon, H. Han, A. Russell, and M. Reed, An ion milling pattern transfer technique for fabrication of three-dimensional micromechanical structures, *J. Microelectromech. Syst.*, 2, 151–159, 1993.
[17] S. Henry, D. McAllister, M. Allen, and M. Prausnitz, Microfabricated microneedles: a novel approach to transdermal drug delivery, *J. Pharm. Sci.*, 87, 922–925, 1998.
[18] B. Stoeber and D. Liepmann, Design, fabrication and testing of a MEMS syringe, in *Solid-State Sensors, Actuator and Microsystems Workshop,* Hilton Head Island, South Carolina, June 2–6, 2002.
[19] P. Griss and G. Stemme, Side-opened out-of-plane microneedles for microfluidic transdermal liquid transfer, *J. of Microelectromechanical Systems*, 12, 296–301, 2003.
[20] H. Gardeniers, R. Luttge, E. Berenschot, M. de Boer, S. Yeshurun, M. Hefetz, R. Oever, and A. Berg, Silicon micromachined hollow microneedles for transdermal liquid transport, *J. of Microelectromechanical Systems*, 12, 855–862, 2003.
[21] E. Mukerjee, S. Collins, R. Isseroff, and R. Smith, Microneedle array for transdermal biological fluid extraction and in situ analysis, *Sensors and Actuators, A*, 114, 267–275, 2004.
[22] D. McAllister, F. Cros, S. Davis, L. Matta, M. Prausnitz, M. Allen, Three-dimensional hollow microneedle and microtube arrays, in *Dig. Transducers'99, Int. Conf. Solid-State Sensors and Actuators*, 1098–1101, 1999.

[23] S. Davis, M. Prausnitz, and M. Allen, Fabrication and characterization of laser micromachined hollow microneedles, in *Dig. Transducers'03, Int. Conf. Solid-State Sensors and Actuators*, 1435–1438, 2003.
[24] K. Kim, D. Park, H. Lu, K-H. Kim, JB Lee, A tapered hollow metallic microneedle array using backside exposure of SU-8, *J. Micromechanics and Microengineering*, 14, 597–603, 2004.
[25] S. Moon and S. Lee, A novel fabrication method of a microneedle array using inclined deep x-ray exposure, *J. Micromechanics and Microengineering*, 15, 903–911, 2005.
[26] P. Stupar and A. Pisano, Silicon, parylene and silicon/parylene microneedles for strength and toughness, in *Dig. Transducers'01, Int. Conf. Solid-State Sensors and Actuators*, 1386, 2001.
[27] S. Davis, B. Landis, Z. Adams, M. Allen, and M. Prausnitz, Insertion of microneedles into skin: measurement and prediction of insertion force and needle fracture force, *J. Biomechanics*, 37, 1155–1163, 2004.
[28] J. Santini, M. Cima, and R. Langer, A controlled-release microchip, *Nature*, 397, 335–338, 1999.
[29] R. Shawgo, A. Grayson, Y. Li, and M. Cima, Bio-MEMS for drug delivery, *Current Opinion in Solid State and Material Science*, 6, 329–334, 2002.
[30] C. Webb, Chip shots, *IEEE Spectrum*, 41, 48–53, 2004.
[31] Y. Su and L. Lin, A water-powered micro drug delivery system, *J. Microelectromechanical Systems*, 13, 75–82, 2004.
[32] Y. Su, L. Lin, and A. Pisano, A water-powered osmotic microactuator, *J. Microelectromechanical Systems*, 11, 736–742, 2002.
[33] G. Voskerician, M. Shive, R. Shawgo, H. von Recum, J. Anderson, M. Cima, and R. Langer, Biocompatibility and biofouling of MEMS drug delivery devices, *Biomaterials*, 24, 1959–1967, 2003.

13

Microchip Capillary Electrophoresis Systems for DNA Analysis

Ryan T. Kelly and Adam T. Woolley

CONTENTS

13.1 Introduction

Nucleic acids are the storage medium for inherited information in living organisms. Thus, scientists have considerable interest in developing enhanced tools for the determination of nucleic acids, and the past twenty years have seen a tremendous expansion in DNA analysis capabilities. Size sorting of DNA, a critical aspect of both genotyping and sequencing, has been transformed from an onerous, slow, and labor-intensive operation involving slab gel electrophoresis to a rapid, automated, and ultra-high-throughput process. The initial miniaturization of electrophoresis into a capillary format enabled higher electric fields to be applied in DNA separations, providing much faster analyses.[1–3] The subsequent development of capillary array electrophoresis (CAE) systems with parallel bundles of lanes[4–6] provided a substantial boost in DNA sample analysis capacity. These advances

were among the first clear manifestations of the benefits of miniaturization and parallel separation in DNA analysis.

While CAE was being developed, researchers were also evaluating next-generation techniques to enhance DNA analysis even more. Indeed, in 1992, the same year that CAE systems for DNA separation were reported, a new technology involving planar capillary electrophoresis (CE) microdevices was described in the literature.[7] CE microchips were quickly recognized as having potential for both miniaturizing chemical separations and integrating various sample handling steps in analyses. The processes involved in the fabrication of planar CE microdevices, such as photolithographic patterning, etching of substrates, growth of thin films, metal deposition, and so on, were in large part developed for integrated circuit manufacturing. These techniques have now been modified to meet the needs of scientists interested in miniaturizing chemical analysis systems. Figure 13.1 depicts schematically the general procedures involved in glass CE microchip fabrication. Importantly, the layout for a micromachined device can be created using computer-aided design software, so rather than having to couple various chambers and capillaries together manually to perform a multistep analysis, different analytical procedures can be integrated on a single, monolithic platform through the clever design of photomasks for batch microfabrication. The advantages of miniaturization looked especially appealing to researchers trying to improve DNA analysis, so CE microchips were soon enlisted for this task.

In this chapter we document how DNA separations in CE microdevices have improved during the past decade. We also discuss how analysis throughput has been enhanced significantly by using CAE microchips. We then detail progress in the integration of DNA sample preparation with CE separation. Finally, we describe a new phase-changing sacrificial layer microfabrication methodology that holds great promise for making low-cost polymeric microdevices for DNA analysis.

13.2 Optimization of DNA Sequencing Separations

In 1994 Effenhauser et al. separated fluorescently labeled oligonucleotides in 45 s,[8] and Woolley and Mathies analyzed PCR products and restriction digests in approximately 100 s,[9] utilizing CE microchips fabricated using procedures similar to those in Figure 13.1. In the following year, four-color DNA sequencing with a read length of approximately 150 bases (97% accuracy) in less than 10 min was demonstrated in a microfabricated CE device.[10] Since these initial publications, significant DNA sequencing improvements have been made in single-lane micromachined systems.[11–15] As discussed below, important parameters, including the sieving matrix, device temperature, electric field, and channel length, have been optimized.

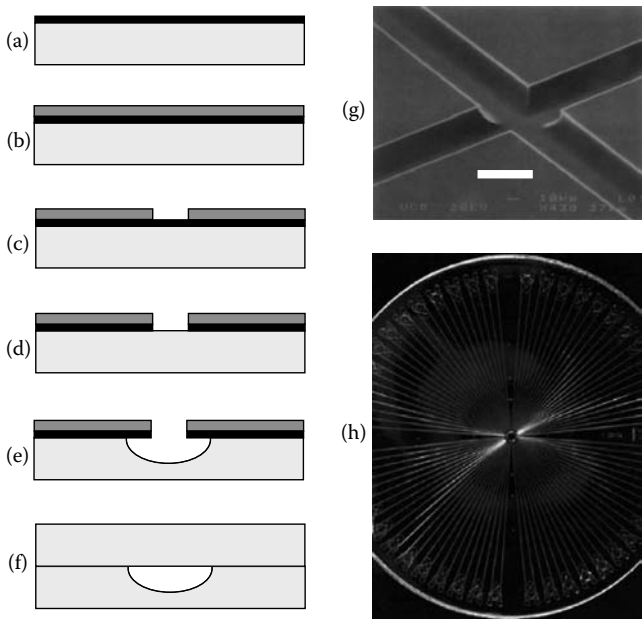

FIGURE 13.1
Schematic overview of typical methods for glass CE microchip fabrication. (a) A thin layer of amorphous silicon (black) is deposited on a clean glass wafer (light gray, side view). (b) Photoresist (dark gray) is spin coated on top of the amorphous silicon. (c) UV radiation on regions of the surface that are not protected by a mask enables the patterned photoresist to be solubilized in a developer solution. (d) Amorphous silicon, which is uncovered by the removal of photoresist, is etched away in a CF_4 plasma. (e) The underlying glass in the pattern of the exposure mask is etched isotropically in HF. (f) Photoresist and amorphous silicon are removed from the etched wafer, which is then bonded in a furnace to another piece of glass. (g) Electron micrograph of channels patterned and etched as described above. Scale bar is 50 μm. (Reprinted with permission from Simpson, P.C., Woolley, A.T., and Mathies, R.A., *J. Biomed. Microdevices*, 1, 7, 1998. Copyright 1998, Springer Science and Business Media.) (h) Top-view photograph of a 96-channel glass microdevice. (Image courtesy of Prof. Richard A. Mathies.)

Because DNA molecules have essentially the same electrophoretic mobility in free solution regardless of fragment length, size-based separation is achieved best in cross-linked gels or entangled polymer solutions. Entangled linear polymers provide convenient sieving matrixes because they can be pumped into capillaries or channels and replaced with fresh solution as needed.[16] Linear polyacrylamide (LPA) has been widely used for DNA sequencing in both capillaries[17] and microdevices, and extensive research effort has led to improved microchip DNA separations with LPA. A systematic study was performed to develop a quantitative model of DNA separation in LPA, resulting in nearly a threefold increase in sequencing read length[11] compared to earlier microchip results.[10] Another group used an optimized polymerization protocol[17] to produce approximately 1 MDa average molecular weight LPA, which provided four-color sequencing to 500 bases in 20 min

with 99.4% accuracy in a microchip.[15] Salas-Solano et al. used a mixture of both high and low molecular weight LPA to improve microchip sequencing.[12] Similar read lengths were obtained using either 4% 10 MDa LPA or a blend of 3% 10 MDa LPA and 1% 50 kDa LPA, but the run time was reduced significantly with the mixed sieving matrix: four-color sequencing to 580 bases with 98.5% accuracy was achieved in 18 min.[12]

A polyacrylamide *nanogel* medium with similar rheological properties to LPA was developed to improve separation performance.[14] The matrix was made by copolymerizing acrylamide with a small amount (approximately 10^{-4} mol %) of *N,N*-methylene bisacrylamide (Bis) cross-linker, such that Bis moieties were present in approximately 75% of the polymer chains, providing intra- and intermolecular covalent linkages. The Bis concentration was sufficiently low to prevent the polymerization of a rigid, cross-linked hydrogel; instead, subcolloidal structures with an average radius of approximately 230 nm were formed. A comparison of performance between nanogel and LPA matrixes using CE showed that average sequencing read lengths were approximately 20% greater with the nanogel matrix, yielding 680 bases with 98.5% accuracy. The nanogel medium was also evaluated in 96-lane CAE microdevices, and average sequence read lengths for the same separation time increased by approximately 4% compared with LPA; importantly, loading of the nanogel matrix into microchannels was much easier than LPA.

Other efforts to create sieving matrixes that are optimized for microchip DNA separations have focused on reducing the solution viscosity because the pressure (greater than 300 psi[13]) required for filling microchannels with LPA can cause thermally bonded glass microdevices to delaminate.[16] One promising approach is to use polymer solutions whose viscosities change abruptly at a certain temperature, allowing easy pumping into channels in the low viscosity state, after which the temperature can be adjusted to create a solution with appropriate sieving properties for DNA separation. A copolymer of *N,N*-diethylacrylamide and *N,N*-dimethylacrylamide was used as such a thermoresponsive sieving medium for DNA sequencing.[18] The low-viscosity solution was loaded into the separation column above 75°C, such that the polymer chains were insoluble and aggregated to form dispersed, colloidal droplets. For CE, the solution was cooled to 44°C, causing the polymer to redissolve and form an entangled matrix. DNA sequence information to approximately 460 bases was obtained with 97% accuracy in a CE system. An alternative viscosity-switching matrix with a *N*-methoxyethylacrylamide/*N*-ethoxyethylacrylamide copolymer has been reported, in which the transition from low to high viscosity occurs when the temperature is raised,[19] allowing facile solution pumping into a capillary at room temperature. At 44°C (above the viscosity transition temperature), CE sequencing to approximately 600 bases with 98.5% accuracy was obtained. Even though these viscosity-switching matrixes have only been evaluated in conventional CE, their rheological properties are especially attractive for microchip DNA separations.

In addition to the composition of the sieving matrix, DNA separation conditions are crucial. For instance, column temperature affects both separation quality and speed; if the temperature is raised to between 35 and 50°C, the run time decreases and the read length increases because compression regions are largely eliminated.[12,15,17] Heating beyond this optimal temperature range further reduces the run time, but the resolution becomes worse, due to a combination of increased analyte diffusion[15] and less favorable DNA interactions with the sieving matrix.[12] Microchannel length and depth also influence separation performance. Longer channels increase read lengths but require greater run times; for example, Koutny et al. sequenced over 800 bases in a 40 cm–long microchannel, but the separation time was 80 min.[13] With sufficiently narrow microchannels (less than 150 μm), Joule heating has little effect on resolution unless electric fields greater than 200 V/cm are applied.[12] Thus, 50 μm–deep channels provided similar resolution to shallower lanes, but the greater optical path length in the deeper microchannels improved detection sensitivity.[15]

13.3 Parallel DNA Separations in Microchips

Microchip systems provide a clear benefit relative to conventional CE in terms of analysis speed;[20] however, single-lane microdevices do not offer an appreciable gain in sample throughput in comparison with either slab gel electrophoresis or CAE instrumentation. To maximize the impact of micromachined analysis systems on DNA separations, it was essential for sample throughput to be increased over that of single-lane devices. Indeed, one of the first papers on microchip CE of DNA recognized this need: each microdevice had fifteen lanes, although separations in individual microcapillaries were performed serially rather than in parallel.[9]

The first demonstration of microchip CAE of DNA was reported in 1997;[21] glass microchips with twelve independent lanes were constructed, and detection was carried out by repeated linear scanning of the bundled channels using a confocal laser-induced fluorescence system. Twelve DNA restriction digest samples were analyzed in less than 160 s in these devices, and excellent lane-to-lane separation reproducibility was evidenced by the less than 1.5% relative standard deviation for band migration times. Practical application of 12-lane CAE microdevices was shown in rapid typing experiments on the *HFE* gene. These CAE microchips provided an order-of-magnitude increase in throughput over single-lane devices, but still lagged behind the sample-handling capabilities of slab gel and conventional CAE systems. Another fourfold increase in sample capacity was gained by carrying out four serial injections in twelve lanes in a CAE microdevice with a modified design;[22] however, the analysis throughput rate remained about the same as in the earlier CAE chip setup.[21] Subsequently, a 48-lane CAE microplate was developed; this system enabled

HFE typing of 96 samples in about 8 min,[23] a severalfold improvement in throughput over previous studies. However, increasing the number of separation lanes beyond approximately 50 would have been difficult in this format, as the parallel bundle of capillaries in the detection region was already approaching a 1 cm width, such that adding channels would have led to less than ideal sampling in the linearly rastered scanning confocal detection system.

To overcome these limitations, a rotary scanning confocal detection setup was constructed,[24] and radial CAE microplates were designed as outlined in Figure 13.2.[25] These microchips had sample loading regions around the

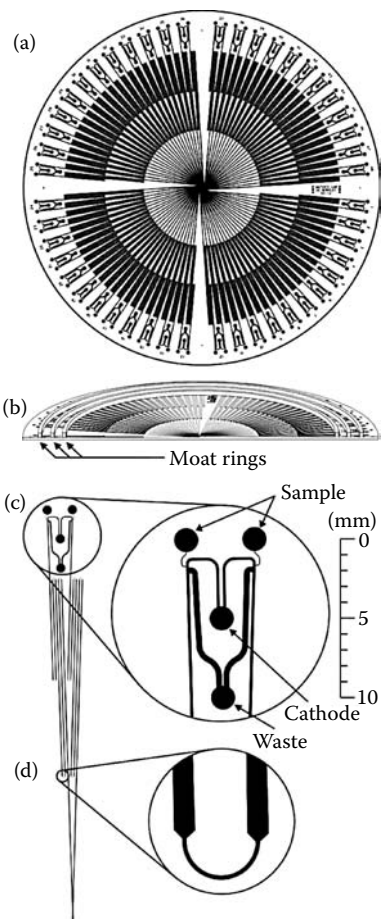

FIGURE 13.2
Microdevice layout for 96-channel CAE sequencing. (a) Top view. (b) Vertical cutaway of a CAE microdevice. Concentric plastic rings create separate "moats" used to provide electrical contact to the drilled cathode and waste ports. (c) Expanded view of the injector region. (d) Expanded view of the channel turn geometry used to reduce dispersion. (Reprinted with permission from Paegel, B.M. et al., High throughput DNA sequencing with a microfabricated 96-lane capillary array electrophoresis bioprocessor, *Proc. Natl. Acad. Sci. USA*, 99, 574, 2002. Copyright 2002, National Academy of Sciences.)

perimeter, and the separation capillaries converged at the center of a device to enable the rotary detection system to probe each lane readily. Sequencing separations on M13mp18 samples were carried out in 96-lane microplates, with a mean read length of 430 bases per channel at 99% accuracy, corresponding to a throughput of 1.7 kilobases per minute.[25] This sequencing rate was fivefold higher than in the best commercial instrumentation and represented a 100-fold increase over the first microchip sequencing paper.[10] Radial CAE microdevices for sizing 384 DNA specimens were also developed in a layout similar to the 96-sample microplates.[26] These microsystems were fabricated on 20 cm–diameter glass disks and had 8 cm–long, gel-filled channels. *HFE* genotyping was performed simultaneously on 384 samples, and the separation time was approximately 325 s, corresponding to a throughput of more than one sample per second. This format provided faster separation times and fourfold more lanes than the best commercial instruments, yielding a 20-fold improvement in throughput.

As a summary of the enhanced throughput enabled by micromachining, Figure 13.3 illustrates how sample processing rates have increased over the past decade for DNA sizing and sequencing by microchip CE. Two key advances led to improved DNA sequencing throughput: first, read lengths increased fourfold between 1995 and 1999 with better sieving matrix formulations and optimized separation conditions (discussed in Section 13.2); second, multichannel sequencing microchips raised sample throughput from one lane in 1995,[10] to 16 lanes in 2000,[27] and 96 lanes in 2002.[25] Is it possible to increase DNA throughput in CE microdevices even more? Several factors influence how many samples can be analyzed in CE microchips. These limitations include the microdevice surface area occupied by sample input systems, the length of separation channels, and the parallel bundling of lanes for detection. For instance, in 20 cm–diameter, 384-lane microplates, approximately 15% of the surface area was occupied by the sample injectors alone.[26] Thus, increasing well beyond several hundred capillaries would require either larger-diameter substrates or microfabrication advances that reduce sample injector dimensions. Moreover, the packing of lanes in the central

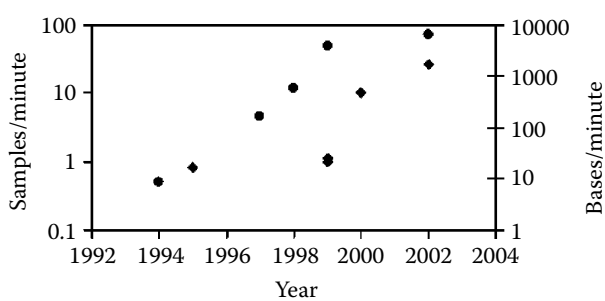

FIGURE 13.3
Throughput improvement over time for DNA analysis in micromachined systems. Circles refer to DNA sizing (left axis) and are from References 9, 21, 23, 24, and 26. Diamonds correspond to four-color sequencing (right axis) and are from References 10, 15, 25, 27, and 52.

detection region is a key factor as the number of separation channels increases. For a 200-μm lane pitch typical of CAE microchips,[23] 384 channels would reach their closest packing approximately 1.2 cm from the center of a device, which is about half of the maximum radius of current rotary scanners.[26] Because the closest packing radius is directly proportional to both the number of capillaries and the pitch between them, the interlane spacing must be decreased, or larger-radius confocal scanning systems must be developed to increase sample capacity in CAE microplates.

13.4 Integrated Microchips for DNA Analysis

Section 13.3 describes how micromachined systems can provide high throughput in DNA separations. Another area where microchips have great potential to streamline DNA analysis is in the integration of multiple steps on a single miniaturized platform. For example, thermal cycling is an important sample processing step in DNA amplification by PCR, and considerable progress has been demonstrated in the integration of PCR with microchip DNA separation. The ease of micromachining submicroliter-volume containers and the efficient heat transfer in such small vessels are important benefits of downsizing PCR.

Microchips that integrate PCR with CE have been demonstrated in two different formats. Whole-device cycling is one approach, where an entire microsystem having a reaction chamber connected to CE channels is heated and cooled in a conventional thermal cycler, and then the microchip is transferred manually to a separate platform for electrophoretic analysis.[28] The more widely applied PCR-CE format involves thermal cycling of only the reaction chamber (and not the integrated separation microfluidics). This approach was first demonstrated using a micromachined silicon PCR chamber attached to a glass CE microchip.[29] A viscous sieving matrix in the separation channel prevented the PCR mixture from entering the analysis microfluidics during amplification; after PCR, the sample was injected into the CE system by a potential applied between the reaction chamber and a waste reservoir. Monolithically integrated PCR-CE systems with localized reaction vessel heating have made important improvements over this initial work. In one study, the PCR chamber was heated with focused infrared radiation, providing approximately 12 s cycle times and completing DNA amplification in approximately 4 min.[30] This device format provided approximately 10 min amplification of a β-globin target, which was analyzed subsequently by microchip CE in the integrated device.[31] Mathies's group developed integrated PCR-CE microdevices with 200 nL reaction chambers.[32] Micropatterned heaters and temperature sensors, as well as valves to control fluid within a microchip, provided exceptional control over processing, such that PCR amplification from a single DNA template with on-chip CE analysis

was feasible.[33] Continuous-flow thermal cycling, which involves transferring the sample between regions of different temperatures in a microfluidic array, is a PCR amplification approach that is well suited for the microchip format.[34] Recent flow PCR microdevice experiments have demonstrated convective[35] and electrokinetic[36] sample movement between temperature zones; future efforts should lead to integration of flow PCR with microchip CE.

Miniaturization and integration of sample handling operations such as DNA extraction and purification are also advantageous, and important progress has been seen in this area. A microchip with silica beads embedded in a sol-gel in a microchannel was developed and shown to be effective in solid-phase extraction of DNA from whole blood in preparation for PCR amplification.[37] Oligonucleotide-modified hydrogels having a sequence complementary to a target analyte[38] have been devised for sample cleanup after DNA sequencing reactions.[39] Prior to microchip CE analysis the raw Sanger extension product sample is passed through the hydrogel, and the target DNA fragments are captured selectively while the high-salt buffer, dNTPs and template, which can interfere with separation, are not retained. The purified target DNA is then eluted with an electric field, heat, or a different buffer to allow facile on-chip CE.

Recent work from Mathies's group[40] has demonstrated that sophisticated DNA analyses for the detection of whole bacterial cells can be integrated in a portable, high-performance microchip setup. Indeed, detection limits of approximately 3 *E. coli* cells were obtained, a specific *E. coli* strain was recognized in the presence of a 10,000-fold higher background of another strain, and methicillin resistance of *S. aureus* was probed in these portable microanalysis systems. Importantly, the miniaturized and integrated format provided rapid (less than 30 min) analysis times for these PCR-CE determinations; such results showcase the power of microchip devices.

13.5 Phase-Changing Sacrificial Layers for Polymer Microchip Fabrication

Challenges associated with micromachining and thermally bonding glass microfluidic devices have led researchers to pursue alternative materials, such as polymers, which offer greater fabrication ease and flexibility. Indeed, polymeric substrates have been effective in carrying out electrophoretic DNA analyses.[41–44] However, DNA sequencing separations in plastic microchips[45,46] have not yet achieved the performance of those in glass microdevices. For low-cost polymer microchips to be legitimate alternatives to glass microsystems for DNA sequencing, two performance-limiting factors must be addressed. First, the maximum internal pressure (approximately 200 psi) that can be applied without delaminating thermally bonded poly(methyl methacrylate) (PMMA) microchips[47] is much lower than can

be sustained in glass (approximately 2,000 psi),[48] making it difficult to fill thermally bonded polymer devices with viscous sieving solutions typically used for DNA sequencing. Second, covalent surface passivation procedures are straightforward for glass microdevices, but less well established in polymers. Therefore, polymer microchips with a stronger bond between substrates and appropriately modified surfaces should perform as well as glass, while offering greater fabrication ease and lower costs.

We have addressed the delamination issue by developing a phase-changing sacrificial layer (PCSL) approach for solvent bonding polymer substrates that can withstand much higher internal pressures than thermally sealed systems.[47] The solvent bonding fabrication procedure is shown in Figure 13.4a–e. First, temporarily enclosed microchannels are formed by sealing poly(dimethylsiloxane) (PDMS, gray, Figure 13.4a) over a patterned PMMA substrate (white), with access holes in the PDMS aligned with the PMMA channel ends. The assembly is heated to 70°C, and a liquid PCSL (paraffin wax, white with gray horizontal lines, Figure 13.4b) is loaded into the microchannels. When the device is cooled to room temperature, the PCSL solidifies (gray with white horizontal lines, Figure 13.4c) and prevents bonding solvent (black) or softened PMMA from filling the channels during the process of affixing a polymer cover plate to the patterned substrate (Figure 13.4d). Once a seal has formed between the PMMA pieces, the microchip is heated to 70°C to melt the PCSL, which is removed easily (Figure 13.4e) by first applying vacuum at the reservoirs and then flushing cyclohexane through the channels. The improved robustness of PCSL-fabricated, solvent-bonded PMMA microdevices has allowed hundreds of CE separations at electric fields as high as 1.5 kV/cm to be performed in a single microchip without any degradation of performance.[47] Moreover, internal pressures greater than 2,200 psi have been applied without delaminating the PMMA substrates,[47] indicating excellent compatibility with conditions for introducing viscous sieving media for DNA sequencing.

In addition, PCSLs can facilitate the interfacing of hydrogel membranes with microfluidic networks in polymers.[49] This capability should be valuable for DNA sample enrichment prior to CE, which has been shown in glass microdevices having a porous sodium silicate thin film,[50,51] although the microchip fabrication was somewhat cumbersome. In contrast, polymerization of an ion-permeable membrane *in situ* using a PCSL is straightforward; a patterned microchannel is filled with PCSL (Figure 13.4a and b) as described above, and a second substrate having an opening to serve as a membrane reservoir is brought into contact with the microchannel-containing piece (Figure 13.4f). The PCSL prevents the prepolymer solution (dark gray, Figure 13.4g) in the well from filling the channel, and after polymerization a rigid, semipermeable hydrogel (gray with white cross-hatching, Figure 13.4h) is formed. Finally, the PCSL is melted and removed (Figure 13.4i) as described previously, providing a microfluidic array interfaced with an ionically conductive hydrogel.

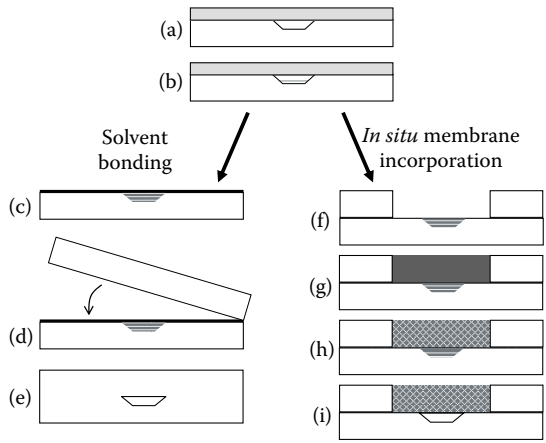

FIGURE 13.4
Phase-changing sacrificial layers for solvent bonding (left) and interfacing polymerized hydrogels with microchannels (right). Additional description is in the text.

Although the initial application of PCSLs in coupling membranes with microfluidics involved protein focusing in an electric field gradient,[49] the same technology should also enable on-column DNA preconcentration for CE. Thus, the newly developed PCSL fabrication approach offers great promise in creating low-cost yet powerful microfluidic systems for DNA analysis.

13.6 Conclusions

Microfabrication technologies have led to the formation of sophisticated microfluidic instrumentation, which has advanced DNA analysis. The development of better sieving matrices and separation conditions has facilitated DNA characterization in both capillary and micromachined systems. In addition, the construction of increasingly parallel microdevice architectures that can handle hundreds of samples simultaneously has raised DNA separation throughput significantly. Moreover, micromachined systems provide a facile platform for the coupling of multiple sample manipulation steps on a single substrate, and this integration has led to versatile and powerful DNA analysis devices for pathogen detection, single-template PCR amplification, and more. Finally, phase-changing sacrificial layer microchip fabrication should facilitate the development of low-cost, high-performance polymer microdevices for DNA characterization. This continued progress in microfluidic systems will further increase DNA separation performance, throughput, and versatility, while driving analysis costs lower.

Acknowledgment

The authors gratefully acknowledge financial support from the National Institutes of Health (1 R01 GM064547-01A1).

References

1. Kasper, T.J. et al., Separation and detection of DNA by capillary electrophoresis, *J. Chromatogr.*, 458, 303, 1988.
2. Cohen, A.S. et al., Rapid separation of DNA restriction fragments using capillary electrophoresis, *J. Chromatogr.*, 458, 323, 1988.
3. Drossman, H. et al., High-speed separations of DNA sequencing reactions by capillary electrophoresis, *Anal. Chem.*, 62, 900, 1990.
4. Huang, X.C., Quesada, M.A., and Mathies, R.A., DNA sequencing using capillary array electrophoresis, *Anal. Chem.*, 64, 2149, 1992.
5. Huang, X.C., Quesada, M.A., and Mathies, R.A., Capillary array electrophoresis using laser-excited confocal fluorescence detection, *Anal. Chem.*, 64, 967, 1992.
6. Mathies, R.A. and Huang, X.C., Capillary array electrophoresis: An approach to high-speed, high-throughput DNA sequencing, *Nature*, 359, 167, 1992.
7. Manz, A. et al., Planar chips technology for miniaturization and integration of separation techniques into monitoring systems: Capillary electrophoresis on a chip, *J. Chromatogr.*, 593, 253, 1992.
8. Effenhauser, C.S. et al., High-speed separation of antisense oligonucleotides on a micromachined capillary electrophoresis device, *Anal. Chem.*, 66, 2949, 1994.
9. Woolley, A.T. and Mathies, R.A., Ultra-high-speed DNA fragment separations using microfabricated capillary array electrophoresis chips, *Proc. Natl. Acad. Sci. USA*, 91, 11348, 1994.
10. Woolley, A.T. and Mathies, R.A., Ultra-high-speed DNA sequencing using capillary electrophoresis chips, *Anal. Chem.*, 67, 3676, 1995.
11. Schmalzing, D. et al., DNA sequencing on microfabricated electrophoretic devices, *Anal. Chem.*, 70, 2303, 1998.
12. Salas-Solano, O. et al., Optimization of high-performance DNA sequencing on short microfabricated electrophoretic devices, *Anal. Chem.*, 72, 3129, 2000.
13. Koutny, L. et al., Eight hundred-base sequencing in a microfabricated electrophoretic device, *Anal. Chem.*, 2000, 3388, 2000.
14. Doherty, E.A.S. et al., Sparsely cross-linked "nanogel" matrixes as fluid, mechanically stabilized polymer networks for high-throughput microchannel DNA sequencing, *Anal. Chem.*, 76, 5249, 2004.
15. Liu, S. et al., Optimization of high-speed DNA sequencing on microfabricated capillary electrophoresis channels, *Anal. Chem.*, 71, 566, 1999.
16. Albarghouthi, M.N. and Barron, A.E., Polymeric matrices for DNA sequencing by capillary electrophoresis, *Electrophoresis*, 21, 4096, 2000.
17. Carrilho, E. et al., Rapid DNA sequencing of more than 1000 bases per run by capillary electrophoresis using replaceable linear polyacrylamide solutions, *Anal. Chem.*, 68, 3305, 1996.

18. Buchholz, B.A. et al., Microchannel DNA sequencing matrices with a thermally controlled "viscosity switch," *Anal. Chem.*, 73, 157, 2001.
19. Kan, C.-W., Doherty, E.A.S., and Barron, A.E., A novel thermogelling matrix for microchannel DNA sequencing based on poly-N-alkoxyacrylamide copolymers, *Electrophoresis*, 24, 4161, 2003.
20. Jacobson, S.C. et al., Microchip structures for submillisecond electrophoresis, *Anal. Chem.*, 70, 3476, 1998.
21. Woolley, A.T., Sensabaugh, G.F., and Mathies, R.A., High-speed DNA genotyping using microfabricated capillary array electrophoresis chips, *Anal. Chem.*, 69, 2181, 1997.
22. Simpson, P.C., Woolley, A.T., and Mathies, R.A., Microfabrication technology for the production of capillary array electrophoresis chips, *J. Biomed. Microdevices*, 1, 7, 1998.
23. Simpson, P.C. et al., High throughput genetic analysis using microfabricated 96-sample capillary array electrophoresis microplates, *Proc. Natl. Acad. Sci. USA*, 95, 2256, 1998.
24. Shi, Y. et al., Radial capillary array electrophoresis microplate and scanner for high-performance nucleic acid analysis, *Anal. Chem.*, 71, 5354, 1999.
25. Paegel, B.M. et al., High throughput DNA sequencing with a microfabricated 96-lane capillary array electrophoresis bioprocessor, *Proc. Natl. Acad. Sci. USA*, 99, 574, 2002.
26. Emrich, C.A. et al., Microfabricated 384-lane capillary array electrophoresis bioanalyzer for ultrahigh-throughput genetic analysis, *Anal. Chem.*, 74, 5076, 2002.
27. Liu, S. et al., Automated parallel DNA sequencing on multiple channel microchips, *Proc. Natl. Acad. Sci. USA*, 97, 5369, 2000.
28. Waters, L.C. et al., Multiple sample PCR amplification and electrophoretic analysis on a microchip, *Anal. Chem.*, 70, 5172, 1998.
29. Woolley, A.T. et al., Functional integration of PCR amplification and capillary electrophoresis in a microfabricated DNA analysis device, *Anal. Chem.*, 68, 4081, 1996.
30. Giordano, B.C. et al., Polymerase chain reaction in polymeric microchips: DNA amplification in less than 240 seconds, *Anal. Biochem.*, 291, 124, 2001.
31. Ferrance, J.P. et al., Developments toward a complete micro-total analysis system for Duchenne muscular dystrophy diagnosis, *Anal. Chim. Acta*, 500, 223, 2003.
32. Lagally, E.T., Emrich, C.A., and Mathies, R.A., Fully integrated PCR-capillary electrophoresis microsystem for DNA analysis, *Lab Chip*, 1, 102, 2001.
33. Lagally, E.T., Medintz, I., and Mathies, R.A., Single-molecule DNA amplification and analysis in an integrated microfluidic device, *Anal. Chem.*, 73, 565, 2001.
34. Kopp, M.U., de Mello, A.J., and Manz, A., Chemical amplification: Continuous-flow PCR on a chip, *Science*, 280, 1046, 1998.
35. Krishnan, N. et al., Reactions and fluidics in miniaturized natural convection systems, *Anal. Chem.*, 76, 6254, 2004.
36. Chen, J.F. et al., Electrokinetically synchronized polymerase chain reaction microchip fabricated in polycarbonate, *Anal. Chem.*, 77, 658, 2005.
37. Breadmore, M.C. et al., Microchip-based purification of DNA from biological samples, *Anal. Chem.*, 75, 1880, 2003.
38. Olsen, K.G., Ross, D.J., and Tarlov, M.J., Immobilization of DNA hydrogel plugs in microfluidic channels, *Anal. Chem.*, 74, 1436, 2002.

39. Paegel, B.M., Yeung, S.H.I., and Mathies, R.A., Microchip bioprocessor for integrated nanovolume sample purification and DNA sequencing, *Anal. Chem.*, 74, 5092, 2002.
40. Lagally, E.T. et al., Integrated portable genetic analysis microsystem for pathogen/infectious disease detection, *Anal. Chem.*, 76, 3162, 2004.
41. Xu, F., Jabasini, M., and Baba, Y., DNA separation by microchip electrophoresis using low-viscosity hydroxypropylcellulose-50 solutions enhanced by polyhydroxy compounds, *Electrophoresis*, 23, 3608, 2002.
42. Wainright, A. et al., Preconcentration and separation of double-stranded DNA fragments by electrophoresis in plastic microfluidic devices, *Electrophoresis*, 24, 3784, 2003.
43. Llopis, S.D., Stryjewski, W., and Soper, S.A., Near-infrared time-resolved fluorescence lifetime determinations in poly(methylmethacrylate) microchip electrophoresis devices, *Electrophoresis*, 25, 3810, 2004.
44. Buch, J.S. et al., DNA mutation detection in a polymer microfluidic network using temperature gradient gel electrophoresis, *Anal. Chem.*, 76, 874, 2004.
45. Shi, Y. and Anderson, R.C., High-resolution single-stranded DNA analysis on 4.5 cm plastic electrophoretic microchannels, *Electrophoresis*, 24, 3371, 2003.
46. Zhu, L., Stryjewski, W.J., and Soper, S.A., Multiplexed fluorescence detection in microfabricated devices with both time-resolved and spectral-discrimination capabilities using near-infrared fluorescence, *Anal. Biochem.*, 330, 206, 2004.
47. Kelly, R.T., Pan, T., and Woolley, A.T., Phase-changing sacrificial materials for solvent bonding of high-performance polymeric capillary electrophoresis microchips, *Anal. Chem.*, 77, 3536, 2005.
48. Scherer, J.R. et al., High-pressure gel loader for capillary array electrophoresis microchannel plates, *BioTechniques*, 31, 1150, 2001.
49. Kelly, R.T. and Woolley, A.T., Electric field gradient focusing, *J. Sep. Sci.*, 28, 1985, 2005.
50. Khandurina, J. et al., Microfabricated porous membrane structure for sample concentration and electrophoretic analysis, *Anal. Chem.*, 71, 1815, 1999.
51. Khandurina, J. et al., Integrated system for rapid PCR-based DNA analysis in microfluidic devices, *Anal. Chem.*, 72, 2995, 2000.
52. Schmalzing, D. et al., Toward real-world sequencing by microdevice electrophoresis, *Genome Res.*, 9, 853, 1999.

14

Bio-MEMS Devices for Proteomics

Justin S. Mecomber, Wendy D. Dominick, Lianji Jin, and Patrick A. Limbach

CONTENTS

14.1 Introduction

The field of proteomics has emerged to directly characterize proteins at a global level. With the advances arising in genomics, the identified functional genes can provide a blueprint for the possible gene products that are the focal point of proteomics. A genome is a static entity whereas a proteome is

dynamic and must be studied individually. Proteomes vary due to splicing of mRNA during transcription and due to posttranslational modification. Moment-by-moment snapshots of a proteome can reflect the up- and down-regulation of proteins, their modification status, and their interacting partners at a given cell state. Proteomics covers a broad range of subjects aimed at understanding complex cellular functions in a systematic manner. It is generally categorized in three areas: (1) large-scale protein identifications including isoforms and posttranslational modifications; (2) quantitative proteomics or global analysis of protein expression; and (3) the characterization of protein–protein interactions.

The identification of all of the proteins present in a cell provides the basis for understanding cell regulation and function. A single gene can produce multiple gene products as a result of alternative splicing, generating a protein having many isoforms, each of which must be characterized. Posttranslational modifications (PTMs) are covalent modifications of protein amino acid residues. PTMs such as phosphorylation and glycosylation can be involved in important cell processes, such as the regulation of enzyme activity, cell signaling, and modulation of molecular interactions.

In addition to identification of proteins present in a proteome, it is often useful to generate quantitative information related to these proteins, most commonly concerning changes in protein abundance. In these experiments, one measures the relative abundance of proteins present in two systems (e.g., cells or biological fluids) to evaluate perturbation-induced protein expression. A technically more challenging measurement is the determination of absolute protein amounts within a given proteome.

The third area of proteomics involves characterizing protein–protein interactions. The success in obtaining genomic information has increased interest in studying the encoded protein networks that govern cellular function. Elucidating protein–protein interactions on a proteome-wide scale often requires combining the techniques associated with protein identification and those required for protein quantitation with additional biochemical techniques that probe protein–protein interactions.

An emerging paradigm in proteomics is the combination of traditional methodology with novel advancements in miniaturization. To rapidly diagnose unhealthy (i.e., diseased) and normal individuals, methods for the early detection and diagnosis of the disease state are most beneficial. With respect to proteomics, a significant constraint is that the proteins of interest in biological samples, such as tissue biopsies or biofluids, are typically very low in abundance. The analytical benchmarks for detecting low abundance proteins in biological samples are helping drive developments in bio-MEMS. To carry out the necessary chemical and biochemical reactions in miniaturized systems requires the fabrication of pumps, valves, storage containers, interconnects, and detection strategies [1]. These components typically have dimensions on the order of a few micrometers to several millimeters in length or width, and are between 100 nm and 100 μm in depth and height. Numerous fabrication techniques for creating these microstructures for proteomic

purposes have been developed [2–8]. This chapter will discuss advances in biological microelectromechanical systems (bio-MEMS), such as assay development, improved separation performance, and enhanced detection strategies, which should eventually contribute to our understanding of the proteome.

14.2 Microarrays and Immunoassays

14.2.1 Peptide and Protein Microarrays

As DNA and oligonucleotide microarrays have greatly accelerated research at the DNA and RNA levels, similar applications are being envisioned at the protein level [9]. MEMS technology offers a host of methods that are being applied to materials processing and production of fast, reliable, and economically feasible array-based devices. Just as in gene-based arrays, processes such as photolighography [10], a development common to the silicon computer industry, can be employed to fabricate the highest possible density of biologically activated regions [11]. Ink-jet printing [12,13], soft lithography [14,15], and scanning probe–based lithography [16] are also promising technologies compatible with bio-MEMS systems. While protein modifications and three-dimensional (3D) structure present obstacles in peptide and protein microarray development, numerous companies, such as ProtoPharm (San Diego, CA), BioSite (San Diego, CA), Zyomyx (Hayward, CA), and Hypromatrix and Diversys (Cambridge, U.K.) are developing approaches to solve these issues.

Hunt and coworkers employed a versatile, highly specific, and biologically friendly technique known as nanoimprint lithography (NIL) for the generation of ultrahigh-resolution protein patterns (Figure 14.1) [17]. Protein patterning of bovine serum albumin (BSA) and rhodamine-labeled streptavidin was completed in both line and dot formats. These proteins feature densities that are more than an order of magnitude greater than those currently available and have the potential for patterning down to 10 nm.

Alternative approaches typically involve creating bio-MEMS devices allowing for parallel peptide synthesis, on-chip, using conventional peptide chemistry to create a miniaturized, spatially addressable peptide microchip [18]. In-solution removal of acid-labile protecting groups, monomer building blocks, photogenerated reagents, and digital photolithography have been used in combination to create a bio-MEMS platform for epitope-binding assays. Proof of principle was demonstrated through the rapid screening for sequences specific to the human p53 antibody. This platform demonstrates the potential of bio-MEMS-based peptide microchips for additional proteomic applications, and is advantageous as it only requires a conventional synthesizer and computer-controllable optical module.

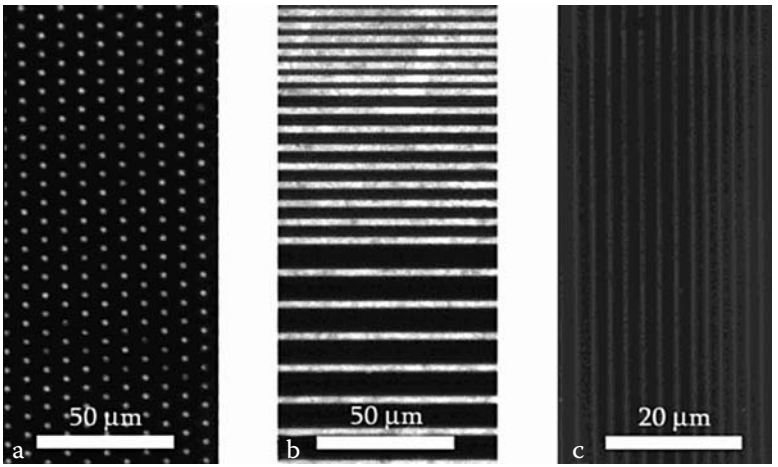

FIGURE 14.1
Epi-fluorescence image of rhodamine-labeled steptavidin bound to sharp uniform microscale dots (a) and lines (b) of biotinylated BSA protein on oxidized Si substrates. Fluorescent intensity signal in the passivated regions is at or below the noise level of the imaging system, indicating the fluorophore concentration in these areas is less than 0.1% of that observed in the patterned regions. (c) Rhodamine-labeled streptavidin bound to patterns of immobilized biotinylated BSA on cover glass.

Han and coworkers have developed the ProteoChip for high-throughput analysis of proteins (Figure 14.2) [19]. Protein linkers, which are calixacrown derivatives with a bifunctional coupling property, allow for efficient immobilization of capture proteins on solid matrixes. The ProteoChip provided benefits in high-density array spots, biomarker assays, and identifying protein–protein interactions. A spot density of 4900 cm^2 was achieved along with a detection sensitivity of 1 fg mL^{1}. The ProteoChip was also used to selectively screen potential drug targets for various integrin-associated diseases such as blood clotting, tumor-induced angiogenesis, and rheumatoid arthritis.

14.2.2 Immunoassays

Immunoassays for identifying proteins exemplify one of the most fundamental devices in environmental analysis, biochemical studies, and clinical diagnostics due to its selectivity and quantitative capabilities. The benefits of the integration of bio-MEMS and immunoassays are reduced cost and consumption, increased speed of analysis, and the ability for portable automation in a single device. Immunoassays can take on various formats in microanalytical systems, with the most common built upon homogenous, heterogeneous, and diffusion immunoassays or immunosorbent assays [4,5,20–27]. For example, Wang and coworkers have developed biochips for simultaneous detection of major renal markers [28] and dual-bioassay single-channel microchips with the integration of immunochemical and enzymatic assays [29].

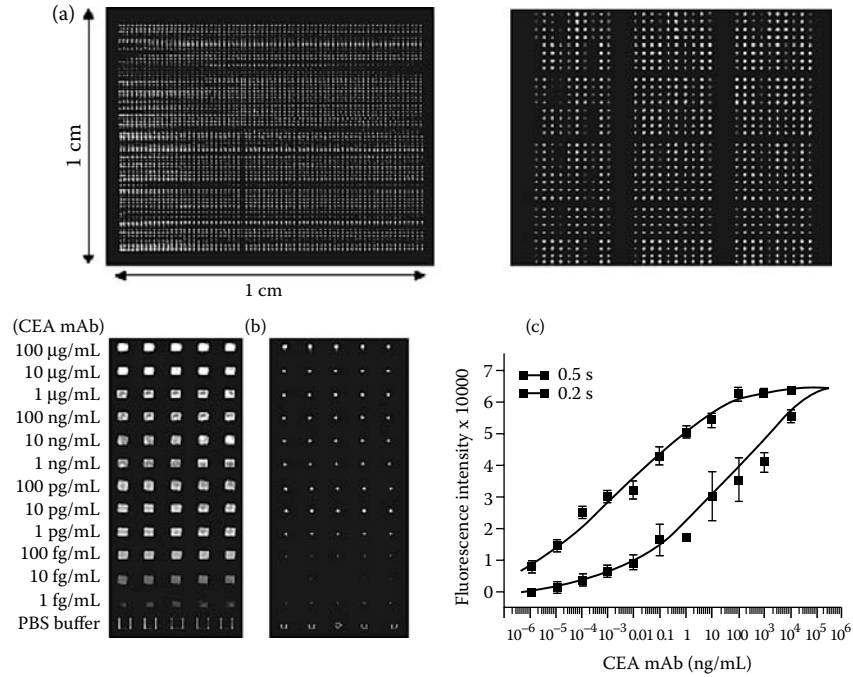

FIGURE 14.2
(a) Microarray images spotted with a Proteogen CM 1000 microarrayer. (Left panel) Spotting test for ProteoChip base plate prepared with an ArrayIt SMP3 (100 mm). The array spot density is 4900 ea/cm2. (Right panel) Spotting tests for ProteoChip base plate prepared with an ArrayIt SMP10 (335 mm). The array spot density is approximately 460 ea/cm2 in this test. The proteins used for the spotting tests are protein A-Alexa546 (yellow). CRP mAb-Cy5 (green) and mouse IgG-Cy3 (red). (b) Rainbow color displays spotted using two different pin sizes, 300 mm (left panel) and 100 mm (right panel), for immobilization of a capture mAB (CEA) in varied concentrations from 1 fg/mL to 100 mg/mL on ProteoChip. The microarrayer and fluorescence scanner used for this experiment were the Proteogen CM 1000 and GSI scanner, respectively. (c) Dose-response curves for immobilized capture mAb represented by fluorescence intensity as a function of mAB concentration. The numerical values of fluorescence intensity were calculated using software from the GSI scanner. The immobilized capture mAb was detectable at a concentration of 1 fg/mL and appeared saturated at a mAb concentration of 100 mg/mL.

The enzyme-linked immunosorbent assay (ELISA) has long been a valuable technique used in the life sciences. Integration of ELISA with MEMS-based devices is advantageous because microchannels provide a vast reduction in volume compared to microtiter plates. This means that reaction volumes can be controlled, shorter incubation times are necessary, and the high surface area-to-volume ratio leads to improvements in dynamic range and sensitivity. Kitamori and coworkers recently presented an idea for microsystem integration that includes affinity capture of a target molecule, separation, and thermal lens detection [30]. In this system, known as microELISA, streptavidin peroxidase was used as a labeling material and thermal lens detection was employed for evaluation of the enzyme reaction

product (Figure 14.3). Polystyrene beads, precoated with recombinant human interferon-γ, were loaded and held at the dam region in the glass microchip. Next, streptavidin peroxidase was loaded, followed by N-ethyl-N-(2-hydroxy-3-sulfopropyl)-3-methylaniline, and sodium salt, with the reaction being detected downstream by a thermal lens microscope. The advantage was a significant reduction in assay time, data error, and the laborious nature of conducting surface measurements.

While glass has been the primary material of choice in bio-MEMS devices, thermoplastics have been implemented due to their ease of fabrication, high aspect ratios, and low cost. Kim and coworkers have developed a polymer-based microfluidic device for immunosensing biochips in handheld diagnostic systems (Figure 14.4) [31]. The device was used in the investigation of the functionalization of ferritin and biotin to the sensing monolayer, and their

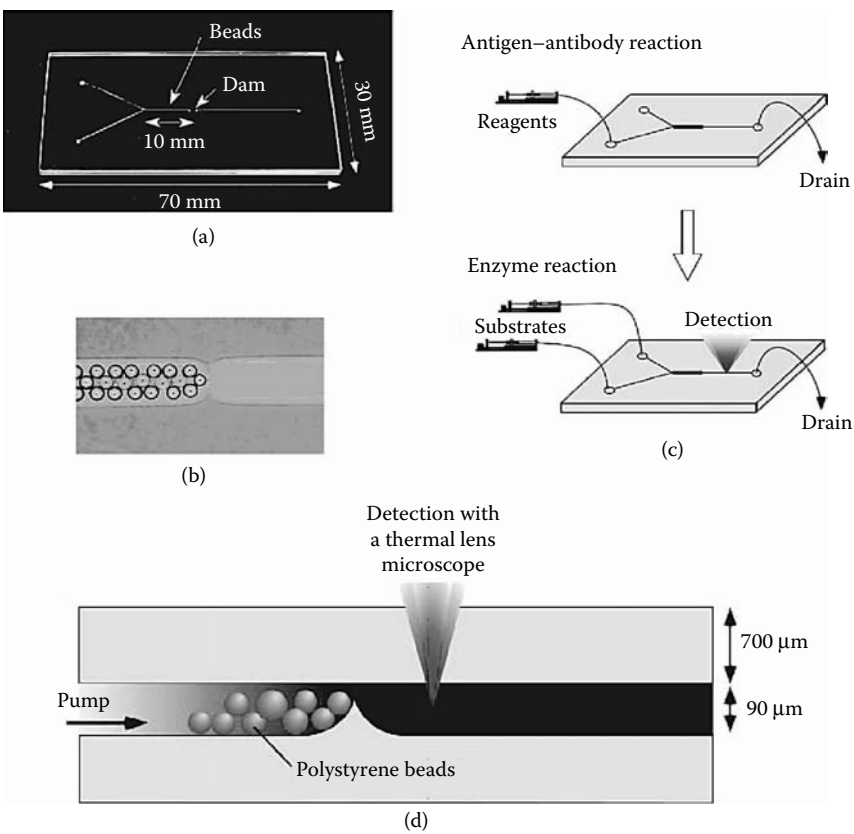

FIGURE 14.3
ELISA microchip, (a) photography of chip, (b) micrograph of dam area with polystyrene beads (45 mm in diameter), (c) operation procedure, and (d) cross-section of the fabricated microchip with microbeads.

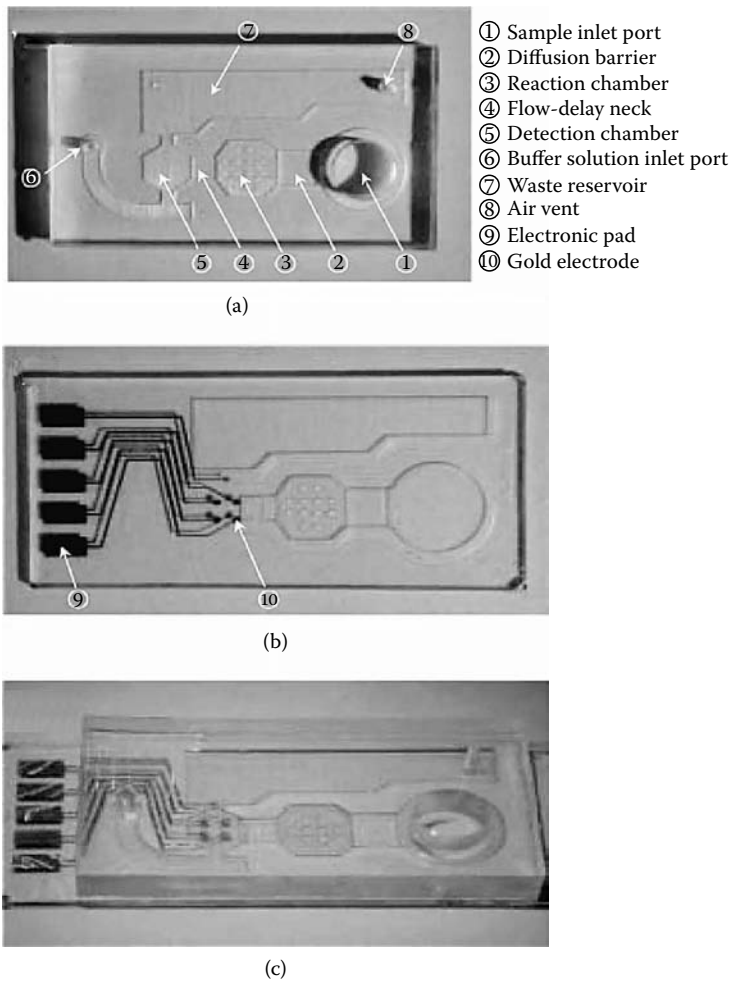

FIGURE 14.4
Photographs of the fabricated polymer microfluidic device. (a) PDMS top substrate. (b) PMMA bottom substrate, and (c) the packaged device. Denotations: 1, sample inlet port; 2, diffusion barrier; 3, reaction chamber; 4, flow-delay neck; 5, detection chamber; 6, buffer solution inlet port; 7, waste reservoir; 8, air vent; 9, electronic pad; and 10, gold electrode.

biospecific interactions with the antiferritin, antiserum, and streptavidin samples. Results show that fluid flow can be passively controlled through surface modifications and geometrical changes of the capillary. With the integration of electrochemical detection, cyclic voltammograms are generated to provide data showing that the device can be employed as a portable diagnostic system.

14.3 Bottom-Up Proteomics

14.3.1 Overview of Proteomics Methodologies

Current proteomics approaches are generally placed in two categories: bottom-up and top-down. In the bottom-up approach, peptides generated from the proteolytic digestion of purified protein(s) are analyzed by mass spectrometric approaches. In the top-down approach, intact proteins are initially characterized by mass spectrometric approaches. This approach is based upon the accurate molecular mass determination of the intact protein followed by gas-phase fragmentation. This approach is most commonly implemented using specialized instrumentation, and will not be discussed further in this chapter. Both approaches, independently or collaboratively, are implemented in current proteomic studies.

Peptide mass fingerprinting (PMF) or peptide mass mapping (PMM), pioneered by Henzel and colleagues for the rapid identification of proteins separated by two-dimensional polyacrylamide gel electrophoresis (PAGE) [32], is the process of identifying an unknown protein by mass determination of its peptide fragments generated by specific enzymatic or chemical cleavage. In PMF, the peptides resulting from cleavage of the unknown protein are identified by matching the mass of the peptide to peptide masses in a database. The analytical methodology most often used for PMF is protein separation by two-dimensional (2D) PAGE followed by in-gel proteolytic digestion, peptide extraction, and detection using matrix-assisted laser desorption/ionization mass spectrometry (MALDI-MS).

An alternative, and often more effective approach, is to sequence peptides by liquid chromatography electrospray ionization tandem mass spectrometry (LC-ESI-MS/MS) to generate sequence tags (i.e., partial sequence information), which can be searched against the database to identify the protein of interest. The protocol begins with the enzymatic digestion of the protein as before. The resulting peptides are applied to a reversed phase high-performance liquid chromatography (RP-HPLC) column (typically C18 columns are used). Peptides are retained on the RP column and contaminating salts and buffer components are washed away. The peptides are then eluted from the RP column into the mass spectrometer using an acetonitrile gradient. As peptides are eluted from the RP column into the ionization source of the mass spectrometer, the instrument acquires tandem (MS/MS) mass spectra of the eluting peptides. The acquired MS/MS spectra of peptides are correlated with predicted amino acid sequences in translated genomic databases and the resulting list of peptide sequences are used to identify the protein. Alternatively, sequence tags can be generated by use of MALDI-TOF/TOF mass spectrometry, wherein particular peptides generated in the standard PMF experiment are selected for gas-phase fragmentation instrumentally.

As an alternative to 2D gel electrophoresis separation of proteins, protein mixtures (e.g., complexes or whole-cell lysates) can be enzymatically digested and analyzed by 2D chromatography coupled with tandem mass spectrometry [33]. This method is particularly useful for identifying proteins, such as hydrophobic membrane proteins or proteins with extreme *p*I values, which are not normally well represented on a 2D polyacrylamide gel. Identification is done by the sequence tag technique with significant bioinformatics support.

14.3.2 Bio-MEMS in Bottom-Up Proteomics

One of the bottlenecks in conventional proteomics is the time required to run standard 2D-PAGE prior to analysis of proteolytic digests by mass spectrometry. These heterogeneous assays can be time consuming and involve often troublesome and costly handling equipment along with bulky instrumentation. These problems also add to the difficulty in making assessments in point-of-care applications. The 2D-PAGE-MS approach also remains deficient in protein coverage because proteins have acute isoelectric points or molecular masses. The advantages bio-MEMS has to offer will seek to alleviate these shortcomings by integrating analytical systems, which will reduce cost (minimal sample and waste), enhance reaction efficiency, and reduce assay time.

Because there is no protein equivalent to the polymerase chain reaction, protein analyses are often sample limited. Bio-MEMS devices allow for the handling of small sample volumes (nanoliter and picoliter) while maintaining sensitivity without any loss of analyte in the sample processing steps prior to detection [27,34,35]. These dimensions also increase the surface area-to-volume ratios. In this dimensional region, the analysis time is now on the order of $\sqrt{Dt}$, (D = diffusion coefficient), which results in faster reaction kinetics. Reaction vessel size is also reduced up to an order of magnitude compared to typical vessels (e.g., microvials). MEMS devices are amenable to automation, which can further reduce analysis time and expense.

14.3.2.1 One-Dimensional Analyte Separations

Fluid manipulation remains one of the primary challenges in bio-MEMS systems for proteomics. Depending on the dimensions of the channel networks, a number of different flow rates, from microliters to nanoliters per minute, are required. The mechanism employed to drive fluids can include thermal capillary pumping, gas pressure, and electrokinetic techniques (i.e., electroosmotic flow (EOF) or electrophoresis) among others [36,37]. While Gyros and Tecan have developed novel microfluidic separation systems using centrifugal forces [38], the two most common approaches are pressure-driven and electrokinetic separations [25,39–48]. Pressure-driven flow generates a laminar profile and is often implemented with the miniaturization

of HPLC on microchips. Pressure-driven flow exhibits a nonuniform parabolic velocity profile, which while beneficial when diffusion is necessary [49], can reduce the separation performance as measured by resolution and theoretical plates. Electokinetic techniques are a more popular avenue for separating molecules in microfluidic devices. Electrokinetic techniques in bioMEMS devices arise from principles found in conventional capillary electrophoresis (CE). Electrophoresis generates a flat flow profile and allows for easier integration in multiplexed systems [50]. Electroomosis in combination with electrophoresis allows for samples that are negative, neutral, and positive to separate based on their charge-to-size ratios.

Shintani and coworkers developed a miniaturized multichannel HPLC for high-throughput analysis of protein tryptic digests [51]. This device incorporates a quartz microchip with polydimethlysiloxane (PDMS) connections between valves. Protein tryptic digests of β-casein are separated and detected by implementation of a single, high-pressure gradient pump, the chip-based module, a monolithic silica capillary column array, and a multichannel UV unit. This HPLC chip device allows for multiple samples to be analyzed for increased biological throughput.

Guo and coworkers fabricated an integrated microfludic device employing micellar electrokinetic capillary chromatography (MEKC) for the analysis of amino acids [52]. The system geometry consisted of a serpentine channel, reaction chamber, and mixer, with an embedded light-emitting diode (LED) in an optical fiber to collect and transfer the fluorescence signal to a photomultiplier tube. Detection limits for the amino acids investigated were as low as 0.5 mM. The device shows promise with proteomic applications through the integration of sample loading, labeling, separation, and detection of various amino acids on a single device.

14.3.2.2 Two-Dimensional Analyte Separations

One-dimensional separations are typically limited to the separation of four or less protein digests and have peak capacities in the hundreds [53]. By contrast, multidimensional separations allow for an eightfold or greater increase in peak capacity, which is becoming necessary for proteomics. While 2D-HPLC has been the chosen technique for multiprotein digests, 2D microchip capillary electrophoresis (MCE) offers advantages such as ease of integration and fabrication, portability, and increased speed of analysis. Multidimensional methods such as micellar electrokinetic capillary chromatography microchip capillary electrophoresis (MEKC-MCE) and high-performance liquid chromatography microchip capillary electrophoresis (HPLC-MCE) offer the more advanced approach of tackling high-throughput proteomics [5,45,54].

Ramsey and coworkers fabricated an MEKC-MCE microfluidic device with relatively long channels in the first dimension (19.6 cm) and shorter channels in the second dimension (1.3 cm) (Figure 14.5a) [55]. With such short channel lengths in the second dimension, care had to be taken with tuning the device (applied electric field strength in both dimensions). To increase peak capacity

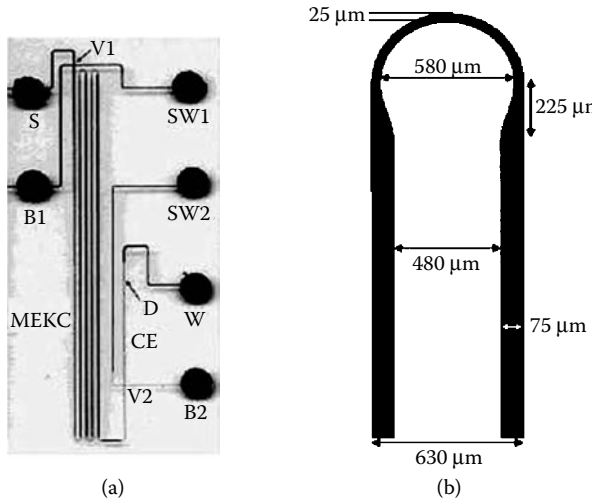

FIGURE 14.5
(a) Image of a microchip with a serpentine channel for two-dimensional separations. (b) Instrumental setup of the coupled system. The dimensions are indicated on the figure and are taken from the top of the channel. The channel was filled with black ink for contrast.

while analyzing a BSA tryptic digest, a novel approach was taken in tapering the serpentine channel (Figure 14.5b) to avoid the "race track" effect. By improving the sampling rate, (each MEKC peak was sampled 6 times), a peak capacity of 4200 (110 in the first dimension and 38 in the second dimension) and an analysis time of 15 min were obtained.

Since the first experimental investigation and performance evaluation of HPLC on a microchip [56], a number of advances have been made using MEMS technology to improve upon design. Yang and coworkers developed a comprehensive 2D separation device employing HPLC-MCE [57]. Fluorescein isothiocyanate-labeled tryptic digests of BSA were separated every 20 seconds and detected using LIF. Kirby and coworkers developed an HPLC-MCE device for the rapid separation of proteins and peptides [58]. In this system, a silica microdevice containing an injector valve and monolithic C18 media was fabricated (Figure 14.6a). The integration of pressure-driven injection allowed for 220 to 800 pL to be linearly metered. Similar to the study mentioned previously, an LED was used in conjunction with laser-induced fluorescence detection. Rapid separations were achieved as well as excellent separation performance. Operating at flow rates of 30 ± 10 nL min^{-1}, column efficiencies of 25,000 plates m^{-1} were obtained (Figure 14.6b).

14.3.2.3 Modifications to Fluidic Networks

Chemical and biochemical modifications to the channel surfaces of bio-MEMS devices for proteomic research are essential for integrating sample cleaning, purification, preconcentration, protein enzymatic digestion, and

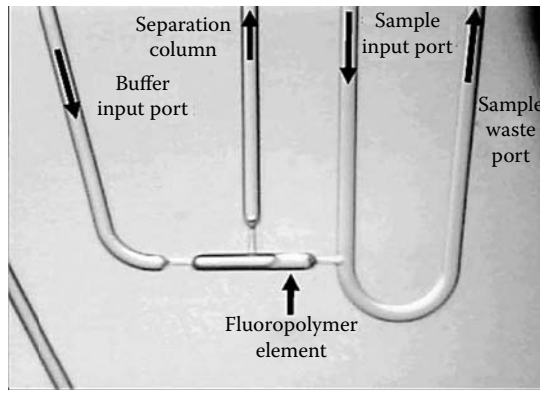

(a)

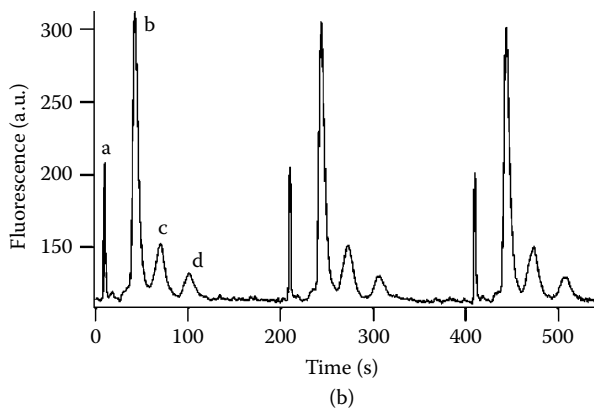

(b)

FIGURE 14.6
(a) Four-port valve allowing rapid sample changes. Sample is changed by flushing at low pressure when the sample waste port is open. Sample is injected by closing sample waste port and pressurizing the sample line. (b) Repeated 6400 pL, 750-ms injections of a protein mixture. Isocratic separation was performed using 24% CAN + 0.16% HFBA in 5 mM phosphate buffer (pH 2.0) at 300 psi. Peak identities and retention factors: a, free dye; b, insulin (3.2); c, anti-biotin (6.0); d, α-lactalbumin (9.1).

solid phase extraction onto the bio-MEMS device. Channel surface modifications can be classified into two categories: dynamic coatings and covalent modifications. Dynamic coatings involve adding small molecules or a polymeric material, which is adsorbed physically to the channel wall [59]. Covalent modifications involve chemically or photochemically derivatizing the wall with an added material. Initially, dynamic coatings were used due to their simplicity; however, covalent modifications are becoming more popular as technical difficulties associated with their use are being resolved [60].

While the electroosmotic mobility is affected by factors such as buffer concentration, ionic strength, viscosity, and applied field strength, one of the most important parameters is the net charge on the surface of the channel

walls. It is essential that the EOF remain stable during an experiment. A drawback of dynamic coatings is their limited lifetime; after sufficient usage, these coatings can be depleted from the channel surface. Additionally, when proteins adhere to the channel walls, they can lead to fluctuations or a reduction in the inherent EOF of the separated device [61].

Wu and coworkers have developed a multilayer adsorbed coating on PDMS microfluidic chips for biopolymer separation (Figure 14.7) [62]. Poly(vinyl

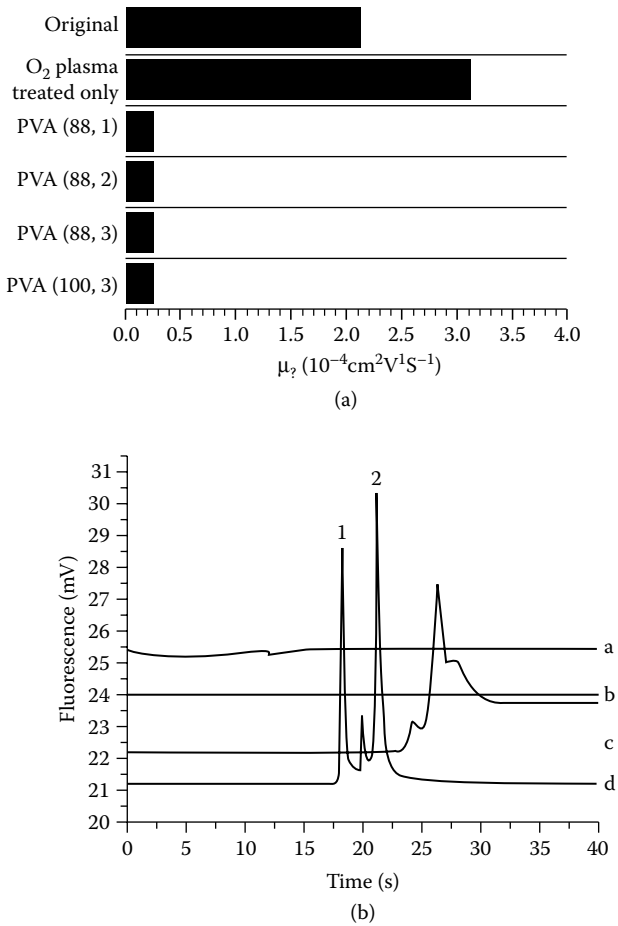

FIGURE 14.7
(a) Electroosmotic mobility in microchannel of original PDMS, O_2 plasma–treated PDMS, one-, two-, and three-layer PVA(88)-coated PDMS pretreated with O_2 plasma, three-layer PVA(100)-coated PDMS pretreated with O_2 plasma. Current monitoring conditions: 12 mM low concentration; 30 mM high-concentration sodium phosphate buffer, pH 9; electric field strength, 400 V/cm; running time was limited within 200 s. (b) Fluorescently labeled basic proteins running in (a) original, (b) O_2 plasma–treated, (c) O_2 plasma–treated and three-layer PVA(100)-coated, and (d) O_2 plasma treated and three-layer PVA(88)-coated PDMS microfluidic chip. Separation conditions: 30 mM phosphate sodium buffer, pH 3.0; 2 cm separation distance. Sample: 50 μg/mL, 1, lysozyme; 2, ribonuclease B.

alcohol) was adsorbed on an oxygen plasma–treated surface of PDMS thereby converting the original hydrophobic surface into a hydrophilic surface. This treatment effectively suppressed the EOF when using solutions in the pH range of 3 to 11. The coating also provided a resistance to protein adsorption and led to exceptional separations of proteins. More than 1×10^6 plates m^{-1} and baseline resolution were obtained during the separation of fluorescently labeled proteins such as lysozyme and ribonuclease B.

Silica surfaces have also been modified to yield improved surface characteristics. Zhang and coworkers modified silicon and gold-patterned silicon for improved biocompatibility and could selectively resist or enhance the adsorption of proteins [63]. In this study, silicon and gold-patterned silicon were modified with methoxy-polyethylene glycol (M-PEG silane) via a self-assembly technique. The dense, stable, self-assembled monolayer provided resistance to fluorescently labeled proteins (fibrinogen and IgG) in the example of bare silicon treated with PEG. A noticeable difference was found in the adsorption of fluorescently labeled proteins.

Baba and coworkers also applied this PEG coating technology to a poly(methylmethacrylate) (PMMA) chip for protein separations [64]. The adsorption of SDS-protein complexes were reduced, and the technique allowed for the separation of proteins ranging from 21.5 to 116.0 kDa. These separations were completed within 8 seconds in a 3 mm separation channel. This research group has also used a dynamic dodecyl sulfate coating for high-speed separations of proteins and peptides [65]. In this study the researchers used, to their advantage, the adsorption of SDS onto the hydrophobic channel PMMA surfaces for the separation of proteins and peptides up to 116.0 kDa. This adsorption essentially created a dynamic coating resulting in a cathodic EOF (Figure 14.8).

14.3.2.4 Sample Purification and Preconcentration

The separation of peptides and proteins from undesirable salts, biological matrix, solvent exchange, and from one another is critical in bio-MEMS devices used for proteome research. One form of sample cleaning, known as solid-phase extraction, has been employed to retain analytes in a stationary phase, while undesired compounds are washed out. For example, a C18 solid phase has been attached to channel surfaces for solid-phase extraction. However, merely coating channel surfaces with hydrophobic media limits the surface area available for sample purification. The surface area of these types of derivatizations is on the order of 230 to 781 mm^1 [66]. Implementation of monoliths solves this surface area deficiency by increasing the surface area-to-volume ratio to 10^4 mm^{-1} or greater [67,68].

Rolando and coworkers have recently investigated novel monolithic devices for proteomics applications [69]. Lauryl methyacrylate, ethylene dimethacrylate, cyclohexanol, and ethylene glycol were used to create a C12

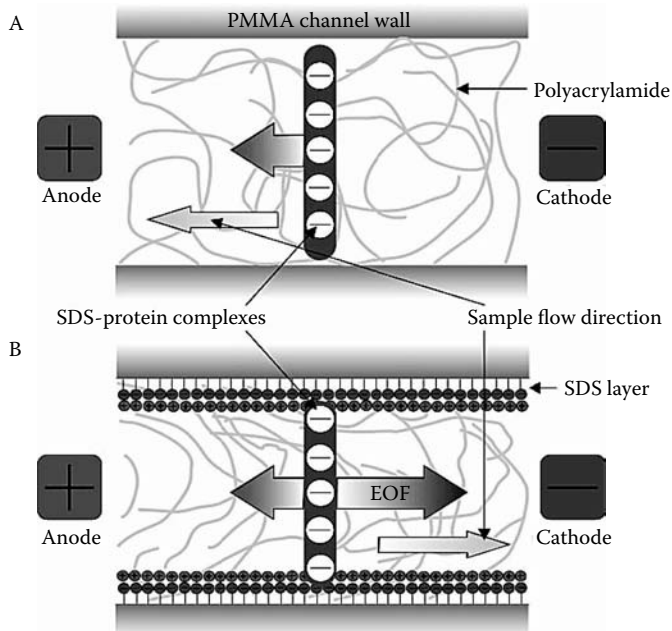

FIGURE 14.8
Schematic image of electrophoretic migration of SDS-protein complexes in a plastic microchip channel. (a) Uncoated microchip. (b) Dynamic SDS-coated chip.

monolithic electrochromatography stationary phase. The monolithic columns were able to separate peptide fragments of a cytochrome C (Cyt-C) digest from as little as 80 fmol of sample at efficiencies up to 145×10^3 plates m^{-1}.

Lee and coworkers presented an approach for microaffinity purification of proteins based on photolytic elution. In this device, bead-based (CutiCore®) affinity chromatography integrated into a glass-silicon microchip was used to purify specific target proteins. Using ligand-coupled beads in combination with elution using ultraviolet irradiation, the target protein was captured with a high specificity, purified, and eluted effectively.

A number of methods in MEMS devices, such as isotachophoresis [70] and isoelectric focusing [71,72] have been shown to further enhance sensitivity by preconcentration and separation of the sample. Han and coworkers developed a simple protein preconcentration device based on electrokinetic trapping by a nanofluidic filter [73]. A 40 nm nanochannel is used as a filtering membrane to generate an ion-depletion region for electrokinetic trapping. The efficiency of the device is controlled by an increase in electrokinetic flow by accumulation of charges on one side of the nanochannel. The resulting nonlinear electroomotic flow and geometrical design yields a 100-fold increase in protein concentration in approximately 60 min of preconcentration. This device, acting as an amplifier for signal intensity, is ideally suited for proteomic studies.

Garrell and coworkers developed a microfluidic device based on the technique of digital microfluidics in which a dried droplet containing peptides or proteins and impurities is moved by an electrowetting-on-dielectric (EWOD) technique (Figure 14.9) [74,75]. This method allows for the reduction of salt adducts, which increase the signal-to-noise ratio in MALDI-MS. By reducing the amount of contaminated peptides, this method also shows enrichment as the signal-to-noise ratio increases with the number of drops

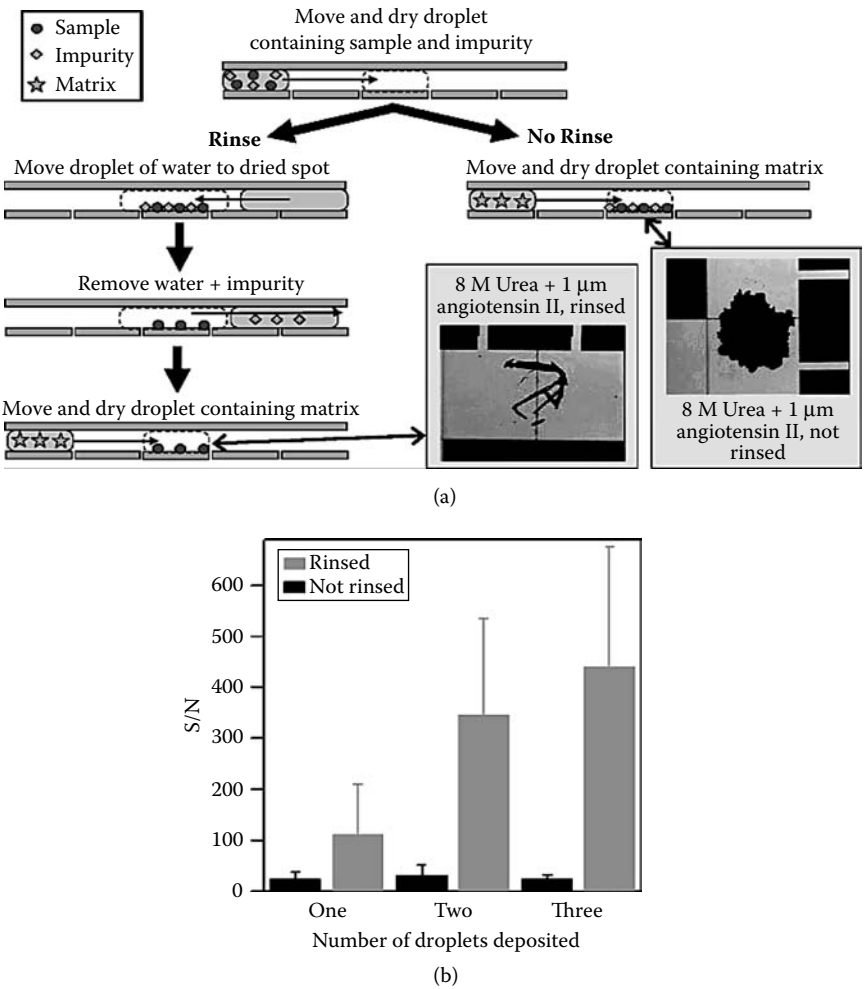

FIGURE 14.9
(a) Schematic of EWOD-driven sample purification and micrographs of dried spots. Insets: The rinsed sample (left) appears to be primarily composed of DHB crystals, while the nonrinsed sample (right) is dominated by urea. (b) MALDI-MS spectra comparing the spectral signal-to-noise ratios from spots of 0.33 µM angiotensin II + 100 mM urea. Spots were prepared by moving and drying one, two, or three droplets (0.17, 0.33, and 0.66 pmol of total peptide, respectively) at the same place on the EWOD device. n = 3 for each condition.

deposited. Consequently, peptide mass fingerprint searches showed an increase in efficiency by employing this technique.

14.3.2.5 Bio-MEMS-Compatible Enzyme Reactors

Typical proteomics involves some sort of enzymatic digestion of a particular protein or set of proteins. Typical in-solution enzymatic digestion of proteins has a number of weaknesses. The digestion time is lengthy (on average 12 hours), and to decrease this time, either the amount of protein or protease has to be increased. However, increasing the amount of protease can lead to autolysis of the protease and additional protein may be unavailable. Traditional enzymatic digestion involves extensive manual sample handling. Immobilization of enzymes has been introduced to decrease these drawbacks. Immobilization of enzymes reduces digestion times, autolysis of enzymes and the diffusional limitations of in-solution digestions [76,77]. Immobilization has been shown to increase the stability of an enzyme [78]. Bio-MEMS devices offer a way to decrease the amount of protein and the time needed for digestion by integrating high surface-to-volume ratios of enzyme into microchannels [79]. The integration and immobilization of enzymes into a microfluidic device can be carried out by a number of different approaches, such as hydrogel and membrane-based immobilization [80–82] and attachment to porous microstructures [35,83,84] including monolithic media [85,86].

Zimmerman and coworkers have fabricated a bio-MEMS enzyme-based electrochemical sensor for glucose monitoring (Figure 14.10) [87]. An in-device immobilization method using a photosensitive poly(vinyl alcohol)-styrylpyridinium (PVA-SbQ) cross-linker is used for entrapment of enzymes. As the enzyme is entrapped, it is not chemically modified, and the result is a preservation of the enzyme's native properties. Enzyme kinetic measurements revealed Michaelis constants of 3.0 mM for an enzyme concentration

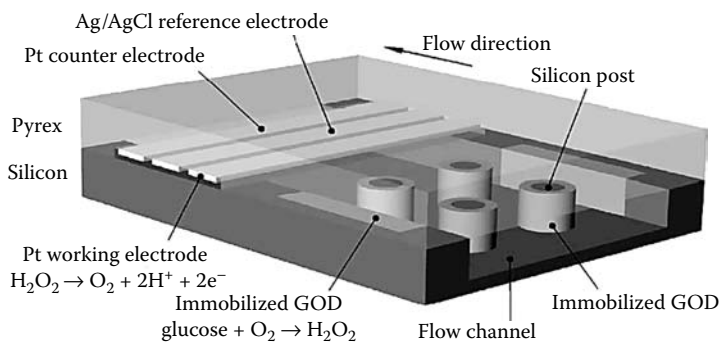

FIGURE 14.10
Schematic diagram of an integrated enzyme-based flow-through glucose sensor. The enzymes are immobilized in side pockets and around silicon posts inside the flow channel. Hydrogen peroxide is transported in the flow direction to the working electrode.

of 22.8 μg mL^{-1}. The sensor also demonstrated stable operation for 24 h with a linear range of 0 to 160 mg dL^{-1}.

Viovy and coworkers fabricated a microfludic device that employed self-assembled magnetic beads for on-chip digestion [88]. Trypsin was grafted on magnetic latex nanoparticles by functionalizing the beads to contain a carboxylate group. The beads were loaded into a device that had magnets integrated on either side of the channel, which generated the immobilizing magnetic field. Human growth hormone and other proteins were then injected into the chip containing the plug of trypsin-immobilized beads. The efficiency of the on-chip microreactor was found to be comparable to the in-solution-based digest, although at a cost of longer digestion time. The researchers noted that the device is reusable and could be applied to other types of microfluidic chromatography.

Kong and coworkers developed a microfluidic device for on-chip digestion through enzyme patterning on PMMA [89]. In this device, a graft copolymer (butyl methacrylate/methylacryloxy)propyltrimethoxysilicane) was used to place a silane functionality (sol-gel) on the polymer wall surface. This allowed a patterned hydrophilic surface to be obtained with enzyme functionality intact. The efficiency of the device was then compared to in-solution-based proteomic methods. The digestion time for Cyt-C and BSA was reduced to less than 5 s for the enzyme reactor, compared to 6 h for solution-based digestions. The efficiency was comparable in both methods, while sequence coverage was slightly less for the microreactor digest of Cyt-C (68 vs 90%). Similarly, Wu and coworkers developed a microfluidic-based enzymatic reactor using sol-gel-derived PDMS substrates [90]. Because PDMS was used, plasma oxidation of the surface was necessary to form silanol groups, which allowed for a tether between the sol-gels (titania and alumina). The sol-gels contained encapsulated trypsin and scanning electron microscope images were taken to show the morphology differences before and after enzyme immobilization. At a flow rate of 7.0 μL min^{-1}, the time required for digestion (2 s) was significantly reduced compared to in-solution digest and other on-chip digestion procedures. For both sol-gels investigated, the efficiency was actually better than in-solution digests. Sequence coverage, peptides matched, and protein scores were all higher in these microreactors. Consequently, with such rapid digestion times and compatible mass spectrometry flow rates, the integrated microfluidic device could be advantageous in future proteomic studies.

14.4 Integrated Bio-MEMS Approaches in Proteomics

Mass spectrometry is an indispensable technique in proteomics due to its sensitivity, separation capability, and resolving power of complex protein

mixtures. Some of the fundamental sample preparation steps that were listed in the preceding sections will only benefit by the integration of MS techniques with bio-MEMS devices. Bio-MEMS task-handling abilities are not only beneficial to MS but the analytical characteristics of MS mesh well with bio-MEMS devices. Those analytical characteristics include the duty cycles of today's MS instrumentation and the high-throughput volumes of bio-MEMS, the flow rate necessary for ion formations (ESI/LC-MS) and the flow rate typically found in microfluidic channels, and finally the complex assay development in bio-MEMS and the performance capabilities of the mass spectrometer. Throughout the past 5 years, there has been an abundant amount of novel research in the application of MEMS devices for proteome research using MS [34,91–97].

14.4.1 Integrated High-Throughput Devices Using MALDI-MS

The analytical properties of MALDI-MS, namely, its automated and high-throughput capabilities, make it amenable for integration with bio-MEMS devices. One of the first reports of this union came from Reinhoudt and coworkers [98]. They imbedded a microfluidic system capable of a complete biochemical reaction with on-line MALDI-MS. The system took advantage of atmospheric pressure (just prior to loading the device into the mass spectrometer) and the vacuum of the instrument to generate the driving force for fluid flow once inside the mass spectrometer. While peptide digestion was done offline, employing the device allowed for minimal sample handling, sample loss, and method development time. Adequate detection of a peptide mixture was noted and the device was also used to detect other analytes such as polymers (PMMA and polystyrene) and oligonucleotides.

Bergman and coworkers have also demonstrated the benefits arising from the integration of microchip devices with MALDI-MS by integrating the sample preparation steps inside a microfluidic compact disk for high-throughput protein identification (Figure 14.11) [99]. Peptide digests are loaded onto the disk, which contains a 10 nL reversed-phase chromatography column. Next, using the Gyrolab workstation, the disk is spun at a specific rate to allow for centrifugal movement of the mixture. This allows for removal of salts, concentration of analytes, and subsequent elution with the matrix all in one step. Once crystallization has taken place, the entire disk is inserted into the mass spectrometer for analysis. With the implementation of robotics, this device allows for the analysis of up to 96 samples with 50 amol detection limits to be obtained. They have also integrated a 16 nL immobilized metal affinity column (IMAC) onto the microfluidic compact disk [100]. This sensitive and selective technique, in combination with the MS-compact disk technology, allowed for high-throughput peptide mass fingerprinting and detection of phosphorylated peptides.

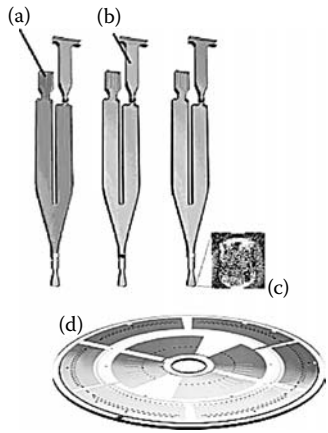

FIGURE 14.11
Microfluidic structure for on-CD processing of samples of up to 1 μL (96 structures per CD). An individual microstructure element is shown separately for the three consecutive steps of sample application (a), washing and elution (b), and co-crystallization with MALDI matrix (c). The dilute and salt-containing crude sample is applied at (a) onto a the 10 nL reversed-phase column. The washing and elution/matrix solutions are applied via a common distribution channel at (b), with the liquid volume defined to 200 nL after activation of an overflow channel (not shown). Co-crystallization of the concentrated and desalted sample with MALDI matrix is taking place at (c) in a 200 × 400 μm target where the crystalline deposit is accessible to the laser beam of the MALDI instrument as shown by photography of the crystals in the desorption area at the outlet. (d) Gryolab MALDI SP1 CD.

14.4.2 Integrated High-Throughput Devices Using ESI-MS

The flow rates typically used in LC-MS instrumentation are of the same magnitude as those found in bio-MEMS devices. Karger and coworkers were one of the first to take advantage of this relationship to develop a high-throughput microfabricated glass chip for automated sampling from a microwell plate [101]. Building on that approach, Henion and coworkers developed an automated chip-based nanoelectrospray system for the analysis of 2D gel samples [102]. This chip serves as both an autosampler and a nano-ESI source. Instead of using one device to sample a microwell plate, the device consisted of a 10 × 10 array of nozzles that allows for the elimination of analyte carryover (Figure 14.12). This system also allows for high sample throughput.

Pointing out future commercial possibilities, Yin and coworkers from Agilent recently integrated nano-LC onto a commercial microfluidic chip for peptide analysis [103]. A packed bed allows for sample enrichment and separation. Reverse-phase gradient separations of tryptic protein digests in the subfemtomole range were obtained. Using an enrichment column, a separation column, a nanoelectrospray tip, and a novel valving scheme, this system demonstrates the utility of integrated bio-MEMS devices in proteomics. The goal of elucidating multiple structural components of complex protein mixtures was recently demonstrated using this chip-MS technology [104].

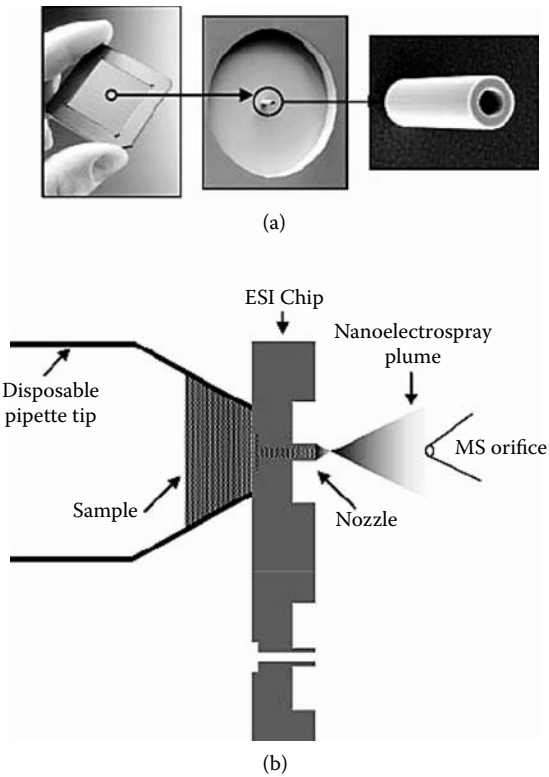

FIGURE 14.12
(a) Sequential photographs of the ESI chip showing the array of microfabricated nanoelectrospray nozzles with successive enlargements of an individual nozzle. The final scanning electron micrograph (SEM) shows a single nanoelectrospray emitter with dimensions of 10 μm ID and 20 μm OD. (b) Schematic representation for a cross-section of a portion of an ESI chip. A disposable pipette tip, containing sample, presses and seals against the inlet side of the chip with the nanoelectrospray plume spraying toward the mass spectrometer ion orifice entrance. Nanoelectrospray is initiated by applying a head pressure and voltage to the sample in the pipette tip.

14.5 Summary

Analytical methods in bio-MEMS have made great strides in the field of proteomics. These techniques are beginning to be used in combination to create systems that are truly totally integrated. The future of bio-MEMS in proteomics holds great promise. While many fabrication and protein-handling techniques have been investigated, and novel advancements will only continue as new doors are opened. While bio-MEMS is about integration and miniaturization, mass spectrometers recently proved amenable for

miniaturization [105], and will become useful if portable systems are to evolve. The goal in future proteomics applications is to make a migration from laboratory settings into point-of-care applications and recent literature only supports this movement [106].

References

[1] Jakeway, S.C., de Mello, A.J., and Russell, E.L., Miniaturized total analysis systems for biological analysis. *Fresenius J. Anal. Chem*. 2000, 366, 525–539.

[2] Madou, M., *Fundamentals of Microfabrication*. CRC Press, Boca Raton, FL (1997).

[3] Gad-el-Hak, M. *The MEMS Handbook.* CRC Press, Boca Raton, FL (2002).

[4] Figeys, D. and Pinto, D., Proteomics on a chip: Promising developments. *Electrophoresis* 2001, 22, 208–216.

[5] Lion, N., Rohner, T.C., Dayon, L., Arnaud, I.L., Damoc, E., Youhnovski, N., Wu, Z., Roussel, C., Josserand, J., Jensen, H., Rossier, J.S., Przybylski, M., and Girault, H.H., Microfluidic systems in proteomics. *Electrophoresis* 2003, 24, 3533–3562.

[6] Ziaie, B., Baldi, A., Gu, Y., and Siegel, R.A., Hard and soft micromachining for Bio-MEMS: Review of techniques and examples of applications in microfluidics and drug delivery. *Advanced Drug Delivery Reviews* 2004, 56, 145–172.

[7] Becker, H. and Gartner, C., Microreplication technologies for polymer-based μTAS applications, in *Lab-on-a-Chip*, Oosterbroek, R.E. and Van Den Berg, A., Eds., Elsevier, Amsterdam, 21–36 (2003).

[8] Gardeniers, J.G.E., Oosterbroek, R.E., and van den Berg, A., Silicon and glass micromachining for μ-TAS, in *Lab-on-a-Chip*, Oosterbroek, R.E. and Van Den Berg, A., Eds., Elsevier, Amsterdam, 37–64 (2003).

[9] Wilson, D.S. and Nock, S., Recent developments in protein microarray technology. *Angew. Chem. Int. Ed*. 2003, 42, 494–500.

[10] Schwartz, A., Rossier, J.S., Roulet, N., Mermod, M.A., Roberts, H.H., and Girault, H.H., Micropatterning of biomolecules on polymer substrates. *Langmuir* 1998, 14, 5526–5531.

[11] Anderson, R.C., McGall, G., and Lipshutz, R.J., Polymucleotite arrays for genetic sequence analysis, in *Microsystem Technology in Chemistry and Life Sciences*, Manz, A. and Becker, H., Eds. Springer-Verlag, Germany, 117–129 (1999).

[12] Cooley, P., Wallace, D., and Antohe, B., Applications of ink-jet printing technology to Bio-MEMS and microfluidic systems. *JALA* 2002, 7, 33–39.

[13] Pawlack, M., Schick, E., Bopp, M.A., Schneider, M.J., Oroszlan, P., and Ehrat, M., Zeptosens' protein microarrays: A novel high performance microarray platform for low abundance protein analysis. *Proteomics* 2002, 2, 383–393.

[14] Zhao, X.M., Xia, Y.N., and Whitesides, G.M., Soft lithographic methods for nano-fabrication. *J. Mat Chem*. 1997, 7, 1069–1074.

[15] Bernard, A., Delamarche, E., Schmid, H., Michel, B., Bosshard, H.R., and Biebuyck, H., Printing patterns of proteins. *Langmuir* 1998, 14, 2225–2229.

[16] Wadu-Mesthrige, K., Xu, S., Amro, N.A., and Liu, G., Fabrication and imaging of nanometer-sized protein patterns. *Langmuir* 1999, 15, 8580–8583.

[17] Hoff, J.D., Cheng, L., Meyhofer, E., Guo, L.J., and Hunt, A.J., Nanoscale protein patterning by imprint lithography. *Nano Letters* 2004, 4, 853–857.

[18] Pellois, J.P., Zhao, X., Srivannavit, O., Zhou, T., Gulari, E., and Gao, X., Individually addressable parallel peptide sythesis on microchips. *Nature Biotechnology* 2002, 20, 922–926.
[19] Lee, Y., Lee, E.K., Cho, Y.W., Matsui, T., Kang, I., Kim, T., and Han, M.H., ProteoChip: A highly sensitive protein microarray prepared by a novel method of protein immobilization for application of protein-protein interaction studies. *Proteomics* 2003, 3, 2289–2304.
[20] Cheng, S.B., Skinner, C.D., Taylor, J., Attiya, S., Lee, W.E., Picelli, G., and Harrison, D.J., Development of a multichannel microfluidic analysis system employing affinity capillary electrophoresis for immunoassay. *Analytical Chemistry* 2001, 73, 1472–1479.
[21] Lee, S.J. and Lee, S.Y., Micro total analysis system (μ-TAS) in biotechnology. *Appl. Microbiol. Biotechnol.* 2004, 64, 289–299.
[22] Khandurina, J. and Guttman, A., Bioanalysis in microfluidic devices. *Journal of Chromatography A* 2002, 943, 159–183.
[23] Sato, K., Hibara, A., Tokeshi, M., Hisamoto, H., and Kitamori, T., Microchip-based chemical and biochemical analysis systems. *Advanced Drug Delivery Reviews* 2003, 55, 379–391.
[24] Vandaveer, W.R., Pasas-Farmer, S.A., Fishcer, D.J., Frankenfeld, C.N., and Lunte, S.M., Recent developments in electrochemical detection for microchip capillary electrophoresis. *Electrophoresis* 2004, 25, 3528–3549.
[25] Weigl, B.H., Bardell, R.L., and Cabrera, C.R., Lab-on-a-chip for drug development. *Advanced Drug Delivery Reviews* 2003, 55, 349–377.
[26] Rossier, J.S., Reymond, F., and Michel, P.E., Polymer microfluidic chips for electrochemical and biochemical analyses. *Electrophoresis* 2002, 23, 858–867.
[27] Sanders, G.H. and Manz, A., Chip-based microsystems for genomic and proteomic analysis. *Trends in Analytical Chemistry* 2000, 19, 364–378.
[28] Wang, J. and Chatrathi, M.P., Microfabricated electrophoresis chip for bioassay of renal markers. *Analytical Chemistry* 2003, 75, 525–529.
[29] Wang, J., Ibanez, A., and Chatrathi, M.P., On-chip integration of enzyme and immunoassays: Simultaneous measurements of insulin and glucose. *J. Am. Chem. Soc*. 2003, 125, 8444–8445.
[30] Sato, K., Yamanaka, M., Hagino, T., Tokeshi, M., Kimura, H., and Kitamori, T., Microchip-based enzyme-linked immonosorbent assay (microELISA) system with thermal lens detection. *Lab Chip* 2004, 4, 570–575.
[31] Ko, J.S., Yoon, H.C., Yang, H., Pyo, H., Chung, K.H., Kim, S.J., and Kim, Y.T., A polymer-based microfluidic device for immonosensing biochips. *Lab Chip* 2003, 3, 106–113.
[32] Henzel, W.J., Billeci, T.M., Stults, J.T., Wong, S.C., Grimley, C., and Watanabe, C., Identifying proteins from two-dimensional gels by molecular mass searching of peptide fragments in protein sequence databases. *Proc. Natl. Acad. Sci. USA* 1993, 90, 5011–5015.
[33] Link, A.J., Eng, J., Schieltz, D.M., Carmack, E., Mize, G.J., Morris, D.R., Garvik, B.M., and Yates, J.R.I., Direct analysis of protein complexes using mass spectrometry. *Nature Biotech*. 1999, 17, 676–682.
[34] Marko-Varga, G., Nilsson, J., and Laurell, T., Micro- and nanotechnology for proteomics, in *Proteome Analysis Interpreting the Genome*, Speicher, D.W., Ed., Elsevier, Amsterdam, 327–365 (2004).
[35] Laurell, T. and Marko-Varga, G., Miniaturization is mandatory unravelling the human proteome. *Proteomics* 2002, 2, 345–351.

[36] Shoji, S., Fluids for sensor systems, in *Microsystem Technology in Chemistry and Life Sciences*, Manz, A. and Becker, H., Eds., Springer, Berlin, 163–188 (1999).
[37] Guzman, N.A., New directions for concentration sensitivity enhancement in CE and microchip technology. LC-GC Europe 2001, 6, 1–9.
[38] Felton, M.J., CD simplicity. *Analytical Chemistry* 2003, 75, 302A–306A.
[39] Crabtree, H.J., Cheong, E.C., Tilroe, D.A., and Backhouse, C.J., Microchip injection and separation anomalies due to pressure effects. *Analytical Chemistry* 2001, 73, 4079–4086.
[40] de Mello, A.J. and Beard, N., *Lab Chip* 2003, 3, 11N–19N.
[41] Dolnik, V., Liu, S., and Jovanovich, S., Capillary electrophoresis on microchip. *Electrophoresis* 2000, 21, 41–54.
[42] Kutter, J., Current developments in electrophoretic and chromatographic separation methods on microfabricated devices. *Trends in Analytical Chemistry* 2000, 19, 352–363.
[43] Bruin, G.J.M., Recent developments in electrokinetically driven analysis on microfabricated devices. *Electrophoresis* 2000, 21, 3931–3951.
[44] Effenhauser, C.S., Integrated chip-based microcolumn separation systems, in *Microsystem Technology in Chemistry and Life Sciences*, Springer, Berlin, 51–82 (1999).
[45] Chang, H.T., Huang, Y.F., Chiou, S.H., Chiu, T.C., and Hsieh, M.M., Advanced capillary and microchip electrophoretic techniques for proteomics. *Current Proteomics* 2004, 1, 325–347.
[46] Binyamin, G., Boone, T.D., Lackritz, H.S., Ricco, A.J., Sassi, A.P., and Williams, S.J., Plastic microfluidic devices: Electrokinetic manipulations, life science applications, and production technologies, in *Lab-on-a-Chip*, Oosterbroek, R.E. and Van Den Berg, A., Eds., Elsevier, Amsterdam, 83–112 (2003).
[47] Khandurina, J. and Guttman, A., Microscale separation and analysis. *Current Opinion in Chemical Biology* 2003, 7, 595–602.
[48] Auroux, P.A., Iossifidis, D., Reyes, D.R., and Manz, A., Micro total analysis systems. 2. Analytica standard operations and applications. *Analytical Chemistry* 2002, 74, 2637–2652.
[49] Yager, P., Transverse diffusion in microfluidic systems, in *Lab-on-a-Chip*, Oosterbroek, R. E. and Van Den Berg, A., Eds., Elsevier, Amsterdam, 115–150 (2003).
[50] Bousse, L., Cohen, C., Nikiforov, T., Chow, A., Kopf-Sill, A.R., Dubrow, R., and Parce, J.W., Electrokinetically controlled microfluidic analysis systems. *Annu. Rev. Biophys. Biomolec. Struct*. 2000, 29, 155–181.
[51] Shintani, Y., Hirako, K., Motokawa, M., Iwano, T., Zhou, X., Takano, Y., Furuno, M., Minakuchi, H., and Ueda, M., Development of miniaturized multi-channel high performance liquid chromatography for high-throughput analysis. *Journal of Chromatography A* 2005, 1073, 17–23.
[52] Guo, Y., Uchiyama, K., Nakagama, T., Shimosaka, T., and Hobo, T., An integrated microfluidic device in polyester for electrophoretic analysis of amino acids. *Electrophoresis* 2005, 1843–1848.
[53] Culbertson, C.T., Jacobson, S.C., and Ramsey, J.M., Microchip devices for high-efficiency separations. *Analytical Chemistry* 2000, 72, 5814–5819.
[54] Molina, M. and Silva, M., Micellar electrokinetic chromatography: Current developments and future. *Electrophoresis* 2002, 23, 3907–3921.
[55] Ramsey, J.D., Jacobson, S.C., Culbertson, C.T., and Ramsey, J.M., High-efficiency, two-dimensional separations of protein digests on microfluidic devices. *Analytical Chemistry* 2003, 75, 3758–3764.

[56] Ocvirk, G., Verpoorte, E., Manz, A., Grasserbauer, M., and Widmer, H.M., High performance liquid chromatography partially integrated onto a silicon chip. *Anal. Methods Instrum*. 1995, 2, 74–82.
[57] Yang, X., Zhang, X., Li, A., Zhu, S., and Huang, Y., Comprehensive two-dimensional separations based on capillary high-performance liquid chromatography and microchip electrophoresis. *Electrophoresis* 2003, 24, 1451–1457.
[58] Reichmuth, D.S., Shepodd, T.J., and Kirby, B.J., Microchip HPLC of peptides and proteins. *Analytical Chemistry* 2005, 77, 2997–3000.
[59] Righetti, P.G., Gelfi, C., Verzola, B., and Castelletti, L., The state of the art of dynamic coatings. *Electrophoresis* 2001, 22, 603–611.
[60] Locascio, L.E., Henry, A.C., Johnson, T.J., and Ross, D., Surface chemistry in polymer microfluidic systems, in *Lab-on-a-Chip*, Oosterbroek, R.E. and Van Den Berg, A., Eds., Elsevier, Amsterdam, 65–82 (2003).
[61] Vreeland, W.N. and Barron, A.E., Functional materials for microscale genomic and proteomic analyses. *Current Opinion in Biotechnology* 2002, 13, 87–94.
[62] Wu, D., Luo, Y., Zhou, X., Dai, Z., and Lin, B., Multilayer poly(vinyl alcohol)-adsorbed coating on poly(dimethylsiloxane) microfluidic chips for biopolymer separation. *Electrophoresis* 2005, 26, 211–218.
[63] Lan, S., Veiseh, M., and Zhang, M., Surface modification of silicon and gold-patterned silicon surfaces for improved biocompatibility and cell patterning selectivity. *Biosensors and Bioelectronics* 2005, 20, 1697–1708.
[64] Nagata, H., Tabuchi, M., Hirano, K., and Baba, Y., High-speed separation of proteins by microchip electrophoresis using a polyethylene glycol-coated plastic chip with a sodium dodecyl sulfate-linear polyacrylamide solution. *Electrophoresis* 2005, 26, 2687–2691.
[65] Nagata, H., Tabuchi, M., Hirano, K., and Baba, Y., Microchip electrophoresis protein separation using electroomotic flow induces by dynamic sodium sulfate-coating of uncoated plastic chips. *Electrophoresis* 2005, 26, 2247–2253.
[66] Kutter, J., Jacobson, S.C., and Ramsey, J.M., Solid phase extraction on microfluidic devices. *Journal of Microcolumn Separations* 2000, 12, 93–97.
[67] van der Wijngaart, W., Anderson, H., and Stemme, G., Handling of beads in microfluidic devices for biotech applications, in *Lab-on-a-Chip*, Oosterbroek, R.E. and Van Den Berg, A., Eds., Elsevier, Amsterdam, 187–204 (2003).
[68] Pumera, M., Microchip-based electrochromatography: Designs and applications. *Talanta* 2005, 66, 1048–1062.
[69] Le Gac, S., Carlier, J., Camart, J.C., Cren-Olive, C., and Rolando, C., Monoliths for microfluidic devices in proteomics. *Journal of Chromatography B* 2004, 808, 3–14.
[70] Huang, H., Xu, F., Dai, Z., and Lin, B., On-line isotachophoretic preconcentration and gel electrophoresis separation of sodium dodecyl sulfate-proteins on a microchip. *Electrophoresis* 2005, 26, 2254–2260.
[71] Li, Y., DeVoe, D.L., and Lee, C.S., Dynamic analyte introduction and focusing in plastic microfluidic devices for proteomic analysis. *Electrophoresis* 2003, 24, 193–199.
[72] Cui, H., Horiuchi, K., Dutta, P., and Ivory, C.F., Isoelectric focusing in a poly(dimethylsiloxane) microfluidic chip. *Analytical Chemistry* 2005, 77, 1303–1309.
[73] Wang, Y.C., Stevens, A.L., and Han, J., Million-fold preconcentration of proteins and peptides by nanofluidic filter. *Analytical Chemistry* 2005, 77, 4293–4299.

[74] Wheeler, A.R., Moon, H., Bird, C.A., Ogorzalek Loo, R.R., Kim, C.J., Loo, J.A., and Garrell, R.L., Digital microfluidics with in-line sample purification for proteomics analyses with MALDI-MS. *Analytical Chemistry* 2005, 77, 534–540.

[75] Wheeler, A.R., Moon, H., Kim, C.J., Loo, J.A., and Garrell, R.L., Electrowetting-based microfluidics for analysis of peptides and proteins by matrix-assisted laser desorption/ionization mass spectrometry. *Analytical Chemistry* 2004, 76, 4833–4838.

[76] Peterson, D.S., Rohr, R., Svec, F., and Frechet, J.M., Enzymatic microreaction on-a-chip: protein mapping using trypsin immobilized on porous polymer monoliths molded in channels of microfluidic devices, *Analytical Chemistry* 2002, 74, 4081.

[77] Slysz, G.W. and Schriemer, D.C., On-column digestion of proteins in aqueous-organic solvents. *Rapid Commun. Mass Spectrom*. 2003, 17, 1044.

[78] Arica, M.Y., Senel, S., Alaeddinoglu, N.G., Patir, S., and Denizli, A., Invertase immobilized on spacer-arm attached poly(hydroxyethyl methacrylate) membrane: Preparation and properties. *J. Appl. Polym. Sci*. 2000, 75, 1685.

[79] Kerenkova, J. and Foret, F., Immobilized microfluidic enzymatic reactors. *Electrophoresis* 2004, 25, 3550–3563.

[80] Gao, J., Xu, J.L., Locascio, L.E., and Lee, C.S., Integrated microfluidic system enabling protein digestion, peptide separation, and protein identification. *Analytical Chemistry* 2001, 73, 2648–2655.

[81] Rubina, A.Y., Dementieva, E.I., Stomakhin, A.A., Darii, E.L., Pan'kov, S.V., Barsky, V.E., Ivanov, S.M., Konovalova, E.V., and Mirzabekov, A.D., Hydrogel-based protein microchips: Manufacturing, properties, and applications. *BioTechniques* 2003, 34, 1008–1022.

[82] Sakai-Kato, K., Kato, M., and Toyo'oka, T., Creation of an on-chip enzyme reactor by encapsulating trypsin in sol-gel on a plastic microchip. *Analytical Chemistry* 2003, 75, 388–393.

[83] Ekstrom, S., Onnerfjord, P., Nilsson, J., Bengtsson, M., Laurell, T., and Marko-Varga, G., Integrated microanalytical technology enabling rapid and automated protein identification. *Analytical Chemistry* 2000, 72, 286–293.

[84] Laurell, T., Marko-Varga, G., Ekstrom, S., Bengtsson, M., and Nilsson, J., Microfluidic components for protein characterization. *Reviews in Molecular Biotechnology* 2001, 82, 161–175.

[85] Wang, C., Oleschuk, R., Ouchen, F., Li, J., Thibault, P., and Harrison, D.J., Integration of immobilized trypsin bead beds for protein digestion within a microfluidic chip incorporating capillary electrophoresis separations and an electrospray mass spectrometry interface. *Rapid Commun. Mass Spectrom*. 2000, 14, 1377–1383.

[86] Jin, L.J., Ferrance, J., Sanders, J.C., and Landers, J.P., A microchip-based proteolytic digestion system driven by electroosmotic pumping. *Lab Chip* 2003, 3, 11–18.

[87] Zimmermann, S., Fienbork, D., Flounders, A.W., and Liepmann, D., In-device enzyme immobilization: Wafer-level fabrication of an integrated glucose sensor. *Sensors and Actuators B* 2004, 99, 163–173.

[88] Slovakova, M., Minc, N., Bilkova, Z., Smadja, C., Faigle, W., Futterer, C., Taverna, M., and Viovy, J.L., Use of self assembled magnetic beads for on-chip protein digestion. *Lab Chip* 2005, 5, 935–942.

[89] Qu, H., Wang, H., Huang, Y., Zhong, W., Lu, H., Kong, J., Yang, P., and Liu, B., Stable microstructured network for protein patterning on a plastic microfluidic channel: Strategy and characterization of on-chip enzyme microreactors. *Analytical Chemistry* 2004, 76, 6426–6433.

[90] Wu, H., Tian, Y., Liu, B., Lu, H., Wang, X., Zhai, J., Jin, H., Yang, P., Xu, Y., and Wang, H., Titania and alumina sol-gel-derived microfluidics enzymatic-reactors for peptide mapping: Design, characterization, and performance. *Journal of Proteome Research* 2004, 3, 1201–1209.

[91] Harrison, D.J., Oleschuk, R.D., and Thibault, P., Microfluidic systems for analysis of the proteome with mass spectrometry, in *Lab-on-a-Chip*, Oosterbroek, R.E. and Van Den Berg, A., Eds., Elsevier, Amsterdam, 249–270 (2003).

[92] Laurell, T., Marko-Varga, G., and Nilsson, J., Interfacing μTAS to matrix assisted laser desorption time-of-flight mass spectrometryóMALDI-TOF-MS, in*Lab-on-a-Chip*, Oosterbroek, R.E. and Van Den Berg, A., Eds., Elsevier, Amsterdam, 271–284 (2003).

[93] Limbach, P.A. and Meng, Z., Integrating micromachined devices with modern mass spectrometry. *Analyst* 2002, 127, 693–700.

[94] Nice, E. and Catimel, B., Affinity-based biosensors, microarrays and proteomics, in *Proteome Analysis Interpreting the Genome*, Speicher, D.W., Ed., Elsevier, Amsterdam, 243–285 (2004).

[95] Zhang, S. and Van Pelt, C.K., Chip-based nanoelectrospray mass spectrometry for protein characterization. *Expert Rev. Proteomics* 2004, 1, 449–468.

[96] de Mello, A.J., Chip-MS: Coupling the large with the small. *Lab Chip* 2001, 1, 7N–12N.

[97] Oleschuk, R.D. and Harrison, D.J., Analytical microdevices for mass spectrometry. *Trends in Analytical Chemistry* 2000, 19, 379–388.

[98] Brivio, M., Fokkens, R.H., Verboom, W., and Reinhoudt, D.N., Integrated microfluidic system enabling (bio)chemical reaction with on-line MALDI-TOF mass spectrometry. *Analytical Chemistry* 2002, 74, 3972–3976.

[99] Gustafsson, M., Hirschberg, D., Palmberg, C., Jornvall, H., and Bergman, T., Integrated sample preparation and MALDI mass spectrometry on a microfluidic compact disk. *Analytical Chemistry* 2004, 76, 345–350.

[100] Hirschberg, D., Jagerbrink, T., Samskog, J., Gustafsson, M., Stahlberg, M., Alvelius, G., Husman, B., Carlquist, M., Jornvall, H., and Bergman, T., Detection of phosphorylated peptides in proteomic analyses using microfluidic compact disk technology. *Analytical Chemistry* 2004, 76, 5864–5871.

[101] Zhang, B., Foret, F., and Karger, B.L., High-throughput microfabricated CE/ESI-MS: Automated Sampling from a MicroWell Plate. *Analytical Chemistry* 2001, 2675–2681.

[102] Zhang, S., Van Pelt, C.K., and Henion, J.D., Automated chip-based nanoelectrospray-mass spectrometry for rapid identification of proteins separated by two-dimensional gel electrophoresis. *Electrophoresis* 2003, 24, 3620–3632.

[103] Yin, H., Killeen, K., Brennen, R., Sobek, D., Werlich, M., and van de Goor, T., Microfluidic chip for peptide analysis with an integrated HPLC column, sample enrichment column, and nanoelectrospray tip. *Analytical Chemistry* 2005, 77, 527–533.

[104] Fortier, M.H., Bonneil, E., Goodley, P., and Thibault, P., Integrated microfluidic device for mass spectrometry-based proteomics and its application to biomarker discovery programs. *Analytical Chemistry* 2005, 77, 1631–1640.

[105] English, R.D. and Cotter, R.J., A miniaturized matrix-assisted laser desorption/ionization time of flight mass spectrometer with mass-correlated acceleration focusing. *Journal of Mass Spectrometry* 2003, 38, 296–304.

[106] Inganas, M., Derand, H., Eckersten, A., Honerud, A.K., Jensen, G., Thorsen, G., Soderman, T., and Anderson, P., Integrated microfluidic compact disc device with potential use in both centralized and point-of-care laboratory settings. *Clinical Chemistry* 2005, 51, 1985–1987.

15

Single-Cell and Single-Molecule Analyses Using Microfluidic Devices

Malgorzata A. Witek, Mateusz L. Hupert, and Steven A. Soper

CONTENTS

15.1 Introduction

15.1.1 What Is a Cell?

The cell is the fundamental structural and functional unit of all living organisms, with organisms consisting of a single cell such as bacteria, or many

cells such as humans, which possess nearly 10^{14} cells. Cells typically function as independently operating machines providing a large heterogeneity in cell characteristics, even for a group of cells that are localized to a specific organ or tissue within a multicellular organism. However, cells do share several common capabilities such as:

- Reproduction by cell division.
- Metabolism, including taking in raw materials, building cell components, converting energy and molecules, and releasing by-products. The functioning of a cell depends upon its ability to extract and use chemical energy stored in organic molecules. This energy is derived from metabolic pathways.
- Synthesis of proteins, the functional workhorses of cells, such as enzymes. A typical mammalian cell contains up to 10,000 different proteins.
- Response to external and internal stimuli, such as changes in temperature, pH, or nutrient levels.

One way to classify cells is whether they live alone or in groups. Organisms vary from single cells (called single-celled or unicellular organisms), which function and survive more or less independently, through *colonial* forms with cells living together, to multicellular forms in which cells are specialized. There are 220 types of cells and tissues that make up the multicellular human body. Cells can also be classified into two categories based on their internal structure.

- *Prokaryotic* cells are structurally simple. They are found only in single-celled and colonial organisms. In the three-domain system of scientific classification, prokaryotic cells are placed in the domains Archaea and Eubacteria.
- *Eukaryotic* cells have organelles with their own membranes. Single-celled eukaryotic organisms such as amoebae and some fungi are very diverse, but many colonial and multicellular forms such as plants, animals, and brown algae also exist.

Cells are comprised of components called organelles, which perform certain functions in this operating machine. The organizational structure and the important organelles comprising a typical eukaryotic animal cell are shown in Figure 15.1. A eukaryotic cell is surrounded by a *plasma membrane*, which serves to separate and protect the cell from its surrounding environment and is composed primarily of a double layer of lipids and proteins. Embedded within this membrane are a variety of other molecules that act as channels and pumps, moving different molecules into and out of the cell.

There is an additional membrane contained within most cells called the nuclear membrane, which forms the cell nucleus and contains the genetic material of the cell. Two different kinds of genetic material exist: deoxyribonucleic

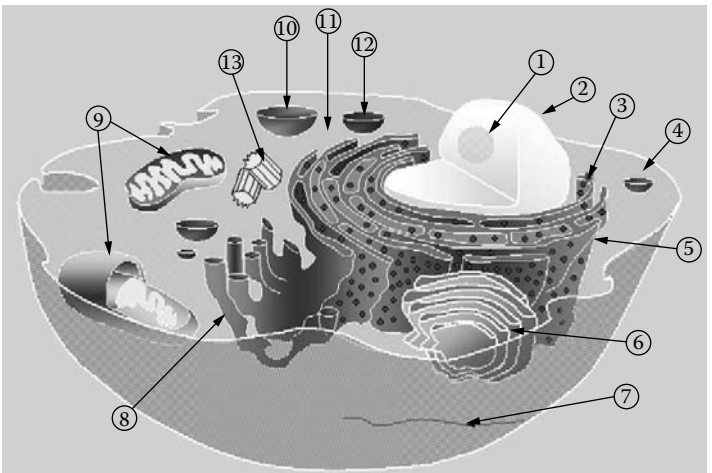

FIGURE 15.1
Schematic of a typical animal cell showing subcellular components. Organelles: (1) nucleolus, (2) nucleus, (3) ribosome, (4) vesicle, (5) rough endoplasmic reticulum (ER), (6) Golgi apparatus, (7) cytoskeleton, (8) smooth ER, (9) mitochondria, (10) vacuole, (11) cytoplasm, (12) lysosome, (13) centrioles.

acid (DNA) and ribonucleic acid (RNA). Most organisms use DNA for their long-term information storage, while the RNA is used for information transport (e.g., mRNA). Transcription is the process by which genomic DNA is used to build mRNA molecules to carry instructional information to the ribosomes for protein production. A human cell has genetic material in the nucleus (the nuclear genome) and the mitochondria (the mitochondrial genome). The nuclear genome is divided into 46 linear DNA molecules called chromosomes. The mitochondrial genome consists of circular DNA molecules that are separate from the nuclear DNA.

The ribosome is a large complex composed of many molecules, including RNAs and proteins, and is responsible for processing the genetic instructions carried by an mRNA. The process of converting an mRNA's genetic code into the exact sequence of amino acids that make up a protein is called *translation*. Protein synthesis is extremely important to all cells, and therefore a large number of ribosomes—sometimes hundreds or even thousands—can be found throughout a cell.

Mitochondria are self-replicating organelles that occur in various numbers, shapes, and sizes in the cytoplasm of all eukaryotic cells. As mentioned earlier, mitochondria contain their own genome, which is separate and distinct from the nuclear genome of a cell. Mitochondria play a critical role in generating energy in the eukaryotic cell, and this process involves a number of complex metabolic pathways.

The endoplasmic reticulum (ER) is the transport network for molecules targeted for certain modifications and specific destinations as compared to molecules that roam freely within the cytoplasm. The ER has two forms: the

rough ER, which has ribosomes on its surface, and the smooth ER, which lacks them. Translation of the mRNA for those proteins that will either stay in the ER or be *exported* from the cell occurs at the ribosomes attached to the rough ER. The smooth ER is important in lipid synthesis, detoxification, and as a calcium reservoir. The Golgi apparatus, sometimes called a *Golgi body* or *Golgi complex,* is the central delivery system for the cell and is a site for protein processing, packaging, and transport. Both organelles consist largely of heavily folded membranes.

Lysosomes and peroxisomes are often referred to as the garbage disposal system of a cell. Both organelles are somewhat spherical, bound by a single membrane, and rich in digestive enzymes—naturally occurring proteins that speed up biochemical processes. For example, lysosomes can contain more than three dozen enzymes for degrading proteins, nucleic acids, and certain sugars called polysaccharides.

15.1.2 The Molecular Makeup of Cells

Cells are comprised of a variety of different types of molecules, such as proteins, peptides, amino acids, DNAs, RNAs, lipids, carbohydrates, and so on. These molecules perform diverse functions within the cell machinery and the presence, absence, structural modification, amount, or location of certain molecules within the cell provides the unique signature or identity of that cell. An example of how a unique cell signature can have significant consequences on the functional state of an organism is evident in cancer. Cancer develops due to a variety of different mutagenic changes that occur in a cell's genome, providing unregulated cell growth in many cases (neoplasm). However, a solid tumor contains a highly heterogeneous collection of neoplastic cells that can originate from a single cancer cell. The heterogeneity within the tumor results from the stochastic cascading mutational events that occur within each cell of the solid mass during tumorigenesis.

The amount (i.e., copy number) of cellular molecules varies considerably and depends on the type of molecule and the size of the cell. For example, most eukaryotic cells contain only two copies of genomic DNA within their nucleus, while the copy number of mRNAs can vary from several to tens of thousands with the exact number dependent on the activity of the gene for which it codes. In addition, there is usually one unique mRNA molecule for each gene that is transcribed, and thus a single cell may contain more than 5000 different mRNA molecules. The number of different proteins found within a single cell varies considerably as well, with a common estimate being somewhere in the neighborhood of 10,000. In addition, the copy number of each protein found within the cell can vary tremendously.

There are a variety of different types of cells, all containing unique structural and morphological features. Several different types of cells and their sizes are listed in Table 15.1.

TABLE 15.1

The Physical Dimensions and Volumes of Different Types of Cells

	Long Dimensions (μm)	Volume (fL)
Mammalian neuron	4–150	—
Lymphocyte	13–16	172–204
Erythrocyte	8–14	53–87
E. coli	0.7–1.5	0.5–1.5
Cancer cell	20–30	4,200–14,100

Source: Hogan, B.L. and Yeung, E.S. (1993). *TrAC, Trends in Analytical Chemistry* 12(1): 4–9.

Cells can be considered ultrasmall-volume containers that possess molecules with a diverse range of concentrations as noted above. For example, genomic DNA is found in eukaryotic cells at 2 molecules per cell, and for a human lymphocyte, this represents a concentration of 19.3 pM (pM = 10^{-12} M). However, for a protein that is modestly expressed (approximately 250,000 copies per cell), the concentration of that protein within the same cell would be 2.14 μM (μM = 10^{-6} M).

The conclusion that can be drawn from these simple calculations is that the concentration of most molecules found within a single cell is relatively high and easily analyzed by most readout modalities, such as laser-induced fluorescence or amperometric detection. However, because many readout or detection strategies are concentration sensitive, dilution of the intracellular contents following cell lysis must be minimized to aid in detection. The use of microsystems for single-cell analysis is particularly attractive because the reaction and processing chambers in these systems are on the same volume scale as that of a single cell. In addition, the closed architecture of most microfluidic systems, and the fact that several processing steps can be integrated into a single system, minimizes sample loss and contamination.

15.1.3 Single-Molecule Analysis

As noted previously, the content of a single cell can vary tremendously, from two copies of a molecule (genomic DNA) to tens of thousands of molecules (mRNA or proteins). Therefore, in many cases when embarking upon the mission of analyzing single cells, it may be necessary to design the system with the capability to detect single molecules as well. In the case of genomic DNA, there are strategies that can be used to amplify the target material (i.e., DNA) using such techniques as the polymerase chain reaction, rolling circle amplification, or strand displacement amplification. While these amplification strategies are attractive for building the copy number of DNA that can be read from the assay, they do have some limitations in terms of their implementation. For example, providing quantitative information is somewhat tenuous when using thermal amplification techniques due to the limited dynamic range associated with these techniques. In addition, there are

parts of the genome that are difficult to amplify, such as highly repetitive regions or regions rich in guanines and cytosine residues. The amplification step would require an additional functional component to be integrated into the system, complicating packaging and assembly of the system. And finally, some molecules that are to be analyzed from a single cell do not lend themselves to amplification, such as proteins, peptides, or amino acids.

Therefore, it is necessary to consider the possibility of reading out the results of a single-cell assay using single-molecule detection. Single-molecule detection is affected by interrogating the signature of a single molecule when it is resident within the sampling volume. To delineate some of the underlying principles associated with single-molecule detection, we will use laser-induced fluorescence readout as an example. During the single molecule's residence within the sampling volume, which in this case is defined by the confocal volume produced by a focused Gaussian laser beam, the molecule is continuously cycled between the ground electronic state and an upper electronic state with relaxation producing a fluorescent photon. This cycling process generates a burst of photons (Mathies et al. 1990), with the number of photons per molecule (n_f) approximately equal to;

$$n_f = \left(Q_f \big/ Q_f \right) \left[1 - e^{-k\tau(k+1)} \right] \tag{15.1}$$

where Q_f is the fluorescence quantum yield, Q_d is the photodestruction quantum yield, τ and k are dimensionless parameters equal to τ_t / τ_d (τ_t = molecular residence time in excitation volume; τ_d = photobleaching lifetime of the molecule), and k_a / k_f (k_a = absorption rate of the single molecule; k_f = fluorescence emission rate of molecule), respectively. As can be seen from Equation 15.1, molecules with high fluorescence quantum yields that are photochemically stable produce large numbers of fluorescent photons. In addition, n_f can be increased by increasing the residence time of the molecule within the sampling volume to a point in time where photobleaching occurs, at which time photon emission ceases.

In any analytical measurement, one is interested in the signal-to-noise ratio (SNR), which provides a criterion by which the analytical signal of interest is statistically greater than the noise in the measurement. For single-molecule detection, the noise is typically comprised of scattering (Raman, Rayleigh, specular), autofluorescence from the sample matrix and shot noise from the detection and processing electronics. In most cases, single-molecule measurements are performed with threshold levels used to provide an acceptable level of confidence that the event scored arises from a single molecule and not from the background (false positive). However, lowering the level of false positives typically provides higher levels of false negatives. To assess the validity of the data and to assure that the scored events are those arising from single molecules and not multiple molecules resident within the sampling volume, one can use the following equations (Soper et al. 1993):

$$P_o = CD_vN_A \tag{15.2}$$

$$N_{ev} = \frac{2P_o vT}{\pi\omega_o} \tag{15.3}$$

Equation 15.2 represents the probability (P_o) of a single molecule occupying the probe volume, and is typically adjusted to less than 0.1 to minimize the probability of double occupancy (C = molecular concentration, molar; D_v is the size of the probe volume in liters; N_A is Avogadro's number). N_{ev} is the number of events expected during a typical experimental run and can be used as a diagnostic to assess the degree of false negatives incurred in an experimental run (v is the linear sample velocity, cm/s; T is the duration of the experiment, s; and ω_o is the laser beam waist, cm).

15.1.4 Why Analyze Single Cells or Single Molecules?

Most biological samples represent a high degree of heterogeneity and as such, making a bulk measurement over many targets, whether they are cells or molecules, will yield an ensemble average of the entire sampling domain. Therefore, fine structure in the heterogeneous sample is lost due to this ensemble averaging phenomenon. Single-cell or single-molecule measurements eliminate such artifacts, and thus can provide fine detail from mixed population samples. Additionally, single-entity measurements produce the ability to study rare events. For example, micrometastasis is typically associated with breast cancer, in which tumor cells are released into circulating blood prior to full-stage metastasis. It is not uncommon to find 1 to 10 cells per milliliter of whole blood with the red blood cell count exceeding 10^7. The detection of these rare cells can be used as an effective early diagnostic for breast cancer (Baker Megan et al. 2003; Husebekk et al. 1988; Kahn Harriette et al. 2004). Another diagnostic example is detecting genetic disorders in embryos at the 6- to 10-cell embryonic developmental stage, in which only 1 to 2 cells can be biopsied for DNA analysis without permanently damaging the embryo.

In the case of single-molecule detection, practical examples of where this can be of importance is in developing biological assays that seek to minimize the number of processing steps required to elicit a response, which can provide near real-time readout and simplify assay processing. DNA fragment sizing following restriction enzyme digestion can be used to score potential mutation sites at specific locations (restriction fragment length polymorphism [RFLP]). This assay typically requires a gel electrophoresis step to sort (by size) the restriction fragments that are generated. Using single-molecule detection, the electrophoresis step can be completely eliminated (Ambrose et al. 1993; Foquet et al. 2002; Habbersett et al. 2004). Another example is the detection of mutations in certain gene fragments

following PCR amplification of the prerequisite gene fragments. The use of single-molecule detection can completely eliminate the need for PCR, reducing assay cost and development time (Wabuyele et al. 2003). From a microsystems point of view, single-molecule detection capabilities eliminate the need for fabricating devices that carry out these amplification processes, simplifying the operation of the system and improving manufacturing success rates.

In this chapter, we will provide some practical examples of using microsystems for analyzing both single cells and single molecules. Special emphasis will be placed on the fabrication of devices and systems capable of detecting single molecules and analyzing single cells as well as substrate material considerations of the microsystem and its effects on single-molecule and single-cell analyses.

15.2 Single-Cell Analysis Using Microfluidic Devices

Each biological cell is self-contained and self-maintaining: it takes in nutrients, converts them into energy, carries out specialized functions, reproduces, and dies. Each cell stores its own set of information for performing each of these activities. The study of cells, what is in them, on them, around them, how they eat, sleep, grow, die, complete tasks, and work by stimulating, influencing, inhibiting and destroying each other is called *cellomics*. Understanding the molecular biology of cells is an active area of research that is fundamental to all of the basic sciences, agriculture, biotechnology, and medicine. Detailed knowledge of the cell biology, cell metabolic processes and pathways, and genetic and proteomic makeup can contribute to the development of new methodologies and drug therapies for prevention or treatment of many disorders and diseases. The stakes involved in single-cell analysis are of great significance, and not surprisingly, the development of single-cell analysis tools has become the focus of significant efforts in the bio-MEMS arena. Well-founded techniques, such as capillary electrophoresis and flow cytometry, have both demonstrated valuable and effective abilities to manipulate large numbers of cells (with few exceptions where single-cell handling was demonstrated) and have rather limited capability to manipulate and analyze *single biological cells*. A disadvantage of currently available cell screening techniques is their low throughput capabilities, making it difficult to obtain data for large cell populations.

New methodologies and rapid developments in micro- and nanofabrication technologies are creating new opportunities for single-cell analysis. There are a number of reasons microfluidic devices and systems are particularly attractive for performing cellomics (Andersson et al. 2003, 2004): (1) micromechanical devices are capable of manipulating *single* objects with cellular dimensions, (2) the size of cells fits very well with that of commonly

used fluidic devices (10 to 100 μm), (3) the ability to integrate standard operations into the microfluidic system, (4) heat and mass transfer characteristics that are very fast in microfluidic systems. The unique ability of microfluidic devices to integrate sample manipulation and processing operations with separations and analyte detection allows for the efficient automation and high-throughput capabilities of chemical analyses. Microdevices possess several advantages over conventional chemical and biochemical analysis instrumentation, including (1) the ability to perform fast separations with no losses in separation efficiency, (2) lower reagent and sample consumption, and (3) the ability to fabricate many parallel systems on the same device making it a convenient platform for single-cell assays with high-throughput capabilities.

Cell studies utilizing microfluidic systems have focused thus far on cytometry (Andersson et al. 2003; Andersson et al. 2004; Beebe 2000; Chan et al. 2003; Chin Vicki et al. 2004; Erickson and Li 2004; Eyal and Quake 2002; Palkova et al. 2004; Sohn et al. 2000; Wu et al. 2004), sorting (Andersson et al. 2003; Emmelkamp et al. 2004; Fu et al. 2002; Fu et al. 1999; Kruger et al. 2002; Lu et al. 2004a; Rao et al. 2004; Sia et al. 2003), cell lysis (Chaiyasut et al. 2002; Dhawan et al. 2002; Gao et al. 2004; Hellmich et al. 2005; Heo et al. 2003; Huang et al. 2003; Lee and Tai 1999; McClain et al. 2003; Waters et al. 1998; Wheeler et al. 2003), followed by extraction (Hong et al. 2004), and separation and analysis of intracellular components (Ocvirk et al. 2004). Microfabrication technology has also enabled the engineering of cell culture environments. Recent microfluidic work has demonstrated successful culturing of biological cells on chips (Balagadde et al. 2005; Chung et al. 2005; Futai et al. 2006; Gu et al. 2004; Hung et al. 2004; Rhee et al. 2005; Shackman et al. 2005; Tourovskaia et al. 2005). These studies addressed certain aspects of cell culture control, including nutrient mass transport and modulation of culture conditions. The ultimate goal, however, is single-cell analyses that can be helpful where culturing processes are difficult (i.e., unculturable microbes, viruses), or when one deals with developing organisms or primary cells.

15.2.1 Cell Sorting and Capture

Cell separation and recognition techniques are fundamental in cell biology. The ability to effectively isolate and recognize single cells from a heterogeneous population is a limiting factor in many sorting technologies. Sohn et al. (2000) developed a capacitance cytometry technique that allows recognition of single cells based on their internal properties. This technique allows probing the polarization response of different biological materials present in a cell. DNA, for example, is a highly charged molecule and when placed in an applied low-frequency AC electric field has a substantial polarization response. Unlike a Coulter counter, which measures the displaced volume, capacitance cytometry measures the response of the polarization of a cell as it passes through an electric field. Sohn et al. observed a linear relationship

between the DNA content of eukaryotic cells and the change in capacitance value that was evoked by the passage of individual cells across a 1 kHz 250 mV rms electric field (Figure 15.2c). The developed microfluidic cytometer was used to quantify the DNA content of eukaryotic cells and to analyze the cell-cycle kinetics of populations of cells. A comparison with standard flow cytometry demonstrated high sensitivity of the method, which was achieved by the use of shallow poly(dimethylsiloxane) (PDMS) channels (30 μm depth and 30 μm width), grounding and shielding the device, and precisely controlling the temperature. Gold electrodes were fabricated photolithographically onto the glass and were 50 μm wide. The interelectrode spacing was 30 μm and the noise magnitude observed was 0.1 to 2 fF. A schematic of the device is presented in Figures 15.2a and b. In contrast to a standard laser flow cytometer, this method required no special sample preparation, such as cell staining.

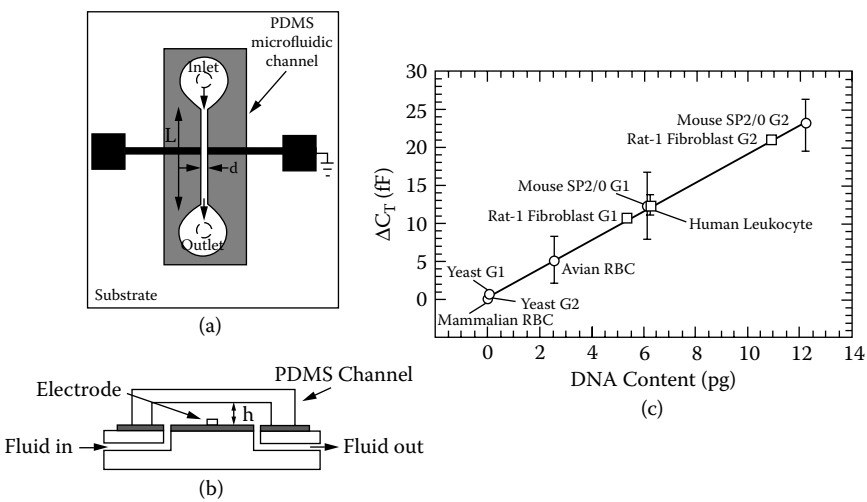

FIGURE 15.2
Schematic illustration of the integrated microfluidic device. (a) Top view shows the entire device, including electrode configuration, inlet and outlet holes for fluid, and the PDMS microfluidic channel. The electrodes are made of gold and are 50 μm wide. The distance, *d*, separating the electrodes is 30 μm. The width of the PDMS microfluidic channel is also *d*, the length, *L*, is 5 mm, and the height, *h*, is either 30 μm or 40 μm. (b) Side view along the vertical axis of the device shows a detailed view of fluid delivery. Fluid delivery is accomplished with a syringe pump at rates ranging from 1 to 300 μl/hr. (c) Change in capacitance C_T vs. DNA content of mouse SP2/0, yeast, avian, and mammalian red blood cells. As shown, there is a linear relationship between C_T and DNA content at 1 kHz frequency. ○–Data taken with a device whose channel height was 30 μm; □–data taken with a device whose channel height was 40 μm. The 40 μm data were scaled by the ratio of the C_T values obtained for mouse SP2/0 cells measured with 30 μm– and 40 μm–high channel devices. All data were obtained at T = 10°C and in PBS solution. (Reprinted with permission from Sohn, L.L., Saleh, O.A., Facer, G.R., Beavis, A.J., Allan, R.S., and Notterman, D.A. (2000). *Proceedings of the National Academy of Sciences of the United States of America* 97(20): 10687–10690. © 2000, The National Academy of Science of the USA.)

Microfluidic devices are being designed in ways that allow the investigation of single-cell phenomena rather than batch culture. Numerous methods are being or have been already developed for the immobilization of particular types of cells in microfluidics (Braschler et al. 2005; Toriello et al. 2005). Among the various immobilization or cell capture methods, several include: (1) chemical surface modifications with microcontact printing, (2) laser trapping, and (3) dielectrophoretic or electromagnetic trapping.

A PDMS and glass microchip that performed direct capture and chemical activation of surface-modified single cells has been presented by Toriello et al. (2005). The cell capture system was comprised of gold electrodes microfabricated on a glass substrate (Figure 15.3a). The cell capturing mechanism involved a labeling of the cell surface with thiol functional groups (using RGD endogenous receptors) and the utilization of spontaneous adsorption of thiol-containing species onto gold surfaces. The off-chip incubation in RGD peptide resulted in approximately 5×10^6 thiol groups per cell. The labeled cells were electrophoretically transported to electrodes and captured on gold surfaces. Once captured, the single cells were activated with an agonist to a membrane-bound receptor, and the response was monitored optically with a fluorescent probe. Multiple cell types were sequentially and

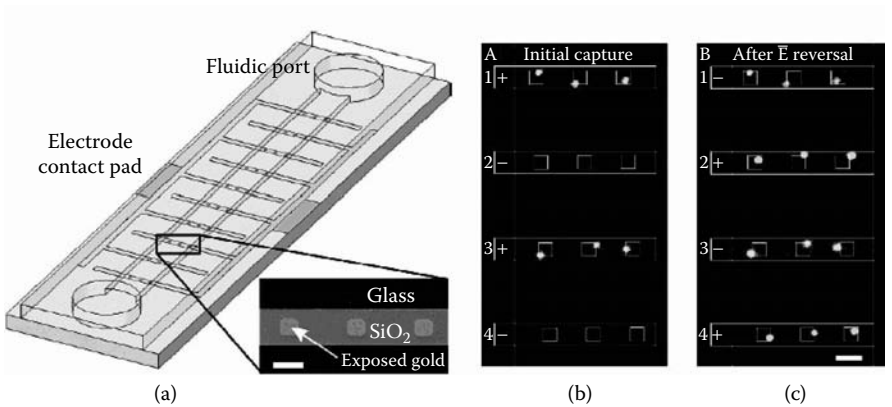

FIGURE 15.3
(a) Schematic of the glass-PDMS microdevice for single cell capture. A cell suspension enters the 200 μm–wide PDMS channel through the 0.5 mm–diameter fluidic port. Cells flow over the PDMA derivitized glass surface in the 32 μm–deep channel and are captured on the 16 μm^2 exposed gold pads centered on the 40 μm–wide gold electrodes. Cells are directed to the desired electrode by applying a 50 V/cm electric field between the interdigitated electrodes (200 μm spacing). Inset: electron micrograph of an electrode showing the three exposed gold pads on the oxide-coated electrode. Bar, 30 μm. (b) Sequential directed capture of two populations of Chinese hamster ovary (CHO) cells. The first population of thiolated K1 cells, labeled with CellTracker Blue, is captured by applying a 50 V/cm potential to the even-numbered electrodes for 10 min. (c) A second population of thiolated K1 cells, labeled with Cell Tracker Green, is introduced into the channel through the opposite fluidic port and field-mediated binding occurs selectively at the odd-numbered electrodes. Bar 40 μm. (Reprinted with permission from Toriello, N.M., Douglas, E.S., and Mathies, R.A. (2005). *Analytical Chemistry* 77(21): 6935–6941. © 2005, American Chemical Society.)

selectively captured on neighboring electrodes by changing the field direction (Figures 15.3b and c). The capture efficiency (defined as the electrode pad rows having a single cell captured) was optimized by variations in the duration of the applied field, which was 63 ± 9% (n = 30) for 10 min and was 90 ± 5% for a 60 min incubation. The use of cell surface thiolation presents several advantages; (1) it relies on the robust and strong gold–thiol bond; (2) it leaves the gold electrodes in their native state, which is useful for sensor applications, and (3) the cell modification approach provides superior adhesion with electrical measurement flexibility.

15.2.2 Cell Lysis

Typical laboratory protocols for cell lysis include the use of enzymes (lysozyme), chemical agents such as detergents (Chaiyasut et al. 2002; Dorre et al. 1997), mechanical forces such as sonication and bead milling (Belgrader et al. 1999; Belgrader et al. 2000; Taylor et al. 2001), and thermal and laser methods (Dhawan et al. 2002; He et al. 2001; Ivanov 1999; Sims et al. 1998). Some of these methods have been successfully implemented into microfluidic formats. For example, an integrated monolithic microchip was fabricated using electrokinetic fluid actuation and thermal cycling to accomplish lysis of *Escherichia coli* and the subsequent amplification of the released DNA (Waters et al. 1998).

In a similar electrokinetic device, the controlled manipulation of *red blood cells* (RBCs) throughout a channel network and chemical lysis of the cells was demonstrated (Dorre et al. 1997). A continuous flow device for rapid RBC lysis and leukocytes isolation from whole blood was also developed by Toner et al. (2005). RBCs lysis was performed on a PDMS chip using a NH_4Cl-based lysing buffer (Toner and Irimia 2005). The advantage of chemical lysis on chip is reduced diffusion time, which allows for fairly short lysing times of 30 s, as opposed to 10 to 20 min for benchtop formats.

The use of microfluidic glass chips for continuous single-cell lysis and detection of β-Galactosidase (β-Gal) content was described by Ocvirk et al. (2004). Cells were transported toward a Y-shaped mixing junction, at which point lytic agents were introduced (Figure 15.4). Flow velocities of approximately 100 and 40 mm/s were used under protein denaturing (35 mM sodium dodecylsulfate [SDS]), and nondenaturing (0.1% Triton X-100) conditions. Complete and reproducible lysis of individual cells on-chip occurred within 30 s using Triton X-100 and 2 s when using SDS. Fluorescence peaks, due to the enzymatic product of the reaction of β–Gal with fluorescein mono-β-D-galactopyranoside (FMG), were detected downstream of the mixing. Unincubated cells were mixed on-chip with both FDG and Triton X-100 with each individual cell generating fluorescence downstream of the mixing point, which was detected within 2 min of mixing. In contrast, viable cells incubated with FDG required 1 h or more in order to generate significant signals.

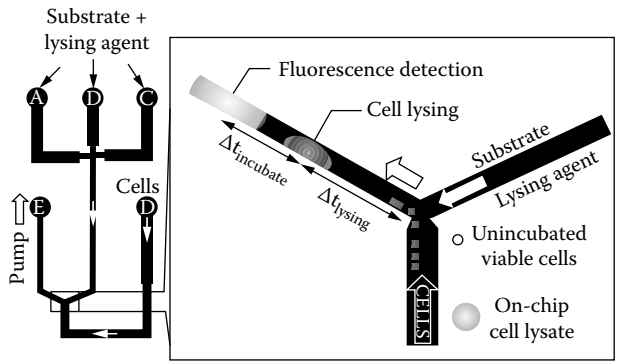

FIGURE 15.4
Scheme of on-chip lysing and on-chip incubation of HL-60 cell with substrate. Substrate and lysing agents were in ports A–C. Cells were placed in port D and suction applied at port E, causing mixing of cells and lytic solution containing enzyme substrate at the intersection. A fluorescence detector was located downstream of the mixing point, and an observation microscope sat over the intersection. (Reprinted with permission from Ocvirk, G., Salimi-Moosavi, H., Szarka, R.J., Arriaga, E.A., Andersson, P.E., Smith, R., Dovichi, N.J. and Harrison, D.J. (2004). *Proceedings of the IEEE* 92(1): 115–125. © 2004, IEEE.)

Another way to disassemble the cell membrane to provide access to the cell's interior is through the use of an electric field. Lysis of cells in an electric field is due to the dielectric breakdown of the membrane as the transmembrane voltage reaches a certain magnitude. In mammalian cells, membrane breakdown leading to pore formation usually begins at a transmembrane voltage of 0.2 to 1.5 V, depending on the buffer concentration and the cell type and size (Tsong 1991). As the transmembrane voltage increases, pores and irreversible holes in the membrane are formed, which cause cell rupture. In designing microfluidic devices for cell lysis, the electrode geometry is very important. The degree of electroporation/lysis of a cell depends on the interelectrode distance when the absolute voltage and pulse duration are constant. The greater the inter-electrode distance, the slower the process of cell lysis. The goal is to utilize an electrode geometry that leads to the fastest formation of irreversible pores at the lowest interelectrode voltage.

Ramsey's group (McClain et al. 2003) implemented electrical lysis into a microfluidic device for the high-throughput chemical analysis of Jurkat cells. Cells loaded with dyes were hydrodynamically transported from the cell-containing reservoir to a region on the microfluidic device where they were focused and rapidly lysed using an electric field. The hydrolyzed, fluorescent dyes in the cell were injected into a separation channel on the device and detected 3 mm downstream of the injection point (Figure 15.5).

The total separation time was 2.2 s with absolute migration time reproducibilities of less than 1% and efficiencies ranging from 2300 to 4000 theoretical plates. Cell analysis rates of 7 to 12 cells/min were demonstrated, which were significantly faster than those reported for standard bench-scale capillary electrophoresis.

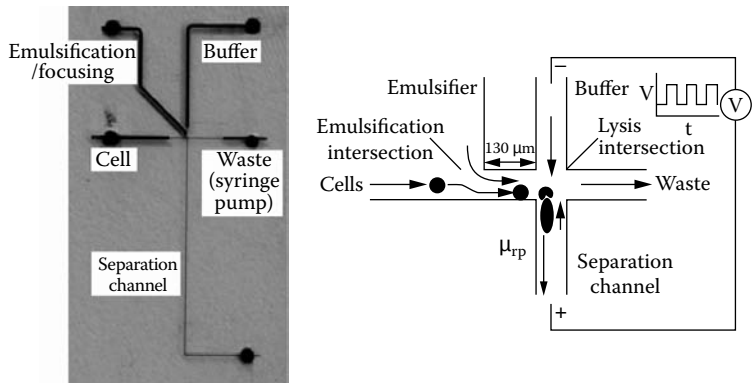

FIGURE 15.5
(a) Image of microchip used for cell analysis experiments. (b) Schematic of the emulsification and lysis intersections for the microchip design shown in (a). The solid arrows show the direction of bulk fluid flow and the dashed arrow shows the electrophoretic migration direction of the labeled components in the cell lysate. (Reprinted with permission from McClain, M.A., Culbertson, C.T., Jacobson, S.C., Allbritton, N.L., Sims, C.E., and Ramsey, J.M. (2003). *Analytical Chemistry* 75(21): 5646–5655. © 2003, American Chemical Society.)

Complete electrical lysis was demonstrated in less than 33 ms using an AC electric field with a DC offset to lower the joule heating and provide sufficient field strength for lysis. Fields of 0.45 kV/cm peak-to-peak square waves (75 Hz) were used with a 0.68 kV/cm DC offset and a 50% duty cycle. Figure 15.6 shows a time series of CCD images demonstrating the lysis of an individual Jurkat cell loaded with Calcein AM. In Figure 15.6a, the Jurkat cell appeared close to one side of the main channel due to the flow from the focusing and emulsification channel. In Figure 15.6b, the cell entered the lysis intersection, encountered the electric field, and was lysed. The fluorescent dyes in the cytosol moved electrophoretically down the channel toward the anode. Spatially separated bands from two dyes could be seen in the third image (Figure 15.6c). Figure 15.6d shows the separation of Oregon green and carboxyfluorescein compounds from eight interrogated cells. These devices should make it feasible to analyze large cell populations.

Another example of a device for single-cell interrogation was introduced by Khine et al. (2005). A PDMS device was designed first to selectively immobilize, and second to locally electroporate cells. The cell suspension was introduced into the device with a syringe and controlled manually to allow cell trapping by applying negative pressure on the trapping channel. When trapped, a cell was pulled laterally into a smaller channel, which acted as a high-resistance component in the fluidic circuit. The localized electroporation was achieved when cells were sequestered in the PDMS channels (Figures 15.7a and b). The electric field was focused with the greatest potential drop occurring across the membrane of the cell inside the channel, which is inversely proportional to its surface area, hence the localized electroporation

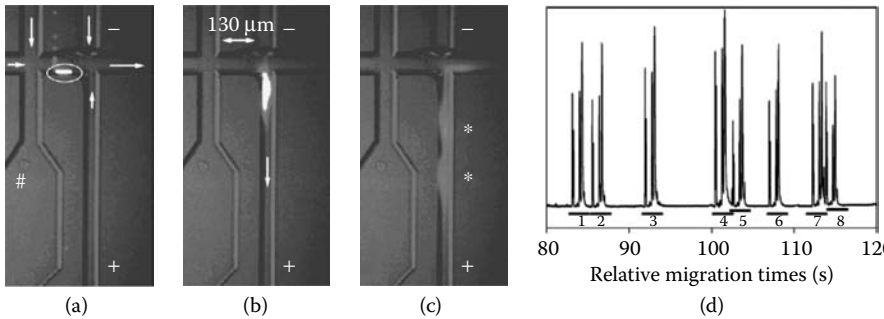

FIGURE 15.6
CCD images of cell lysis. (a) The Jurkat cell loaded with Calcein AM (within white oval) is being hydrodynamically transported to the lysis intersection. The cell image is distorted because the integration (exposure) time of the CCD camera was long compared to the cell velocity. The arrows depict the direction of fluid flow in the channels. The faint line and spots above the cell are the result of pixel blooming during readout in the frame-transfer mode of the camera. (b) The cell has encountered the electric field and been lysed. The fluorescently labeled contents are injected into the separation channel and migrate toward the anode. The arrow depicts the direction of lysate migration in the channel. (c) The separation of two of the fluorescently labeled components (marked by asterisks) in the separation channel is seen. (d) Electrophoretic separation of cytosolic dyes released from individual cells. This is a 40s segment of a 2 min run. The peak envelopes from eight cells are shown and are demarcated by the thick black horizontal lines and labeled 1 through 8. (Reprinted with permission from McClain, M.A., Culbertson, C.T., Jacobson, S.C., Allbritton, N.L., Sims, C.E., and Ramsey, J.M. (2003). *Analytical Chemistry* 75(21): 5646–5655. © 2003, American Chemical Society.)

was achieved at relatively low voltages (approximately 0.75 V/cm). The effectiveness of the device was demonstrated by electroporating HeLa cells. Additionally, the average transmembrane poration potential of these cells has been determined to be 0.51 ± 0.13 V. The required field was maintained by measuring characteristic increases in the current that corresponded to a drop in the cell resistance and microscopically by recording either the escape of cytoplasmic dye Calcein AM or the entrance of Trypan blue stain. Time-lapsed images of electroporation are shown in Figure 15.7d and consist of Trypan blue moving into the cell. The data also provided evidence of the occurrence of cell resealing after the first sequence of the applied field.

15.2.3 Cellular Physiology and Signaling

Studies of cellular physiology require maintaining cells in a life-supporting environment while measurements are made on them. Such studies are typically performed on a laboratory bench, with cells suspended in a physiological medium while immobilized in a macroscale perfusion system. Microfabricated fluidic systems offer the potential to develop experimental stations that incorporate multiparameter measurements on cells that are viable (Shackman et al. 2005). Shackman et al. reported on a microfluidic device that perfused cells and monitored the insulin secretion from single

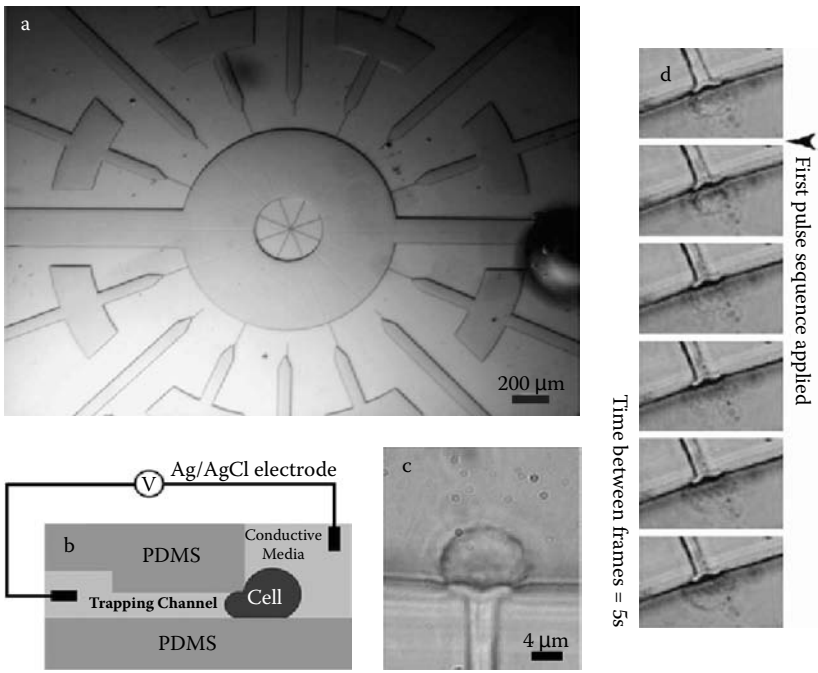

FIGURE 15.7
The layout of the chip and cell. (a) The two wide inlet channels on the left and right are used for cell input and output. An electrode is connected to one of these main channels. The other electrode is connected to the small channel where the cell is trapped. (b) A schematic of the cross-section of the chip. When trapped, a cell is pulled laterally into the small trapping channel by applying a negative pressure. The trapped cell acts as a high resistance component in the circuit. (c) An image showing the cell trapped in the channel. The cell extends into the channel leaving a tail-like structure in the channel. Because of its viscoelastic nature, the cell retains its shape after the negative pressure is removed. (d) Time-lapsed video of Trypan blue entering the cell. The cell is trapped in a channel when the pulse sequence is applied. After the pulse sequence application, the cell turns distinctly blue as the dye diffuses through the electropores and concentrates inside the cell. It can be observed that the blue dye first appears in the cell at the region within the channel, and gradually migrates throughout the cell. (Reprinted with permission from Khine, M., Lau, A., Ionescu-Zanetti, C., Seo, J., and Lee, L.P. (2005). *Lab on a Chip* 5(1): 38–43. © 2005, The Royal Society of Chemistry.)

islets of Langerhans. Islets are 75 to 200 mm–diameter spheroid microorgans located in the pancreas, which contain endocrine cells. Most islet cells secrete insulin as part of the glucose homeostasis mechanism. Upon exposure to glucose, an initial burst of insulin is released followed by a lower rate oscillatory release. This process is of interest because weakened secretion is associated with type II diabetes and drugs that treat diabetes target this process (Shackman et al. 2005). The assay on a chip allowed the quantitative monitoring of insulin secretion in a highly automated fashion. The results were comparable to those of the offline method utilizing ELISA (enzyme linked immunosorbent assay). The micromethod also allowed longer cell survival and rapid change of solutions contacting the cells as compared to the macroscale version. The

technique could be amenable to studies involving other tissues or cells that release chemicals. The detection method (i.e., optical, electrochemical) could be customized for the particular analyte of interest.

Another cellular metabolite, lactate, was assayed in a microfluidic format. Lactate is the final product of glycolysis and is one of the most important cellular metabolites. It is produced in small concentrations during aerobic respiration and in larger concentrations during cell death. Measurements of its concentration provide information on the complex timeline of metabolic changes. Cai et al. (2002) presented ultra-low-volume, real-time measurements of lactate from single heart cells utilizing amperometric detection. The rod-shaped myocyte cell membrane integrity was compromised by permeabilization with saponin, which caused immediate cell contracture (Figure 15.8).

Lactate was released from the cell immediately after the addition of saponin. Dynamic electrochemical measurements of lactate during cell permeabilization

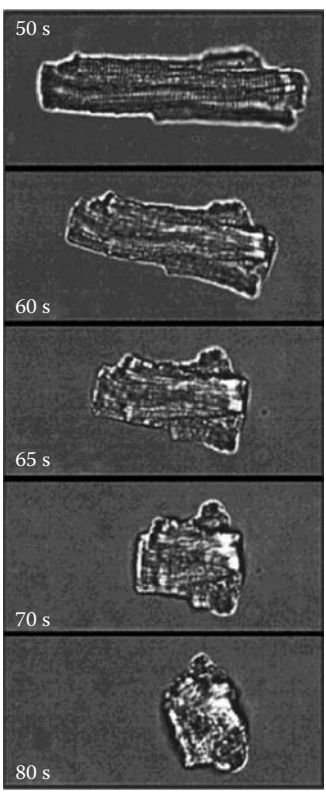

FIGURE 15.8
Healthy "dormant" rod-shaped myocyte being permeabilized with saponin. Upon addition of the saponin (at 8 s to 80 g/mL), the myocyte shortened and rounded up. Images from 50 s onward are shown (those from 0 to 50 s are identical). Observation of the cell within the chamber showed that lactate was released immediately when saponin was added to the cell. (Reprinted with permission from Shackman, J.G., Dahlgren, G.M., Peters, J.L., and Kennedy, R.T. (2005). *Lab on a Chip* 5(1): 56–63. © 2005 The Royal Society of Chemistry.)

found that the lactate content after metabolic inhibition was three times that in the healthy cell. The method provided a generic assay to make single-cell sensing in picoliter volumes.

The detection of lactate was optimized using an enzyme-linked assay with lactate oxidase involving amperometric detection of H_2O_2 at +0.64 V versus a Ag/AgCl reference electrode, according to Equations 15.4 and 15.5.

$$\text{L-lactate} + O_2 \rightarrow \text{pyruvate} + H_2O_2 \tag{15.4}$$

$$H_2O_2 \rightarrow O_2 + 2H^+ + 2e^- \tag{15.5}$$

A two-electrode microamperometric system was developed based on a platinized working microelectrode and an integrated Ag/AgCl electrode serving as a counter and reference electrode. The platinized microelectrode possessed a very large surface area, which increased the signal-to-background ratio and improved the detection limits. Also, this working electrode is highly catalytic with a reduced overpotential for the oxidation of hydrogen peroxide (H_2O_2). The entire device consisted of an electrochemical sensor and a dispensation technology capable of delivering small volumes (6.5 pL), and single cells into a microelectrochemical cell.

There is tremendous interest in understanding not only how cells react to environmental stimuli, but also how they receive and process signals. Cellular signal transduction has been found to be important in multiple physiological functions, including their role in the immune system, neural activity, and proper organ development. Molecular-level communication between adjacent cells is essential for proper functioning of living tissue. It has been noted for years that membrane contact with neighboring cells can cause changes in morphology, gene expression, and growth. Impaired cell–cell communication has been implicated in numerous diseases, and is correlated with most forms of cancer (Lee et al. 2005). Lee et al. (2005) fabricated a device to study cell–cell communication between neighboring cells. The developed microfluidic device consisted of a module that selectively trapped cell pairs followed by optical characterization. Microfluidic devices were intended to trap individual cells within one cell diameter of an adjacent cell (Figure 15.9). A single pair of trapping sites was designed to be separated by 20 μm on opposite sides of a microfluidic channel. The cell line used averaged 12 μm in diameter, and hence the channel was wide enough to allow cells to flow through unhindered and yet narrow enough to allow membrane contact when the cell pairs were trapped across from each other. The cell-trapping design consisted of two different heights of channels molded in PDMS. The cell trapping array had four fluidic ports connected to control valves. The west and east ports were used for the flow of cells into the device and the north and south ports controlled the corresponding row of cell-trapping sites. Independent control of the two trapping ports (north and south) allowed trapping of one cell.

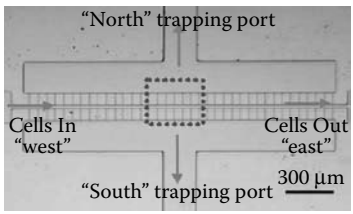

(a)

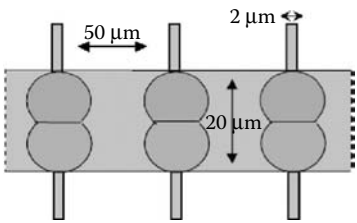

(b)

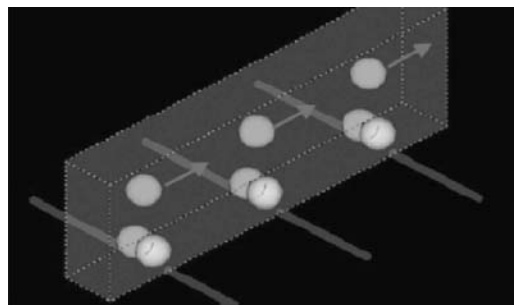

(c)

FIGURE 15.9
A layout of microfluidic cell-trapping device. (a) Microscope image of the arrayed device. The four inlets are referred to as north, south, west, and east according to the depicted layout for clarity. Cells are flowed through the main channel from west to east. Trapping is controlled by altering fluid flow using valves connected to the four outlets. (b) The trapping design allows two independently controlled sets of channels for localizing different cell populations either to the north or south trapping sites. (c) Three-dimensional schematic view depicting channel geometry, trapped cells, and cell flow. (Reprinted with permission from Lee, P.J., Hung, P.J., Shaw, R., Jan, L., and Lee, L.P. (2005). *Applied Physics Letters* 86(22): 223902/223901–223902/223903. © 2005, American Institute of Physics.)

Device operation was verified by observation of dye transfer between mouse fibroblasts placed in membrane contact. The intracellular fluorescent dye was permeable through cell–cell junctions and was used to study dye transfer. After fluorescent and nonfluorescent cell pairs were selectively trapped, the device was placed in a standard cell culture incubator to promote dye diffusion. Dye transfer was observed for incubation times between 3 and 16 h for cells in membrane contact (Figure 15.10), but not for cells that were not in contact.

The objective of much research is to measure and understand cellular signaling in order to explain the complex relationships between intracellular pathways leading to, for example, cell death. Apoptotic cell death dynamics of HL60 cells studied using a microfluidic cell trap device were presented by Valero et al. (2005). The term *apoptosis* defines a genetically encoded cell death program, which is morphologically, biochemically, and molecularly distinct from necrosis. Apoptosis is a kinetic event and the entire duration of it, from onset to total disintegration of the cell, is relatively short. The various inducers of apoptosis start the process by activation of intracellular cysteine-aspartic acid proteases (i.e., caspases). These enzymes participate in a series of reactions that are triggered in response to pro-apoptotic signals and result in the cleavage of protein substrates, causing the disassembly of

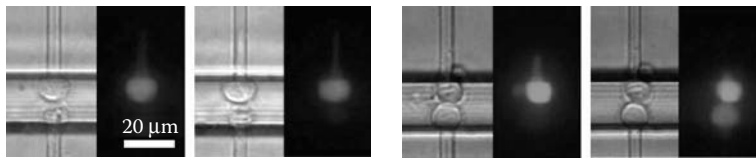

FIGURE 15.10
Diffusion of intracellular dye between fibroblasts in membrane contact. The north cell in both cell pairs was initially labeled with calcein AM, while the south cell was not. When the two trapped cells were not in membrane contact (left), no dye transfer occurred. When membrane contact was present (right), fluorescent dye was able to transfer to the adjacent cell within 16 h. Phase contrast and fluorescence images are depicted for the same field of view. Reprinted with permission from Lee, P.J., Hung, P.J., Shaw, R., Jan, L., and Lee, L.P. (2005). *Applied Physics Letters* 86(22): 223902/223901–223902/223903. © 2005, American Institute of Physics.)

the cell. The process of their activation is considered to be the key event of apoptosis and is studied as a target for drug discovery. Suppression or enhancement of apoptosis is known to cause or contribute to many diseases, such as cancer, neurodegenerative diseases, and AIDS (Valero et al. 2005).

Valero et al. 2005 fabricated a microfluidic cell trap device for analysis of apoptosis. The microfluidic silicon-glass chip enabled the immobilization of cells and real-time monitoring of the apoptotic process. The device consisted of two channels joined together in a crossway (Figure 15.11a). The cell-trapping microstructures were located in the vicinity of this crossway acting as a filter; buffer flew through the trap while the cells were captured. The cell-trapping structures varied in terms of shape, size, and the number of trapping sites. Figures 15.11b and c show photographs of two different trapping layouts. The layout shown in Figure 15.11b contains traps that differ in size. The diameters of the capturing sites varied between 8 µm and 12 µm and openings between traps were of 3 µm. The second layout in Figure 15.11c shows a mechanical trap with identical trap diameters (10 µm) and no exit channels between them. Figure 15.11d shows a SEM of the trapping sites designed in the first layout.

Cells were interrogated with different apoptosis-inducing factors, either electric or chemical, followed by the exposure of treated cells to the appropriate fluorescent dyes, FLICA™ and propidium iodide (PI). This allowed discrimination between viable, apoptotic, and necrotic cells. For example, FLICA is a reagent that measures apoptosis via detection of caspase activity. It is a cell-permeable, noncytotoxic peptide reagent, called flourochrome inhibitor of caspase, that binds active caspases within cells. When added to a population of cells, the probe enters the cell and covalently binds to a reactive cysteine residue on the subunit of the target active caspase, thereby inhibiting further enzymatic activity. Unbound reagent diffuses out of the cell. The remaining fluorescent signal is a direct measure of the number of active caspase enzymes present in the cell at the time the reagent is added.

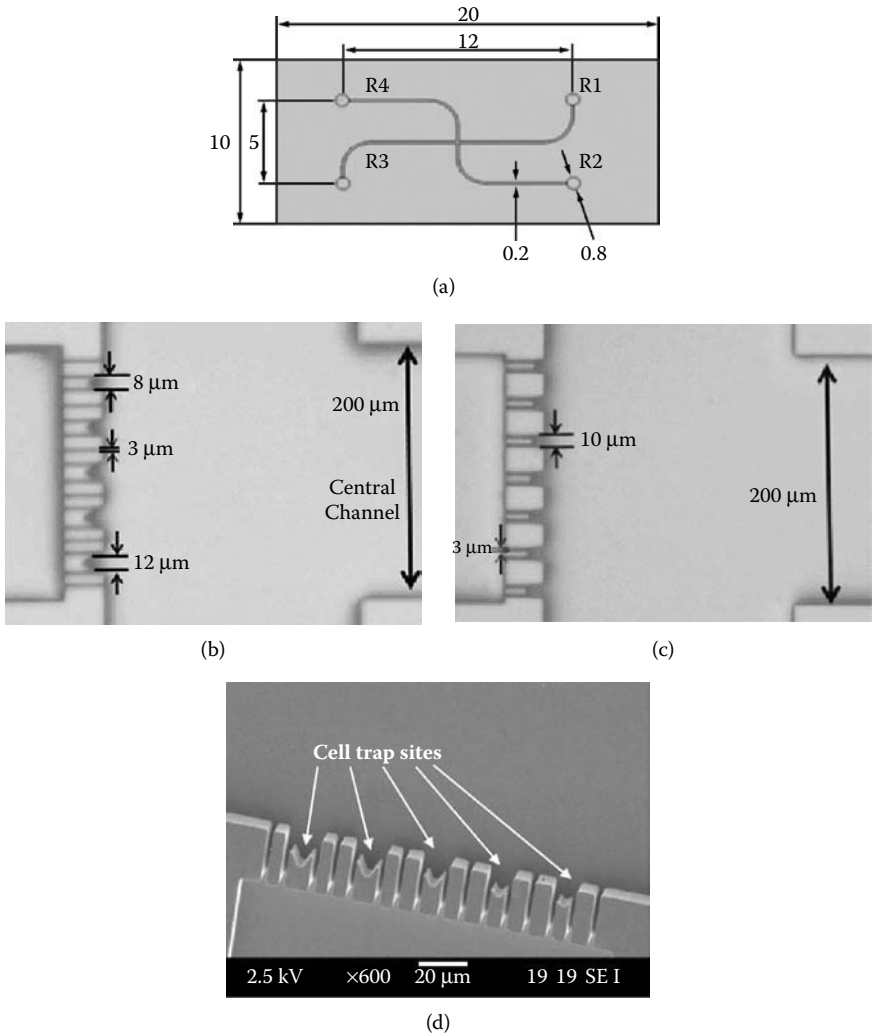

FIGURE 15.11
(a) Drawing of the microfluidic chip with dimensions in mm. Photographs of the trapping sites, (b) layout 1 and (c) layout 2, in the microfluidic chip design. (d) SEM picture of the trapping sites (close-up) for layout 1. (Reprinted with permission from Valero, A., Merino, F., Wolbers, F., Luttge, R., Vermes, I., Andersson, H., and van den Berg, A. (2005). *Lab on a Chip* 5(1): 49–55. © 2005, The Royal Society of Chemistry.)

Propidium iodide (PI) binds to DNA by intercalating between the bases with little or no sequence preference and with a stoichiometry of one dye per 4.5 base pairs of DNA. PI is a membrane-impermeable dye and generally is excluded from viable cells. PI is commonly used for identifying dead cells with open membranes. HL60 cells incubated with different factors transitioned from viable to early apoptotic and eventually to late apoptotic during the course of the cell death cascade (Figure 15.12).

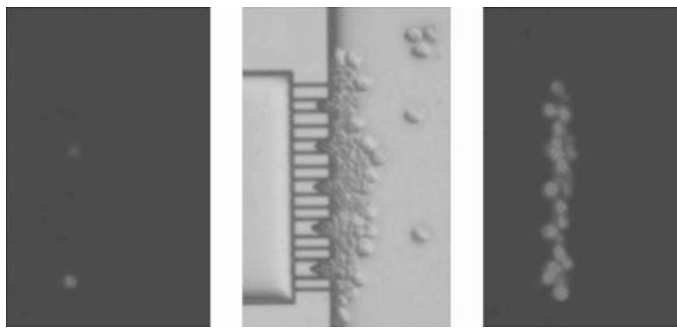

FIGURE 15.12
PI uptake in HL60 cells sitting at the trap due to the high electric field line density. (a) Fluorescence image at the time the HL60 cells arrive at the trap. (b) Light microscopy image of the cells 10 s after EOF control was stopped. (c) Fluorescence image from image (b). Reprinted with permission from Valero, A., Merino, F., Wolbers, F., Luttge, R., Vermes, I., Andersson, H., and van den Berg, A. (2005). *Lab on a Chip* 5(1): 49–55. © 2005, The Royal Society of Chemistry.)

15.2.4 Molecular Analysis of Cells

Conventional benchtop approaches for the molecular analysis of cells typically starts with thousands to millions of cells from which sufficient molecular material is harvested (i.e., DNA, proteins) to enable a successful analysis. However, individual cells isolated from a specific location and contained within a large population pool may possess unique genomes due to their response to external stimuli resulting in unique expression profiles produced by the individual cell imposing upon it a distinct phenotype. Thus, the isolation of genetic material from single cells is of great interest. The ability to analyze cells (mutational content, identification, etc.) via signature sequences elucidated from their genomic DNA (gDNA) or mRNA requires the ability to effectively recover or purify the DNA and RNA from the whole cell lysate. Following cell lysis, it is often necessary to remove cellular debris, proteins and other intracellular components that may potentially interfere with subsequent bioenzymatic reactions. Hong et al. (2004) recently described a pneumatic microsystem for DNA and RNA isolation from a single mammalian cell. All processes (i.e., cell isolation, cell lysis, DNA or mRNA purification, and recovery) were performed on a single microfluidic chip in nanoliter volumes.

The process for mRNA purification consisted of stacking an affinity column with oligo-dT polymer magnetic beads, isolating the cells of interest, measuring and mixing reagents, lysing cells, flushing lysate over the affinity column, and recovering mRNA from the column (Figure 15.13). Batch processing took place in a linear fashion; valves and cross-junctions were used to load different segments of a channel with reagents. Opening the valve between the lysis buffer and the cell chamber allowed diffusive mixing and

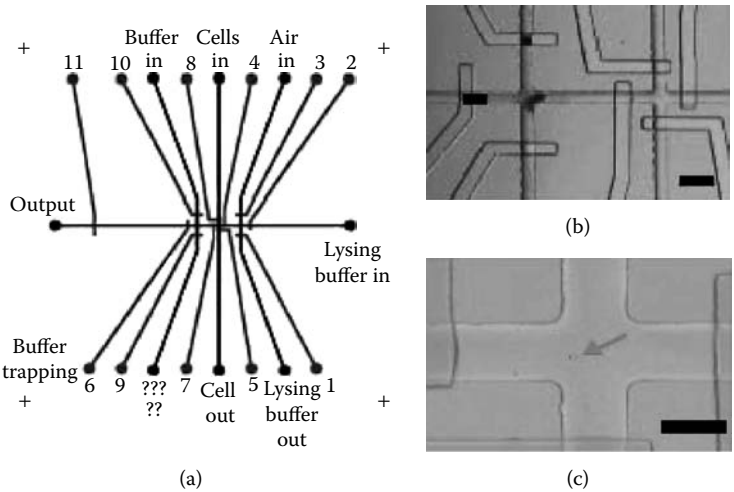

FIGURE 15.13
mRNA purification chip. (a) Layout of the microfluidic chip. The blue lines represent the 100 μm–wide fluidic channels, the red lines are the 100 μm–wide valve actuation channels. The fluidic ports are named; the actuation ports are numbered 1 to 11. The lysing buffer chamber is composed of the channel space delineated by valves 1, 2, 3 and 4. The *cell chamber* is composed of the channel space delineated by valves 4, 5, 6 and 7 (see also b and c). The *bead chamber* is composed of the channel space delineated by valves 7, 8, 9 and 10 (see also b). (b) Photograph of the *in situ* affinity column construction. A column of 2.8 μm–diameter paramagnetic beads covered with oligo dT is being built against a partially closed microfluidic valve (valve 8). Scale bar, 200 μm. (c) One cell is loaded in the cell chamber before the lysis step. (The channels are 100 μm wide). Scale bar, 100 μm. (Reprinted with permission from Hong, J.W., Studer, V., Hang, G., Anderson, W.F., and Quake, S.R. (2004). *Nature Biotechnology* 22(4): 435–439. © 2004, Nature Publishing Group.)

cell lysis. Reverse transcription and amplification (RT-PCR) were carried out directly on the beads. Gel electrophoresis of the RT-PCR products revealed that for high abundant actin mRNA, detection was down to the single-cell level, while for the moderately abundant type of mRNA (only zinc finger [OZF]) detection was at the level of 2 to 10 cells.

One of the strong attributes of microfluidic devices is the ability to integrate standard operations onto a single device. An example of such integration can be found in work by Wu et al. (2004). A microfluidic chip for analyzing the chemical contents of a single cell was designed to accomplish four different functions: (i) cell handling, (ii) metering and delivering of chemical reagents, (iii) cell lysis with derivatization, and (iv) separation of labeled compounds and detection by laser-induced fluorescence (LIF). All of these functions were accomplished using a device equipped with two three-state valves and a picopipette. The valves prevented diffusion or pumping of reagents from the chamber, which allowed sufficient time for the derivatization reaction to reach completion.

Three-way valves were constructed by multilayer soft lithography. Their performance depended upon the elastomeric property of poly(dimethylsiloxane)

(PDMS). The upper layer contained a closed chamber that was connected to an external pressure controller; the lower layer contained the microfluidic network. Between the layers was a thin elastomeric membrane that deformed under pressure to close the fluidic channel. The three stages of valve operation were: (1) when no pressure is applied, the PDMS membrane does not deform and the fluidic channel is open; (2) when slight pressure is applied,

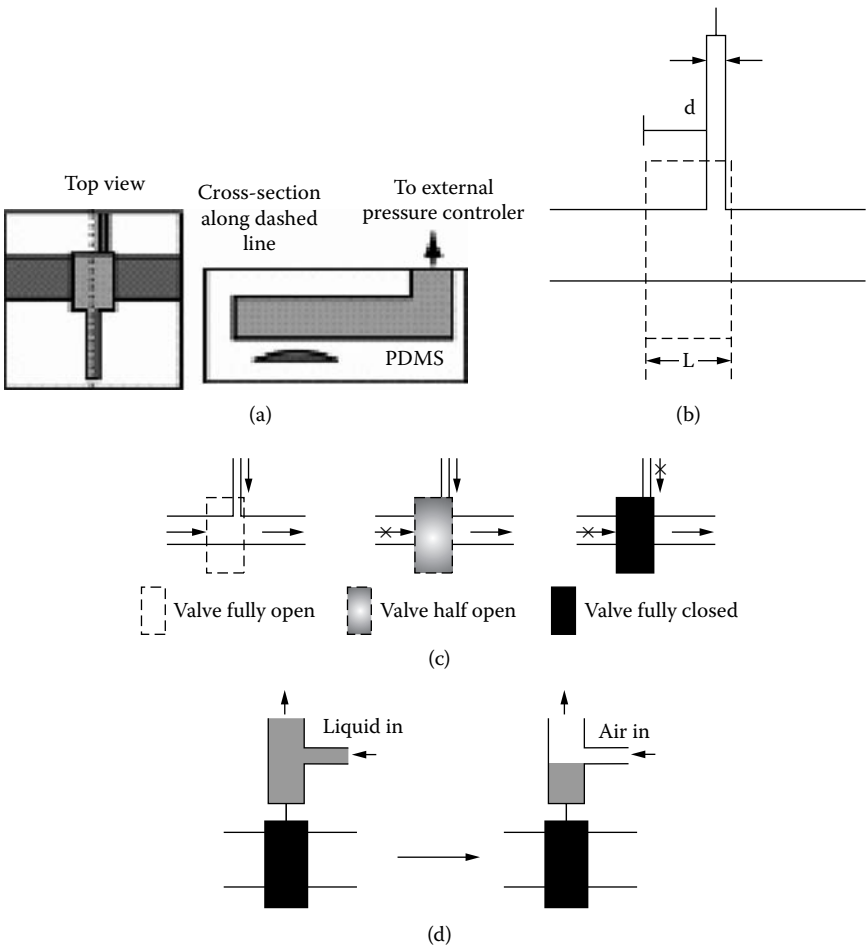

FIGURE 15.14
Three-state valve and picopipette. (a) Schematic illustration of three-state valve (top view and cross-section). Channels on the upper layer (light shade) are filled with water and connected to an external pressure controller; channels of the lower layer (dark shade) are the microfluidic channels with smoothly curved surfaces. The pressure from the upper channel deforms the membrane between the layers and controls the opening and closing of the lower channel. (b) A simplified diagram of a three-state valve. (c) Schematic of the three states of this valve. (d) Scheme of the function of a picopipette. (Reprinted with permission from Wu, H., Wheeler, A., and Zare Richard, N. (2004). *Proceedings of the National Academy of Sciences of the United States of America* 101(35): 12809–12813. © 2004, Proceedings of the National Academy of Sciences of the USA.)

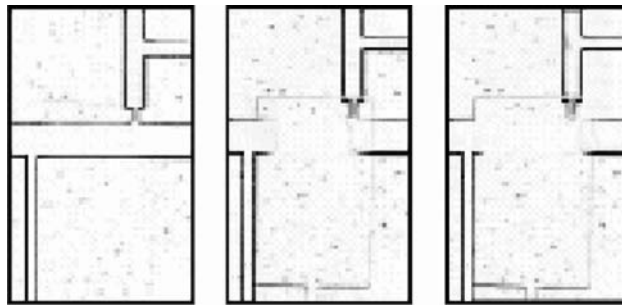

(e)

FIGURE 15.14 (continued)
Three-state valve and picopipette. (e) Pictures of a three-state valve that is connected to a picopipette. (Reprinted with permission from Wu, H., Wheeler, A., and Zare Richard, N. (2004). *Proceedings of the National Academy of Sciences of the United States of America* 101(35): 12809–12813. © 2004, Proceedings of the National Academy of Sciences of the USA.)

the membrane starts to deform and the left horizontal channel is blocked, but the side channel remains open to the right horizontal channel; and (3) when more pressure is applied, the side channel is also blocked and no flow takes place through the valve (Figure 15.14a). The operation of the picopipette is achieved by injection of the liquid from an inlet channel by pressure, with the three-state valve closed (Figure 15.14d). Because PDMS is permeable to air, liquid is pushed toward the closed valve; as air is displaced through the PDMS, the chamber between the inlet and the valve is filled with fluid. Injecting air from the inlet forces most of the liquid from the channel and traps a small volume of liquid that can be loaded through the three-state valve into a reaction chamber. The volume of the remaining liquid is accurately defined by the channel dimensions and the distance from the inlet to the valve. This method can accurately deliver picoliter amounts of liquid. Although fast evaporation of water makes it difficult to meter lower volumes accurately with an air–water interface, it might be possible to meter aqueous solutions with subpicoliter volume by using oil as the second fluid to prevent evaporation.

A reaction volume of approximately 70 pL was used for the lysis and derivatization of the contents of a single Jurkat cell, which limited the dilution of the contents of the single cell. The total analysis time of one cell (cell injection, fluorescence derivatization, and separation) was 1 h. An electropherogram of amino acids from single cells was recorded and compared with those collected from a multiple-cell homogenate. Differences in the separation traces between the single-cell and multicell samples were assumed to be from insoluble single-cell debris, as this sample was not filtered, whereas it was filtered in the case of the large cell population.

(Wheeler et al. 2003) developed a microfluidic device constructed from PDMS for the analysis of single cells designed for two functions: (1) rapid isolation of an individual cell from a mixture of cells in bulk solution, and (2) precise delivery of minute volumes of reagents to the selected cell.

Isolating individual cells from bulk solution was achieved by utilizing fluid dynamics in microfluidics. The behavior of fluids at the microscale differs from the macroscale. In microfluidics, the surface tension, energy dissipation, and fluidic resistance start to dominate and the fluid flow thus exhibits a number of characteristic features, the most important of which is laminar flow. Fluids flowing in channels with dimensions on the order of micrometers and at flow speeds of 1 mm/s are characterized by low Reynolds numbers (R_e). The R_e is usually much less than 100, and oftentimes less than 1.0 in microscale channels. In this Reynolds number regime, flow is completely laminar and no turbulence occurs.

To increase the efficiency of capture in flows that are dominated by laminar flow, cells were hydrodynamically focused between two buffer streams. Additional side inlet channels delivered reagents directly to a docked cell for cell viability assays and measurements of calcium fluxes at the level of single cells. The reagent delivery system utilized PDMS pumps and valves that were actuated with a manifold of three-way pneumatic switch valves. The manifold was controlled by compressed nitrogen or helium applied to the device (approximately 20 psi). Two channels were positioned to the left of the cell dock (Figure 15.15c). The channel close to the dock delivered a shield buffer; the channel farther from the dock delivered reagents. By actuating pumps and valves such that the contents of both channels were flowing by the dock, reagents were loaded within a few micrometers from the cell (Figure 15.15c, main). If the shield buffer valve was closed, the reagent could perfuse over the cell (Figure 15.15c, inset). The microfluidic network enabled the passive separation of a single cell from a bulk cell suspension, and integrated valves and pumps allowed the delivery of nL (10^{-9} L) volumes of reagents to the cell. Various applications of this system were demonstrated, including cell viability assays and measurements of intracellular Ca^{+2} flux.

Microfluidic devices play a key role in handling small quantities of material, delivering those materials to different locations within the device, and controlling the movement of cells within the channels. Microfluidic devices have found numerous applications in biology, biochemistry, and medicine because of their ability to efficiently control and replicate microenvironments. They also offer practical benefits, such as limiting human exposure to large amounts of hazardous samples (Shelby et al. 2003). The ability to fabricate micrometer-sized features in glass, silicon, and polymers makes these materials attractive options for making capillary-sized structures. Many of these devices are integrated into far-reaching formats with the ability to control physical parameters such as flow rate, temperature, and pressure. Microsystems can closely mimic *in vivo* environments, and can be helpful in characterizing biological cell surface area, volume, deformability, and so forth.

For instance, Shelby et al. (2003) developed a microfluidic for observations and characterization of *Plasmodium falciparum*–infected erythrocytes (i.e., red blood cells [RBCs]). Normal erythrocytes are highly deformable cells, and they owe their high degree of flexibility to low internal viscosity, high sur-

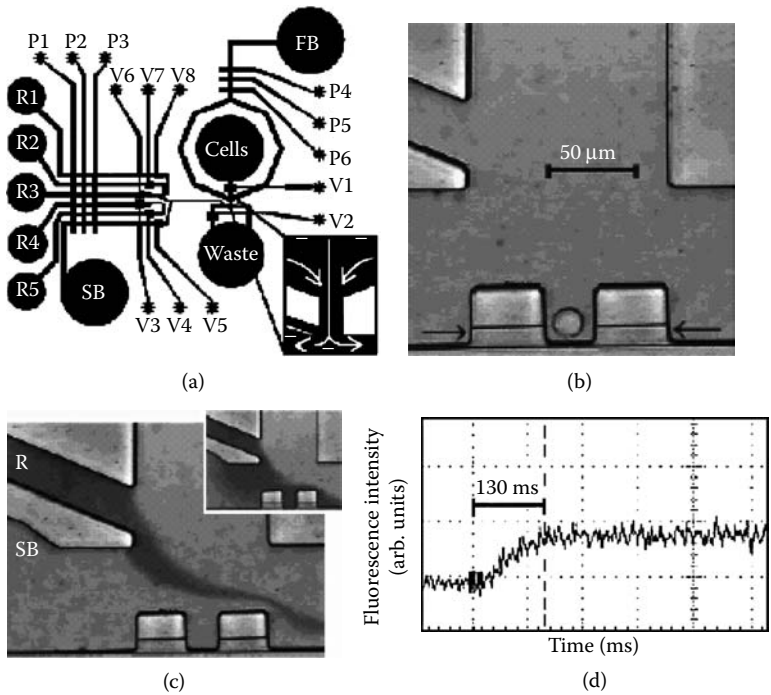

FIGURE 15.15
Single-cell analysis device. (a) Schematic of device: fluidic channels are dark; control channels are light. R1 through R5 are reactant inlets, SB and FB are shield and focusing buffer inlets, respectively. Valves are actuated by applying pressure to control inlets V1 through V8. Pumps are activated by actuating P1 through P3 or P4 through P6 in series. The serpentine regions of reagent and shield buffer channels diminish flow pulsing resulting from pump activation. Inset: close-up of cell trapping region. Cells are pushed by hydrostatic pressure from cell inlet to waste; they are focused to the center of the stream by the focusing buffer. Note the point of stagnation formed at *. (b) CCD image of an individual Jurkat T-cell trapped in cell dock. Note the drain channels (arrows) on the dock. (c) Images of "load" (main) and "perfuse" (inset) states. In the load state, reagents (R) and shield buffer (SB) are both pumped over the dock. In the perfuse state, the shield buffer valve is closed, and the reagents flow onto the dock. (d) Oscilloscope screen capture of dye-marked solution change during a switch from load to perfuse. A complete solution change is achieved in approximately 100 ms. (Reprinted with permission from Wheeler, A.R., Throndset, W.R., Whelan, R.J., Leach, A.M., Zare, R.N., Liao, Y.H., Farrell, K., Manger, I.D., and Daridon, A. (2003). *Analytical Chemistry* 75(14): 3581–3586. © 2003, American Chemical Society.)

face-area-to-volume ratio, and the highly elastic nature of the membrane and cytoskeleton (Shelby et al. 2003). When invaded by *Plasmodium falciparum*, RBCs become rigid, which causes occlusions of capillaries and symptoms of malaria. *Plasmodium falciparum*, a parasitic protozoan, has been implicated in causing the most lethal form of human malaria. After the parasites enter the body by a mosquito bite, they disappear from circulating blood within an hour and gather in the liver. After several days, infected RBCs emerge from the liver and infect other RBCs. Severe malaria is potentially fatal, and

frequently unresponsive to even the most aggressive treatments. There are two distinct stages of *P. falciparum* erythrocytic stage asexual development—trophozoite and schizont.

Shelby et al. (2003) developed a microfluidic device for observation and *in vitro* modeling of cell deformability. The authors demonstrated the unique abilities of elastomeric PDMS microchannels to characterize complex behaviors of the cells of interest (Figure 15.16). Microchannels were fabricated to mimic capillaries between 2 and 8 μm in diameter. The average flow velocity in the channel constriction modeled the flow rates in capillaries (100 to 500 μm/s). Channels ranging in width between 2 and 8 μm were readily traversed by the 8 μm–wide, highly elastic, uninfected RBCs, as well as by infected cells. Trophozoite stages failed to freely traverse 2 to 4 μm channels. However, some emerged with morphological deformations. Heavily infected RBCs failed to traverse 6 μm channels and rapidly formed a capillary blockage. Uninfected RBCs, though, readily squeezed through the blockages of a 6 μm capillary. The individual erythrocytes in the trophozoite stage of infection (Figure 15.16b) and in the late schizont stages of infection after being hydrodynamically forced through a 4 μm channel are shown in Figure 15.16c. It was observed that the trophozoites recovered their spherical appearance within approximately 30 s, however, the schizonts did not fully recover their

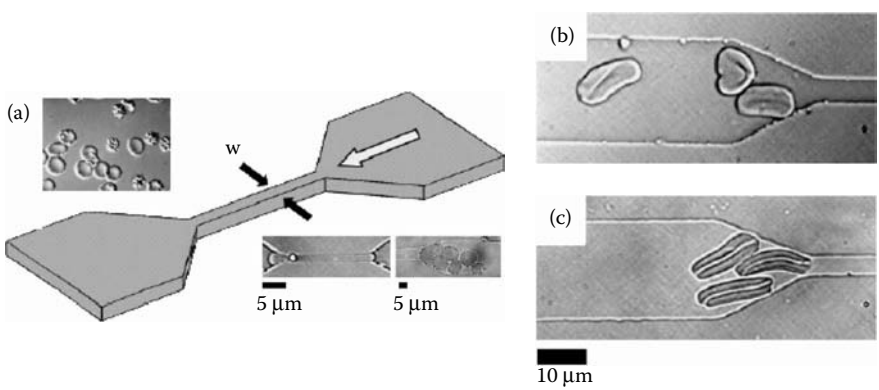

FIGURE 15.16
(a) Schematic illustrating the geometry of the microchannel. The constricted segment of the channel (width denoted by *w*) was sized at 8, 6, 4, and 2 μm. The white arrow represents the direction of fluid flow. (Upper inset) A differential interference contrast image of normal (smooth) and infected RBCs. (Lower left inset) A normal RBC passing through a 2 μm constriction. (Lower right inset) Infected RBCs blocking a 6 μm constriction. (b–c) Differences in recovery of compressed infected cells; (b) Early trophozoite stages of infected RBCs were partially distorted after passage through a 4 μm constriction and remained compressed for 30 sec after emerging from the channels. (c) Schizont forms of RBC infections were more severely deformed and did not relax back to their original shape after passage through a 4 μm constriction even 1 to 2 min after compression. (Reprinted with permission from Shelby, J.P., White, J., Ganesan, K., Rathod, P.K., and Chiu, D.T. (2003). *Proceedings of the National Academy of Sciences of the United States of America* 100(25): 14618–14622. © 2003, The National Academy of Sciences of the USA.)

spherical shape even after 1 to 2 min. It was concluded that both the RBC's membrane rigidity and internal viscosity increase as the parasite matures; therefore, erythrocytes in the later stages of infection have longer recovery times than cells in the early stages of infection. Such devices can thus be used to screen antimalarial drugs or agents that can reverse the biomechanical effects of malaria parasites on RBCs.

15.2.5 Organelle Manipulation in Microfluidics

A typical single organelle may range in size from tens of nanometers to a couple of micrometers with a corresponding volume of approximately 6×10^{-20} L for a 50 nm synaptic vesicle to approximately 8×10^{-15} L for a 2 μm mitochondrion (Chiu 2003). Within a volume of 6×10^{-20} L, even at a relatively high concentration of 100 mM, the number of molecules present is only approximately 3600. At this small scale, most proteins would be present as a single copy or only as a few copies. Therefore, the analysis of subcellular compartments necessitates an approach that is both highly sensitive and capable of isolating each organelle and then analyzing the various components of the organelle for characterization and quantitation (Lu et al. 2004a).

Lu et al. (2004a) reported a microfabricated field flow fractionation device for continuous separation of subcellular organelles by isoelectric focusing. The microdevice provided fast separation while avoiding large voltages and heating effects. The authors presented the separation of mitochondria from whole cells and nuclei (Figure 15.17) as well as the separation of two mitochondrial subpopulations. When automated and operated in parallel, these microdevices could facilitate high-throughput analysis in studies requiring separation of specific organelles.

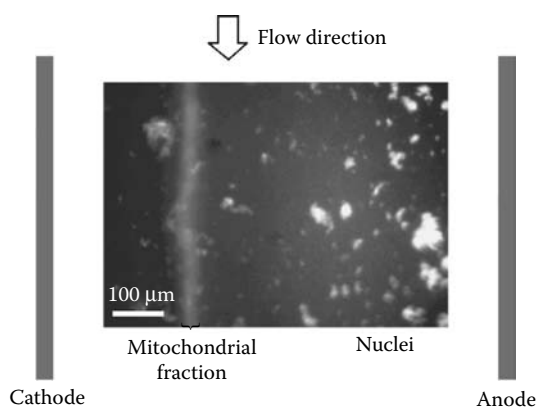

FIGURE 15.17
IEF of mitochondria from lysate of NR6WT cells stained with MitoTracker Green and propidium iodide. The mitochondria focus into a distinct narrow band while the nuclei migrate to a broad band. A pH 3 to 6 buffer was used; the mitochondria focused at pI between 4 and 5. (Reprinted with permission from Lu et al. (2004a). © 2004, American Chemical Society.)

Strömberg et al. (2001) described an electrofusion-based technique for combinatorial synthesis of individual liposomes. A device with containers for liposome fusion was constructed. Optical trapping (Chiu et al. 1996) was used to transport individual liposomes and cells through the microchannels into the fusion container, where pairs of liposomes were fused together. Optical trapping is a technique that utilizes laser light to trap and manipulate small (nm scale) spherical objects using the radiation pressure produced from a focused laser beam.

Sequential fusion of liposomes with different dyes incorporated into their membranes is shown in Figures 15.18a through h. The first fusion (Figures 15.18a through d) involves a liposome with no membrane dye incorporated and a green fluorescent liposome in the membrane. The product liposome, shown in Figure 15.18d, was then fused with a red fluorescent liposome

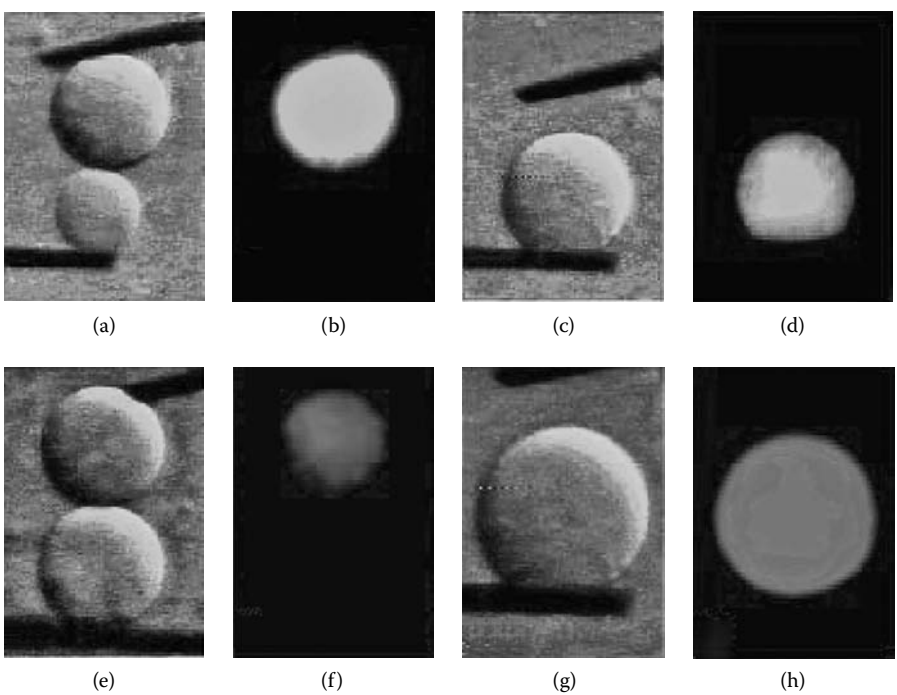

FIGURE 15.18
Sequential pairwise fusion of three different liposomes. The first fusion involves a *plain* liposome (no membrane dye in the membrane) and a liposome with the membrane fluorescent dye DiO (a–c). The membrane dye distributes evenly over the entire membrane surface in the product liposome (d). In the next fusion the created *hybrid* liposome with DiO was fused with a liposome with the membrane fluorescent dye DiI (e–g). DiI was distributed over the entire membrane surface of the product hybrid liposome (h). Black-and-white fluorescence images were pseudo-color-coded and enhanced digitally. The scale bar is 10 μm. (Reprinted with permission from Stromberg, A., Karlsson, A., Ryttsen, F., Davidson, M., Chiu, D.T., and Orwar, O. (2001). *Analytical Chemistry* 73(1): 126–130. © 2001, American Chemical Society.)

within the membrane (Figures 15.18e through h). The fluorescent membrane dyes were evenly distributed after each fusion. This procedure allowed for a large number of synthesized liposomes with complex components and reaction systems to be obtained from small sets of precursor liposomes. The use of optical trapping for the handling of cells required that trapping leave the cells undamaged, which could be achieved using near-IR lasers. They demonstrate excellent spatial resolution (10 nm to 100 μm) and confer a large degree of dexterity and accuracy in the manipulation of micron-scale objects. For biological applications, the fact that the lasers are noninvasive, sterile, and operate in the near-IR (λ = 700 to 1064 nm) means that there are little to no biological effects on cells. In the future the cell selection and fusion concept should be advantageously used for the production of hybridomas, cloning, and cell–liposome fusions.

Sinclair et al. (2002) presented a cell-based bar code reader for screening of ion channel–ligand interactions. The microfluidic platform performed a high-throughput screening and characterization of weak-affinity ion channel–ligand interactions. The device integrated a microfluidic chip with multiple channels entering an open volume with standard patch clamp equipment (Figure 15.19). The microfluidic chip was placed on a motorized scanning stage (ms scan rate capabilities). A patch-clamped cell was rapidly scanned across zones of different solutions. This method had the capacity to obtain kinetically resolved patch clamp measurements and dose-response curves of up to 1000 ligands in a single day.

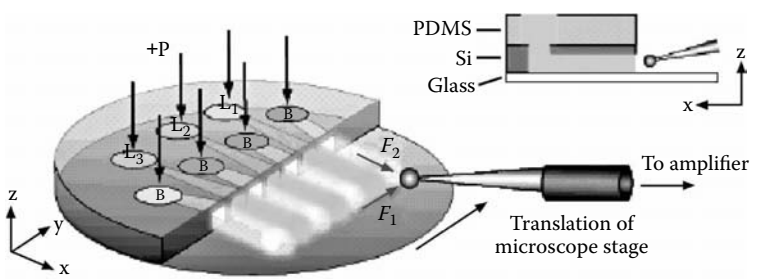

FIGURE 15.19
Schematic showing the design of a microfluidic device for generating chemical bar codes in open volumes. The microfluidic chip is mounted on a programmable scanning stage (not shown) that can move the channel outlets relative to a patch-clamped cell. The patch clamp electrode is positioned using micromanipulators. B represents buffer reservoirs and channels, and L1-3 represents the different ligand reservoirs and channels. F1 is the drag force acting on the cell due to scanning, and F2 is the force created by fluid flow from the microchannel outlets. The inset shows a cross-section of the device with the channel structure in Si bonded to glass and PDMS. PDMS was used to increase the height of the reservoirs and sensor chamber. Each channel is 50 μm wide and 100 μm high, and the flow rate was 3 mm/s. The stream remains collimated in the open volume. B and L depict channels filled with buffer solution and dye, respectively. (Reprinted with permission from Sinclair, J., Pihl, J., Olofsson, J., Karlsson, M., Jardemark, K., Chiu, D.T., and Orwar, O. (2002). *Analytical Chemistry* 74(24): 6133–6138. © 2002, American Chemical Society.)

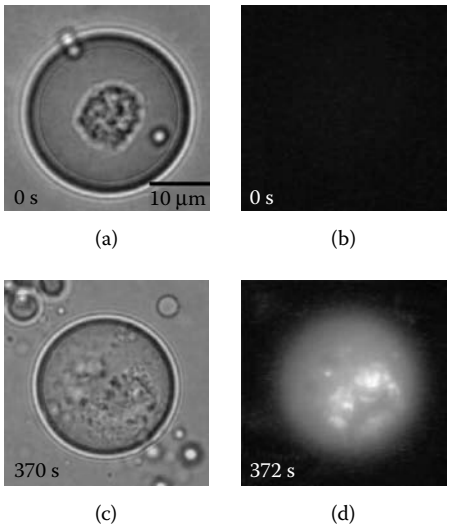

FIGURE 15.20
Single-cell enzymatic assay within an aqueous droplet in soybean oil. (a) A mast cell was encapsulated in an aqueous droplet that contained the fluorogenic substrate FDG. (b) Prior to photolysis of the cell, there was little fluorescent product within the droplet because the intracellular enzyme β-galactosidase was physically separated from FDG by the cell membrane. (c, d) After laser induced cell lysis (c), β-galactosidase catalyzed the formation of the product fluorescein, which caused the droplet to become highly fluorescent (d). (Reprinted with permission from He, M., Edgar, J.S., Jeffries, G.D.M., Lorenz, R.M., Shelby, J.P., and Chiu, D.T. (2005). Selective encapsulation of single cells and subcellular organelles into picoliter- and femtoliter-volume droplets. *Analytical Chemistry* 77(6): 1539–1544. © 2005, American Chemical Society.)

A method, which combined the optical trapping and microfluidic-based droplet generation, was developed by He et al. (2005). This work described a method for selective and controlled encapsulation of a single cell or subcellular structure into a picoliter or femtoliter volume of an aqueous droplet surrounded by an immiscible phase. Once the selected moiety was encased within the droplet, rapid laser photolysis within the droplet was demonstrated (Figure 15.20). The process confined the cell lysate within the pL volume of the droplet. With further development, the droplet manipulations could be combined with droplet fusion for initiating chemical reactions, such as derivatization reactions. The biggest advantage of such an approach is that the cell lysate and cell biocomponents are confined within a small volume, minimizing the dilution and diffusion of the analytes of interest.

15.3 Single-Molecule Detection in Microfluidic Devices

Initial studies on SMD (single-molecule detection) in microfluidic devices have indicated how powerful this marriage can become (Dorre et al. 1997;

Effenhauser et al. 1997; Fister et al. 1998; Mathis et al. 1997). Higher sensitivities, minimized sample consumption, increased throughput and speed, and full automation of the assays were pointed out as the most appealing benefits. To this point, genomic-based studies are probably the area that has gained the most from the powerful combination of SMD and microfluidics. Many new tools for DNA sequencing, mapping and sizing have been developed over the last 10 years with some already commercialized or being introduced to the market as we speak. SMD and microfluidics have also proven invaluable in studies of protein folding kinetics (Lipman et al. 2003) and mechanistic studies of DNA–enzyme interactions (Lee et al. 2006; van Oijen et al. 2003). Furthermore, advancements in microfabrication technologies allow the fabrication of submicrometer-sized or even nanometer-sized channels as well as new, on-chip optical detection schemes (e.g., zero-mode waveguides or near field scanner) (Levene et al. 2003; Tegenfeldt et al. 2001), which significantly extend the range of capabilities of this powerful technique. In the following sections, a description and discussion of some of the applications of SMD in microfluidics will be presented. Anyone interested in this topic should also consult the following reviews: de Mello (2003), Dittrich and Manz (2005), and Tegenfeldt et al. (2004).

15.3.1 DNA Fragment Sizing

Separation of DNA molecules distinguished by their size (in base pairs [bp]) is a fundamental requirement in most molecular biology assays. For example, the isolation of certain fractions of DNA samples based on size may be required for further experiments, such as the preparation of bacterial artificial chromosome (BAC) or plant artificial chromosome (PAC) libraries. DNA sizing is also an important tool in a wide range of diagnostic applications, such as restriction fragment length polymorphism (RFLP). Conventional DNA sizing techniques typically rely on gel electrophoretic sorting, which are time-consuming processes, require the use of relatively large amounts of sample, and have limited sensitivity and resolution. To alleviate some of these limitations, various microfluidic approaches with SMD have been proposed. Two general approaches can be distinguished. The first one, practical for sizing shorter DNA fragments, uses on-chip microcapillary gel electrophoresis with highly sensitive single-molecule fluorescence burst counting for detection. In the second approach, the electrophoretic step is completely eliminated from the assay as single DNA molecules are directly detected and sized using specially designed microfluidic or nanofluidic chips. This second approach is especially useful for sizing very long (e.g., genome-sized) DNA fragments. The size of the DNA is transduced by quantitatively measuring the fluorescence signal generated from a single DNA molecule traveling through a focused laser beam. The DNA is made fluorescent by adding to it an intercalating dye, which acts like a molecular light switch, in which the fluorescence is "turned on" when the dye is incorporated into the double-stranded

DNA molecule and is "turned off" when the dye is in the surrounding fluid. Because the loading of these dyes to double-stranded DNA is quantitative, the intensity of the fluorescence signal is proportional to the size of the DNA molecule. On-chip capillary gel electrophoresis combined with a single-molecule fluorescence burst counting for the separation and detection of fluorescently labeled DNA fragments was introduced by Haab and Mathies (1999). On-chip microcapillary gel electrophoresis for DNA separations offers several advantages over conventional gel and capillary gel electrophoreses. These include shorter separation times, improved control of the sample injection plug, reduction in sample and buffer consumption, and increased throughput via high-density parallelism (e.g., 384 analyses running at the same time) (Aborn et al. 2005; Tian et al. 2005). On the other hand, using SMD significantly improves the sensitivity of the assay. For example, 100 to 1000 bp DNA sizing ladder can be separated in approximately 300 s with a mass detection limit of approximately 1000 molecules using a microchip with an effective separation length of 4 cm (Haab et al. 1999). The unique feature

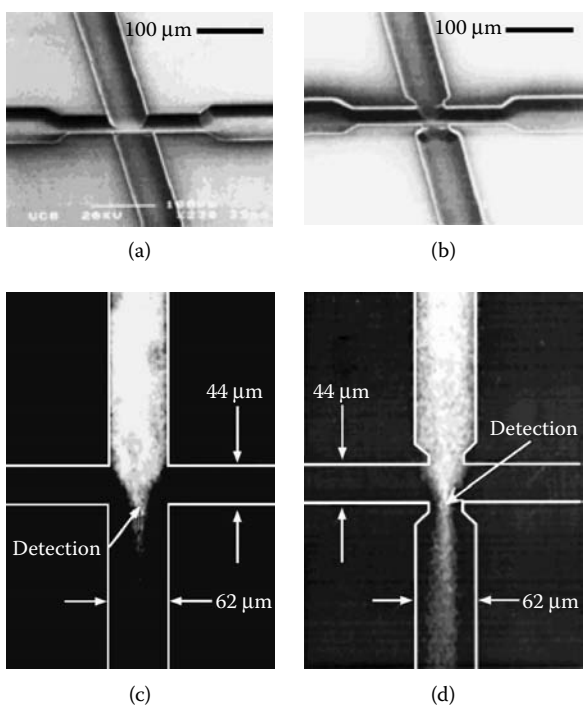

FIGURE 15.21
Scanning electron micrographs of the straight (a) and pinched (b) detectors. Fluorescence images of continuously injected fluorescein electrophoresing through the straight (c) and pinched (d) detectors. The electrophoresis medium was 3% LPA and 1× TAE. The separation channel current was 3.2 μA, and each cross-channel carried a focusing current of 1.6 μA (current ratio 0.5). (Reprinted with permission from Haab, B.B. and Mathies, R.A. (1999). *Analytical Chemistry* 71(22): 5137–5145. © 1999, American Chemical Society.)

of Haab's design was the capability of focusing the DNA sample through a confocal detection volume in order to increase the percentage of DNA molecules that could be detected without increasing the background. Focusing of the sample was achieved by physical narrowing (or tapering) of the channel dimensions and electrodynamic focusing (a sheath flow delivered from cross channels) (Figure 15.21). The detection efficiency of this assay was shown to be 3 times higher than that of normal chip-based separations.

A second SMD approach toward DNA sizing is based on direct measurement of fluorescent signals of DNA molecules labeled with intercalating dyes. Because the amount of the intercalating dye bound to the DNA molecule is proportional to the size of the molecule, the length of the DNA molecule can be found simply by quantifying the total fluorescent signal detected from the molecule. The first application of this concept in a microfluidic format was demonstrated by Quake and coworkers (Chou et al. 1999). The authors successfully used confocal detection of DNA flowing through a simple T-channel fabricated in PDMS. Sizing of DNA molecules ranging in size from 2 to 200 kbp was achieved in less than 10 min using only 28 femtograms (approximately 3000 molecules) of DNA (Figure 15.22). There are two important features of this approach that clearly differentiate it from gel electrophoresis methods. First, the sizing time is independent of the length of the DNA molecules, whereas in gel electrophoresis it increases proportionally with the fragment length and can take days to size genomic DNA. Second, the resolution of the assay increases with increasing DNA length, as more fluorescent signal is generated by longer molecules. In the case of electrophoresis, longer DNAs typically result in reduced sizing resolution.

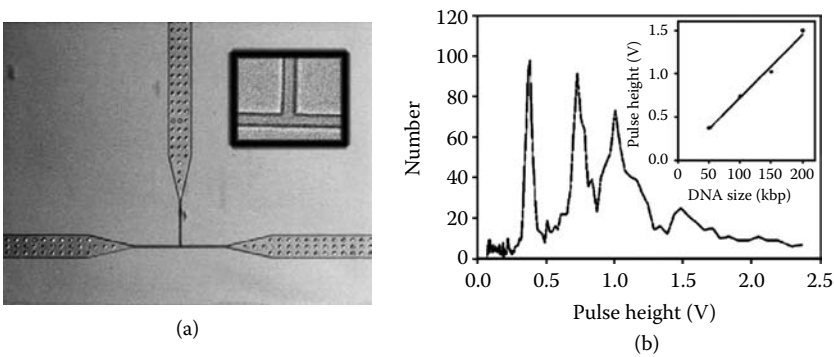

FIGURE 15.22
(a) Optical micrograph of T-channel device. The large channels have lateral dimensions of 100 μm, which narrow down to 5 μm at the T-junction. The depth of the channels is 3 μm. (b) Analysis of ladder. To test the upper length limit of the device, a ladder was analyzed. Peaks corresponding to 50, 100, 150, and 200 kbp can clearly be resolved. (Inset) The peak height measurement is linear even out to 200 kbp. (Reprinted with permission from Chou, H.-P., Spence, C., Scherer, A., and Quake, S. (1999). *Proceedings of the National Academy of Sciences of the United States of America* 96(1): 11–13. © 1999, The National Academy of Sciences of the USA.)

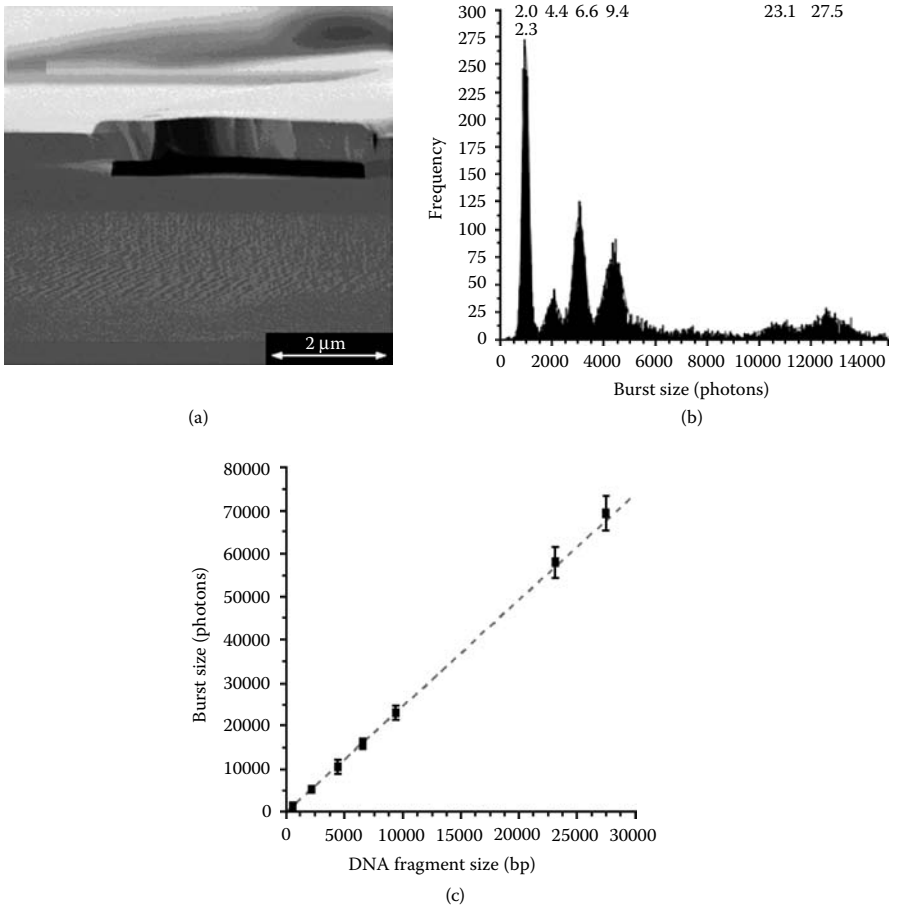

FIGURE 15.23
(a) SEM showing the cross-section of channel (10 µm width, 270 nm height). The width appears smaller in this image because the channel is viewed from a side angle. (b) Photon burst histogram obtained for a mixture of several DNA fragments. The red curves correspond to the fitting of a set of six Gaussian peaks by a least-squares method. The positions of the peaks depend on the size of DNA fragments; the peak area is proportional to the relative concentration of each fragment. (c) Plot of the burst size as a function of the (known) fragment size. Error bars correspond to the standard deviation of the peak sizes. The dashed line is a linear least-squares fit. The intercept was 256 photons, and the slope was 2.498 photons/bp. The correlation coefficient is 0.9998. (Reprinted with permission from Foquet, M., Korlach, J., Zipfel, W., Webb, W.W., and Craighead, H.G. (2002). *Analytical Chemistry* 74(6): 1415–1422. © 2002, American Chemical Society.)

Further improvements to direct single-molecule sizing of DNA samples was provided by the use of submicrometer-sized fluidic channels (Foquet et al. 2002) (Figure 15.23). By using ultrasmall channels, high signal-to-noise ratios (SNR) were achieved even for very fast flow speeds, up to 5 mm/s, thereby shortening the analysis time per molecule to less than a few milliseconds.

15.3.2 Sequencing of Single DNA Molecules

The Sanger reaction combined with electrophoretic separations has become a workhorse for most DNA sequencing projects. However, this technology has inherent limitations, especially in terms of cost, read length, and sensitivity. For example, it took over 9 months at a total cost of over $3 billion to sequence genomes from only five persons (http://www.ornl.gov/sci/techresources/Human_Genome/project/whydoe.shtml). These limitations make conventional Sanger sequencing rather impractical for massive comparative genomic studies. Deciphering the genomes of thousands of people will make it easier to track down genetic risk factors for many genetic disorders (e.g., diabetes or heart diseases) and eventually lead to a discovery of new medical treatments. Inexpensive DNA sequencing technologies could be used to monitor the environment for specific microorganisms, including biowarfare agents. Applications of single-molecule detection to DNA sequencing has monumental potential to alleviate the cost and speed issues associated with classical Sanger sequencing. Two examples of SMD in microfluidic formats for DNA sequencing are briefly described below.

Sequencing by controlled enzymatic digestion performed in microfluidic channels was proposed by Dorre and colleagues (1997). In this assay, DNA is first synthesized with each nucleotide labeled with a fluorescent dye. The DNA is fixed within a flow stream and an exonuclease enzyme is used to sequentially cleave the terminal nucleotide, which is then released into the flow and detected (Figure 15.24). As long as the nucleotides can be detected in the order that they were released, the sequence of the DNA of interest can

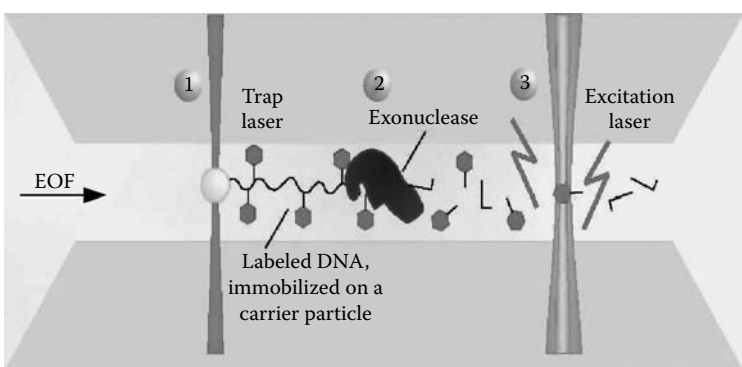

FIGURE 15.24
The principle of single-molecule sequencing. (1) A bead loaded with a labeled DNA molecule is held by a trap laser (D 1064 nm) inside a transparent microstructure. (2) The DNA is degraded sequentially by an exonuclease. The liberated monomers are transported to the detection focus via electroosmotic flow (EOF). (3) Passing the focus, the labeled monomers are excited by a laser and emit photon bursts that are recorded with respect to their fluorescence characteristics (wavelength, lifetime). (Reprinted with permission from Dorre, K., Brakmann, S., Brinkmeier, M., Han, K.-T., Riebeseel, K., Schwille, P., Stephan, J., Wetzel, T., Lapczyna, M., Stuke, M., Bader, R., Hinz, M., Seliger, H., Holm, J., Eigen, M., and Rigler, R. (1997). *Bioimaging* 5(3): 139–152. © 1997, John Wiley and Sons.)

be established. The speed of this assay is, in principle, limited only by the rate of an enzymatic digestion (100 to 1000 bases/min). The complete detection of all dye-labeled monomers, which are cleaved off of the isolated DNA template during the sequencing reaction, is an essential requirement. This can be addressed by use of a microfluidic system with a confocal multielement setup (Dorre et al. 1997; Dorre et al. 2001). A linear array of adjacent multimode optical fibers, each connected to its own avalanche photodiode detector, is set at each microfluidic channel. The entire cross-section of the microchannel is illuminated at the detection area. This arrangement generates a number of overlapping femtoliter detection volumes across the channel and ensures high detection efficiency.

On-chip DNA sequencing can be also performed using sequencing-by-synthesis approaches (Braslavsky et al. 2003; Kartalov and Quake 2004). A primed DNA template is anchored within a microfluidic reactor and its position is recorded using high-sensitivity digital cameras connected to a microscope. The DNA template is then exposed to a mixture of a known type of standard nucleotide, its fluorescently tagged analog, and DNA polymerase. If the tagged nucleotide is complementary to the template base next to the primer's end, the polymerase extends the primer with it and a fluorescence signal is detected after a washing step. Iteration with each type of nucleotide reveals the DNA sequence. By imaging many reactors, the sequence of multiple DNA molecules can be obtained in parallel. The proof of principle of sequencing-by-synthesis with an average read length of 3 bp has been demonstrated in a fully integrated PDMS microfluidic system (Figure 15.25). This approach to DNA sequencing has advantages in economy of material and integration under the lab-on-a-chip paradigm, and has the ability to obtain sequence information from millions of independent molecules in parallel.

15.3.3 Other SMD Bioassays On-Chip

Many types of genomic studies, such as comparative studies of differences among species or among individuals within a given species, do not require single-base resolution provided by DNA sequencing. DNA mapping, which provides low resolution information about DNA sequence, is especially useful in such cases as it is much faster and less expensive for long, genome-sized DNA. An interesting approach to DNA mapping using SMD in microfabricated devices is called direct linear analysis (DLA) (Chan et al. 2004) (Figure 15.26). In the first step, double-stranded DNA molecules are labeled with intercalating dyes and with sequence-specific fluorescent tags (e.g., fluorescent peptide nucleic acids [PNAs]), which target 7 to 8 bp of DNA. In the next step, the sample is introduced into a microfluidic chip containing micropost arrays and tapered channels. By interaction with microposts, DNA molecules uncoil and finally stretch into a linear form in the tapered region of the channel. Individual DNA molecules are then interrogated with laser

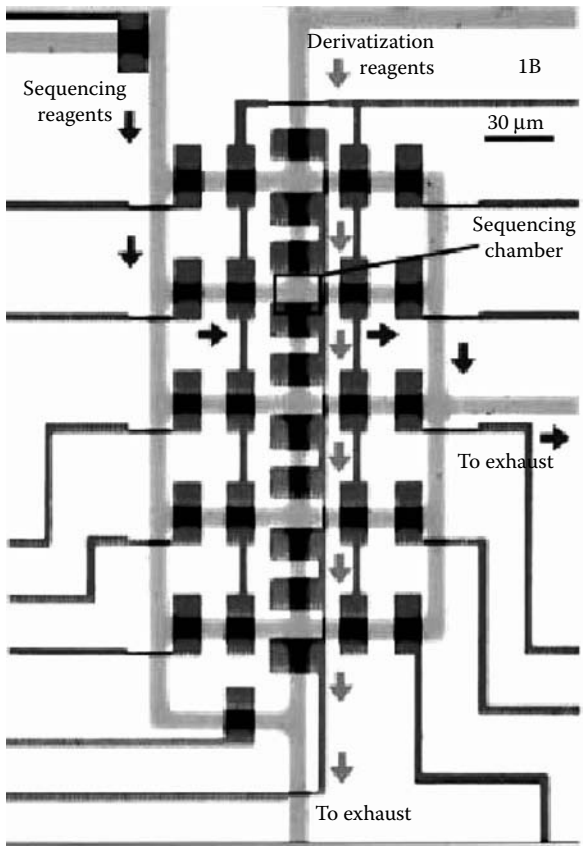

FIGURE 15.25
Chip architecture. The microchannels are filled with food dyes to accentuate features. The derivatization tree supplies reagents to form surface chemistry in all five sequencing chambers at once. Lane controls direct flow of sequencing reagents from the sequencing tree into any chamber of choice. Valves are formed only where wide control segments cross over flow segments. Arrows indicate the flow direction during operation–derivatization and sequencing. (Reprinted with permission from Kartalov, E.P. and Quake, S.R. (2004). *Nucleic Acids Research* 32(9): 2873–2879. © 2004, Oxford University Press.)

radiation to reveal the length of the molecule as well as the number and location of site-specific tags.

Detection of single nucleotide polymorphisms (SNPs) has high analytical value for early detection of such diseases as cystic fibrosis, Alzheimer's, sickle cell anemia, and certain cancers. The most difficult problem of detecting SNPs in real samples is that the mutant DNA is present in a much lower concentration than normal DNA. Thus, SNP detection assays have to be capable of distinguishing between both forms of DNA with high sensitivity. New assays for the detection of SNPs by combination of ligase detection reaction (LDR) and single-pair fluorescence resonance energy transfer (spFRET) with molecular beacons have been proposed by Soper and colleagues (Wabuyele et al.

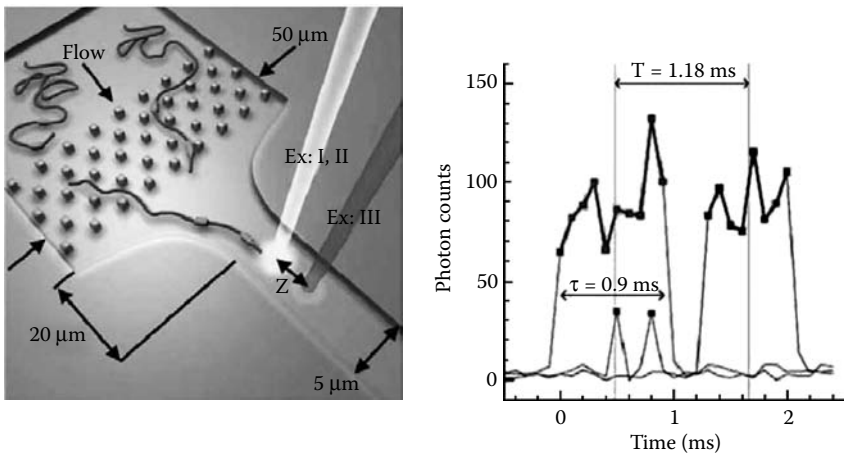

FIGURE 15.26
(a) Schematics of the direct linear analysis (DLA) technology. (b) Typical raw data traces from data channels 1 through 3 for a single tagged DNA molecule. The traces arise from fluorescence of the intercalating dye when the DNA backbone travels through the excitation spots ExII and ExIII (ex = 633 nm), respectively. The spikes are detected when the DNA-bound PNA tags pass through the excitation spot ExI (ex = 532 nm) and emit bursts of photons. (Reprinted with permission from Chan, E.Y., Goncalves, N.M., Haeusler, R.A., Hatch, A.J., Larson, J.W., Maletta, A.M., Yantz, G.R., Carstea, E.D., Fuchs, M., Wong, G.G., Gullans, S.R., and Gilmanshin, R. (2004). *Genome Research* 14(6): 1137–1146. © 2004, Cold Spring Harbor Laboratory Press.)

2003). By using single-molecule approaches, the authors were able to detect low abundant point mutations in K-ras oncogenes without the initial PCR amplification required by other assays. This assay could be performed in less than 5 min at a frequency of 1 mutant DNA per 10 normals using PMMA microfluidic chips and sheath flows for sample stream focusing.

15.3.4 Submicrometer-Sized Fluidic Channels

Typical microfluidic channels have cross-sections that are still much larger than the cross-sections associated with most confocal detection volumes. Relatively large channel dimensions impose some restrictions with respect to the optimal resolution that can be obtained. For example, large channel dimensions require relatively large observation windows for uniform illumination of the entire channel width. Therefore, only slow flow speeds or low sample concentrations can be employed to avoid multiple molecular occupancies. Also, noise contributions from buffer solutions increase with increasing channel size. In addition, hydrodynamic and electric-current focusing techniques require additional fluidic control systems that may lead to off-center focusing. In order to alleviate these problems, fluidic channels with sizes smaller than the confocal detection volume may be used.

In order to match a typical confocal detection volume of less than 1 fL, channels with dimensions of less than 1 μm × 1 μm have to be fabricated. Some of the techniques that have been successfully used for fabrication of submicrometer-sized and nanometer-sized channels for SMD are listed in Table 15.2.

With submicrometer or nanometer channel dimensions, the detection volumes on the order of tens of attoliters can be generated, which are roughly 100 times smaller than the effective observation volume of typical confocal setups. Thus, nearly all of the individual molecules can be detected rapidly with high signal-to-noise ratios. This is extremely important for the SMD-based assays, which depend on 100% sampling efficiencies, such as the DNA sequencing-by-digestion assays described in the previous section. Higher counting efficiencies also improve the statistical accuracy of any single-molecule characterization because all molecules are counted and contribute to the analysis. Another advantage of extremely small detection volumes is that higher sample concentrations can be used without a risk of detection errors resulting from multiple occupancy of the detection volume. This is especially useful for studying biochemical processes, which occur efficiently only at much higher than the pico- or nanomolar concentration regime. Thus, nanofabricated devices offer the potential to study these processes at physiologically more appropriate concentrations. Finally, extremely higher linear velocities can be used with submicron channel shortening analysis time per molecule, significantly reducing analysis time (Foquet et al. 2004).

TABLE 15.2

Techniques Used for Fabrication of Submicrometer-Sized and Nanometer-Sized Channels

Fabrication technique	Channel characteristics	Example application	Reference
Sacrificial layer	350 nm wide × 250 nm tall channels in fused silica	DNA fragment sizing	(Foquet et al. 2002; Foquet et al. 2004)
Focused ion beam (FIB)	individual 150–900 nm trapezoidal trenches in silicon	Electrophoretic behavior of single, fluorescently labeled DNA molecules	(Campbell et al. 2004)
Reactive ion etch (RIE)	500 nm square cross-section channels in fused silica	Detection of individual quantum dots conjugated with organic fluorophores	(Stavis et al. 2005)
Nanoimprint lithography (NIL)	Array of 10 nm–200 nm trenches	Sizing of genome-length (>1 million bp) DNA	(Cao et al. 2002a,b; Tegenfeldt et al. 2004a,b)
Polymer fibers as sacrificial layer	Suspended glass nanotubes, 100–500 nm diameter	Detection of single fluorescently labeled proteins	(Verbridge et al. 2005)

One has to remember, however, that when using submicrometer- and nanometer-sized channels, new issues can arise. These include channel clogging, increased molecule-to-surface interactions, high levels of background caused by increased refraction from channel surfaces, interfacing nanometer-sized channels to macroscale instrumentation, and extremely high back pressures induced by nanometer-sized channels when hydrodynamic pumping is used. Some of these issues can be addressed by proper design of the nanofluidic devices. For example, nanochannels can be accessed by microfluidic channel networks, which are easier to interface to macroscale instrumentation (Cao et al. 2002a, b; Foquet et al. 2004). Dense arrays of parallel nanochannels can be used to reduce clogging issues as well (Cao et al. 2002a; Tegenfeldt et al. 2004b) (Figure 15.27), whereas suspended glass nanotubes with extremely thin walls reduce the problem of substrate-related background (Verbridge et al. 2005) (Figure 15.28). Surface coatings can reduce the problems associated with molecule adhesion to the channel walls and electrokinetic forces can be used to drive the fluids eliminating the problems of high back pressures.

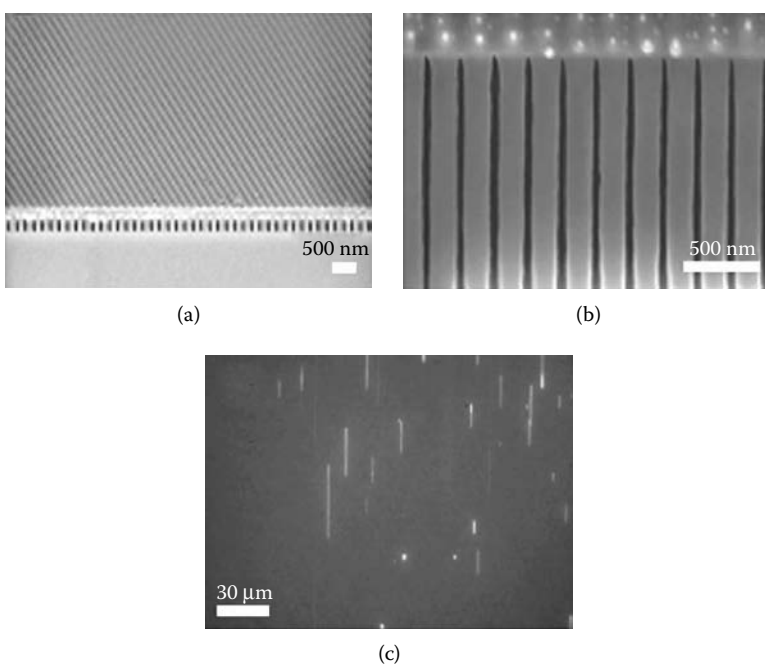

FIGURE 15.27
(a) SEM image shows the "roof" and profile of the nanochannels fabricated with NIL and sealed by the SiO2 sputtering process. (b) Buried nanochannels under the sealing roof were shown to be perfectly intact after sealing. (c) CCD image of λ-phage DNA concatemers stretched in nanofluidic channels. (Reprinted with permission from Cao et al. 2002b, © 2002, American Institute of Physics.

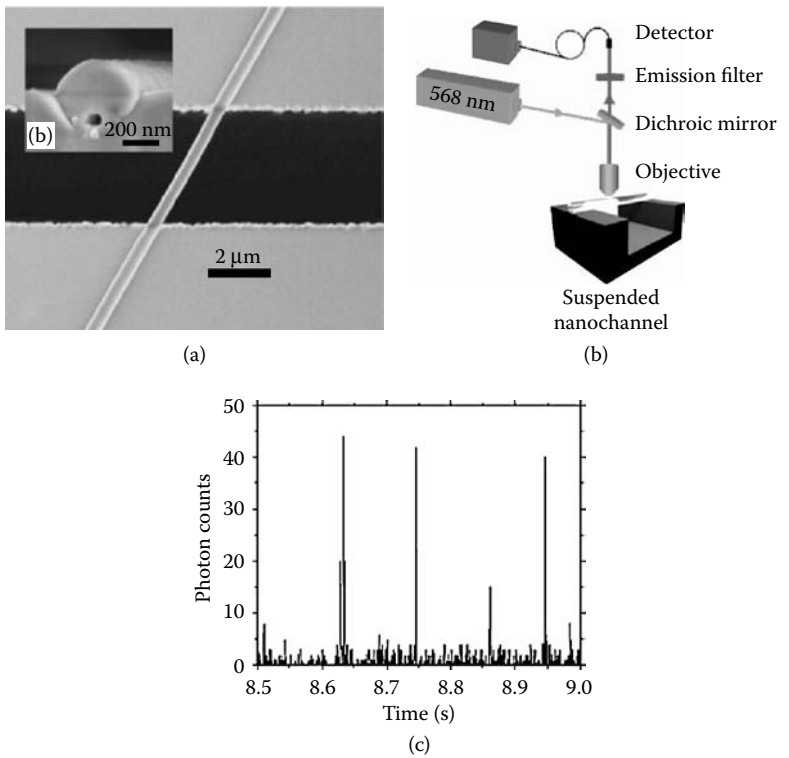

FIGURE 15.28
Scanning electron micrograph of (a, b) 400 nm outer diameter, 100 nm inner diameter sputtered glass channel suspended over a 5 μm–wide, 25 μm–deep trench etched in silicon. (c) Schematic for the optical apparatus used for fluorescent measurement and (d) a 0.5 s portion of a photon burst scan for 2 nM Rhodamine Red-X cellulase enzyme. At a 2 nM sample, the average volume per molecule was a factor of 100 greater than the focal volume of approximately 10×10^{-18} L for a 100-nm inner diameter channel. (Adapted with permission from Verbridge, S.S., Edel, J.B., Stavis, S.M., Moran-Mirabal, J.M., Allen, S.D., Coates, G., and Craighead, H.G. (2005). *Journal of Applied Physics* 97(12): 124317/124311–124317/124314. © 2005, American Institute of Physics.)

15.3.5 Selection of the Right Substrate Material for SMD

The material for microfluidic chip fabrication has to fulfill several requirements in order to be successfully used for SMD with optical methods. These include optical clarity, low-level background fluorescence, compatibility with a wide range of potential chemistries, and biocompatibility. Glass is an ideal material for such applications as it fulfills most of these requirements. Despite the appealing and promising developments of microfluidic devices fabricated in glass, it is considered relatively expensive for applications where disposability of the device is often required. Polymers are viewed as promising alternative substrates for such applications as they are

less expensive and offer greater flexibility in fabrication strategies for mass producing microstructures.

Many polymeric materials possess good light transmission properties for use in optical detection (see Figure 15.29a). Unfortunately, most polymers also show high fluorescent backgrounds in the visible range of the electromagnetic spectrum as compared to glass (see Figure 15.29b). This high autofluorescence can be attributed to either the polymer itself or to different additives, such as plasticizers, commonly used in commercial-grade polymers (compare autofluorescence values for different types of PMMA in Figure 15.29b). The autofluorescence of polymeric material is strongly dependent on excitation wavelength with higher autofluorescence values observed for shorter wavelengths (Piruska et al. 2005; Wabuyele et al. 2001). PDMS and PMMA (especially high purity grade) are the only polymeric materials used for microfluidic chip applications that come close to glass in terms of its low autofluorescence properties using a relatively wide range of excitation wavelengths ($\lambda_{exc} > 480$ nm). These properties of both PDMS and PMMA have already been widely used in SMD (Braslavsky et al. 2003; Chou et al. 1999; Effenhauser et al. 1997; Wabuyele et al. 2003; Wabuyele et al.

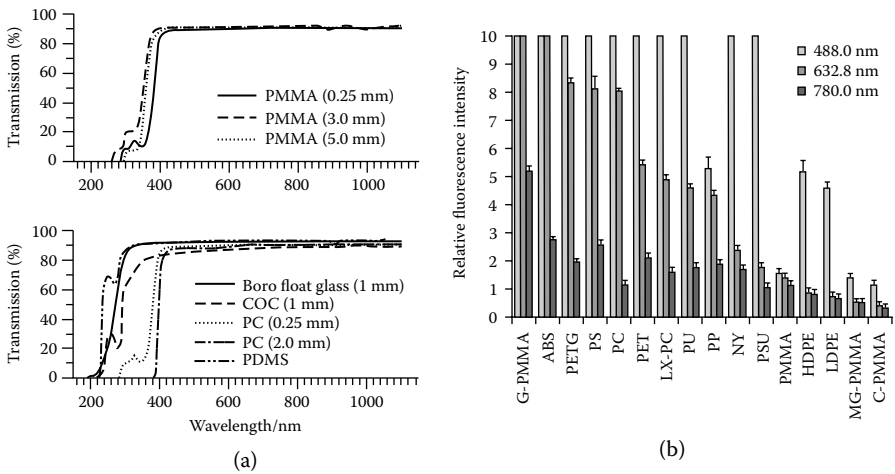

FIGURE 15.29
(a) The transmission spectra of the plastic materials taken at normal incidence. (Reprinted with permission from Piruska, A., Nikcevic, I., Lee, S.H., Ahn, C., Heineman, W.R., Limbach, P.A., and Seliskar, C.J. (2005). *Lab on a Chip* 5(12): 1348–1354. © 2005, The Royal Society of Chemistry.) (b) LIF background levels of different polymers measured at three different excitation wavelengths, 488 nm, 632.8 nm, or 780 nm. The average fluorescence intensity (cps) of the polymers was normalized with respect to the value obtained for glass at the same excitation wavelength. COC: cyclic olefin copolymer; PDMS: poly(dimethylsiloxane); PMMA: poly(methylmethacrylate); MG-PMMA: medical-grade PMMA; G-PMMA: grey acrylic; C-PMMA: clear acrylic; ABS: poly(acrylonitirle-butadiene-styrene); PETG: polyethylene terephtalate glycolate; PS: polystyrene; PC: polycarbonate; LX-PC: Lexan-grade PC; PET: polyethylene terephtalate; PU: polyurethane; PP: polypropylene; NY: nylon; PSU: polysulfone; HDPE: high-density polyethylene; LDPE: low-density polyethylene. (Reprinted with permission from Shadpour et al. 2005 , © 2005, Elsevier B.V.)

2001). Other polymers, such as PC, may be used as long as near-IR chromophores are utilized (Wabuyele et al. 2001).

15.4 Concluding Remarks

The development of microfluidic chip systems provides an attractive platform for the study of single cells, and the very low number of molecules comprising those cells, due to the fact that the volume scale of microfluidics is on the same scale as a whole cell, which minimizes dilution of the molecular intracellular contents of those cells. When the size scale of fluidic networks is reduced below 1 μm, then new opportunities exist for sampling single molecules using biologically and chemically relevant concentrations, for such applications as bioenzymatic reactions and chemical derivatization reactions. Due to the extensive level of integration of processing steps into a single device, sample loss due to sample transfer is eliminated as well as contamination effects. For further information on this topical area, a number of different books and valuable journal review articles on the general use of microfluidic devices are available: Erickson and Lu (2004), Huang et al. (2002), Jakeway et al. (2000), Lagally and Mathies (2004), and Lu et al. (2004a, b). For further information on single-cell manipulation and analysis using microfluidic devices, see Andersson and van den Berg (2003), Andersson et al., Beebe (2000), Beebe et al. (2002), Brehm-Stecher and Johnson (2004), Chovan and Guttman (2002), Olson et al. (2005), and Toner and Irimia (2005).

References

Aborn, J.H., El-Difrawy, S.A., Novotny, M., Gismondi, E.A., Lam, R., Matsudaira, P., McKenna, B.K., O'Neil, T., Streechon, P., and Ehrlich, D.J. (2005). A 768-lane microfabricated system for high-throughput DNA sequencing. *Lab on a Chip* 5(6): 669–674.

Ambrose, W.P., Goodwin, P.M., Jett, J.H., Johnson, M.E., Martin, J.C., Marrone, B.L., Schecker, J.A., Wilkerson, C.W., Keller, R.A., Haces, A., Shih, P.J., and Harding, J.D. (1993). Application of single-molecule detection to DNA-sequencing and sizing. *Berichte Der Bunsen-Gesellschaft-Physical Chemistry Chemical Physics* 97(12): 1535–1542.

Andersson, H. and van den Berg, A. (2003). Microfluidic devices for cellomics: A review. *Sensors and Actuators, B: Chemical* B92(3): 315–325.

Andersson, H. and van den Berg, A. (2004). Microtechnologies and nanotechnologies for single-cell analysis. *Current Opinion in Biotechnology* 15(1): 44–49.

Baker Megan, K., Mikhitarian, K., Osta, W., Callahan, K., Hoda, R., Brescia, F., Kneuper-Hall, R., Mitas, M., Cole David, J., and Gillanders William, E. (2003). Molecular detection of breast cancer cells in the peripheral blood of advanced-stage

breast cancer patients using multimarker real-time reverse transcription-polymerase chain reaction and a novel porous barrier density gradient centrifugation technology. *Clinical Cancer Research* 9(13): 4865–4871.

Balagadde, F.K., You, L., Hansen, C.L., Arnold, F.H., and Quake, S.R. (2005). Long-term monitoring of bacteria undergoing programmed population control in a microchemostat. *Science* (Washington, DC, United States) 309(5731): 137–140.

Beebe, D.J. (2000). Microfabricated fluidic devices for single-cell handling and analysis. *Emerging Tools for Single-Cell Analysis*, 95–113.

Beebe, D.J., Mensing, G.A., and Walker, G.M. (2002). Physics and applications of microfluidics in biology. *Annual Review of Biomedical Engineering* 4, 261–286.

Belgrader, P., Hansford, D., Kovacs, G.T.A., Venkateswaran, K., Mariella, R., Jr., Milanovich, F., Nasarabadi, S., Okuzumi, M., Pourahmadi, F., and Northrup, M.A. (1999). A minisonicator to rapidly disrupt bacterial spores for DNA analysis. *Analytical Chemistry* 71(19): 4232–4236.

Belgrader, P., Okuzumi, M., Pourahmadi, F., Borkholder, D.A., and Northrup, M.A. (2000). A microfluidic cartridge to prepare spores for PCR analysis. *Biosensors & Bioelectronics* 14(10–11): 849–852.

Braschler, T., Johann, R., Heule, M., Metref, L., and Renaud, P. (2005). Gentle cell trapping and release on a microfluidic chip by in situ alginate hydrogel formation. *Lab on a Chip* 5(5): 553–559.

Braslavsky, I., Hebert, B., Kartalov, E., and Quake, S.R. (2003). Sequence information can be obtained from single DNA molecules. *Proceedings of the National Academy of Sciences of the United States of America* 100(7): 3960–3964.

Brehm-Stecher, B.F. and Johnson, E.A. (2004). Single-cell microbiology: Tools, technologies, and applications. *Microbiology and Molecular Biology Reviews* 68(3): 538–559.

Campbell, L.C., Wilkinson, M.J., Manz, A., Camilleri, P., and Humphreys, C.J. (2004). Electrophoretic manipulation of single DNA molecules in nanofabricated capillaries. *Lab on a Chip* 4(3): 225–229.

Cao, H., Tegenfeldt, J.O., Austin, R.H., and Chou, S.Y. (2002a). Gradient nanostructures for interfacing microfluidics and nanofluidics. *Applied Physics Letters* 81(16): 3058–3060.

Cao, H., Yu, Z., Wang, J., Tegenfeldt, J.O., Austin, R.H., Chen, E., Wu, W., and Chou, S.Y. (2002b). Fabrication of 10 nm enclosed nanofluidic channels. *Applied Physics Letters* 81(1): 174–176.

Chaiyasut, C., Tsuda, T., Khansuwan, U., and Ong-Chai, S. (2002). Red blood cell lysis at the single cell level by using a mini electrophoresis apparatus. *Chromatography* 23(1): 33–38.

Chan, E.Y., Goncalves, N.M., Haeusler, R.A., Hatch, A.J., Larson, J.W., Maletta, A.M., Yantz, G.R., Carstea, E.D., Fuchs, M., Wong, G.G., Gullans, S.R., and Gilmanshin, R. (2004). DNA mapping using microfluidic stretching and single-molecule detection of fluorescent site-specific tags. *Genome Research* 14(6): 1137–1146.

Chan, S.D.H., Luedke, G., Valer, M., Buhlmann, C., and Preckel, T. (2003). Cytometric analysis of protein expression and apoptosis in human primary cells with a novel microfluidic chip-based system. *Cytometry, Part A* 55A(2): 119–125.

Chin Vicki, I., Taupin, P., Sanga, S., Scheel, J., Gage Fred, H., and Bhatia Sangeeta, N. (2004). Microfabricated platform for studying stem cell fates. *Biotechnology and Bioengineering* 88(3): 399–415.

Chiu, D.T. (2003). Micro- and nano-scale chemical analysis of individual sub-cellular compartments. *TrAC, Trends in Analytical Chemistry* 22(8): 528–536.

Chiu, D.T. and Zare, R.N. (1996). Biased diffusion, optical trapping, and manipulation of single molecules in solution. *Journal of the American Chemical Society* 118(27): 6512–6513.

Chou, H.-P., Spence, C., Scherer, A., and Quake, S. (1999). A microfabricated device for sizing and sorting DNA molecules. *Proceedings of the National Academy of Sciences of the United States of America* 96(1): 11–13.

Chovan, T. and Guttman, A. (2002). Microfabricated devices in biotechnology and biochemical processing. *Trends in Biotechnology* 20(3): 116–122.

Chung, B.G., Flanagan, L.A., Rhee, S.W., Schwartz, P.H., Lee, A.P., Monuki, E.S., and Jeon, N.L. (2005). Human neural stem cell growth and differentiation in a gradient-generating microfluidic device. *Lab on a Chip* 5(4): 401–406.

de Mello, A.J. (2003). Focus: Seeing single molecules. *Lab on a Chip* 3(2): 29N–34N.

Dhawan, M.D., Wise, F., and Baeumner, A.J. (2002). Development of a laser-induced cell lysis system. *Analytical and Bioanalytical Chemistry* 374(3): 421–426.

Dittrich, P.S. and Manz, A. (2005). Single-molecule fluorescence detection in microfluidic channels-the Holy Grail in μTAS? *Analytical and Bioanalytical Chemistry* 382(8): 1771–1782.

Dorre, K., Brakmann, S., Brinkmeier, M., Han, K.-T., Riebeseel, K., Schwille, P., Stephan, J., Wetzel, T., Lapczyna, M., Stuke, M., Bader, R., Hinz, M., Seliger, H., Holm, J., Eigen, M., and Rigler, R. (1997). Techniques for single molecule sequencing. *Bioimaging* 5(3): 139–152.

Dorre, K., Stephan, J., Lapczyna, M., Stuke, M., Dunkel, H., and Eigen, M. (2001). Highly efficient single molecule detection in microstructures. *Journal of Biotechnology* 86(3): 225–236.

Effenhauser, C.S., Bruin, G.J.M., Paulus, A., and Ehrat, M. (1997). Integrated capillary electrophoresis on flexible silicone microdevices: Analysis of DNA restriction fragments and detection of single DNA molecules on microchips. *Analytical Chemistry* 69(17): 3451–3457.

Emmelkamp, J., Wolbers, F., Andersson, H., DaCosta, R.S., Wilson, B.C., Vermes, I., and van den Berg, A. (2004). The potential of autofluorescence for the detection of single living cells for label-free cell sorting in microfluidic systems. *Electrophoresis* 25(21–22): 3740–3745.

Erickson, D. and Li, D. (2004). Integrated microfluidic devices. *Analytica Chimica Acta* 507(1): 11–26.

Eyal, S. and Quake, S.R. (2002). Velocity-independent microfluidic flow cytometry. *Electrophoresis* 23(16): 2653–2657.

Fister, J.C., III, Jacobson, S.C., Davis, L.M., and Ramsey, J.M. (1998). Counting single chromophore molecules for ultrasensitive analysis and separations on microchip devices. *Analytical Chemistry* 70(3): 431–437.

Foquet, M., Korlach, J., Zipfel, W., Webb, W.W., and Craighead, H.G. (2002). DNA fragment sizing by single molecule detection in submicrometer-sized closed fluidic channels. *Analytical Chemistry* 74(6): 1415–1422.

Foquet, M., Korlach, J., Zipfel, W.R., Webb, W.W., and Craighead, H.G. (2004). Focal volume confinement by submicrometer-sized fluidic channels. *Analytical Chemistry* 76(6): 1618–1626.

Fu, A.Y., Chou, H.-P., Spence, C., Arnold, F.H., and Quake, S.R. (2002). An integrated microfabricated cell sorter. *Analytical Chemistry* 74(11): 2451–2457.

Fu, A.Y., Spence, C., Scherer, A., Arnold, F.H., and Quake, S.R. (1999). A microfabricated fluorescence-activated cell sorter. *Nature Biotechnology* 17(11): 1109–1111.

Futai, N., Gu, W., Song, J.W., and Takayama, S. (2006). Handheld recirculation system and customized media for microfluidic cell culture. *Lab on a Chip* 6(1): 149–154.

Gao, J., Yin, X.-F., and Fang, Z.-L. (2004). Integration of single cell injection, cell lysis, separation and detection of intracellular constituents on a microfluidic chip. *Lab on a Chip* 4(1): 47–52.

Gu, W., Zhu, X., Futai, N., Cho Brenda, S., and Takayama, S. (2004). Computerized microfluidic cell culture using elastomeric channels and Braille displays. *Proceedings of the National Academy of Sciences of the United States of America* 101(45): 15861–15866.

Haab, B.B. and Mathies, R.A. (1999). Single-molecule detection of DNA separations in microfabricated capillary electrophoresis chips employing focused molecular streams. *Analytical Chemistry* 71(22): 5137–5145.

Habbersett, R.C. and Jett, J.H. (2004). An analytical system based on a compact flow cytometer for DNA fragment sizing and single-molecule detection. *Cytometry Part A* 60A(2): 125–134.

He, M., Edgar, J.S., Jeffries, G.D.M., Lorenz, R.M., Shelby, J.P., and Chiu, D.T. (2005). Selective encapsulation of single cells and subcellular organelles into picoliter- and femtoliter-volume droplets. *Analytical Chemistry* 77(6): 1539–1544.

He, Y., Zhang, Y.H., and Yeung, E.S. (2001). Capillary-based fully integrated and automated system for nanoliter polymerase chain reaction analysis directly from cheek cells. *Journal of Chromatography.* 924(1–2): 271–284.

Hellmich, W., Pelargus, C., Leffhalm, K., Ros, A., and Anselmetti, D. (2005). Single cell manipulation, analytics, and label-free protein detection in microfluidic devices for systems nanobiology. *Electrophoresis* 26(19): 3689–3696.

Heo, J., Thomas, K.J., Seong, G.H., and Crooks, R.M. (2003). A microfluidic bioreactor based on hydrogel-entrapped *E. coli*: Cell viability, lysis, and intracellular enzyme reactions. *Analytical Chemistry* 75(1): 22–26.

Hogan, B.L. and Yeung, E.S. (1993). Single-cell analysis at the level of a single human erythrocyte. *TrAC, Trends in Analytical Chemistry* 12(1): 4–9.

Hong, J.W., Studer, V., Hang, G., Anderson, W.F., and Quake, S.R. (2004). A nanoliter-scale nucleic acid processor with parallel architecture. *Nature Biotechnology* 22(4): 435–439.

Huang, Y., Chen, N., Borninski, J., and Rubinsky, B. (2003). A novel microfluidic cell-chip for single cell analysis and manipulation. Proceedings—IEEE Annual International Conference on Micro Electro Mechanical Systems, 16th, Kyoto, Japan, January 19–23, 403–406.

Huang, Y., Mather Elizabeth, L., Bell Janice, L., and Madou, M. (2002). MEMS-based sample preparation for molecular diagnostics. *Analytical and Bioanalytical Chemistry* 372(1): 49–65.

Hung, P.J., Lee, P.J., Sabounchi, P., Lin, R., and Lee, L.P. (2004). Continuous perfusion microfluidic cell culture array for high-throughput cell-based assays. *Biotechnology and Bioengineering* 89(1): 1–8.

Husebekk, A., Skogen, B., and Husby, G. (1988). High-density lipoprotein has different binding capacity for different apoproteins. The amyloidogenic apoproteins are easier to displace from high-density lipoprotein. *Scandinavian Journal of Immunology* 28(6): 653–658.

Ivanov, I.T. (1999). Investigation of surface and shape changes accompanying the membrane alteration responsible for the heat-induced lysis of human erythrocytes. *Colloids and Surfaces, B: Biointerfaces* 13(6): 311–323.

Jakeway, S.C., de Mello, A.J., and Russell, E.L. (2000). Miniaturized total analysis systems for biological analysis. *Fresenius' Journal of Analytical Chemistry* 366(6–7): 525–539.

Kahn Harriette, J., Presta, A., Yang, L.-Y., Blondal, J., Trudeau, M., Lickley, L., Holloway, C., McCready David, R., Maclean, D., and Marks, A. (2004). Enumeration of circulating tumor cells in the blood of breast cancer patients after filtration enrichment: Correlation with disease stage. *Breast Cancer Research and Treatment* 86(3): 237–247.

Kartalov, E.P. and Quake, S.R. (2004). Microfluidic device reads up to four consecutive base pairs in DNA sequencing-by-synthesis. *Nucleic Acids Research* 32(9): 2873–2879.

Khine, M., Lau, A., Ionescu-Zanetti, C., Seo, J., and Lee, L.P. (2005). A single cell electroporation chip. *Lab on a Chip* 5(1): 38–43.

Kruger, J., Porta, P., Morrison, A., Singh, K., O'Neill, A., and O'Brien, P. (2002). Micro-optical laser induced fluorescence detection on a miniaturized flow cytometry device. Micro Total Analysis Systems 2002, *Proceedings of the mTAS 2002 Symposium*, 6th, Nara, Japan, November 3–7, 290–292.

Lagally, E.T. and Mathies, R.A. (2004). Integrated genetic analysis microsystems. *Journal of Physics D: Applied Physics* 37(23): R245–R261.

Lee, J.-B., Hite, R.K., Hamdan, S.M., Sunney Xie, X., Richardson, C.C., and van Oijen, A.M. (2006). DNA primase acts as a molecular brake in DNA replication. *Nature* (London, United Kingdom) 439(7076): 621–624.

Lee, P.J., Hung, P.J., Shaw, R., Jan, L., and Lee, L.P. (2005). Microfluidic application-specific integrated device for monitoring direct cell-cell communication via gap junctions between individual cell pairs. *Applied Physics Letters* 86(22): 223902/223901–223902/223903.

Lee, S.-W. and Tai, Y.-C. (1999). A micro cell lysis device. *Sensors and Actuators, A: Physical* A73(1–2): 74–79.

Levene, M.J., Korlach, J., Turner, S.W., Foquet, M., Craighead, H.G., and Webb, W.W. (2003). Zero-mode waveguides for single-molecule analysis at high concentrations. *Science* (Washington, DC, United States) 299(5607): 682–686.

Lipman, E.A., Schuler, B., Bakajin, O., and Eaton, W.A. (2003). Single-molecule measurement of protein folding kinetics. *Science* (Washington, DC, United States) 301(5637): 1233–1235.

Lu, H., Gaudet, S., Schmidt Martin, A., and Jensen Klavs, F. (2004a). A microfabricated device for subcellular organelle sorting. *Analytical Chemistry* 76(19): 5705–5712.

Lu, X., Huang, W.-H., Wang, Z.-L., and Cheng, J.-K. (2004b). Recent developments in single-cell analysis. *Analytica Chimica Acta* 510(2): 127–138.

Mathies, R.A., Peck, K., and Stryer, L. (1990). Optimization of high-sensitivity fluorescence detection. *Analytical Chemistry* 62(17): 1786–1791.

Mathis, H.P., Kalusche, G., Wagner, B., and McCaskill, J.S. (1997). Steps towards spatially resolved single molecule detection in solution. *Bioimaging* 5(3): 116–128.

McClain, M.A., Culbertson, C.T., Jacobson, S.C., Allbritton, N.L., Sims, C.E., and Ramsey, J.M. (2003). Microfluidic devices for the high-throughput chemical analysis of cells. *Analytical Chemistry* 75(21): 5646–5655.

Ocvirk, G., Salimi-Moosavi, H., Szarka, R.J., Arriaga, E.A., Andersson, P.E., Smith, R., Dovichi, N.J. and Harrison, D.J. (2004). b-Galactosidase assays of single-cell lysates on a microchip: A complementary method for enzymatic analysis of single cells. *Proceedings of the IEEE* 92(1): 115–125.

Olson, K.J., Ahmadzadeh, H., and Arriaga, E.A. (2005). Within the cell: Analytical techniques for subcellular analysis. *Analytical and Bioanalytical Chemistry* 382(4): 906–917.

Palkova, Z., Vachova, L., Valer, M., and Preckel, T. (2004). Single-cell analysis of yeast, mammalian cells, and fungal spores with a microfluidic pressure-driven chip-based system. Cytometry A 59(2): 246–253.

Piruska, A., Nikcevic, I., Lee, S.H., Ahn, C., Heineman, W.R., Limbach, P.A., and Seliskar, C.J. (2005). The autofluorescence of plastic materials and chips measured under laser irradiation. *Lab on a Chip* 5(12): 1348–1354.

Rao, S.R., Yamamura, S., Takamura, Y., and Tamiya, E. (2004). Multiplexed microfluidic devices for single-cell manipulation and analysis. Special Publication—Royal Society of Chemistry 296 (*Micro Total Analysis Systems 2004, Volume 1*): 61–63.

Rhee, S.W., Taylor, A.M., Tu, C.H., Cribbs, D.H., Cotman, C.W., and Jeon, N.L. (2005). Patterned cell culture inside microfluidic devices. *Lab on a Chip* 5(1): 102–107.

Shackman, J.G., Dahlgren, G.M., Peters, J.L., and Kennedy, R.T. (2005). Perfusion and chemical monitoring of living cells on a microfluidic chip. *Lab on a Chip* 5(1): 56–63.

Shelby, J.P., White, J., Ganesan, K., Rathod, P.K., and Chiu, D.T. (2003). A microfluidic model for single-cell capillary obstruction by plasmodium falciparum-infected erythrocytes. *Proceedings of the National Academy of Sciences of the United States of America* 100(25): 14618–14622.

Sia, S.K. and Whitesides, G.M. (2003). Microfluidic devices fabricated in poly(dimethylsiloxane) for biological studies. *Electrophoresis* 24(21): 3563–3576.

Sims, C.E., Meredith, G.D., Krasieva, T.B., Berns, M.W., Tromberg, B.J., and Allbritton, N.L. (1998). Laser-micropipet combination for single-cell analysis. *Analytical Chemistry* 70(21): 4570–4577.

Sinclair, J., Pihl, J., Olofsson, J., Karlsson, M., Jardemark, K., Chiu, D.T., and Orwar, O. (2002). A cell-based bar code reader for high-throughput screening of ion channel–ligand interactions. *Analytical Chemistry* 74(24): 6133–6138.

Sohn, L.L., Saleh, O.A., Facer, G.R., Beavis, A.J., Allan, R.S., and Notterman, D.A. (2000). Capacitance cytometry: Measuring biological cells one by one. *Proceedings of the National Academy of Sciences of the United States of America* 97(20): 10687–10690.

Soper, S.A., Mattingly, Q.L., and Vegunta, P. (1993). Photon burst detection of single near-infrared fluorescent molecules. *Analytical Chemistry* 65(6): 740–747.

Stavis, S.M., Edel, J.B., Samiee, K.T., and Craighead, H.G. (2005). Single molecule studies of quantum dot conjugates in a submicrometer fluidic channel. *Lab on a Chip* 5(3): 337–343.

Stromberg, A., Karlsson, A., Ryttsen, F., Davidson, M., Chiu, D.T., and Orwar, O. (2001). Microfluidic device for combinatorial fusion of liposomes and cells. *Analytical Chemistry* 73(1): 126–130.

Taylor, M.T., Belgrader, P., Furman, B.J., Pourahmadi, F., Kovacs, G.T.A., and Northrup, M.A. (2001). Lysing bacterial spores by sonication through a flexible interface in a microfluidic system. *Analytical Chemistry* 73(3): 492–496.

Tegenfeldt, J.O., Bakajin, O., Chou, C.-F., Chan, S.S., Austin, R., Fann, W., Liou, L., Chan, E., Duke, T. and Cox, E.C. (2001). Near-field scanner for moving molecules. *Physical Review Letters* 86(7): 1378–1381.

Tegenfeldt, J.O., Prinz, C., Cao, H., Chou, S., Reisner, W.W., Riehn, R., Wang, Y.M., Cox, E.C., Sturm, J.C., Silberzan, P., and Austin, R.H. (2004a). The dynamics of genomic-length DNA molecules in 100-nm channels. *Proceedings of the National Academy of Sciences of the United States of America* 101(30): 10979–10983.

Tegenfeldt, J.O., Prinz, C., Cao, H., Huang, R.L., Austin, R.H., Chou, S.Y., Cox, E.C., and Sturm, J.C. (2004b). Micro- and nanofluidics for DNA analysis. *Analytical and Bioanalytical Chemistry* 378(7): 1678–1692.

Tian, H., Emrich, C.A., Scherer, J.R., Mathies, R.A., Andersen, P.S., Larsen, L.A., and Christiansen, M. (2005). High-throughput single-strand conformation polymorphism analysis on a microfabricated capillary array electrophoresis device. *Electrophoresis* 26(9): 1834–1842.

Toner, M. and Irimia, D. (2005). Blood-on-a-chip. *Annual Review of Biomedical Engineering* 7: 77–103.

Toriello, N.M., Douglas, E.S., and Mathies, R.A. (2005). Microfluidic device for electric field-driven single-cell capture and activation. *Analytical Chemistry* 77(21): 6935–6941.

Tourovskaia, A., Figueroa-Masot, X., and Folch, A. (2005). Differentiation-on-a-chip: A microfluidic platform for long-term cell culture studies. *Lab on a Chip* 5(1): 14–19.

Tsong, T.Y. (1991). Electroporation of cell membranes. *Biophysical Journal* 60(2): 297–306.

Valero, A., Merino, F., Wolbers, F., Luttge, R., Vermes, I., Andersson, H., and van den Berg, A. (2005). Apoptotic cell death dynamics of HL60 cells studied using a microfluidic cell trap device. *Lab on a Chip* 5(1): 49–55.

van Oijen, A.M., Blainey, P.C., Crampton, D.J., Richardson, C.C., Ellenberger, T., and Xie, X.S. (2003). Single-molecule kinetics of l exonuclease reveal base dependence and dynamic disorder. *Science* (Washington, DC, United States) 301(5637): 1235–1239.

Verbridge, S.S., Edel, J.B., Stavis, S.M., Moran-Mirabal, J.M., Allen, S.D., Coates, G., and Craighead, H.G. (2005). Suspended glass nanochannels coupled with microstructures for single molecule detection. *Journal of Applied Physics* 97(12): 124317/124311–124317/124314.

Wabuyele, M.B., Farquar, H., Stryjewski, W., Hammer, R.P., Soper, S.A., Cheng, Y.-W., and Barany, F. (2003). Approaching real-time molecular diagnostics: Single-pair fluorescence resonance energy transfer (spFRET) detection for the analysis of low abundant point mutations in K-ras oncogenes. *Journal of the American Chemical Society* 125(23): 6937–6945.

Wabuyele, M.B., Ford, S.M., Stryjewski, W., Barrow, J., and Soper, S.A. (2001). Single molecule detection of double-stranded DNA in poly(methylmethacrylate) and polycarbonate microfluidic devices. *Electrophoresis* 22(18): 3939–3948.

Waters, L.C., Jacobson, S.C., Kroutchinina, N., Khandurina, J., Foote, R.S., and Ramsey, J.M. (1998). Microchip device for cell lysis, multiplex PCR amplification, and electrophoretic sizing. *Analytical Chemistry* 70(1): 158–162.

Wheeler, A.R., Throndset, W.R., Whelan, R.J., Leach, A.M., Zare, R.N., Liao, Y.H., Farrell, K., Manger, I.D., and Daridon, A. (2003). Microfluidic device for single-cell analysis. *Analytical Chemistry* 75(14): 3581–3586.

Wu, H., Wheeler, A., and Zare Richard, N. (2004). Chemical cytometry on a picoliter-scale integrated microfluidic chip. *Proceedings of the National Academy of Sciences of the United States of America* 101(35): 12809–12813.

16

Pharmaceutical Analysis Using Bio-MEMS

Celeste Frankenfeld and Susan Lunte

CONTENTS

16.1 Advantages of the Microworld for Pharmaceutical and Biomedical Analysis

Pharmaceutical analysis deals with the detection of any drug compound or biological molecule that elicits a pharmacological response. Fast, efficient, and selective analytical methods are important for drug research and development as well as the clinical diagnosis of disease. The emergence of biological microelectromechanical systems (bio-MEMS) provides a new opportunity for the creation of high-throughput and portable analysis systems that can be used for a variety of pharmaceutical applications. These include *in vivo* sensing, point-of-care diagnostics, and high-throughput screening of drug candidates.

Bio-MEMS and lab-on-a-chip devices offer several advantages over conventional analytical methods for pharmaceutical analysis. First, the small

sample requirements of these devices (mid-to-low picoliter range) mean that only a few microliters of blood or micrograms of protein are necessary for clinical or biological assays. The small footprint of the device also makes it possible to perform multiple assays on a single chip.[1–3] The integration of several procedures including sample preparation, separation, and detection, all in one device also means that sample loss and handling errors are minimized.

Three additional advantages afforded by microchips are due to their small size. First, the overall shorter channel dimensions make it possible to perform separations within seconds as opposed to the minutes required when using conventional analytical systems. Secondly, the smaller dimensions of the individual components make them portable. This offers the potential for point-of-care analysis in the field, at home, or in a physician's office. Lastly, plastics and other inexpensive substrate materials can be used to generate the microchips, making the production of disposable devices feasible. Disposable devices are particularly attractive for the analysis of blood and other biological fluids that may contain biohazardous substances (such as HIV or hepatitis B virus). It also eliminates many of the problems with cross-contamination that can occur when a single chip is employed for several analyses.

Perhaps the greatest advantage that microchip devices offer to the pharmaceutical industry is the capability of high-throughput analysis. Multiple channels and detectors may be fabricated onto a single chip, allowing anywhere between two and several hundred online analyses to occur simultaneously. This saves time and allows pharmaceutical companies to screen molecular libraries that contain hundreds of thousands of potential drugs.

16.2 Basic Components of Bio-MEMS and Lab-on-a-Chip Devices for Pharmaceutical Analysis

Most bio-MEMS and lab-on-a-chip devices used for pharmaceutical or biomedical analysis have several common components that are employed for sample introduction, sample processing, and detection. Figure 16.1 shows a schematic outlining the different functions of the components that are commonly employed for pharmaceutical and clinical applications.

Sample introduction into an analytical microchip is most often accomplished by manually pipetting the sample into a low-volume reservoir that is built into the chip. Alternatively, a syringe pump may be connected to chip fittings to reproducibly introduce the sample via a pressure-driven flow. A portion of the sample is then injected from the reservoir into the analytical system using either pressure-driven flow or electrokinetic gating. If pressure-driven flow is employed, the sample is forced from the sample well into the processing channel hydrodynamically.[4,5] In electrokinetic gating, the sample

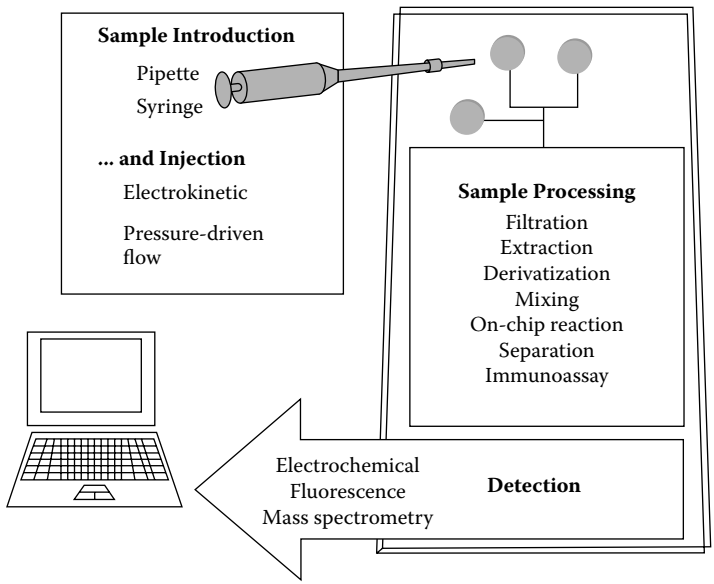

FIGURE 16.1
Components of bio-MEMS chips for pharmaceutical and biomedical analysis.

is injected into the processing channel by application of voltages that generate electroosmotic flow (EOF).[6,7] The magnitude of the EOF is dependent on pH, ionic strength, and the type of substrate employed for the device as well as the field strength. In general, EOF forces the bulk fluid toward cathodic buffer reservoirs; in the process it carries the analyte along with other sample components into the sample processing region of the chip.

A recent trend in sample injection into microchips is the introduction of discrete samples from a flowing stream.[8] In 2001, Harrison's group first published a paper entitled, "Allowing microfluidic chips to drink from the fire hose of the external environment."[9] In this application, discrete injections were made from a solution flowing at one mL/min and then analyzed by electrophoresis. Later, Chen et al. described an interface that could be employed at lower flow rates (1 μl/min) and was employed for a flow injection-based immunoassay.[10] More recently, our group has further modified this approach to incorporate microdialysis as an online sample preparation method.[11] Figure 16.2 shows a schematic of the online microdialysis-microchip CE system and data obtained for the near real-time monitoring of an enzymatic reaction.

Once a sample has been introduced into the chip, additional processing steps such as sample preparation, mixing, reactions, and separation are usually necessary prior to analyte detection. Some commonly employed sample preparation strategies include filtration, solid-phase extraction, and derivatization. Filtration can be accomplished using pillars fabricated directly into the device, beads packed into a channel, or microdialysis membranes sandwiched within the chip.[12–14] For solid-phase extraction, particles

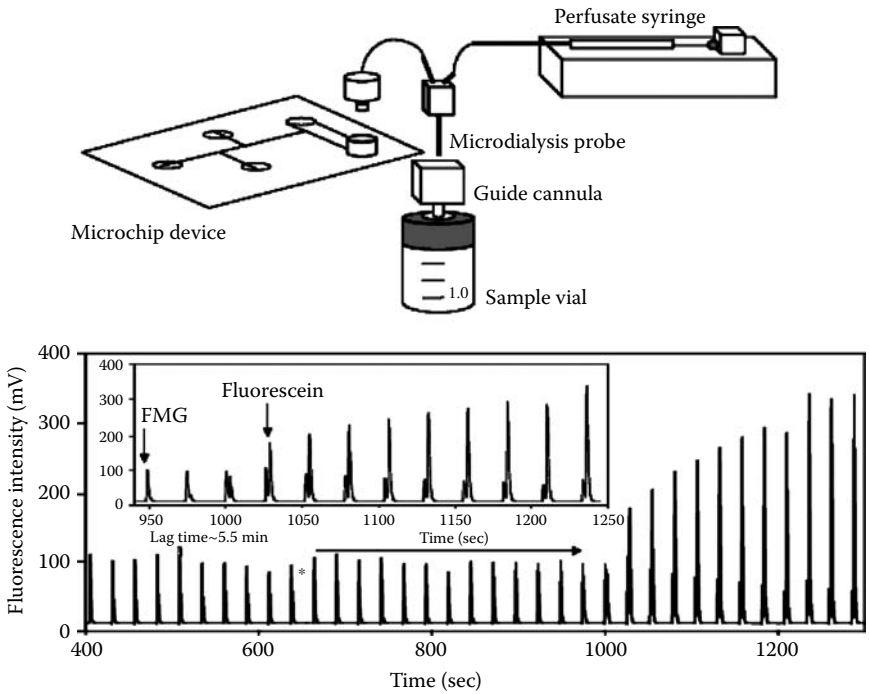

FIGURE 16.2
Online microdialysis microchip electrophoresis continuous monitoring of hydrolysis of fluorescein mono--D-galactopyranoside by galactosidase. (From Huynh, B. et al., *Anal. Chem.* 76, 6440-6447, 2004. With permission.)

and monolithic chromatographic materials have been used to isolate the compound(s) of interest from the other components of the sample.[15,16] Several types of supports have been investigated for this purpose, including reversed phase[17] and immunoaffinity chromatography.[18]

In some cases, derivatization is necessary to make the analyte of interest detectable. Derivatization can be accomplished precolumn, postcolumn, or on-column. James Landers has employed on-chip derivatization for the detection of proteins following sodium dodecyl sulfate-polyacrylamide gel electrophoresis (SDS-PAGE).[19] Ramsey's group has used postcolumn derivatization for the detection of peptides following electrophoretic separation.[20,21]

Control of fluid flow is essential to carry out the diverse functions required of analytical bio-MEMS, including derivatization, mixing,[22] and other on-chip chemical reactions.[23] Valves may be incorporated into the chip to direct fluid flow and promote mixing of two fluid streams. These valves can be pressure driven[24] or electrokinetic.[25] Valves produced by soft lithography can also be used as pneumatic pumps within the chip or simply act as isolation points where fluid flows may be separated from one another.[24]

Electrophoresis is commonly employed for the separation of analytes on microchip devices.[26] Several forms of electrophoresis have been accomplished

on-chip, including zone electrophoresis,[27] polyacrylamide gel electrophoresis (PAGE), SDS-PAGE,[28] and micellar electrokinetic chromatography (MEKC) separations.[29] In zone electrophoresis, the analytes are separated based on their charge-to-mass ratio. This approach is most commonly employed for the separation of amino acids and peptides. SDS-PAGE and PAGE are size-based separations and are used for separations of proteins and DNA, respectively. MEKC separates compounds based on their hydrophobicity and is most commonly employed for the separation of nonionic pharmaceuticals.

Chromatographic supports have also been incorporated into microchips to effect a separation. This can be accomplished through the incorporation of porous hydrophobic beads, commonly utilized in conventional HPLC, into micron-sized channels.[17] Alternatively, *in situ* production of monoliths has been accomplished by several groups. The separation can be accomplished by the application of pressure-driven flow or an electric field (electrochromatography).

Antibodies have been used for both sample processing and detection. If the antibodies are immobilized on a chromatographic support, they can be used for sample preparation and concentration. Alternatively, antibodies can be employed for sample detection by immunoassay. Both of these methods take advantage of the high selectivity of binding of an antigen to an antibody.[30–32] In the case of immunoaffinity, the antibodies are used to trap the antigen of interest and isolate it from potential interferences. This approach was discussed above under the sample preparation methods.

Separation-based immunoassays have also been performed on-chip.[33] In the competitive immunoassay format, labeled antigens compete with endogenous antigens for antibody binding sites. Then electrophoresis or chromatography is used to separate the bound from the free fraction of labeled antigen. An alternative approach is to immobilize a specific known quantity of antibodies on beads or the channel walls in the chip. A sample containing both endogenous antigen and labeled antigen is introduced into the channel. Both compete for the binding sites. When the labeled antigens are measured (via fluorescence or an enzyme reaction), the concentration of target analyte may be determined.

There are many forms of detection that may be incorporated into a bio-MEMS device. An entire chapter of this book is devoted to one of those methods, electrochemical detection (EC).[34–37] Another common form of integrated detection is laser-induced fluorescence (LIF).[38] Other optical forms of detection, less commonly included on microchips, are thermal lens spectroscopy,[39] deep UV spectroscopy,[40] and fiber-optic methods of capturing emission intensity.[41] Mass spectrometry (MS) is an important detection method that is highly desirable to the pharmaceutical industry. Although MS has not been incorporated on-chip, several chips have been developed with microfabricated interfaces that allow analyte to be injected from the microdevice onto the mass spectrometer.[42–45]

16.3 Challenges of Pharmaceutical Bio-MEMS

The greatest challenge to face pharmaceutical bio-MEMS is that of compatibility with biological fluids, tissues, and cells. Devices used for monitoring the release of substances from cells or tissue culture or those that are implanted into a tissue must be constructed of biocompatible materials that will resist biofouling. A review by Grayson et al.[46] addresses many of these issues.

The analysis of complex biological fluids, including blood, saliva, or urine, also presents a challenge. In this case, cells, proteins, large molecules, and other components that may interfere with analysis must be separated or removed completely. Otherwise, they may adhere to channel walls, foul detector electrodes (diminishing electrode response), physically clog the channel, or co-elute or co-migrate with analytes of interest, hindering detection. Samples are usually filtered either pre-, or on-chip, and channel walls can be coated to resist adherents.

For cells or tissue studies on-chip, it is important to provide an environment in which cells can grow and tissue will remain viable. Also, in neural networks, the brain cells must remain in contact with the electrodes that are stimulating or recording their activity without fouling them. Commonly employed materials and substrates in microfabrication of bio-MEMS include silicon, silicon nitride, silicon dioxide, gold, SU-8, higher noble metals (platinum, titanium), and activated carbon electrodes have all been found to be biocompatible in the short term, although different forms (porous as opposed to smooth silicon) elicited different degrees of biocompatibility.[46]

Another potential problem for lab-on-a-chip devices can be the high salt concentrations characteristic of physiological samples. This can be a particular problem for electrophoretic-based analyses. The mismatch between the ionic strengths of the samples and the run buffer can lead to peak dispersion and loss of efficiency. It is possible to increase the ionic strength of the run buffer, however this can lead to joule heating. In most cases, physiological samples are simply diluted to overcome the high salt concentrations, but this also dilutes the sample. Therefore, the detector must have limits of detection that are low enough to allow sample dilution.

Blood can be a particularly difficult sample for microchip-based assays. Over 46% of the components of blood are solids, including red blood cells, white blood cells, and platelets. In standard clinical assays involving blood, these solid components are removed through centrifugation. However, this approach is not easily transferred to the microchip format. Recently, a variety of filters and techniques that take advantage of the slower flow of the larger particles have been incorporated into chips to isolate small molecules from the larger components.

16.4 Applications: Clinical Chemistry and Bioanalysis

16.4.1 Clinical Chemistry

Lab-on-a-chip devices have been developed for a number of clinical analyses, including those to detect exposure to biological warfare agents. Recently, Moorthy et al.[47] described a microassay for botulinum neurotoxin in whole blood. This toxin is one of the most deadly substances known, and can be lethal at concentrations as low as 1 ng/kg. Because the only known antidote for this toxin is an antitoxin that binds the toxin before it can bind to nerves, fast analysis is critical.

In the microchip-based assay, whole blood is first mixed with a hypotonic solution that causes the red blood cells to swell. The swollen cells are retained behind a porous polymer filter, allowing the serum to pass into the processing part of the chip where a bead-based sandwich enzyme-linked immunosorbent assay (ELISA) is performed. Valves are used to control the flow and addition of reagents in the immunoassay. For this assay, quantitation was not necessary, as just an indication of the presence of the toxin was needed to confirm contamination. Hence, a simple colorimetric response generated by the enzyme label in the immunoassay was used as an indicator for the existence of the toxin.

A more common clinical application of microchip-based assays is the detection of endogenous compounds or biomarkers. Table 16.1 provides an extensive list of clinical assays reported in the literature. One example of such an assay is the detection of homocysteine in blood. Homocysteine has been identified as an independent risk factor for cardiovascular disease. Therefore, a point-of-care device for analysis of homocysteine levels would be a useful tool for cardiologists to monitor their patients' heart health. In this microchip-based assay, a cobalt (II) phthalocyanine (coPC)-modified carbon paste electrode was used to detect the three major thiols in blood (glutathione, homocysteine, and cysteine). The modified electrode showed high selectivity for thiols compared to other easily oxidized compounds found in blood.[48]

Another microchip electrophoresis device currently under investigation in our laboratory has clinical possibilities for the detection of nitrate and nitrite. Nitric oxide is an important signaling molecule that plays a role in neural signal mediation, inflammation, and vasodilation. Nitric oxide degrades quickly into nitrate (NO_3^-) and nitrite (NO_2^-) under physiological conditions. The presence of nitrite in urine frequently indicates a bacterial infection.

Kikura-Hanajiri et al. developed a microchip-based analytical method for the detection of nitrate and nitrite as an indirect measurement of NO production. Two separate measurements were used to determine the total concentration of NO because only nitrite could be analyzed directly using

TABLE 16.1

Clinical and Bioanalytical Applications

Analyte	Significance	Device/Technique	Notes
Carnitine/acetylcarnitine standards, also imipramine and desipramine in fortified human plasma	Amino acid derivative important in fatty acid oxidation; deficiency leads to cardiac, CNS, and skeletal problems	Microchip electrophoresis to separate analytes,-coupled with mass spectrometry for detection[57]	Linear calibration curve obtained, demonstrating ability for robust, reproducible quantitation
		Sequential injection analysis with amperometric biosensor detection[58]	
Carnitine, acylcarnitine, butylcarnitine		Microchip electrophoresis coupled to mass spec[59]	Separated small, polar molecules w/o channel treatment on-chip, ion-sprayed into MS
		Microchip electrophoresis with online electrospray to MS[42]	Carnitine and three acylcarnitines in urine separated in 48 s
Potassium in blood	Electrolyte involved in signaling	Microarray sensor in a potassium-selective electrode[60]	
Potassium, sodium, lithium	Electrolytes	Microchip electrophoresis with contactless conductivity detection[61]	
Blood gases and electrolytes (CO_2, O_2, Ca^{2+}, Na^+, K^+)		6-channel fluorescence sensor array[62]	Superblue LED acted as light sources
Creatine, creatinine, p-aminohippuric acid, uric acid	Renal markers used to assess health of renal system	Microchip electrophoresis coupled with enzymatic reaction using amperometric detection[56]	
Glucose, uric acid, ascorbic acid, acetaminophen		Enzyme reaction on-chip, separation by electrophoresis, and electrochemical detection[63]	Enzyme mixed with glucose on-chip, reaction products separated from ascorbic acid and internal standard, uric acid
Glucose and lactate	Blood sugar monitored in diabetes and related metabolic disorders and ubiquitous by-product of cellular metabolism	Microdialysis interface, microflow manifold, and biosensor array for detection[64]	*In vivo* microdialysis of core blood of dogs
		Microdialysis probe coupled to flow cell/ enzyme biosensor array[65]	

(continued)

TABLE 16.1 (continued)

Clinical and Bioanalytical Applications

Analyte	Significance	Device/Technique	Notes
Lactate in serum		On-chip enzyme reaction, mixing, flow injection analysis, and chemiluminescence detection[66]	
Lactate, glucose, glutamate		Enzymatic microsensor for FIA[67]	Dialysis tube traps enzyme—substrates (lactate, etc.) flow past and react, releasing hydrogen peroxide, which is then detected electrochemically
Glucose		Microchip electrophoresis with electrochemical detection[68]	Amperometric detection of glucose in diluted human plasma
Amino acids in urine	Building blocks of proteins, serve various functions in the body	Microchip electrophoresis with indirect fluorescence detection[69]	
		Micellar electrokinetic capillary chromatography on-chip with LIF detection of amino acids in urine and serum[70]	Cyclic channel design allows column switching and variable separation channel lengths
Hydrolysis of fluorescein mono-D-galactopyranoside		Microdialysis coupled to microchip electrophoresis with laser-induced fluorescence detection[11]	Microdialysis may be used to monitor biological compounds *in vivo* as well as a sample cleanup technique
Neuropeptides	Bioactive compounds in the brain that act as neurotransmitters and signal regulators	Microdialysis coupled to MS for *in vivo* monitoring of neurochemicals[71, 72]	Microdialysis sampling of brain peptides of live rats
Homocysteine	High blood level a risk factor for heart disease	Microchip electrophoresis with electrochemical detection[73]	Homocysteine and glutathione standards separated on-chip
Lipoproteins (LDL and HDL)	Concentrations correlated to heart disease	Microchip electrophoresis with LIF detection[74]	Sodium dodecyl sulfate (SDS) added to sample to increase peak efficiency
Hepatitis C virus	A cause of liver disease	Post-PCR microchip electrophoresis with LIF detection[75]	

(continued)

TABLE 16.1 (continued)

Clinical and Bioanalytical Applications

Analyte	Significance	Device/Technique	Notes
ATP	Energy molecule in cellular metabolism	Microchip flow-through channels with chemiluminescence detection[76]	Channels mimic blood vessels, ATP released from erythrocytes that are physically deformed in those channels
Catecholamines (epinephrine, norepinephrine, dopamine, L-dopa)	Neurotransmitters	Mixing and reacting on-chip with thermal lens microscopy detection[77]	Sodium metaperiodate oxidized analytes to aminochromes (detectable via TLS) in only 15 s on-chip
Ascorbic acid	Vitamin C	Flow injection analysis with thermal lens microscopy detection[78]	Mixing, reactions, extraction, and detection all occurred on-chip; AA and dehydroascorbic acid (DHAA) determined in urine samples
Amino sugars (glucosamine, galactosamine, and reduced forms)		Microchip electrophoresis with LIF detection[79]	
Uric acid	Measured in urine to monitor diverse conditions such as kidney stones, lead poisoning, gout, alcoholism	Microchip electrophoresis with amperometric electrochemical detection of urine samples[80]	
Reactive oxygen species (ROS)/ glutathione (GSH)	Cellular oxidants / endogenous antioxidant	Microchip electrophoresis with LIF detection of apoptic leukemia cell extracts[81]	DHR-123 converted to fluorescent Rh-123 by ROS; GSH reacts with NDA to form fluorescent adduct so each is visible via LIF
Insulin secretion		Mixing, reaction, electrophoretic separation with LIF detection[30,82]	Single islet of Langerhans placed into reservoir and surrounding fluid continually sampled for secretion of insulin

(continued)

TABLE 16.1 (continued)

Clinical and Bioanalytical Applications

Analyte	Significance	Device/Technique	Notes
NO	Dilates blood vessels; modulates synaptic signal transmission	Cells grown in channels of microfluidic chip with amperometric detection[83]	Bovine pulmonary artery endothelial cells stimulated to release NO, detected with C ink electrode coated with nafion to block interfering species.
		Cell culture, enzyme reactions, and detection by a colorimetric reaction and laser-induced thermal lens microscopy[50]	Indirect detection via Griess reagent of NO released from mouse macrophages
Cytokine	Cellular proteins that regulate immune response	Immunoaffinity capture, dye-labeling, electrophoresis, and LIF detection[31]	Immobilized antibodies in injection port–captured cytokines in serum and CSF of head-trauma patients
Botulinum toxin	Bacterial toxin used in biological warfare	ELISA, including sample prep of blood, on-chip[47]	Filtration, mixing, incubation coupled to microfluidic channels, valves, filters, and enzymatic reaction for colorimetric detection
Cortisol	Stress hormone	Competitive immunoassay, electrophoretic separation of bound and free labeled antigen, and LIF detection on-chip[84]	Determination of cortisol in blood serum in clinical range without extraction or other sample prep (separation in less than 30 s)

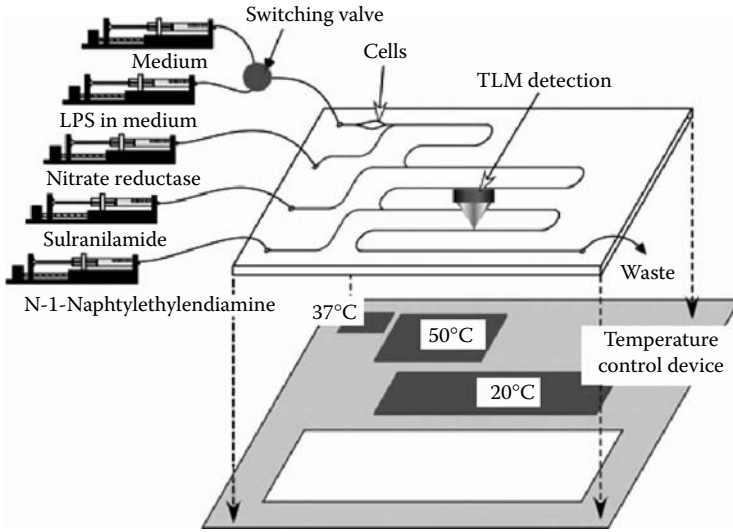

FIGURE 16.3
Microsyringe pumps, microchip, and temperature control device for bioassay of NO release from macrophages. (From Goto, M. et al., *Anal. Chem.*, 77, 2125, 2005. With permission.)

electrochemical detection. First, the total amount of NO_2 was determined by zone electrophoresis with amperometric detection at a carbon electrode. Second, NO_3 was reduced to NO_2^- on-chip with copper-coated cadmium granules, separated, and detected. The total concentration of NO_3^- was calculated by subtracting the first run (NO_2^-) from the second (NO_2^- + NO_2^- from reduction of NO_3^-).[49]

A different microchip-based bioassay was developed for the detection of nitric oxide release from macrophage cells stimulated by lipopolysaccharide (LPS).[50] A diagram of the microchip is shown in Figure 16.3. Cells were cultured on-chip in a microchamber and incubated at 37°C by a Peltier element-based temperature control device. In order to stimulate NO production, LPS in medium was introduced through a reservoir upstream from the cells. The NO quickly degraded to generate NO_2^- and NO_3^-. Nitrate reductase was introduced through another reservoir to reduce the nitrate to nitrite. The resulting nitrite (from both NO_2^- and NO_3^-) was then reacted with sulfanilamide and N-1-naphthylethylendiamine to form a colored product that was detected using a thermal lens microscope.

Another application of microchips to clinical analysis is immunoassays. These are frequently used to detect the presence of certain proteins or antibodies in blood or other tissues. Examples of microchip assays of this type include those for simple protein analytes such as bovine serum albumin (BSA)[51,52] or IgG.[51,53,54] Other on-chip assays are more complex. One example is a chip that is designed to aid in the diagnosis of Duchene muscular dystrophy.[55] In this assay, genomic DNA was extracted from whole blood and amplified using an on-chip IR-mediated polymerase chain reaction

(PCR). The resulting DNA related to the disease was detected following electrophoretic separation.

Wang et al. have coupled an enzymatic bioassay with an electrophoretic separation on-chip for the measurement of the renal markers creatine, creatinine, p-aminohippuric acid, and uric acid.[56] These markers are routinely monitored to assess kidney function. Sample and a mixture of creatinase, creatininase, and sarcosine oxidase were combined and allowed to react. The enzyme reactions produced hydrogen peroxide, which is neutral and can be electrophoretically separated from other anionic analytes of interest, urate, and p-aminohippuric acid. Amperometric detection was used for quantitation.

In large clinical labs, most assays take place at a location that is far from the patient. In these cases, the analysis can take a great deal of time and the sample may be mishandled, mislabeled, or lost. Microfluidic devices offer the opportunity for point-of-care analysis, giving both the patient and the doctor instant feedback. These small, fast, and disposable devices offer the potential for quick, less error-prone analyses—at the doctors' office or at home. Table 16.1 lists a majority of the current research toward development of microchip-based clinical assays.

16.4.2 Therapeutic Drug Monitoring

Microchip-based assays have also been developed for therapeutic drug monitoring as Table 16.2 shows. An on-chip competitive immunoassay for serum theophylline was developed by Chiem and Harrison.[51,85] Theophylline is an antiasthmatic drug. Physicians can adjust the dosage for maximum efficacy if serum theophylline levels are followed. In this study, the antibody, labeled theophylline, and sample serum were mixed on-chip by electroosmotic pumping. The antibodies were allowed to react with the antigen and then the bound versus free fractions were separated by electrophoresis and detected by fluorescence. Limits of detection for theophylline of 26 mg/L in serum were achieved.

Vrouwe et al.[86] created a microchip analysis system for measurement of Li^+ in whole blood. Li^+ is normally not present in the body; however, it is used in the treatment of manic-depressive illnesses. The upper therapeutic level of this drug is dangerously close to toxic concentrations; therefore, careful monitoring of blood concentration is important. Vrouwe exploited the fact that in an electric field, Li^+ ions move more quickly than the much larger blood cells. The sample was injected electrokinetically, and Li^+ was loaded into the separation channel before the blood cells had a chance to enter the injection T. Glucose was also added to the run buffer to match the osmotic strength of the run buffer to that of blood so that the cells did not lyse and release contents that could interfere with Li^+ detection. Because sodium concentrations are high and fairly constant in blood, sodium was used as an internal standard. The Li^+ peak areas were normalized to Na^+

and quantitated after calibration. Channels were coated with polyacrylamide so that the chip might be reused (protein adhesion to channel walls would otherwise not allow more than one run). Conductivity detection was employed in this study.

A mixture of serotonin, propranolol, 3-phenoxy-1,2-propandiol, and tryptophan, as well as a distinct mixture of unlabeled lysozyme, trypsinogen, and chymotrypsinogen were analyzed by microchip electrophoresis with deep UV LIF detection.[40] The significance of this particular study is the sensitivity with which the low molecular weight biomolecules could be detected and the simplicity of the chip design. The use of deep UV fluorescence detection also meant that proteins could be detected by native fluorescence, obviating any deriviatization steps normally required. Figure 16.4 shows a comparison of the sensitivity obtained using deep UV fluorescence detection versus other detection systems.

TABLE 16.2

Therapeutic Drug Monitoring

Analyte	Significance	Device/Technique	Notes
Propanolol, serotonin, tryptophan, and a diol (also, unlabeled basic proteins, and egg white protein)		Microchip electrophoresis to separate analytes, deep UV fluorescence for detection[40]	Deep UV fluorescence detection enabled post-separation detection at low micromolar concentrations w/o first labeling analytes
β-blockers (oxprenolol, atenolol, timolol, propanolol, metoprolol, acebutolol)	Drug for regulation of cardiovascular system	Mixtures of β-blockers in urine SPE treated, then separated and detected with CD and LIF[87]	Coupled channel on-chip allowed preconcentration in one channel, and separation in another
Octopamine, doxylamine, ephedrine, noradrenaline, isoproterenol, adrenaline		Microchip electrophoresis with contactless conductivity detection[88]	
Amphetamines	Drugs of abuse that affect the CNS, also over-the-counter decongestants	FITC-derived amphetamines from spiked urine separated in microchip and detected with LIF[89]	
		Chiral separations using cyclodextrins and microchip electrophoresis with LIF detection[90]	Direct separation of chiral molecules through addition of chiral selector to the run buffer

(continued)

TABLE 16.2 (continued)

Therapeutic Drug Monitoring

Analyte	Significance	Device/Technique	Notes
Lithium	Used as treatment in manic-depressive illness, therapeutic range dangerously close to toxic level	Microchip electrophoresis separation of Li+, K+, and Na+ with AC conductivity detection[86]	Whole blood mixed with anticoagulant, loaded on-chip, channels coated to resist contamination by proteins, voltage controlled so that sample entered separation channel, yet RBC did not
Phenytoin	Anticonvulsant	Competitive immunoassay of whole blood with fluorescence detection[91]	T-sensor allows diffusion of side-by-side streams of antigen and antibody; binding of antigen (small and thus fast) to antibody (larger thus slower) slows their diffusion; diffusion profile changes compared to profile of freely diffusing antigen. Albumin bound to iophenoxate to decrease binding assay interference.
General immunoassay microfabrication technique		Patterning protein antigens on-chip with surface plasmon resonance, then probed antigens with complementary antibodies to visualize patterning[92]	Fabrication of chip microarray for immunoassay
Theophylline	Drug for respiratory diseases	On-chip competitive immunoassay, detection down to 1.25 ng/mL, linear in therapeutic range[51,85,93]	Reagent and serum samples mixed, reacted, separated, and analyzed all on one chip

16.4.3 High-Throughput Screening

As mentioned previously, microchips and bio-MEMS are of great value to the pharmaceutical industry for the purpose of high-throughput screening.

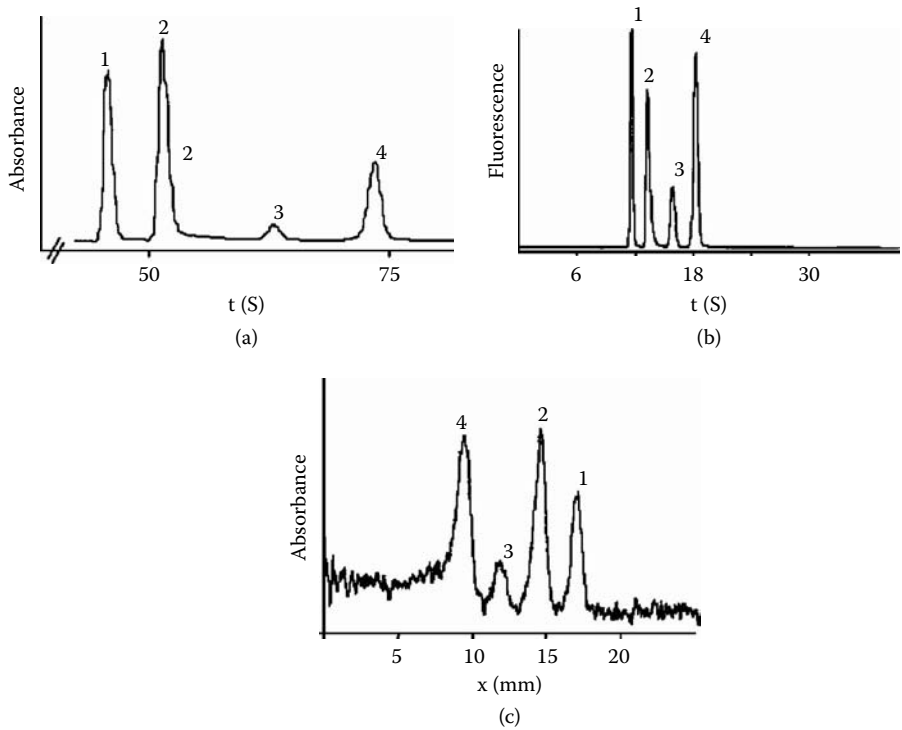

FIGURE 16.4
Electropherograms of separations of a mixture of (1) serotonin, (2) propranolol, (3) 3-phenoxy-1,2-propandiol, and (4) tryptophan using different detection systems. (a) Conventional capillary electrophoresis with UV absorbance detection. (b) Microchip electrophoresis with deep UV fluorescence detection. (c) Commercial microchip electrophoresis system with UV absorbance detection. (From Schulze, P. et al., *Anal. Chem.*, 77, 1325, 2005. With permission.)

Multiple channels and detectors on one chip greatly increase the number of analyses that can be run. To that end, several research groups have developed microchips to investigate high volumes of samples. This enables drug screening of molecular libraries to identify successful drug candidates.[94]

Currently, many high-throughput screenings involve microarrays. Numerous physiological processes involve protein–carbohydrate interactions, and the ideal microanalysis tool to study these interactions in the high-throughput format is the carbohydrate microarray.[95,96] These chips consist of carbohydrates immobilized on glass slides. Detection is external, frequently fluorescence detection. A high-throughput carbohydrate array microchip was developed and used to determine the binding affinities between lectins and carbohydrates.[97] A different carbohydrate microarray was used to screen 85 compounds to find inhibitors of fucosyltransferases.[98]

Another form of high-throughput screening, multiplexed enzyme assay, was developed to screen enzymatic activity of MAP, IR, and PKA kinases.[51,99] These assays were especially valuable because they were multiplexed; three

enzymes, each from a different kinase family, were assayed simultaneously within each channel. Although sample preparation was conducted off-chip, enzymes and product were separated in a double-T microchip design. Using this device, drugs were screened for activity, cross-reactivity, specificity, and potential side effects. In a separate high-throughput application, a 6-channel microfluidic immunoreactor/immunoassay was developed for the simultaneous assay of ovalbumin and antiestradiol within 30 to 60 s.[51,100] Another high-throughput immunoassay was used to screen affinity complexes of phenobarbitol antibody and nine barbiturates, including phenobarbitol. Sample loading, washing, and dissociation steps were performed on-chip, and the device was then coupled to ESI-MS for detection.[101]

Tabuchi et al. developed an integrated cell-culture chip that incorporated protein separation and detection along with cell culture. Washing, stimulation, and lysis could be accomplished on-chip and were coupled to a commercial Agilent microelectrophoresis chip.[102] The culture chip contained 48 to 96 wells 5 to 6.5 mm in diameter, with a second layer that contained molded cups that fit into the wells of the first chip. Jurkat cells were cultured in the first row of wells in the strip of cups that fit into those wells. For a medium change, the cups in which the cells were cultured were removed and placed into the next row of wells, which were filled with fresh medium. This process was repeated for each new step, that is, stimulation, lysis, and protein extraction, until finally the cups were placed in wells fitted with the wires for the electrophoretic separation chip. This Agilent chip has 12 channels; in this application, 11 samples from the cells and a protein ladder sample were run and detected by LIF. The cell density remained constant in contrast to conventional cell culture and CE analysis, where cells are consistently lost to dilution, washing, medium change, and pipetting. Ultimately, this device enabled analysis of extracted proteins without sample loss at a rate of 12 samples per minute.

DNA sequencing is the most popular application of microchips in the high-throughput world; however, Chapter 13 addresses DNA directly, and discussion of this topic will be left to that chapter.

16.5 Conclusion

Although many examples of useful clinical and bioanalytical pharmaceutical applications have been presented in this chapter, most of the bio-MEMS used in these are prototypes. There is still much work to be done to improve the limits of detection, reproducibility, and ruggedness of these devices. In addition, the integration and fabrication of several components onto a single chip has been accomplished by only a few groups thus far. However, the potential utility of these microchip devices for high-throughput and point-of-care analyses makes this research well worth the effort.

References

1. Gawron, A.J., Martin, R.S., and Lunte, S.M., Microchip electrophoretic separation systems for biomedical and pharmaceutical analysis, *Eur. J. Pharm. Sci.*, 14, 1, 2001.
2. Kricka, L.J. and Wilding, P., Micromachining: a new direction for clinical analyzers, *Pure Appl. Chem.*, 68, 1831, 1996.
3. Verpoorte, E., Microfluidic chips for clinical and forensic analysis, *Electrophoresis*, 23, 677, 2002.
4. Wang, J. et al., Single-channel microchip for fast screening and detailed identification of nitroaromatic explosives or organophosphate nerve agents, *Anal. Chem.*, 74, 1187, 2002.
5. Fang, Q., Xu, G.M., and Fang, Z.L., A high-throughput continuous sample introduction interface for microfluidic chip-based capillary electrophoresis systems, *Anal. Chem.*, 74, 1223, 2002.
6. Alarie, J.P., Jacobson, S.C., and Ramsey, J.M., Electrophoretic injection bias in a microchip valving scheme, *Electrophoresis*, 22, 312, 2001.
7. Jacobson, S.C., Ermakov, S.V., and Ramsey, J.M., Minimizing the number of voltage sources and fluid reservoirs for electrokinetic valving in microfluidic devices, *Anal. Chem.*, 71, 3273, 1999.
8. Roddy, E.S., Xu, H., and Ewing, A.G., Sample introduction techniques for microfabricated separation devices, *Electrophoresis*, 25, 229, 2004.
9. Attiya, S. et al., Design of an interface to allow microfluidic electrophoresis chips to drink from the fire hose of the external environment, *Electrophoresis*, 22, 318, 2001.
10. Chen, S.H. et al., Flow-through sampling for electrophoresis-based microchips and their applications for protein analysis, *Anal. Chem.*, 74, 5146, 2002.
11. Huynh, B.H. et al., On-line coupling of microdialysis sampling with microchip-based capillary electrophoresis, *Anal. Chem.*, 76, 6440, 2004.
12. Wilding, P. et al., Integrated cell isolation and polymerase chain reaction analysis using silicon microfilter chambers, *Anal. Biochem.*, 257, 95, 1998.
13. Foote, R.S. et al., Preconcentration of proteins on microfluidic devices using porous silica membranes, *Anal. Chem.*, 77, 57, 2005.
14. Xu, N. et al., A microfabricated dialysis device for sample cleanup in electrospray ionization mass spectrometry, *Anal. Chem.*, 70, 3553, 1998.
15. Yu, C. et al., Preparation of monolithic polymers with controlled porous properties for microfluidic chip applications using photoinitiated free-radical polymerization, *J. Polym. Sci., Part A: Polym. Chem.*, 40, 755, 2002.
16. Kutter, J.P., Jacobson, S.C., and Ramsey, J.M., Solid phase extraction on microfluidic devices, *J. Microcolumn Sep.*, 12, 93, 2000.
17. Oleschuk, R.D. et al., Trapping of bead-based reagents within microfluidic systems: on-chip solid-phase extraction and electrochromatography, *Anal. Chem.*, 72, 585, 2000.
18. Delaunay-Bertonicini, N. and Hennion, M.C., Immunoaffinity solid-phase extraction for pharmaceutical and biomedical trace-analysis-coupling with HPLC and CE-perspectives, *J. Pharm. Biomed. Anal.*, 34, 717, 2004.
19. Giordano, B. et al., Microchip laser-induced fluorescence detection of proteins at submicrogram per milliliter levels mediated by dynamic labeling under pseudonative conditions, *Anal. Chem.*, 76, 4705, 2004.

20. Gottschlich, N. et al., Integrated microchip-device for the digestion, separation and postcolumn labeling of proteins and peptides, *J. Chromatog. B*, 745, 243, 2000.
21. Jacobson, S.C. et al., Microchip structures for submillisecond electrophoresis, *Anal. Chem.*, 70, 3476, 1998.
22. Veenstra, T.T. et al., Characterization method for a new diffusion mixer applicable in micro flow injection analysis systems, *J. Micromech. Microeng.*, 9, 199, 1999.
23. Eijkel, J.C.T. et al., Micromachined heated chemical reactor for pre-column derivatisation, *J. Chromatog. A*, 815, 265, 1998.
24. Unger, M.A. et al., Monolithic microfabricated valves and pumps by multilayer soft lithography, *Science*, 288, 113, 2000.
25. Jacobson, S.C., McKnight, T.E., and Ramsey, J.M., Microfluidic devices for electrokinetically driven parallel and serial mixing, *Anal. Chem.*, 71, 4455, 1999.
26. Weinberger, R., *Practical Capillary Electrophoresis*. 2nd ed., San Diego, CA: Academic Press, 2000.
27. Culbertson, C.T., Jacobson, S.C., and Ramsey, J.M., Microchip devices for high-efficiency separations, *Anal. Chem.*, 72, 5814, 2000.
28. Han, J. and Singh, A.K., Rapid protein separations in ultra-short microchannels: microchip sodium dodecyl sulfate-polyacrylamide gel electrophoresis and isoelectric focusing, *J. Chromatog. A*, 1049, 205, 2004.
29. Rodriguez, I., Lee, H.K., and Li, S.F., Microchannel electrophoretic separation of biogenic amines by micellar electrokinetic chromatography, *Electrophoresis*, 20, 118, 1999.
30. Shackman, J.G. et al., Perfusion and chemical monitoring of living cells on a microfluidic chip, *Lab Chip*, 5, 56, 2005.
31. Phillips, T.M., Rapid analysis of inflammatory cytokines in cerebrospinal fluid using chip-based immunoaffinity electrophoresis, *Electrophoresis*, 25, 1652, 2004.
32. Wang, J., Ibanez, A., and Chatrathi, M.P., On-chip integration of enzyme and immunoassays: simultaneous measurements of insulin and glucose, *J. Am. Chem. Soc.*, 125, 8444, 2003.
33. Wang, J., Ibanez, A., and Chatrathi, M.P., Microchip-based amperometric immunoassay using redox tracers, *Electrophoresis*, 23, 3744, 2002.
34. Wooley, A.T. et al., Capillary electrophoresis chips with integrated electrochemical detection, *Anal. Chem.*, 70, 684, 1998.
35. Wang, J., Tian, B.M., and Sahlin, E., Micromachined electrophoresis chips with thick-film electrochemical detectors, *Anal. Chem.*, 71, 5436, 1999.
36. Tantra, R. and Manz, A., Integrated potentiometric detector for use in chip-based flow cells, *Anal. Chem.*, 72, 2875, 2000.
37. Martin, R.S. et al., In-channel electrochemical detection for microchip capillary electrophoresis using an electrically isolated potentiostat, *Anal. Chem.*, 74, 1136, 2002.
38. Lui, Y. et al., Electrophoretic separation of proteins on a microchip with noncovalent, postcolumn labeling, *Anal. Chem.*, 72, 4608, 2000.
39. Tamaki, E. et al., Single cell analysis by a scanning thermal lens microscope with a microchip: direct monitoring of cytochrome-c distribution during apoptosis process, *Anal. Chem.*, 74, 1560, 2002.
40. Schulze, P. et al., Deep UV laser-induced fluorescence detection of unlabeled drugs and proteins in microchip electrophoresis, *Anal. Chem.*, 77, 1325, 2005.
41. Chau, L.K. et al., Microfabricated silicon flow-cell for optical monitoring of biological fluids, *Anal. Sci.*, 15, 721, 1999.

42. Deng, Y. et al., Chip-based capillary electrophoresis/mass spectrometry determination of carnitines in human urine, *Anal. Chem.*, 73, 639, 2001.
43. Deng, Y., Zhang, H., and Henion, J., Chip-based quantitative capillary electrophoresis/mass spectrometry of drugs in human plasma, *Anal. Chem.*, 73, 1432, 2001.
44. Li, J. et al., Integration of microfabricated devices to capillary electrophoresis-electrospray mass spectrometry using a low dead volume connection: application to rapid analyses of proteolytic digests, *Anal. Chem.*, 71, 3036, 1999.
45. Zhang, B. et al., Microfabricated devices for capillary electrophoresis-electrospray mass spectrometry, *Anal. Chem.*, 71, 3258, 1999.
46. Grayson, A.C.R. et al., A bioMEMS review: MEMS technology for physiologically integrated devices, *IEEE*, 2, 6, 2004.
47. Moorthy, J. et al., Microfluidic tectonics platform: a colorimetric, disposable botulinum toxin enzyme-linked immunosorbant assay system, *Electrophoresis*, 25, 1705, 2004.
48. Pasas-Farmer, S.A., New analytical methods for the determination of homocysteine in human plasma, Ph.D. thesis, Pharmaceutical Chemistry, University of Kansas, Lawrence, 2004.
49. Kikura-Hanajiri, R., Martin, R.S., and Lunte, S.M., Indirect measurement of nitric oxide production by monitoring nitrate and nitrite using microchip electrophoresis with electrochemical detection, *Anal. Chem.*, 74, 6370, 2002.
50. Goto, M. et al., Development of a microchip-based bioassay system using cultured cells, *Anal. Chem.*, 77, 2125, 2005.
51. Guijt, R.M., Baltussen, E., and Van Dedem, G.W.K., Use of bioaffinity interactions in electrokinetically controlled assays on microfabricated devices, *Electrophoresis*, 23, 823, 2002.
52. Qui, C.X. and Harrison, D.J., Integrated self-calibration via electrokinetic solvent proportioning for microfluidic immunoassays, *Electrophoresis*, 22, 3949, 2001.
53. Martynova, L. et al., Fabrication of plastic microfluid channels by imprinting methods, *Anal. Chem.*, 69, 4783, 1997.
54. Dodge, A. et al., Electrokinetically driven microfluidic chips with surface-modified chambers for heterogeneous immunoassays, *Anal. Chem.*, 73, 3400, 2001.
55. Ferrance, J.P. et al., Developments toward a complete micro-total analysis system for Duchene muscular dystrophy diagnosis, *Anal. Chim. Acta*, 500, 223, 2003.
56. Wang, J. and Chatrathi, M.P., Microfabricated electrophoresis chip for bioassay of renal markers, *Anal. Chem.*, 75, 525, 2003.
57. Deng, Y., Zhang, H., and Henion, J., Chip-based quantitative capillary electrophoresis/mass spectrometry determination of drugs in human plasma, *Anal. Chem.*, 73, 1432, 2001.
58. Stefan, R. et al., Simultaneous determination of L- and D-carnitine using a sequential injection analysis/amperometric biosensors system, *J. Pharm. Biomed. Anal.*, 33, 323, 2003.
59. Kameoka, J. et al., A polymeric microfluidic chip for CE/MS determination of small molecules, *Anal. Chem.*, 73, 1935, 2001.
60. Uhlig, A. et al., Miniaturised ion-selective sensor chip for potassium measurement in a biomedical application, *Sens. Actuators B*, 34, 252, 1996.
61. Lichtenberg, J., De Rooij, N.F., and Verpoorte, E., A microchip electrophoresis system with integrated in-plane electrodes for contactless conductivity detection, *Electrophoresis*, 23, 3769, 2002.

62. Bruno, A.E. et al., All-solid-state miniaturized fluorescence sensor array for the determination of critical gases and electrolytes in blood, *Anal. Chem.*, 69, 507, 1997.
63. Wang, J. et al., Microfabricated electrophoresis chips for simultaneous bioassays of glucose, uric acid, ascorbic acid, and acetaminophen, *Anal. Chem.*, 72, 2514, 2000.
64. Freaney, R. et al., Novel instrumentation for real-time monitoring using miniaturized flow systems with integrated biosensors., *Ann. Clin. Biochem.*, 34, 291, 1997.
65. Dempsey, E. et al., Design and development of a miniaturised total chemical analysis system for on-line lactate and glucose monitoring in biological samples, *Anal. Chim. Acta*, 346, 341, 1997.
66. Nakamura, H. et al., A compactly integrated flow cell with a chemiluminescent FIA system for determining lactate concentration in serum, *Anal. Chem.*, 73, 373, 2001.
67. Bohm, S. et al., A flow-through amperometric sensor based on dialysis tubing and free enzyme reactors, *Biosens. Bioelectron.*, 16, 391, 2001.
68. Du, Y. et al., Direct electrochemical detection of glucose in human plasma on capillary electrophoresis microchips, *Electrophoresis*, 25, 3853, 2004.
69. Munro, N.J. et al., Indirect fluorescence detection of amino acids on electrophoretic microchips, *Anal. Chem.*, 72, 2765, 2000.
70. Von Heeren, F. et al., Micellar electrokinetic chromatography separations and analyses of biological samples on a cyclic planar microstructure, *Anal. Chem.*, 68, 2044, 1996.
71. Kennedy, R.T. et al., In vivo neurochemical monitoring by microdialysis and capillary separations, *Curr. Opin. Chem. Biol.*, 6, 659, 2002.
72. Haskins, W.E. et al., Discovery and neurochemical screening of peptides in brain extracellular fluid by chemical analysis of in vivo microdialysis samples, *Anal. Chem.*, 76, 5523, 2004.
73. Pasas, S.A. et al., Detection of homocysteine by conventional and microchip capillary electrophoresis/electrochemistry, *Electrophoresis*, 23, 759, 2002.
74. Ceriotti, L. et al., Low-density lipoprotein analysis in microchip capillary electrophoresis systems, *Electrophoresis*, 23, 3615, 2002.
75. Chen, Y. et al., Plastic microchip electrophoresis for analysis of PCR products of hepatitis C virus, *Clin. Chem.*, 45, 1938, 1999.
76. Price, A.K. et al., Deformation-induced release of ATP from erythrocytes in a poly(dimethylsiloxane)-based microchip with channels that mimic resistance vessels, *Anal. Chem.*, 76, 4849, 2004.
77. Sorouraddin, H.M., Hibara, A., and Kitamori, T., Use of a thermal lens microscope in integrated catecholamine determination on a microchip, *Fresenius J. Anal. Chem.*, 371, 91, 2001.
78. Sorouraddin, H.M. et al., Integrated FIA for the determination of ascorbic acid and dehydroascorbic acid in a microfabricated glass-channel by thermal-lens microscopy, *Anal. Sci.*, 16, 1033, 2000.
79. Suzuki, S. et al., Rapid analysis of amino sugars by microchip electrophoresis with laser-induced fluorescence detection, *Electrophoresis*, 22, 4023, 2001.
80. Fanguy, J.C. and Henry, C.S., The analysis of uric acid in urine using microchip capillary electrophoresis with electrochemical detection, *Electrophoresis*, 23, 767, 2002.
81. Qin, J. et al., Simultaneous and ultrarapid determination of reactive oxygen species and reduced glutathione in apoptotic leukemia cells by microchip electrophoresis, *Electrophoresis*, 26, 1155, 2005.

82. Roper, M.G. et al., Microfluidic chip for continuous monitoring of hormone secretion from live cells using an electrophoresis-based immunoassay, *Anal. Chem.*, 75, 4711, 2003.
83. Spence, M.D. et al., Amperometric determination of nitric oxide derived from pulmonary artery endothelial cells immobilized in a microchip channel, *Analyst*, 129, 995, 2004.
84. Koutny, L.B. et al., Microchip electrophoretic immunoassay for serum cortisol, *Anal. Chem.*, 68, 18, 1996.
85. Chiem, N.H. and Harrison, D.J., Microchip systems for immunoassay: an integrated immunoreactor with electrophoretic separation for serum theophylline determination, *Clin. Chem.*, 44, 591, 1998.
86. Vrouwe, E.X., Luttge, R., and Van Den Berg, A., Direct measurement of lithium in whole blood using microchip capillary electrophoresis with integrated conductivity detection, *Electrophoresis*, 25, 1660, 2004.
87. Kriikku, P. et al., Isotachophoresis of β-blockers in a capillary and on a poly(methyl methacrylate) chip, *Electrophoresis*, 25, 1687, 2004.
88. Tanyanyiwa, J. and Hauser, P.C., Capillary and microchip electrophoresis of basic drugs with contactless conductivity detection, *Electrophoresis*, 25, 3010, 2004.
89. Ramseier, A., Von Heeren, F., and Thormann, W., Analysis of fluorescein isothiocyanate derivatized amphetamine and analogs in human urine by capillary electrophoresis in chip-based and fused-silica capillary instrumentation, *Electrophoresis*, 19, 2967, 1998.
90. Wallenborg, S.R. et al., On-chip chiral and achiral separation of amphetamine and related compounds labeled with 4-fluoro-7-nitrobenzofurazane, *Electrophoresis*, 21, 3257, 2000.
91. Hatch, A. et al., A rapid diffusion immunoassay in a T-sensor, *Nature Biotech.*, 19, 461, 2001.
92. Kanda, V. et al., Label-free reading of microarray-based immunoassays with surface plasmon resonance imaging, *Anal. Chem.*, 76, 7257, 2004.
93. Chiem, N. and Harrison, D.J., Microchip-based capillary electrophoresis for immunoassays: analysis of monoclonal antibodies and theophylline, *Anal. Chem.*, 69, 373, 1997.
94. Sundberg, S.A. et al., Microchip-based systems for target validation and HTS, *Drug Discov. Today*, 5, 92, 2000.
95. Khan, I., Desai, D.V., and Kumar, A., Carbochips: a new energy for old biobuilders, *J. Biosci. Bioeng.*, 98, 331, 2004.
96. Wang, D., Carbohydrate microarrays, *Proteomics*, 3, 2167, 2003.
97. Park, S. et al., Carbohydrate chips for studying high-throughput carbohydrate-protein interactions, *J. Am. Chem. Soc.*, 126, 4812, 2004.
98. Bryan, M.C., Lee, L.V., and Wong, C.H., High-throughput identification of fucosyltransferase inhibitors using carbohydrate microarrays, *Bioorg. Med. Chem. Lett.*, 14, 3185, 2004.
99. Xue, Q. et al., Multiplexed enzyme assays in capillary electrophoresis single-use microfluidic devices, *Electrophoresis*, 22, 4000, 2001.
100. Cheng, S.B. et al., Development of a multichannel microfluidic analysis system employing affinity capillary electrophoresis for immunoassay, *Anal. Chem.*, 73, 1472, 2001.

101. Jiang, Y. et al., Integrated plastic microfluidic devices with ESI-MS for drug screening and residue analysis, *Anal. Chem.*, 73, 2048, 2001.
102. Tabuchi, M. and Baba, Y., Self-contained on-chip cell culture and pretreatment system, *J. Proteom. Res.*, 3, 871, 2004.